AD 683314

Bulletin 38
Part 3
(of 3 Parts)

THE SHOCK AND VIBRATION BULLETIN

NOVEMBER 1968

A Publication of
THE SHOCK AND VIBRATION
INFORMATION CENTER
Naval Research Laboratory, Washington, D.C.

1969

Office of
The Director of Defense
Research and Engineering

Reproduced by the
CLEARINGHOUSE
for Federal Scientific & Technical
Information Springfield Va. 22151

This document has been approved for public release and sale; its distribution is unlimited.

335

Bulletin 38
Part 3
(of 3 Parts)

THE SHOCK AND VIBRATION BULLETIN

NOVEMBER 1968

A Publication of
THE SHOCK AND VIBRATION
INFORMATION CENTER
Naval Research Laboratory, Washington, D.C.

The 38th Symposium on Shock, Vibration and Associated Environments was held in St. Louis, Missouri, on 1-2 May 1968.

Office of
The Director of Defense
Research and Engineering

PAGES _____

ARE

MISSING

IN

ORIGINAL

DOCUMENT

SYMPOSIUM MANAGEMENT

THE SHOCK AND VIBRATION INFORMATION CENTER

William W. Mutch, Director
Henry C. Pusey, Coordinator
Rudolph H. Volin, Coordinator
Katherine G. Jahnel, Administrative Secretary

Bulletin Production

Graphic Arts Branch, Technical Information Division,
Naval Research Laboratory

CONTENTS

PART 3

Damping and Isolation

DESIGN OF A DAMPED MACHINERY FOUNDATION FOR HIGH-SHOCK LOADING 1
E. V. Thomas, Annapolis Division, Naval Ship Research and Development Center, Annapolis, Maryland

CONSTRAINED LAYER DAMPING WITH PARTIAL COVERAGE 5
D. S. Nokes and F. C. Nelson, Tufts University, Medford, Massachusetts

THE EFFECTS OF ROTATORY INERTIA AND SHEAR DEFORMATION ON THE FLEXURAL VIBRATIONS OF A TWO-LAYERED VISCOELASTIC-ELASTIC BEAM 13
T. Nicholas, Air Force Materials Laboratory, Wright-Patterson AFB, Ohio

METHODS OF DAMPING VERY STIFF STRUCTURAL MEMBERS 29
H. T. Miller, Lord Manufacturing Company, Erie, Pennsylvania

THE OPTIMUM DESIGN OF FIVE-PLY VISCOELASTIC ISOLATION FLEXURES FOR POINT-INERTIA LOADING 37
D. A. Frohrib, University of Minnesota, Minneapolis, Minnesota

APPLICATION OF DAMPING DEVICE FOR CRITICAL SPEED CONTROL 45
J. F. Mullen and M. R. Kulina, Curtiss-Wright Corporation, Wood-Ridge, New Jersey

DEVELOPMENT OF PRACTICAL TUNED DAMPERS TO OPERATE OVER A WIDE-TEMPERATURE RANGE 57
A. D. Nashif, University of Dayton Research Institute, Dayton, Ohio

MULTIFREQUENCY RESPONSE OF VISCOELASTIC DAMPERS 71
R. K. Newman and D. C. Kraft, University of Dayton, Dayton, Ohio

THE CRITICAL DAMPING CALCULATOR AND A COMPARISON OF SELECTED STRUCTURAL DAMPING EVALUATION SYSTEMS 89
B. E. Douglas, Annapolis Division, Naval Ship Research and Development Center, Annapolis, Maryland

FORCED RESPONSE OF LUMPED-PARAMETER SYSTEM WITH APPLICATIONS TO MISSILE DYNAMICS 95
J. D. Sowers, Chrysler Corporation Space Division, New Orleans, Louisiana

A NONFLUID VELOCITY DAMPER 111
W. G. Flannelly, Kaman Aircraft Division, Kaman Corporation, Bloomfield, Connecticut

THE DYNAMIC RESPONSE OF LINEARLY VISCOELASTIC CYLINDRICAL SHELLS TO PERIODIC OR TRANSIENT LOADING 121
E. A. Fitzgerald, Missile and Space Systems Division, McDonnell Douglas Corporation, Santa Monica, California

DAMPING OF MULTISPAN STRUCTURES BY MEANS OF VISCOELASTIC LINKS 139
D. I. G. Jones, Air Force Materials Laboratory, Wright-Patterson AFB, Ohio

DAMPING MEASUREMENTS ON SOFT VISCOELASTIC MATERIALS USING A TUNED DAMPER TECHNIQUE 151
C. M. Cannon and A. D. Nashif, University of Dayton, Dayton, Ohio, and D. I. G. Jones, Air Force Materials Laboratory, Wright-Patterson AFB, Ohio

AIRCRAFT STRUCTURAL RESPONSE DUE TO GROUND IMPACT 165
J. D. Weber, Convair Division of General Dynamics, San Diego, California

EFFECT OF TEMPERATURE ON THE VISCOELASTIC HIGH POLYMER MATERIALS 175
J. M. Ohno, Aerospace Systems Division, The Bendix Corporation, Ann Arbor, Michigan

BROADBAND EXTENSIONAL DAMPING MATERIALS 199
D. R. Blenner and T. J. Dudek, Lord Manufacturing Company, Erie, Pennsylvania

A SINUSOIDAL PULSE TECHNIQUE FOR ENVIRONMENTAL VIBRATION TESTING 207
J. T. Howlett and D. J. Martin, NASA, Langley Research Center, Hampton, Virginia

Isolation

A STUDY OF THE PERFORMANCE OF AN OPTIMUM SHOCK MOUNT 213
K. T. Cornelius, Naval Ship Research and Development Center, Washington, D.C.

AN INVESTIGATION OF THE PERFORMANCE OF GAS-BEARING MACHINERY SUBJECTED TO LOW-FREQUENCY VIBRATION AND SHOCK 221
P. W. Curwen and A. Frost, Mechanical Technology Inc., Latham, New York

AN EXPERIMENTAL INVESTIGATION OF AN ACTIVE VIBRATION ABSORBER 235
T. D. Dunham, Southwest Research Institute, San Antonio, Texas, and D. M. Egle, University of Oklahoma, Norman, Oklahoma

INTEGRATED SHOCK AND ACOUSTIC MODULAR DESIGN CONCEPT FOR SUBMARINES 243
M. Pakstys, Jr. and G. A. Ziegra, Electric Boat Division of General Dynamics, Groton, Connecticut

CYCLIC DEFORMATION CREW ATTENUATOR STRUTS FOR THE APOLLO COMMAND MODULE 255
D. L. Platus, Mechanics Research, Inc., El Segundo, California

DEVELOPMENT OF THE KINEMATIC FOCAL ISOLATION SYSTEM FOR HELICOPTER ROTORS 263
R. W. Balke, Bell Helicopter Company, Fort Worth, Texas

A TOOL FOR PARAMETRIC ANALYSIS OF COMPLEX ISOLATION SYSTEMS 285
P. J. Jones and F. A. Smith, Martin Marietta Corporation, Denver, Colorado

AN ACTIVE STABILIZATION SYSTEM FOR VEHICLES AND OTHER MASSIVE BODIES.... 317
T. H. Putman, Westinghouse Research Laboratories, Pittsburgh, Pennsylvania

CRASH CONSIDERATIONS IN THE DESIGN OF THE NEW YORK STATE SAFETY SEDAN .. 325
S. Davis and N. B. Nissel, Fairchild Hiller, Republic Aviation Division, Farmingdale, L.I., New York

PAPERS APPEARING IN PART 1

Vibration Analysis

VIBRATION RESPONSES OF SIMPLE CURVED PANELS TO HIGH INTENSITY RANDOM AND DISCRETE FREQUENCY NOISE
C. E. Rucker, NASA, Langley Research Center, Hampton, Virginia

RANDOM VIBRATION USING FINITE ELEMENT APPROACH
K. K. Kapur, Ching-U Ip and E. P. Howard, Aerospace Corporation, San Bernardino, California

FREQUENCY ANALYSIS OF REPETITIVE BURSTS OF RANDOM VIBRATION
W. E. Noonan, McDonnell Company, St. Louis, Missouri

SIMPLIFIED RANDOM VIBRATION COMPUTATIONS
LaVerne W. Root and A. S. Henry, Collins Radio Company, Cedar Rapids, Iowa

CONCENTRATED MASS EFFECTS ON THE VIBRATION OF CORNER SUPPORTED RECTANGULAR PLATES
R. L. Barnoski, Measurement Analysis Corporation, Los Angeles, California, and T. D. Schoessow, Aerospace Corporation, El Segundo, California

VIBRATION OF ECCENTRICALLY STIFFENED PLATES
B. R. Long, Defence Research Establishment Suffield, Raleton, Alberta, Canada

CRACK DETECTION IN A STRUCTURAL BEAM THROUGH CROSS-CORRELATION ANALYSIS
F. Baganoff, Baganoff Associates, Inc., St. Louis, Missouri, and
D. Baganoff, Stanford University, Stanford, California

A THEORETICAL MODAL STUDY FOR THE LATERAL VIBRATIONS OF BARS HAVING VARIABLE CROSS SECTION AND FREE END CONDITION
A. F. Witte, Sandia Corporation, Albuquerque, New Mexico

*VARIABLE RESONANT VIBRATION GENERATOR FOR EXPERIMENTAL VIBRATIONAL ANALYSIS OF STRUCTURES
H. Soulant and S. Lee, Naval Ship Research and Development Center, Washington, D.C.

*THE PREDICTION OF INTERNAL VIBRATION LEVELS OF FLIGHT VEHICLE EQUIPMENT
R. W. Sevy and D. L. Earls, Air Force Flight Dynamics Laboratory, Wright-Patterson AFB, Ohio

SATURN V COMPONENT VIBRATION TESTS USING SEGMENTED SHELL SPECIMENS
C. Hwang, Northrop Corporation, Norair Division, Hawthorne, California, and
C. E. Lifer, NASA, Marshall Space Flight Center, Huntsville, Alabama

AN APPLICATION OF FLOWGRAPHS TO THE FREE VIBRATION OF STRUCTURES
P. M. Wright, University of Toronto, Toronto, Canada, and
C. C. Feng, University of Colorado, Boulder, Colorado

DUAL SPECIFICATIONS IN VIBRATION TESTING
W. B. Murfin, Sandia Corporation, Albuquerque, New Mexico

SUBSTITUTE ACOUSTIC TESTS
T. D. Scharton and T. M. Yang, Bolt Beranek and Newman Inc., Van Nuys, California

SIMPLIFIED METHOD OF CALCULATING NATURAL FREQUENCIES AND NORMAL MODES OF VIBRATION FOR SHIPS
H. B. Ali and H. F. Alma, Naval Ship Research and Development Center, Washington, D.C.

RESPONSE SPECTRA FOR SWEEPING SINUSOIDAL EXCITATIONS
D. L. Cronin, TRW Systems Group, Redondo Beach, California

PAPERS APPEARING IN PART 2

Structural Analysis

AN OVERALL VIEW OF STRUCTURAL DYNAMICS
R. M. Mains, Washington University, St. Louis, Missouri

DYNAMIC SUBSTRUCTURES METHOD FOR SHOCK ANALYSIS
M. Paketys, Jr., General Dynamics, Electric Boat Division, Groton, Connecticut

IDENTIFICATION OF COMPLEX STRUCTURES USING NEAR-RESONANCE TESTING
J. P. Raney, NASA, Langley Research Center, Hampton, Virginia

PROPAGATION OF LONGITUDINAL STRESS WAVES IN A COMPLEX BAR TYPE STRUCTURE
D. L. Block, Martin Marietta Corporation, Orlando, Florida

ALSEP SYSTEM STRUCTURAL DYNAMICS STUDY
M. M. Bahn, Aerospace Systems Division, The Bendix Corporation, Ann Arbor, Michigan

REDUCING THE NUMBER OF MASS POINTS IN A LUMPED PARAMETER SYSTEM
M. T. Soifer and A. W. Bell, Dynamic Science, Monrovia, California

LATERAL DYNAMIC RESPONSE OF LARGE SUBSYSTEMS DURING LAUNCH TRANSIENT CONDITIONS
J. S. Gaffney and P. E. Campos, Atlantic Research Corporation, Costa Mesa, California

*This paper appears in Shock and Vibration Bulletin 38, Supplement.

A NEW APPROACH TO THE INTERACTION PROBLEMS OF FLUID FILLED ELASTIC MEMBRANE SHELLS
C. L. Tai and S. Uchiyama, Space Division, North American Rockwell Corporation, Downey, California

STRUCTURAL AND VIBRATION ANALYSIS OF NAVY CLASS HIGH IMPACT MEDIUMWEIGHT SHOCK TEST
W. P. Welch and P. D. Saunders, Westinghouse Electric Corporation, Sunnyvale, California

TRANSIENT RESPONSES OF A LINEAR MECHANICAL SYSTEM BY USE OF EXPERIMENTALLY DETERMINED UNIT IMPULSE RESPONSES
V. P. Warkulwiz, General Electric Company, Valley Forge Space Technology Center, Pennsylvania

A MOMENT TECHNIQUE FOR SYSTEM PARAMETER IDENTIFICATION
F. Kozin and C. H. Kozin, Midwest Applied Science Corporation, West Lafayette, Indiana

REINFORCED CONCRETE BEAM RESONANCES
F. G. Krach, Barry Controls Division, Barry Wright Corporation, Watertown, Massachusetts

STRUCTURAL DYNAMIC ANALYSIS OF THE MARINER MARS '69 SPACECRAFT
H. J. Helbeck, Jet Propulsion Laboratory, Pasadena, California, and T. D. Arthurs and W. J. Gaugh, Northrop Systems Laboratory, Northrop Corporation, Hawthorne, California

LINE SOLUTION TECHNOLOGY AS A GENERAL ENGINEERING APPROACH TO THE STATIC, STABILITY, AND DYNAMIC RESPONSE OF STRUCTURAL MEMBERS AND MECHANICAL ELEMENTS
W. D. Pilkey, IIT Research Institute, Chicago, Illinois, and R. Nielsen, Jr., Department of Transportation, Washington, D.C.

UPPER AND LOWER BOUNDS TO BENDING FREQUENCIES OF NONUNIFORM SHAFTS, AND APPLICATIONS TO MISSILES
N. Rubinstein, V. G. Sigillito and J. T. Stadter, Applied Physics Laboratory, The Johns Hopkins University, Silver Spring, Maryland

DAMAGE PREDICTION FOR OPEN FRAME STRUCTURES SUBJECT TO LIQUID PROPELLANT EXPLOSIONS
G. C. Kao and V. M. Conticelli, Wyle Laboratories, Huntsville, Alabama, and M. J. Rosenfield, U.S. Army Corps of Engineers, Ohio River Division Laboratories, Cincinnati, Ohio

SIMPLIFIED DYNAMICS OF HARDENED BURIED BUILDINGS
J. V. Poppitz, Bell Telephone Laboratories, Inc., Whippany, New Jersey

INFLUENCE COEFFICIENT MATRIX QUICK CHECK PROCEDURE
G. W. Bishop, Bishop Engineering Company, Princeton, New Jersey

Mechanical Impedance

DETERMINATION OF FIXED BASE NATURAL FREQUENCIES OF DUAL FOUNDATION SHIPBOARD EQUIPMENTS BY SHAKE TESTS
L. P. Petak and G. J. O'Hara, Naval Research Laboratory, Washington, D.C.

*VIBRATION TRANSMISSION METHODS FOR FOUNDATION STRUCTURES
E. V. Thomas, Annapolis Division, Naval Ship Research and Development Center, Annapolis, Maryland

VIBRATION ANALYSIS OF A STRUCTURAL FRAME USING THE METHOD OF MOBILITY
J. Verga, Hazeltine Corporation, Little Neck, New York

APPLICABILITY OF MECHANICAL ADMITTANCE TECHNIQUES
D. U. Noiseux and E. B. Meyer, Bolt Beranek and Newman Inc., Cambridge, Massachusetts

*This paper appears in Shock and Vibration Bulletin 38, Supplement

APPLICATION OF THE MECHANICAL RECEPTANCE COUPLING PRINCIPLE TO SPACECRAFT SYSTEMS
E. Heer, Jet Propulsion Laboratory, Pasadena, California, and
L. D. Lutes, Rice University, Houston, Texas

A VERIFICATION OF THE PRACTICALITY OF PREDICTING INTERFACE DYNAMICAL ENVIRONMENTS BY THE USE OF IMPEDANCE CONCEPTS
F. J. On, NASA, Goddard Space Flight Center, Greenbelt, Maryland

EXPERIMENTAL TECHNIQUE FOR DETERMINING FIXED-BASE NATURAL FREQUENCIES OF STRUCTURES ON SINGLE NONRIGID ATTACHMENT POINTS
G. M. Remmers, Naval Research Laboratory, Washington, D.C.

DETERMINATION OF MODAL MASS FROM TEST DATA
I. P. Vatz, Brown Engineering, A Teledyne Company, Huntsville, Alabama

DAMPING AND ISOLATION

DESIGN OF A DAMPED MACHINERY FOUNDATION FOR HIGH-SHOCK LOADING

E. V. Thomas
Annapolis Division of Naval Ship Research
and Development Center*
Annapolis, Maryland

A simplified design procedure is set forth for pipe within-a-pipe members supported by a viscoelastic adhesive. The safety of the design procedure has been verified by three separate exposures to high-shock testing.

INTRODUCTION

The design of machinery foundations using elastic materials has been advanced to a relatively sophisticated state by Belsheim and O'Hara for impulsively loaded structures [1]. However, their method becomes analytically unmanageable if a viscoelastic material is incorporated as a load-carrying member in the design. When such a viscoelastic material has a high damping coefficient, plus normal nonlinear elastic properties, the differential equations of motion of the dynamic analysis method grow beyond the capabilities for solution of the largest computers.

Prior to the development of the dynamic analysis method for shock design, the only available methods for evaluation of a design were shock machine testing or explosive testing on a shock barge facility. These methods are adequate for testing damped structures, but are primarily designed for testing machinery rather than foundation structures. For machinery foundation structures designed to be attached directly to a ship hull, rather than to a deck or intermediate structure, the shape of the hull as it affects the foundation must be simulated for testing on a shock machine. This requires fabrication of an intermediate simulated hull. The foundation to be evaluated must then be fabricated on the hull share. Loading of the foundation requires the use of shipboard-type isolation mounts supporting a mass simulating the shipboard machine. This procedure requires design simulation of the hull structure of the ship plus nonresonant machine-simulation masses.

The design procedure discussed in this paper was developed specifically for a pipe within a pipe supported by a viscoelastic cylinder adhered to inner and outer elastic pipes (Fig. 1). This foundation member was developed for vibration attenuation of the attached machinery. The design for shock safety in combat vessels is required for containment of supported machinery.

VISCOELASTIC MATERIAL PARAMETERS

The viscoelastic material used for the pipe-in-pipe leg is a lead-filled, flexible epoxy resin. This material, like most long-chain, cross-linked polymeric materials, is highly rate sensitive for shear loading beyond the nonreversible loading limit. This rate sensitiveness is caused by the superelastic uncoiling

*The opinions and assertions herein are those of the author and are not to be construed as those of the Annapolis Division, The Center, the Navy, or the naval service at large.

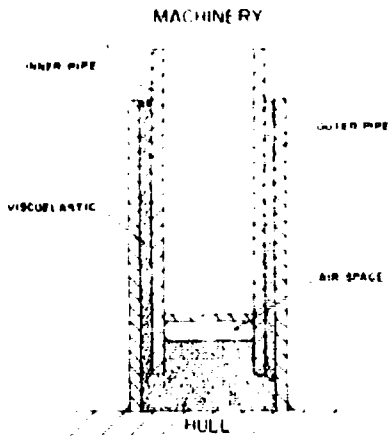

Fig. 1. Pipe within a pipe supported by viscoelastic cylinder adhered to inner and outer pipes

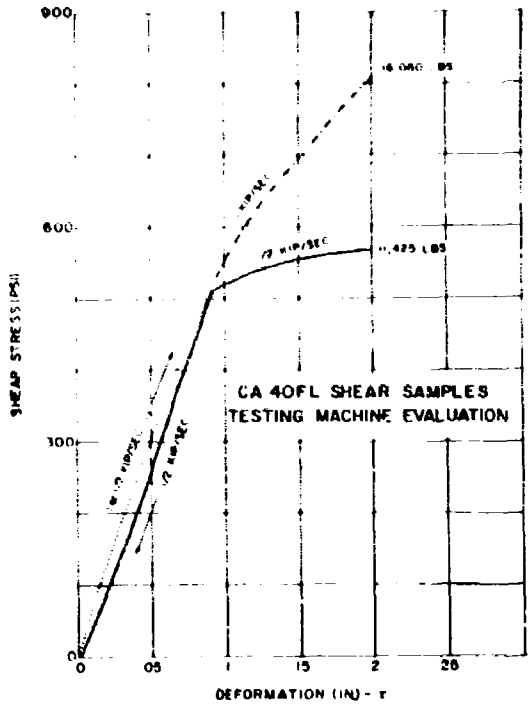

Fig. 2. Stress-deformation curves

of cross-linked molecular structure. This difference in rate was measured experimentally on a testing machine with a programable rate of force application up to 1000 lb/sec. With 500 and 1000 lb/sec as loading rates on many samples of pipe-in-pipe specimens, the stress-deformation curves seen in Fig. 2 were generated. The linear stress-deformation portion of the curve terminates at a shear stress level of 510 psi. Beyond this point all the way to failure, superelastic nonrecoverable, rate-sensitive deformation occurs. Failure occurs at the same shear deflection, regardless of loading rate. The average failure stress of samples at the 1000 lb/sec loading rate was 40 percent higher than the average failure stress for the samples tested at the 500 lb/sec loading rate. The testing machine data (Fig. 2) do not approximate the high loading rates of shock inputs. They do, however, provide an indication of the added design factor of safety owing to the composition of the viscoelastic adhesive used in the pipe-within-a-pipe leg.

DESIGN PROCEDURE

The testing machine data on the viscoelastic adhesive will be used as design stress load at the extent of the repeatable shear stress-deformation limit of 510 psi. This limit is used with Navy shock-design curves (Fig. 3) to determine a total shock design number (SDN) based on the installed weight of machinery. With the viscoelastic adhesive data from the testing machine used as a base, the total shear length of viscoelastic adhesive required for a pipe-within-a-pipe foundation is

$$L = \frac{P}{\pi d s} = \frac{W \cdot SDN}{\pi \cdot d \cdot 510} \text{ (in.)},$$

where

W = weight of machine in pounds,

SDN = shock design number from Fig. 3,

3.1416 = π,

d = outside diameter of inner pipe in inches

EXPERIMENTAL EVALUATION

This method has been used successfully for design of a double-damped portal frame foundation, a highly damped torsional-beam foundation, and a braced cantilever foundation for shipboard use. These foundations were tested on a medium weight shock machine under MIL-S-901C specifications with no damage. A foundation was also designed for future evaluation in a Naval Research vessel under explosive loading.

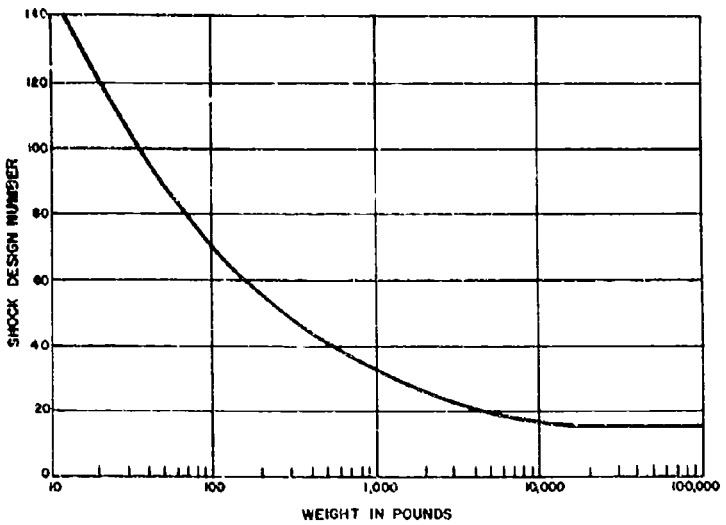

Fig. 3. Navy shock-design curves

REFERENCE

1. R. O. Belsheim and G. J. O'Hara, "Shock Design of Shipboard Equipment, Part 1 — Dynamic Design — Analysis Method," NAVSHIPS 250-423-30

* * *

CONSTRAINED LAYER DAMPING WITH PARTIAL COVERAGE

David S. Nokes and Frederick C. Nelson
Tufts University
Medford, Massachusetts

A theoretical and experimental study is presented for the damping of beams by constrained viscoelastic layers when only a portion of the beam is covered. The results of Ungar and Kerwin are extended to nonsinusoidal mode shapes and to partial coverage in which only the central portion of the beam is covered with a constrained viscoelastic layer. Both theory and experiment show that for stiff viscoelastic layers the loss factor is greater for partial coverage than for full coverage.

INTRODUCTION

This paper deals with the damping of beams by constrained viscoelastic layers when only a portion of the beam is covered. A layer of viscoelastic material is applied to one surface of the beam and covered with a metal constraining layer. This produces large shear strains in the viscoelastic layer and, thus, high damping.

The first treatment of this problem appears to have been by Kerwin [1] in 1959. Shortly thereafter a more general treatment was given by Ross, Ungar, and Kerwin [2]. They later developed a simpler method of derivation using energy methods [3], which led to the currently accepted form of the equations for the loss factor of the beam [4]. Their results have since been extensively checked against experiment, the most complete works being by Yin et al. [5] and Ruzicka et al. [6]. These works report good agreement for the case considered by the Ungar and Kerwin theory.

The theory of Ungar and Kerwin was derived for an infinitely long beam with a sinusoidal waveform. The theory applies to a pinned-pinned finite-length beam but not to other cases of finite beams. DiTaranto [7,8] has developed a general theory that is valid for any end conditions but still assumes the entire beam is covered.

Recently, Yoos and Nelson [9], in attempting to damp floor panel vibration in a building, performed tests that indicated that partial coverage could give as much damping as full coverage. These tests indicated a peak in the damping at about 60 percent coverage of the beam. While no other cases of increased damping with reduced coverage have been reported in the literature, comments at the presentation of their paper indicated that other people had observed this effect but had attributed it to experimental error. At that time there was apparently no theory available for predicting the effect of partial coverage.

As a result, it was decided to conduct a theoretical and experimental study of the effects of covering only the central portion of the beam and also evaluating the effects of different beam end conditions. In this paper, a theory is developed that is applicable to any symmetrical boundary conditions and assumes the mode shape is the same as that of the corresponding undamped beam. The theory predicts that for stiff viscoelastic layers the damping will be higher for partial coverage than for full coverage. The loss factor was measured and agreed with the theory to within limits of accuracy of the property data.

ANALYTICAL

The following derivation uses the same assumptions as the Ungar and Kerwin theory [4], with two exceptions. The mode shape is assumed to be the same as that of the undamped beam, but not necessarily sinusoidal. The mode shape for any symmetric boundary conditions can be used. Also, only a fraction of the beam is assumed covered. The damping layer is a

single section of length ℓ which is centered on the length of the main beam as shown in Fig. 1.

Fig. 1. Beam and damping layer geometry

A differential equation is developed for δ_3, the horizontal displacement of the neutral axis of the constraining layer. The viscoelastic material is represented by a complex modulus $G = G' + iG'' = G'(1 + i\beta)$. In all the following equations, steady-state sinusoidal motion is assumed, that is, all quantities can be taken as multiplied by $e^{i\omega t}$ where ω is the frequency of oscillation.

The geometry of deformation is shown in Fig. 2. From the geometry, the shear strain in the viscoelastic layer, Ψ, is

$$\Psi = \frac{\delta_3 - \delta_1 - (c_1 + h + c_3)\Phi}{h} . \tag{1}$$

For equilibrium in the x direction of the constraining layer, the tensile force in the constraining layer, F_3, and the shear stress in the viscoelastic layer, τ, are related by

$$\frac{dF_3}{dx} = \tau W \tag{2}$$

and overall equilibrium in the x direction gives the tensile force in the main beam, F_1, equal to F_3.

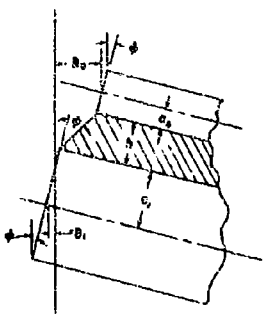

Fig. 2. Geometry of deformation

Using these equations and the stress-strain laws, the following equation is found for δ_3 in terms of the beam slope, Φ, and constants (see Ref. [10] for a detailed derivation):

$$\frac{d^2\delta_3}{d\xi^2} - R\delta_3 = -HRL\Phi \tag{3}$$

where

$$R = \frac{GWL^2}{h}\left(\frac{1}{E_3A_3}\right) + \left(\frac{1}{E_1A_1}\right) \tag{4}$$

$$H = \frac{c_1 + h + c_3}{L\left(1 + \frac{E_3A_3}{E_1A_1}\right)} \tag{5}$$

$$\xi = \frac{x}{L} . \tag{6}$$

If $x = 0$ at the center of the beam, then the mode shape for any symmetric boundary conditions is given by

$$y = \cos\lambda\xi + \sigma\cosh\lambda\xi \tag{7}$$

for symmetric mode shapes, and

$$y = \sin\lambda\xi + \sigma\sinh\lambda\xi \tag{8}$$

for antisymmetric mode shapes. The solution is given below only for the symmetric modes; see Ref. [10] for the antisymmetric mode solution. The damping layer is assumed to cover a fraction of the total beam length, $\theta = \ell/L$.

Using the symmetric mode shape and the boundary conditions of $\delta_3 = 0$ and $\xi = 0$ from symmetry and $d\delta_3/d\xi = 0$ at $\xi = \theta/2$ for a free end of the constraining layer gives

$$\delta_3 = -\frac{HR\lambda}{(\lambda^2 + R)}\sin\lambda\xi - \frac{HR\lambda}{(\lambda^2 - R)}\sigma\sinh\lambda\xi + \left[\frac{\frac{HR\lambda^2}{(\lambda^2 + R)}\cos\lambda\frac{\theta}{2} + \frac{HR\lambda^2}{(\lambda^2 - R)}\sigma\cosh\lambda\frac{\theta}{2}}{\sqrt{R}\cosh\sqrt{R}\frac{\theta}{2}}\right]\sinh\sqrt{R}\,\xi . \tag{9}$$

The tensile strain in the constraining layer is the derivative of Eq. (9) or

$$\epsilon_3 = \frac{1}{L}\frac{d\delta_3}{d\xi}$$

$$= D(-\cos\lambda\xi - B\cosh\lambda\xi + E\cosh\sqrt{R}\,\xi) , \tag{10}$$

where

$$D = \frac{HR}{\left[1 + \frac{R}{\lambda^2}\right] L} \tag{11}$$

$$B = \frac{\left[1 + \frac{R}{\lambda^2}\right]}{\left[1 - \frac{R}{\lambda^2}\right]} \sigma \tag{12}$$

$$E = \frac{\cos \lambda \frac{\theta}{2} + B \cosh \lambda \frac{\theta}{2}}{\cosh \sqrt{R} \frac{\theta}{2}} . \tag{13}$$

By substituting into Eq. (1), the shear strain in the viscoelastic layer is found to be

$$\Psi = A(\sin \lambda\xi - B \sinh \lambda\xi + C \sinh \sqrt{R}\, \xi) \tag{14}$$

where

$$A = \frac{\lambda H}{h\left[1 + \frac{R}{\lambda^2}\right]} \left(1 + \frac{E_3A_3}{E_1A_1}\right) \tag{15}$$

$$C = \frac{\sqrt{R}}{\lambda} E . \tag{16}$$

Using the energy expressions of Ref. [3], the loss factor of the beam is given in terms of the strain energies by

$$\eta = \frac{\beta G' A_2 L \int_0^{\theta/2} |\Psi|^2 \, d\xi}{\frac{E_1 I_1}{L^3} \int_0^{1/2} \left(\frac{d^2y}{d\xi^2}\right)^2 d\xi + \frac{E_3 I_3}{L^3} \int_0^{\theta/2} \left(\frac{d^2y}{d\xi^2}\right)^2 d\xi + G' A_2 L \int_0^{\theta/2} |\Psi|^2 \, d\xi + E_3 A_3 L \left(1 + \frac{E_3A_3}{E_1A_1}\right) \int_0^{\theta/2} |\epsilon_3|^2 d\xi} . \tag{17}$$

Because all quantities containing R are complex numbers, the expansion of Eq. (17) is lengthy. The complete set of resulting equations and a Fortran computer program for calculation are given in Ref. [10].

The loss factor was calculated for a rectangular steel beam (0.125-in. thick, 2.0-in. wide, 20.0-in. long) with a 0.050-in. thick viscoelastic layer and a 0.031-in. thick steel constraining layer. The material loss factor β, was taken as 1.0 and the shear storage modulus G', was varied to give different values of R' (the real part of R). The resulting damping vs fraction of length covered for a free-free beam in the first mode is shown in Fig. 3.

For full coverage, Yin et al. [5] had suggested using the Ungar and Kerwin theory modified by substituting an equivalent wavelength equal to 1.10 L. Results using this assumption are compared to the present analysis in Table 1. Thus, it appears that this procedure is not a valid extrapolation of the Ungar and Kerwin theory.

R' is the ratio of the stiffness of the viscoelastic layer in shear to the tensile stiffness of the constraining layer. It can also be viewed as a measure of the coupling between the main beam and the constraining layer (see Fig. 4). As $R' \to 0$, the two layers deform independently with no stretching of the constraining layer. As

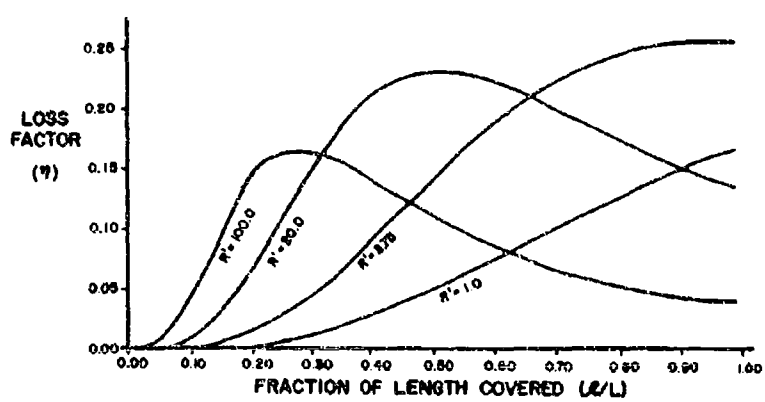

Fig. 3. Damping vs coverage, first free-free mode

TABLE 1
Comparison of Loss Factors for Fully Covered Free-Free Beams

R'	η from Present Analysis	η from Modified Ungar and Kerwin Theory
1.0	0.162	0.066
6.0	0.238	0.222
20.0	0.132	0.239
100.0	0.036	0.095

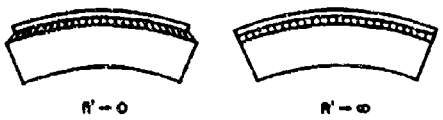

Fig. 4. Deformation for low and high R'

$R' \to \infty$, the layers are rigidly coupled together and deform as a single Bernoulli-Euler beam.

For small R', the damping decreases continuously as coverage is decreased. This is expected because if the constraining layer has not stretched, the shear strain at any point is independent of the fraction covered. Removing coverage simply eliminates a portion of the viscoelastic material without affecting the energy stored in the remainder, thereby reducing the loss factor.

For large R', the damping initially increases as coverage is decreased. In this case, the stretching of the constraining layer has an important effect. As coverage is removed, the end of the layer will contract. Therefore, the shear strain at any point in the remaining viscoelastic material will increase. In effect, for very large R', the shear strain tends to concentrate in a boundary layer at the ends of the constraining layer.* Thus the energy dissipation will depend mostly on the beam curvature beneath the ends of the constraining layer. Because the free-free beam has zero curvature at the ends, but a peak at the center, the shear strain at the end of the damping layer will rise as coverage is reduced, as shown in Fig. 5. Thus, larger shear strains occur for less coverage but the length over which the dissipation can accumulate is reduced. These competing effects result in a maximum of damping at some partial coverage.

This analysis has also been applied to a fixed-fixed beam that has a maximum curvature at the ends and a local maximum at the center (see Fig. 6). As the explanation above implies, for large R' the loss factor has a maximum at full coverage and another peak at partial coverage.

EXPERIMENTAL

To measure the beam loss factor, steady-state forcing in the first free-free mode was employed. A schematic diagram of the test setup is shown in Fig. 7. The test beam was mounted on a load cell to give the force input to the beam. An accelerometer was used to give an approximate center amplitude. For more accurate center amplitude measurements, as well as amplitude measurements at other points along the beam, a traveling telescope was used to sight on a line on the beam, which was frozen by a stroboscope.

The loss factor was obtained from the force required to drive the beam at resonance and also from the bandwidth to half-power points. A test beam of the same dimensions as that used in the theoretical calculations was used. Du Pont LR3-606 was used as the viscoelastic material. Du Pont data indicated $G' = 8200.0$ psi (therefore, $R' = 80.0$) and $\beta = 0.73$ at the test conditions of 105 Hz and 77°F. The results are shown in Fig. 8. The data shows good agreement, with some indication that the effective shear storage modulus is less than that given by Du Pont.

The assumption that the mode shape remains the same as that of the undamped beam was checked by measuring the mode shape at different coverages. The maximum error of 5 percent of the tip deflection occurred for 40 percent coverage as shown in Fig. 9. Because this was a very heavy damping treatment, it is concluded that the assumption of constant mode shape is valid for any practical damping layer.

CONCLUSIONS

1. The theory can predict the damping for partial coverage of any beam with symmetric boundary conditions.

*This tendency is evident in Eq. (3) if it is written in the form

$$\frac{1}{R}\frac{d^2\delta_3}{d\xi^2} - \delta_3 = -HL\Phi .$$

As $R \to \infty$, the coefficient of the highest derivative approaches zero. This behavior is characteristic of boundary layer problems [11].

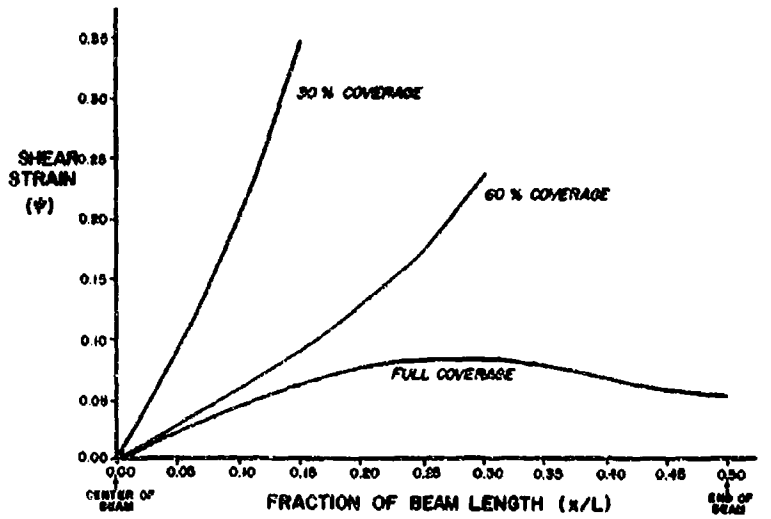

Fig. 5. Shear strains in viscoelastic layer for R' = 100.0; free-free beam, center amplitude = 1.215 in.

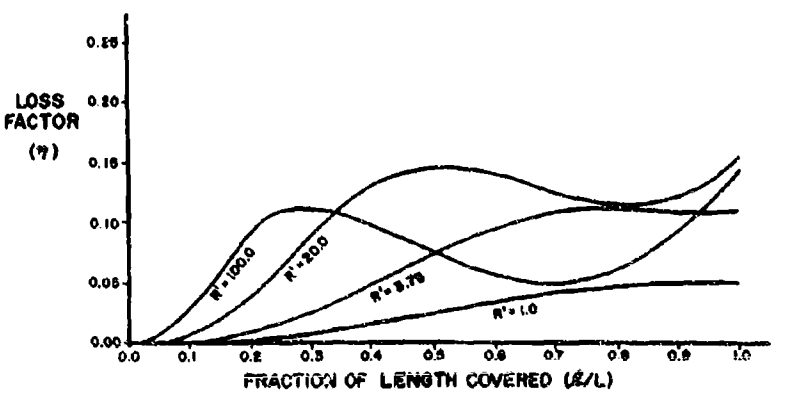

Fig. 6. Damping vs coverage, first fixed-fixed mode

2. It is not necessary to cover the entire beam to achieve good damping. Partial coverage is more practical, particularly if one is limited to a relatively stiff material.

3. The Ungar and Kerwin theory should not be used for other than pinned-pinned beams by substituting an equivalent wavelength as suggested by Yin et al.

ACKNOWLEDGMENT

The first author is indebted to NSF and NASA for financial support during this work.

REFERENCES

1. E. M. Kerwin, "Damping of Flexural Waves by a Constrained Viscoelastic Layer," J. Am. Acoust. Soc. 31(7):952-962 (1959)

2. D. Ross, E. E. Ungar, and E. M. Kerwin, "Damping of Plate Flexural Vibrations by Means of Viscoelastic Laminae," Section 3

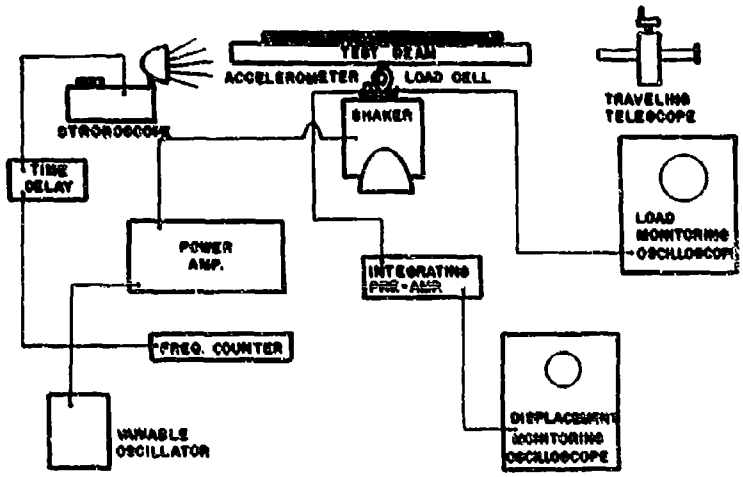

Fig. 7. Schematic diagram of test apparatus

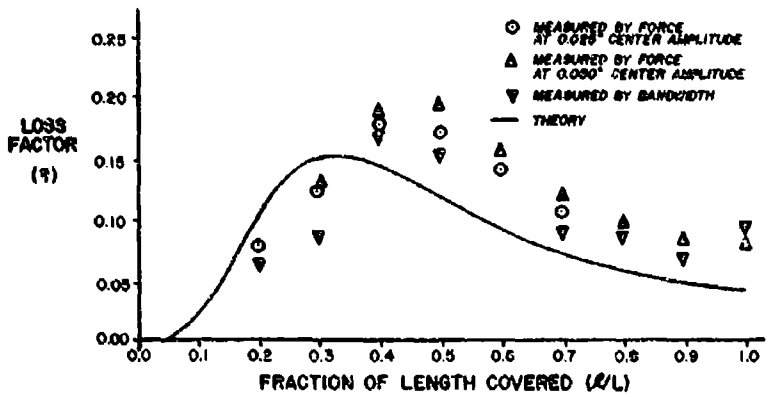

Fig. 8. Measured loss factor, first free-free mode

of Structural Damping (J. E. Ruzicka, Ed.) (ASME, New York), 1959

3. E. E. Ungar and E. M. Kerwin, "Loss Factors of Viscoelastic Systems in Terms of Energy Concepts," J. Am. Acoust. Soc., 34(7):954-957 (1962)

4. E. E. Ungar, "Loss Factors of Viscoelastically Damped Beam Structures," J. Am. Acoust. Soc., 34(8):1082-1089 (Aug. 1962)

5. T. P. Yin, T. J. Kelley, and J. E. Barry, "A Quantitative Evaluation of Constrained-Layer Damping," ASME Paper No. 67-Vibr-26, 1967

6. J. E. Ruzicka et al., "Damping of Structural Composites with Viscoelastic Shear-Damping Mechanisms," NASA Contractor Rept. NASA CR-742, 1967

7. R. A. DiTaranto, "Theory of Vibratory Bending for Elastic and Viscoelastic Layered Finite-Length Beams," J. Appl. Mech., pp. 881-886, ASME (Dec. 1965)

8. R. A. DiTaranto and W. Blasingame, "Composite Damping of Vibrating Sandwich Beams," ASME Paper No. 67-Vibr-6, 1967

9. T. R. Yoos and F. C. Nelson, "Damping of Low-Frequency Vibration by Constrained Viscoelastic Layers," ASME Paper No. 67-Vibr-62, 1967

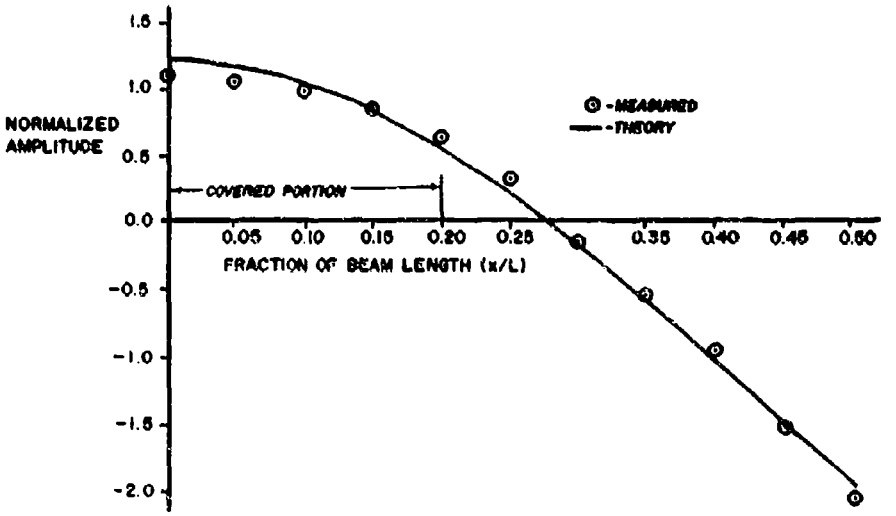

Fig. 9. Measured mode shape with 40 percent coverage

10. D. S. Nokes, "Constrained Layer Damping of Beams with Partial Coverage," Ph.D. Thesis, Tufts Univ., June 1968, available from Univ. Microfilms, Ann Arbor, Mich.

11. F. C. Nelson, "An Introduction to the Geckeler Approximation Based on a Boundary Layer Analysis of Beams-on-Elastic Foundation," Bull. Mech. Engr. Educ., 5: 35-39 (1966)

DISCUSSION

Mr. Conlisk (Monsanto): I got the impression that you took only the shear of the damping layer into account, as Kerwin and Ungar did. However, you also stated that, with the stiffer damping materials, you got some stretch in the constraining layer which implies stretch of the viscoelastic layer; yet your experiments agreed. Do you have any explanation for that?

Mr. Nokes: Probably the easiest way is to look at it in terms of the energy stored in each of these different types of things. As a matter of fact, Ungar and Kerwin do allow stretching of the constraining layer, although it is not quite as obvious. Even with the stiff material I used here, we are still talking stiff moduli, which means about 8000 psi as compared with a modulus of 30 million psi for steel. We also know that the tensile strains are going to be about the same order of magnitude. Therefore the actual tensile strain energy in the viscoelastic material is simply negligible.

Mr. Blenner (Lord Manufacturing Corp.): When you tested this, did you use one particular frequency or a band of frequencies? A constrained layer treatment is very frequency sensitive. Might this have given a frequency effect?

Mr. Nokes: No, those data are all at the first free-free mode so there is comparatively little variation in frequency, but there was some variation. It varied from about 100 to 80 Hz as a result of changes in natural frequency of the overall configuration; but the theory curve has, in fact, been corrected for this. In other words, I used the manufacturer's property data variation over this frequency range to correct the theory curve.

Mr. DiTaranto (PMC Colleges): I think your work is very interesting. I wonder if you have given any consideration to the effect of what you found on the higher modes?

Mr. Nokes: The theory was developed to the extent that the computer program, in fact, calculates answers for the higher modes; however, I did not do any experimental work on the

higher modes. My assumption that the mode shapes stay the same as those of the undamped beam is highly questionable at the higher modes. If you want a guess, I would say that I might have been able to do the third mode with this sort of analysis. I certainly would not have been able to do something like the sixth mode.

Mr. Brooks (NASA, Langley Research Ctr.): I notice that you had R as a ratio which was the extensional stiffness of the layer on top of the beam. I believe you had numbers of R up to 100. What is a realistic value for R? Was the R that you had on your curve the absolute value of the magnitude of that parameter?

Mr. Nokes: What I had on the curve was the real part of the parameter. In other words, it was just the real part of g in the equation. What a realistic value is depends pretty much on what you have available for material. If you were going to use the previously available theory you would have said that for this geometry you wanted an R of 1 to 5, simply because it is in this region that you had a very inefficient layer. One of the materials that was available to me just happened to be quite stiff. There would have been no way of using that material although it might be very good for other purposes. In that case using the value of R quite high might be practical. The experimental beam, for instance, had an R value of 80.

* * *

THE EFFECTS OF ROTATORY INERTIA AND SHEAR DEFORMATION ON THE FLEXURAL VIBRATIONS OF A TWO-LAYERED VISCOELASTIC-ELASTIC BEAM

T. Nicholas
Air Force Materials Laboratory
Wright-Patterson AFB, Ohio

The equations of motion for a two-layered sandwich beam consisting of viscoelastic and elastic layers have been solved considering the effects of deformation owing to shear and rotatory inertia. It is shown that the effects of rotatory inertia may be neglected for flexural vibrations of most beams, while the effects of shear deformation are small in calculations relating moduli to frequency. For calculations relating the damping of the composite to the damping of the viscoelastic layer, it is shown that shear effects are not always negligible, and curves are presented showing the errors involved when using "elementary beam theory" in which shear deformations are not considered.

INTRODUCTION

The analysis of the flexural vibrations of beams is commonly carried out with the aid of the well-known Bernoulli-Euler beam equations in which it is assumed that plane cross sections before deformation remain plane and perpendicular to the center line after deformation and, furthermore, that rotatory inertia effects are negligible. This analysis is known to be accurate for low frequencies but becomes less accurate as the vibrational frequency is increased and is quite inaccurate at frequencies near the first thickness shear mode of a beam. Although these remarks apply to a beam of an elastic material, they are no less true for the analysis of a beam of a viscoelastic material if the elastic modulus E is replaced by the complex modulus $E_1(1 - i\eta)$.

For improved accuracy in the analysis of such beams at higher frequencies, one may include the effects of rotatory inertia in the equations of motion [1], and for a more accurate solution the effects of deformation owing to shear must also be considered [2]. The resulting equations are the Timoshenko beam equations which are known to be accurate up to the first thickness shear frequency of the beam.

In considering vibrations of multilayered beams of different materials, the analysis takes on added complexities. In these configurations the flexural and shear vibrations are generally coupled together. Hence the knowledge of the effects of shear deformation and rotatory inertia on the homogeneous beams is of little help in weighing their effects on multilayered beams. These effects will depend in general not only on the frequency (and wavelength) of the vibration but on parameters such as the ratio of thicknesses of the layers and the modulus ratio. Equations including these effects have been derived previously for many different geometries [3] but solutions have been obtained only for very specialized cases because of the complexity of the equations. In particular, the three-layered sandwich beam having thin metal facings and a soft thick core has been studied previously in Ref. [4] where it was pointed out that for certain geometries the predominant deformation mode involved shear deformation in the core. For other configurations, it is generally difficult to assess the importance of shear deformation from physical intuition without solving the equations of motion.

One of the more common experimental techniques for determining the complex modulus of a viscoelastic material is to sandwich it to an elastic beam and observe the vibrational modes of the two-layered composite. This technique was first proposed by Oberst [5] and has been used by Schwarzl [6] and subsequently by many other investigators. The analysis is based on the assumptions of simple beam

theory; namely that plane sections remain plane and perpendicular to the deformed neutral axis of the beam. In other words, the effects of deformation owing to shear and rotatory inertia are not considered. The question of the validity of this assumption arises because there is a tendency to use this experimental technique for materials having wide ranges of moduli and damping and a wide range of thickness ratios. It was therefore decided to check the validity of the assumptions inherent in the Oberst beam calculations by performing a more rigorous analysis of the problem and comparing results.

In this paper, the effects of deformation owing to shear and rotatory inertia are studied separately for a two-layered beam of materials having different moduli and thicknesses by first solving the appropriate differential equations of motion for free undamped vibrations. The method is extended to the case of a viscoelastic layer sandwiched to an elastic layer by introducing the complex modulus into the equations of motion and through the introduction of a "complex frequency" into the free vibration solution. Finally, the calculations from elementary beam theory for the loss factor, η, of the viscoelastic layer from the damping of the composite beam are compared with those from a more exact theory which considers the effects of shear deformation. The results are compared for a wide range of geometric and material parameters and are presented in graphical form.

NOMENCLATURE

- E Young's modulus
- G Shear modulus
- h Thickness
- i Unit imaginary number
- I Moment of inertia about center of layer
- M Bending moment
- ℓ Length of beam
- N Axial force
- Q Transverse shear force
- t Time
- T Kinetic energy
- u Displacement component along axis of beam
- U Potential energy
- w Displacement component normal to axis of beam
- W Work of external forces
- x Coordinate along axis of beam
- δ Logarithmic decrement, variation
- η Loss factor for viscoelastic material
- λ Wavelength
- ξ Wave number
- ρ Mass density
- ψ Rotation of cross section
- ω Circular frequency
- Ω Reference frequency
- $*$ Superscript denoting dimensionless quantity
- 1 Subscript denoting viscoelastic layer
- 2 Subscript denoting elastic layer

ANALYSIS

Elastic Beam

The equations of motion of a two-layered beam are derived first for the case where both layers are linear elastic materials. The beam shown in Fig. 1 is analyzed by applying Hamilton's principle for a conservative system in the form

$$\delta \int_{t_0}^{t} (T - U)dt + \int_{t_0}^{t} \delta W \, dt = 0 \qquad (1)$$

where the first term represents the variation of the kinetic minus potential energy of the entire system from some initial time, t_0, to some other time, t. W represents the work done by external forces acting on the system and will be taken as zero hereafter for the case of free vibrations.

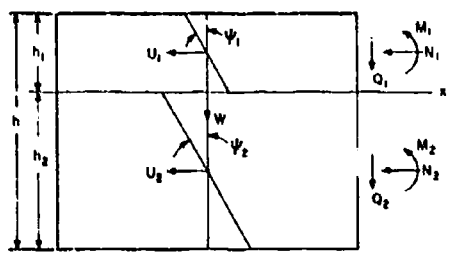

Fig. 1. Notation for two-layered beam

Both layers of the beam are treated as Timoshenko beams including the effects of resultant normal forces. This analysis thus assumes that plane sections of each layer remain plane but not necessarily perpendicular to the

deformed centerline, that is, shear deformation is considered. In addition, the effects of rotatory inertia are considered. The width of the beam is taken as unity in all subsequent discussion.

Subscripts 1 and 2 are used to denote the top and bottom layers of the beam respectively, the top layer being the one with the lower modulus. The rotation of a cross section and the axial displacement of the centerline of a layer are denoted by ψ and u respectively; w represents the transverse displacement; and thickness changes are neglected. The expression for the kinetic energy per unit length of beam is written for the top layer as

$$2T_0 = \rho_1 h_1 \left(\frac{\partial w}{\partial t}\right)^2 + \rho_1 h_1 \left(\frac{\partial u_1}{\partial t}\right)^2 + \rho_1 I_1 \left(\frac{\partial \psi_1}{\partial t}\right)^2 \quad (2)$$

where ρ_1 is the mass density, h_1 the thickness, and I_1 the moment of inertia about the centerline of the top layer. The potential energy is

$$2U_0 = G_1 h_1 \left(\psi_1 + \frac{\partial w}{\partial x}\right)^2 + E_1 I_1 \left(\frac{\partial \psi_1}{\partial x}\right)^2 + E_1 h_1 \left(\frac{\partial u_1}{\partial x}\right)^2 \quad (3)$$

where E_1 and G_1 are Young's modulus and the shear modulus respectively. The energy expressions for the bottom layer are identical to Eqs. (2) and (3) with subscript 2 replacing subscript 1.

The displacement components u_1 and u_2 are not independent; to insure continuity of displacements across the interface

$$u_2 = u_1 - \frac{h_1}{2}\psi_1 - \frac{h_2}{2}\psi_2 \quad (4)$$

Equations (2) and (3) and the equivalent expressions for the bottom layer constitute expressions for the kinetic and potential energies in terms of four independent displacement components, w, ψ_1, ψ_2, u_1, after applying the continuity condition, Eq. (4). These expressions are substituted into Eq. (1) and the variation is carried out for a beam occupying the region $x = 0$ to $x = \ell$ leading to a statement of Hamilton's principle in the form

$$\int_{t_0}^{t} dt \int_0^{\ell} dx \left\{ \left[G_1 h_1 \left(\frac{\partial \psi_1}{\partial x} + \frac{\partial^2 w}{\partial x^2}\right) + G_2 h_2 \left(\frac{\partial \psi_2}{\partial x} + \frac{\partial^2 w}{\partial x^2}\right) - (\rho_1 h_1 + \rho_2 h_2)\frac{\partial^2 w}{\partial t^2} \right] \delta w \right.$$

(5) (Cont.)

$$+ \left[-G_1 h_1 \left(\psi_1 + \frac{\partial w}{\partial x}\right) + E_1 I_1 \frac{\partial^2 \psi_1}{\partial x^2} - E_2 \frac{h_1 h_2}{2}\frac{\partial^2 u_2}{\partial x^2} - \rho_1 I_1 \frac{\partial^2 \psi_1}{\partial t^2} + \rho_2 \frac{h_1 h_2}{2}\frac{\partial^2 u_2}{\partial t^2} \right] \delta\psi_1$$

$$+ \left[-G_2 h_2 \left(\psi_2 + \frac{\partial w}{\partial x}\right) + E_2 I_2 \frac{\partial^2 \psi_2}{\partial x^2} - E_2 \frac{h_2^2}{2}\frac{\partial^2 u_2}{\partial x^2} - \rho_2 I_2 \frac{\partial^2 \psi_2}{\partial t^2} + \rho_2 \frac{h_2^2}{2}\frac{\partial^2 u_2}{\partial t^2} \right] \delta\psi_2$$

$$+ \left[E_1 h_1 \frac{\partial^2 u_1}{\partial x^2} + E_2 h_2 \frac{\partial^2 u_2}{\partial x^2} - \rho_1 h_1 \frac{\partial^2 u_1}{\partial t^2} - \rho_2 h_2 \frac{\partial^2 u_2}{\partial t^2} \right] \delta u_1 \Bigg\}$$

$$+ \left\{ \left[-G_1 h_1 \left(\psi_1 + \frac{\partial w}{\partial x}\right) - G_2 h_2 \left(\psi_2 + \frac{\partial w}{\partial x}\right) \right] (\delta w) \Bigg|_{x=0}^{x=\ell} \right\}$$

$$+ \left\{ \left[-E_1 I_1 \frac{\partial \psi_1}{\partial x} + E_2 \frac{h_2 h_1}{2}\frac{\partial u_2}{\partial x} \right] (\delta\psi_1) \Bigg|_{x=0}^{x=\ell} \right\}$$

$$+ \left\{ \left[-E_2 I_2 \frac{\partial \psi_2}{\partial x} + E_2 \frac{h_2^2}{2}\frac{\partial u_2}{\partial x} \right] (\delta\psi_2) \Bigg|_{x=0}^{x=\ell} \right\}$$

$$+ \left\{ \left[-E_1 h_1 \frac{\partial u_1}{\partial x} - E_2 h_2 \frac{\partial u_2}{\partial x} \right] (\delta u_1) \Bigg|_{x=0}^{x=\ell} \right\}$$

$$+ \int_0^{\ell} F(\delta w, \delta\psi_1, \delta\psi_2, \delta u_1) \Big|_{t_0}^{t} dx = 0 . \quad (5)$$

The last term involves variations of the four independent displacement components evaluated at times t and t_0 and is made equal to zero by specifying the values of these four quantities for all values of x at time t_0, that is, by specifying the initial conditions in the problem. Equation (5) can be made equal to zero for any and all variations of w, ψ_1, ψ_2, and u_1 only by setting each of the coefficients of the variations in the first four terms equal to zero identically, and by specifying one term of each of the products in the next four terms at the boundaries $x = 0$ and $x = \ell$. After rearranging

$$E_1 I_1 \frac{\partial^2 \psi_1}{\partial x^2} - G_1 h_1 \left(\psi_1 + \frac{\partial w}{\partial x}\right) + E_1 \frac{h_1^2}{2}\frac{\partial^2 u_1}{\partial x^2}$$

(6) (Cont.)

$$- \rho_1 \frac{h_1^2}{2} \frac{\partial^2 u_1}{\partial t^2} - \rho_1 I_1 \frac{\partial^2 \psi_1}{\partial t^2} = 0$$

$$E_2 I_2 \frac{\partial^2 \psi_2}{\partial x^2} - G_2 h_2 \left(\psi_2 + \frac{\partial w}{\partial x}\right) + E_1 \frac{h_1 h_2}{2} \frac{\partial^2 u_1}{\partial x^2}$$

$$- \rho_1 \frac{h_1 h_2}{2} \frac{\partial^2 u_1}{\partial t^2} - \rho_2 I_2 \frac{\partial^2 \psi_2}{\partial t^2} = 0$$

$$G_1 h_1 \left(\frac{\partial \psi_1}{\partial x} + \frac{\partial^2 w}{\partial x^2}\right) + G_2 h_2 \left(\frac{\partial \psi_2}{\partial x} + \frac{\partial^2 w}{\partial x^2}\right)$$

$$- (\rho_1 h_1 + \rho_2 h_2) \frac{\partial^2 w}{\partial t^2} = 0$$

$$E_1 h_1 \frac{\partial^2 u_1}{\partial x^2} + E_2 h_2 \left[\frac{\partial^2 u_1}{\partial x^2} - \frac{h_1}{2} \frac{\partial^2 \psi_1}{\partial x^2} - \frac{h_2}{2} \frac{\partial^2 \psi_2}{\partial x^2}\right]$$

$$- \rho_1 h_1 \frac{\partial^2 u_1}{\partial t^2} - \rho_2 h_2 \left[\frac{\partial^2 u_1}{\partial t^2} - \frac{h_1}{2} \frac{\partial^2 \psi_1}{\partial t^2} - \frac{h_2}{2} \frac{\partial^2 \psi_2}{\partial t^2}\right] = 0 \tag{6}$$

and the natural boundary conditions in the form

$$\begin{aligned} &(Q_1 + Q_2)\ (w) \\ &\left(M_1 - \frac{h_1}{2} N_2\right)\ (\psi_1) \\ &\left(M_2 - \frac{h_2}{2} N_2\right)\ (\psi_2) \\ &(N_1 + N_2)\ (u_1) \end{aligned} \tag{7}$$

where one of the products in each expression must be specified on the boundary to insure a unique solution.

M_1, Q_1, N_1, the bending moment, transverse shear, and axial force, respectively, for the top layer in the beam are given by

$$\begin{aligned} M_1 &= E_1 I_1 \frac{\partial \psi_1}{\partial x} \\ Q_1 &= G_1 h_1 \left(\psi_1 + \frac{\partial w}{\partial x}\right) \\ N_1 &= E_1 h_1 \frac{\partial u_1}{\partial x} \end{aligned} \tag{8}$$

and similarly for M_2, Q_2, N_2.

The solution to a problem involving the free vibrations of a two-layered sandwich beam is seen to be based on a set of four coupled partial differential equations given by Eqs. (6). Because the solution of these equations is cumbersome, the effects of rotatory inertia and shear deformation will be studied separately.

Consider first the equations when only rotatory inertia is taken into account and shear deformation is neglected. The shear deformation in each layer is taken equal to zero, requiring plane sections to remain plane and perpendicular to the deformed centerline; thus

$$\psi_1 + \frac{\partial w}{\partial x} = 0 \qquad \psi_2 + \frac{\partial w}{\partial x} = 0 \tag{9a}$$

$$\psi_1 = \psi_2 = \psi = - \frac{\partial w}{\partial x}\,. \tag{9b}$$

However, because the shear forces in each layer are not zero, this can be accomplished only by making the shear modulus infinite, such that the products

$$\begin{aligned} G_1 h_1 \left(\psi + \frac{\partial w}{\partial x}\right) &\neq 0 \\ G_2 h_2 \left(\psi + \frac{\partial w}{\partial x}\right) &\neq 0\,. \end{aligned} \tag{10}$$

Substituting Eqs. (9) and (10) into the equations of motion, Eq. (6), and rearranging leads to the simpler set of equations

$$(E_1 h_1 + E_2 h_2) \frac{\partial^2 u_1}{\partial x^2} - (\rho_1 h_1 + \rho_2 h_2) \frac{\partial^2 u_1}{\partial t^2}$$

$$+ E_2 h_2 \frac{(h_1 + h_2)}{2} \frac{\partial^3 w}{\partial x^3} - \rho_2 h_2 \frac{(h_1 + h_2)}{2} \frac{\partial^3 w}{\partial x \partial t^2} = 0$$

$$- (E_1 I_1 + E_2 I_2) \frac{\partial^4 w}{\partial x^4} - (\rho_1 h_1 + \rho_2 h_2) \frac{\partial^2 w}{\partial t^2}$$

$$+ E_1 h_1 \frac{(h_1 + h_2)}{2} \frac{\partial^3 u_1}{\partial x^3} - \rho_1 h_1 \frac{(h_1 + h_2)}{2} \frac{\partial^3 u_1}{\partial x \partial t^2}$$

$$+ (\rho_1 I_1 + \rho_2 I_2) \frac{\partial^4 w}{\partial x^2 \partial t^2} = 0\,. \tag{11}$$

which will be referred to subsequently as the equations that consider rotatory inertia only.

In a similar manner, the effects of rotatory inertia can be neglected while considering the shear deformation. In this case

$$\frac{\partial^2 u_1}{\partial t^2} = \frac{\partial^2 u_2}{\partial t^2} = \frac{\partial^2 \psi_1}{\partial t^2} = \frac{\partial^2 \psi_2}{\partial t^2} = 0 \qquad (12)$$

and the resulting equations of motion are

$$E_1 I_1 \frac{\partial^2 \psi_1}{\partial x^2} - G_1 h_1 \left(\psi_1 + \frac{\partial w}{\partial x}\right) + \frac{E_1 h_1 E_2 h_2}{4(E_1 h_1 + E_2 h_2)} \left(h_1^2 \frac{\partial^2 \psi_1}{\partial x^2} + h_1 h_2 \frac{\partial^2 \psi_2}{\partial x^2}\right) = 0$$

$$E_2 I_2 \frac{\partial^2 \psi_2}{\partial x^2} - G_2 h_2 \left(\psi_2 + \frac{\partial w}{\partial x}\right) + \frac{E_1 h_1 E_2 h_2}{4(E_1 h_1 + E_2 h_2)} \left(h_1 h_2 \frac{\partial^2 \psi_1}{\partial x^2} + h_2^2 \frac{\partial^2 \psi_2}{\partial x^2}\right) = 0$$

$$G_1 h_1 \frac{\partial \psi_1}{\partial x} + G_2 h_2 \frac{\partial \psi_2}{\partial x} + (G_1 h_1 + G_2 h_2) \frac{\partial^2 w}{\partial x^2} - (\rho_1 h_1 + \rho_2 h_2) \frac{\partial^2 w}{\partial t^2} = 0 . \qquad (13)$$

These equations will be referred to as the equations that consider shear deformation only.

Finally, the "elementary beam" equations are obtained by neglecting both rotatory inertia effects, Eq. (9), and deformation owing to shear, Eq. (12), leading to

$$\left[E_1 I_1 + E_2 I_2 + \frac{E_1 h_1 E_2 h_2 (h_1 + h_2)^2}{4(E_1 h_1 + E_2 h_2)}\right] \frac{\partial^4 w}{\partial x^4} + (\rho_1 h_1 + \rho_2 h_2) \frac{\partial^2 w}{\partial t^2} = 0 . \qquad (14)$$

The sets of Eqs. (11), (13), and (14) are each solved for a wave traveling in the x direction in an infinite beam, with the corresponding displacement components

$$\begin{aligned} w &= A_0 \exp[i(\xi x - \omega t)] \\ \psi_1 &= A_1 \exp[i(\xi x - \omega t)] \\ \psi_2 &= A_2 \exp[i(\xi x - \omega t)] \end{aligned} \qquad (15)$$

for the set of three equations in Eq. (13), for example, where ξ is the wave number and ω the frequency. The wave number ξ is related to the wavelength λ through

$$\xi = \frac{2\pi}{\lambda} . \qquad (16)$$

The displacement components, Eq. (15), are substituted into the differential equations and lead to a set of three homogeneous equations in the unknowns A_0, A_1, and A_2. For a nonzero solution, the determinant of the coefficients of the unknowns is set equal to zero and results in a frequency equation relating ω, ξ, and the parameters of the sandwich beam. In the solution, nondimensional quantities are introduced in the form

$$\begin{aligned} \frac{h}{\lambda} &= \frac{(h_1 + h_2)}{\lambda} = \frac{(h_1 + h_2)\xi}{2\pi} \\ E^* &= \frac{E_1}{E_2} \\ h^* &= \frac{h_1}{h_2} \\ \omega^* &= \frac{\omega}{\Omega_1} \end{aligned} \qquad (17)$$

where Ω_1 is a fictitious thickness shear frequency of a beam having the geometric average properties of the sandwich beam and is given by

$$\Omega_1 = \frac{\pi}{(h_1 + h_2)} \sqrt{\frac{E_{avg}}{3\rho_{avg}}} = \frac{\pi}{h_2(1 + h^*)} \sqrt{\frac{E_2(1 + E^* h^*)}{3\rho_2(1 + h^*)}} \qquad (18)$$

and where $\rho_1 = \rho_2$ for simplicity.

The frequency equations for the three cases considered are

$$\omega_1^* = \frac{(1 + h^*)}{\pi} \xi_0^2 \sqrt{\frac{b + 4f\xi_0^2}{d + e\xi_0^2 + f\xi_0^4}}$$

$$\omega_2^* = \frac{(1 + h^*)}{\pi} \xi_0 \times \sqrt{\frac{(36 + m\xi_0^2) - \sqrt{36 + m\xi_0^2)^2 - 12n\xi_0^2(1 + h^*\xi_0^2)}}{6(1 + h^*\xi^2)}}$$

$$\omega_3^* = \frac{(1 + h^*)}{\pi} \xi_0^2 \sqrt{\frac{b}{(1 + E^* h^*)^2}} \qquad (19)$$

where ω_1^*, ω_2^*, and ω_3^* represent the cases considering (a) only shear deformation, (b) only rotatory inertia, and (c) the elementary beam solution, and where the following symbols have been introduced:

$$\xi_0 = \frac{\pi}{(1+h^*)} \frac{h}{\lambda}$$

$$b = 4\left[(1+E^*h^*)(1+E^*h^{*3}) + 3E^*h^*(1+h^*)^2\right]$$

$$d = (1+E^*h^*)^2$$

$$e = (1+E^*h^*)\left[(1+4E^*h^*) + h^{*2}(4+E^*h^*)\right]$$

$$f = \left[2h^*(1+E^*h^*)\right]^2$$

$$n = \frac{144}{(1+E^*h^*)^2}\left[3(1+h^*)^2 - (1+E^*h^{*3})(1+E^*h^*)\right]$$

$$m = \frac{36h^*(1+E^*)(1+h^*)}{(1+E^*h^*)} + \frac{11(1+h^{*3})}{(1+h^*)} + \frac{12(1+E^*h^{*3})}{(1+E^*h^*)} . \tag{20}$$

Viscoelastic Layer

The case of a beam consisting of a viscoelastic layer sandwiched to an elastic layer is easily analyzed by taking the results of the two-layered elastic beam and making the replacements

$$\begin{aligned} E_1 &\rightarrow E_1(1+i\eta) \\ G_1 &\rightarrow G_1(1+i\eta) \\ \omega &\rightarrow \omega\left(1+i\,\frac{\delta}{2\pi}\right) \end{aligned} \tag{21}$$

where the damping in shear and extension is assumed identical and δ represents the logarithmic decrement. The introduction of a complex frequency into free vibrations of the form $\exp(i\omega t)$ leads to free damped oscillations of the form

$$\sim\exp(i\omega t)\ \exp\left(-\frac{\omega\delta}{2\pi}t\right) .$$

Solutions to the resulting complex frequency equation are obtained by setting the real and imaginary portions equal to zero identically and solving the two resulting equations simultaneously.

CONSIDERATIONS

The equations of motion of a two-layered elastic beam were solved for a wave having wavelength λ and circular frequency ω traveling in an infinite beam. Three particular cases were considered: (a) The elementary solution including only the additional effects of shear deformation, (b) the elementary solution including only the additional effects of rotatory inertia, and (c) the elementary solution. The equations that considered combined shear and rotatory inertia effects were not solved because of their complexity. The three sets of equations were solved numerically with the aid of an IBM 7094 computer and the results were plotted as curves of nondimensional frequency ω^* against h/λ, where $\omega^* = 1$ represents a thickness shear mode of a beam having the geometrical average properties of the composite two-layered beam given by Eq. (18), and h/λ represents the ratio of the total beam thickness to the wavelength of the vibration. Two typical curves are presented as Figs. 2 and 3. The curves showed that the effects of rotatory inertia and shear deformation could be neglected in modulus and frequency calculations for h/λ ratios less than about 0.2 for a range of E^* values from 10^{-1} to 10^{-5} and for h^* values from 0.1 to 10. The curves also showed that the effects of shear deformation were more significant than those of rotatory inertia for the ratios of moduli and thicknesses considered in this investigation; for this reason the effects of rotatory inertia were not considered subsequently. The conclusions that can be drawn are that rotatory inertia and shear effects can be neglected in flexural vibration problems except when considering very short, thick beams or when considering higher numbered modes of flexural vibration. An h/λ ratio of 0.20 is equivalent to a fifth mode of vibration of a cantilever beam having a length to thickness ratio of approximately 11.

The same equations discussed above were solved again, this time considering the damping of the softer layer, by the introduction of the complex modulus $E(1+i\eta)$ (and $G(1+i\eta)$) into the equations of motion and considering the frequency ω to be complex also. This results in a free damped vibration expressed as the product of a sinusoidal term and an exponential decay term. Values of the damping, η, up to unity had little or no effect on the relationships between the real part of the frequency and h/λ, that is, they did not significantly affect calculations of the real part of the complex modulus.

The effect of η on the damping of the composite sandwich beam given by the logarithmic decrement δ was studied for the elementary beam solution and for the case where deformation owing to shear was considered. The numerical solutions were plotted as δ against h/λ for four values of η ranging from 0.25 to 1.0; some typical curves are presented in Figs. 4 through 7. In these curves, the elementary solution is not plotted but is represented by a horizontal line intersecting the curves shown at $h/\lambda = 0$. The elementary solution gives a logarithmic decrement or composite damping that

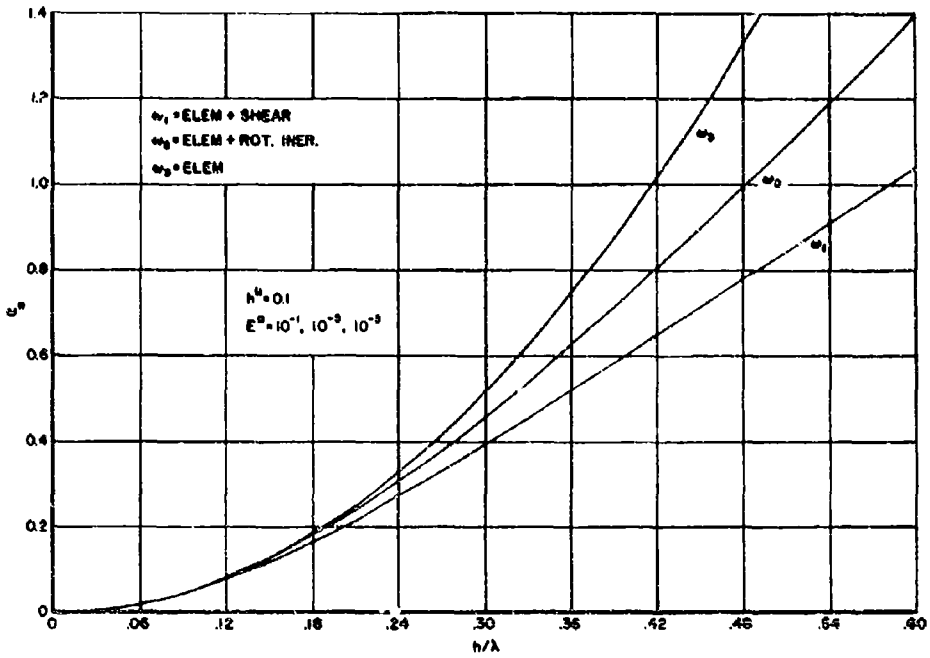

Fig. 2. Frequency spectrum for $h^* = 0.1$, $E^* = 10^{-1}, 10^{-3}, 10^{-5}$

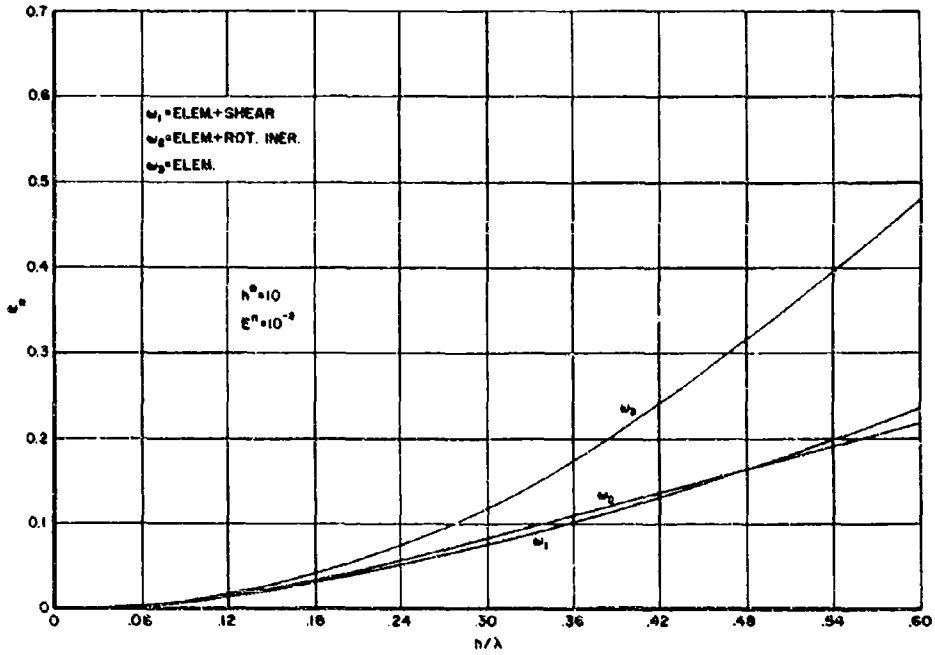

Fig. 3. Frequency spectrum for $h^* = 10$, $E^* = 10^{-3}$

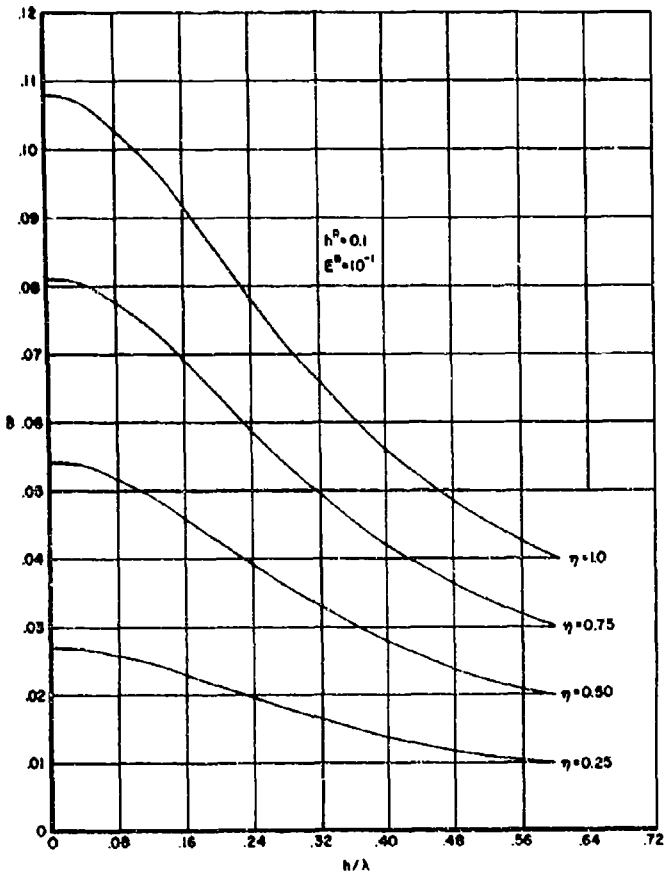

Fig. 4. Logarithmic decrement vs h/λ for $h^* = 0.1$, $E^* = 10^{-1}$

is independent of frequency, whereas the inclusion of effects of shear deformation makes it frequency dependent. It can be seen from these curves that the effects of shear deformation on the composite damping become important for h/λ values greater than 0.1 and even less for certain geometries.

To study the effects of the various parameters on the damping of a composite beam, calculations were carried out and curves were plotted of δ/E^*h^* against the thickness ratio h^* for two specific values of h/λ ($h/\lambda = 0, 0.1$) for a typical value of η of 0.333. The curves for $h/\lambda = 0$ correspond to the elementary beam solution; the curves for $h/\lambda = 0.1$ are for higher modes of flexural vibration or for very short thick beams. The plots are presented as Fig. 8, and each curve gives a measure of the composite damping per thickness of the damping layer as a function of thickness of damping layer for a specific value of E^*. For a relatively stiff damping layer having $E^* = 10^{-1}$, the optimum thickness ratio is about unity while for decreasing E^* ratios the optimum damping of composite per volume of damping layer corresponds to increasingly thicker layers. It can be seen from the curves that the inclusion of the effects of deformation owing to shear had little or no effect on these conclusions with respect to the optimization of damping by varying the thickness of the damping layer.

Finally, a comparison was made of the value of η calculated from the Oberst beam experiment which was based on frequency and composite beam damping observations; the elementary beam equations were used in the experiment with the value of η calculated for the more exact equations which take into

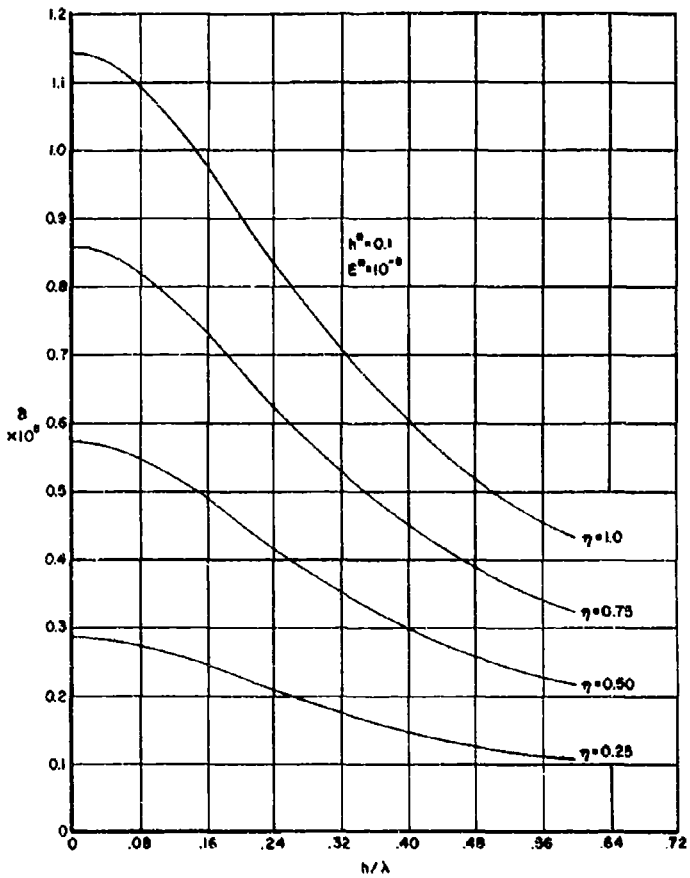

Fig. 5. Logarithmic decrement vs h/λ for $h^* = 0.1$, $E^* = 10^{-5}$

account the deformations owing to shear. Calculations of η as a function of δ were carried out using the two theories for various values of E^* and h^* for a range of frequencies corresponding to h/λ values between 0 and 0.2. The results are presented as Figs. 9 through 13 in the form of a set of curves of the ratio η_{calc}/η_{act} where η_{calc} is the value of η calculated from the elementary beam equations and η_{act} is the "actual" or more exact value as calculated from the equations that consider the effects of shear deformation. The nondimensional frequency ω^* is the ratio of actual ω to a fictitious thickness shear frequency Ω_1 given by Eq. (18). The calculations were found to be insensitive to the actual value of η since δ was related to η almost linearly for most of the combinations of parameters. The calculations were carried out for the specific value of $\eta_{act} = 0.1$ but are approximately valid for η values up to unity.

It is seen from the curves in Figs. 9 through 13 that the calculated value of η from an Oberst beam-type experiment using the elementary beam theory equations may be in error at frequencies that are within the range of those encountered in laboratory experiments of this type. The degree of error depends not only on the frequency or the h/λ ratio but on the E^* and h^* ratios in the particular experiment. The error increases with increasing thickness and decreasing modulus of the damping layer. The curves presented are not "exact" in that the equations used are only higher order approximations. In addition the difference in the calculated frequencies between the "exact" and elementary solutions is not considered. They are presented to aid in the assessment of the validity of the assumption that shear deformation may be neglected in the experimental determination of the complex modulus of a material

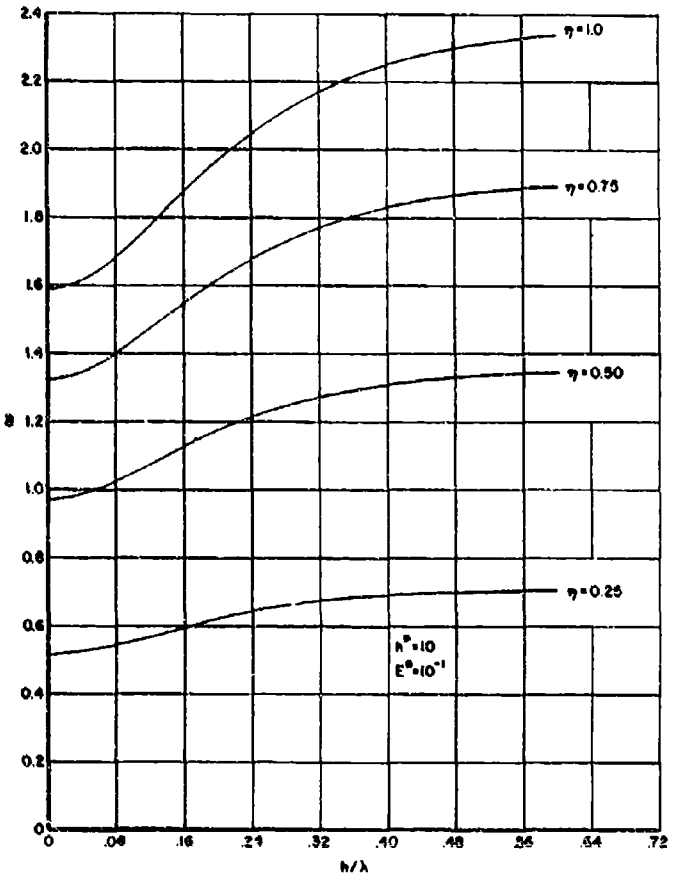

Fig. 6. Logaritumic decrement vs h/λ for $h^* = 10$, $E^* = 10^{-1}$

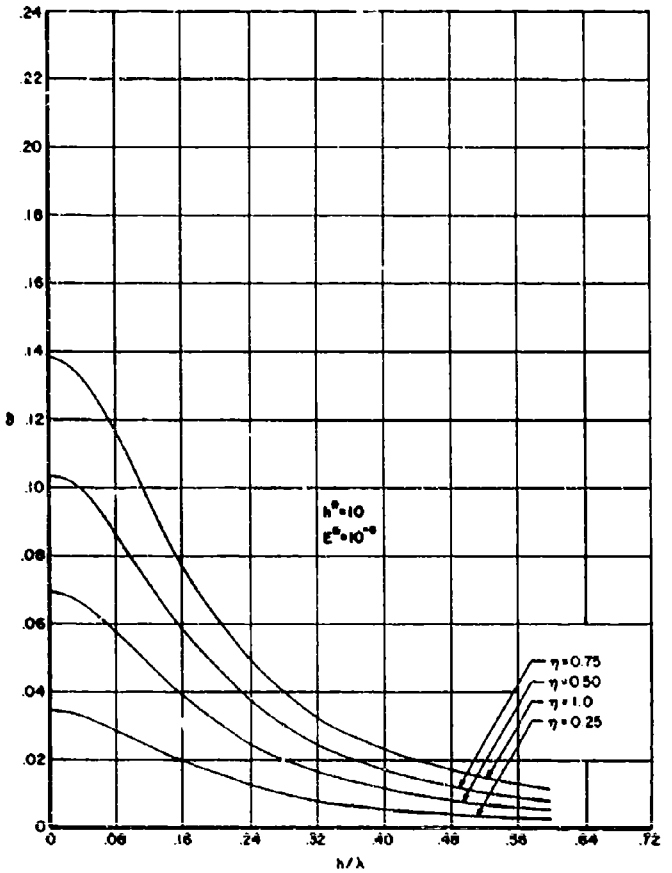

Fig. 7. Logarithmic decrement vs h/λ for $h^* = 10$, $E^* = 10^{-5}$

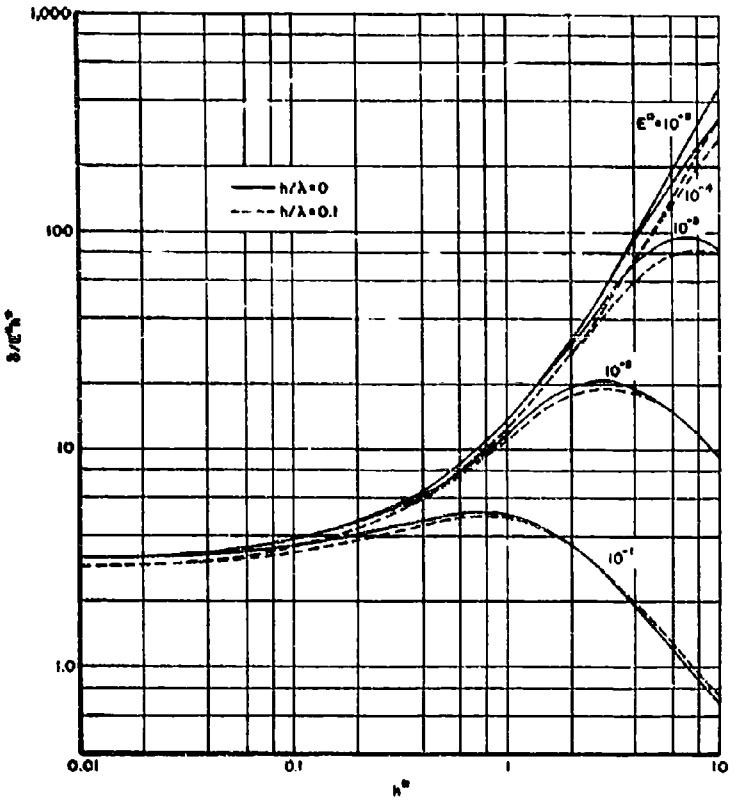

Fig. 8. Damping of composite beam as a function of thickness of damping layer

using the Oberst beam technique. An approximate method for correcting calculated η values follows:

1. Record the frequency and damping in the composite beam.

2. Calculate the real and imaginary portions of the complex modulus of the damping layer (elementary beam equations).

3. Calculate the reference frequency Ω_1 for the geometry used.

4. Calculate $\tilde{\omega}^*$.

5. Locate the point on the appropriate curve corresponding to the experimental parameters by interpolation (approximate).

6. Record the value η_{calc}/η_{act} and correct the calculated η by dividing by this value.

CONCLUSIONS

The results of calculations based on theories that consider the effects of shear deformation and rotatory inertia for a two-layered viscoelastic-elastic sandwich beam indicate that the elementary beam theory commonly used is adequate for the real modulus and the frequency calculations, while rotatory inertia may be neglected for all calculations involving flexural vibrations. For calculations involving the damping of the viscoelastic material and the composite beam, the effects of shear deformation must be considered for short thick beams and higher flexural modes of vibrations, that is, when the wavelength is less than 10 times the thickness. Finally, it appears that the largest errors in calculations occur for beams with increasingly thick damping layers of relatively soft materials. The effects of shear deformation must therefore be considered and evaluated before using the Oberst beam complex modulus

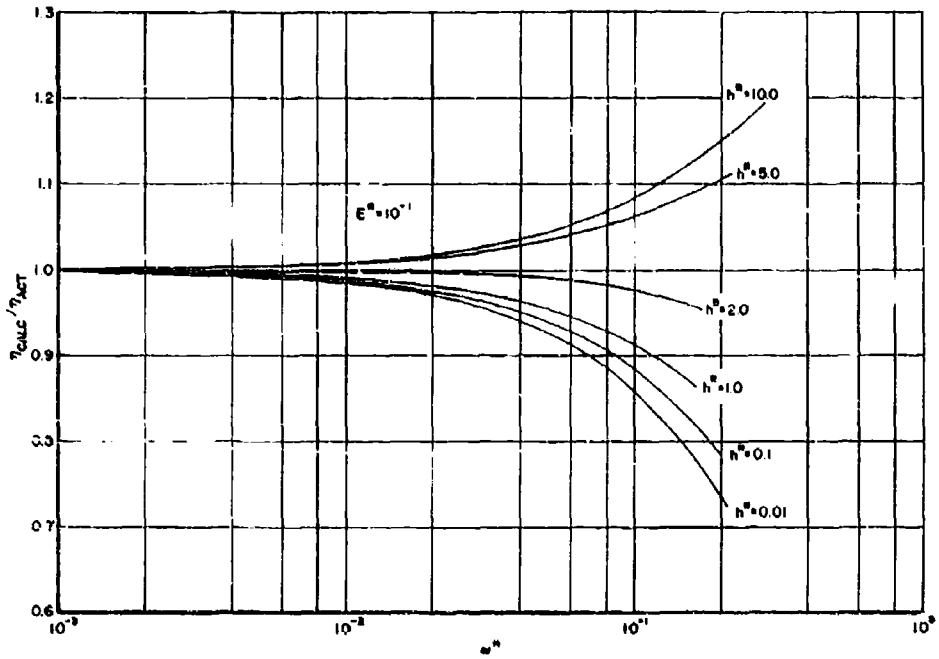

Fig. 9. Error in damping calculations using elementary beam theory for $E^* = 10^{-1}$

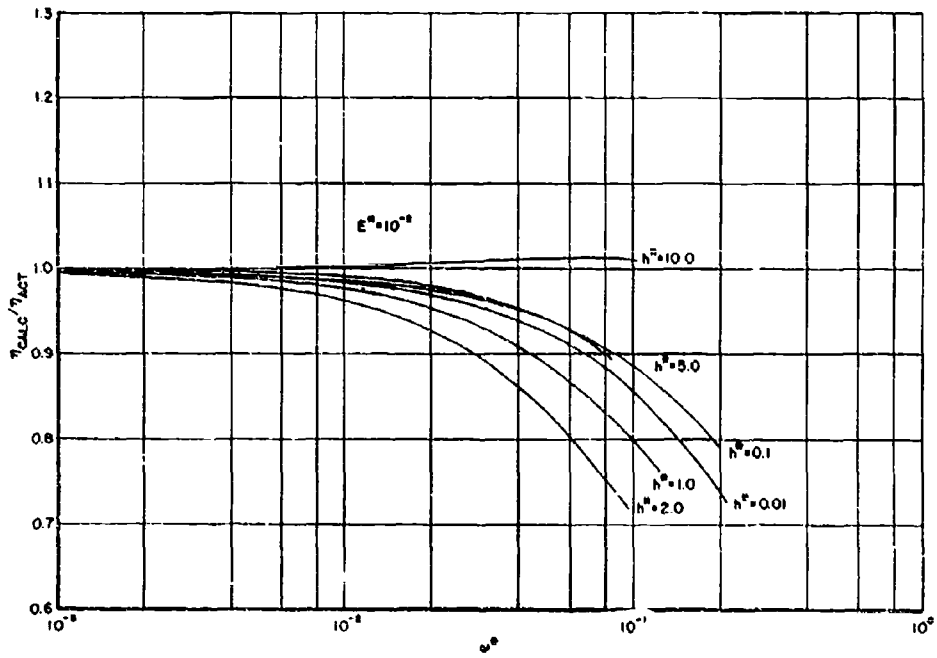

Fig. 10. Error in damping calculations using elementary beam theory for $E^* = 10^{-2}$

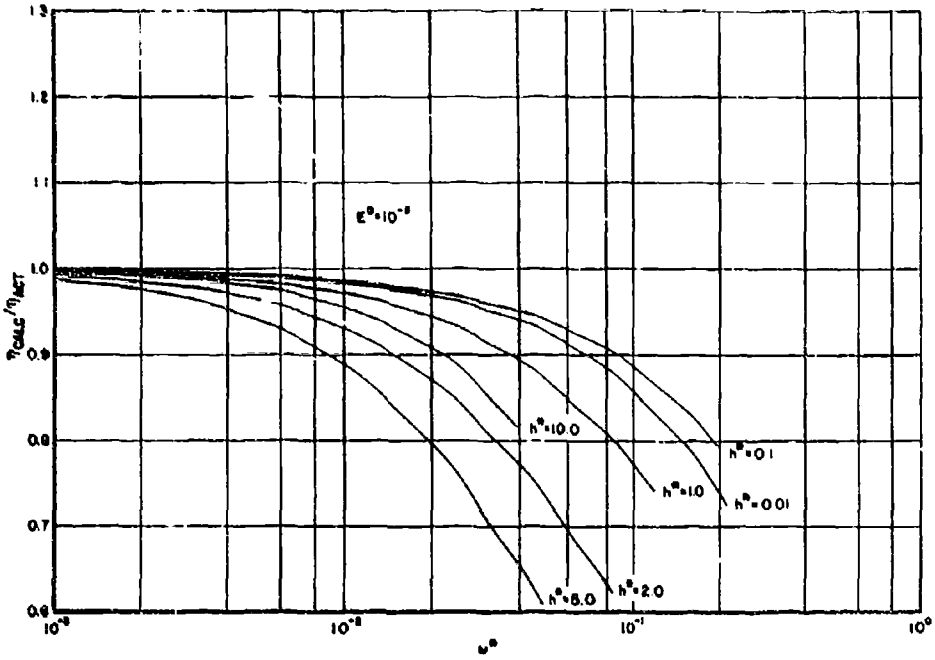

Fig. 11. Error in damping calculation using elementary beam theory for $E^* = 10^{-3}$

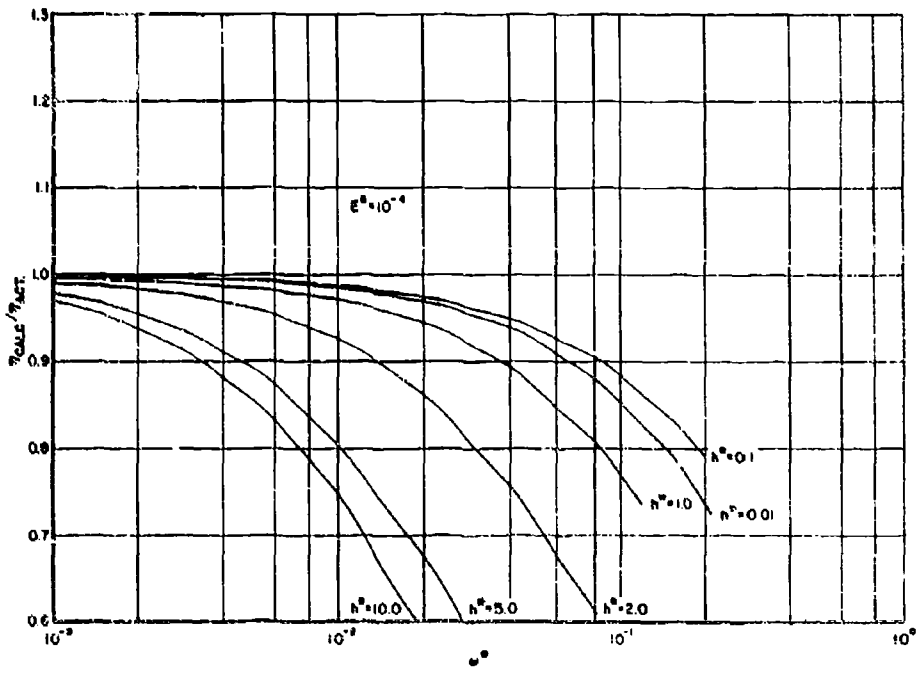

Fig. 12. Error in damping calculations using elementary beam theory for $E^* = 10^{-4}$

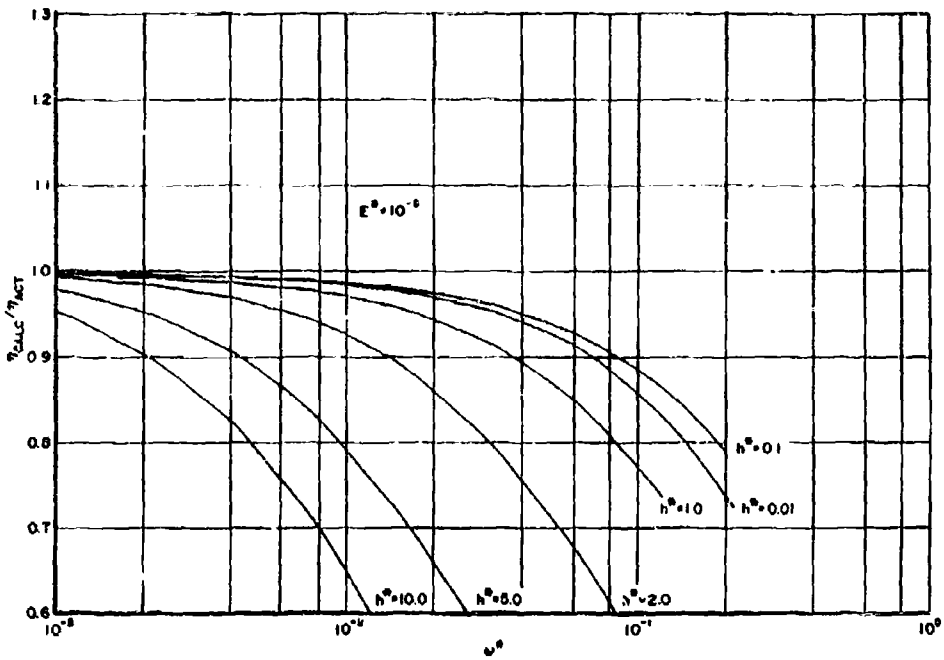

Fig. 13. Error in damping calculations using elementary beam theory for $E^* = 10^{-5}$

technique for the determination of the damping properties of viscoelastic materials. For other geometries involving three or more layers, a similar analysis would have to be applied before assumptions could be made regarding the importance of considering shear deformation in deriving the equations of motion.

ACKNOWLEDGMENTS

The author would like to express his appreciation to D. I. G. Jones and A. D. Nashif for their many helpful discussions and to Connie Gillmore for the typing of the manuscript. The work described in this paper was carried out under Project No. 7351, "Metallic Materials," Task No. 735106, "Behavior of Metals." This paper may be reproduced for purposes of the U.S. Government.

REFERENCES

1. J. W. S. Rayleigh, The Theory of Sound, Vol. II (Dover Publications, New York), 1945, p. 293

2. S. Timoshenko, Vibration Problems in Engineering, 3rd ed. (D. Van Nostrand Co., New York), 1955, p. 330

3. Yi-Yuan Yu, "A New Theory of Elastic Sandwich Plates — One Dimensional Case," J. Appl. Mech. 26:415-421 (1959)

4. T. Nicholas and R. A. Heller, "Determination of the Complex Shear Modulus of a Filled Elastomer from a Vibrating Sandwich Beam," Experimental Mechanics 7:110-116, 1967

5. H. Oberst, "Über die Dämfung der Biegeschwingungen dünner Bleche durch fest haftende Belage," Acustica (Acustische Beihefte), 2(2):181-194 (1952)

6. F. Schwarzl, "Forced Bending and Extensional Vibrations of a Two-Layer Compound Linear Viscoelastic Beam," Acustica, 8: 164-172 (1958)

* * *

METHODS OF DAMPING VERY STIFF STRUCTURAL MEMBERS

H. T. Miller
Lord Manufacturing Company
Erie, Pennsylvania

The problem of damping any structure becomes increasingly difficult as the stiffness of the structure increases. Practical methods have been worked out and parts have been constructed and tested for providing a significant amount of damping (composite loss factors on the order of 0.10) for very stiff structures. The damping can be accomplished through proper design of the structure, if possible, or through the use of the spaced-damping concept. This paper will present theory and test data on both of these damping methods.

Damping can be added to any structure to reduce the effects of a resonant response. The specific reasons for wanting to accomplish this are many. Control of resonant amplitudes limits motions and stresses in the structure, improving fatigue life for sustained disturbances, and reducing the damaging effects of shock by limiting the amplitude and the number of high stress cycles in the residual response. In submarines and surface ships, damping may be helpful in reducing structure-borne vibration that causes self and radiated noise.

Damping is achieved by adding a lossy material, usually in the form of some elastomer, to the structure. These lossy materials have the ability to turn part of the energy required to deform them into heat. A simple way of adding damping is to adhesively bond a layer of damping material to the structure. In this manner, when the structure bends, the damping material deforms in extension and compression, thus dissipating some of the energy it took to bend the structure and the material. The amount of energy that is dissipated is a function of the amount of energy required to deform the structure compared with that needed to deform the damping material. Obviously, if it takes 99 percent of the available energy to deform the structure and only 1 percent to deform the damping material, no more than 1 percent of the original energy can be dissipated. This would be the case if the damping material were completely lossy and dissipated all the energy it took to deform it. Thus, it is desirable to have the damping material control as much as possible the deformation of the structure being damped. This paper will discuss methods of accomplishing this.

We can conclude that damping the bending waves in a structure becomes more difficult as the stiffness of the structure increases. In some cases, the stiffness of the structure is so high as to make the application of damping more trouble than it is worth. This can be illustrated by considering the equation for the composite loss factor of a structure being damped by means of a free layer of damping material.

$$\eta_c = \frac{B_3'' + K_3'' H_{31}^2}{B_1 + B_3' + K_3' H_{31}^2} \qquad (1)$$

where

η_c = composite loss factor of structure

$B_1 = E_1 I_1$

E_1 = Young's modulus of structure being damped

I_1 = moment of inertia of structure being damped around its own neutral axis

$B_3' = E_3' I_3$

E_3' = real part of Young's modulus of damping material being used

I_3 = moment of inertia of damping layer around its own neutral axis

$K_3' = E_3' A_3$

A_3 = cross-section area of damping layer

$D_3' = E_3'' I_3$

E_3'' = imaginary part of Young's modulus of damping layer

$K_3'' = E_3'' A_3$

H_{31} = distance between neutral axis of damping layer and neutral axis of structure being damped.

The bending stiffness of the structure appears in the denominator, where an increase will, of course, cause a decrease in the composite loss factor.

The other variables in the equation, except H_{31}, are dependent on either the damping material properties, or its dimensions. During the design of a damping treatment, these variables will be at least partially controlled by factors other than the composite loss factor that is to be achieved. These other factors could be environmental limitations on the type of damping materials available for use, or overall weight, which would limit the amount of damping material that could be used. This leaves H_{31} as the only other variable for the designer to work with to increase damping. The distance H_{31} is thus potentially a very powerful tool that can be used in the design of a damping treatment. Added to this, H_{31} appears in the equation as a squared function, making its impact even greater.

The value of H_{31} can be varied by a designer in several different ways. An obvious way is to place the damping material on the structure in such way that its neutral axis is as far from the neutral axis of the structure as possible. Another way, if possible, is to design the structure itself in such way that it has its neutral axis at a location that is far away from an area that will be available for the application of damping material.

To illustrate these concepts, take the structure of Fig. 1(a) as an example. This figure shows the base structure, essentially a hat section, with a layer of damping material bonded to the top. The damping material is located on the structure at the top where the distance to the neutral axis of bending of the structure is the greatest. The damping layer is 0.150-in. thick and runs the entire length of the beam. With the damping treatment as shown, the value of the normalized composite loss factor (η/η_3) is 0.050 (η_3 is the loss factor of the damping material). The Young's modulus of the damping material was assumed to be 5.0×10^5 psi and the base structure is made from aluminum.

Now, consider the configuration in Fig. 1(b). The base structure is the same, but the damping layer has been modified. The same amount of damping material has been used, but the width of the layer has been cut in half and the thickness doubled compared with the damping layer of Fig. 1(a). This modification increases the distance between the neutral axis of the base and that of the damping layer and also increases the moment of inertia of the damping layer. The structure has a normalized composite loss factor of 0.067. This constitutes an increase of about 35 percent over the structure of Fig. 1(a).

If one has the freedom to modify the base structure, even more can be done. Figure 1(c) is an example of this. The structure is like the previous one, except that material has been removed from the top and added to the flanges at the bottom of the structure. This lowers the neutral axis of the structure toward the base. The damping material configuration used is the same as in Fig. 1(b). The bending stiffness of this structure compared with the first one is only slightly reduced (from 1.46×10^5 to 1.28×10^5). This new structure has a normalized composite loss factor of 0.12, more than double that of the first structure.

In this example, we have three different configurations that will structurally do about the same job. However, from the standpoint of reduced vibrations, the third one will do the best job. Comparing one and two, it can be seen that choosing the best location and configuration for the damping layer causes an improvement. However, if one designed the original structure with the possibility of damping in mind as in the third case, the best results are achieved. However, it may at times be impossible or impractical to try these variations (especially changing the base structure), so that it becomes necessary to have other ways of accomplishing the same results.

There is another way to increase the distance between the neutral axis of the structure to be damped and the neutral axis of the damping layer. This is through the use of a spacing layer between the base structure and the damping layer (Fig. 2). This layer spaces the damping material away from the base and, thus, increases H_{31}. The general characteristics of a spacing layer are low extensional stiffness and high shear stiffness. The low extensional stiffness insures that the spacing layer will not add

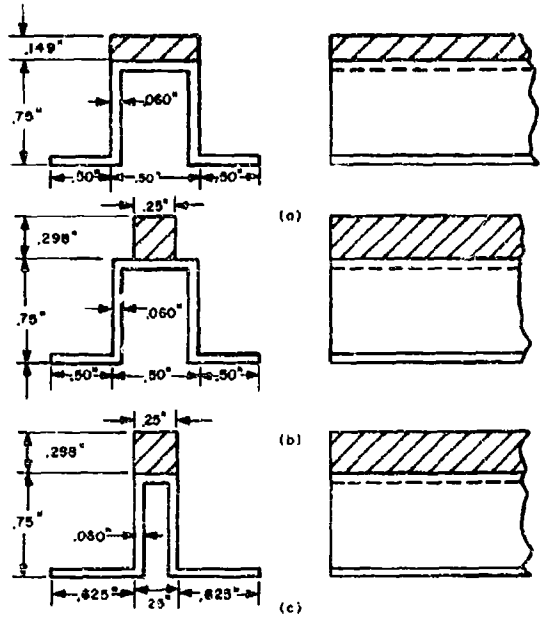

Fig. 1. Damped sections

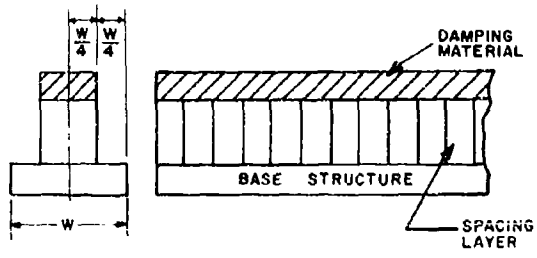

Fig. 2. General spaced damping treatment

any bending rigidity to the base structure, making it more difficult to damp. The high shear stiffness insures that the bending strains in the base will be coupled into the damping layer.

Figure 3 shows typical data for a spaced damping treatment. The configuration from which these measurements were made appears in Fig. 2. The damping material used is the one that conforms to Mil-P-23653A, Class II. The spacing layer has a thickness of 1 in and the base bar is 0.25-in. thick. Tests on the spaced treatment show that the composite loss is flat with frequency up to about 500 Hz with a value of 0.45. Above 500 Hz, the loss factor then falls with increasing frequency. Also shown in Fig. 3 is the loss factor vs frequency data from a test bar that has the same amount of material attached directly to the base bar. This comparison shows the values of composite loss factor of the spaced treatment to be higher than the total frequency range of the test.

Generally, all spaced damping treatments have the type of composite loss factor vs frequency curve shown in Fig. 3. All will have an area of constant composite loss factor at lower frequencies and an area where loss factor falls with increasing frequency. The flat area of the curve is where the spacer is acting as an ideal

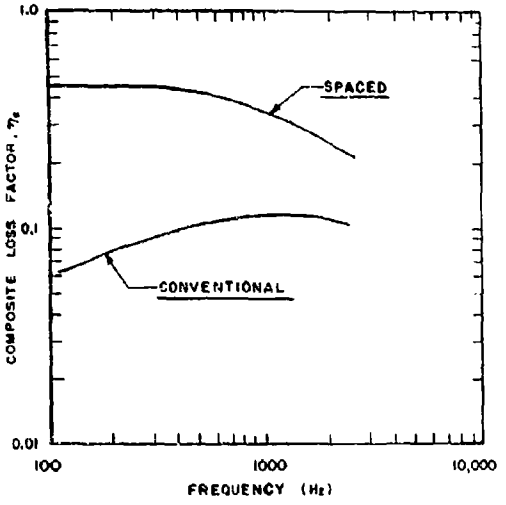

Fig. 3. Composite loss factor vs frequency for spaced treatment compared with conventional treatment

one (that is, infinite shear stiffness, zero extensional stiffness). The falling portion is a result of the actual finite shear stiffness of the spacing layer. At the lower frequencies, the composite loss factor will be given by Eq. (1). This equation assumes perfect coupling between the base structure and the damping layer which is what an ideal space accomplishes. With perfect coupling, the entire configuration bends as a unit about some composite neutral axis. By doing this, the damping layer makes the greatest possible contribution to the overall bending stiffness of the damping material and base combination and, thus, produces the highest damping. At the higher frequencies, neither the assumption nor the equation continues to hold. At the point where the loss factor starts to fall, the damping layer is becoming uncoupled from the base. If the frequency is increased far enough, a condition is reached where both the damping layer and the base are bending about their own neutral axis independent of each other. At this condition, the damping layer will have very little effect on the bending of the base structure. The frequency at which the decoupling process starts is controlled to a large extent by the shear stiffness of the spacer. If the shear stiffness of the spacer is infinite (ideal spacer), the uncoupling never occurs no matter how high the frequency. However, an infinite shear stiffness can never be achieved in practice. One must try to get the shear stiffness as high as possible within the limits of a design.

We can now take a look at what magnitudes of loss factors can be achieved with spaced damping. If we assume that we are damping a beam-like structure and that the damping layer cross-section is rectangular, we can rewrite Eq. (1) as

$$\eta_c = \frac{\eta_3 \left[\frac{W_3 H_3^3}{12} + W_3 H_3 H_{31}^2\right]}{\frac{E_1}{E_3} I_1 + \frac{W_3 H_3^2}{12} + W_3 H_3 H_{31}^2} \qquad (2)$$

where

η_3 = loss factor of damping material

W_3 = width of damping layer

H_3 = thickness of damping layer.

Figure 4 shows composite loss factor (η_c) vs moment of inertia of the base structure (I_1) for various values of H_{31} constructed from the above equation. For the construction of this curve, the damping layer width was taken to be the same as the base and 0.50 in. thick. Damping material properties of $E_3 = 4.50 \times 10^5$ psi and $\eta_3 = 0.45$ were assumed with a steel-base structure.

Figure 4 may be interpreted as follows: Taking a 4-in.-sq tube as an example, the moment of inertia of this structure is 1.17 in.^{3}. (This is a per unit width value.) If we look at the figure, we can find the composite loss factor associated with the various values of H_{31}. It is known that the neutral axis of bending of a square tube is at its center and the neutral axis of the damping layer is also at its center. This says that for a spaced damping treatment of the beam, H_{31} is equal to one-half the thickness of the beam plus one-half the thickness of the damping layer, plus the total thickness of the spacer, or in this case:

$$H_{31} = 2.5 \text{ in.} + H_s$$

H_s = thickness of spacer.

Thus, if a spacer 1 in. thick is used, H_{31} is 3.5 in. and the composite loss factor is 0.035. The type of plot shown in Fig. 4 may be developed for any damping material and any configuration of the damping layer. The plot will give a designer an idea of what magnitude of loss factor he can hope to achieve. It will not, however, tell when the loss factor will start to fall with frequency. This is a separate problem.

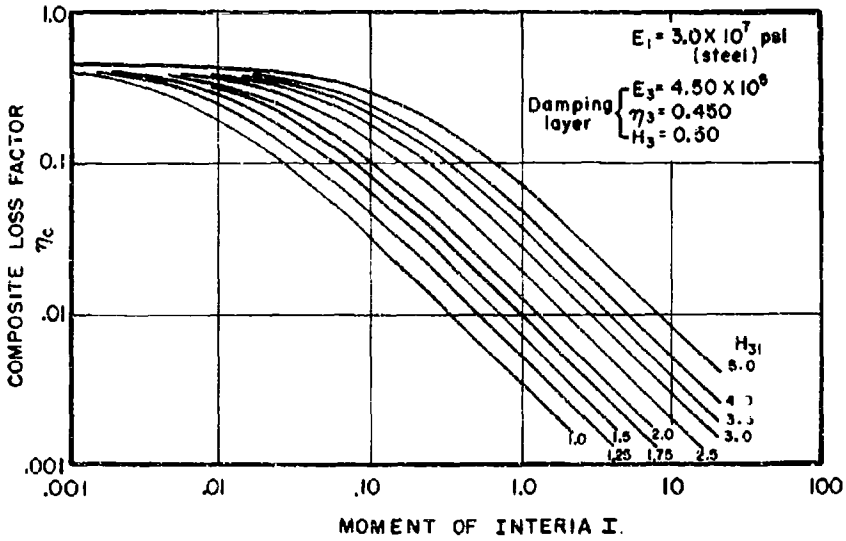

Fig. 4. Composite loss factor vs moment of inertia of structure being damped for various values of H_{31} (distance between neutral axis of layers)

We now come to the problem of what kinds of material can be used as a spacer layer. It has been suggested that such items as honeycomb or like materials be used as spacers. However, we have found that for most applications the shear stiffness of honeycomb is not high enough to maintain the coupling between damping material and base to high enough frequencies. The use of these materials is all right for some lower frequency applications (less than 200 Hz), but is insufficient when high damping is needed over a broad frequency range.

One class of materials we have found that can be used as spacers are structural sections such as tees or channels. These sections have high shear stiffness and also have suitable areas for the attachment of damping material.. However, these sections in their normal form also have a high extensional or bending stiffness. This problem can be solved by cutting the sections into short lengths before installing them in the damping treatment. The idea here is to make the length of each individual spacer shorter than the wavelength of the bending waves traveling in the structure. Selecting the length of each spacer is more involved than just considering wavelength. The tradeoff between maintaining a high shear stiffness and keeping the extensional stiffness low must be considered. Figure 5 shows an example of a spaced damping treatment optimized for a particular structure. The spacers are made from tee sections. The tees have been cut into 2-in. lengths and are attached into the treatment with a 0.25-in. gap between each. The width of this gap is critical and is involved with the tradeoff of high shear stiffness and low extensional stiffness in the spacer layer. The loss factor vs frequency curve is shown in Fig. 3. Channel sections can also be used as spacers, and the design problem is similar to the tee sections.

Normal extensional or free layer damping treatments may be difficult and time consuming to apply. The surfaces to which they are to be applied must be cleaned and specially prepared to insure a good bond between the structure and the damping material. In some locations it will also be necessary to construct special fixtures to hold the damping material in place while the adhesive is curing.

Spaced damping treatments offer a big advantage because they can be welded to the structure being damped with no degradation of the damping material. The entire damping treatment can be constructed under controlled conditions at a location remote from the final application area, brought to this area and simply welded in place. The special preparation for

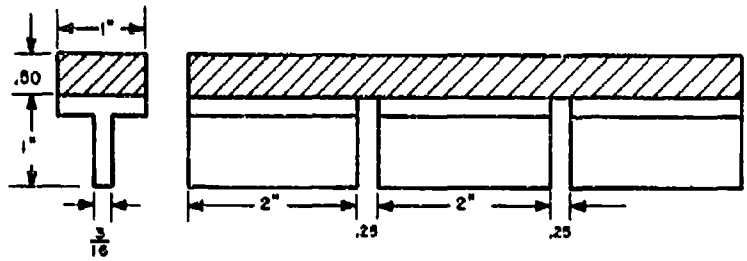

Fig. 5. Tee section spaced damping treatment

bonding of the surfaces of the structure being damped is eliminated. Also, the possible need for fixturing to hold the treatment in place while the adhesive is curing is eliminated. These facts make spaced damping treatments faster and cheaper to apply.

Figure 6 shows loss factor vs frequency data for a spaced damping treatment applied to a length of 1.5 square tubing. Also shown for comparison purposes is loss factor vs frequency results from the same tube damped by a layer of damping material the same size as that used in the spaced treatment. These samples were tested by hanging them in a free-free condition, attaching a small shaker to one end, and recording the response with an accelerometer at the opposite end. The composite loss factor was determined from the relationship $\eta_c = \Delta F/F_n$ where F_n is natural frequency and ΔF is frequency bandwidth of the half-power points. The spacing layer used in the sample was short lengths of 1-in. high, 1.5-in. wide channel. The damping material covered the top of the channels and was 0.50 in. thick. As shown by the data, the composite loss factors of the spaced treatment are about four times higher than those of the simple one layer treatment.

So far all the spaced damping treatments we have discussed are one-dimensional treatments. That is, they efficiently damp bending waves in only one direction. However, in many applications it is desirable to damp structures that have bending waves traveling in two directions. For instance, any plate has waves traveling in two directions. We have found that applying the spaced damping treatments, previously discussed, in two-dimensional patterns will do a good job of damping these structures. Figure 7 is an example of this. This figure shows a 2 by 3 ft, 0.25-in. steel plate with the damping treatment applied. The strips of spaced damping are applied in a checkerboard pattern on approximately 8-in. centers. The damping treatment used is the one made from the tee

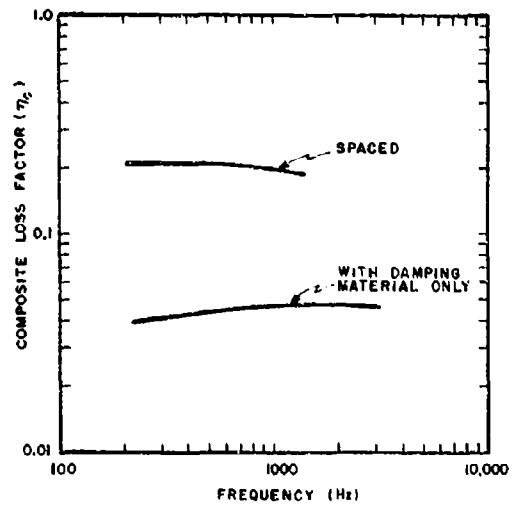

Fig. 6. Comparison of loss factor of 1.5-in.-sq-tube treated with spaced damping and with extensional damping

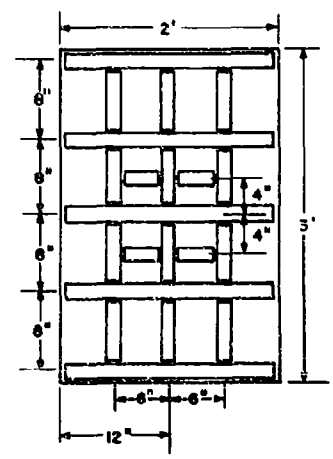

Fig. 7. Two-dimensional spaced damping treatment

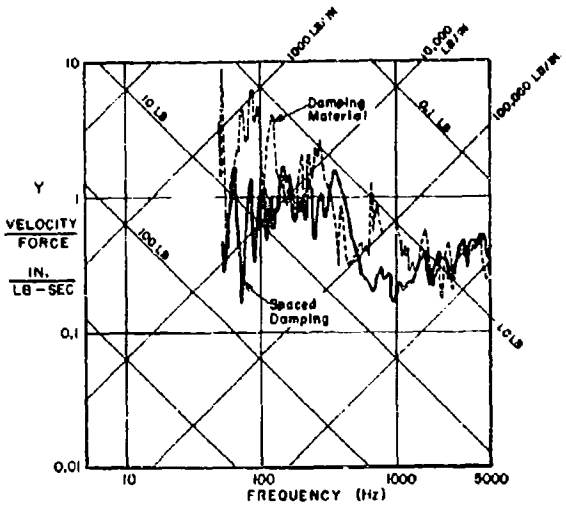

Fig. 8. Driving point admittance of spaced damping treatment as compared to complete damping material coverage

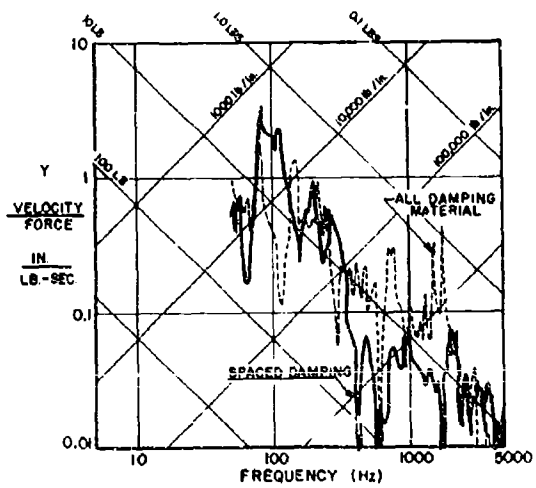

Fig. 9. Transfer admittance of spaced damping treatment compared to complete damping material coverage

section (Fig. 5). Figures 8 and 9 show the driving point admittance and corner-to-corner transfer admittance for the configuration shown in Fig. 8 as compared with data from the same plate covered with 4.5 lb/ft^2 of Class II Navy damping tiles. As can be seen, the checkerboard pattern is at least equivalent to the complete coverage treatment and in many areas is better. The spaced damping treatment of this plate actually weighs less than the all damping material treatment (about 4.0 lb/ft^2 as compared with 4.5 lb/ft^2). Spacing layers that are optimized to work in two directions may also be built. These, however, are more difficult to work with and will not be discussed here.

This paper has shown methods of damping the bending waves in structures that are quite stiff. The damping may be accomplished through optimum positioning of the damping

material or through the use of spaced damping. This technique offers the designer improved damper for a given weight of treatment and greater flexibility in installation.

BIBLIOGRAPHY

Bolt, Beranek & Newman, Inc., "Damping of Flexural Vibrations in Plates by Free and Constrained Visco-Elastic Layers," Rept. No. 632, May 1959

Ungar, E. E., "Loss Factors of Viscoelastically Damped Beam Structures," JASA, 34(8): 1082-1089 (July-Dec. 1962)

DISCUSSION

Mr. Kraft (Univ. Dayton): Depending upon the particular application, it seems that you are paying a considerable penalty in weight in using a spaced damping treatment like this as opposed to some other type of treatment that could be used.

Mr. Miller: I guess I neglected to mention that the plate that was covered with the spaced treatment was actually done with less weight. A plate with the spaced treatment weighs less than if the plate were entirely covered with damping material of the same thickness.

* * *

THE OPTIMUM DESIGN OF FIVE-PLY VISCOELASTIC ISOLATION FLEXURES FOR POINT-INERTIA LOADING

Darrell A. Frohrib
Mechanical Engineering Department
University of Minnesota

The engineering theory for the interaction between elastic and viscoelastic strata developed by Kerwin and DiTaranto is applied to the inertialess flexure treated on both surfaces with constrained viscoelastic layers. The absolute transmissibility expression is developed; equivalence to the elastically supported dashpot model is discussed for certain conditions on the loss ratio G_2/G_1 and surface constraining layer to elastic properties of the viscoelastic layer. Design equations are presented to expedite calculation of size and shape properties of the flexure to optimize response at the fixed point.

INTRODUCTION

The use of viscoelastic materials as damping mechanisms in engineering practice has been studied extensively in recent years. An understanding of the dynamical properties of polymers [1], coupled with knowledge of the response of treated engineering structures [2-4], has permitted a prediction of the design approach to the use of viscoelastic materials in certain cases. Until Kerwin's and DiTaranto's work, the interactions between the constraining elastic and the viscoelastic media were largely unknown. Current investigations appear to be largely directed toward the response of beams and plates with distributed mass and elasticity, when treated with viscoelastic applications.

In the case of a viscoelastically treated support subjected to point-inertia loading (Fig. 1), one can anticipate the support to act as the discrete-element model including an elastically supported dashpot, as studied by Ruzicka and Cavanaugh (Fig. 2). A quantitative understanding of the equivalence between the model parameters k, N, and c and those of a strata-like treated flexure appear not to have been clearly defined. Furthermore, it is well known that the complex modulus of viscoelastic materials is frequency sensitive. Therefore, a clear understanding of the single-degree-of-freedom transmissibility expression and its equivalence to the elastically supported dashpot model should be established to enable prediction of response over a wide frequency spectrum. The purpose of this paper is to develop these expressions in the framework of DiTaranto's theory and to set forth conditions under which the general statement is approximated by the discrete-element model.

NOMENCLATURE

A_i	Cross-sectional area of ith layer
B	$(EI)_1 + (EI)_3 + (EI)_5$
b	Flexure width
C_i's	Deflection amplitude coefficients
c	Dashpot viscous damping constant
E_i	Modulus of elasticity of ith layer
F_i	Axial force in ith elastic layer
G^*, G_1, G_2	Shear moduli of viscoelastic layers
H_i	Half-thickness of ith layer
I_i	Area moment of inertia about individual neutral axis of ith layer
i	Imaginary number
k	Stiffness constant of linear spring

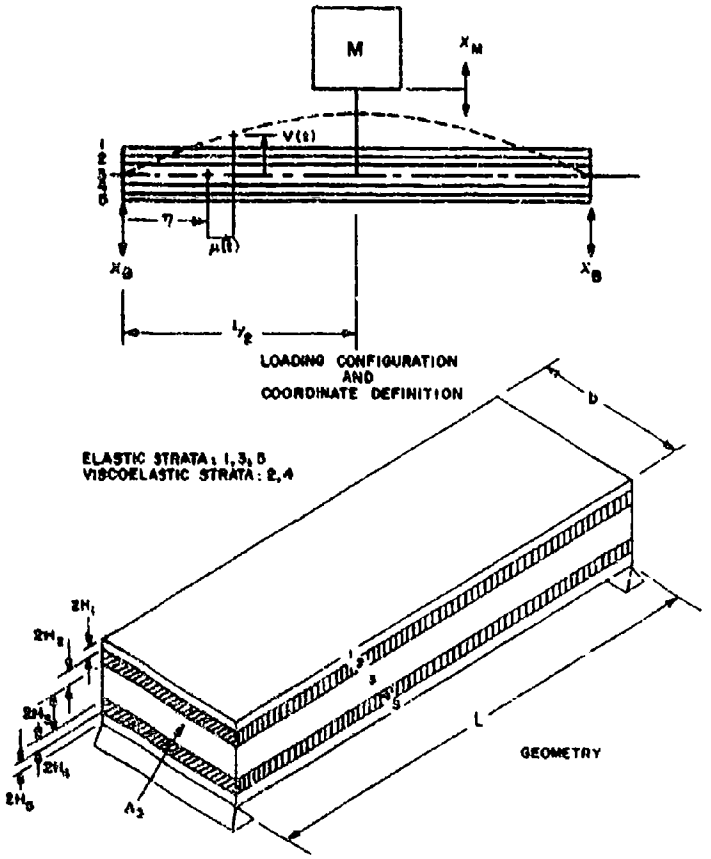

Fig. 1. Viscoelastically treated support subjected to point-inertia loading

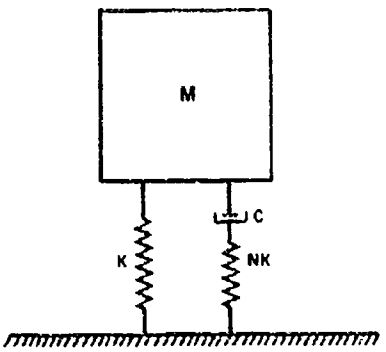

Fig. 2. Elastically supported dashpot model

L Flexure length

M Mass at flexure midspan

N Spring stiffness ratio of linear model

q, q^*, q^{**} Frequency ratios

R $bG^*/(2H_2(EA)_1)$

T_A, T_R Absolute and relative transmissibilities

u_i Axial dynamic displacement of centerline of ith elastic layer

Δu $u_1 - u_5$

U, V Functions of exponentials of viscoelastic layer stiffnesses

v Transverse dynamic displacement of flexure

x_M Output displacement response of flexure at mass mounting location

x_B Input displacement at flexure ends

α $(EA)_1 s^2 / (2B)$

β Square root of amplitude coefficient, Eq. (4)

γ $2(H_1 + 2H_2 + H_3)$

ζ Percent of critical damping

η Axial reference position of element in flexure

θ $\tan^{-1}(G_2/G_1)$

$\lambda, \bar{\lambda}$ Natural frequencies, rad/sec

μ $\beta L/2$

ϕ Flexure dynamic slope

ω Input frequency, rad/sec

ANALYSIS

Equations of Motion

The analysis is developed for a model of symmetric cross section, composed of a parent beam and two identical surface applications of viscoelastic material and constraining layers. ($H_1 = H_5$, $H_2 = H_4$, $E_1 = E_5$, $G_2^* = G_4^*$ — see Fig. 1.) Extending DiTaranto's engineering theory to this five-ply inertialess flexure, the moment-deflection equilibrium equation can be written in terms of beam curvature, ϕ, and the relative axial motion between outer strata centerlines, Δu, as follows:

$$M = (EA)_1 \frac{s^2}{2} (\Delta u)' + B\phi' \qquad (1)$$

where

$$(\ )' = \frac{d}{d\eta}(\ ).$$

From geometry, the auxiliary equation for the five-ply symmetric section becomes

$$\phi = \frac{1}{s}\Delta u - \frac{1}{Rs}(\Delta u)'' \qquad (2)$$

Combining Eqs. (1) and (2) into one equation in the variable, Δu,

$$(\Delta u)'' - \frac{4G^*}{2H_2(EA)_1}\left[1 + \frac{(EA)_1}{B}\frac{s^2}{2}\right](\Delta u)''' = 0. \qquad (3)$$

Solution

Defining the complex square root of the coefficient of the third derivative term as $\beta = \beta_1 + i\beta_2$, the equation has the general solution

$$\Delta u = C_1 + C_2\eta + C_3\eta^2 + C_4 \exp[-(\beta_1 + i\beta_2)\eta] + C_5 \exp[+(\beta_1 + i\beta_2)\eta]. \qquad (4)$$

For the problem under consideration, Eq. (4) is specialized to the following boundary conditions:

Force boundary conditions:

1. Axial forces (F) at $\eta = 0$ on the strata are zero:

$$F_1 = F_5 = (EA)_1 (\Delta u)' \quad \text{(from DiTaranto).}$$

2. Moment (M) is zero on the ends:

$$M(0) = (EA)_1 \frac{s^2}{2}(\Delta u)'\Big|_{\eta=0} + B\phi'\Big|_{\eta=0} = 0.$$

Geometric boundary conditions:

3. Beam deflection $v(0) = 0$.

Symmetry about $\eta = L/2$:

4. $\Delta u(L/2) = 0$.

5. $\phi(L/2) = 0$

From these boundary conditions, the equations governing the C_i's can be shown to be

$$\begin{bmatrix} 0 & 1 & 0 & 1 & 1 \\ 1 & \frac{L}{2} & \left(\frac{L}{2}\right)^2 & \exp\left(-\frac{L}{2}\right) & \exp\left(\frac{L}{2}\right) \\ 1 & \frac{L}{2} & \left[\left(\frac{L}{2}\right)^2 - \frac{2}{R}\right] & \exp\left(-\frac{L}{2}\right)\left(1 - \frac{\beta^2}{R}\right) & \exp\left(\frac{L}{2}\right)\left(1 - \frac{\beta^2}{R}\right) \\ \frac{L}{2} & \frac{1}{2}\left(\frac{L}{2}\right)^2 & \left[\frac{1}{3}\left(\frac{L}{2}\right)^3 - \frac{2}{R}\frac{L}{2}\right] & \left(\frac{L}{2} - \frac{1}{R}\right) & \left(\frac{L}{2} - \frac{1}{R}\right) \\ & & & -\left[1 - \exp\left(-\frac{L}{2}\right)\right] & +\left[1 - \exp\left(\frac{L}{2}\right)\right] \\ 0 & \left[\frac{(EA)_1}{B}\frac{s^2}{2} - 1\right] & 0 & \left\{-\left[\frac{(EA)_1}{B}\frac{s^2}{2} - 1\right]\right. & \left\{-\left[\frac{(EA)_1}{B}\frac{s^2}{2} - 1\right]\right. \\ & & & \left. + \frac{\beta^2}{R}\right\} & \left. - \frac{\beta^2}{R}\right\} \end{bmatrix} \begin{bmatrix} C_1 \\ C_2 \\ C_3 \\ C_4 \\ C_5 \end{bmatrix} = \begin{bmatrix} 0 \\ 0 \\ 0 \\ -\left(\frac{L}{2}\right) \\ 0 \end{bmatrix}$$

As $t \to \infty$, the solution for Δu and its derivatives can be substituted into Eq. (2) and integrated directly to determine the suspension deflection, $v(\eta)$. This deflection is

$$\frac{2\alpha}{\mu^3}\left[\exp(\mu\eta) - \exp(-\mu\eta)\right]$$

$$\frac{v(\eta)}{v(L/2)} = \frac{-\left[\left(\frac{2\alpha}{\mu^2} + 1\right)\left(\frac{\eta}{L/2}\right) - \frac{1}{3}\left(\frac{\eta}{L/2}\right)^3\right] V}{\frac{2\alpha}{\mu^3} U - \left[\frac{2\alpha}{\mu^2} + \frac{2}{3}\right] V} \qquad (5)$$

where

$$U = \exp(\mu) - \exp(-\mu), \qquad V = \exp(\mu) + \exp(-\mu)$$

$$\alpha = \frac{(EA)_1 \lambda^2}{2B}, \qquad \mu = \lambda^2 \frac{L}{2}.$$

Satisfying the shear requirement imposed by the inertia force at midspan, the equation governing the center deflection $v(L/2)$ can be written in terms of end displacement amplitude x_B:

Relative transmissibility T_R

$$= \frac{\frac{\lambda^2}{\mu^2}}{\frac{\lambda^2}{\mu^2} - \frac{1 + \alpha}{1 + i\left[\frac{3}{\mu^2}\left(1 - \frac{U}{\mu V}\right)\right]}} \qquad (6)$$

where $\lambda^2 = (48B/ML^3)$, the undamped natural frequency of the three-beam suspension without shear interaction.

The absolute transmissibility T_A is determined from $x_M = x_B + v(L/2)$ where

$$x_M = X_M \exp(i\lambda t)$$

$$x_B = X_B \exp(i\lambda t)$$

$$v(L/2) = V(L/2) \exp(i\lambda t)$$

and the amplitudes are complex. T_A is

$$T_A = \frac{1}{1 + i\left(\frac{\lambda^2}{\mu^2}\right)\left[1 + \frac{3}{\mu^2}\right]} \qquad (7)$$

The complex quantity in Eq. (7) is a function of μ and represents the effect of the viscoelastic

$$\mu = \lambda^2 \frac{L}{2} = \frac{L}{2}\left[\left(\frac{bG^*}{2H_2(EA)_1}\right)\left(1 + \frac{(EA)_1}{B}\frac{\lambda^2}{2}\right)\right]^{1/2} \qquad (8)$$

where G^* is the complex shear modulus of the layer:

$$G^* = G_1\left(1 + i\frac{G_2}{G_1}\right).$$

Writing μ as

$$\mu_1 = (1 + \alpha)^{1/2}\left(\frac{G_1}{E}\right)^{1/2}\left(\frac{L}{2H_1}\right)^{1/2}\left(\frac{L}{2H_2}\right)^{1/2}$$

$$\cdot\left[1 + \left(\frac{G_2}{G_1}\right)^2\right]^{1/4} \cos\frac{\theta}{2}$$

$$\mu_2 = (1 + \alpha)^{1/2}\left(\frac{G_2}{E}\right)^{1/2}\left(\frac{L}{2H_1}\right)^{1/2}\left(\frac{L}{2H_2}\right)^{1/2}$$

$$\cdot\left[1 + \left(\frac{G_2}{G_1}\right)^2\right]^{1/4} \sin\frac{\theta}{2}$$

where

$$\tan^{-1}\left(\frac{G_2}{G_1}\right)$$

and

$$\frac{\mu_2}{\mu_1} = \left(\frac{G_2}{G_1}\right)^{1/2} \tan\left(\frac{\theta}{2}\right)$$

The elastic effects of the viscoelastic layer are represented by μ_1, the dissipative effects by μ_2.

DISCUSSION OF TRANSMISSIBILITY EQ. (7)

Small Values of μ

[illegible] we regard [illegible] the bracket [illegible] Eq. [illegible] can be shown to approach unity in the limit [illegible]. Then T_A becomes

$$\frac{1}{1 - \frac{\lambda^2}{\mu^2}}$$

the undamped linear oscillator response

Large Values of μ

The bracket { } approaches 0 in the limit $\mu \to \infty$, and T_A becomes

$$T_A \underset{\mu\to\infty}{=} \frac{1}{1 - \left[\frac{\omega^2}{\lambda^2(1+\alpha)}\right]},$$

which again represents linear oscillator response with zero damping. The quantity

$$\lambda^2(1+\alpha) = \frac{48(1+\alpha)(EI_1 + EI_3 + EI_5)}{ML^3}$$

signifies response of the suspension as an integral beam, in which fibers of the three parallel elastic layers respond as a combined cross section which remains plane during distortion.

Intermediate Values of μ

For the general case when $\mu_1 \neq 0$, but $\mu_2 = 0$, bracket { } can be written

$$\left\{\frac{3}{\mu_1^2}\left(1 - \frac{U}{\mu_1 V}\right)\right\} = \frac{3}{\mu_1^3}(\mu_1 - \tanh\mu_1). \qquad (9)$$

The response for zero damping, and for finite and infinite values of μ_1 is then

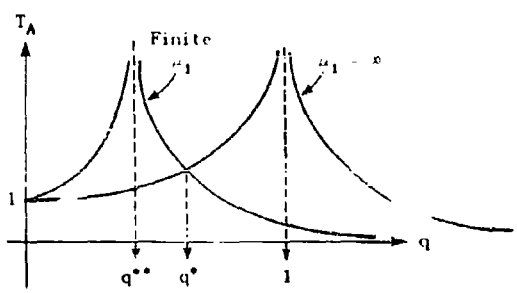

$$q = \frac{\omega^2}{\lambda^2(1+\alpha)},$$

$$q^{**} = \frac{1}{1 + \alpha\frac{a_1}{c_1}},$$

$$q^* = \frac{1}{1 + \frac{1}{2}\alpha\frac{a_1}{c_1}}$$

For nonzero values of μ_2, the absolute transmissibility T_A can be expressed by expanding the bracket { } using the relationships

$$U = \exp\mu_1 \exp i\mu_2 - \exp(-\mu_1)\exp(-i\mu_2)$$

$$= \exp\mu_1\{\cos\mu_2 + i\sin\mu_2\}$$

$$- \exp(-\mu_1)\{\cos\mu_2 - i\sin\mu_2\}$$

and similarly for V; multiplying and collecting terms,

$$T_A = \frac{1}{1 - q\left[1 + \alpha\frac{a+ib}{c+id}\right]} \qquad (10)$$

where

$$a = a_1(\mu_1) + a_2(\mu_1,\mu_2)$$

$$b = b(\mu_1,\mu_2)$$

$$c = c_1(\mu_1) + c_2(\mu_1,\mu_2)$$

$$d = d(\mu_1,\mu_2)$$

$$a_1 = 3[\mu_1 - \tanh\mu_1]$$

$$a_2 = -3\mu_2\tan\mu_2\tanh\mu_1$$

$$b = 3[(\mu_2 - \tan\mu_2) + \mu_2\tanh\mu_1\tan\mu_2]$$

$$c_1 = \mu_1^3$$

$$c_2 = -\mu_1^3\left(\frac{\mu_2}{\mu_1}\right)\left\{3\frac{\mu_2}{\mu_1} + \left[3 - \left(\frac{\mu_2}{\mu_1}\right)^2\right]\tan\mu_2\tanh\mu_1\right\}$$

$$d = \mu_1^3\left\{\left[1 - 3\left(\frac{\mu_2}{\mu_1}\right)^2\right]\tan\mu_2\tanh\mu_1 + \frac{\mu_2}{\mu_1}\left[3 - \left(\frac{\mu_2}{\mu_1}\right)^2\right]\right\}.$$

T_A may be rewritten

$$T_a^2 = \frac{1 + \left(\frac{d}{c}\right)^2}{\left[1 - q\left(1 + \alpha\frac{a}{c}\right)\right]^2 + \left(\frac{d}{c}\right)^2\left[1 - q\left(1 + \alpha\frac{b}{d}\right)\right]^2}. \qquad (11)$$

Equation (11) enables the engineer to predict the vibration transmission over a wide frequency range, q, where $\mu = f(q)$, which is typical of viscoelastic materials.

Equivalence with the Elastically Supported Dashpot Model

Under certain conditions, Eq. (11) can be approximated by the elastically supported

dashpot isolator considered by Ruzicka and Cavanaugh. That transmissibility is

$$T_A^2 = \frac{1 + 4\left(\frac{N+1}{N}\right)^2 \rho^2 \frac{\omega^2}{\lambda^2}}{\left[1 - \frac{\omega^2}{\lambda^2}\right]^2 + \frac{4}{N^2}\rho^2 \frac{\omega^2}{\lambda^2}\left[N + 1 - \frac{\omega^2}{\lambda^2}\right]^2} . \quad (12)$$

These authors have shown that the fixed point may be located in the spectrum and used to control maximum (resonance) transmissibility by appropriate adjustment of N and c:

$$T_A^* = 1 + \frac{2}{N}$$

$$\beta_A^* = \left[\frac{2(N+1)}{N+2}\right]^{1/2}$$

$$\rho^*_{opt\,A} = \frac{N}{4(N+1)}\,[2(N+2)]^{1/2}.$$

This motivates the reconsideration of Eq. (11) to determine under what conditions it is equivalent to Eq. (12). If equivalence can be demonstrated, parametric analogies between the viscoelastic suspension and the model of Eq. (12) may be made, and optimum design parameters identified.

To show this, Eq. (11) is cast into the form of Eq. (12) in the following way:

$$T_A^2 = \frac{1 + \left(\frac{d}{c}\right)^2}{\left[1 - \frac{\omega^2}{\bar{\lambda}^2}\right]^2 + \left(\frac{d}{c}\right)^2 \left(\frac{1 + \alpha\frac{b}{d}}{1 + \alpha\frac{a}{c}}\right)^2 \left[\frac{1 + \alpha\frac{a}{c}}{1 + \alpha\frac{b}{d}} - \frac{\omega^2}{\bar{\lambda}^2}\right]^2} \quad (13)$$

where

$$\bar{\lambda}^2 = \frac{(1+\alpha)}{\left(1 + \alpha\frac{a}{c}\right)}\lambda^2 .$$

Studying the ratios a/c and b/d, we recognize that

$$\frac{a}{c} \approx \frac{a_1}{c_1}$$

and

$$\alpha\frac{b}{d} = 3\alpha\left(\frac{\mu_2}{\mu_1}\right)^2$$

for $\mu_2 << \mu_1 << 1$. For viscoelastic materials, G_2/G_1 seldom exceeds unity, and therefore

$$\left(\frac{\mu_2}{\mu_1}\right)_{max} = \left[\left(\frac{G_2}{G_1}\right)^{1/2} \tan\frac{\theta}{2}\right]_{max} \approx 0.4 .$$

The ratio μ_2/μ_1 is usually substantially smaller than 0.4.

Retaining only first order terms in $(\mu_2/\mu_1)^2$, Eq. (13) may be written

$$T_A^2 = \frac{1 + (3\mu_2/\mu_1)^2}{\left[1 - \frac{\omega^2}{\bar{\lambda}^2}\right]^2 + \left(3\frac{\mu_2}{\mu_1}\right)^2 \left[\frac{1}{1 + \alpha\frac{a_1}{c_1}}\right]^2 \left[1 + \alpha\frac{a_1}{c_1} - \frac{\omega^2}{\bar{\lambda}^2}\right]^2} . \quad (14)$$

Then, the following analogies may be established:

Elastically Connected Dashpot	S-Ply Viscoelastic Flexure
Stiffness Ratio: N	$\alpha\frac{a_1}{c_1}$
Damping Ratio: ρ	$\dfrac{\frac{3}{2}\left(\frac{G_2}{G_1}\right)^{1/2}\tan\frac{\theta}{2}\left(\alpha\frac{a_1}{c_1}\right)\left[1 + \frac{3}{2}\left(\alpha\frac{a_1}{c_1}\right) + \frac{1}{2}\left(\alpha\frac{a_1}{c_1}\right)^2\right]^{1/2}}{1 + \alpha}$

DESIGN PROCEDURE

The above analogies permit calculations to follow the pattern developed for the elastically connected dashpot isolator. Selecting the maximum permissible transmissibility and locating it at the fixed point is equivalent to determining both N_{opt} and ρ_{opt}. The four equations relating N_{opt} and ρ_{opt} to the physical and geometric properties of the flexure may be written:

From the definition of α:

$$\alpha = G\frac{H_1}{H_3}\frac{\left[1 + 2\frac{H_2}{H_3} + \frac{H_1}{H_3}\right]^2}{\left[1 + 2\left(\frac{H_1}{H_3}\right)^3\right]} . \quad (15)$$

Location of resonance ω^*:

$$\omega^{*2} = \frac{1}{12}\left(\frac{Eb}{M}\right)\left(\frac{2H_3}{L}\right)^2 \left[1 + 2\left(\frac{H_1}{H_3}\right)^3\right] \frac{1 + \alpha}{1 + \frac{1}{2}\alpha\frac{a_1}{c_1}} . \quad (16)$$

From the definition of μ_1:

$$\mu_1 = (1+d)^{1/2}\left(\frac{G_1}{E}\right)^{1/2}\left(\frac{L}{2H_3}\right)^{1/2}\left(\frac{H_3}{H_1}\right)^{1/2}\left(\frac{H_3}{H_2}\right)^{1/2}$$

$$\times\left[1+\left(\frac{G_2}{G_1}\right)^2\right]^{1/4}\cos\frac{\theta}{2}\,. \tag{17}$$

From required damping:

$$\alpha = \frac{\frac{3}{2}\left(\frac{G_2}{G_1}\right)^{1/2}\tan\frac{\theta}{2}\left(\alpha\frac{a_1}{c_1}\right)\left[1+\frac{3}{2}\left(\alpha\frac{a_1}{c_1}\right)+\frac{1}{2}\left(\alpha\frac{a_1}{c_1}\right)^2\right]^{1/2}}{\rho_{opt}} - 1. \tag{18}$$

For given material properties, Eqs. (15) through (18) may be regarded as four equations in the unknown geometric parameters b, H_1/H_3, H_2/H_3, and H_3/L. Of course, they may be used in various ways depending on design criteria.

For discussion purposes, consider the problem in which we want to minimize the thickness of the damping layers for a given maximum transmissibility, T_A. Furthermore, consider $H_1/H_3 = H_2/H_3$. Minimizing these parameters implies minimization of α. As

$$\left(\alpha\frac{a_1}{c_1}\right)_{opt} = N_{opt}$$

and

$$0 \le \frac{a_1}{c_1} \le 1 \qquad \text{(see Fig. 3)},$$

$$N_{opt} \le \alpha_{opt} \le \infty\,.$$

This requires $\alpha_{opt\,min} = N_{opt}$ and $a_1/c_1 = 1$.

For design purposes, $\mu_1 \approx 0.1$. Then H_1/H_3 is determined from Eq. (15), H_3/L from Eq. (17), b from Eq. (16), and the required material loss modulus G_2/G_1 from Eq. (18).

From Eq. (18)

$$\frac{\mu_2}{\mu_1} = \left(\frac{G_2}{G_1}\right)^{1/2}\tan\frac{\theta}{2}$$

$$= \frac{2}{3}\,\frac{(1+N_{opt})\,\rho_{opt}}{N_{opt}\left[1+\frac{3}{2}N_{opt}+\frac{1}{2}N_{opt}^2\right]^{1/2}}$$

$$= f(T_A)\,.$$

By assumption in Eq. (14), $3\alpha(\mu_2/\mu_1)^2 \ll 1$. For small μ_1, $\alpha(a_1/c_1) \approx \alpha$, and for $\alpha_{opt} = N_{opt}$, $\mu_2/\mu_1 \ll 1/(3N)^{1/2}$ or

$$\rho_{opt} \ll \frac{(3)^{1/2}N_{opt}^{1/2}}{2}\,\frac{\left[1+\frac{3}{2}N_{opt}+\frac{1}{2}N_{opt}^2\right]^{1/2}}{1+N_{opt}}$$

which is reasonable for the elastically supported damper isolator.

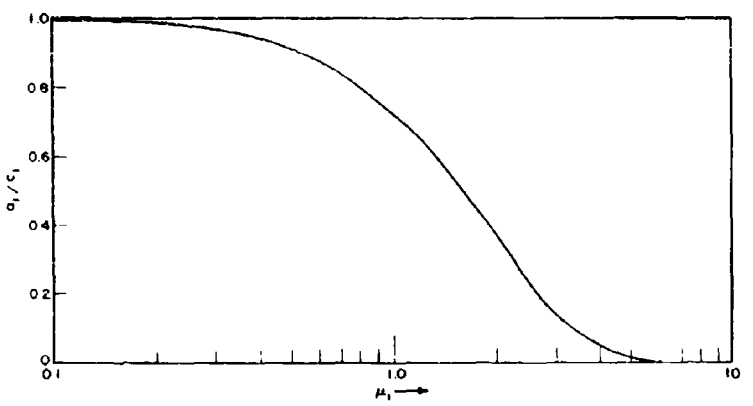

Fig. 3. a_1/c_1 as a function of μ_1

REFERENCES

1. J. D. Ferry, Viscoelastic Properties of Polymers (John Wiley & Sons, Inc., New York), 1960

2. E. M. Kerwin, Jr., "Damping of Flexural Waves by a Constrained Viscoelastic Layers," J. Am. Acoust. Soc., 31:952-962 (July 1959)

3. R. A. DiTaranto, "Theory of Vibratory Bending for Elastic and Viscoelastic Layered Finite-Length Beams," J. of Appl. Mech., Series E, 32(4):881-886 (Dec. 1965)

4. Structural Damping (J. E. Ruzicka, Ed.) (ASME, New York), 1959

DISCUSSION

Mr. Verga (Hazeltine Corp.): Is there any opinion at this time as to whether we can ever possibly hope to find this type of isolator better, in terms of mass volume for the same type of damping and for the same natural frequency, than the typical standard type of linear isolator such as Cavanaugh's and Ruzicka's model?

Mr. Frohrib: I am afraid I would be presumptuous in making claims at this point. I would like to think that there will be evidence of real design opportunity as we proceed with our optimization. Depending of course upon the design criteria and the volume characteristics, as well as the specific package size, I can not say whether it is going to be competitive. It is not intended as a competitive kind of thing of course, but it will be more opportune. It would indeed depend upon the design problem. We should be able to answer your question more specifically after our optimization effort.

* * *

APPLICATION OF DAMPING DEVICE FOR CRITICAL SPEED CONTROL

John F. Mullen and Mark R. Kulina
Curtiss-Wright Corporation
Wood-Ridge, New Jersey

A device for the control of critical speeds of rotating shafts has been developed. It is a bearing support consisting basically of a film of oil between two nonrotating parts in parallel with a flexible mechanical support. A mathematical model of the physical system is developed and response of the system predicted from the model. Results from operation of an experimental rig are presented which confirm the model and provide data for damper design. Design details of applications to operating rigs and engines, as well as test results from them, are given, indicating the damper to be effective in controlling the effects of critical speed. The device should find application in retrofitting engines known to have rotor induced vibration or noise problems and in insuring successful control of rotor amplitude and/or rig vibration in first-time operation of development rigs and engines. It may also be used during the design stage in lightweight, multipurpose engines where control of critical speed by other means imposes weight or other penalties.

INTRODUCTION

Avoiding the detrimental effects of operating at or near critical speeds (shaft bending natural frequencies) has always been a consideration, explicit or implied, in the design of rotating machinery. In most cases, this is done by appropriate selection of mass and stiffness to place the critical speeds outside the operating range. With the advent of lightweight, multipurpose engines, however, the operating range often covers a wider percentage of design speed, while the designer has less latitude in the selection of mass and stiffness.

Another parameter for the control of critical speeds is damping. A previous paper [1] detailed development of a mathematical model and component testing of an oil-squeeze bearing damper and presented a bibliography of related work. This paper reviews the previous work and reports development work, including rig and engine testing, on the bearing damper.

OIL-SQUEEZE BEARING DAMPER

A schematic of the physical parts of the bearing damper is shown in Fig. 1. The shaft bearing is supported in two ways: structurally by the flexible support and hydrodynamically by the oil in the cavity. Oil under pressure enters the squeeze film cavity through one or more inlet passages and exits through the drain holes beneath the oil rings. Viscous damping is produced in the high pressure cavity as motion of the rotor causes the oil to be pumped or forced circumferentially around the cavity and through the drain holes. In addition to the damping provided by the oil, there is also a nonlinear spring rate associated with the oil. This spring rate, however, can be maintained at a low value by proper design of the oil cavity. The flexible bearing support performs three functions: It helps to control the location of the critical speed, it restricts the deflection of the rotor when not rotating, and it permits the squeeze film to operate as a damper.

Additional design features of the oil-squeeze bearing damper are:

1. The oil film is between two nonrotating parts, thus eliminating the possibility of oil whip which occurs when the film is between rotating and nonrotating members, as in journal bearings.

2. The annulus adds little to the damping but provides distribution of the oil around the cavity from the inlet holes.

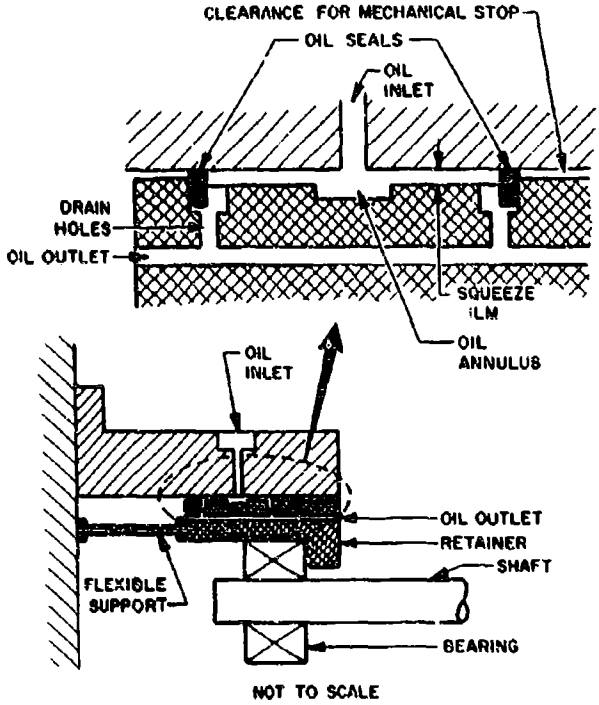

Fig. 1. Oil-squeeze bearing damper schematic

3. As a fail-safe device, mechanical stops can be incorporated in the design outside the high pressure oil cavity to permit only limited radial and torsional motion of the retainer ring.

MATHEMATICAL MODEL

The simplest method of understanding the operation of the oil-squeeze bearing damper is by developing an analogous mathematical model. Such a model is shown in Fig. 2.

In this model, the spring, K, and mass, m, of the main system represent the original system to which the damper is to be applied. The spring represents all of the flexibility from the mass to the ground; that is, if the true system has flexibilities between both the damper and the mass and the damper and ground, they may both be represented by an equivalent spring, K, as shown in the model.

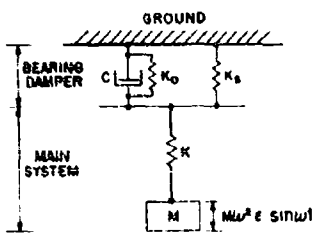

Fig. 2. Mathematical model

In the damper, the oil provides both a flexibility, K_o, and a damping, c, while the flexible support results in a flexibility, K_s. By judicious choice of damper and spring dimensions, K_o can be kept much smaller than K_s. Because the two springs are in parallel, the effect of K_o can then be neglected.

A cursory examination of the model will show that the natural frequency will vary as a function of damping. For no damping, the natural frequency of the system is a function of the flexibilities K_s and K acting in series and will be relatively low. For infinite damping, the flexible support spring, K_s, is effectively short circuited and the natural frequency is a function only of the main system flexibility, K. This latter is effectively the system natural frequency before the bearing damper was added. For convenience, we will refer to the former – that with

no damping — as the soft system, and the latter — that with infinite damping — as the hard system.

For the mathematical model, the amplitude of vibration was determined in a previous paper [1] as

$$\frac{X}{\epsilon} = m\omega^2 \sqrt{\frac{(K_s + K)^2 + \omega^2 c^2}{(K_s K - K_s m\omega^2 - Km\omega^2)^2 + \omega^2 c^2 (K - m\omega^2)^2}}$$

while the force transmissibility is expressed as

$$T = \frac{F_T}{M\omega_s^2 \epsilon}$$

$$= \left(\frac{\omega}{\omega_s}\right)^2 \sqrt{\frac{K^2 (K_s^2 + \omega^2 c^2)}{(K_s K - K_s m\omega^2 - Km\omega^2)^2 + \omega^2 c^2 (K - m\omega^2)^2}}$$

Using these equations, response curves for a particular configuration ($K_s/K = 0.15$) were generated as a function of damping and are given in Figs. 3 and 4. The amplitude curves show the peaks of the soft and hard system, but also indicate that for a reasonably wide range of damping values, magnification is held to a reasonable level. For one damping value, the amplitude optimum, both the hard and soft system peaks are completely suppressed.

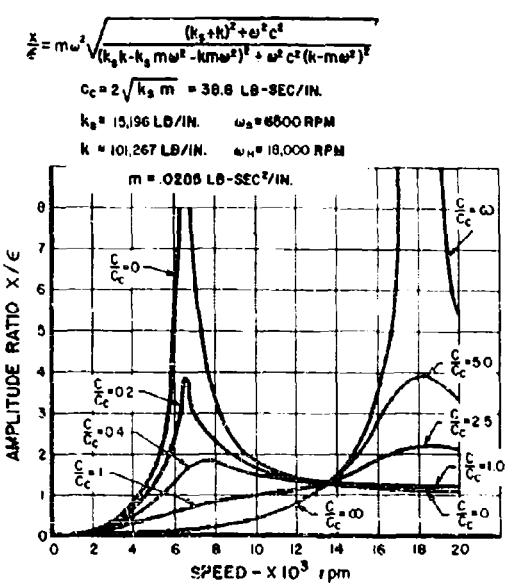

Fig. 3. Theoretical amplitude response as a function of damping

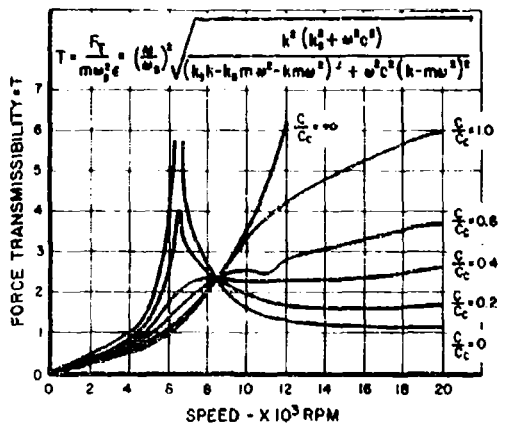

Fig. 4. Theoretical force response as a function of damping

The force transmissibility curves show similar characteristics to those of amplitude response, but the optimum force damping must be defined for a particular speed range and may not be the same as the optimum damping for amplitude. It should be noted that transmitted force does not increase indefinitely with speed for positive values of damping, as the figure would appear to indicate. At some speed beyond the range of the figure, the transmissibility will peak and then begin to decrease.

Thus an optimum damping can not be arbitrarily set, but must be a function of the details of the application; for example, the location of the operating range of the machine with respect to the response curves, the operating clearances between rotating and stationary parts, and the load capacity of the bearings and related structure must all be functions of the details of the application.

An obvious question in the design of the flexible support for the system is the degree of flexibility required. A lower bound can be established in that it must be an order of magnitude larger than the flexibility of the oil film to prevent the nonlinear oil spring from affecting the response. To accomplish this, load-deflection calculations similar to those shown in Fig. 5 must be developed. Note that the spring rate of the oil is significantly lowered by an increase in the oil film thickness.

An upper bound on the spring rate of the flexible support may be established relative to the spring rate of the main system by considering its effect on the response curves. As was noted in discussing Fig. 3, a minimum amplitude

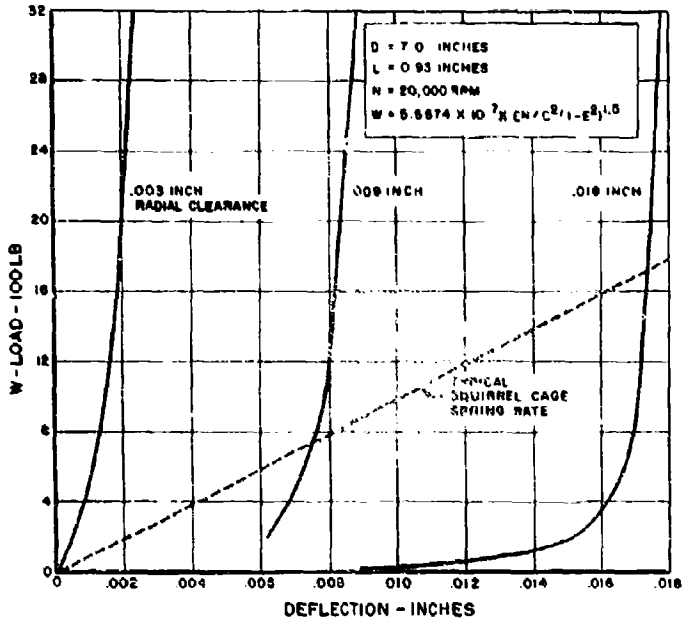

Fig. 5. Typical load-deflection relationships for oil film

can be attained as a function of damping for a particular configuration. However, this minimum amplitude (and the damping value to attain it) is also a function of the relative values of the flexibilities of the main system and the flexible support. This relationship is shown in Fig. 6. It may be seen that the value of magnification is relatively small for a wide range of support spring rate, provided that the support spring rate is not significantly greater than the original spring rate of the system. The lower the flexible support spring rate, the lower the magnification that can be attained. This may also be observed intuitively from the response curves of Fig. 3. It is observed that the optimum magnification is at the intersection of the response curves for the hard and soft systems. The w er the separation between these curves (and thus, the lower the flexible support spring rate) the lower the optimum magnitification will be.

TESTING TO VERIFY MODEL

To verify the mathematical model, investigate the effect of various design parameters, and demonstrate the control of critical speeds by the damper, a two-bearing test rig simulating in scale a gas generator engine was designed, fabricated, and operated. Because these test results have been previously reported [1], results will only be summarized.

Figure 7 shows typical test data obtained of shaft amplitude vs speed with varying oil flows. With low flow (under damping) the soft system peak is observed while with high flow (over damping) the peak is at the hard system critical. The medium flow produces optimum damping and peaks as both hard and soft systems criticals are suppressed.

The major conclusions derived from operation of this test rig were as follows:

1. The oil-squeeze bearing damper has the capability of controlling rotor amplitudes and transmitted force at critical speeds, even with relatively high unbalance.

2. The mathematical model adequately describes the operation of the actual damper.

3. Variation in oil flow to the damper produces significant changes in damping.

4. Damping values greater than $c/c_c = 1$ are readily attainable.

5. Increasing the film thickness results in decreased damping.

6. Maintenance of a high pressure cavity by a device such as the oil seals is important to the operation of the damper.

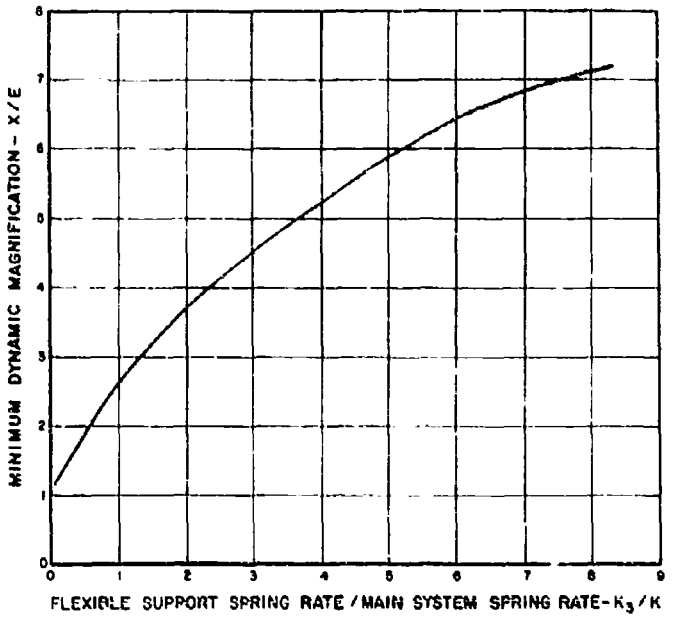

Fig. 6. Minimum-amplitude magnification as a function of flexible support spring rate

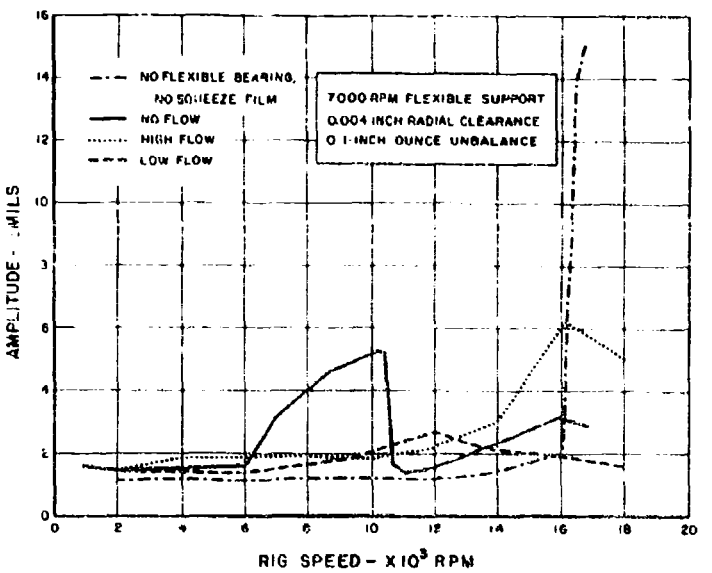

Fig. 7. Damper rig test results -- effect of oil flow

7. A suddenly applied unbalance produces no large transients, but simply an increase in amplitude owing to an increase in applied force.

8. Variation of the soft system critical speed in the range of ω_s/ω_h from 0.16 to 0.51 produces no significant effect.

9. Sizing of the damper can be established by the relationship

$$\frac{R^3 L}{h^3 m \omega_s} = 3 \times 10^4$$

where

R is the radius of the oil film in inches,

L is the length of the oil film in inches,

h is the thickness of the oil film in inches,

m is the mass of the rotating system in lb-sec^2/in., and

ω_s is the soft system natural frequency in rad/sec.

APPLICATIONS

The success of the bearing damper in the test rig in controlling the detrimental effects of critical speeds encouraged us to install the damper on various test-stand rig and engine configurations. Some of the present and planned applications are shown in Table 1. In all configurations tested to date, amplitude has been well controlled and in no case have the effects of critical speed limited rotor operation. Results of some of these applications will now be reviewed in detail.

Compressor Rig

The first application of the bearing damper was to an hp compressor rig. The physical configuration of the damper is shown in Fig. 8, while the significant damper dimensions are given in Fig. 9. This rig was operated in four builds for more than 229 test hours, using a single set of damper parts. At the completion of this testing, all parts were in excellent condition.

Typical test data from this rig are shown in Fig. 10. All amplitudes observed were well within monitored limits. The 1.25-lb/min flow resulted in an optimum damping condition for the first critical speed, producing a peak amplitude midway between the hard and soft systems first mode critical speeds. It is therefore likely that the amplitude at 18,000 rpm also represents an optimum peak for the second mode, and further increases in speed would have resulted in decreasing amplitudes. On the other hand, the 5-lb/min flow represents an overdamped condition, and increases in speed would have resulted in increases in amplitude up to the second critical of the hard

TABLE 1
Applications of the Oil-Squeeze Bearing Damper

Application	Bearing Type	Critical Speeds (rpm)	Design Speed (rpm)
Test rig	Roller	3000 to 9000 (soft) 17,000 (hard)	18,000
Hp compressor	Ball	6100 and 18,800 (soft) 10,200 and 20,200 (hard)	17,800
Gas generator	Ball	6050 and 11,500 (soft) 7500 and 16,800 (hard)	17,500
Prototype turbo fan	Ball	6000 and 17,500 (soft) 9300 and 22,000 (hard)	20,000
Single rotor rig	Roller	See text	30,000
Small mixed-flow compressor rig	Roller	10,000 (soft) 40,000 (hard)	50,000[a]
Fan drive	Roller	5000 (soft) 9000 (hard)	15,000[b]

[a]Test in progress.
[b]Test to be run.

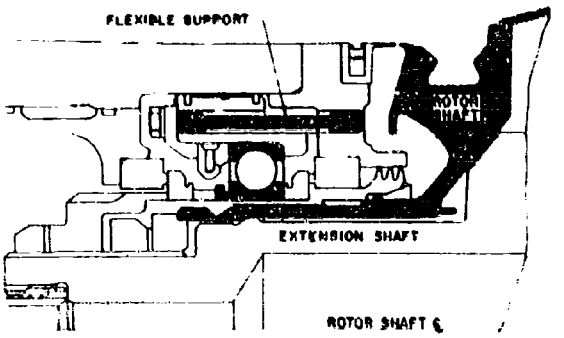

Fig. 8 HP compressor rig bearing damper configuration

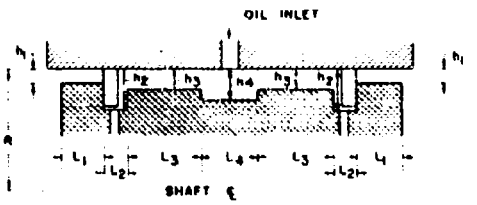

CONFIGURATION	COMPRESSOR RIG	TWIN SPOOL ENGINE	SINGLE ROTOR RIG
OUTER RADIUS R	3.281	3.492	1.700
LAND			
h_3	.019 ± .001	.019 ± .0005	.0085 ± .0005
L_3	.300 ± .010	.250 ± .005	.160 ± .010
ANNULUS			
h_4	.119 ± .011	.119 ± .0055	.060 ± .005
L_4	.261 ± .044	.225 ± .020	.0805 ± .0005
OIL SEAL GROOVE			
h_2	.182 ± .003	.172 ± .003	.155 ± .001
L_2	.0945 ± .0005	.1263 ± .0015	.0805 ± .0005
MECHANICAL STOP			
h_1	.013 ± .001	.013 ± .0005	.0055 ± .0005
L_1	.100 ± .010	.152 ± .0255	.080 ± .005
OIL INLET	ONE HOLE	ONE HOLE	ONE HOLE
	.188 ± .010	.125 ± .010 DIA	.125 ± .010 DIA
OIL OUTLET	THREE HOLES .040 ± .012 BENEATH EACH RING	THREE HOLES .040 ± .002 BENEATH EACH RING	THREE HOLES .040 ± .002 BENEATH EACH RING

Fig. 9. Significant dimensions of bearing damper configurations

system at 20,000 rpm, although amplitudes would be lower than if the damper were not installed. Unfortunately, operation to higher speeds on this rig was not feasible.

Prototype Fan Jet Engine

Upon successful completion of the compressor testing, the hp compressor discussed in the previous section was installed in a twin-spool engine. Slight changes were required in the bearing damper design because of geometry and changed critical speeds. The significant dimensions of the test configuration are shown in Fig. 9.

Test results are shown in the table below. In the operation of the engine, a single oil flow

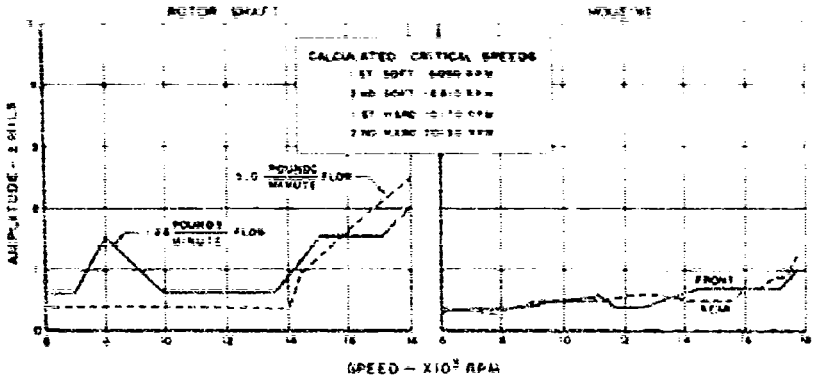

Fig. 10. Test results – hp compressor rig

Hp Speed (rpm)	Probable Mode	Peak Amplitudes (+ mils)		
		Rotor Shaft		Housing
		Front (Damped) Bearing	Rear Bearing	
8700	First soft	0.46	0.81	0.81
15,000	Second soft	0.61	1.50	1.00
19,000	Maximum speed	0.18	1.54	0.96

value of 6 lb/min was chosen initially and was not varied throughout the testing because amplitude results were acceptable. For this configuration, the calculated critical speeds are 6500, 9400, 17,400, and 22,000 rpm for first soft, first hard, second soft, and second hard modes of the system.

The response of the system to a suddenly applied unbalance was obtained unintentionally during the full-scale engine test program. This occurred when three early stage hp compressor rotor blades failed while operating at 90 percent design speed. Continuously recorded data during the failure and subsequent shutdown showed that rotor displacement had no significant transient response beyond the increase in amplitude owing to the increased unbalance. The oil damper successfully controlled the amplitude so that there was no contact at the mechanical stops of the damper. The clearance of these stops was chosen to prevent contact between rotating and nonrotating parts of the engine.

Single Rotor Rig

Because of the success of the bearing damper in controlling critical speeds in our large scale engine the device found ready acceptance in other rigs that had vibration problems. Such a rig was the single rotor rig, which combines a compressor and turbine in a single-axial plane. This rig had consistent vibration problems which at times caused radial rubs or restricted operation. Because of the complexity of the rotating parts and the supporting system, critical speeds were difficult to estimate analytically, but it was felt that the problem was most probably critical-speed induced. A bearing damper was therefore incorporated in the design. Detail dimensions are shown in Fig. 9.

The vibration problem on the original rig was evidenced by high housing amplitude in the 25,000-rpm range, averaging about 3 mils and, on particular builds, running three times higher. With the bearing damper installed, and a constant oil flow of 6 lb/min, amplitudes have been consistently below 1 mil on the last six builds. Typical test data for an identical pickup both with and without the damper are shown in Fig. 11. As a verification that the elimination of the problem resulted from the addition of the damper and not simply from a change in critical speed caused by the flexible support, the rig was run with no oil flow to the damper. Test results are again shown in Fig. 11. Testing was terminated in this case at 24,000 rpm to protect against damage to the rig.

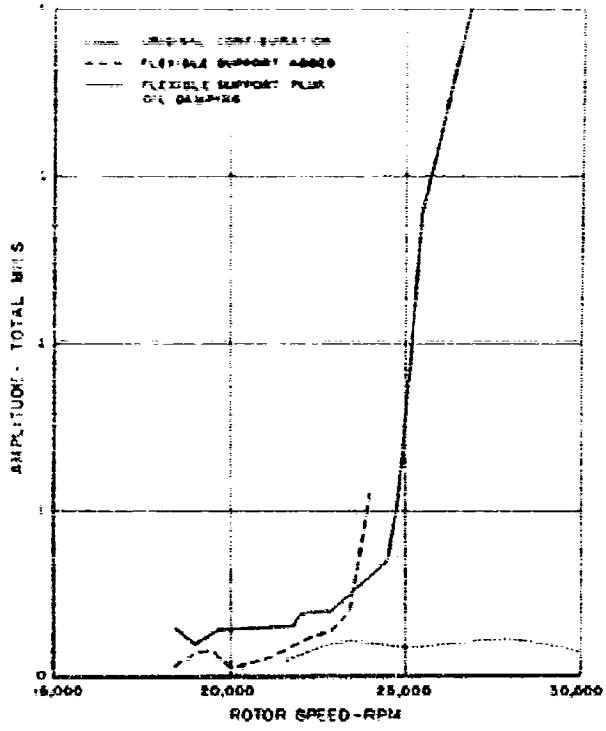

Fig. 11 Test results -- single rotor rig

DAMPER WITHOUT FLEXIBLE SUPPORT

A limited amount of testing was also done on the use of the oil film without the flexible support. This configuration is called the squeeze film damper. Analytically, this is basically the same concept as the bearing damper previously discussed, but because the flexible support spring rate is eliminated, the nonlinear spring rate of the oil becomes the significant spring in the system. This type damper has been applied to two fan rigs. The first application was to a roller bearing that had a known (after testing) critical speed near design speed. The squeeze film configuration and significant dimensions are shown in Fig. 12. Test results of shaft and housing amplitude vs speed are given in Fig. 13 for the configuration with and without the damper. There is no physical difference between these builds beyond the squeeze film.

USE OF FLEXIBLE SUPPORT

Given the success of the squeeze film alone on the fan rig, an obvious question is whether a flexible support is necessary or desirable. The squeeze film alone has the advantage that few additional parts and little additional space are required compared with conventional designs. These combine into the further advantage that it is therefore easier to use in modification of existing systems. With the current state-of-the-art, however, the flexible support appears to be at least desirable if not necessary. The use of the flexible support has the following advantages:

1. It permits the separation of the two functions of the control device, in that it acts as the spring of the device and permits the oil to act only as a damper by minimizing the effect of the spring rate of the oil.

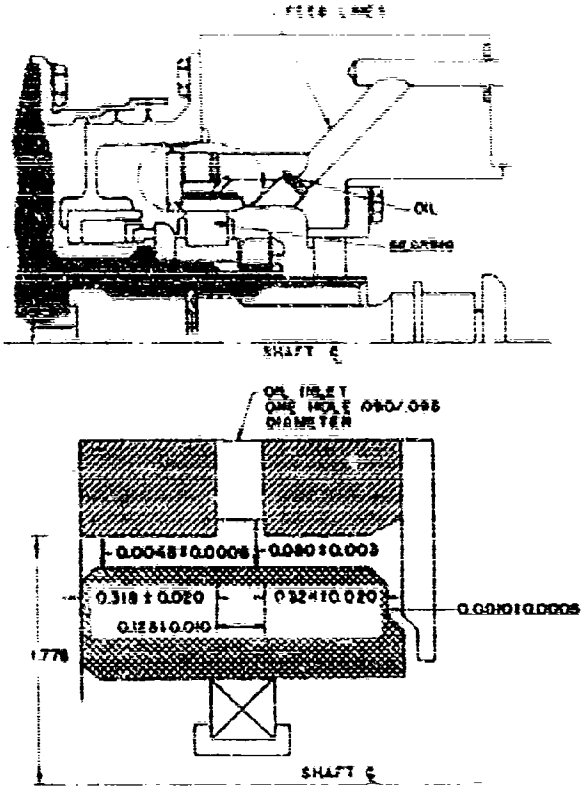

Fig. 12. Fan rig squeeze film configuration

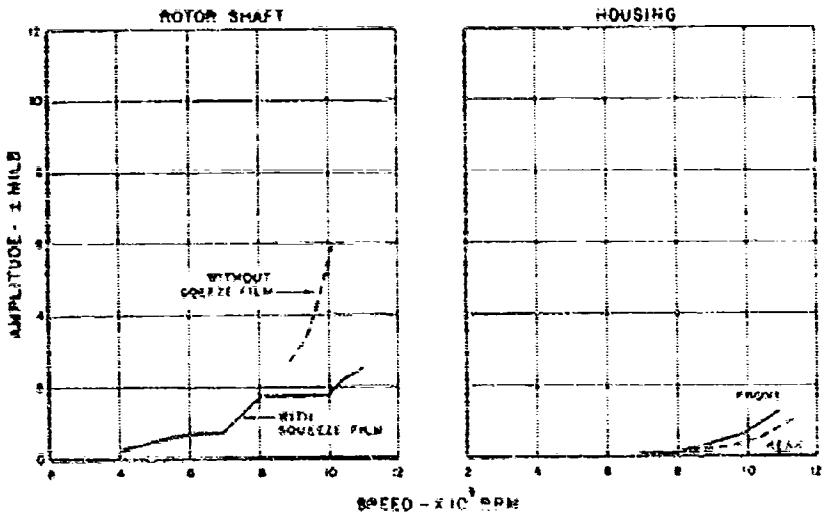

Fig. 13. Test results -- fan rig

2. The result of this separation of functions is that the critical speed can be accurately predicted with the flexible support while, without it, the nonlinear oil spring must be considered.

3. A second result of the separation of functions is that during initial operation of the rig to which the device is applied, should a variation in damping be required, it can be applied without a variation in spring rate, which is not the case without the damper.

4. The flexible support restricts the deflection of the rotor when not rotating.

5. Because the thickness of the oil is much larger in the bearing damper than in the squeeze film system, machining tolerances of the parts that form the oil cavity are not as critical.

FUTURE APPLICATIONS

The oil squeeze bearing damper is not viewed as a required or even a desirable addition to all existing rotating machinery. In those cases where the effects of critical speeds can be adequately controlled by mass and stiffness alone, incorporation of a damper is economically unjustified. However, it may be readily applied in the following cases:

1. In lightweight, high performance engine designs where critical speed solutions by mass and stiffness parameters result in weight or other penalties.

2. As a retrofit to service operated machinery with vibration and/or noise problems induced by the rotating parts.

3. As an integral part of new rigs or engines to insure satisfactory initial operation where there is any possibility of critical speed problems. The damper has the advantage of permitting operation at the hard system, the soft system, or at an optimized condition by variation in oil flow. Thus the need for a damper or for a flexible support alone can be evaluated in a single build.

REFERENCE

1. M. Kulina et al., "A New Concept for Critical Speed Control," SAE No. 670347, Nat. Aeronautics Meeting, New York, Apr. 24-27, 1967

DISCUSSION

Mr. Nelson (Tufts Univ.): Have you extended the analysis to nonaxisymmetric situations such as rotors which have unequal stiffnesses?

Mr. Mullen: No, we have not.

Mr. Nelson: Are you planning to?

Mr. Mullen: Probably, yes. Most of our development was done specifically for particular compressor rigs. I hope we will continue in this area.

Mr. Orelup (Allison Div., GMC): During your test work did you observe any whirl, instability or nonsynchronous type of response?

Mr. Mullen: If by instability you mean self-excited vibrations, no we did not. During some of our early test work on the critical speed rig we did notice some nonsynchronous vibration. Almost always we could attribute it to low oil flow and high amplitudes which were probably giving us snubbing at the mechanical stops.

Mr. Orelup: Was there any effect of oil viscosity in this respect?

Mr. Mullen: We have done a limited amount of study on the effect of oil viscosity. We did find that changing the oil viscosity could help us in adding damping to the system. We used the same oil and changed the temperature. In any case we did not see any nonsynchronous vibrations in this connection.

Mr. Jones (Air Force Materials Lab.): You mentioned temperature as a means of controlling viscosity. Were there any problems with regard to temperature in service as a result of this?

Mr. Mullen: No, because the oil flow generally was fairly large. It flowed fairly well through the bearing. We used the same oil which was used for our bearing lubrications. Therefore it all went to a general reservoir and was cooled. I should add that we do not have this in service. This has been run only on compressor rigs and prototype engines. It is not in a service application yet. I do believe

that Rolls Royce has a similar design, but I do not know the details, other than knowing that it is a squeeze film damper in service on the Conway bypass engines

DEVELOPMENT OF PRACTICAL TUNED DAMPERS TO OPERATE OVER A WIDE-TEMPERATURE RANGE

Abid O. Nashif
University of Dayton Research Institute
Dayton, Ohio

Design procedures are outlined for developing lightweight and compact tuned viscoelastic dampers to operate over a wide-temperature range and to withstand severe vibrational environments. The effectiveness of such a design is demonstrated experimentally on a radar antenna, representing a typical vibrating single-degree-of-freedom system.

INTRODUCTION

Several techniques using high damping materials have been developed for reducing vibration amplitudes in structural members. Among these, the tuned viscoelastic dampers have been widely investigated in recent years because of their high damping capabilities [1,2]. A special purpose, tuned, viscoelastic damper, developed recently at the Air Force Materials Laboratory, has been very successful in increasing the service life of an IFF radar antenna subjected to a severe vibrational environment [3]. As a result of that program, it was concluded that it is possible to produce tuned damping devices that will effectively reduce vibration damage in a structure over a wide range of temperatures by utilizing the viscoelastic material in the rubbery region, that is, above the glass transition temperature.

It was therefore considered advantageous to investigate the possibility of developing practical tuned viscoelastic dampers that meet the following requirements: (a) compact size, (b) lightweight, (c) simplicity of inspection, (d) simplicity of attachment to structures, (e) high damping properties over a temperature range from -100°F to +500°F, and (f) ability to withstand severe vibrational environments over this temperature range.

It is the purpose of this paper to outline design procedures for developing tuned viscoelastic dampers that meet all the above requirements. The effectiveness of such a design is demonstrated experimentally on the same IFF radar antenna, using a commercial Silicone material that exhibits good damping and high strength properties over a temperature range of -100° to +500°F.

NOMENCLATURE

- A Amplification factor at resonance
- E Real part of Young's modulus of viscoelastic material (lb/in.^{2})
- k Stiffness of tuned damper link (lb/in.)
- m Mass of tuned damper (slug)
- S Cross-sectional area of viscoelastic link (in.^{2})
- η Loss factor of viscoelastic material
- ℓ Height of viscoelastic link (in.)
- μ Mass ratio between the mass of tuned damper and that of the structure
- μ_{eff} Effective mass ratio (see Ref. [4])
- ω_s Natural frequency of structure (rad/sec)
- ω_D Natural frequency of damper unit (rad/sec)

DESIGN PROCEDURE

Consider a tuned viscoelastic damper consisting of a mass, m, connected through a

viscoelastic link of stiffness k [illegible] to a point on a vibrating structure as shown in Fig. 1. For this structure/damper system to be optimally tuned, it is necessary to select the mass and the link stiffness of the damper to give it the appropriate natural frequency. The relationship between the natural frequency, ω_D, of the tuned damper and that of the structure, ω_1, has been derived [4] for structures that exhibit widely separated resonance frequencies as a function of the loss factor, η, of the viscoelastic link and the effective mass ratio, μ_{eff}, between the mass of the damper and that of the structure; or

$$\omega_D = (1+\mu_{eff})^{-1/2}(1+\eta^2)^{-1/4}\,\omega_1 \qquad (1)$$

where

$$\omega_D = (k/m)^{1/2}. \qquad (2)$$

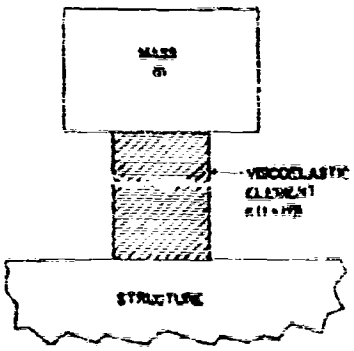

Fig. 1. Idealized tuned viscoelastic damper

Because the weight penalty is, in most cases, a critical item in designing tuned dampers, it is usually advantageous to assume an allowable mass, m, and then proceed to solve for the link stiffness, k, from Eqs. (1) and (2). By obtaining the link stiffness and using

$$k = ES/t \qquad (3)$$

where E is the real part of Young's modulus, S is the cross-sectional area, and t is the thickness, a relationship between the properties of the viscoelastic material and the geometry of the link can be easily determined.

The discussion above outlines a procedure for designing tuned dampers to most frequencies. However, it should be emphasized here that the critical parameter affecting the tuning frequency when the damper is to operate over a wide-temperature range is the modulus of the viscoelastic material. This is because the modulus of most viscoelastic materials changes rapidly with temperature around the transition region (between the glassy and the rubbery regions of the material). Therefore, it is necessary to utilize viscoelastic materials having their rubbery regions over the entire operational temperature range.

A PRACTICAL APPLICATION

Definition of the Problem

The application of a tuned viscoelastic damper to reduce the failure rate in a typical aircraft radar antenna has recently been demonstrated [3]. This failure was caused by airframe vibrations induced by gunfire in the neighborhood of the antenna and was simulated in a shaker test by the random input acceleration spectrum illustrated in Fig. 2. Rapid failures occurred around the rim of the antenna as shown in Figs. 3 and 4. The rim was the only area subjected to severe bending stresses, and the mode of vibration was observed to be almost piston-like, with an effective pivot near the rim, with high bending stress.

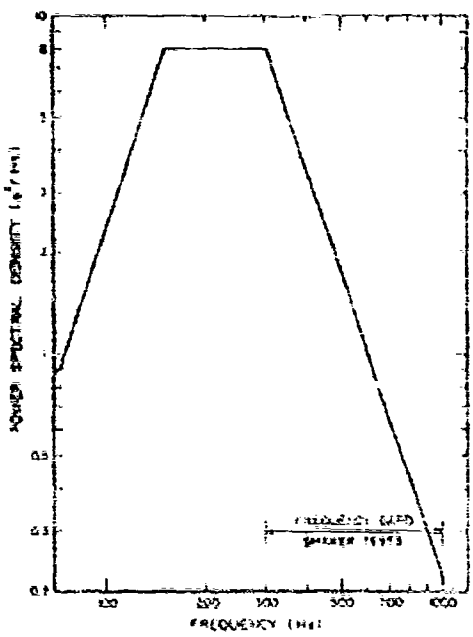

Fig. 2. Derived broadband random spectrum

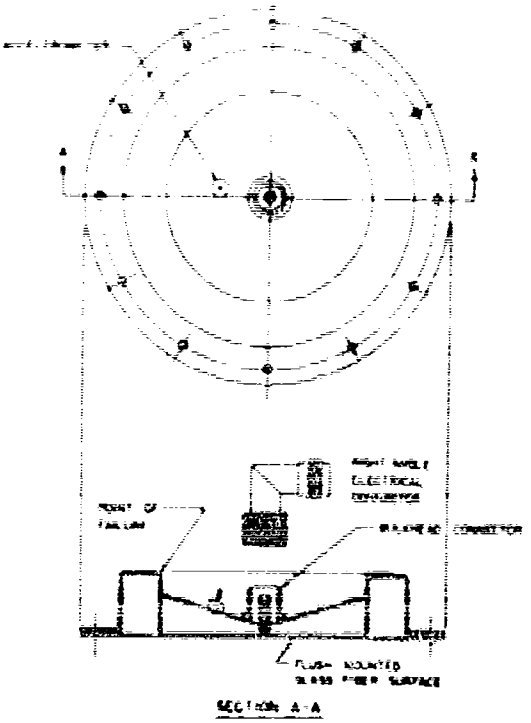

Fig. 3. Schematic of radar antenna

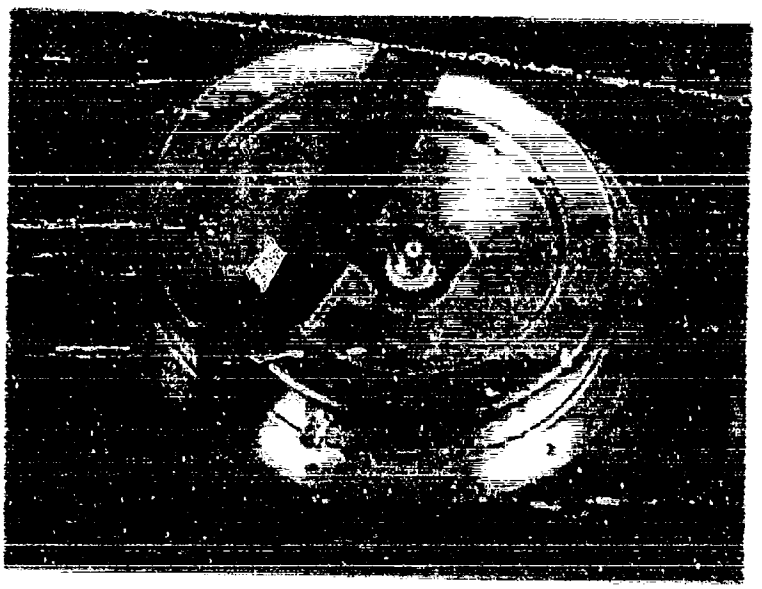

Fig. 4. Failure in antenna

To better determine the nature of the problem and to seek means of avoiding failure, or at least increasing the service life of the antenna, a sample antenna was excited harmonically on an electromagnetic shaker. Amplification factors (ratio of output acceleration to input acceleration at resonance) of the order of 30 were observed to occur near the electrical connector at a frequency of about 485 Hz in the absence of damping additions. The antenna appeared to act as a single-degree-of-freedom system as no further response peaks were observed up to several thousand hertz.

The surface strains at all points apart from the rim edge were very small, and all attempts to use commonly available layered damping treatments were, consequently, fruitless. In fact, because the energy dissipation depends on the local acceleration level rather than the strain level, a tuned damper was the only possibility apart from a complete redesign of the antenna.

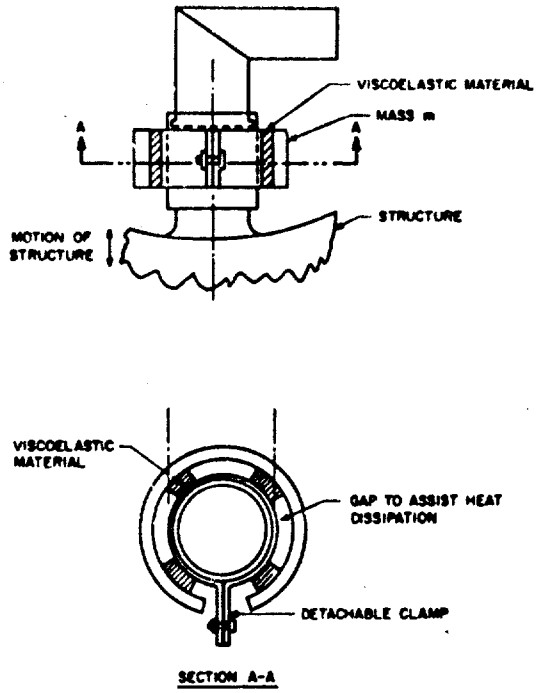

Fig. 5. Location of damper on connector

Initial Approach to Damper Design

The initial damper designs of the type shown in Fig. 5 were built on a largely ad hoc basis, utilizing readily available viscoelastic materials. These dampers fitted onto the electrical connector at the center of the antenna. Several viscoelastic materials and damper dimensions were tested, and each individual damper configuration was tuned by varying the mass, m, because this was far more convenient than varying the stiffness of the viscoelastic link. These tests were carried out over a temperature range of 75° to 150°F in an attempt to achieve low amplification factors over as wide a range of temperatures as possible. It became clear from these initial tests that the variables involved — namely tuning mass, geometry of the viscoelastic link, and variation of the viscoelastic material properties with temperature — were too great in number for a simple design procedure to be adopted. A great simplification could be achieved, however, if the material damping properties varied very little with temperature. For this purpose, the ideal material would have a good loss factor and a rubbery region behavior over the operating temperature range which was from 50° to about 200°F.

A viscoelastic material satisfying the above criterion was found to be a medium acrylonitrile rubber known as Paracril-BJ. To give this material adequate strength to withstand the severe vibrational environment, 25 PHR of carbon black were added to it. The damping properties of this material were evaluated as functions of temperature and plotted as shown in Fig. 6 for a frequency of 500 Hz by use of symmetric cantilever beam specimens in a complex modulus apparatus [5].

Several tuned viscoelastic dampers were molded using Paracril-BJ with 25 PHR carbon black as shown in Fig. 7. These dampers will be referred to as the Paracril-BJ dampers. The antenna/damper system (Fig. 8) was then evaluated under sinusoidal excitation at 10- and 20-g input levels. Graphs of measured amplification factor A against temperature for the antenna/damper system are shown in Fig. 9 for six different dampers. These results indicate that the Paracril-BJ tuned dampers were very effective in reducing the vibration amplitude of the antenna throughout the operating temperature range.

In view of the results shown in Fig. 9, several antenna/damper systems were subjected to the simulated operational environment. These tests indicated that the life of the antenna was increased considerably by use of tuned dampers. This fact was later verified by field test data which indicated that the average life was increased up to a factor of 12 times.

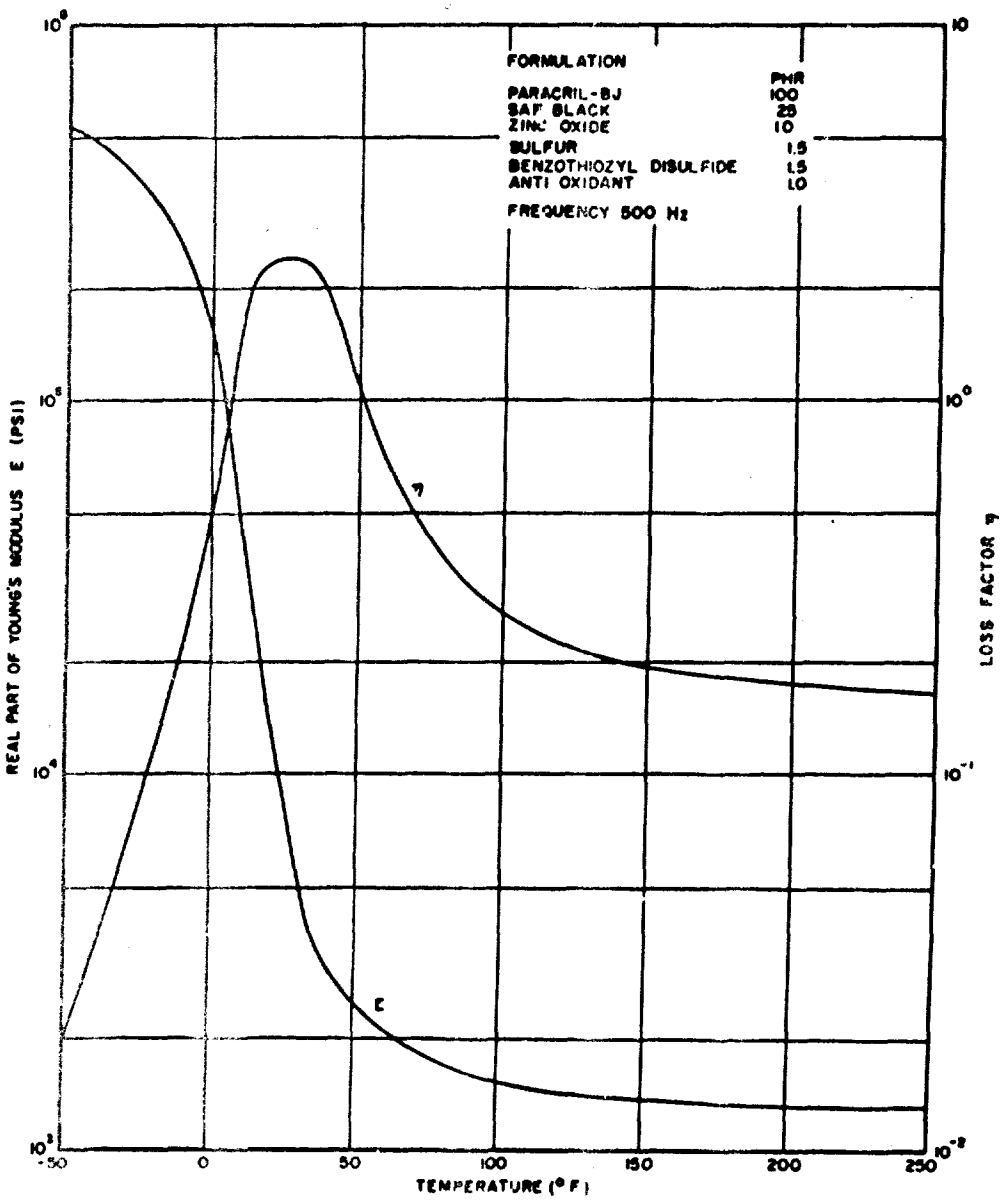

Fig. 6. Damping properties of Paracril-BJ with 25 PHR carbon

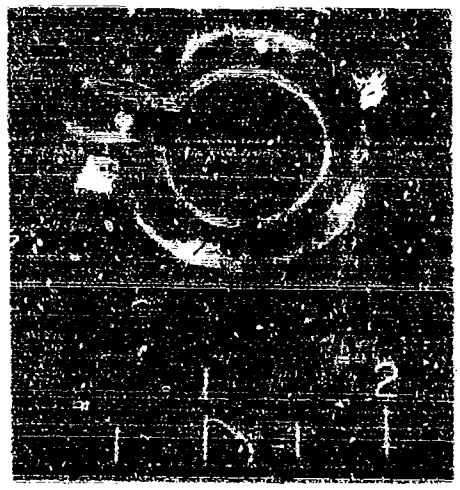

Fig. 7. Photograph of Paracril-BJ damper

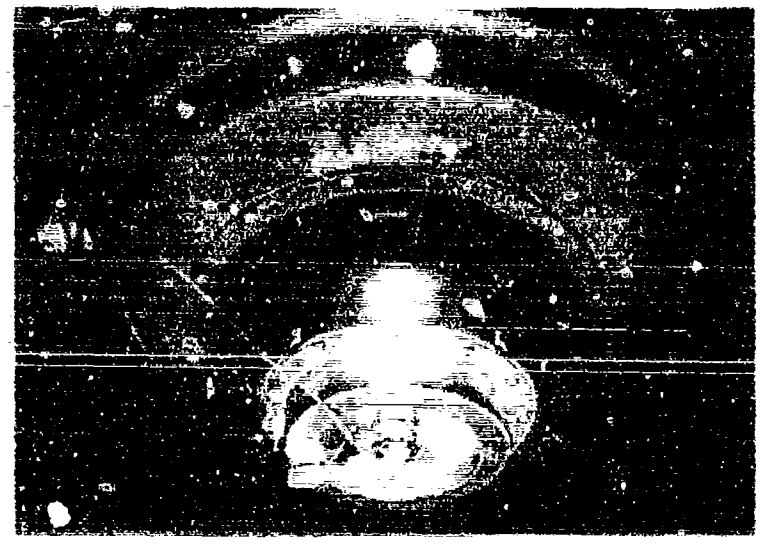

Fig. 8. Photograph of antenna/Paracril-BJ damper system

General Approach to Damper Design

Apart from the solution of the field problem, the main conclusion is that it is possible to produce tuned damping devices that will effectively reduce vibration damage in a structure over a wide temperature range by utilizing the viscoelastic material in the so-called rubbery region. In an attempt to extend the operating temperature range of tuned viscoelastic dampers to cover approximately a 600°F temperature range, it was necessary to obtain a viscoelastic material with the following properties: (a) a rubbery region that extends from -100° to +500°F, (b) good damping properties over the same temperature range (a loss factor of 0.2 or greater), and (c) a good tensile strength over the same temperature range.

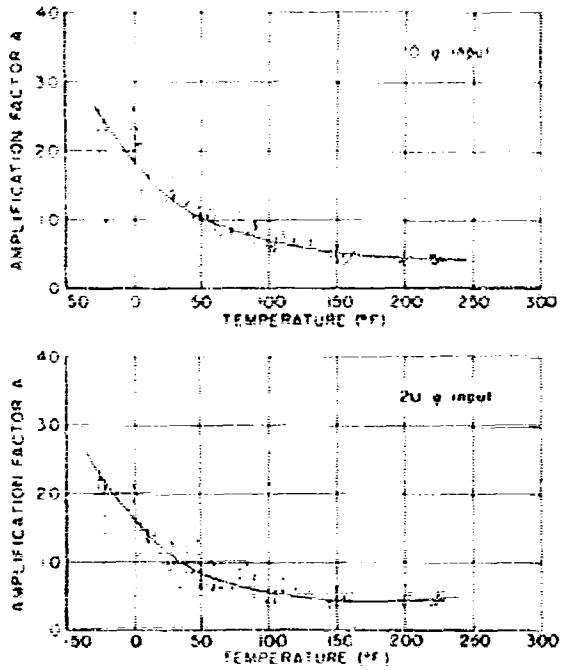

Fig. 9. Graphs of amplification factor against temperature for antenna/Paracril-BJ damper system

After an extensive evaluation of the damping properties of several viscoelastic materials as a function of temperature, commercially available Silicone materials were found to satisfy the above requirements. One such material is a high strength Silicone sealant manufactured by the Dow Corning Corp. The loss factor and the real part of Young's modulus for this material were evaluated in the linear range as a function of temperature and frequency by a suitable technique [6]. These results are shown in Fig. 10 for a frequency of 500 Hz. The loss factor and Young's modulus are also shown in Fig. 11 as functions of the acceleration input level for the same frequency of 500 Hz at room temperature. The effectiveness of this material, in a general design approach, was demonstrated by building several tuned viscoelastic dampers to reduce the vibration amplitude of the same radar antenna.

A significant fraction of the maximum damping that can be introduced into simple structures by use of tuned viscoelastic dampers having a loss factor of 0.2 can be achieved with a mass ratio (between the mass of the damper and that of the structure) of only $\mu = 0.05$ [1]. Hence, using a loss factor of 0.2 and putting $\mu_{eff} = \mu = 0.05$ (because the antenna behaved as a single-degree-of-freedom system with its dish-like inner surface acting as a massless spring and its electrical connector and cable acting as a concentrated mass at the center), Eq. (1) gives $\omega_D^2 = \omega_1^2$. Therefore, the tuned damper was designed to have a natural frequency of 485 Hz. Figures 10 and 11 were used in calculating the geometry of the damper. The damper was tuned for the middle of the temperature range and for high acceleration level inputs. This was because the antenna itself was subjected to extremely high accelerations.

Several tuned viscoelastic dampers were built to the design of Fig. 12. The damper itself had a diameter of 0.7 in., a height of 0.6 in., and a tuning mass of 0.03 lb. These dampers, which will be referred to as the Silicone dampers, were adhered to flat-top electrical connectors, and tests on the antenna/damper system were carried out. Graphs of the measured amplification factor against temperature are shown in Fig. 13 for 1-, 5-, and 10-g acceleration input levels and in Fig. 14 for 15-, 20-, and 25-g acceleration input levels. It can be seen from these figures that the amplification factors of the antenna/damper system are much lower in

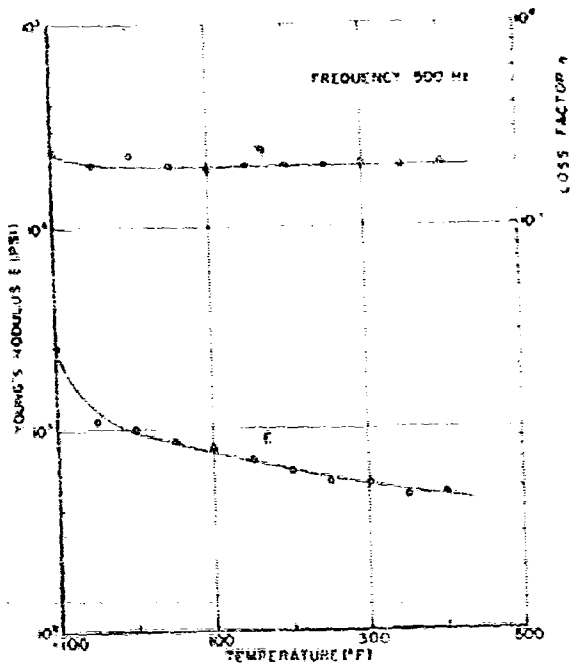

Fig. 10. Damping properties of Dow Corning high strength Silicone sealant against temperature

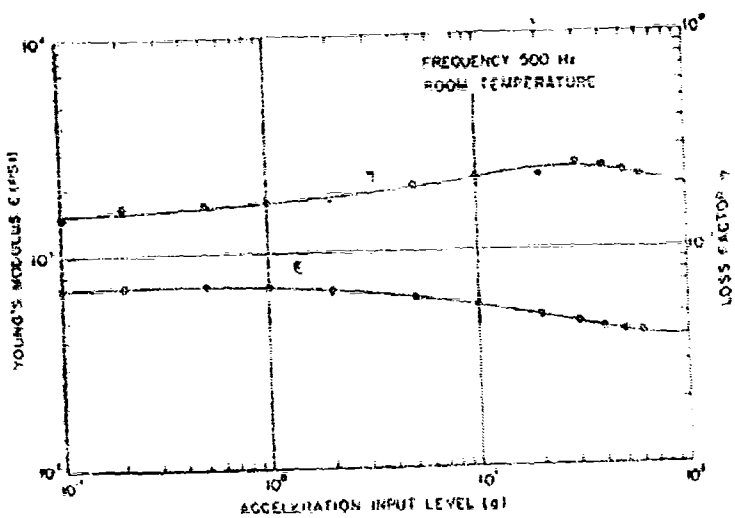

Fig. 11. Damping properties of Dow Corning high strength Silicone sealant against acceleration input (t = 0.25 in.)

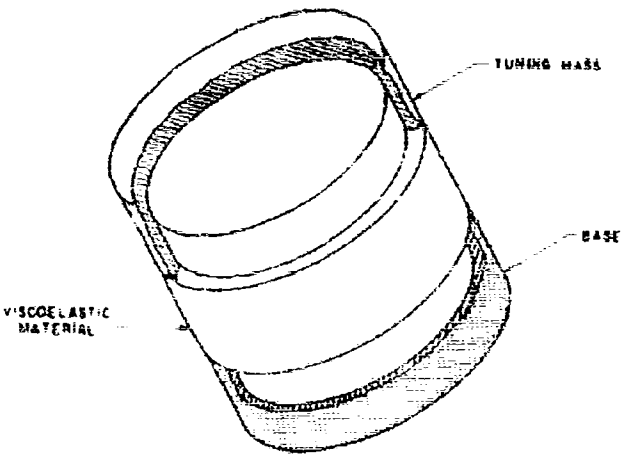

Fig. 12. Sketch of Silicone damper

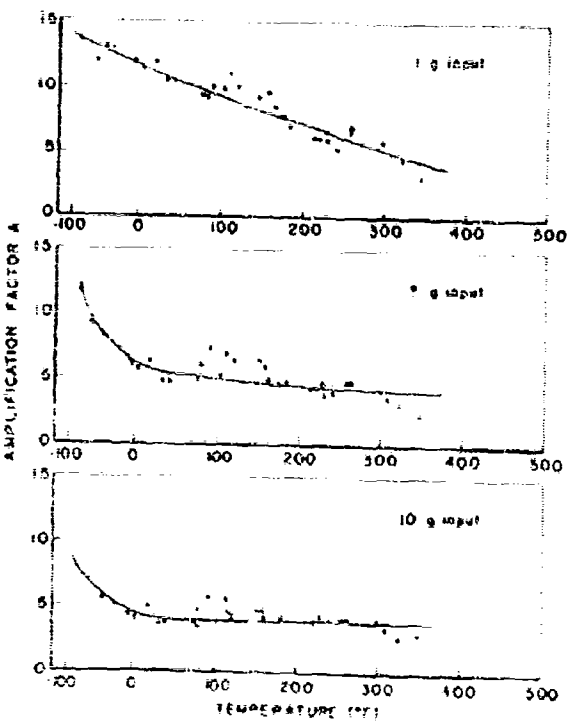

Fig. 13. Graphs of amplification factors against temperature for antenna/Silicone damper system (1-, 5-, and 10-g inputs)

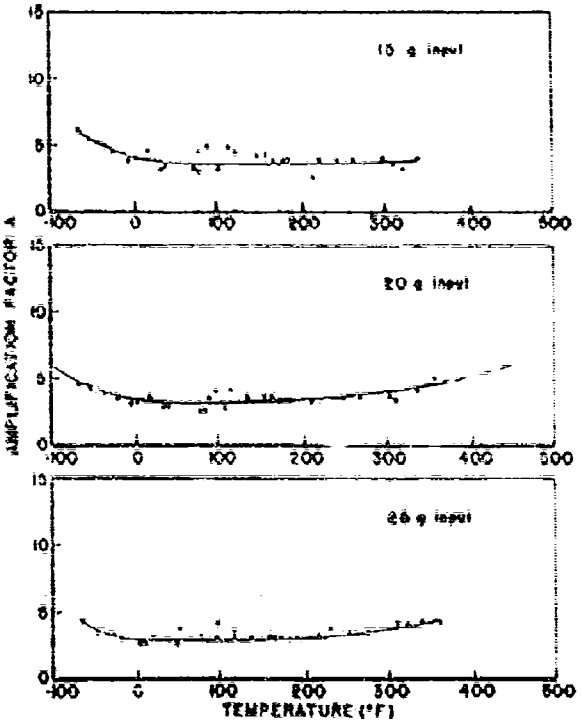

Fig. 14. Graphs of amplification factors against temperature for antenna/Silicone damper system (15-, 20-, and 25-g inputs)

Fig. 14 than in Fig. 13 because the damper was tuned for the high acceleration input levels. Because of temperature limitations on the measuring accelerometers, tests on the system were carried out up to +350°F only. However, it is expected that these dampers would operate up to +500°F with low amplification factors, because the material properties change only slightly between +350° and +500°F. A comparison is made in Fig. 15 of the amplification factors accomplished by the initial tuned damper and the wide temperature Silicone tuned damper. It can be seen from this figure that the Silicone damper introduced higher damping into the antenna over a considerably wider temperature range than the Paracril-BJ damper. No field tests are available on these Silicone tuned dampers; however, because of the low amplification factors introduced, it is expected that they would increase the life of the antenna by at least as much as, and possibly more than, the initial Paracril-BJ tuned dampers.

A more practical design than the experimental one of Fig. 12 is shown in Fig. 16. To minimize stress concentration conditions, this design gives more attention to the geometry of the viscoelastic material. The cap in this design serves as a protective measure for the tuning mass in case of failure. Tuned dampers with a wide range of different natural frequencies can be made by use of this compact lightweight design. This can be accomplished by varying the mass of the damper, the stiffness of the link, or both.

CONCLUSIONS

It has been demonstrated that, using the design procedure outlined, tuned viscoelastic dampers can be designed and built to work effectively over a wide temperature range and under a severe vibrational environment.

ACKNOWLEDGMENTS

The author wishes to thank D. I. G. Jones, of the Air Force Materials Lab., for his continued guidance and interest in this investigation; H. A. DeMarey, of the Univ. of Dayton, for

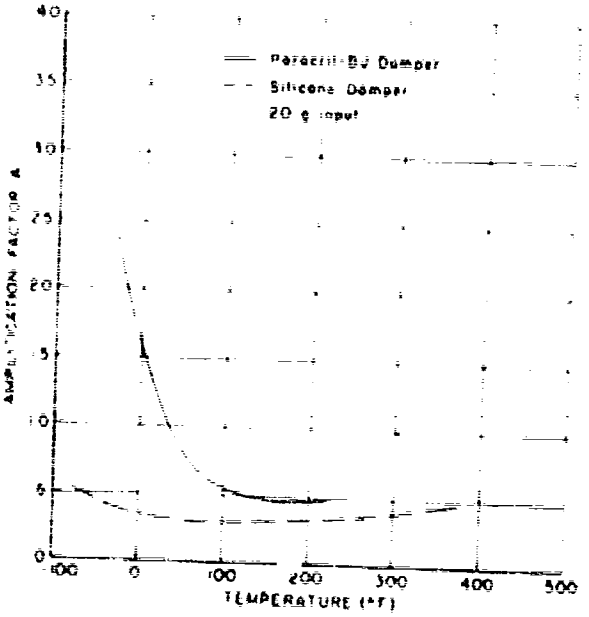

Fig. 15. Comparison of the effectiveness of the Paracril-BJ damper and the Silicone damper

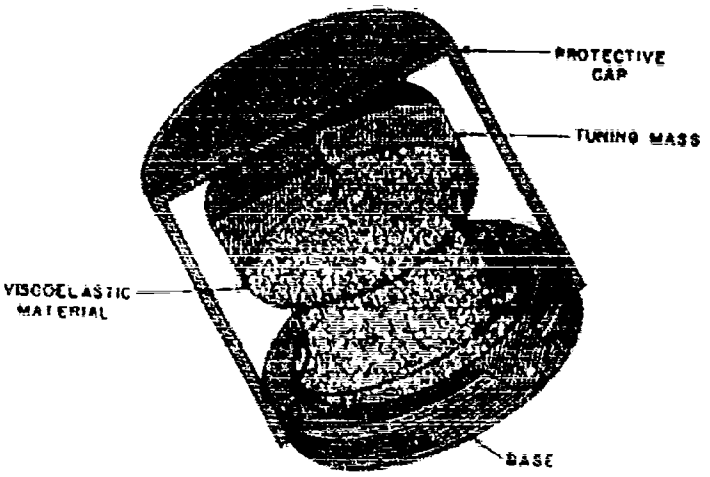

Fig. 16. Sketch of a practical tuned damper design

his assistance in preparing the figures, Connie Gillmore for typing the manuscript; and the Dow Corning Corp. for providing the viscoelastic material.

This work represents part of the Vibrations and Damping Research and Development Program at the Air Force Materials Lab., Metals and Ceramics Div., Strength and Dynamics Branch, under Project No. 7351, "Metallic Materials," Task No. 735100, "Behavior of Metals," under USAF Contract No. F 33615-67-C1187
This paper may be reproduced for purposes of the U.S. Government

REFERENCES

1. D. I. G. Jones, A. D. Nashif, and R. Adkins, "Effect of Tuned Dampers on Vibrations of Simple Structures," J. AIAA, 5(2):210-215 (Feb. 1967)

2. D. I. G. Jones and G. R. Drunn, "Effect of Tuned Viscoelastic Dampers on Response of Multi-Span Structures," 38th Shock and Vibration Bulletin, Part 4, Apr. 1967, pp. 49-64

3. D. I. G. Jones et al., "Development of a Tuned Damper to Reduce Vibration Damage in an Aircraft Radar Antenna," AFML-TR-67-307, Sept. 1967

4. D. I. G. Jones, "Analytical and Experimental Investigation of the Effect of Tuned Viscoelastic Dampers on Response of Simple Beams with Various Boundary Conditions," AFML-TR-67-214, June 1967

5. A. D. Nashif, "A New Method for Determining the Damping Properties of Viscoelastic Materials," 38th Shock and Vibration Bulletin, Part 4, Apr. 1967, pp. 34-47

6. C. M. Cannon, A. D. Nashif, and D. I. G. Jones, "Damping Measurements on Soft Viscoelastic Materials Using a Tuned Damper Technique," to be presented at the 38th Shock and Vibration Symp. in St. Louis, Mo., May 1969

DISCUSSION

Mr. Thrasher (B. F. Goodrich Co.): I was concerned with the large temperature range, that is from -100° to +500°F. Did you look at the aging properties of your materials? I think that that would be a very important factor in any design. The dynamic properties of the materials would change considerably with any exposure time to these high temperatures.

Mr. Nashif: You are right about aging of viscoelastic materials and the change of the properties of these materials with service life. We are planning to conduct some tests on some of these materials to find their effectiveness with time.

Mr. Thrasher: I think you will find quite a change between the dynamic and the static properties.

Mr. Nashif: On some of these Silicone materials the aging is not very important.

Mr. Bouche (Endevco Corp.): I understand that you would select the stiffness of the material and the size of the mass to make the tuned damper resonant frequency coincide with the frequency of the structure. However, I would like to mention that this is an excellent application for mechanical impedance measurements. Mechanical impedance measurements in designing a damper of this type would permit you not only to know the frequency for designing the damper, but it would also determine how large a mass to use to damp the structure effectively. In other words, if instrumentation were available, it would be possible to measure the mechanical impedance of the structure at the connector without the damper, then add a damper and measure its mechanical impedance. You could then predict the amount of attenuation that would result from attaching the damper.

Mr. Nashif: We never tried to adopt that procedure; however, it does sound interesting.

Mr. Wallerstein (Lord Manufacturing Co.): I would be interested to know the strain amplitudes at which you ran your test, because you mentioned that there were severe vibratory conditions. Also, for how long a period of time did you conduct the vibration testing at elevated temperatures?

Mr. Nashif: We do not have any figures on the Silicone damper in service. However, we

have some figures that the Paracril-BJ damper was subjected to. The first damper was subjected to an environment of approximately 3 g's/Hz and it operated effectively for several months. The Silicone dampers have comparable tensile strength and it is expected that they would operate also for that length of time.

Mr. Jones (Air Force Materials Lab.): I would like to add a comment about the degradation of material properties with time. There is a huge variety of materials from most of the chemical companies as most of us are well aware. Each one has its own characteristics, and in most areas there are materials available which will meet almost any condition. The main problem is to get a combination of all the desirable properties together into one material. We do not pretend to have all the answers. I do not know if anybody else does either.

Mr. Nelson (Tulsa Univ.): Did you notice any effects due to dissipative heating in the viscoelastic material itself?

Mr. Nashif: Yes, we measured temperature rise of 30° or 50°F on the Paracril-BJ damper. On the Silicone dampers we did not attempt to measure the heat dissipation because, as you see from the damping properties of the material, that was not very significant.

Mr. Trapp (Air Force Materials Lab.): I would like to add a few words here on the deterioration of these materials. They certainly do deteriorate, but our problems at the moment in the Air Force are of very short-term duration. We are very happy to solve them with any material at the moment.

* * *

MULTIFREQUENCY RESPONSE OF VISCOELASTIC DAMPERS

Ronald K. Newman and David C. Kraft
University of Dayton
Dayton, Ohio

A theoretical approach for the determination of the response of damped structural components to periodic nonsinusoidal and transient dynamic loadings is available through use of superposition principles for linear viscoelastic materials. Only a small amount of experimental data is available, however, which verifies the applicability of this approach to damping materials that exhibit a fair degree of linearity under single-frequency excitation.

The vibration response of a viscoelastic material under double-frequency input excitation is investigated analytically and experimentally. Comparisons between theoretical predicted and measured peak accelerations, and force-acceleration hysteresis loops were made for an experimental single-degree-of-freedom damped system. The correlation of measured and theoretical response was favorable (± 10 percent).

An experimental procedure for determining the damping properties of viscoelastic materials is developed. The equations for determining these properties using experimental data are detailed.

INTRODUCTION

The use of viscoelastic materials as damping treatments on structural aircraft components has received considerable attention as a means of reducing vibrational levels, with a consequent reduction in fatigue failures as a result of dynamic loadings. In recent years the trend has been to achieve even higher performance and lighter weight structures. This, along with the high acoustic energy levels that can excite vibrations over a broadband of frequency, has forced the engineer to rely more on techniques that damp the resonant response rather than avoidance of natural frequencies in design situations.

The use of constrained layer, viscoelastic link, and tuned damping techniques depends on the applicability of the linear theory of viscoelasticity for determination of the response of damped structures. The concept of structural (or hysteretic) damping which is based on linear viscoelastic response of damping materials has been used for many years in connection with aircraft flutter and vibration problems. The relationships involved in the use of structural damping concepts have been well defined by Soroka [1], Myklestad [2], and Bishop [3], and a thorough summary of many of the presently used techniques developed in recent years by application of these structural damping concepts has been compiled by Jones [4].

While the response of linear viscoelastic materials to single-frequency harmonic loadings has been well defined both theoretically and experimentally, many loading conditions occur that are either periodic nonsinusoidal or transient in character. A theoretical approach to these nonharmonic loadings is available through use of the Boltzman [5] superposition principle for linear viscoelastic materials. It would appear from a review of available literature that only a small amount of experimental data is available that would demonstrate the validity of this approach to the nonharmonic excitation of damping materials that exhibit a fair degree of linearity under single-frequency excitation.

This report presents the development of the equations for analyzing a single-degree-of-freedom damped system under single and multifrequency dynamic loadings. The single-frequency solution equations, when combined with data taken from the experimental test system developed, permit the determination of the structural damping parameters (k and h) of a linear viscoelastic material under single-

frequency excitation. Experimental evidence is then presented providing comparisons between the theoretically predicted response (based on the material parameters derived from single-frequency tests) and experimentally measured response of the damped test system under double-frequency excitation.

NOMENCLATURE

A_m Peak acceleration of the mass

A_o Peak input acceleration

A_{oj} Peak input acceleration of jth frequency component

A_r Peak relative acceleration

b Thickness of viscoelastic material in each joint

c Arbitrary constant

e Base of natural logarithms

E Energy loss

f Frequency

f_n Natural frequency

F_b Force on the base of the damper

F_r Relative force (force in the viscoelastic material)

G' Storage shear modulus

G'' Loss shear modulus

h Loss component of the complex stiffness

h_j Loss component of the complex stiffness at jth frequency

H Absolute value of the ratio of the peak acceleration of the mass block to the peak input acceleration

i $\sqrt{-1}$

j Designates frequency component other than lowest frequency

k Storage component of the complex stiffness

k_j Storage component of the complex stiffness at the jth frequency

K^* Complex modulus ($K^* = k + ih$)

m Mass of suspended block

m_o Mass of the base or frame of the damper

s Shear area of each damper joint

t Time

X_b Peak displacement of the base of the damper

$x_b, \ddot{x}_b$ Displacement and acceleration of the base of the damper

$x_m, \ddot{x}_m$ Displacement and acceleration of the mass block

$x_r, \ddot{x}_r$ Relative displacement and acceleration

α_j Phase angle between the jth frequency component (ω_j) and lowest frequency component (ω_1) of the input acceleration ($\ddot{x}_b$)

β Phase angle between the acceleration of the mass block and the acceleration of the base

π Pi

ϕ Phase angle between the relative acceleration and the acceleration of the base

ω Frequency ($\omega = 2\pi f$)

DEVELOPMENT OF ANALYSIS EQUATIONS

Single Frequency

If a single-degree-of-freedom system consisting of a mass, m, suspended by a viscoelastic material as shown in Fig. 1 is considered for dynamic loading conditions, the differential equation of motion can be written as

$$m\ddot{x}_m = \Sigma \text{ forces on mass} = K^*(-x_r) \qquad (1)$$

where

$$K^* = k + ih$$

and (2)

$$i = \sqrt{-1}.$$

The complex modulus, K^*, is composed of the storage term, k, and the dissipative term, h, which often are referred to as the structural

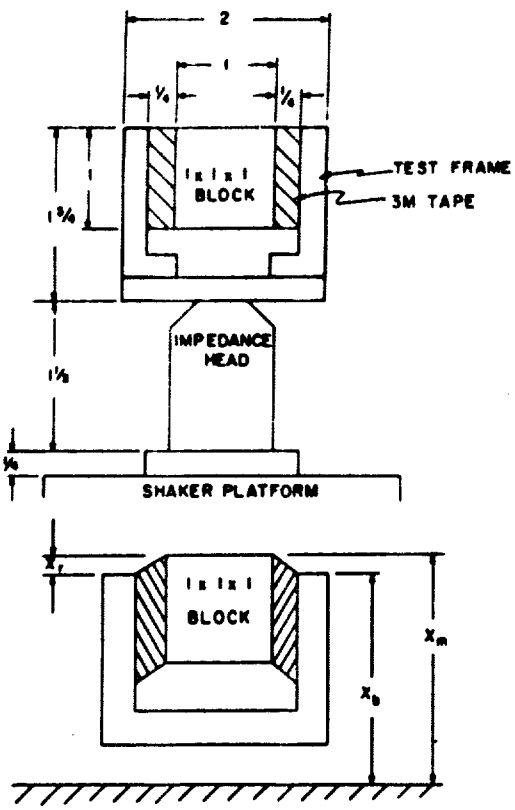

(all dimensions in inches)

Fig. 1. Single-degree-of-freedom damper system

(hysteretic) damping parameters. In Eq. (1), the inertia of the viscoelastic material has been neglected as small compared to the mass, m. The structural damping parameters, k and h, are related to the complex shear moduli, G' and G'', as

$$G' = \frac{bk}{2s}$$
$$G'' = \frac{bh}{2s} \tag{3}$$

where b = thickness of viscoelastic materials and s = shear area of each joint.

The displacement of the mass expressed in terms of the displacement of the base and the relative displacement between the mass and base (see Fig. 1) is given by

$$x_m = x_b + x_r \tag{4}$$

and

$$\ddot{x}_m = \ddot{x}_b + \ddot{x}_r . \tag{5}$$

Substitution of Eq. (5) into Eq. (1) gives

$$\ddot{x}_r + (k/m + ih/m)x_r = -\ddot{x}_b \tag{6}$$

which is the basic differential equation to be solved for x_r. If this system is excited by a harmonic displacement of the form

$$x_b = X_b e^{i\omega t} ; \tag{7}$$

then

$$\ddot{x}_r + (k/m + ih/m)x_r = X_b \omega^2 e^{i\omega t} . \tag{8}$$

Assuming a solution of the form $x_r = c e^{i\omega t}$ gives

$$x_r = \frac{X_b \omega^2 m e^{i\omega t}}{k - m\omega^2 + ih} . \tag{9}$$

Rationalizing Eq. (9) and writing the result in polar form produces

$$x_r = \frac{X_b \omega^2 m \, [\cos(\omega t - \phi) + i \sin(\omega t - \phi)]}{\left[(k - m\omega^2)^2 + h^2\right]^{1/2}} \tag{10}$$

$$\phi = \tan^{-1}\left[\frac{h}{k - m\omega^2}\right] . \tag{11}$$

Realizing that the imaginary part of Eq. (10) is the particular integral corresponding to a forcing function of $X_b \sin \omega t$, the solution for this type of forcing function can be written as

$$x_r = \frac{X_b \omega^2 m \sin(\omega t - \phi)}{\left[(k - m\omega^2)^2 + h^2\right]^{1/2}} \tag{12}$$

where $X_b \omega^2$ = peak acceleration of the base and ϕ = phase angle between the relative acceleration and the acceleration of the base.

Because the relative displacement or acceleration could not be measured directly in the test program, it was necessary to express the response of the system in terms of the acceleration of the mass ($\ddot{x}_m$) and the acceleration of the base ($\ddot{x}_b$). This is accomplished by substituting Eqs. (7) and (12) into Eq. (5) which yields

$$\ddot{x}_m = -A_o \sin \omega t - \frac{A_o m\omega^2 \sin(\omega t - \phi)}{\left[(k - m\omega^2)^2 + h^2\right]^{1/2}} \tag{13}$$

where $A_o = X_b \omega^2$.

The energy dissipated per cycle of the system can be expressed as

$$E = \oint F_r \, dx_r \tag{14}$$

where

$$F_r = (k + ih)x_r \tag{15}$$

and differentiating Eq. (12) gives

$$dx_r = \frac{\omega A_o m \cos(\omega t - \phi)}{\left[(k - m\omega^2)^2 + h^2\right]^{1/2}} dt . \tag{16}$$

Substitution of Eq. (9) into Eq. (15) and retention of the imaginary component yields

$$F_r = \frac{A_o m}{(k - m\omega^2)^2 + h^2} \left\{ \left[k(k - m\omega^2) + h^2\right] \sin \omega t - hm\omega^2 \cos \omega t \right\} \tag{17}$$

from which Eq. (14) can be written as

$$E = \int_0^{2\pi/\omega} \frac{A_o^2 m^2 \omega \cos(\omega t - \phi)}{\left[(k - m\omega^2)^2 + h^2\right]^{3/2}} \left\{ \left[k(k - m\omega^2) + h^2\right] \times \sin \omega t - hm\omega^2 \cos \omega t \right\} dt . \tag{18}$$

Upon integration of Eq. (18), the energy per cycle can be expressed as

$$E = \frac{A_o^2 m^2 h \pi}{(k - m\omega^2)^2 + h^2} . \tag{19}$$

Again, because the relative force and displacement could not be measured directly in the test program, but realizing that the forces involved are small and that consequently the only energy dissipated in the system must be in the viscoelastic material, the energy per cycle can also be expressed by

$$E = \oint F_b \, dx_b \tag{20}$$

for which

$$F_b = (k + ih)\, x_r + m_o A_o \sin \omega t \tag{21}$$

where m_o = mass of base or frame of test figures, and

$$dx_b = (A_o/\omega) \cos \omega t . \tag{22}$$

Substitution of Eqs. (21) and (22) into Eq. (20) and integrating yields the same expression for energy dissipated per cycle as given by Eq. (19). Consequently, the energy loss in the viscoelastic material can be obtained by recording the total force to the base vs the displacement of the base over a full cycle.

Multifrequency

Using the principle of superposition, the response of the single-degree-of-freedom system to an n-multiple frequency input is given by

$$\ddot{x}_m = -A_{o1} \sin \omega_1 t - \frac{A_{o1} m\omega_1^2 \sin(\omega_1 t - \phi_1)}{\left[(k_1 - m\omega_1^2)^2 + h_1^2\right]^{1/2}} - \sum_{j=2}^{n} \left\{ A_{oj} \sin(\omega_j t - \alpha_j) - \frac{A_{oj} m \omega_j^2 \sin(\omega_j t - \phi_j - \alpha_j)}{\left[(k_j - m\omega_j^2)^2 + h_j^2\right]^{1/2}} \right\} \tag{23}$$

where α_j = phase angle between the jth frequency component (ω_j) and the lowest frequency component (ω_1).

The energy loss from a multiple frequency input is not as evident as the response equation. Using superposition, the relative force and differential relative displacement become

$$F_r = \frac{A_{o1} m}{(k_1 - m\omega_1^2)^2 + h_1^2} \left\{ \left[k_1(k_1 - m\omega_1^2) + h^2\right] \times \sin \omega_1 t - h_1 m\omega_1^2 \cos \omega_1 t \right\} + \sum_{j=2}^{n} \left[\frac{A_{oj} m}{(k_j - m\omega_j^2)^2 + h_j^2} \left\{ \left[k_j(k_j - m\omega_j^2) + h_j^2\right] \times \sin(\omega_j t - \alpha_j) - h_j m\omega_j^2 \cos(\omega_j t - \alpha_j) \right\} \right] \tag{24}$$

and

$$dx_r = \left\{ \frac{\omega_1 A_{o1} m \cos(\omega_1 t - \phi_1)}{\left[(k_1 - m\omega_1^2)^2 + h_1^2\right]^{1/2}} + \sum_{j=2}^{n} \frac{\omega_j A_{oj} m \cos(\omega_j t - \phi_j - \alpha_j)}{\left[(k_j - m\omega_j^2)^2 + h_j^2\right]^{1/2}} \right\} dt . \tag{25}$$

Substituting Eqs. (24) and (25) into Eq. (14) and integrating over one cycle of the lowest frequency component gives the following equation for multiple cycle energy loss:

$$E = \frac{A_{o1}^2 \omega^2 m h_1}{(k_1 - m\omega_1^2)^2 + h_1^2} + \sum_{j=2}^{n} \frac{\omega_j}{\omega_1} \frac{A_{oj}^2 \omega^2 m h_j}{(k_j - m\omega_j^2)^2 + h_j^2} \tag{26}$$

Upon inspection of Eqs. (19) and (26), it is evident that

$$E = E_1 + \sum_{j=2}^{n} \frac{\omega_j}{\omega_1} E_j \tag{27}$$

This energy expression is valid when ω_j is an integral multiple of ω_1, because the quantity E is an energy loss only if an integral number of cycles is considered. It should be noted that x_b and F_b are the measurable quantities and, as in the single-frequency problem, the energy loss can also be obtained from $\oint F_b dx_b$ over one cycle of the lowest frequency component.

Material Vibration Parameters

The parameters k, h, and ϕ, as given in Eqs. (13) and (19), are properties of the material and depend on the physical size of the particular damping pieces used in the experiment (see Eq. (3)). These parameters, then, are of considerable interest and must be evaluated over the frequency range of interest.

Because ϕ could not be directly measured but the phase angle β between the acceleration of the base and the acceleration of the mass could be, it was necessary to calculate the peak relative acceleration and ϕ from the vector diagram shown in Fig. 2. Using the law of cosines,

$$A_r = \left(A_o^2 + A_m^2 - 2A_o A_m \cos \beta\right)^{1/2} \tag{28}$$

where A_r, A_o, and A_m are the experimentally determined peak relative, input, and mass accelerations respectively. The angle ϕ, between relative acceleration and the acceleration of the base, must then be given as two separate equations, which are

$$\phi = \sin^{-1}\left[(A_m / A_r) \sin \beta\right] \quad \text{for } A_m \cos \beta \geq A_o$$

and (29)

$$\phi = -\sin^{-1}\left[(A_m / A_r) \sin \beta\right] \quad \text{for } A_m \cos \beta < A_o$$

Having determined ϕ, and knowing the value of the peak acceleration of the mass, it is then necessary to determine the value of ωt at which this peak occurs. Differentiating Eq. (13) and

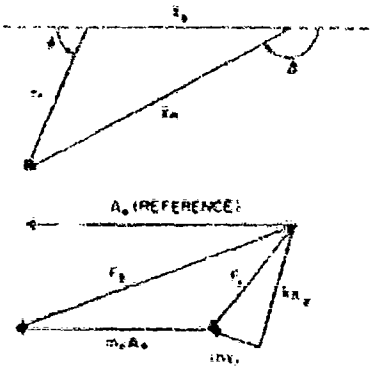

Fig. 2. Acceleration and force diagrams

setting the result equal to zero yields the value of ωt where $\ddot{x}_m$ is a maximum as given by

$$\omega t = \tan^{-1}\left\{\frac{-\left[(k - m\omega^2)^2 + h^2\right]^{1/2} - m\omega^2 \cos \phi}{m\omega^2 \sin \phi}\right\}. \tag{30}$$

Substituting Eqs. (11) and (30) into Eq. (13) and solving for the parameter k gives

$$k = m\omega^2 \left\{\frac{1 - \cos^2\phi \pm \cos \phi \left[\cos^2\phi - (1 - H^2)^2\right]^{1/2}}{(1 - H^2)}\right\} \tag{31}$$

where

$$H = \left|\frac{A_m}{A_o}\right| \tag{32}$$

Thus the values of ϕ, k, and h can be determined directly from Eqs. (29), (31), and (11), respectively, based on experimental measurements of A_o, A_m, and β. Care must be used when solving Eq. (31) for k. The only sure way of determining the correct root of the quadratic is to plug the values of k and h back into Eq. (13) and solve for $\ddot{x}_m$ which will prove to be equal to A_m for the correct root of Eq. (31). Also, knowing k, h, and A_o permits energy loss determinations for single and multifrequency excitations by use of Eqs. (19) and (27). To facilitate the evaluation of experimental data, computer programs were written for the Univ. of Dayton Burroughs 220 digital computer to calculate k, h, and ϕ, and also to calculate F_b and x_b vs time, and $\ddot{x}_m$ vs time for multiple frequency excitations.

TEST PROCEDURE

The test setup developed and used in the experimental evaluation of k, b, and ζ and in determination of the response of a single-degree-of-freedom system to double-frequency excitation is shown in Fig. 1. The viscoelastic material chosen was Scotch Mount Pressure Sensitive Tape No. 9033C, manufactured by the 3M Co. This damping material was chosen because of its relatively low elastic modulus as necessitated by the limited capacity of the shaker, its significant change in modulus and phase angle with frequency, and its linear response in the frequency and acceleration range of interest. Sensitivity to temperature and change in properties with age are undesirable characteristics of this material that were overcome by holding the test temperature constant (±1°F) and by collecting the experimental data for comparison purposes over a one-day period.

Assembly of the damper was accomplished by attaching the tape to mass and assembling the frame with the tape to mass in place (see Fig. 1). The damper was mounted atop an impedance head that was then fastened to the shaker. The impedance head permitted the measurement of the force and acceleration applied to the test frame. A miniature accelerometer was attached to the top of the vibrating mass block. In addition, three thermocouples were inserted in the viscoelastic material during the tests to monitor the temperature variations. The characteristics of the test setup are detailed in Table 1.

To insure that the motion of the test setup was that of a single-degree-of-freedom system in the frequency range of interest (100 to 1000 Hz), the resonant frequency of the cantilever motion of the test frame was determined (f_n > 2000 Hz) and verified experimentally.

The basic circuitry network used for excitation, amplification, and recording is schematically represented in Fig. 3. This network consisted essentially of a square wave generator for signal excitation followed by two band pass filters for selecting the two frequency components for the double frequency tests and an amplifier network for combining the two frequency components and conditioning the signal previous to input to the shaker. In single frequency tests, only one band pass filter was used.

As indicated previously, the impedance head permitted measurement of the input force and acceleration while the accelerometer measured the acceleration of the mass block. The signals from these transducers were fed to a three-channel vibration amplifier-meter system and the force and acceleration levels were read directly from these three meters. The recording instrumentation used for the single-frequency tests was not suitable for the double frequency tests because the signals were no longer sinusoidal. The impedance head and accelerometer signals from double-frequency tests were fed to a data sampler which provided a one-third hertz replica of the signal which was then recorded on an x-y plotter. The following recordings were made by the x-y plotter for all double frequency tests:

1. Input acceleration vs time (combined double frequency, and each of the component frequencies).

2. Acceleration of the mass block vs time (combined double frequency, and each component frequency).

3. Force vs acceleration (combined double frequency, and each component of frequency).

The acceleration axis of the force vs acceleration plot for the single-frequency excitation could then be scaled to force vs displacement (hysteresis loop) by dividing acceleration by ω^2. The vibration amplifier meters were also read for the individual component frequencies to provide a scale for the plots.

EXPERIMENTAL RESULTS

Single Frequency

The frequency range of interest for the test program was between 100 and 1000 Hz, within

TABLE 1
Characteristics of the Test System

Component	Dimensions (in.)	Weight (g)
Frame	(side pieces) 1-1/2 x 1-1/2 x 1/4 in. (base) 2 x 2 x 1/4 in.	107.7
Suspended mass	1 x 1 x 1 in.	44.4
Accelerometer	3/8 in. Hexagonal x 1/2 in. high	5.1

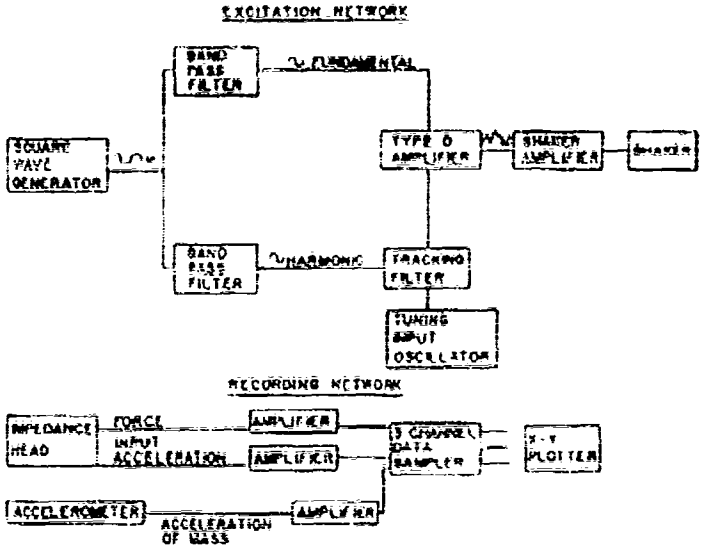

Fig. 3. Signal generating and recording network

which range the test fixture acted as a single-degree-of-freedom system. Tests were initially conducted to determine linearity of response of the damping material. The results of these tests, as given by the ratio of normalized acceleration vs the acceleration of the mass block for several frequencies, are shown in Fig. 4. Reference to Fig. 4 indicates that the damping material is approximately linear (±4 percent) within an acceleration of the mass block range of 0 to 3 g. All tests were conducted within this range.

Tests were also conducted to determine the temperature rise of the viscoelastic material during sustained vibration. Three thermocouples were inserted into the damping material (one at the mass block face, one at the frame face, and one in the middle of the damping material) to provide temperature monitoring. A

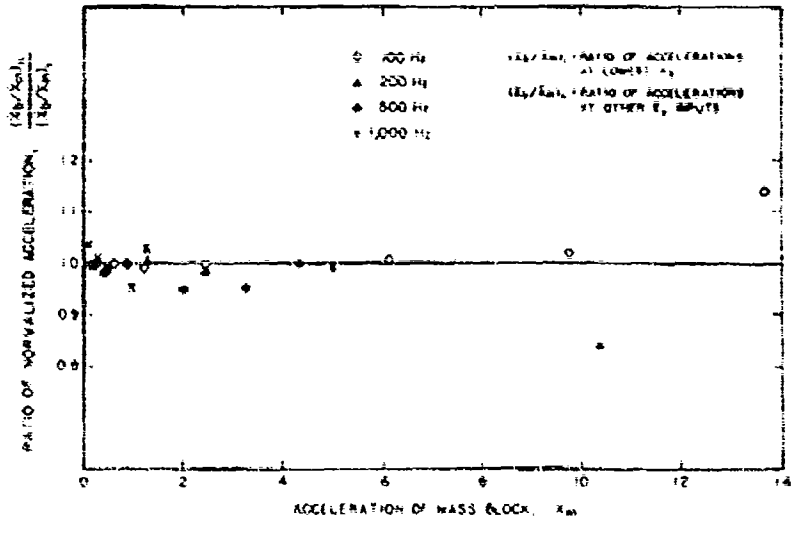

Fig. 4. Linearity of response

sustained input acceleration of 2 g for a 3-min period produced a temperature increase of less than 1°F. Temperature monitoring of the damping material was also conducted during all tests. All tests were conducted at a temperature of 70°F (±1°F).

As indicated previously, aging effects are observed for the damping material selected. Tests were conducted to determine k, h, ϕ, and H (amplification factor) on three different dates covering a 3-month period. The effects of aging on the above parameters are shown in Figs. 5, 6, and 7. The effects of aging on the damping material are to increase the values of the material property parameters k and h, and to increase the resonant frequency. The Jan. 6 single-frequency test data were taken the same day as the double-frequency test data, and consequently these k, h, and ϕ values were used in the prediction of the response of the system under double-frequency excitation.

A plot of the energy loss vs frequency is shown in Fig. 8 as developed from the Jan. 6 data. The energy loss has been normalized by dividing the energy loss by the square of displacement to make the result independent of acceleration. Values of G' and G'' as given by Eq. (3) are shown in Fig. 9. For comparison purposes, these values are compared with the moduli values previously reported by Henderson [6]. All moduli values were referenced to 75°F using a procedure described by Henderson [6]. The difference in moduli values may be a result of the effect of aging and the difference between batches of the damping material.

Double Frequency

If the k, h, and ϕ values as a function of frequency developed from single-frequency tests are combined with Eq. (23) for selected combinations of frequency, then a prediction of the response of the damped single-degree-of-freedom system under double-frequency excitation could be made. The test program used for comparing predicted and measured response is given in Table 2.

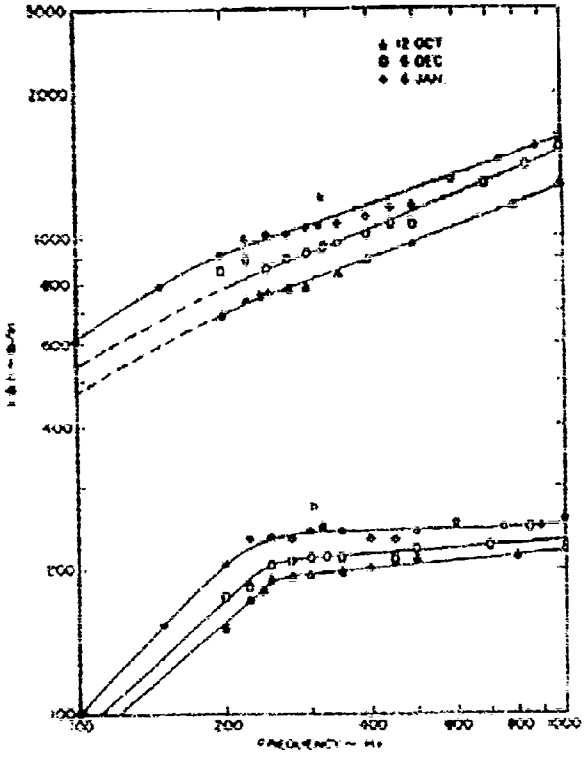

Fig. 5. k and h vs frequency

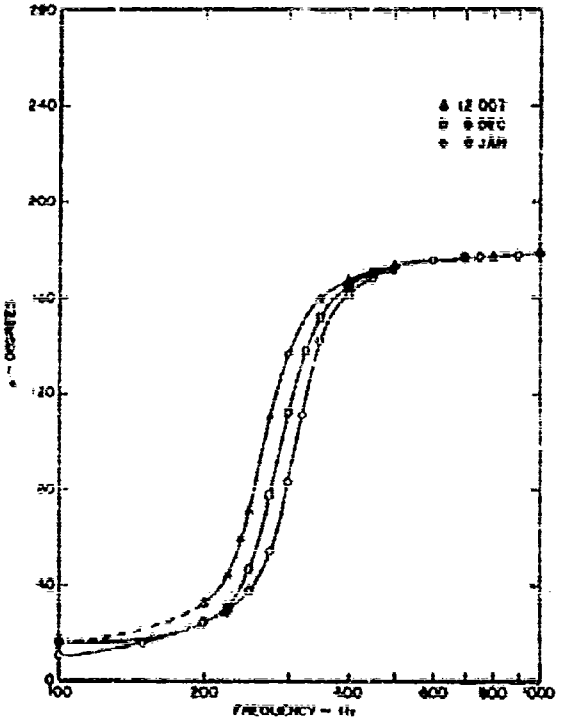

Fig. 6. Phase angle vs frequency

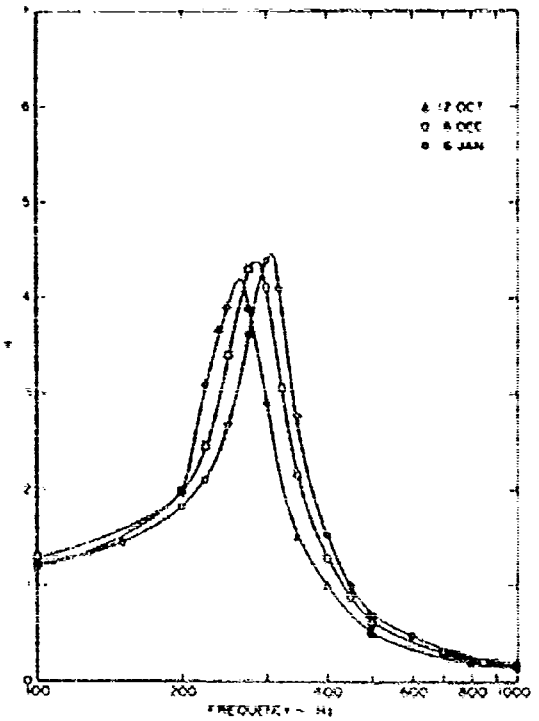

Fig. 7 Amplification factor vs frequency

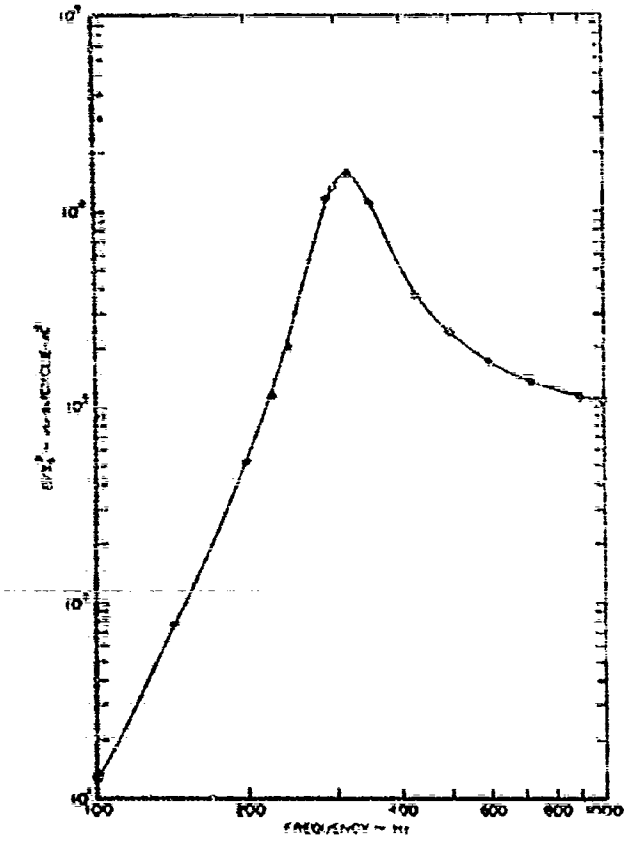

Fig. 8 Energy loss vs frequency

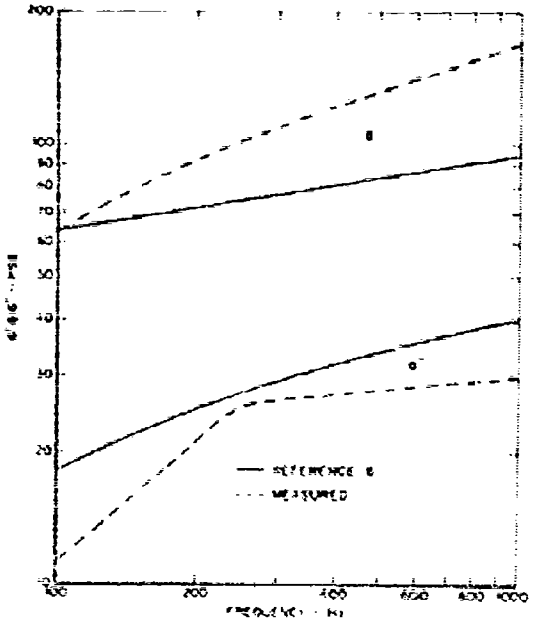

Fig. 9. Complex modulus vs frequency

TABLE 2
Experimental Comparison Program

Double Frequency (hertz)		k (lb/in.), h (lb/in.) and ϕ (degrees)	
f_1	f_2	f_1	f_2
100	300	k = 605 h = 90 ϕ = 10	k = 1040 h = 230 ϕ = 83
150	450	k = 790 h = 153 ϕ = 25	k = 1260 h = 241 ϕ = 160
150	750	k = 790 h = 153 ϕ = 26	k = 1425 h = 247 ϕ = 177
250	750	k = 985 h = 231 ϕ = 38	k = 1425 h = 247 ϕ = 177

Comparisons of the theoretical response, using superposition and the measured response of the system to a double-frequency input, are shown in Figs. 10, 11, 12, and 13. The acceleration of the mass block for one full cycle of the lower frequency is shown. Reference to Figs. 10 through 13 indicates that the measured response is very near the predicted response in both peak accelerations (±10 percent) and in waveform.

Additional comparisons were made based on the relative sizes of the predicted and measured double-frequency force-acceleration diagrams (in the form of a hysteresis loop). Figures 14, 15, 16, and 17 show the theoretical and measured single- and double-frequency force-acceleration diagrams for the frequency combinations of interest. Figure 18 shows an overlay of theoretical and measured diagrams for the 100- and 300-Hz test condition. The measured force-acceleration diagrams involving the 750-Hz frequency are suspect, because it was observed that the one-third hertz data sampler did not seem to follow the event satisfactorily. The results of the force-acceleration comparisons for theoretical and measured response were not as favorable as the acceleration-time comparisons. Discounting the 750 component which leaves only a limited basis for comparison does give a favorable comparison. In fact, the diagram for 100 and 300 Hz is exceptionally good.

It should be noted that the force-acceleration diagrams for the double-frequency tests are not energy loss diagrams. With a single-frequency input, where the peak displacement is directly proportional to the peak acceleration, the energy loss can be obtained from a force-acceleration diagram by use of a constant scaling factor (ω^{-1}) on the acceleration axis. With multifrequency input this is no longer possible. The components of the displacement derived from the basic frequencies are proportional to the component

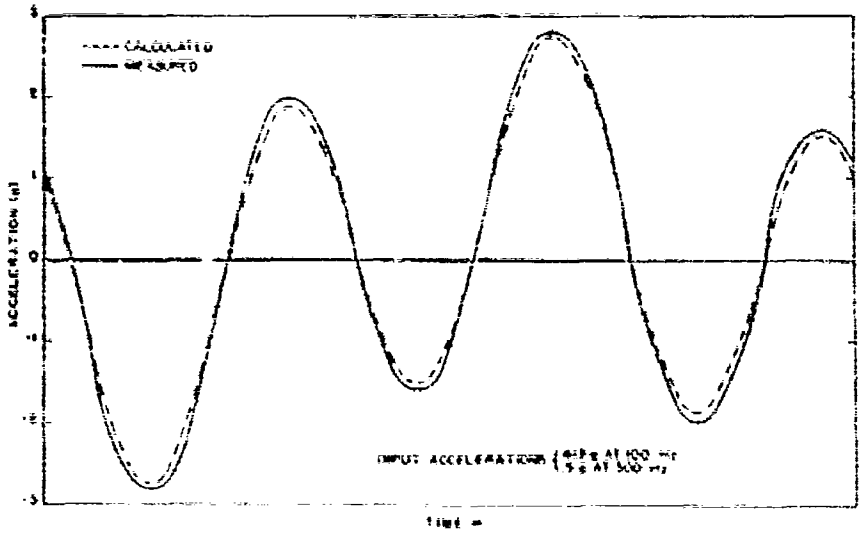

Fig. 10. Theoretical vs measured response, 100 and 300 Hz

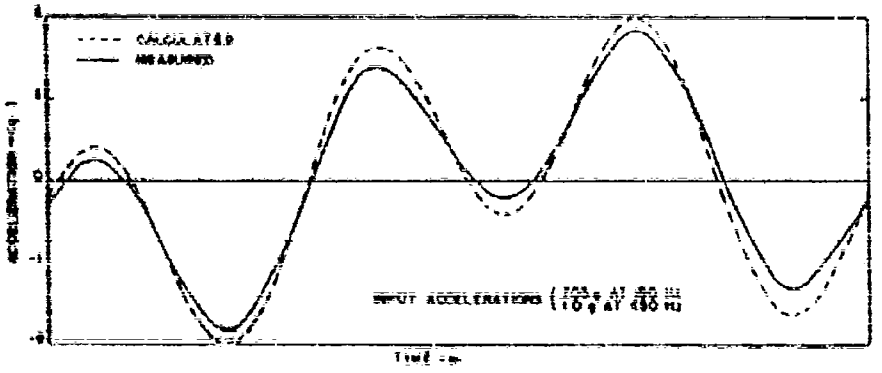

Fig. 11. Theoretical vs measured response, 150 and 450 Hz

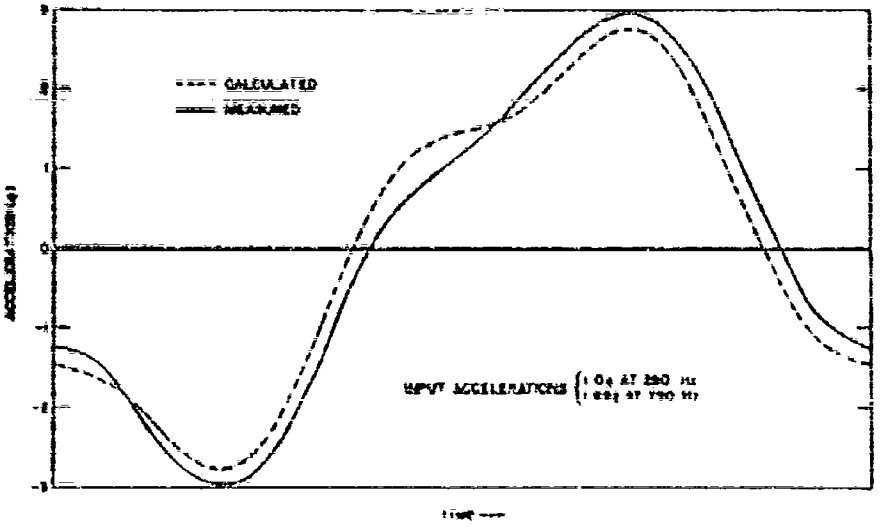

Fig. 12. Theoretical vs measured response, 250 and 750 Hz

accelerations, but the resultant displacement can no longer be derived from the resultant acceleration because the scaling factor changes with acceleration. If the assumption is made that the scaling factor is identical for predicted and measured force-acceleration diagrams, then the results do reflect energy loss comparisons.

CONCLUSIONS

The experimental technique and associated equations developed for determining the material property parameters k, h, and ϕ (or G', G'', and ϕ) from a single-frequency test were shown to be both convenient and satisfactory. Although the test system used provided material property parameters with sufficient accuracy only for the 100- to 1000-Hz range (this range is defined by the mass of the block and the spring stiffness of the damper which determines the resonant frequency), this range can easily be extended by use of a variable mass block.

The results of the theoretical and predicted response comparisons of the damped single-degree of freedom system under double-frequency excitation were consistent, based on the use of

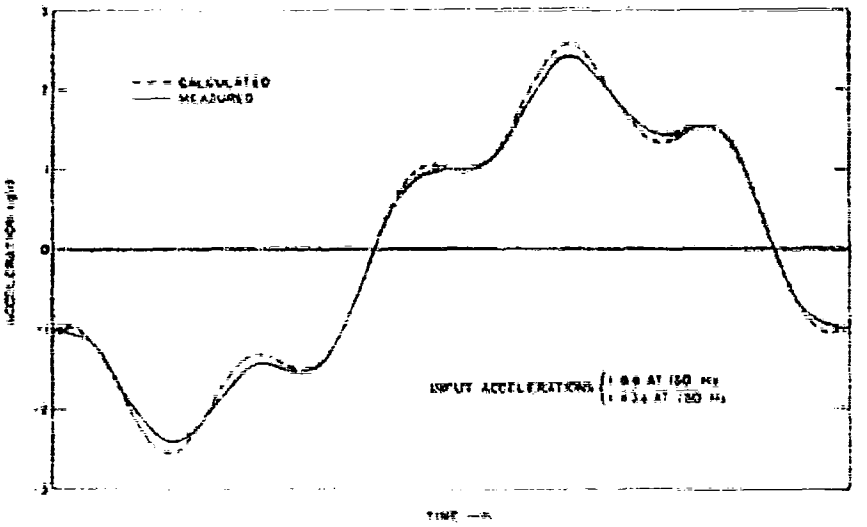

Fig. 13. Theoretical vs measured response, 150 and 750 Hz

the principle of superposition as developed for linear viscoelastic damping materials. This verification was based primarily on the results of acceleration vs time comparisons although the force vs acceleration diagrams were consistent with the exception of the 750-Hz frequency component tests for which recording difficulties were encountered.

The effects of aging on the material property parameters of the damping material, which shifted the resonant frequency approximately 50 Hz upwards over a 3-month period, is an important factor that should not be overlooked in selecting damping materials for aging situations.

ACKNOWLEDGMENTS

The authors wish to express their appreciation to Dr. D. I. G. Jones and Mr. J. P. Henderson of the Air Force Materials Laboratory for their helpful suggestions; to Mr. Ahid Nashif of the Univ. of Dayton for his guidance in selection and use of instrumentation techniques, to Mr. J. R. Schmermund of the Air Force Materials Laboratory for providing equipment setup of the instrumentation; and to Mr. D. J. Sopp, representing the 3M Co., for providing the viscoelastic tape.

REFERENCES

1. W. W. Soroka, "Note on the Relations Between Viscous and Structural Damping Coefficients," J. Aeron. Sci., pp. 409-10 and 448 (July 1949).

2. N. O. Myklestad, "The Concept of Complex Damping," J. Appl. Mech., pp. 284-86 (Sept. 1952).

3. R. E. D. Bishop, "The General Theory of 'Hysteretic Damping,'" The Aeronautical Quarterly, pp. 60-70 (Feb. 1956).

4. D. I. G. Jones, "Some Aspects of the Analysis of Damping and Vibrations in Simple Structures," A. F. Mat. Lab., Tech. Rept. AFML-TR-65-151, Dec. 1965.

5. T. Alfrey, Jr., Mechanical Behavior of High Polymers (Interscience Publ., Inc., New York), 1948.

6. J. P. Henderson, "Energy Dissipation in a Vibration Damper Utilizing a Viscoelastic Suspension," A. F. Mat. Lab., Tech. Rept. AFML-TR-65-403, Nov. 1965.

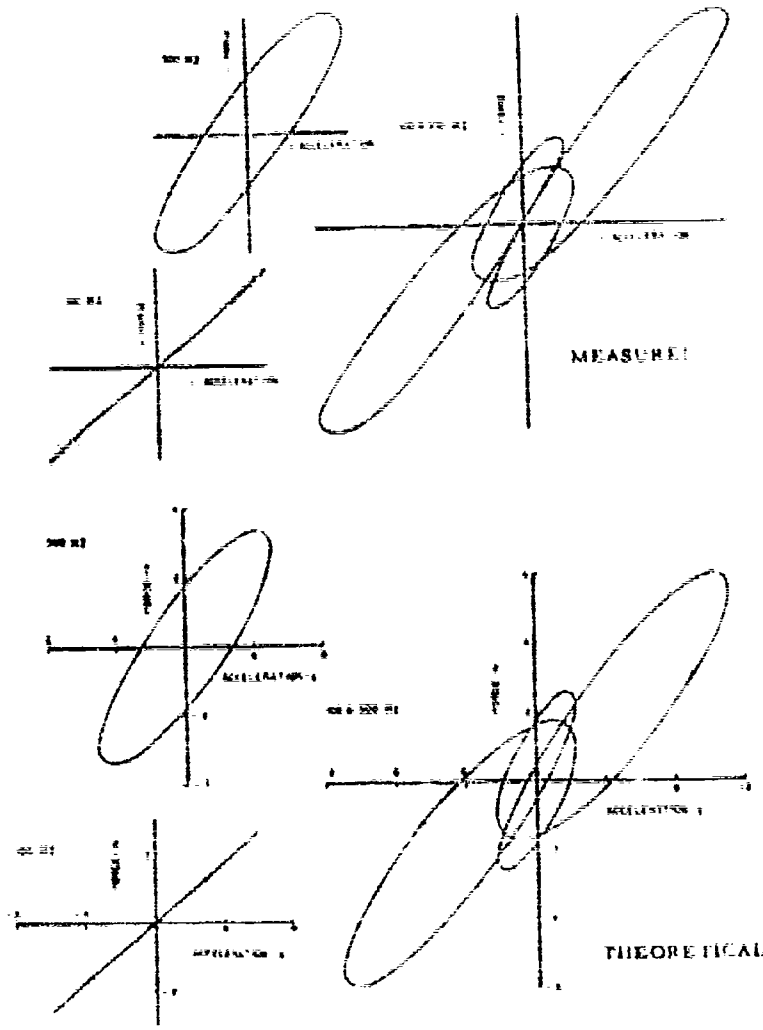

Fig. 14 Measured and theoretical force-acceleration diagrams, 100 and 400 Hz

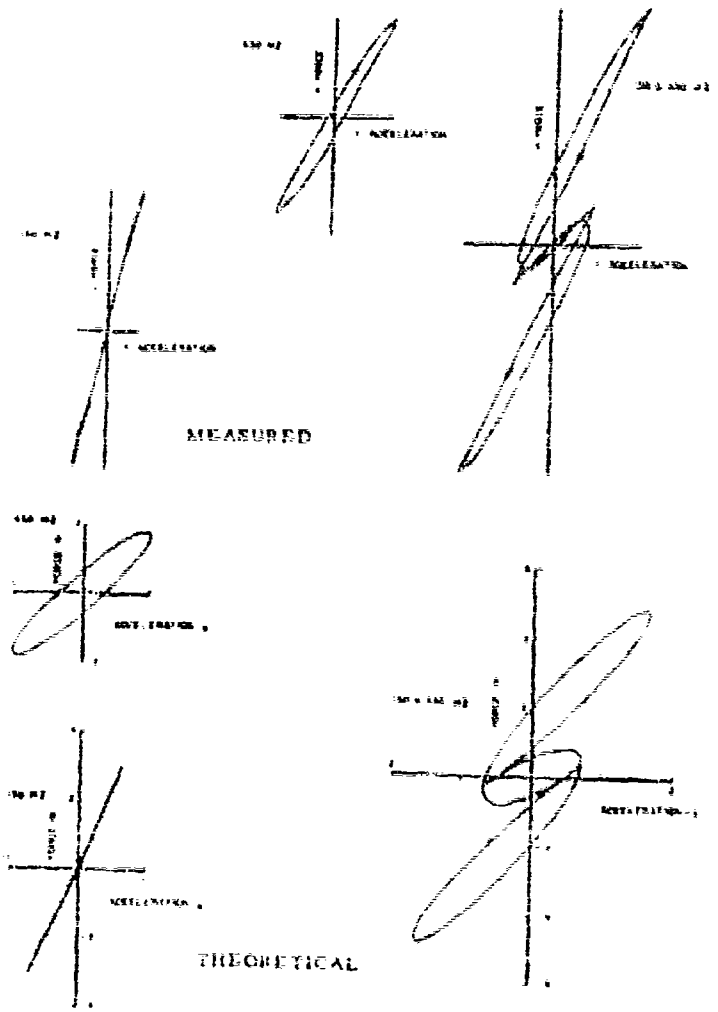

Fig. 15. Measured and theoretical force-acceleration diagrams, 150 and 450 Hz.

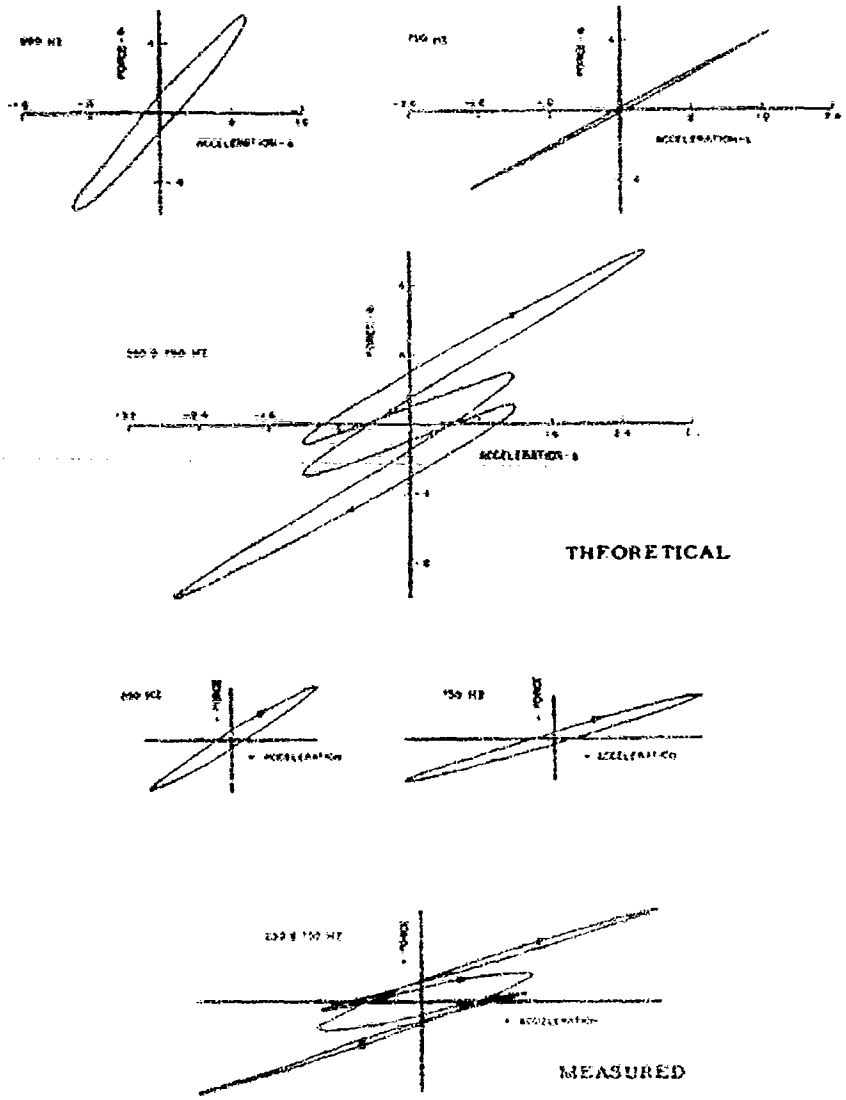

Fig. 16. Theoretical and measured force-acceleration diagrams, 250 and 750 Hz

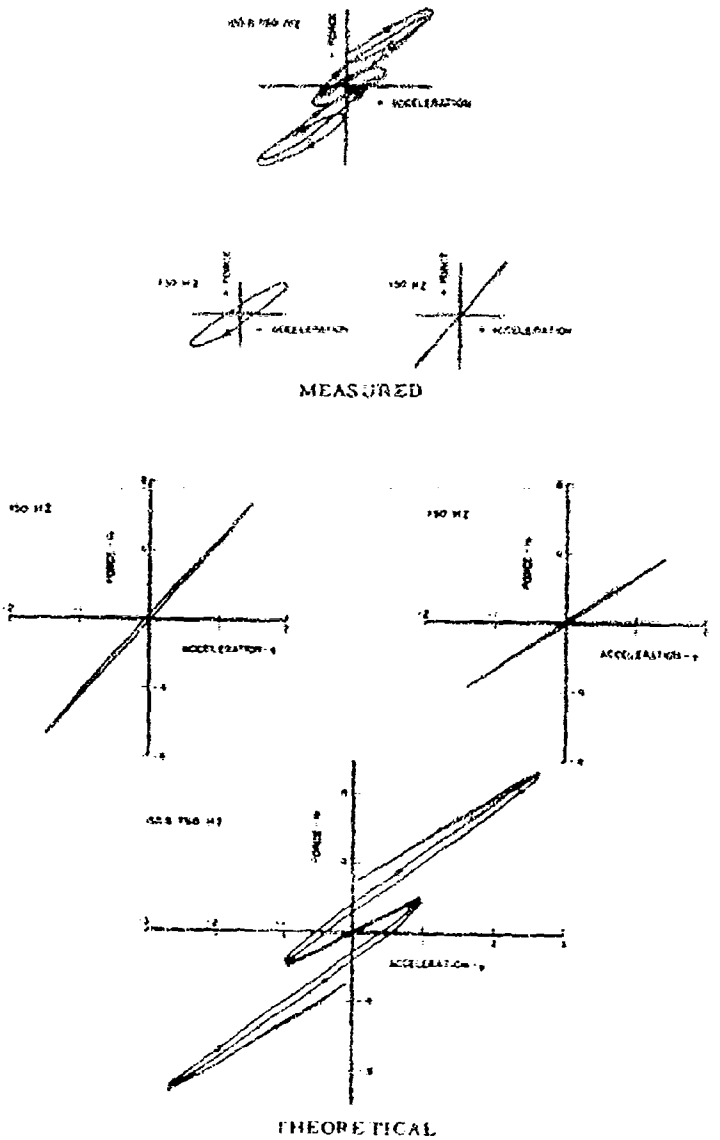

Fig. 17. Measured and theoretical force-acceleration diagrams, 150 and 750 Hz

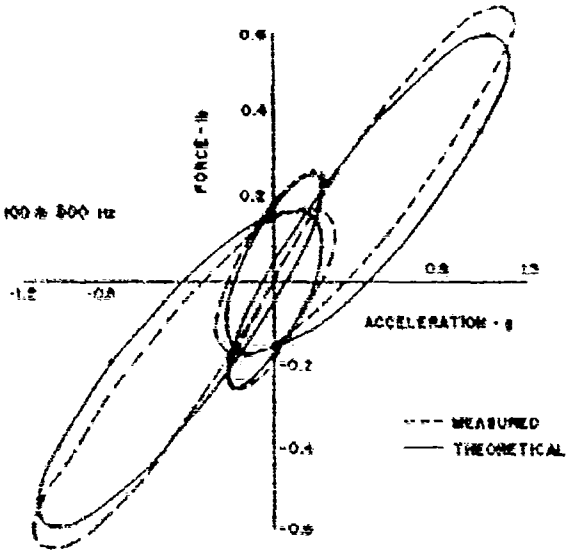

Fig. 18. Comparison of double-frequency force-acceleration diagrams, 100 and 300 Hz

DISCUSSION

Mr. McConnell (Iowa State Univ.): Did you run any other tests to compare these properties or were these tests all run with the same setup?

Mr. Kraft: Using other types of techniques?

Mr. McConnell: Yes.

Mr. Kraft: On this particular damping material we did not. However, other people have run different types of tests on the same damping material and our results compared fairly well, particularly when you consider the effects of aging which were indicated in the one figure. The data to which we compared it did not give any time period during which this damping material had been used. But they did compare fairly well to other independently run test results.

Mr. McConnell: What was the ratio of the mass that was shaking to the mass of the visco-elastic material?

Mr. Kraft: The ratio was large. I can not recall the figure, but I would guess it is between 20 and 50 to 1. In essence we ignored the mass of the damping material. This was a small test figure. We have a larger one also, with the variable mass block built into it which we hope will extend the range of capability a little bit.

* * *

THE CRITICAL DAMPING CALCULATOR AND A COMPARISON OF SELECTED STRUCTURAL DAMPING EVALUATION SYSTEMS

B. E. Douglas
Annapolis Division Naval Ship Research
and Development Center*
Annapolis, Maryland

This paper introduces and evaluates the critical damping calculator (a combination of transparent overlays for mechanical impedance or mobility graphs) and compares it with other selected damping-evaluation systems. All methods discussed are derived from a single-degree-of-freedom system. The restrictions that are explored can be classified broadly as instrumentation and application to multiple-degree-of-freedom systems.

INTRODUCTION

Designing an effective damping treatment is basically a two-part problem. The first phase is to select a structural configuration that yields high composite loss factors. This selection is based on an examination of the modes of vibration that the structure can assume in the frequency range of interest. The second phase is to find the damping material best suited to the selected structural configuration. The damping performance of a viscoelastic material can be determined from a knowledge of two of its dynamic moduli (usually the complex shear modulus and the complex Young's modulus). Evaluating these dynamic moduli is, however, a difficult experimental problem. One widely used approach is the resonance method which requires the accurate determination of damping coefficients [1]. Thus, to adequately study both phases of this design problem, it is important to establish an acceptable measuring technique that is reliable over a broad range of damping values. Toward that end, this paper will examine and compare several popular damping-evaluation systems.

All the measuring systems to be discussed are derived from the consideration of a single-degree-of-freedom system (that is, $M\ddot{x} + C\dot{x} + Kx = Fe^{i\omega t}$) and, thus, are subject to the same basic limitations. However, each of the methods has additional restrictions which can be broadly classed as (a) instrumentation and (b) application of methods described to multiple-degree-of-freedom systems.

METHODS DESCRIBED

Free-Decay Measurements

The free-decay method takes advantage of the decay with time of vibrational energy at the resonant frequencies of a test structure. In this method the acceleration signal is maximized with respect to the input force signal, thus determining the resonant frequency. The force generator is then cut off, and the resulting free-damped vibration is recorded, usually by photograph, on an oscilloscope capable of storage. The loss factor, η, is then obtained graphically from the photograph by taking the ratio of the initial amplitude, A_1, to the amplitude, A_n, n cycles later.

$$\eta = 2\frac{C}{C_c} = \frac{0.732}{n}\log_{10}\frac{A_1}{A_n} \qquad (1)$$

*The opinions or assertions made in this paper are those of the author(s) and are not to be construed as official or reflecting the views of the Department of the Navy or the naval service at large.

Figure 1 is a schematic of the instrumentation used in this method. The half-octave band filter is used to eliminate the effects of other modes of vibration. A narrowband filter is impractical because the decay of the filter would mask out the test results from the structure. With the half-octave band filter, reliable data are limited to $C/C_c < 0.05$. The relay in the switch disconnects when the force is momentarily zero and helps insure repeatable results, as no partially completed stress wave will be applied to the test item.

Equation (1) is an abbreviated form of the general solution given by Eq. (2):

$$\frac{(C/C_c)^2}{1 - (C/C_c)^2} = \left(\frac{1}{2.72_n} \log_{10} \frac{A_1}{A_2}\right)^2. \qquad (2)$$

But, Eq. (1) is generally used because of the instrumentation limitations discussed above.

Damping Properties from Mechanical Impedance and Associated Phase-Angle Data

Because mechanical impedance (or mobility) and the associated phase-angle information are widely used vibration-analysis tools, the advantage of obtaining damping coefficients from this information is to consolidate instrumentation and manpower. The three basic variations of the single-degree-of-freedom system will be discussed here. Two variations measure damping from mechanical impedance or mobility information and one from phase-angle information. In all cases, it is assumed that the resonant mechanical circuit can be represented schematically as a parallel network (Fig. 2) and that the antiresonant mechanical circuit can be represented by a series network (Fig. 3).

MARINE ENGINEERING LABORATORY

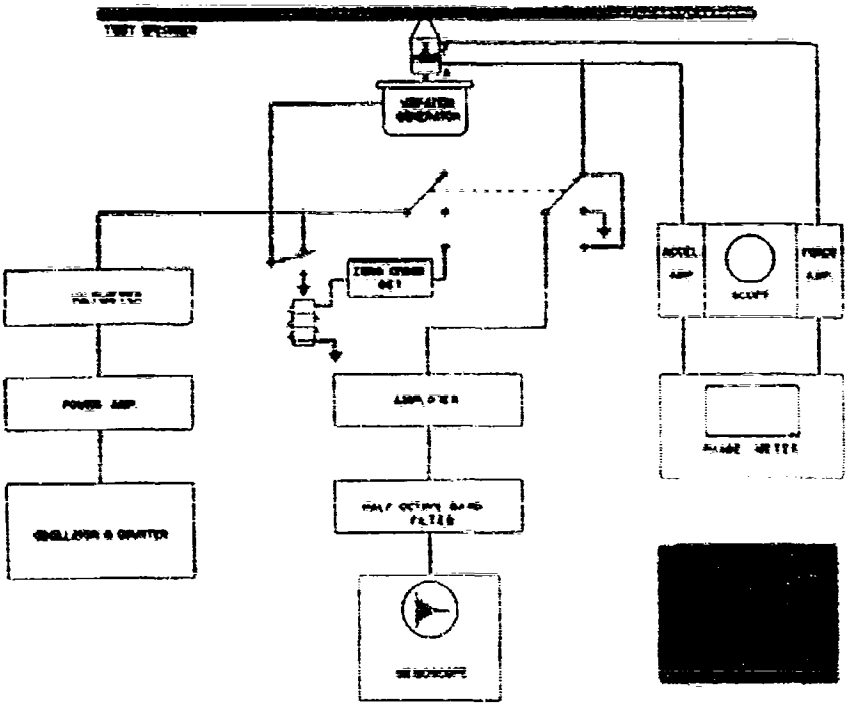

Fig. 1. Instrumentation for damping evaluation by free decay

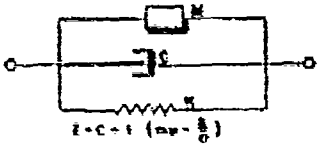

Fig. 2. Resonant circuit

Fig. 3. Antiresonant circuit

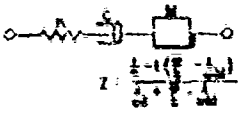

Resonant Bandwidth Transparency

Damping evaluation by this method involves a calibrated, transparent overlay (Fig. 4) for mechanical impedance or mobility graphs. This overlay is constructed from the impedance magnitude of the parallel network pictured in Fig. 2:

$$|Z| = \sqrt{KM}\left(4\frac{C}{C_c}^2 - 2 + \omega^2\frac{M}{K} + \frac{K}{M}\frac{1}{\omega^2}\right)^{1/2} \quad (3)$$

Once the desired impedance scale factor is chosen, the damping scale can then be calculated from Eq. (3). For example, 6 db above the resonance the mechanical impedance is twice the value than at resonance. Thus, Eq. (3) can be rewritten

$$\frac{C}{C_c} = 0.29\left[\omega^2\frac{M}{K} + \frac{K}{M}\frac{1}{\omega^2} - 2\right]^{1/2} \quad (4)$$

(the 6-db scale), where ω = rotational frequency at $|Z| = 2|Z_r|$. The 6-db scale is then calculated by arbitrarily selecting the resonant frequency, $\sqrt{K/M}$, and solving Eq. (4) for ω. The results can then be scaled to fit the mechanical impedance graph to be used. The arrow on the overlay is placed directly over the value of mechanical impedance at resonance and the damping is then read from the lowest scale that will give readable results.

Several limitations are inherent in this measuring system. For instance, the instrumentation will again place a lower limit on the measuring range which is governed by its dynamic range (as high as 120 db in some systems). The transducers used in connection with this system must be small enough not to apply outside constraints to the structure under test.

The upper limit is governed by the type of structure being measured. In multiple-degree-of-freedom systems, the damping coefficients obtained from resonant bandwidth measurements become somewhat questionable as the damping increases. This method reaches an upper bound also dependent on the frequency density of adjacent resonances. For example, if an antiresonance is located close to the resonance to be measured, the curve shape is not likely to be symmetrical about that resonance (as is the case of a single-degree-of-freedom system plotted on a log frequency scale). In this case, measurements should be made to favor the side away from the closest antiresonance.

Resonant Amplitude Transparency

The resonant amplitude transparency (Fig. 5) measures damping from the impedance

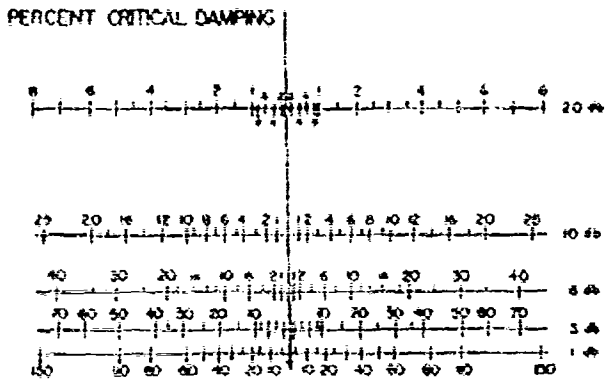

Fig. 4. Resonant bandwidth transparency

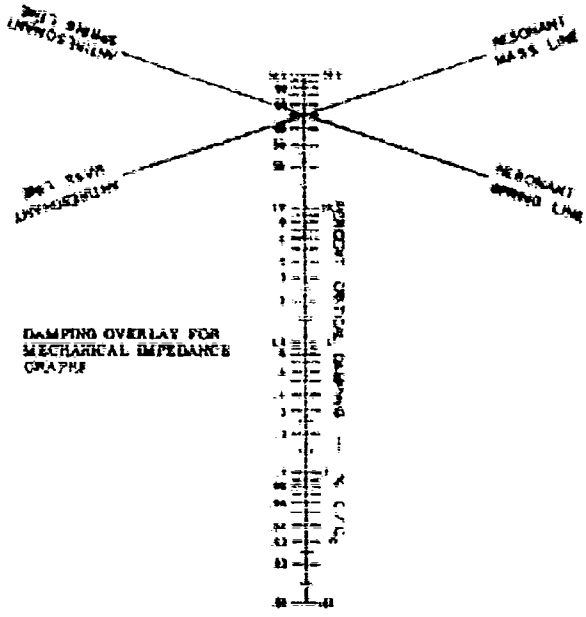

Fig. 5. Resonant amplitude transparency

magnitude of the resonance relative to its interacting spring and mass lines. This overlay extends the lower limit of the resonant bandwidth transparency and is intended to complement it. It can be computed from the equation for mechanical impedance at resonance,

$$|Z_r| = 2\sqrt{KM}\,\frac{C}{C_c}$$

by arbitrarily choosing an interacting spring and mass and scaling off the results to fit the impedance graphs to be used.

The main disadvantage of the resonant amplitude overlay is that additional information is needed to use it. Besides the resonant frequency, either the resonant mass or spring must be known. The overlay is placed on the mechanical impedance plot so that the resonant frequency coincides with the vertical damping scale. The overlay is then adjusted up or down so that the mass or spring line of the resonance in question lines up with the mass or spring line on the overlay, and the degree of damping is read at the impedance magnitude of the resonance. From symmetry considerations the same procedure can be applied to antiresonances.

The resonant amplitude overlay is preferred to the resonant bandwidth overlay when the frequency density of resonances and antiresonances is high and the damping is low, such as in the shell modes of small structures. A tacit assumption has to be made to use it properly in this case because the interacting spring and mass lines may be masked out. The spring or mass line can be located from the inflection point between the adjacent resonance and antiresonance. If the inflection point is difficult to determine, the spring line can be assumed to lie halfway (on a log scale) between the adjacent antiresonance and resonance. The basis for this assumption is that in most structural configurations the composite loss factor changes little with small changes in frequency for the same type of vibrational mode. Care has to be taken when using the overlay in this manner.

The resonant bandwidth overlay is preferred on highly damped structures with a low resonant-antiresonant frequency density because of the difficulty in locating the interacting spring and mass lines of the resonances.

Phase-Angle Method

In the single-degree-of-freedom system represented schematically in Fig. 2, the damping is directly proportional to slope of the phase-angle curve as the system passes through resonance.

$$\frac{C}{C_c} = \frac{57.3}{f_n} \frac{d\phi}{df} \qquad (5)$$

where f_n = resonant frequency (Hz) and ϕ = phase-angle measured in degrees. Note: Eq. (5) is derived from a differentiation of secant ϕ.

Unlike the two measuring systems involving impedance or mobility measurements, this system requires the experimenter to measure the phase angle at discrete frequencies rather than using the graphs that are easily obtained by the newer automatic impedance-measuring systems. This procedure is followed to assure maximum accuracy over the full range of this system. The slope is assumed to be a straight line and is measured as close to the resonance as possible. This measuring system has a lower limit, around $C/C_c = 0.005$ which is governed by the instrumentation, and an upper limit which is governed by the type of structure being measured. In the case of the flexural bending modes in beams, this limit is about $C/C_c = 0.12$.

CONCLUSIONS

It would be best to give a rigid range of accuracy for each of the methods previously discussed. This would, however, result in an oversimplification that could mislead the experimenter. The outside limits of each measuring system could be established on the basis of instrumentation and application of each method to a single-degree-of-freedom system; but this seems futile because each instrumentation setup has its own limitations and multi-degree-of-freedom structures are usually the test items.

Of the systems discussed, the combination of calibrated overlays (the so-called damping calculator) for impedance graphs seems to be the most versatile. The state-of-the-art in mechanical impedance measurements has progressed to a stage where the instrumentation presents only minor limitations compared with free decay and phase measurements. Above all, the experimenter can determine (from an examination of the mechanical impedance or mobility of the test structure) how a particular resonance can be approximated by a single-degree-of-freedom system. For this reason the upper limit of the damping calculator is somewhat higher than the other systems discussed.

REFERENCE

1. A. J. Roscoe, E. V. Thomas, and W. Blasingame, "Measurement of Complex Shear Modulus of Viscoelastic Materials by Mechanical Impedance Methods," 35th Shock and Vibration Bull., Part 7, Apr. 1966

BIBLIOGRAPHY

Bishop, R. E. D. and D. C. Johnson, The Mechanics of Vibration (Cambridge Univ. Press), 1960

DISCUSSION

Mr. Jones (Air Force Materials Lab.): You stated that there were considerable difficulties in measuring the damping properties; namely, the elastic modulus, either Young's modulus or the shear modulus and the loss factor of viscoelastic materials. I would query what grounds you have for making this statement?

Mr. Douglas: If you just use the material itself you have a limitation placed on it by the range of the moduli. In other words, by just simply making a column, applying a torque, and using transfer impedance or measurements to determine the moduli, you have the many experimental difficulties in applying your transducer to such a small system. Usually, we found that it is best to build a large test item such as a beam and invert some of the equations, say of Dr. DiTaranto in viscoelastic beams, and study that large beam because of the smaller effect the transducers would induce into the test structure itself.

* * *

FORCED RESPONSE OF LUMPED-PARAMETER SYSTEM WITH APPLICATIONS TO MISSLE DYNAMICS

John D. Sowers
Chrysler Corporation Space Division
New Orleans, Louisiana

This report presents a general method for computer solution of forced-vibration problems associated with space launch vehicles. Lumped-parameter, finite degree-of-freedom systems with damping and arbitrary forcing functions are considered. Real and complex eigenvalue problems are discussed and a method for solving forced-response problems is presented in detail.

INTRODUCTION

The object of this report is to present a general method for computer solution of forced-vibration problems associated with space launch vehicles. The report considers finite degree-of-freedom systems with damping and arbitrary forcing functions. The finite element* approach, although less rigorous than a continuum approach, is felt to be justified, because practical structures are rarely continuous. Many discontinuities, such as abrupt changes in thickness or material and numerous connections, are the norm. The matrix method is employed, not only to simplify notation and digital computer solution, but because the method is ideally suited to account for structural discontinuities.

This report presents, first, the Lagrange method of obtaining the generalized equations of motion and the arrangement of these equations into matrix format. Second, there follows a discussion of the complex eigenvalue problem and a development of the orthogonality relations for the complex eigenvectors. It is shown that the real eigenvalue problem for undamped systems is a degenerate case of the complex system and is more easily solved.

*By "finite element," it is implied that the distributed system has been reduced to discrete form by lumping its mass and stiffness into a series of masses connected by massless springs.

Third, an iterative method for solving the real eigenvalue problem is presented. The semidefinite case is discussed in detail and an approach to solving the complex eigenvalue problem is suggested.

Fourth, a practical method for solving the forced-response problem is presented. The method uses the orthogonality property of the classical normal modes to decouple the equations of motion. The uncoupled equations are then modified to account for damping.

Finally, the method is illustrated by application to the wind-gust response of a typical space launch vehicle. Digital computer routines are used to solve the matrix equations of motion for the example problem.

NOMENCLATURE

- c Damping coefficient
- e Exponential
- q Generalized coordinate
- i Indicates imaginary part of complex number
- k Stiffness coefficient
- m Mass coefficient; also bending moment

ν Complex eigenvalue

$\bar{\nu}$ Complex conjugate eigenvalue

t Time

x, y, z Cartesian coordinates

A Cross-sectional area

D Dissipation energy function

E Young's modulus; also indicates multiplication by powers of ten

F External force

G Generalized force; also shear modulus

I Area moment of inertia

L Length of beam segment

T Kinetic energy function

$[A], [B]$ Dynamic matrices defined in text

$[C]$ Damping matrix

$[I]$ Identity matrix

$[K]$ Stiffness matrix

$[M]$ Mass matrix

$[V]$ Matrix of normal mode vectors

$[K_r]$ Modal stiffness matrix

$\{q\}$ Generalized coordinate vector

$\{v\}$ Complex eigenvector

$\{v_r\}$ Real part of complex eigenvector

$\{v_i\}$ Imaginary part of complex eigenvector

$[\ ]^T$ Indicates matrix transpose

$[\ ]_d$ Indicates diagonal matrix

ω Circular frequency

τ Inverse of circular frequency

ζ Critical damping ratio

d/dt Time derivative (also indicated by dot above quantity to be differentiated)

$\partial/\partial q$ Indicates partial derivative

THE GENERALIZED EQUATIONS OF MOTION

In the following discussion it will be assumed that the system has been reduced to finite form by lumping the distributed mass at discrete points, connected by massless springs. The lumped parameters are assumed invariant with time. This procedure will lead to ordinary differential equations with constant coefficients.

If we consider a holonomic mechanical system with n degrees of freedom, its configuration can be defined by a set of independent generalized coordinates, q_k. Lagrange's equations are derived in Ref. [1] from the concept of virtual displacements and d'Alembert's principle. Reference [2] presents a derivation from a more general concept known as Hamilton's principle.

The Lagrange equations for a finite degree-of-freedom system are:

$$\frac{d}{dt}\left(\frac{\partial T}{\partial \dot{q}_k}\right) - \frac{\partial T}{\partial q_k} = G_k \qquad (1)$$

where G_k is the generalized force. In deriving the Lagrange equations there is no requirement that the force field be conservative. The generalized force may therefore consist of: (a) the forces resulting from changes in potential energy, (b) the damping or energy dissipation forces in a nonconservative system, and (c) the forces externally applied to the system.

If we choose a set of generalized coordinates such that q_k is zero in the datum configuration,* assume small oscillations about the datum, and neglect all terms higher than second order, we can express the kinetic and potential energies of the system in quadratic form as

$$T = \frac{1}{2}\sum_{j=1}^{n}\sum_{i=1}^{n} m_{ij}\dot{q}_i\dot{q}_j \qquad (2)$$

and

$$U = \frac{1}{2}\sum_{j=1}^{n}\sum_{i=1}^{n} \frac{\partial^2 U}{\partial q_i \partial q_j} q_i q_j \qquad (3)$$

As indicated by Ref. [1], Rayleigh's dissipation function may also be expressed in quadratic form as

*The datum configuration, in which $q_k = 0$, is assumed to be one of stable equilibrium.

$$D = \frac{1}{2}\sum_{i=1}^{n}\sum_{j=1}^{n}\frac{\partial^2 D}{\partial \dot{g}_i \partial \dot{g}_j}\,\dot{g}_i\dot{g}_j \tag{4}$$

Combining the dissipation forces with the forces resulting from changes in potential energy, the generalized forces, G_k, may be expressed as

$$G_k = -\frac{\partial D}{\partial \dot{g}_k} - \frac{\partial U}{\partial g_k} + F_k \tag{5}$$

where F_k denotes the applied external force corresponding to g_k. Substituting Eq. (5) into Eq. (1), Lagrange's equations can be written as

$$\frac{d}{dt}\left(\frac{\partial T}{\partial \dot{g}_k}\right) - \frac{\partial T}{\partial g_k} + \frac{\partial D}{\partial \dot{g}_k} + \frac{\partial U}{\partial g_k} = F_k\,. \tag{6}$$

The Lagrange equations lead immediately to a convenient matrix formulation. For example, considering the potential energy function, U, we have

$$\frac{\partial U}{\partial g_k} = \sum_{i=1}^{n} k_{ij} g_i \tag{7}$$

or

$$\left\{\frac{\partial U}{\partial g}\right\} = [K]\{g\}$$

where*

$$k_{ij} = \frac{\partial^2 U}{\partial g_i \partial g_j}\,. \tag{8}$$

Similarly,

$$\frac{\partial D}{\partial \dot{g}_k} = \frac{\partial}{\partial \dot{g}_k}\left(\frac{1}{2}\sum_{i=1}^{n}\sum_{j=1}^{n}\frac{\partial^2 D}{\partial \dot{g}_i \partial \dot{g}_j}\,g_i g_j\right) = \sum_{i=1}^{n} c_{ij}\dot{g}_i$$

or (9)

$$\left\{\frac{\partial D}{\partial \dot{g}}\right\} = [C]\{\dot{g}\}$$

*We have used the theorem of complimentary strain energy:

$$\frac{\partial U}{\partial g_j} = p_j\,;$$

therefore

$$\frac{\partial p_j}{\partial g_i} = \frac{\partial}{\partial g_i}\left(\frac{\partial U}{\partial g_j}\right) = \frac{\partial^2 U}{\partial g_i \partial g_j} = k_{ij} = k_{ji}$$

where k_{ij} is the force at i resulting from a unit deflection at j.

and

$$\frac{d}{dt}\left(\frac{\partial T}{\partial \dot{g}_k}\right) = \frac{d}{dt}\left(\sum_{i=1}^{n} m_{ij}\dot{g}_i\right) = \sum_{i=1}^{n} m_{ij}\ddot{g}_i \tag{10}$$

or

$$\frac{d}{dt}\left\{\frac{\partial T}{\partial \dot{g}}\right\} = [M]\{\ddot{g}\}.$$

For a Cartesian coordinate system,

$$\frac{\partial T}{\partial g_k} = 0\,.$$

Combining, we obtain the matrix equations of motion:

$$[M]\{\ddot{g}\} + [C]\{\dot{g}\} + [K]\{g\} = \{F\}\,. \tag{11}$$

As an example, the equations developed above will be applied to the three-mass problem shown in Fig. 1. From Eq. (2) the kinetic energy of the system is

$$T = \frac{1}{2}\sum_{i=1}^{3}\sum_{j=1}^{3} m_{ij}\dot{x}_i\dot{x}_j = \frac{1}{2}\left(M_1\dot{x}_1^2 + M_2\dot{x}_2^2 + M_3\dot{x}_3^2\right).$$

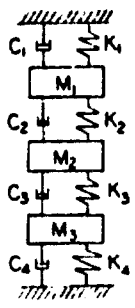

Fig. 1. Spring mass system

Note that in the above expression $m_{ij} = 0$, for $i \neq j$, because we have assumed x_i measured from the center of gravity of each mass.

The potential energy is found by Eq. (3) to be

$$U = \frac{1}{2}\sum_{i=1}^{3}\sum_{j=1}^{3} k_{ij}g_i g_j = \frac{1}{2}\left(k_{11}x_1^2 + 2k_{12}x_1x_2 + 2k_{13}x_1x_3 + k_{22}x_2^2 + 2k_{23}x_2x_3 + k_{33}x_3^2\right)$$

$$= \frac{1}{2}(k_1 + k_2)x_1^2 - k_2x_1x_2 + \frac{1}{2}(k_2 + k_3)x_2^2 - k_3x_2x_3 + \frac{1}{2}(k_3 + k_4)x_3^2\,.$$

Similarly applying Eq. (4), the dissipation energy is

$$D = \frac{1}{2}(c_1 + c_2)\dot{x}_1^2 - c_2\dot{x}_1\dot{x}_2 + \frac{1}{2}(c_2 + c_3)\dot{x}_2^2 - c_3\dot{x}_2\dot{x}_3 + \frac{1}{2}(c_3 + c_4)\dot{x}_3^2\,.$$

By performing the required differentiation of the above energy expressions and arranging in the matrix format of Eq. (9), we obtain the equations of motion for the system,

$$\begin{bmatrix} M_1 & 0 & 0 \\ 0 & M_2 & 0 \\ 0 & 0 & M_3 \end{bmatrix} \begin{Bmatrix} \ddot{x}_1 \\ \ddot{x}_2 \\ \ddot{x}_3 \end{Bmatrix} + \begin{bmatrix} (c_1 + c_2) & -c_2 & 0 \\ -c_2 & (c_2 + c_3) & -c_3 \\ 0 & -c_3 & (c_3 + c_4) \end{bmatrix} \begin{Bmatrix} \dot{x}_1 \\ \dot{x}_2 \\ \dot{x}_3 \end{Bmatrix}$$

$$+ \begin{bmatrix} (k_1 + k_2) & -k_2 & 0 \\ -k_2 & (k_2 + k_3) & -k_3 \\ 0 & -k_3 & (k_3 + k_4) \end{bmatrix} \begin{Bmatrix} x_1 \\ x_2 \\ x_3 \end{Bmatrix} = \begin{Bmatrix} 0 \\ 0 \\ 0 \end{Bmatrix}.$$

Note that all the coefficient matrices $[M]$, $[C]$, and $[K]$ are symmetric, that is, $[K] = [K]^T$, and so forth.

THE COMPLEX EIGENVALUE PROBLEM

It has been shown that the equations of motion for a multi-degree-of-freedom system with light (or small) damping can be expressed in matrix form as

$$[M]\{\ddot{q}\} + [C]\{\dot{q}\} + [K]\{q\} = \{F\} . \qquad (12)$$

In this section we will investigate the free-vibration case where $\{F\} = \{0\}$.

Considering only the homogeneous part of Eq. (12), we assume a solution of the complex form

$$\{q\} = \{u\} e^{pt} .$$

Differentiating, we obtain

$$\{\dot{q}\} = p\{u\} e^{pt}$$

and

$$\{\ddot{q}\} = p^2\{u\} e^{pt} .$$

Substituting into Eq. (12),

$$(p^2[M] + p[C] + [K])\{u\} = \{0\} . \qquad (13)$$

Equation (13) is a complex eigenvalue problem, where $\{u\}$ is the complex eigenvector and p is the complex eigenvalue. By considering any two solutions p_r and p_s, we will now establish orthogonality relations that the eigenvectors $\{u_r\}$ and $\{u_s\}$ must satisfy.

$$(p_r^2[M] + p_r[C] + [K])\{u_r\} = \{0\} \qquad (14)$$

$$(p_s^2[M] + p_s[C] + [K])\{u_s\} = \{0\} \qquad (15)$$

Multiplying Eq. (14) by $\{u_s\}^T$,

$$\{u_s\}^T(p_r^2[M] + p_r[C] + [K])\{u_r\} = 0 \qquad (16)$$

and Eq. (15) by $\{u_r\}^T$,

$$\{u_r\}^T(p_s^2[M] + p_s[C] + [K])\{u_s\} = 0 . \qquad (17)$$

Transposing Eq. (17),

$$\{u_s\}^T(p_s^2[M] + p_s[C] + [K])\{u_r\} = 0 \qquad (18)$$

and subtracting Eq. (16) from Eq. (18), we see that

$$(p_s^2 - p_r^2)\{u_s\}^T[M]\{u_r\} + (p_s - p_r)\{u_s\}^T[C]\{u_r\} = 0.$$

By dividing out the common factor, $(p_s - p_r)$, we obtain

$$(p_s + p_r)\{u_s\}^T[M]\{u_r\} + \{u_s\}^T[C]\{u_r\} = 0, \quad r \neq s. \qquad (19)$$

Also if we add Eq. (16) and Eq. (18)

$$(p_s^2 + p_r^2)\{u_s\}^T[M]\{u_r\} + (p_s + p_r)\{u_s\}^T[C]\{u_r\}$$

$$+ 2\{u_s\}^T[K]\{u_r\} = 0 \qquad (20)$$

which can be rewritten as

$$(p_s + p_r)^2\{u_s\}^T[M]\{u_r\} + (p_s + p_r)\{u_s\}^T[C]\{u_r\}$$

$$- 2p_sp_r\{u_s\}^T[M]\{u_r\} + 2\{u_s\}^T[K]\{u_r\} = 0 \qquad (21)$$

Multiplying Eq. (19) by $(p_s + p_r)$ and subtracting from Eq. (21), we obtain

$$-p_sp_r\{u_s\}^T[M]\{u_r\} + \{u_s\}^T[K]\{u_r\} = 0, \quad r \neq s. \qquad (22)$$

The complex eigenvectors satisfy the orthogonality relations given by Eqs. (19) and (22).

If $\{u_r\}$ and p_r are solutions to Eq. (13), then the complex conjugates $\{\bar{u}_r\}$ and $\bar{p}_r$ are also solutions. Therefore

$$(\bar{p}_r^2[M] + \bar{p}_r[C] + [K])\{\bar{u}_r\} = \{0\} . \qquad (23)$$

We will take p_r to be of the same form as the usual single-degree-of-freedom solution:

$$p_r = -\zeta_r\omega_r + j\omega_r\sqrt{1-\zeta_r^2}\,. \tag{24}$$

Then the complex conjugate is

$$\bar{p}_r = -\zeta_r\omega_r - j\omega_r\sqrt{1-\zeta_r^2} \tag{25}$$

Also we can express the complex eigenvectors in the form of real and imaginary parts as

$$\{u_r\} = \{v_r\} + j\{w_r\} \tag{26}$$

Then the conjugate eigenvector is

$$\{\bar{u}_r\} = \{v_r\} - j\{w_r\}\,. \tag{27}$$

Multiplying Eq. (14) by $\{\bar{u}_r\}^T$,

$$\{\bar{u}_r\}^T(p_r^2[M] + p_r[C] + [K])\{u_r\} = 0\,. \tag{28}$$

And multiplying Eq. (23) by $\{u_r\}^T$,

$$\{u_r\}^T(\bar{p}_r^2[M] + \bar{p}_r[C] + [K])\{\bar{u}_r\} = 0\,, \tag{29}$$

Transposing Eq. (28),

$$\{u_r\}^T(p_r^2[M] + p_r[C] + [K])\{\bar{u}_r\} = 0 \tag{30}$$

Subtracting Eq. (29) from Eq. (30),

$$(p_r^2 - \bar{p}_r^2)\{u_r\}^T[M]\{\bar{u}_r\} + (p_r - \bar{p}_r)\{u_r\}^T[C]\{\bar{u}_r\} = 0. \tag{31}$$

Dividing out the common term $p_r - \bar{p}_r$,

$$(p_r + \bar{p}_r)\{u_r\}^T[M]\{\bar{u}_r\} + \{u_r\}^T[C]\{\bar{u}_r\} = 0 \tag{32}$$

From Eqs. (24) and (25),

$$(p_r + \bar{p}_r) = -2\zeta_r\omega_r\,. \tag{33}$$

Therefore

$$2\zeta_r\omega_r = \{u_r\}^T[C]\{\bar{u}_r\}(\{u_r\}^T[M]\{\bar{u}_r\})^{-1}\,. \tag{34}$$

Also if we add Eqs. (29) and (30),

$$(p_r^2 + \bar{p}_r^2)\{u_r\}^T[M]\{\bar{u}_r\} + (p_r + \bar{p}_r)\{u_r\}^T[C]\{\bar{u}_r\} + 2\{u_r\}^T[K]\{\bar{u}_r\} = 0. \tag{35}$$

From Eqs. (24) and (25),

$$p_r^2 = \omega_r^2\omega_r^2 - 2\zeta_r^2\omega_r\sqrt{1-\zeta_r^2} - (1-\zeta_r^2)\omega_r^2\,,$$

and

$$\bar{p}_r^2 = \omega_r^2\omega_r^2 - 2\zeta_r^2\omega_r\sqrt{1-\zeta_r^2} - (1-\zeta_r^2)\omega_r^2$$

Therefore

$$p_r^2 + \bar{p}_r^2 = 4\zeta_r^2\omega_r^2 - 2\omega_r^2\,. \tag{36}$$

Substituting Eqs. (33) and (36) into Eq. (35)

$$(4\zeta_r^2\omega_r^2 - 2\omega_r^2)\{u_r\}^T[M]\{\bar{u}_r\} - 2\zeta_r\omega_r\{u_r\}^T[C]\{\bar{u}_r\} + 2\{u_r\}^T[K]\{\bar{u}_r\} = 0\,. \tag{37}$$

From Eq. (34) we see that

$$4\zeta_r^2\omega_r^2\{u_r\}^T[M]\{\bar{u}_r\} = 2\zeta_r\omega_r\{u_r\}^T[C]\{\bar{u}_r\}\,.$$

Therefore Eq. (37) yields

$$-2\omega_r^2\{u_r\}^T[M]\{\bar{u}_r\} + 2\{u_r\}[K]\{\bar{u}_r\} = 0$$

or rewriting,

$$\omega_r^2 = \{u_r\}^T[K]\{\bar{u}_r\}(\{u_r\}^T[M]\{\bar{u}_r\})^{-1}\,. \tag{38}$$

Turning our attention to the undamped system, we see that if $c_{ij} = 0$ in Eq. (13), the complex eigenvalue problem reduces to the real eigenvalue problem with $p_r = -j\omega_r$ and $\{u_r\} = \{v_r\}$. Equation (13) becomes

$$\omega^2[M]\{v_r\} = [K]\{v_r\}\,. \tag{39}$$

The orthogonality relations given by Eqs. (19) and (22) reduce to

$$\{v_r\}^T[M]\{v_s\} = \{v_r\}^T[K]\{v_s\} = 0\,, \quad r \neq s\,. \tag{40}$$

The undamped natural frequency can be obtained from Eq. (38):

$$\omega_r^2 = \{v_r\}^T[K]\{v_r\}(\{v_r\}^T[M]\{v_r\})^{-1}\,. \tag{41}$$

The eigenvector $\{v_r\}$ is referred to as the "normal mode vector" or "mode shape vector," because its ith element is the relative displacement of the ith mass of a system vibrating in its rth mode.

ITERATIVE SOLUTION FOR EIGENVALUES

The purpose of this section is to present an iterative method for obtaining numerical solutions to the real eigenvalue problem discussed in the previous section. In addition, an approximate complex eigenvalue solution for damped systems will be suggested.

Equation (39) could be written in either one of the following forms:

$$[A]\{v_r\} = \{v_r\}\lambda_r^2 \tag{42}$$

or

$$[B]\{v_r\} = \{v_r\}\omega_r^2 \tag{43}$$

where

$$[A] = [K]^{-1}[M]$$

$$[B] = [M]^{-1}[K]$$

and

$$\omega_r = \lambda_r^{-1}.$$

Considering Eq. (42), let $\lambda_1^2, \lambda_2^2, \ldots, \lambda_n^2$ denote the eigenvalues of matrix $[A]$ in descending order and let $\{v_1\}, \{v_2\}, \ldots, \{v_n\}$ be the corresponding eigenvectors. Further, let $\{v^0\}$ denote a linear combination of $\{v_1\}, \{v_2\}, \ldots, \{v_n\}$ such that

$$\{v^0\} = a_1\{v_1\} + a_2\{v_2\} + a_3\{v_3\} + \ldots + a_n\{v_n\}. \tag{44}$$

Premultiplying by $[A]$ gives

$$[A]\{v^0\} = a_1[A]\{v_1\} + a_2[A]\{v_2\} + \ldots a_n[A]\{v_n\} \tag{45}$$

which by Eq. (42) can be written as

$$\{v^1\} = a_1\lambda_1^2\{v_1\} + a_2\lambda_2^2\{v_2\} + \ldots + a_n\lambda_n^2\{v_n\}. \tag{46}$$

Multiplying Eq. (46) by $[A]$ yields

$$[A]\{v^1\} = \{v^2\} = a_1\lambda_1^4\{v_1\} + \ldots + a_n\lambda_n^4\{v_n\}. \tag{47}$$

Repeating m times we obtain

$$[A]\{v^{m-1}\} = \{v^m\} = a_1\lambda_1^{2m}\{v_1\} + a_2\lambda_2^{2m}\{v_2\} + \ldots + a_n\lambda_n^{2m}\{v_n\} \tag{48}$$

Because

$$\lambda_n < \lambda_{n-1} < \ldots < \lambda_2 < \lambda_1$$

we can write

$$\{v^m\} \simeq a_1\lambda_1^{2m}\{v_1\}, \quad m \to \infty \tag{49}$$

and

$$\{v^{m+1}\} \simeq a_1\lambda_1^{2(m+1)}\{v_1\}, \quad m \to \infty. \tag{50}$$

Equation (50) can be written as

$$\{v^{m+1}\} = \lambda_1^2(a_1\lambda_1^{2m}\{v_1\}) = \lambda_1^2\{v^m\} \tag{51}$$

but

$$\{v^{m+1}\} = [A]\{v^m\} \tag{52}$$

Therefore

$$[A]\{v^m\} = \lambda_1^2\{v^m\} \tag{53}$$

Similarly it could be shown that

$$[B]\{v^m\} = \omega_1^2\{v^m\}. \tag{54}$$

It is obvious that Eq. (53) converges to the lowest natural frequency, while Eq. (54) converges to the highest natural frequency.

To illustrate the above iteration process, consider the three-mass problem shown in Fig. 1. For simplicity, let $k_1 = k_2 = k_3 = k_4 = 1$; $m_1 = m_3 = 1$; $m_2 = 2$. Then we have

$$[K] = \begin{bmatrix} 2 & -1 & 0 \\ -1 & 2 & -1 \\ 0 & -1 & 2 \end{bmatrix}, \quad [K]^{-1} = \begin{bmatrix} 0.75 & 0.50 & 0.25 \\ 0.50 & 1.00 & 0.50 \\ 0.25 & 0.50 & 0.75 \end{bmatrix}$$

and

$$[M] = \begin{bmatrix} 1 & 0 & 0 \\ 0 & 1 & 0 \\ 0 & 0 & 2 \end{bmatrix}; \quad [K]^{-1}[M] = \begin{bmatrix} 0.75 & 0.50 & 0.50 \\ 0.50 & 1.00 & 1.00 \\ 0.25 & 0.50 & 1.50 \end{bmatrix}$$

Let the starting vector, $\{v^0\}$, be

$$\begin{Bmatrix} 1 \\ 1 \\ 1 \end{Bmatrix}$$

$$\begin{bmatrix} 0.75 & 0.5 & 0.50 \\ 0.50 & 1.0 & 1.00 \\ 0.25 & 0.5 & 1.50 \end{bmatrix}\begin{Bmatrix} 1 \\ 1 \\ 1 \end{Bmatrix} = \begin{Bmatrix} 1.75 \\ 2.50 \\ 2.25 \end{Bmatrix}$$

$$= 2.25\begin{Bmatrix} 0.785 \\ 1.110 \\ 1.000 \end{Bmatrix} = \{v^1\}.$$

Using $\{v^1\}$ as the next approximation,

$$\begin{bmatrix} 0.75 & 0.5 & 0.50 \\ 0.50 & 1.0 & 1.00 \\ 0.25 & 0.5 & 1.50 \end{bmatrix} \begin{Bmatrix} 0.785 \\ 1.110 \\ 1.000 \end{Bmatrix} = \begin{Bmatrix} 1.645 \\ 2.502 \\ 2.251 \end{Bmatrix}$$

$$2.2510 \begin{Bmatrix} 0.737 \\ 1.110 \\ 1.000 \end{Bmatrix} .$$

After a few more trials we obtain

$$\begin{bmatrix} 0.75 & 0.5 & 0.50 \\ 0.50 & 1.0 & 1.00 \\ 0.25 & 0.5 & 1.50 \end{bmatrix} \begin{Bmatrix} 0.710832 \\ 1.102775 \\ 1.000000 \end{Bmatrix}$$

$$= 2.22909490 \begin{Bmatrix} 0.710837 \\ 1.102775 \\ 1.000000 \end{Bmatrix} .$$

$$\lambda_1^2 = 2.22909490$$

$$\omega_1^2 = 0.44661257 .$$

Having obtained the fundamental natural frequency and mode shape, it is now necessary to modify the matrix $[A]$ to obtain the second mode. Although there are many methods for doing this, the following discussion will be limited to the method of Ref. [3]. For this purpose we need a generalized orthogonality relation for the eigenvectors of the matrix $[A]$.

To develop this orthogonality relation let us consider the equation

$$\{y_s\}^T[A] = \lambda_s^2 \{y_s\}^T \tag{55}$$

in conjunction with Eq. (56):

$$[A]\{v_r\} = \lambda_r^2 \{v_r\} \tag{56}$$

Postmultiplying Eq. (55) by $\{v_r\}$ and premultiplying Eq. (56) by $\{y_s\}^T$ we obtain

$$\{y_s\}^T[A]\{v_r\} = \lambda_s^2 \{y_s\}^T\{v_r\}$$

and

$$\{y_s\}^T[A]\{v_r\} = \lambda_r^2 \{y_s\}^T\{v_r\} .$$

Subtracting, we obtain the desired orthogonality relation

$$(\lambda_s^2 - \lambda_r^2)\{y_s\}^T\{v_r\} = 0$$

or

$$\{y_s\}^T\{v_r\} = 0 . \quad r \neq s . \tag{57}$$

It follows from the above orthogonality condition that we can obtain a dynamic matrix with the first mode removed by the equation,

$$[A_2] = [A_1] - [A_1][S_1] \tag{58}$$

where $[S_1]$ is a square matrix, whose first row is the characteristic row $\{y_1\}^T$ and those other rows are zero. The characteristic row $\{y_1\}^T$ can, of course, be obtained by iteration of Eq. (55). Continuing the example problem, we have corresponding to Eq. (55):

$$\{1.0 \quad 1.0 \quad 1.0\} \begin{bmatrix} 0.75 & 0.50 & 0.50 \\ 0.50 & 1.00 & 1.00 \\ 0.25 & 0.50 & 1.50 \end{bmatrix}$$

$$= \{1.50 \quad 2.0 \quad 3.0\} .$$

The next iteration yields

$$\{1.0 \quad 1.3 \quad 2.0\} \begin{bmatrix} 0.75 & 0.50 & 0.50 \\ 0.50 & 1.00 & 1.00 \\ 0.25 & 0.50 & 1.50 \end{bmatrix}$$

$$= 1.91 \{1.0 \quad 1.48 \quad 2.51\} .$$

After a few more iteration we obtain the characteristic row

$$\{y_1\}^T = \{1.0 \quad 1.551377 \quad 2.813558\} .$$

The dynamic matrix for the second mode is

$$[A_2] = \begin{bmatrix} 0.75 & 0.50 & 0.50 \\ 0.50 & 1.00 & 1.00 \\ 0.25 & 0.50 & 1.50 \end{bmatrix} \left[\begin{bmatrix} 1 & 0 & 0 \\ 0 & 1 & 0 \\ 0 & 0 & 1 \end{bmatrix} - \begin{bmatrix} 1.0 & 1.551377 & 2.813558 \\ 0.0 & 0.0 & 0.0 \\ 0.0 & 0.0 & 0.0 \end{bmatrix} \right]$$

or

$$[A_2] = \begin{bmatrix} 0.0 & -0.6635338 & -1.6101685 \\ 0.0 & 0.2243120 & -0.4067790 \\ 0.0 & 0.1121560 & 0.7966105 \end{bmatrix}$$

Iterating $[A_2]$ we obtain

$$\lambda_2 = 0.70086053$$

and

$$\{v_2\} = \begin{Bmatrix} -1.489287 \\ -0.653633 \\ -1.000000 \end{Bmatrix}.$$

In general the dynamic matrix for higher modes is

$$[A_{i+1}] = [A_i] - [A_i][S_i] . \qquad (59)$$

Let us now consider the case of semidefinite systems. As we have seen above, the normal mode and natural frequencies of a vibrating system can be found by iteration of the equation

$$[M]^{-1}[K]\{v\} = \omega^2\{v\} . \qquad (60)$$

Because the stiffness matrix $[K]$ for a semidefinite system is singular, its inverse does not exist, and the equation cannot be solved.

However, by making use of a few matrix theorems we can form a pseudo stiffness matrix that can be inverted. The following theorems are presented without proof.*

Theorem 1: If the eigenvalues of a matrix $[A]$ are λ_i, and the corresponding eigenvectors are $\{x_i\}$, then eigenvalues of $[B]$, where $[B] = [A]^r$, are λ_i^r and the corresponding eigenvectors are $\{x_i\}$. In equation form we have: if

$$[A]\{x_i\} = \lambda_i\{x_i\}$$

and

$$[B] = [A]^r$$

then

$$[B]\{x_i\} = \lambda_i^r\{x_i\} = \{x_i\} .$$

Theorem 2: If the matrix $[B]$ can be formed as a polynomial of matrix $[A]$ such that

$$[B] = a_0[I] + a_1[A] + a_2[A]^2 + \dots a_n[A]^n ,$$

and if the eigenvalues and eigenvectors of $[A]$ are λ_i and $\{x_i\}$, then the eigenvalues and eigenvectors of $[B]$ are μ_i and $\{x_i\}$, where

$$\mu_i = a_0 + \Sigma a_r \lambda_i^r .$$

That is, if

$$[A]\{x_i\} = \lambda_i\{x_i\}$$

then

$$[B]\{x_i\} = \left(a_0[I] + \sum_r a[A]\right)\{x_i\}$$

$$= \left(a_0 + \sum_r a_r \lambda_i^r\right)\{x_i\} .$$

Corollary: if

$$[B] = a_0[I] + [A]$$

and

$$[A]\{x_i\} = \lambda_i\{x_i\}$$

then

$$[B]\{x_i\} = (a_0 + \lambda_i)\{x_i\} .$$

Returning to Eq. (60), let

$$[M]^{-1}[K] = [A]$$

and

$$[B] = a_0[I] + [M]^{-1}[K] ;$$

then

$$(a_0[I] + [M]^{-1}[K])\{v_r\} = (a_0 + \omega_r^2)\{v_r\} .$$

Premultiply by $[M]$ to obtain

$$(a_0[M] + [K])\{v_r\} = (a_0 + \omega_r^2)[M]\{v_r\}$$

or (61)

$$(a_0[M] + [K])^{-1}[M]\{v_r\} = \mu_r\{v_r\} .$$

Equation (61) can be iterated in the same manner as Eq. (42) to obtain the free-free modes for semidefinite systems. The eigenvalue of Eq. (61) is

$$\mu_r = \frac{1}{a_0 + \omega_r^2}$$

from which the system natural frequencies can be recovered:

$$\omega_r = \sqrt{\frac{1}{\mu_r} - a_0} .$$

To apply the iteration method to systems with viscous damping we write the homogeneous part of Eq. (12) as

*For proofs see Refs. [4] and [5].

$$\begin{bmatrix} [0] & [M] \\ [M] & [C] \end{bmatrix} \begin{Bmatrix} \{\ddot{g}\} \\ \{\dot{g}\} \end{Bmatrix} + \begin{bmatrix} -[M] & [0] \\ [0] & [K] \end{bmatrix} \begin{Bmatrix} \{\dot{g}\} \\ \{g\} \end{Bmatrix} = \{0\} \qquad (62)$$

Note that upon substitution of the function, $\{g\} = \{u\}e^{pt}$, and its derivatives we obtain an equation of the same form as Eq. (39):

$$p \begin{bmatrix} [0] & [M] \\ [M] & [C] \end{bmatrix} \begin{Bmatrix} \{p(u)\} \\ \{u\} \end{Bmatrix} + \begin{bmatrix} -[M] & [0] \\ [0] & [K] \end{bmatrix} \begin{Bmatrix} \{p(u)\} \\ \{u\} \end{Bmatrix} = \{0\} \qquad (63)$$

The orthogonality relations, Eq. (19) and (22) can be written as

$$\begin{Bmatrix} \{p_s(u_s)\} \\ \{u_s\} \end{Bmatrix}^T \begin{bmatrix} [0] & [M] \\ [M] & [C] \end{bmatrix} \begin{Bmatrix} \{p_r(u_r)\} \\ \{u_r\} \end{Bmatrix} = 0, \quad r \neq s, \qquad (64)$$

and

$$\begin{Bmatrix} \{p_s(u_s)\} \\ \{u_s\} \end{Bmatrix}^T \begin{bmatrix} -[M] & [0] \\ [0] & [K] \end{bmatrix} \begin{Bmatrix} \{p_r(u_r)\} \\ \{u_r\} \end{Bmatrix} = 0, \quad r \neq s. \qquad (65)$$

Rewriting Eq. (63):

$$-\begin{bmatrix} -[M]^{-1} & [0] \\ [0] & [K]^{-1} \end{bmatrix} \begin{bmatrix} [0] & [M] \\ [M] & [C] \end{bmatrix} \begin{Bmatrix} \{p(u)\} \\ \{u\} \end{Bmatrix} = \frac{1}{p} \begin{Bmatrix} \{p(u)\} \\ \{u\} \end{Bmatrix}$$

or (66)

$$\begin{bmatrix} [0] & [I] \\ -[K]^{-1}[M] & -[K]^{-1}[C] \end{bmatrix} \begin{Bmatrix} \{p(u)\} \\ \{u\} \end{Bmatrix} = \frac{1}{p} \begin{Bmatrix} \{p(u)\} \\ \{u\} \end{Bmatrix}.$$

A method for iterating Eq. (66) may be found in Ref. [6]. This is obviously more difficult than the real eigenvalue problem because the roots and modal columns are both complex and will occur as complex conjugate pairs.

FORCED-RESPONSE SOLUTION USING CLASSICAL NORMAL MODES

Equations of motion of the form

$$[M]\{\ddot{g}\} + [C]\{\dot{g}\} + [K]\{g\} = \{F\} \qquad (67)$$

for forced systems with damping are simultaneous linear differential equations. The equations are coupled through off-diagonal terms in the coefficient matrices $[M]$, $[C]$, or $[K]$. Closed form or direct solutions to these equations are difficult or impossible to obtain except for the most elementary forcing functions.

The classical method of solving these equations is to first find the principle modes for the homogeneous equations

$$[M]\{\ddot{g}\} + [K]\{g\} = \{0\} \qquad (68)$$

and to make use of the orthogonality property of the principle modes to de-couple the equations of motion. It has been shown that solutions to Eq. (68) are such that

$$[K]^{-1}[M]\{v_r\} = \frac{1}{\omega_r^2}\{v_r\}, \quad r = 1, 2, \ldots, n. \qquad (69)$$

If we now form a linear transformation matrix of the mode vectors, we can write

$$\{g\} = [V]\{N\} \qquad (70)$$

where the rth column of $[V]$ is the rth mode vector and the rth element of $\{N\}$ is the corresponding normal coordinate. Differentiating Eq. (70) twice, we obtain,

$$\{\ddot{g}\} = [V]\{\ddot{N}\}. \qquad (71)$$

Substitute Eqs. (70) and (71) into (67) and premultiply by $[V]^T$ to obtain

$$[V]^T[M][V]\{\ddot{N}\} + [V]^T[K][V]\{N\} = [V]^T\{F\} \qquad (72)$$

Now from the orthogonality property (Eq. (40)) it is obvious that

$$[V]^T[M][V] = [\kappa_r] \qquad (73)$$

and

$$[V]^T[K][V] = [K_r] = [\omega^2\kappa_r] \qquad (74)$$

where κ_r is called the generalized mass for the rth mode and K_r is called the generalized stiffness for the rth mode.

Substituting Eqs. (73) and (74) into Eq. (72), we see that we have decoupled the equations of motion into independent modes:

$$[\kappa_r]\{\ddot{N}\} + [\omega_r^2\kappa_r]\{N\} = [V]^T\{F\}. \qquad (75)$$

The set of independent equations (Eq. (75)) can be easily solved for the response of each mode. The response in the physical coordinate can then be found by the use of Eqs. (70) and (71).

For the case of light damping, Eq. (75) is modified by a velocity coefficient matrix analogous to the single-degree-of-freedom viscous damping term:

$$[n_r]\{\ddot{N}\} + \left[2n_r\omega_r n_r\right]\{\dot{N}\} + \left[\omega_r^2 n_r\right]\{N\} = \{V\}^T\{F\}. \tag{76}$$

The introduction of the velocity dependent terms in Eq. (76) is justified only for systems with "small" physical damping. In general, the modal transformation of the form of Eq. (70) will fail to diagonalize the velocity coefficient matrix for the damped system described by Eq. (67). It has been shown by Caughey [7] that if the damping matrix of Eq. (67) is diagonalized by the same transformation that uncouples the undamped system, then the system possesses "classical" normal modes.* This condition is met if the damping matrix is a linear combination of the mass and stiffness matrices:†

$$[C] = \alpha[M] + \beta[K] \tag{77}$$

where α and β are constants. It is possible, of course, to use the complex eigenvectors (see Eq. (66)) to uncouple the damped system. However, as has been previously noted, this is difficult and less practical.

To demonstrate the transformation indicated by Eq. (70), let us again consider the dynamic system shown in Fig. 1. The modal matrix is formed from the mode vectors calculated in Iterative Solution for Eigenvalues.

$$[V] = \begin{bmatrix} 0.710832 & -1.489288 & 3.778454 \\ 1.102775 & -0.853634 & -4.249137 \\ 1.000000 & 1.000000 & 1.000000 \end{bmatrix}.$$

It is easily verified that

$$\left[K_r\right] = \begin{bmatrix} 1.669465 & 0.0 & 0.0 \\ 0.0 & 7.057995 & 0.0 \\ 0.0 & 0.0 & 107.2724 \end{bmatrix}$$

$$\left[n_r\right] = \begin{bmatrix} 3.721395 & 0.0 & 0.0 \\ 0.0 & 4.946669 & 0.0 \\ 0.0 & 0.0 & 34.331898 \end{bmatrix}$$

$$\left[\omega_r^2\right] = \begin{bmatrix} 0.448613 & 0.0 & 0.0 \\ 0.0 & 1.426817 & 0.0 \\ 0.0 & 0.0 & 3.124570 \end{bmatrix}.$$

*As defined by Caughey and O'Kelley [8] classical normal modes exist when, for any particular mode, the various parts of the system pass through their minimum point at the same time.

†This result is from Lord Rayleigh [9].

APPLICATIONS

The normal mode approach to solving forced-vibration problems has wide application in calculating dynamic loads for space vehicles. Typical problems are longitudinal response at liftoff, lateral response to wind gusts, response to maneuvering loads, and the like.

To complete this report, the methods presented in the previous sections were applied to the case of a space vehicle launched during a ground wind and associated gust. The analysis was limited to a determination of the lateral vibration response to the gust loads on the restrained vehicle and the effect of releasing the hold-down restraints at liftoff.

The vehicle stiffness and mass distribution assumed for this analysis are shown in Fig. 2, and the distributed mass was lumped at the vehicle stations indicated. The Appendix presents a formulation of the mathematical model and stiffness matrix for this vehicle. For the captive phase the vehicle was assumed to be cantilevered at station 1. The calculations for the normal modes and natural frequencies, presented in Tables 1 and 2, were performed on the IBM 7090 digital computer.

The first five cantilever modes and frequencies were used for calculating the response of the restrained vehicle. The equations of motion corresponding to Eq. (76) were written and solved on the IBM 7090, using a numerical integration routine. The generalized force $\{F\}$ was expressed as

$$\{F\} = \{c_s\}f(t) \tag{78}$$

where $\{c_s\}$ describes the distribution of the dynamic pressure to the vehicle stations. The function $f(t)$ was assumed to be a wedge-shaped gust of 4-sec duration, superimposed on a steady wind, as shown in Fig. 3. The distribution vector, $\{c_s\}$, is given in Table 3. One percent of critical damping was assumed for each mode. The steady wind portion of $f(t)$ was neglected for the captive phase because it does not affect the acceleration response. The initial conditions used were

$$\ddot{N}_r = \dot{N}_r = N_r = 0 \tag{79}$$

The shear and bending moment at the jth station were calculated by

$$(\text{shear})_j = \sum_{i=1}^{j} A_i \tag{80}$$

and

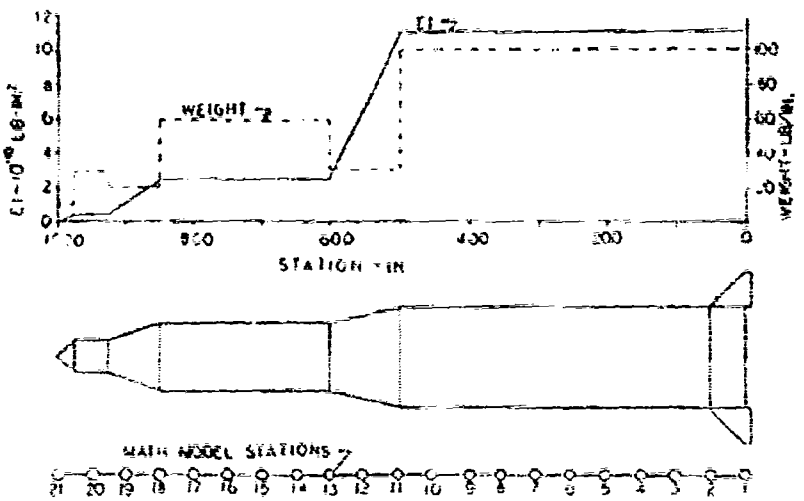

Fig. 2. Vehicle stiffness and weight distribution

TABLE I
Normal Modes and Natural Frequencies, Cantilever Conditions

STATION	Mode 1	Mode 2	Mode 3	Mode 4	Mode 5
	0.548 cps	2.356 cps	5.716 cps	11.395 cps	17.815 cps
1	0.00000000E-39	0.00000000E-39	0.00000000E-39	0.00000000E-39	0.00000000E-39
2	-4.09150250E-03	-1.06605980E-02	-2.49163230E-02	-4.26352800E-02	-6.17164770E-02
3	-1.59327940E-02	-3.99170570E-02	-8.54511410E-02	-1.34760510E-01	-1.79743040E-01
4	-3.46713380E-02	-6.17436150E-02	-1.60833600E-01	-2.26301770E-01	-2.65646010E-01
5	-6.02592090E-02	-1.31131130E-01	-2.31974490E-01	-2.77419160E-01	-2.63385430E-01
6	-9.14545050E-02	-1.83120130E-01	-2.82847120E-01	-2.64959120E-01	-1.63530050E-01
7	-1.27825700E-01	-2.33178650E-01	-3.01796950E-01	-1.86045860E-01	-2.55137820E-03
8	-1.68758110E-01	-2.77368600E-01	-2.82477270E-01	-5.70961220E-02	1.54597410E-01
9	-2.13655280E-01	-3.12506340E-01	-2.24191530E-01	5.19603030E-02	2.42371200E-01
10	-2.61966650E-01	-3.36304380E-01	-1.31521550E-01	2.27120890E-01	2.21791490E-01
11	-3.13155370E-01	-3.47465150E-01	-1.32273450E-02	3.21186170E-01	5.95443150E-02
12	-3.67073730E-01	-3.43904690E-01	1.21065030E-01	3.54305810E-01	-1.04048150E-01
13	-4.24420200E-01	-3.18147250E-01	2.58575350E-01	2.99066120E-01	-3.17976970E-01
14	-4.86741440E-01	-2.54352690E-01	3.66064360E-01	1.24815810E-01	-4.05598960E-01
15	-5.54684460E-01	-1.45745880E-01	4.01307690E-01	-1.18203640E-01	-2.53716830E-01
16	-6.24556470E-01	-2.61630560E-04	3.44302940E-01	-3.13561090E-01	5.54207120E-02
17	-6.98130300E-01	1.72537790E-01	1.94526680E-01	-3.66584440E-01	3.27573300E-01
18	-7.72657320E-01	3.64847620E-01	-3.19306370E-02	-2.46473510E-01	3.94417470E-01
19	-8.46006070E-01	5.69410790E-01	-3.17975290E-01	4.79139070E-02	1.72330100E-01
20	-9.23910730E-01	7.83060290E-01	-6.50159610E-01	4.92317680E-01	-3.46278310E-01
21	-1.00000000E 00	1.00000000E 00	-1.00000000E 00	1.00000000E 00	-1.00000000E 00

$$(\text{moment})_i = \sum_{i=1}^{i} A_i \bar{x}_i \qquad (81)$$

where $\bar{x}_i$ is the distance from the ith station to the ith station and A_i is the inertia force at the ith station:

$$A_i = -m_i \bar{y}_i \qquad (82)$$

The results presented in Figs. 4 and 5 indicate that the response is predominantly first mode and that inclusion of additional modes is unnecessary.

For the liftoff phase, the first five semi-definite or free-free modes were used. The zero-frequency modes (representing rigid body translation and rotation) were omitted, because the objective was only to investigate the vibration response of the vehicle. A release time of 2.25 sec was chosen based on maximum tip deflection during the captive phase.

The initial conditions for release were calculated from the terminal conditions of the captive phase. The terminal velocity in terms of the free-free normal coordinates is

TABLE 2
Normal Modes and Natural Frequencies, Free-Free Condition

STATION	Mode 1	Mode 2	Mode 3	Mode 4	Mode 5
	2.265 cps	5.710 cps	11.317 cps	17.668 cps	27.620 cps
1	-3.75175450E-01	-4.07096360E-01	-3.70274620E-01	-3.49726770E-01	-3.33333330E-01
2	-2.83215750E-01	-2.54767050E-01	-1.70607480E-01	-1.09774950E-01	-4.32367740E-02
3	-1.91568980E-01	-1.07173390E-01	1.50525680E-02	9.45668990E-02	1.70645320E-01
4	-1.02791020E-01	2.74659540E-02	1.56331150E-01	2.18842420E-01	2.31922170E-01
5	-1.76331490E-02	1.38765410E-01	2.33332660E-01	2.31034900E-01	1.27667180E-01
6	6.12547270E-02	1.14805400E-01	2.37072570E-01	1.37240300E-01	-6.46710400E-02
7	1.31554620E-01	2.54225240E-01	1.65244120E-01	-1.75673070E-02	-1.19255920E-01
8	1.91136190E-01	2.47649140E-01	4.03513910E-02	-1.66655860E-01	-2.35026990E-01
9	2.38266670E-01	1.98425830E-01	-1.05217680E-01	-2.44778320E-01	-5.70910390E-02
10	2.71740900E-01	1.12507230E-01	-2.36546440E-01	-2.15345370E-01	1.17650350E-01
11	2.91122310E-01	-5.08008550E-04	-3.26267370E-01	-6.35247770E-02	2.95344030E-01
12	2.94641190E-01	-1.30621580E-01	-3.54659610E-01	1.17155080E-01	3.45581050E-01
13	2.75193420E-01	-2.65108800E-01	-2.95582570E-01	3.26932310E-01	2.03674320E-01
14	2.16764650E-01	-3.70923900E-01	-1.19238440E-01	4.06153940E-01	-1.10758460E-01
15	1.13294640E-01	-4.05570190E-01	1.23058780E-01	2.47011610E-01	-3.32031250E-01
16	-2.68666750E-02	-3.48428260E-01	3.16347630E-01	-6.36044730E-02	-2.76562500E-01
17	-1.94527700E-01	-1.98543600E-01	3.66152230E-01	-3.32394120E-01	1.15885420E-01
18	-3.80733890E-01	2.92574660E-02	2.44146630E-01	-3.92759560E-01	3.90625000E-01
19	-1.79647180E-01	3.15034410E-01	-5.06685570E-02	-1.66666670E-01	3.22916660E-01
20	-7.87970740E-01	6.48474380E-01	-4.94124030E-01	3.52459010E-01	-2.08333330E-01
21	-1.00000000E 00	1.00000000E 00	-1.00000000E 00	1.00000000E 00	-1.00000000E 00

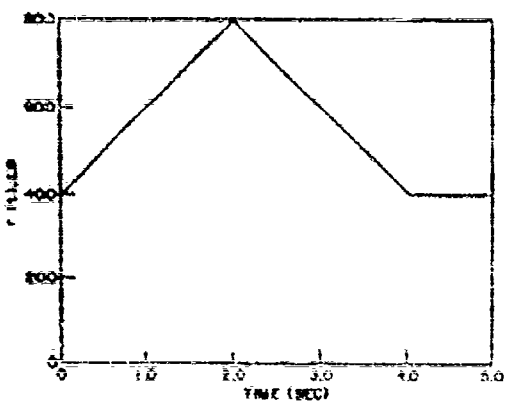

Fig. 3. Forcing function steady wind and gust

$$(\dot{y})_{\substack{(1.25)\\ sec}} = [V](\dot{N})_{(0)} \qquad (85)$$

Premultiplying by $[V]^T[M]$,

$$[V]^T[M](\dot{y})_{\substack{(1.25)\\ sec}} = [V]^T[M][V](\dot{N})_{(0)}$$

Or rewriting

$$(\dot{N})_{(0)} = [\omega_i]^{-1}[V]^T[M](\dot{y})_{\substack{(2.25)\\ sec}}$$

Similarly the initial displacement in the free-free normal coordinates is

TABLE 3
Dynamic Pressure Distribution

Station	C_N	Station	C_N	Station	C_N
1	0.0988	9	0.0988	17	0.0658
2	0.0988	10	0.0988	18	0.0658
3	0.0988	11	0.0988	19	0.0495
4	0.0988	12	0.0821	20	0.0329
5	0.0988	13	0.0658	21	0.0165
6	0.0988	14	0.0658		
7	0.0988	15	0.0658	Total	1.6626
8	0.0988	16	0.0685		

$$(N)_{(0)} = [\omega_i]^{-1}[V]^T[M]\left((y)_{\substack{(1.25)\\ sec}} + (y)_{sw}\right) \qquad (85)$$

where $(y)_{sw}$ is the static displacement resulting from the wind force at 2.25 sec and was calculated by

$$(y)_{sw} = [K]^{-1}(c_y)(400) \qquad (86)$$

It is to be noted that although the steady wind does not affect the velocity and acceleration response of the system or the dynamic bending moments, it does contribute to the deflection of the vehicle and to the total energy stored in the hold-down spring and must be included in the initial conditions for liftoff. The response for the liftoff phase is presented for typical stations in Figs. 6 and 7.

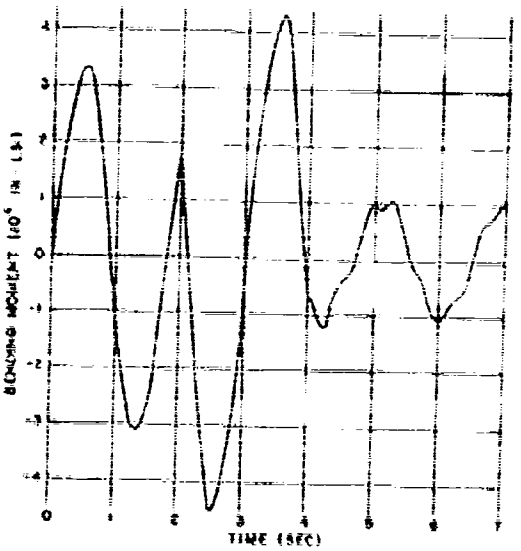

FIG. 4. Bending moment vs time, station 1, cantilever condition

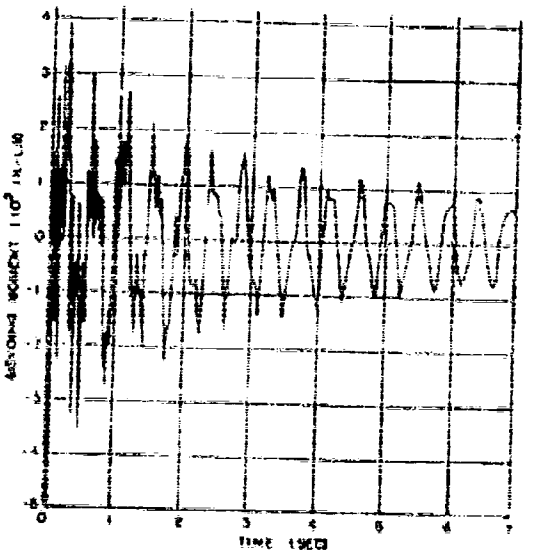

FIG. 6. Moment vs time, station 10, free-free condition

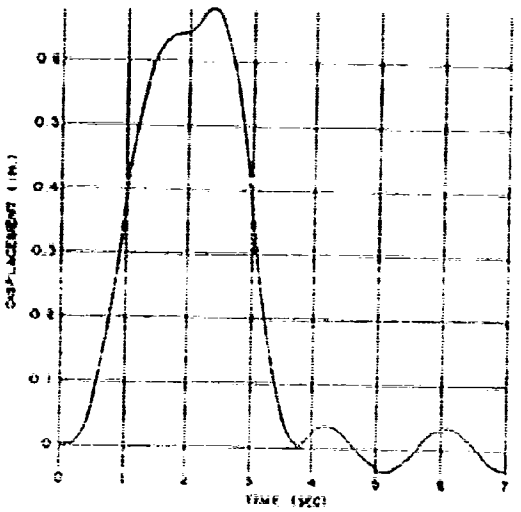

FIG. 5. Displacement vs time, station 21, cantilever condition

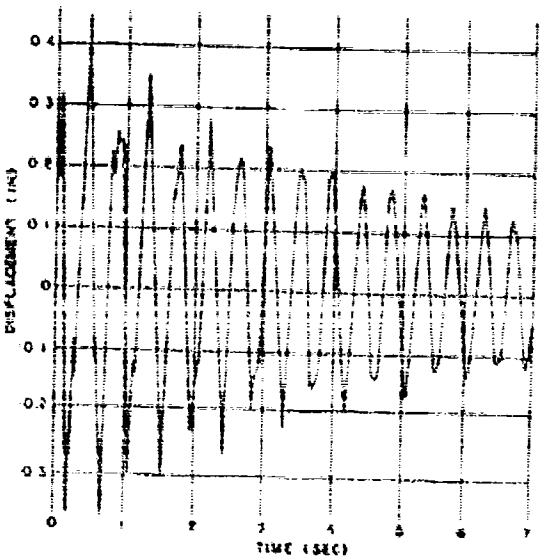

FIG. 7. Displacement vs time, station 21, free-free condition

ACKNOWLEDGMENT

This report was originally submitted as a Master's Report to the Department of Engineering Mechanics, Louisiana State Univ., Baton Rouge, La. (Dr. Robert Thome, Major Professor, Dr. Dale Carver, Head, Department of Engineering Mechanics.)

REFERENCES

1. F. S. Tse, I. E. Morse, and R. T. Hinkle, Mechanical Vibrations (Allyn & Bacon, Inc., Boston), 1963
2. S. W. McCuskey, Introduction to Advanced Dynamics (Addison-Wesley Publishing Co., London), 1959
3. R. H. Scanlan and R. Rosenbaum, Introduction to the Study of Aircraft Vibration and Flutter (The Macmillan Co., New York), 1951
4. S. J. McMinn, Matrices for Structural Analysis (John Wiley & Sons, New York), 1962
5. L. A. Pipes, Matrix Methods for Engineering (Prentice-Hall, Englewood Cliffs, N.J.), 1963
6. R. A. Frazer, W. J. Duncan, and A. R. Collar, Elementary Matrices (Cambridge Univ. Press, London), 1950
7. T. K. Caughey, "Classical Normal Modes in Damped Linear Dynamic Systems," J. Appl. Mech., Paper No. 59-A-62 (1959)
8. T. K. Caughey and M. E. O'Kelly, "Effect of Damping on Natural Frequencies of Linear Dynamic Systems," J. Am. Acoust. Soc. 33 (11) (Nov. 1961)
9. Lord Rayleigh, Theory of Sound, I (Dover Publications, New York), 1945
10. G. E. Thomann, "Aeroelastic Problems of Low Aspect Ratio Wings," Aircraft Engineering, Feb. 1956
11. E. C. Pestel and F. A. Leckie, Matrix Methods in Elastomechanics (McGraw-Hill, New York), 1963

BIBLIOGRAPHY

Bishop, R. E., G. M. L. Gladwell, and S. Michaelson, The Matrix Analysis of Vibration (Cambridge Univ. Press), 1965

Appendix

STIFFNESS MATRIX FORMULATION

The stiffness matrix for a single beam element as given in Ref. [10] is

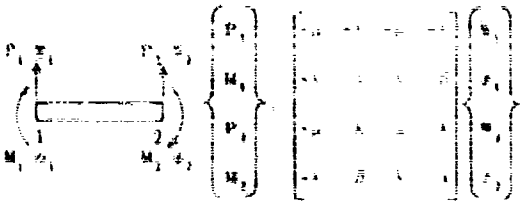

where

$$= \frac{12\,EI}{L^3 K}$$

$$= \frac{EI}{L}\left(1 + \frac{3}{K}\right)$$

$$= \frac{6EI}{L^2 K}$$

$$= \frac{EI}{L}\left(\frac{3}{K} - 1\right)$$

$$K = 1 + \frac{12\,EI}{GAL^2}$$

The above matrix is the same as that given in Ref. [11], except for the inclusion of shear deformation defined by K above.

The vehicle analyzed in this report was divided into 20 beam segments and 21 mass stations as shown in Fig. 2. The physical properties for these beam segments are summarized in Table A-1. The stiffness elements for each beam segment are given in Table A-2.

The stiffness matrix for the connected beam segments is formed by adding the stiffness elements at common node points. This is shown in Table A-3. The matrix in Table A-3 is for the free-free vehicle. For the cantilevered condition the deflection and slope at station 1 are both zero. Therefore, the stiffness matrix for the cantilevered vehicle is found by simply eliminating rows 1 and 2 and columns 1 and 2 from the free-free matrix.

TABLE A-1
Beam Element Physical Properties

Station No.	EI (lb-in.^{2})	Weight (lb)	Coordinate
1	11.0 E10	2500	0
2	11.0 E10	5000	50
3	11.0 E10	5000	100
4	11.0 E10	5000	150
5	11.0 E10	5000	200
6	11.0 E10	5000	250
7	11.0 E10	5000	300
8	11.0 E10	5000	350
9	11.0 E10	5000	400
10	11.0 E10	5000	450
11	6.5 E10	3250	500
12	4.8 E10	1500	550
13	2.5 E10	2250	600
14	2.5 E10	3000	650
15	2.5 E10	3000	700
16	2.5 E10	3000	750
17	2.5 E10	3000	800
18	1.8 E10	2000	850
19	1.0 E10	1000	900
20	1.9 E10	1500	950
21	0	250	1000

TABLE A-2
Beam Segment Stiffness Elements

Beam	α	β	γ	δ
1	1.647468 E6	4.118670 E7	3.229668 E9	-1.170332 E9
2	1.647468 E6	4.118670 E7	3.229668 E9	-1.170332 E9
3	1.647468 E6	4.118670 E7	3.229668 E9	-1.170332 E9
4	1.647468 E6	4.118670 E7	3.229668 E9	-1.170332 E9
5	1.647468 E6	4.118670 E7	3.229668 E9	-1.170332 E9
6	1.647468 E6	4.118670 E7	3.229668 E9	-1.170332 E9
7	1.647468 E6	4.118670 E7	3.229668 E9	-1.170332 E9
8	1.647468 E6	4.118670 E7	3.229668 E9	-1.170332 E9
9	1.647468 E6	4.118670 E7	3.229668 E9	-1.170332 E9
10	1.647468 E6	4.118670 E7	3.229668 E9	-1.170332 E9
11	1.337705 E6	3.344262 E7	2.536065 E9	-8.629344 E8
12	1.001739 E6	2.504348 E7	1.586087 E9	-3.339130 E8
13	7.058824 E5	1.764706 E7	9.411765 E8	-5.882352 E8
14	7.058824 E5	1.764706 E7	9.411765 E8	-5.882352 E7
15	7.058824 E5	1.764706 E7	9.411765 E8	-5.882352 E7
16	7.058824 E5	1.764706 E7	9.411765 E8	-5.882352 E7
17	7.058824 E5	1.764706 E7	9.411765 E8	-5.882352 E7
18	5.082353 E5	1.270588 E7	6.776470 E8	-4.235294 E7
19	4.114286 E5	1.028571 E4	4.571428 E8	5.714286 E7
20	4.114286 E5	1.028571 E4	4.571428 E8	5.714286 E7

TABLE A-3
Vehicle Stiffness Matrix

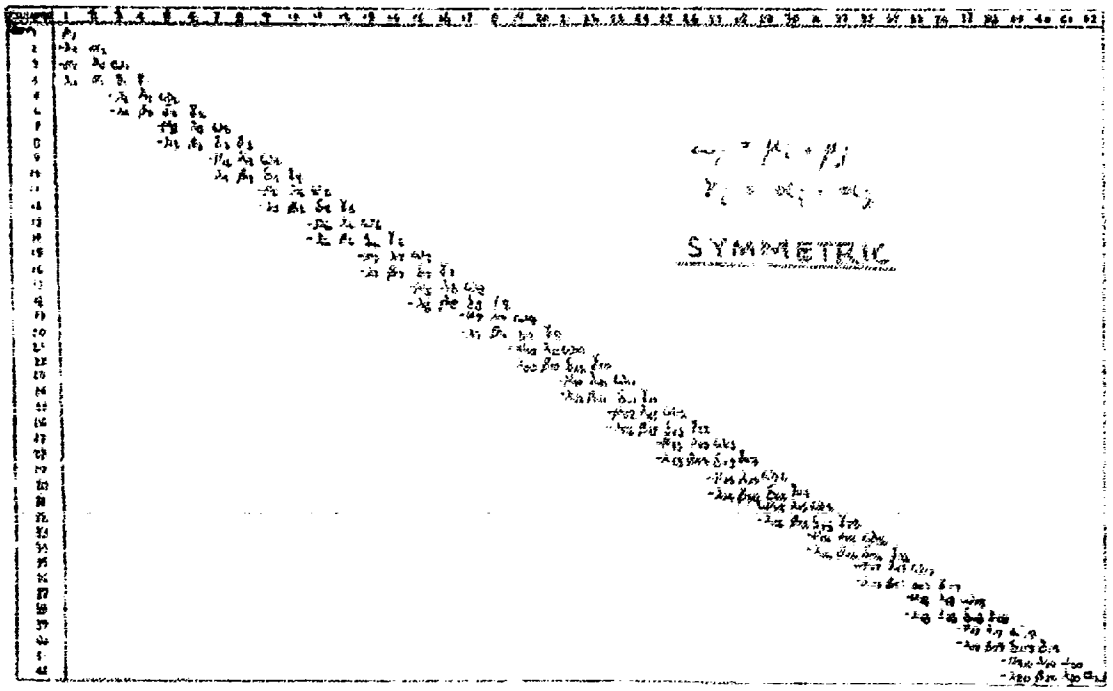

DISCUSSION

Mr. Jones (Air Force Materials Lab.): Did you incorporate damping into your equations of motion in any form?

Mr. Sowers: Yes, I did have damping. It was 1 percent modal damping.

* * *

A NONFLUID VELOCITY DAMPER

William G. Flannelly
Kaman Aircraft
Division of Kaman Corporation
Bloomfield, Connecticut

It is shown that a grooved block sliding axially on two dry rotating shafts acts as a velocity damper in the axial direction. The effective coefficient of damping is a function of the shaft diameter, shaft speed, and the normal force. Through experiments, the axial force is found to correlate very closely with viscous damping and it is found possible to reduce the damping to negligible values if desired. The maximum values of viscous damping coefficients obtainable with fractional friction horsepower are sufficiently high to cover a practical range of small-specimen laboratory testing. Experimental means for measurement of sliding coefficient of friction and spring structural damping are illustrated.

A laboratory rig for restraining specimens to unidirectional motion with negligible resistance was constructed and is described in this paper.

NOMENCLATURE

c_a Coefficient of velocity (viscous) damping in the axial direction (lb-sec/in.)

d Shaft diameter (in.)

e Base of natural logarithm

F_a Resistive force in the axial direction (lb)

F_f Force owing to Coulomb friction (lb)

g Structural damping ratio

G Acceleration owing to gravity (386 lb-sec^2/in.)

HP Horsepower

n Shaft speed (rpm)

N Normal force (lb)

T Torque (in.-lb)

v_a Axial velocity (in./sec)

v_t Tangential velocity (in./sec)

W Weight (lb)

μ_f Coefficient of sliding friction, dry

ζ Viscous damping ratio

ζ_{STR} Equivalent viscous damping ratio of structural damping

ω_n Natural frequency (rad/sec)

Ω Shaft speed (rad/sec)

THEORY

It was observed by Timoshenko [1] that a rotating shaft can oscillate in the axial direction with very little resistance to motion. This occurs when the axial velocity is small compared with the tangential velocity. Figure 1 shows the forces and velocities on either of the shafts of Fig. 2. The force of friction, F_f, must be in opposition to the velocity, v; the frictional force component in the axial direction is, therefore,

$$F_a = \frac{F_f v_a}{\sqrt{v_a^2 + v_t^2}} \tag{1}$$

Ideally, the frictional force, F, is the product of the normal force, N, and the coefficient of friction, μ_f, between the slider and the shafts; if the tangential velocity, v_t, is much greater than the axial velocity, v_a, then

$$\frac{F_a}{v_a} = \frac{\mu_f N}{v_t} \tag{2}$$

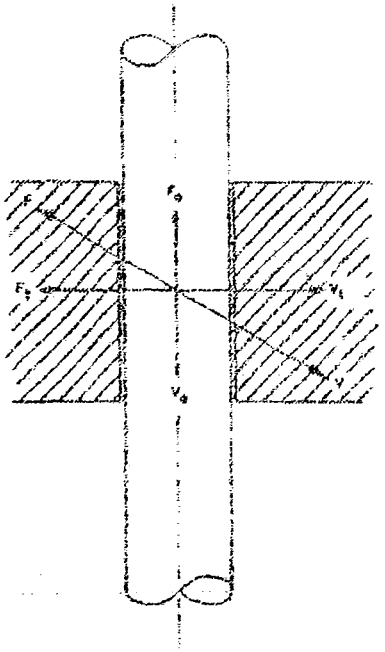

Fig. 1. Force and velocity components on shaft

This amounts to nearly pure "viscous" or velocity-proportional damping in the axial direction resulting from dry friction.

Taking the tangential velocity as constant and large compared with the axial velocity, it is seen from Eq. (1) that the nature of the resisting force, F, is immaterial provided that its magnitude is insensitive to small changes in velocity. Any passive force of resistance (for example, viscous, velocity squared, Coulomb-Morin friction, and so forth) that dissipates energy will, under the above conditions, appear as velocity damping in the axial direction on a shaft.

From the plot of Eq. (1) in Fig. 3, it is seen that there are three distinct regions of "damping" depending on the ratio of the axial and the tangential velocities. At high v_a/v_t ratios, the axial resistance is in the nature of Coulomb-Morin friction. The axial force departs noticeably from Coulomb friction at v_a/v_t of about 5.

Taking the derivative of Eq. (1), with respect to v_a, gives the viscous damping coefficient

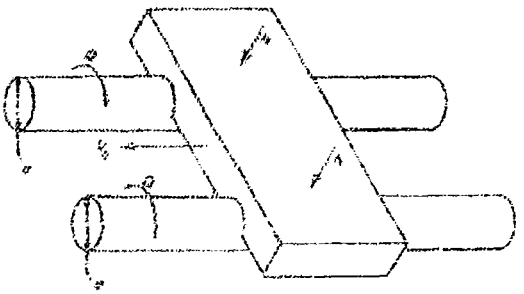

Fig. 2. Grooved slider on rotating shafts with normal force N per shaft

$$\frac{dF_a}{dv_a} = c_a = \frac{F_t\, v_t}{\sqrt[3]{1 + \frac{v_a^2}{v_t^2}}}\left(1 - \frac{1}{1 + \frac{v_t^2}{v_a^2}}\right) \qquad (3)$$

In the plot of Eq. (3), Fig. 4, it is seen that the axial resistive force is within 6 percent of pure viscous damping when the axial-to-tangential velocity ratio is 20 percent and comes within 2 percent of pure viscous damping when the ratio is 10 percent. The region of v_a/v_t below about 20 percent may be considered as velocity damping and the region between $0.2 < v_a/v_t < 5.0$ as a "transition zone."

Taking the v_a/v_t ratio of 0.20 and below as the region of velocity damping, one may describe the maximum accelerations, for various frequencies of sinusoidal motion and various tangential velocities, at which the axial resistive force is essentially velocity damping. This is shown in Fig. 5 for an arbitrary 1-in. diameter shaft. The ordinate values of Fig. 5 increase linearly with shaft diameter.

An approximation to the minimum power required to produce a given magnitude of axial viscous damping is given by the shaft speed and friction torque,

$$HP = \frac{Tn}{63{,}000} = \frac{F_t d n}{63{,}000};$$

but

$$F_t = c_a d n = \frac{n}{60};$$

therefore

$$HP = \frac{c_a d^2 n^2}{378 \times 10^4} \qquad (4)$$

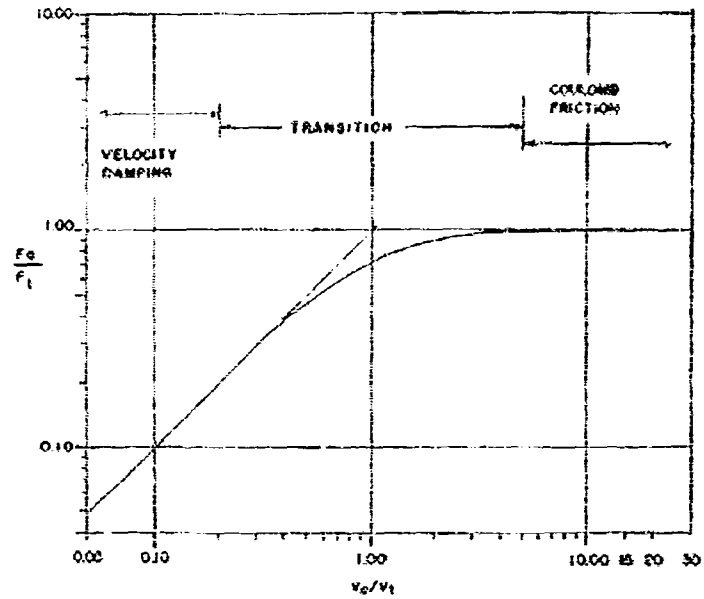

Fig. 3. Axial-tangential force ratio vs velocity ratio

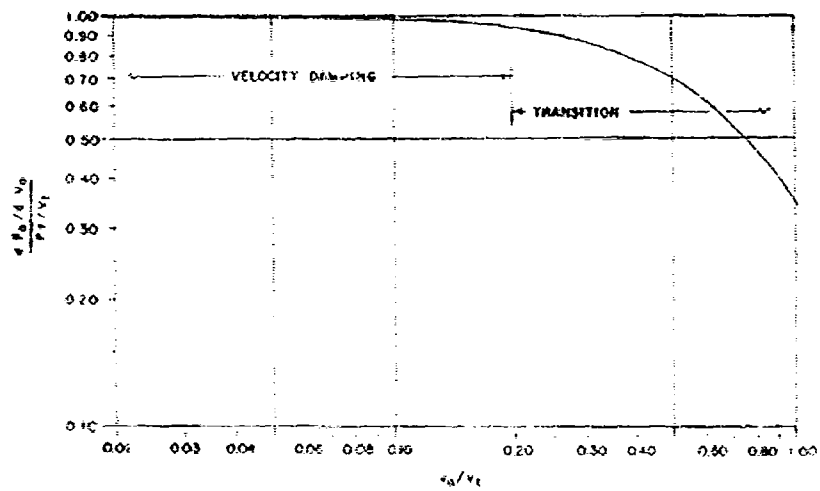

Fig. 4. At low axial-to-tangential velocity ratio, the axial resistive force is of the nature of velocity damping

A plot of Eq. (4) for a 1-in. diameter shaft is shown in Fig. 6. Comparison of Figs. 6 and 7 show that fractional horsepower is sufficient to cover the range of damping coefficient needed in most small-specimen laboratory vibration testing.

EXPERIMENTAL DEVICE

The device shown in Fig. 8 was constructed to test the theoretical conclusions, particularly the conclusion that axial motion is velocity damped. The test device consists of two parallel

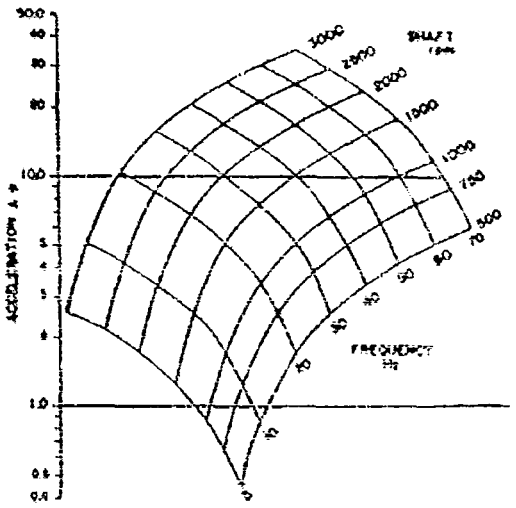

Fig. 5. Maximum acceleration for velocity damping on 1-in. diameter shafts

model, shown in Fig. 9, had counterrotating shafts geared together.

The motor speed was controlled by a commercial electronic speed adjuster and the shaft speed was monitored by feeding a signal from a magnetic pickup to an oscillograph. The magnetic pickup signaled once per revolution as a steel screw on the shaft coupling passed the pickup head. The sliding block was fitted with bronze bushings that fit freely on the 0.317-in. diameter steel shafts.

Substantial static friction was observed with the shafts not turning. With the shafts rotating, all static friction disappeared, as would be expected, and no static angle of repose could be measured. When one end of the test device was displaced from the horizontal by even a few thousandths of an inch in a foot, the slider block translated to the low side; it had the sensitivity of a carpenter's bubble level.

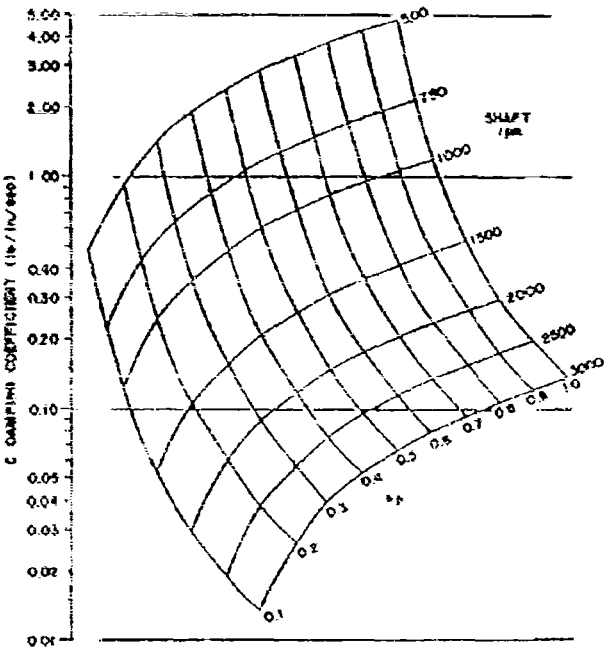

Fig. 6. Damping coefficient in axial direction on 1-in. diameter shaft as a function of friction horsepower and rpm

shafts, one of which is driven by a 1/15th horsepower universal electric motor and, in turn, drives the other shaft either by a belt connection, as shown in Fig. 8, or by gearing. The modified

To obtain accurate measurements of the axial resistance to motion, the sliding block was axially restrained by springs preloaded in compression, as shown in Fig. 9. A velocity

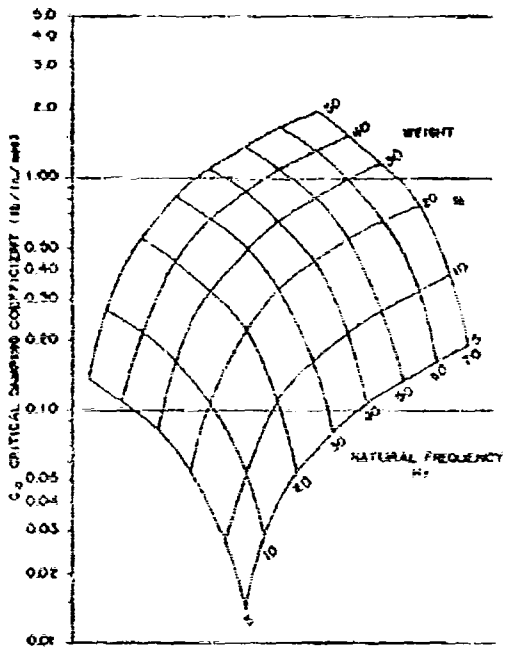

Fig. 7 Critical damping coefficient vs weight and natural frequency

transducer, reading in the axial direction, was fitted to the sliding block and its signal fed to an oscillograph.

With the shafts rotating, the block was displaced from its neutral position and suddenly released. A typical decay curve is shown in Fig. 10.

Because the block oscillates axially, going through zero velocity twice per cycle, Coulomb damping effects will be observed in the decay curve only if the maximum vibratory velocity in the axial direction is very high compared with the tangential velocity, let us say 100 times; then the energy dissipated per cycle is approximately by $F_n = F_t$. This behavior of the decay curve is of little interest in this investigation. The low rate of d[illegible] in the initial stages of the experimental trace shown in Fig. 10 results, in the main, from bottoming of the moving element in the transducer and that section of the trace can be ignored. The high frequency evident in the trace in Fig. 10 is 60 Hz and is caused by electrical noise.

EXPERIMENTAL APPROACH

Vibration decay traces were recorded for free motion of blocks carrying various weights and at various shaft rpm. Figure 11 shows plots of successive normalized peak amplitudes (numbered as shown in the inset) for four values of shaft rpm; the natural frequency of the slider block against its springs is 12.5 Hz in Fig. 11. The cycles on the abscissa are sequentially numbered from an arbitrary reference cycle occurring early in the time history after the transducer element had ceased bottoming.

The expected pattern of successive maximum amplitudes for pure velocity damping is a straight line on semilogarithmic paper, as shown by Den Hartog [2], for example. The negatively sloped lines about which the test points cluster in Fig. 11 are least squares lines of regression [3,4]. It is readily shown that the statistically best value of viscous damping ratio for N measured peaks each of amplitude Y_n at chronological peak number n is given by

$$\zeta = \frac{1}{2\pi \log_{10} e} \frac{N \sum n \log_{10} Y_n - \sum n \sum \log_{10} Y_n}{N \sum n^2 - (\sum n)^2} \qquad (5)$$

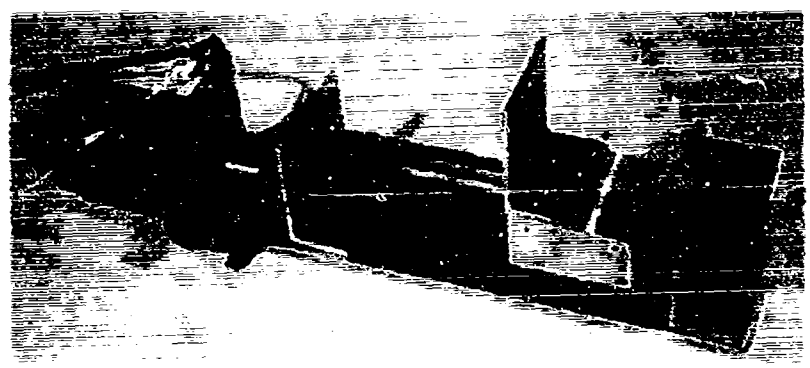

Fig. 8 Original laboratory test device

for a plot on (common) semilogarithmic paper. The damping ratio is the slope of the line of regression, on semilog paper, divided by $2\pi \log_{10} e$.

The coefficient of correlation [3,4] of the data to pure viscous damping is given by

$$r = \left| \sqrt{2\pi(\log_{10} e)\left(\frac{N\sum n \log_{10} Y_n - \sum n \sum \log_{10} Y_n}{N\sum(\log_{10} Y_n)^2 - (\sum \log_{10} Y_n)^2} \right)} \right| \qquad (6)$$

With the shafts not rotating, the slider block was initially displaced approximately the same amount as in the rotating shaft cases. When suddenly released, the block motion decayed to absolute rest in about three cycles. Such rapid and absolute decay is expected with dry friction and starkly contrasts with the performance on rotating shafts.

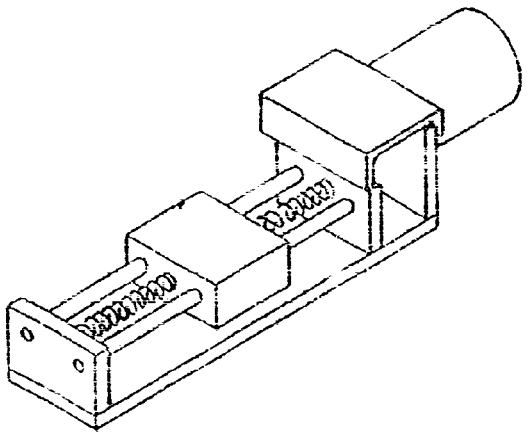

Fig. 9. Modified laboratory test device showing restraining springs

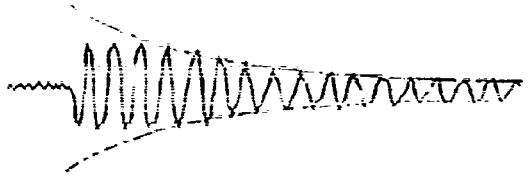

Fig. 10. Typical decay of free axial vibration on test device showing viscous damping decay envelope

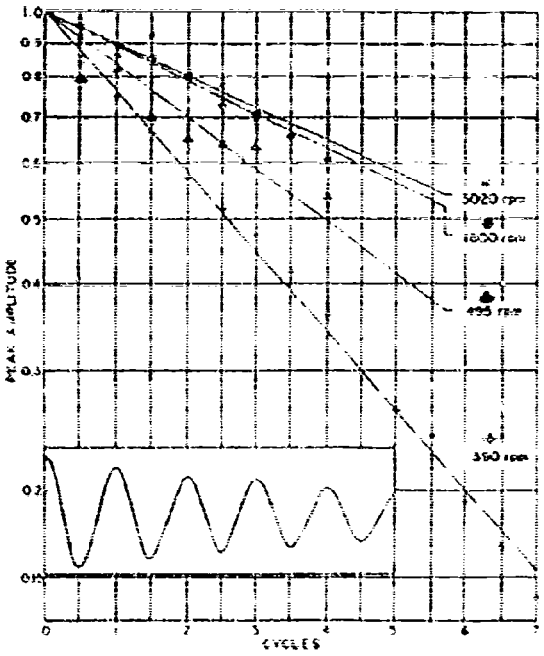

Fig. 11. Test points and lines of regression

The decay decrement per cycle under Coulomb-Morin friction is a constant as shown, for example, by Jacobsen and Ayre [5]. With the weight of the block providing the normal force the free vibration decrement per cycle is given by

$$\Delta = \frac{G\mu_f}{\omega_n^2} \tag{7}$$

EXPERIMENTAL DATA

Results of some tests with rotating shafts are shown in Table 1. The coefficients of correlation, calculated using the data of Fig. 11, are all sufficiently high that it may be concluded that the resistance to axial motion is pure velocity damping. Although the data correlates very well with a curve representing viscous damping, the magnitude of the measured damping ratios are not reasonably close to that which would be predicted from Eq. (2) above; that is, the damping ratio for a system with a given natural frequency does not vary inversely as the shaft rpm. This is shown by Fig. 12 in which the damping ratios of the 12.5-Hz systems of Table 1 appear to approach a finite damping ratio asymptotically at high rpm.

It may be hypothesized that the existence of this asymptote results from structural damping in the springs [6]. Because the normal force is simply the weight of the sliding block, the critical damping

$$C_c = \frac{2W}{G}\omega_n \tag{8}$$

Dividing Eq. (2) by Eq. (8) gives

$$\zeta = \frac{\mu_f G}{2r_b W\omega_n} \tag{9}$$

TABLE 1
Correlation of Test Data with Velocity Damping

Shaft Speed (rpm)	Natural Frequency (Hz)	Damping Ratio (%)	Coefficient of Correlation (%)
4020	12.5	1.39	N.A.*
3020	12.5	1.79	91.04
2100	6.5	1.60	99.56
1300	12.5	1.72	94.65
495	12.5	2.79	98.35
390	12.5	4.29	99.64

*N.A. - Not available.

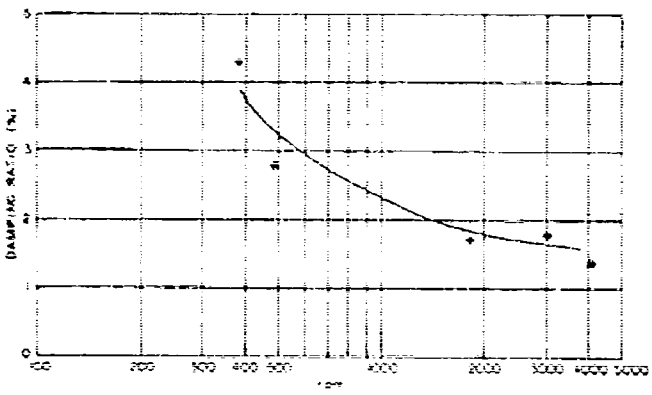

Fig. 12. Experimentally determined damping ratios (percent critical) for 12.5-Hz system and line of regression

But the damping coefficient actually measured, ζ_m, is the sum of the viscous damping given by Eq. (9) and one-half the structural damping, g, for small values of structural damping, because the dissipation of energy through hysteresis in the spring acts independently of and in addition to the axial velocity damping. It follows, therefore, that the equation for the measured damping coefficient at low v_a/v_t ratios is

$$\zeta_m = \frac{\mu_f G}{2r_b}\left(\frac{1}{\omega_n M}\right) + \frac{1}{2} g \qquad (10)$$

or

$$\zeta_m = \frac{a}{M} + \zeta_{STR} \qquad (11)$$

for constant natural frequency.

The constant a is unknown, because the friction coefficient μ_f is unknown, and the structural damping coefficient is unknown. From the admittedly limited data of Fig. 12 the statistically best values of the unknown constants may be determined by a least-squares fit; set the partial derivative of the sum of the squares of the differences between the measured values of Fig. 12 and the ideal value ζ_m, with respect to ζ_{STR}, equal to zero, and the similar partial derivative with respect to the constant a equal to zero, and solve for a and ζ_{STR}. This calculation yields ζ_{STR} = 1.20 percent or g = 2.4 percent. The value for g thus obtained is reasonable; Soroka [6] states that g, in the absence of deliberate damping, should lie in the neighborhood of 2 to 4 percent. It may therefore be concluded that the asymptote is a result of structural damping.

Solving for the constant a and substituting the values of a and ζ_{STR} into Eq. (11), the analyst may plot the solid line curve of Fig. 12 as the line of regression. The equation of the line of regression is

$$\zeta_m = \frac{1035}{rpm} + 0.0120 \qquad (12)$$

for a system of natural frequency of 12.5 Hz. Equation (9), for 12.5-Hz natural frequency and a shaft diameter of 0.317 in., gives

$$\zeta = 925.31\,\frac{\mu_f}{f_n\ rpm} \qquad (13)$$

from which it is seen that

$$\mu_f = \frac{f_n\ rpm}{925.31}\,\zeta$$

or (14)

$$\mu_f = \frac{rpm}{73.5}\,\zeta$$

for a 12.5-Hz natural frequency. Subtracting the viscous damping ratio owing to structural damping from the calculated damping ratio ζ_m in Eq. (12) (the line of regression) gives the actual viscous damping ratio, ζ_{act}, as listed in Table 2. Substituting the values of ζ_{act} for ζ in Eq. (14), one obtains the coefficients of friction shown in Table 2. It will be noted that the calculations of the coefficient of friction are reasonably consistent and agree favorably, within 8 percent, of the value of 0.152 given by Kent [7] for bronze on steel.

APPLICATION

To confirm analytical predictions of the performance of a vibration device it is often necessary to shake in one principal direction, and no other, in which the resistance to motion is ideally zero. It was to approximate these conditions in laboratory testing that the device shown in Fig. 13 was constructed.

Two H-shaped sliders are used; the left slider in Fig. 13 is the input and is shown attached to a shaker. The slider to the right holds the "output" mass. In Fig. 13, a dynamic antiresonant vibration isolator, placed between the input and output sliders, is under test. The

TABLE 2
Calculation of Friction Coefficient from Dynamic Test Data

Rpm	ζ_{act} from Line of Regression (%)	Natural Frequency f_n (Hz)	Coefficient of Friction μ_f
4020	0.357	12.5	0.140
3020	0.342	12.5	0.140
1600	0.575	12.5	0.142
495	2.09	12.5	0.140
390	2.65	12.5	0.140

Fig. 11 One-hp laboratory rig

shafts are 1-1/2 in. in diameter and 31 in. long and are driven by a 1.00 hp motor through right-angle gearboxes, 1725 rpm. As the tests were conducted at vibratory accelerations of less than 1/2 g on systems with natural frequencies between 4.7 and 15.0 Hz the axial resistance to motion was pure viscous damping-to-ground and of such a small value that it could, for most practical purposes, be ignored.

Characteristic of rotating machinery, a noise problem had to be dealt with; the predominant extraneous signal was at the frequency of shaft rotation which made it easy to discriminate and filter. Some gear tooth frequency noise was evident. Noise, or undesired signals, is particularly troublesome when tests in the immediate region of antiresonance are of primary concern, as was the case with much of the experimentation at Kaman in which this machine was used. However, the problem was not so severe that it could not be lived with even without filters and, except in the near vicinity of the rotational frequency, it was possible to tune antiresonances with a transmissibility as low as 0.006 percent.

REFERENCES

1. S. Timoshenko, Vibration Problems in Engineering, 3rd ed. (D. Van Nostrand Co., Princeton, N.J.), 1956, p. 68
2. J. P. Den Hartog, Mechanical Vibrations, 3rd ed. (McGraw-Hill, New York), 1947, pp. 52-56
3. I. Miller and J. E. Freund, Probability and Statistics for Engineers (Prentice-Hall, Inc., Englewood Cliffs, N.J.), 1965
4. A. J. Duncan, Quality Control and Industrial Statistics (Richard D. Irwin, Inc., Homewood, Ill.) 1953
5. L. S. Jacobsen and R. S. Ayre, Engineering Vibrations (McGraw-Hill, New York), 1958
6. W. W. Soroka, "Note on the Relations Between Viscous and Structural Damping Coefficients," J. Aero. Sci. 16(8):409ff, July 1949
7. Kent's Mechanical Engineers' Handbook, 12th ed. (John Wiley & Sons, Inc., New York), 1950, pp. 7-28

DISCUSSION

Mr. Brooks (NASA Langley Res. Ctr.): One point that you made was that you are getting about 0.024 g on the springs. You were looking at the effect of the mass on the spring during this vibration, were you not? It seems to me that that is a fairly high structural damping for the system because essentially most of the mass of the system is not undergoing any deformation.

Mr. Flannelly: It is. The restraint of the springs was not the best either. I think we got a fair amount of rubbing and deformation on the back of this little device. This was done on the small one. We did not take pains to weld the ends shut, so there might have been rotation.

* * *

THE DYNAMIC RESPONSE OF LINEARLY VISCOELASTIC CYLINDRICAL SHELLS TO PERIODIC OR TRANSIENT LOADING

Eugene A. Fitzgerald
Missile and Space Systems Division
McDonnell Douglas Corporation
Santa Monica, California*

The development in recent years of polymeric materials with improved energy absorption characteristics has led to an increased interest in the use of these materials as coatings or shear layers providing viscoelastic damping for the structure. This paper reports the results of an investigation that extended the previous work by other authors (on beams, plates, and axisymmetrically loaded shells) to nonsymmetrically loaded cylindrical shells with a more general class of cross sections. The various configurations were evaluated for response to random, harmonic, and impulsive loads using the well-known modal-displacement summation technique. In addition to obtaining equations and numerical results for cylindrical shells, results were also found for a dynamic correspondence principle for damped structures, and a transverse shear correction factor.

The numerical results obtained led to the following conclusions: (a) Even large amounts of damping are ineffective in reducing the peak response to an impulsive load; however, ringing at later times may be significantly reduced. (b) The addition of viscoelastic layers produces a significant reduction in response to broadband and near-resonant harmonic loads. (c) Constrained and unconstrained layer treatments show about the same effectiveness.

INTRODUCTION

In recent years, the addition of viscoelastic coatings or viscoelastic layers to increase the damping in structures has become increasingly attractive. Also, there is a natural desire to take advantage of the presence of viscoelastic materials that have already been added for other reasons, such as insulative or bonding purposes, but whose contributions to structural damping have hitherto been ignored. As a result, some analytical methods have already been developed for the rational analysis and design of the multilayered constructions which are prevalent in viscoelastically damped structures. In a few of the simpler structures, such as beams and plates, some first attempts at optimization have been made. However, shells with viscoelastic layers have not yet received comparable attention and the literature on viscoelastically damped, multilayer shells appears rather restricted, especially in comparison with the extensive literature on elastic shells and elastic shell vibrations. Most of the efforts in viscoelastic shell analysis has been devoted to the development of governing equations and to a qualitative investigation of the motion.

Baylor and Oberndorfer derive equations for the quasi-static response of cylindrical sandwich shells [1,2]. Scipio has done the same for other homogeneous cylindrical shells [3]. For homogeneous cylindrical shells, Librescu and Grigolyuk found frequency equations, but did not generate numerical results, while others considered axisymmetric wave propagation [4,5].

Damping factors or loss factors, as well as frequencies, have been found for a few cases. Biot has considered the correspondence between elastic and viscoelastic shell motions [6]. Bieniek and Freudenthal have considered a three-layer cylindrical shell with transverse shear effects, valid for a stiff core [7]. Yu has developed a set of equations for three-layer

*This work was done at the Virginia Polytechnic Institute, Blacksburg, Virginia, in partial satisfaction of the requirements for the Ph.D in Engineering Mechanics.

shells, including transverse shear effects like Bieniek's but probably valid for slightly thicker shells which he used to find damping parameters for a sandwich cylinder [8]. Haile has developed a more general shell theory, with a somewhat different accounting for transverse shear, valid for a stiff core that was used to find a few frequencies and loss factors for a shell similar to that of Yu's [9]. Salerno and Jones have used Yu's equations to examine two damped cylindrical shell configurations under resonant loading [10].

Differential equations similar to those of Yu are used in this paper (with a changed treatment of the transverse shear) to find loss factors and frequencies for selected cylindrical shells. In addition, the effectiveness of the damping in reducing response to transient or random loads is considered.

THE VISCOELASTIC SHELL PROBLEM

A general correspondence theorem exists for viscoelastic solids which guarantees that, under certain not-too-restrictive conditions, the solution for the response of an elastic body (called the associated elastic body) will be the Laplace (or Fourier) transform of the solution for the response of a corresponding viscoelastic body. For harmonic motion this general correspondence theorem can be applied to get a particularly convenient result, as follows:

> If and only if correspondence exists, then classical uncoupled normal modes exist in the viscoelastic solid and are identical to those of the associated elastic solid. Furthermore, the natural frequencies and logarithmic decrements of the motion in the viscoelastic body can be found from the natural frequencies of the elastic body by an algebraic relation.

Also, because the normal modes form a complete, orthogonal set, loads and initial conditions can be represented in a Fourier series of these modes, and both transient and steady-state forced motion problems can be solved.

For the cases in which correspondence does exist, it can then be seen that the central problem in viscoelastic shell analysis changes from that of finding the response of the viscoelastic body directly, to that of finding the normal modes and natural frequencies of the associated elastic problem and performing the algebraic manipulation necessary to extract natural frequencies and damping factors from the natural frequencies of the elastic system.

A direct attack on the viscoelastic problem can be made whether correspondence exists or not. It is likely to be very difficult to get a meaningful solution, however, unless correspondence exists (whether one takes advantage of it or not) and, indeed, in not one of the cited papers is there a deliberate lack of correspondence.

Because of the great variety of elastic vibration problems that have been solved, it may appear that solution of the associated elastic problem either has already been done or is very straightforward. In actual practice, this does not usually turn out to be the case because the viscoelastic layers that are added for damping are usually relatively soft and flexible with elastic moduli of perhaps only 1/10th to 1/10,000th of those of a metallic substructure. Therefore, in many cases additional deformations such as transverse shear and transverse normal strain, which are neglected in the classical elastic theories, must be taken into account.

To summarize briefly: The viscoelastic shell problem in many cases can be reduced to the following:

1. Establishment of correspondence between the viscoelastic problem and an associated elastic problem.

2. Solution of the associated elastic problem for normal modes and natural frequencies. (This may require development or adaptation of differential equations containing higher order approximations). This is likely to be the most difficult step in a dynamic viscoelastic shell problem.

3. Algebraic manipulation of the natural frequencies of the associated elastic problem to get damping factors and damped natural frequencies.

4. Application of the results of the above to a series of problems with different geometries, loads, and so forth, to develop insight into the response and to find optimum designs.

THEORETICAL CONSIDERATIONS

The existence of a correspondence between the solutions of dynamic elastic and viscoelastic problems has been noted in the Introduction as the key to the solution of a great many viscoelastic

structure problems. Several correspondence principles have been stated for different classes of motion or systems.

A very general correspondence principle for the free vibrations of a viscoelastic solid has been stated by Fisher and Leitman [11]. The existence of uncoupled normal modes in damped systems was considered by Rayleigh who stated conditions sufficient for their existence in discrete systems [12]. These results were generalized by Caughey and O'Kelly, who were also able to state both necessary and sufficient conditions for existence of normal modes in second order, viscously-damped, continuous systems [13,14]. In this paper, their results are extended to include viscoelastically damped, nth order systems.

The correspondence principle itself can be stated, in a form slightly different from that given by Biot [6], as the following:

> The stresses and displacements of the transformed viscoelastic problem correspond to those of the associated elastic problem if and only if the normal modes are identical.

Existence conditions can be stated as follows:

1. Normal modes exist in a nonablating viscoelastic solid with nondissipative boundary conditions, and they are identical to those of the associated elastic solid, if one of the following is true:

a. The viscoelastic material has a homogeneous relaxation spectrum, that is, the loss factors are the same in dilatation and shear, which for isotropic materials requires Poisson's ratio to be constant [11].

b. The motion is purely solenoidal or purely dilatational.

c. A product solution is known.

d. The damping is light and the natural frequencies of the associated elastic body are well separated.

2. For bodies for which the equations of motion can be reduced to a single partial differential equation of the type

$$L_n \frac{\partial^n y}{\partial t^n} + L_{n-2} \frac{\partial^{n-2} y}{\partial t^{n-2}} + \dots L_o y = -M \frac{\partial^2 y}{\partial t^2} \quad (1)$$

where L and M are complex and real partial differential spatial operators, respectively, and n is even, then normal modes and solutions of the type

$$y(\bar{x}, t) = \Phi(\bar{x})\, e^{i\omega^* t} \quad (2)$$

will exist, if, and only if

a. The damping operator is a linear combination of the stiffness and mass operators, that is,

$$\left[\mathrm{Im}\left(\sum_n (i\omega)^n L_n\right)\right] = a\left[\mathrm{Re}\left(\sum_n (i\omega)^n L_n\right)\right] + b\omega^2 M. \quad (3)$$

b. The damping operator is commutative with the stiffness and mass operators, that is,

$$\left[\mathrm{Re}\left(\sum_n (i\omega)^n L_n\right)\right] M^{-1} \left[\mathrm{Im}\left(\sum_n (i\omega)^n L_n\right)\right]$$
$$= \left[\mathrm{Im}\left(\sum_n (i\omega_n) L_n\right)\right] M^{-1} \left[\mathrm{Re}\left(\sum_n (i\omega)^n L_n\right)\right] \quad (4)$$

and the boundary conditions for the stiffness operator are derivable from those on the damping operator or vice versa.

c. The body is homogeneous and the boundary conditions on the stiffness operator are derivable from those on the damping operator or vice versa.

As an example, we can consider the Timoshenko beam. The governing equation for the Timoshenko beam with rotatory inertia is

$$\left[\frac{\rho I \rho A}{KAG}\right] \frac{\partial^4 y}{\partial t^4} + \left[\left(-\rho I - \frac{\rho A E I}{KAG}\right) \frac{\partial^2}{\partial x^2}\right] \frac{\partial^2 y}{\partial t^2}$$
$$+ (EI) \frac{\partial^4 y}{\partial x^4} = -\rho A \frac{\partial^2 y}{\partial t^2}. \quad (5)$$

Let

$$y = \Phi(x)\, e^{i(\omega + i\delta)t} \quad (6)$$

$$E^* = E(1 + i\eta_1) \quad (7)$$

and

$$G^* = G(1 + i\eta_2) \quad (8)$$

and, noting the undamped natural frequencies as ω_0, and the damped natural frequencies as ω, where

$$\omega^2 = \omega_0^2 - \delta^2, \quad (9)$$

upon substitution into Eq. (5) and separation

into real and imaginary parts, it is found that the real parts yield

$$\left\{\rho I\omega^2 + \frac{EI\rho A}{KAG}\left[\omega^2 - 2\,\frac{(\eta_1-\eta_2)}{1+\eta_1\eta_2}\,\delta\omega_0\right]\right\}\frac{\partial^2\phi}{\partial x^2} + EI\,\frac{\partial^4\phi}{\partial x^4}$$

$$= \left\{\rho A\omega^2 - \frac{\rho I\rho A}{KAG}\left[\omega^4 - 4\delta^2\omega_0^2 + 4\eta_2\delta\omega_0\omega^2\right]\right\}\phi \quad (10)$$

and the imaginary parts yield

$$\left\{\rho I(2\delta\omega_0) + \frac{EI\rho A}{KAG}\left[2\delta\omega_0 + \frac{(\eta_1-\eta_2)}{1+\eta_1\eta_2}\,\omega^2\right]\right\}\frac{\partial^2\phi}{\partial x^2} + EI\eta_1\,\frac{\partial^4\phi}{\partial x^4}$$

$$= \left\{\rho A(2\delta\omega_0) - \frac{\rho I\rho A}{KAG}\left[-\omega^4\eta_2 + 4\delta\eta_2\omega_0^2 + 4\delta\omega_0\omega^2\right]\right\}\phi\,. \quad (11)$$

Both equations must be satisfied for all values of x. Assuming that one of the equations, let us say Eq. (10) has been solved for the eigenvalues and eigenfunctions that satisfy it, then $\partial^4\phi/\partial x^4$ can be found. Upon substitution for $\partial^4\phi/\partial x^4$, Eq. (11) becomes

$$\left\{\rho I(2\delta\omega_0 - \omega^2\eta_1) + \frac{EI\rho A}{KAG}\left[(2\delta\omega_0 - \eta_1\omega^2) + \frac{\eta_1-\eta_2}{1+\eta_1\eta_2}\,(\omega^2 + 2\eta_1\delta\omega_0)\right]\right\}\frac{\partial^2\phi}{\partial x^2}$$

$$= \left\{\rho A(2\delta\omega_0 - \eta_2\omega^2) - \frac{\rho A\rho I}{KAG}\,\frac{1}{1+\eta_2^2}\left[-\omega^4(\eta_1+\eta_2) + 4\delta^2\omega_0^2(\eta_1+\eta_2) + 4\delta\omega_0\omega^2(1-\eta_1\eta_2)\right]\right\}\phi\,. \quad (12)$$

If $\eta_1 = \eta_2$, then both the coefficient of $\partial^2\phi/\partial x^2$ and ϕ will be zero (for $2\delta\omega_0 = \eta\omega^2$), so this equation is always satisfied. Of course, from the general rule given by the Fisher-Leitman equation, Eq. (11), this was anticipated [1]. If the loss factors are not equal then the eigenfunctions in Eqs. (10), (11), and (12) will be the same only if the boundary conditions are compatible.

To determine the compatibility of the boundary conditions, Eq. (12) is written as

$$\beta_L\phi'' = \beta_R\phi\,. \quad (13)$$

Suppose that one set of boundary conditions is

$$\phi(a) = \phi(b) = 0\,. \quad (14)$$

Then from Eq. (13)

$$\phi''(a) = \frac{\beta_R}{\beta_L}\,\phi(a) = 0\,,$$
$$\phi''(b) = \frac{\beta_R}{\beta_L}\,\phi(b) = 0\,. \quad (15)$$

Similarly if $\phi'(a) = 0$, then $\phi''(a)$ must equal zero, and so on. In particular it can be seen that fixed-fixed beams, free-free beams, or cantilevered beams, do not have compatible boundary conditions, while a simply supported beam does. Because the mode shapes of a simply supported beam are known to be sinusoidal, infinite beams with sinusoidal waves will also have dynamic correspondence.

This result is of some importance because it shows that most theoretical analyses correctly assumed correspondence, as they were done for simply supported or infinite beams, while most experimental results usually have at best only approximate correspondence, as they are done with cantilevers and free-free beams.

Difficulties with lack of correspondence (although not labeled as such) have arisen in elasticity-type solutions in which sinusoidal modes, in all relevant directions, could not be assumed a priori. Biot and Pohle suppressed any coupling by assuming light damping, but Hertelendy and Goldsmith's report is unclear regarding the approximation they used [15,16].

Based upon a limited series of experiments, and an otherwise commendable analysis, DiTaranto and Blasingame have concluded that the damping factors of a beam do not depend upon the boundary conditions [17,18]. Their error results from assuming that there will be at least one real eigenfunction for any beam, but, as we have shown above, there are none except for simply supported beams. Therefore, DiTaranto and Blasingame have assumed, in effect, that at least one eigenfunction is sinusoidal. Ruzicka handles nonsimply supported boundary conditions by assuming sinusoidal mode shapes and light damping, which gives the same result as in Ref. [17], but in a more straightforward way [19].

For reasons related to experimental technique almost all tests have been done on specimens that lack correspondence. While the errors resulting from lack of correspondence may be acceptable in the context of the present test accuracy, at the least an estimate of their size should be made. Apparently one investigator has noticed substantial modal coupling [20].

As in other structures, shells of any shape and with any boundary conditions will exhibit correspondence if they have homogeneous relaxation spectra. However, for the multilayered shells considered in this paper, a homogeneous relaxation spectrum is unlikely, so the existence of correspondence must depend upon the particular geometries and motions being considered.

For the most general vibration, bending, stretching, and shearing motions will be significant, and as a result it will be found that correspondence exists only for sinusoidal mode shapes; this, of course, requires simple supports for a cylindrical shell.

If correspondence can be established then elastic shell equations can be used to solve for the motion.

Equations containing higher order terms have been derived by Yu for nonaxisymmetric motion and used (in a reduced form, of course) by him and by Jones et al. to study axisymmetric motion. Rotatory and translatory inertia terms were included and normals were assumed to remain straight but not normal [7,8]. Bieniek and Freudenthal dropped all higher order terms and used the resulting equations to consider nonaxisymmetric motion also [4]. Their assumptions regarding transverse shear and inertia terms are the same as Yu's. In this paper, some of Yu's higher order terms have been dropped but the resulting equations, while slightly more complicated than Bieniek's and Freudenthal's, are still approximately Donnell-type. The tangential translatory inertia terms have been neglected but the same assumption is made for transverse shear as was used by the others. The notation of Ref. [4] has been adopted as more suggestive than Yu's and a more general method is given for finding the constitutive equation for transverse shear.

It is assumed that the motion of the shell is such that the stress resultants shown in Fig. 1, can be related to the displacements by the following:

$$\left.\begin{aligned}
N_1 &= B_1 \frac{1}{R}\frac{\partial u}{\partial \alpha} + B_{12}\frac{1}{R}\left[\frac{\partial v}{\partial \beta} + w\right] \\
N_2 &= B_2 \frac{1}{R}\left[\frac{\partial v}{\partial \beta} + w\right] + B_{12}\frac{1}{R}\frac{\partial u}{\partial \alpha} \\
N_{12} &= C\frac{1}{R}\left[\frac{\partial u}{\partial \beta} + \frac{\partial v}{\partial \alpha}\right] \\
M_1 &= D_1 \frac{1}{R}\frac{\partial \phi}{\partial \alpha} + D_{12}\frac{1}{R}\frac{\partial \psi}{\partial \beta} \\
M_2 &= D_2 \frac{1}{R}\frac{\partial \psi}{\partial \beta} + D_{12}\frac{1}{R}\frac{\partial \phi}{\partial \alpha} \\
M_{12} &= H\frac{1}{R}\left[\frac{\partial \phi}{\partial \beta} + \frac{\partial \psi}{\partial \alpha}\right] \\
Q_1 &= \overline{KAG}\left[\phi + \frac{1}{R}\frac{\partial w}{\partial \alpha}\right] \\
Q_2 &= \overline{KAG}\left[\psi + \frac{1}{R}\frac{\partial w}{\partial \beta}\right]
\end{aligned}\right\} \quad (16)$$

(Cont.)

where the geometry of the cross section is shown in Fig. 2 and

$$\left.\begin{aligned}
B_1 &= B_2 = \sum_n \frac{E_i}{1-\nu_i^2} h_i \\
B_{12} &= \sum_n \frac{\nu_i E_i}{1-\nu_i^2} h_i \\
C &= \sum_n G_i h_i \\
D_1 &= D_2 = \sum_n \frac{E_i}{1-\nu_i^2}\left[\frac{1}{12} h_i^3 + h_i \bar{d}_i^2\right] \\
D_{12} &= \sum_n \frac{\nu_i E_i}{1-\nu_i^2}\left[\frac{1}{12} h_i^3 + h_i \bar{d}_i^2\right] \\
H &= \sum_n G_i \left[\frac{1}{12} h_i^3 + h_i \bar{d}_i^2\right]
\end{aligned}\right\} \quad (17)$$

and $\overline{KAG}$ is defined below and the reference surface is located so that

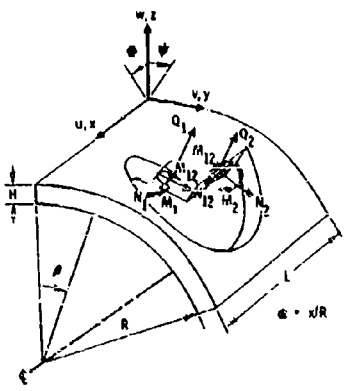

Fig. 1. Geometry and stress resultants for a cylindrical shell

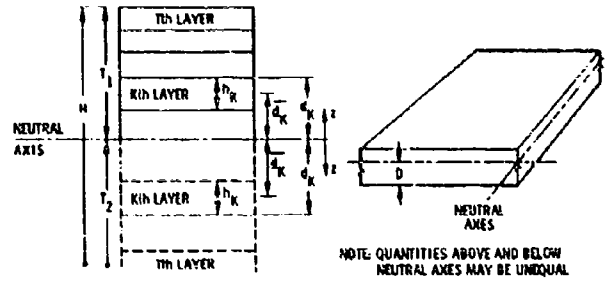

Fig. 2. Cross section geometry

$$\int \frac{zE}{1-\nu^2}\, dA = 0 . \qquad (18)$$

The equilibrium equations are obtained from those of [6] by dropping certain higher order terms involving coupling between stretching and bending terms. They are shown below with all translatory inertia and surface load terms included, although only those in the z direction (radial) will be retained.

$$\left.\begin{aligned}
&\frac{\partial N_1}{\partial x} + \frac{\partial N_{12}}{\partial y} + \left[p_1 - M\frac{\partial^2 u}{\partial t^2}\right] = 0\\
&\frac{\partial N_{12}}{\partial x} + \frac{\partial N_2}{\partial y} + \frac{Q_2}{R} + \left[p_2 - M\frac{\partial^2 v}{\partial t^2}\right] = 0\\
&\frac{\partial Q_1}{\partial x} + \frac{\partial Q_2}{\partial y} - \frac{N_2}{R} + \left[p_3 - M\frac{\partial^2 w}{\partial t^2}\right] = 0\\
&\frac{\partial M_1}{\partial x} + \frac{\partial M_{12}}{\partial y} - Q_1 - I\frac{\partial^2 \phi}{\partial t^2} = 0\\
&\frac{\partial M_2}{\partial y} + \frac{\partial M_{12}}{\partial x} - Q_2 - I\frac{\partial^2 \psi}{\partial t^2} = 0
\end{aligned}\right\} \qquad (19)$$

where

$$M = \sum \rho_i h_i , \quad I = \sum \rho_i \left[\frac{1}{12} h_i^3 + h_i d_i^2\right] \qquad (20)$$

where ρ_i is the mass density, and p_i is the external load.

Substituting Eq. (16) in Eq. (19), the governing equations are found as follows:

$$\left(B_1 \frac{\partial^2}{\partial \alpha^2} + C\frac{\partial^2}{\partial \beta^2}\right)u + (B_{12}+C)\left(\frac{\partial^2}{\partial\alpha\partial\beta}\right)v + B_{12}\frac{\partial w}{\partial \alpha} = 0$$

(21) (Cont.)

$$(B_{12}+C)\left(\frac{\partial^2}{\partial\alpha\partial\beta}\right)u + \left(B_2\frac{\partial^2}{\partial\beta^2} + C\frac{\partial^2}{\partial\alpha^2}\right)v + (B_{22}+\overline{KAG})\frac{\partial w}{\partial\beta} + \overline{KAG}\,R\psi = 0$$

$$-B_{12}\frac{\partial u}{\partial\alpha} - B_{11}\frac{\partial v}{\partial\beta} + \left(\overline{KAG}\frac{\partial^2}{\partial\alpha^2} + \overline{KAG}\frac{\partial^2}{\partial\beta^2} - B_1\right)w + \overline{KAG}\,R\frac{\partial\phi}{\partial\alpha} + \overline{KAG}\,R\frac{\partial\psi}{\partial\beta} = -p_3R^2 + MR^2\frac{\partial^2 w}{\partial t^2}$$

$$-\overline{KAG}\,R\frac{\partial w}{\partial\alpha} + \left(D_1\frac{\partial^2}{\partial\alpha^2} + H\frac{\partial^2}{\partial\beta^2} - \overline{KAG}\,R^2\right)\phi + (D_{12}+H)\frac{\partial^2\psi}{\partial\alpha\partial\beta} = IR^2\frac{\partial^2\phi}{\partial t^2}$$

$$-\overline{KAG}\,R\frac{\partial w}{\partial\beta} + (D_{12}+H)\frac{\partial^2\phi}{\partial\alpha\partial\beta} + \left(D_1\frac{\partial^2}{\partial\beta^2} + H\frac{\partial^2}{\partial\alpha^2} - \overline{KAG}R^2\right)\psi = IR^2\frac{\partial^2\psi}{\partial t^2}$$

(21)

where $\alpha = x/R$.

Equation (21) together with boundary conditions will form a complete boundary value problem. On the ends $x = 0$ and L, one of each of the following pairs

$$N_1 u, \quad N_{12} v, \quad M_1\phi, \quad M_{12}\psi, \quad Q_1 w$$

must be prescribed [7].

The transverse shear correction factor $\overline{KAG}$ must be evaluated for use in the constitutive equation, Eq. (16).

Recently Cowper developed a method for deriving the Timoshenko beam approximation

in a way that greatly clarifies the nature of the approximation [21]. This technique has been extended herein to multilayer cross sections.

To evaluate the transverse shear correction factor by Cowper's method it is necessary to make some sort of assumption, such as the existence of a particular strain, stress, or displacement distribution or condition. In this case it will be assumed that the shape of the shear stress distribution is the same as in the static case for which normals to the middle surface remain straight and for which the shell is axisymmetrically loaded. The coefficient that will be derived on this basis will be equally valid for dynamic, nonaxisymmetrically loaded shells to the extent that the shape of the shear stress distribution does not change under the new conditions. Of course, the magnitude of the shear stress can change drastically without affecting the accuracy of the approximation. With this assumption then the normal stress is

$$\sigma_{xx} = \frac{z}{D_1} \frac{E}{1-\nu^2} M \tag{22}$$

where D_1 is defined by Eq. (17), and the geometry is shown in Fig. 2. Then the stress is (for $Q = \partial M/\partial x$)

$$\sigma_{xz} = \int_z^T \frac{\partial \sigma_{xx}}{\partial x} dz = \frac{Q}{D_1} \int_z^T \frac{E}{1-\nu^2} z dz . \tag{23}$$

Then the constitutive relation,

$$\frac{Q}{KAG} = \frac{1}{D_1} \int_A \frac{zE}{1-\nu^2} \int_0^z \frac{\sigma_{xz}}{G} dz dA$$

becomes

$$\frac{Q}{KAG} = \frac{Q}{D_1^2} \int_A \frac{zE}{1-\nu^2} \int_0^z \frac{1}{G} \int_z^T \frac{zE}{1-\nu^2} dz\, dz\, dA. \tag{24}$$

This integration can be performed for a layered section (Fig. 2) to give the shear coefficient

$$\overline{KAG} = \frac{D_1^2}{I_{top} + I_{bottom}} \tag{25}$$

where

$$I_{\substack{top,\\ bottom}} = \sum_{i=1}^{k=T_1 \text{ or } T_2} \left\{ \frac{E_k}{1-\nu_k^2} \left[\left(\frac{C_k + D_k}{2} \right) (d_k^2 - d_{k-1}^2) - \frac{A_k + B_k}{3G_k} (d_k^3 - d_{k-1}^3) - \frac{E_k}{30G_k(1-\nu_k^2)} (d_k^5 - d_{k-1}^5) \right] \right\} \tag{26}$$

(Cont.)

where I is evaluated separately for the $k = T_1$ layers above the neutral axis and the $k = T_2$ layers below the neutral axis, and

$$\left.\begin{aligned} A_k &= \sum_{i=1}^{i=T-k} \frac{E_{k+i}}{1-\nu_{k+i}^2} \bar{d}_{k+i} h_{k+i} \quad \text{for } T > k \\ A_k &= 0 \quad \text{for } T = k \end{aligned}\right\} \tag{27}$$

$$B_k = \frac{E_k}{2(1-\nu_k^2)} d_k^2 \tag{28}$$

$$\left.\begin{aligned} C_k &= \sum_{i=1}^{i=k} \left[\frac{(A_i + B_i)}{G_i} (d_i - d_{i-1}) - \frac{E_i}{6G_i(1-\nu_i^2)} (d_i^3 - d_{i-1}^3) \right] \quad \text{for } k > 1 \\ C_k &= 0 \quad \text{for } k = 1 \end{aligned}\right\} \tag{29}$$

$$D_k = -\frac{A_k + B_k}{G_k} (d_{k-1}) + \frac{E_k}{6G_k(1-\nu_k^2)} (d_{k-1}^3). \tag{30}$$

For the simply supported shell considered in this paper the natural frequencies of the associated elastic problem can be found in closed form by assumption of a product solution of known functions. Damping factors and damped natural frequencies of the viscoelastic shell can then be found by substitution of complex constants for the elastic constants. Both side-on (Fig. 3) and axisymmetric loads are considered.

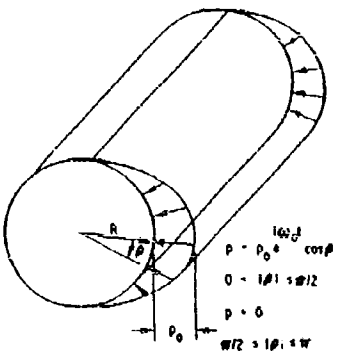

Fig. 3. Side-on load

The boundary conditions at $x = 0$ and L are

$$N_1 = v = M_1 = \psi = w = 0$$

Then, if the load can be represented by

$$p_3 = \sum_m \sum_n P_{mn} (\sin \lambda_m \alpha \sin n\beta) e^{i\omega_0 t} \quad (31)$$

where m and n are not equal to zero, solutions can be found in the form

$$\left.\begin{aligned}
u &= \sum_m \sum_n U_{mn} (\cos \lambda_m \alpha \sin n\beta) e^{i\omega_0 t} \\
v &= \sum_m \sum_n V_{mn} (\sin \lambda_m \alpha \cos n\beta) e^{i\omega_0 t} \\
w &= \sum_m \sum_n W_{mn} (\sin \lambda_m \alpha \sin n\beta) e^{i\omega_0 t} \\
\phi &= \sum_m \sum_n \phi_{mn} (\cos \lambda_m \alpha \sin n\beta) e^{i\omega_0 t} \\
\psi &= \sum_m \sum_n \psi_{mn} (\sin \lambda_m \alpha \cos n\beta) e^{i\omega_0 t}
\end{aligned}\right\} \quad (32)$$

where $\lambda_m = (m\pi R)/L$ and m is the number of half waves in the x direction and n is the number of full waves in the circumferential direction.

Substitution of the solutions of Eq. (32) in the governing equations of Eq. (21) leads to a set of algebraic equations for U_{mn}, V_{mn}, W_{mn}, ϕ_{mn}, ψ_{mn} and the load P_{mn}. These can be solved to give relations between the displacements

$$\left.\begin{aligned}
U_{mn} &= \frac{\underline{F} W_{mn} - \underline{F}_1 \Psi_{mn}}{\underline{D}} \\
V_{mn} &= \frac{\underline{G} W_{mn} - \underline{G}_1 \Psi_{mn}}{\underline{D}} \\
\Phi_{mn} &= \frac{(\underline{M} R^2 I \omega_0^2 - \underline{H}) W_{mn}}{R^4 I^2 \omega_0^4 - R^2 I \omega_0^2 \underline{C} + \underline{D}} \\
\Psi_{mn} &= \frac{(\underline{N} R^2 I \omega_0^2 + \underline{J}) W_{mn}}{R^4 I^2 \omega_0^4 - R^2 I \omega_0^2 \underline{C} + \underline{D}}
\end{aligned}\right\} \quad (33)$$

and the magnitude of the displacement

$$\frac{W_{mn}}{P_{mn}} = R^2 \Bigg/ \left\{ \frac{\underline{P}}{\underline{D}} + \underline{E} - MR^2 \omega_0^2 + \frac{\underline{I}}{\underline{D}} \left[\frac{R^2 I \omega_0^2 \underline{H} + \underline{J}}{R^4 I^2 \omega_0^4 - R^2 I \omega_0^2 \underline{C} + \underline{D}} \right] + \left[\frac{R^2 I \omega_0^2 \underline{R} + \underline{S}}{R^4 I^2 \omega_0^4 - R^2 I \omega_0^2 \underline{C} + \underline{D}} \right] \right\} \quad (34)$$

where

$$\begin{aligned}
\underline{B} &= (B_1 \lambda^2 + Cn^2)(B_1 n^2 + C\lambda^2) - (B_{12} + C)^2 \lambda^2 n^2 \\
\underline{C} &= (D_1 + H)(\lambda^2 + n^2) + 2\,\overline{KAG}\, R^2 \\
\underline{D} &= (D_1 n^2 + H\lambda^2 + \overline{KAG}\, R^2)(D_1 \lambda^2 + Hn^2 + \overline{KAG}\, R^2) \\
&\quad - (D_{12} + H)^2 \lambda^2 n^2 \\
\underline{E} &= B_1 + \overline{KAG}\,(\lambda^2 + n^2) \\
\underline{F} &= B_{12}(B_1 n^2 + C\lambda^2)\lambda - (B_{12} + C)(B_1 + \overline{KAG})\lambda n^2 \\
\underline{F}_1 &= \overline{KAG}\, R(B_{12} + C)\lambda n \\
\underline{G} &= (B_1 + \overline{KAG})(B_1 \lambda^2 + Cn^2) n - (B_{12} + C) B_{12} \lambda^2 n \\
\underline{G}_1 &= \overline{KAG}\, R(B_1 \lambda^2 + Cn^2) \\
\underline{H} &= \overline{KAG}\, R\lambda \left[-(D_1 n^2 + H\lambda^2 + \overline{KAG}\, R^2) + (D_{12} + H) n^2 \right] \\
\underline{J} &= \overline{KAG}\, Rn \left[-(D_1 \lambda^2 + Hn^2 + \overline{KAG}\, R^2) + (D_{12} + H)\lambda^2 \right] \\
\underline{M} &= \overline{KAG}\, R\lambda \\
\underline{N} &= \overline{KAG}\, Rn \\
\underline{P} &= -B_{12}^2 (B_1 n^2 + C\lambda^2)\lambda^2 + B_{12}(B_{12} + C)(B_1 + \overline{KAG})\lambda^2 n^2 \\
&\quad - B_1 (B_1 + \overline{KAG})(B_1 \lambda^2 + Cn^2) n^2 + B_1 B_{12} (B_{12} + C)\lambda^2 n^2 \\
\underline{R} &= \overline{KAG}^2\, R^2 (n^2 + \lambda^2) \\
\underline{S} &= \overline{KAG}^2\, R^2 \left[2(D_{12} + H) n^2 \lambda^2 - (D_1 \lambda^2 + Hn^2 + \overline{KAG}\, R^2) n^2 \right. \\
&\quad \left. - (D_1 n^2 + H\lambda^2 + \overline{KAG}\, R^2)\lambda^2 \right] \\
\underline{T} &= \overline{KAG}\, Rn \left[B_{12}(B_{12} + C)\lambda^2 - B_1 (B_1 \lambda^2 + Cn^2) \right] .
\end{aligned} \quad (35)$$

Then the natural frequencies, for $m \neq 0$, $n \neq 0$, can be found from Eq. (34) as

$$\begin{aligned}
MI^2 R^6 \omega_0^6 &+ I^2 R^4 \omega_0^4 \left[-\underline{E} - \frac{\underline{P}}{\underline{D}} - \underline{C} \frac{M}{I} \right] \\
&+ IR^2 \omega_0^2 \left[\underline{C}\underline{E} + \frac{\underline{C}\underline{P}}{\underline{D}} + \underline{D} \frac{M}{I} - \frac{\underline{N}\underline{T}}{\underline{D}} - \underline{R} \right] \\
&+ \left[-\underline{D}\underline{E} - \frac{\underline{D}\underline{P}}{\underline{D}} - \frac{\underline{J}\underline{T}}{\underline{D}} - \underline{S} \right] = 0. \quad (36)
\end{aligned}$$

For axisymmetric motion $n = 0$ and it is necessary to rederive the frequency equation starting with the governing equations of Eq. (21) and the assumed solution

$$
\left.\begin{aligned}
v &= \phi = 0 \\
u &= \sum_m (U_m \cos \lambda_m t)\, e^{i\omega_0 t} \\
w &= \sum_m (W_m \sin \lambda_m t)\, e^{i\omega_0 t} \\
\Phi &= \sum_m (\Phi_m \sin \lambda_m t)\, e^{i\omega_0 t}
\end{aligned}\right\} \tag{37}
$$

for the load

$$
p_3 = \sum_m P_m \sin \lambda_m t\, e^{i\omega_0 t} .
$$

Then the displacement become

$$
\left.\begin{aligned}
U_m &= \frac{B_{12}}{B_1 \lambda} W_m \\
\Phi_m &= \frac{\overline{KAG}\, R\lambda}{IR^2 \omega_0^2 - (D_1 \lambda^2 + \overline{KAG}\, R^2)} W_m \\
\frac{W_m}{P_m} &= 1 \Bigg/ \left\{ \frac{(\overline{KAG}\, \lambda)^2}{IR^2 \omega_0^2 - (D_1 \lambda^2 + \overline{KAG}\, R^2)} - M\omega_0^2 \right. \\
&\qquad \left. + \frac{(\overline{KAG}\, \lambda^2 + B_1)\, B_1 \lambda - B_{12}^2 \lambda}{B_1 \lambda R^2} \right\} .
\end{aligned}\right\} \tag{38}
$$

The natural frequencies are given by

$$
\omega_0^4 [MIR^4] - \omega_0^2 [M \underline{C}_0 + I \underline{E}_0] R^2 + [-\underline{M}_0^3 R^2 + \underline{C}_0 \underline{E}_0] = 0 \tag{39}
$$

where

$$
\left.\begin{aligned}
\underline{C}_0 &= D_1 \lambda^2 + \overline{KAG}\, R^2 \\
\underline{E}_0 &= (\overline{KAG}\, \lambda^2 + B_1) - D_1 - \frac{B_{12}^2}{B_1} \\
\underline{M}_0 &= \overline{KAG}\, \lambda
\end{aligned}\right\} \tag{40}
$$

and the effective mass per unit area is

$$
M_{min} = M + I \left(\frac{\Phi_m}{W_m} \right)^2 \tag{41}
$$

where (Φ_m / W_m) is defined in Eq. (38).

It is known from the correspondence principle that the solution for the viscoelastic shell can be gotten from the solution for the associated elastic problem by (a) replacing $e^{i\omega_0 t}$ in Eq. (33) by $e^{i\omega^* t}$, where $\omega^* = \omega + i\delta$, and ω is the damped natural frequency and δ is the decay rate, and (b) transforming the elastic constants.

Because any viscoelastic stress-strain relationship can be written as

$$
P_{rs}^M \sigma_{rs} = \sum_{k,l}^N Q_{rskl}^N \epsilon_{kl} \tag{42}
$$

where P and Q are differential time operators,

$$
P_{rs}^M = p_{rs}^0 + p_{rs}^1 \frac{\partial}{\partial t} + p_{rs}^2 \frac{\partial^2}{\partial t^2} + \cdots p_{rs}^M = \frac{\partial^M}{\partial t^M}
$$

and

$$
Q_{rskl}^N = q_{rskl}^0 + q_{rskl}^1 \frac{\partial}{\partial t} + q_{rskl}^2 \frac{\partial^2}{\partial t^2} \cdots q_{rskl}^N \frac{\partial^N}{\partial t^N} \tag{43}
$$

it can be seen by direct substitution of

$$
\left.\begin{aligned}
\sigma_{rs} &= \sigma_{rs}^0 e^{i\omega^* t} \\
\text{and} \qquad \epsilon_{kl} &= \epsilon_{kl}^0 e^{i\omega^* t}
\end{aligned}\right\} \tag{44}
$$

that for this special type of motion, the differential relation equation, Eq. (42) is reduced to an algebraic relation

$$
\sigma_{rs} = \sum_{k,l} \left[\bar{H}_{rskl}(\omega^*) + i \bar{\bar{H}}_{rskl}(\omega^*) \right] \epsilon_{kl} . \tag{45}
$$

For an isotropic material the stress-strain relations in Eq. (45) take the particularly simple form

$$
\left.\begin{aligned}
\sigma &= 3(K_1 + i K_2)\, \epsilon_{ii} = 3K^* \epsilon_{ii} \\
\text{and} \qquad s_{ij} &= 2(G_1 + i G_2)\, e_{ij} = 2G^* e_{ij}
\end{aligned}\right\} \tag{46}
$$

where σ and s_{ij} are the hydrostatic tension and deviatoric stress respectively, e_{ij} is the deviatoric strain, ϵ_{ii} is the cubical dilatation and K_1, K_2, G_1, G_2 play the same role as the bulk modulus and shear modulus in elasticity. From Eq. (46) quantities analogous to E and ν can be derived, so that relations of the type

$$
\sigma_{ij} = \frac{\nu^* E^*}{(1 + \nu^*)(1 - 2\nu^*)} \epsilon_{kk} \delta_{ij} + 2G^* e_{ij} \tag{47}
$$

where

$$
\left.\begin{aligned}
\nu^* &= \nu_1(\omega^*) + i \nu_2(\omega^*) \\
E^* &= E_1(\omega^*) + i E_2(\omega^*) \\
\text{and} \qquad G^* &= G_1(\omega^*) + i G_2(\omega^*)
\end{aligned}\right\} \tag{48}
$$

can be formed. From the correspondence between the structure of Eqs. (47) and (48), and the usual Hooke's law for elastic bodies, it can be seen that transformation from elastic constants to viscoelastic constants can actually be made merely by making the substitutions

$$E \to E_1 + i E_2 = E^* ,$$

$$G \to G_1 + i G_2 = G^* ,$$

and

$$\nu \to \nu_1 + i \nu_2 = \nu^*$$

in all the relevant equations. In particular, Eq. (17) must be changed to the * form, and all subsequent equations such as Eqs. (21), (33), (34), and (35), and frequency equation, Eq. (36) will reflect this change. The frequency equation will take the form

$$MI^2R^6\omega^{*6} + I^2R^4\omega^{*4}f_4(\omega^*) + IR^2\omega^{*2}f_2(\omega^*) + f_0(\omega^*) = 0 \tag{49}$$

where f_4, f_2, and f_0 contain real geometric quantities and the complex viscoelastic constants E^*, G^*, ν^*, which are functions of the complex frequency ω^*.

In principle, Eq. (49) can be solved for its roots, by an iterative technique. It is more common to make a simplifying assumption such as (a) the damping is light, that is, $\delta \ll \omega$ and E_2 and $G_2 \ll E_1$ and G_1, respectively, or (b) E^*, G^*, and ν^* are approximately constant. In the first case it will be found that the damped natural frequencies are the same as the undamped natural frequencies, that is, $\omega = \omega_0$. Because the ω_0 are known, Eq. (49) can be used immediately to find the decay rate δ. In the second case f_0, f_2, and f_4 become complex constants, and Eq. (49) can be solved as an ordinary cubic equation.

The second approach is used in this investigation. This is justified on the basis that the most interesting design range is in the vicinity of the glass transition temperature where the energy absorption is relatively high and the rates of change of material properties are small.

From the frequency ω and the decay rate δ it will be possible to compute the loss factor $\eta = 2\delta/\omega$, the logarithmic decrement $\Delta = 2\pi\delta/\omega$, the critical damping ratio $c/c_0 = \delta/\omega$, or other common measures of the damping capacity.

The expressions for natural frequencies, decay rates, receptances, stiffness coefficients, and so forth, are too complicated for closed form evaluation. However, their numerical evaluation is relatively straightforward when using a digital computer with a complex arithmetic capability, such as the IBM 7040 used during this research, and will not be discussed further.

NUMERICAL EXAMPLES

As can be seen from Fig. 4 a shell of radius 10 in. was used with an L/R of three for most cases although values as low as L/R of 1/2 were considered for a few cases. Five cross section geometries with a radius/thickness ratio of either 25 or 50 were chosen as shown in Fig. 5. In each case the "elastic" layers are aluminum and the viscoelastic layers are made of an imaginary material, in most cases similar to Lord LD-400, a butyl rubber. Material properties are shown in Table 1. Calculation will show that these properties correspond to elastic behavior in dilatation, and viscoelastic behavior in shear. It will also be noted that all cross sections have the same total weight.

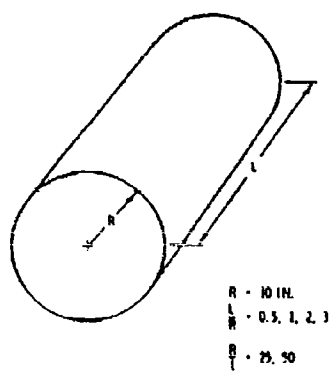

Fig. 4. Exterior geometry

The construction of each shell has been coded in the following format: Length; H, M, L, or X; cross section number (loss factor), where H, M, or L indicates the stiffness of the viscoelastic material (Table 1), X indicates the absence of a viscoelastic layer, the cross section numbers are shown in Fig. 5, and the loss factor is the loss factor of the viscoelastic layer in shear. For example, 30M3(0.1) is a three-layer sandwich shell with L = 30 in., made of a medium stiffness viscoelastic material, and with a loss factor in shear of 0.1.

Results for Axisymmetric Impulsive Load

The response to the axisymmetric impulsive load was evaluated for each of the shells

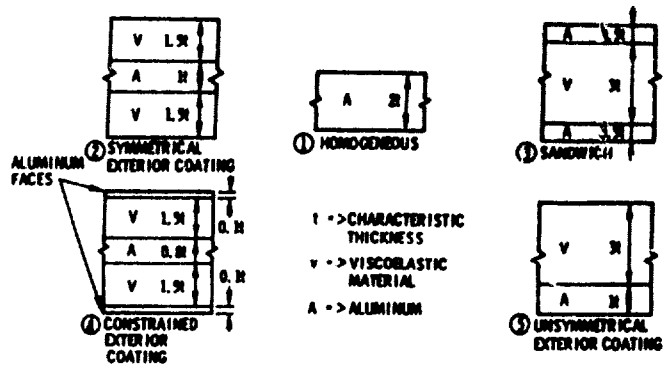

Fig. 5. Constructions

TABLE 1
Material Properties

Aluminum	
Young's modulus, E	10.6×10^6 psi
loss factor, η_1	0.001
Shear modulus, G	4.1×10^6 psi
loss factor, η_2	0.001
Poisson's ratio, $\lvert\nu\rvert$	0.30
Weight density	0.100 pci
Viscoelastic Material	
Young's modulus, E ..... (Material D)	10×10^4 psi
..... (Material M)	10×10^3 psi
..... (Material L)	10×10^2 psi
loss factor, η_1	0.536, 0.437, 0.240, 0.083, 0.001
Shear modulus, G ..... (Material H)	4×10^4 psi
..... (Material M)	4×10^3 psi
..... (Material L)	4×10^2 psi
loss factor, η_2	1.00, 0.6, 0.3, 0.1, 0.001
Poisson's ratio, $\lvert\nu\rvert$	0.29
Weight density	0.0333 pci

at two times — one-fourth and ten times the period of the fundamental mode which in this case is always the $m = 1$ mode. From Figs. 6 and 7 it can be seen that the shells with stiffer viscoelastic layers (H shells) and the shorter shell (5M3) are affected by the viscoelastic damping more than are the softer or longer shells. However, the reductions in peak response are so small that an all-aluminum shell (X1) of the same cross section weight has a smaller response at $t = T/4$ than any of the layer shells. But, at a later time, $t = 10T$ the viscoelastic layered shells have considerably smaller responses than the aluminum shell.

This confirms the usual supposition that damping is of little importance in changing the peak response to single impulsive load. However,

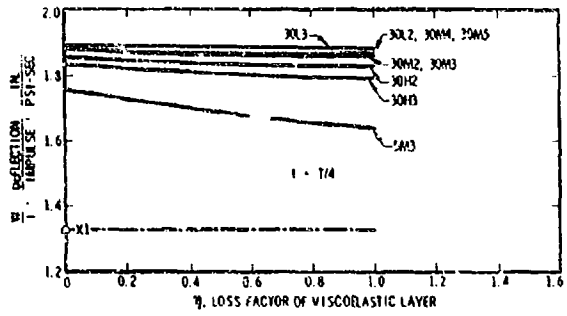

Fig. 6. Impulsive response at t = 1/4 period

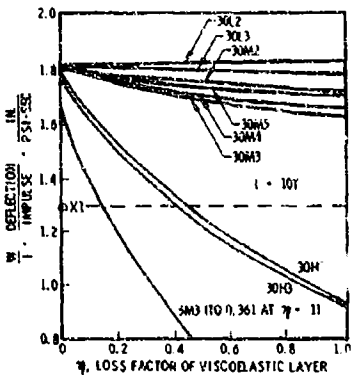

Fig. 7. Impulsive response at t = 10 periods

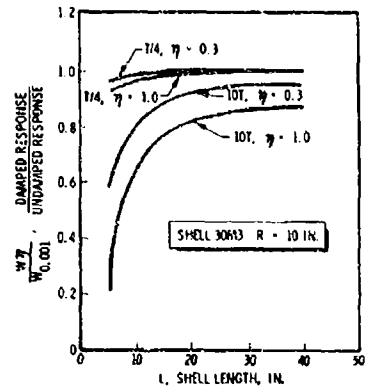

Fig. 8. Damping effectiveness for an impulsive load

the significant decrease in response at t = 10T suggests that viscoelastic damping might be considered for increasing fatigue life or lessening the response to a series of shocks.

The damping effectiveness for different length shells is shown in Fig. 8. The large increase in damping effectiveness with shorter lengths is primarily a result of the greater amounts of bending (and shearing) associated with these lengths. It will be noticed in the following discussion of the other loads that the ratio of bending energy to stretching energy, in each mode, is of great importance in determining the damping effectiveness in those other situations, too.

It can be seen from the curves for 30H2 and 30H3 that somewhat greater effectiveness can be gotten even in those modes that are predominantly stretching by using stiffer viscoelastic materials, even if they have lower loss factors than the softer materials.

Results for Axisymmetric Harmonic Load

The admittance for an axisymmetric harmonic load on the all-aluminum (30 x 1) shell is shown in Fig. 9. The most striking feature is the enormous magnification in response at the natural frequencies. This is also true for the three-layer sandwich shell (30M3) shown in Fig. 10. However, as can be seen from the curves for 30M3 (1.0) on Figs. 10 and 11 and from the curve for 30M3 (0.1), Fig. 12, these peaks can be lessened or eliminated by the addition of damping. This is also true for the externally coated shell (30M2) and the five-layer sandwich (30M4) as is shown in Fig. 13. As a result both the peak response and the response to a broadband (or random) load are decreased to below the response for the aluminum shell (30 x 1). Because broadband loads are difficult to avoid and although it is generally unnecessary to operate a system at a natural frequency, the results shown in Fig. 14 are more

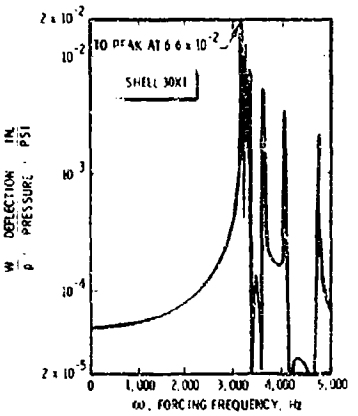

Fig. 9. Admittance for axisymmetric load, homogeneous shell

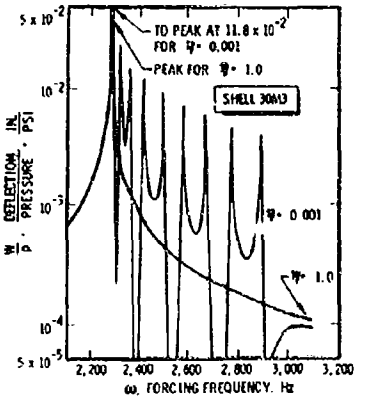

Fig. 11. Admittance for axisymmetric harmonic load, 2100-3100 Hz

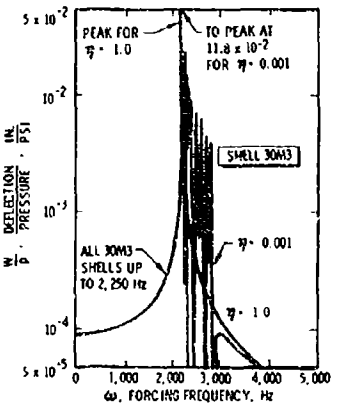

Fig. 10. Admittance for axisymmetric harmonic load, 0-5000 Hz

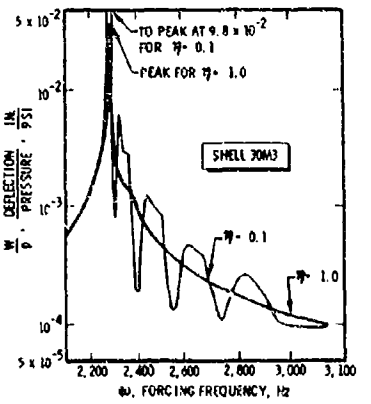

Fig. 12. Admittance for axisymmetric harmonic load, 2100-3100 Hz

significant indicators of damping effectiveness than a comparison of peak admittances would give.

The higher response of the internally damped constructions (30M3, 30M4) compared with the externally damped constructions (30M2, 30M5) is apparently a result of shear deflection.

Results for Nonsymmetric Harmonic Load

The higher damping associated with modes in which bending predominates, is shown clearly in Fig. 15, in which the ratio of damping to critical damping c/c_0 is stated for each of the modes shown. Because the lowest frequency belongs to a mode for which bending predominates, the addition of viscoelastic layers is particularly effective over the frequency range investigated, 0-500 Hz, as is shown in Figs. 16 and 17.

CONCLUSIONS

The investigation of the dynamic response of viscoelastically damped shells led to the following conclusions:

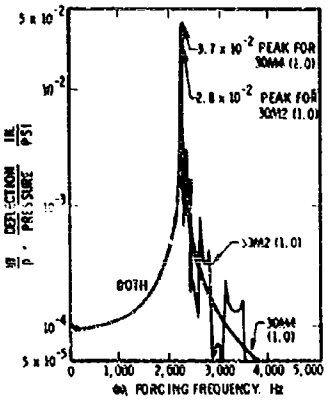

Fig. 13. Admittance for axisymmetric load, shells 30M2 and 30M4

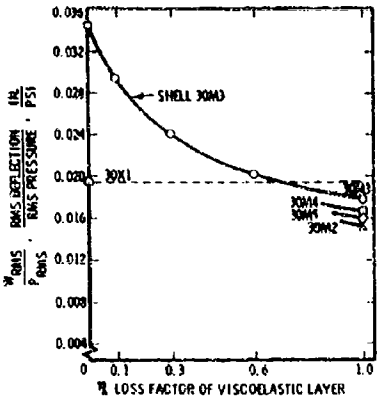

Fig. 14. Admittance for broadband axisymmetric load

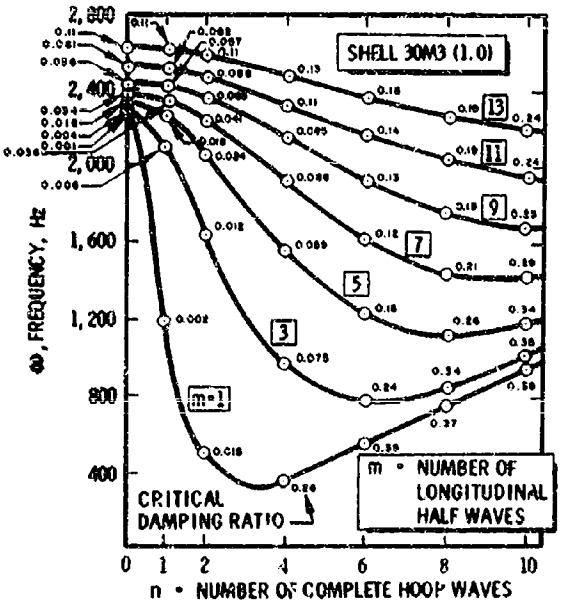

Fig. 15. Frequencies and damping ratios, shell 30M3 (1.0)

1. The dynamic response of viscoelastically damped shells to periodic or transient loading can be found by solving an associated elastic problem and transforming the solution by the substitution of complex viscoelastic constants.

2. The transverse shear deflections can be taken into account for a general multilayered cross section by summing to find the appropriate correction factor as in a Timoshenko beam formulation.

3. Complete correspondence between the viscoelastic shell and an associated elastic shell will usually exist only for shells with sinusoidal mode shapes. A useful degree of correspondence will exist for almost all shells.

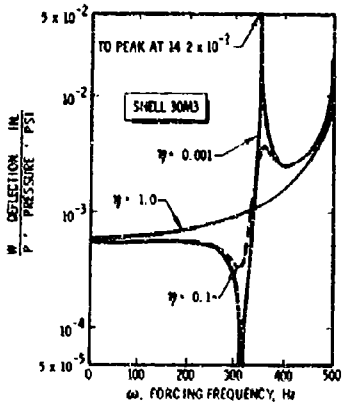

Fig. 16. Admittance for nonsymmetric harmonic load

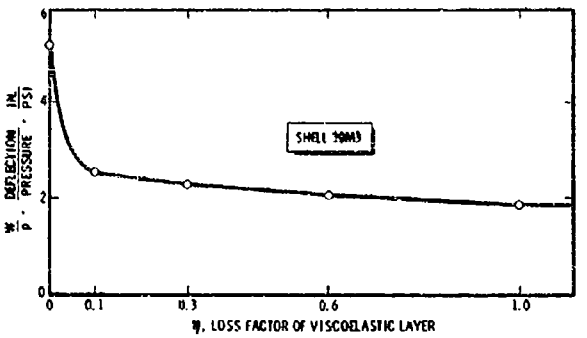

Fig. 17. Admittance for broadband nonsymmetric load

4. Numerical evaluation of the shell response is straightforward using a computer with a complex arithmetic capability.

5. The addition of viscoelastic layers will produce only small damping in modes that are predominantly extensional, but can produce significant damping in predominantly bending modes.

6. Even large amounts of damping are ineffective in reducing the peak response to an impulsive load. Ringing at later times may be significantly reduced however.

7. The addition of viscoelastic layers produces a significant reduction in response to broadband and near-resonant harmonic loads.

8. A valid comparison of the peak response of various systems to transient loads can be made by comparing the root-mean-square values of the different responses.

9. Constrained and unconstrained layer treatments show about the same effectiveness.

ACKNOWLEDGMENTS

The author wishes to extend his thanks to the Douglas Aircraft Co. for support of this work under their Corporate Scholarship Program. In addition, the College of Engineering of the Virginia Polytechnic Institute is thanked for their support of the necessary computer operations.

Special thanks are given to Dr. Daniel Frederick for his encouragement during this investigation.

REFERENCES

1. J. L. Baylor, "A Theory of Anisotropic Viscoelastic Sandwich Shells," NASA Contractor Rept., CR-396, Mar. 1966

2. W. J. Oberndorfer, "Equations for Thermoelastic and Viscoelastic Cylindrical Sandwich Shells," NASA Contractor Rept., CR-645, Nov. 1966

3. L. A. Scipio and J. A. Moses, "Viscoelastic Behavior of Shells Under Combined Load Conditions," in Proc., 4th Natl. Congress of Appl. Mech., 2:1087-1102, 1962

4. L. Librescu, "Dynamic Problem of Shallow Viscoelastic Shells," Studii si Cercetari de Mecanica Applicata, 13(1):137-14' Jan. 1962

5. E. I. Grigolyuk, "Dynamics of Viscoelastic Shells and Plates," from Doklady Akad. Nauk SSR, 138 (6):1317-1320, 1961, translated as NASA TT-F-8058, N66-27036

6. M. A. Biot, "Variational and Lagrangian Methods in Viscoelasticity," in Deformation and Flow of Solids (R. Grammel, Ed.) (Springer-Verlag, Berlin), 1956, pp. 251-263

7. M. P. Bieniek and A. M. Freudenthal, "Forced Vibrations of Cylindrical Sandwich Shells," J. Aero. Sci., 29(2):180-206, Feb. 1962

8. Y.-Y. Yu, "Viscoelastic Damping of Vibrations of Sandwich Plates and Shells," in Non-Classical Shell Problems (W. Olszak and A. Sawczuk, Eds.) (North-Holland Publishing Co., Amsterdam), 1964, pp. 551-571

9. W. B. Haile, "A Study of Linearly Viscoelastic Anisotropic Shell Structures," Ph.D. Dissertation, V. P. I., June 1967

10. I. W. Jones and V. L. Salerno, "The Effect of Structural Damping on the Forced Vibrations of Cylindrical Shells," Paper No. 65-WA/UNT-1, Am. Soc. Mech. Engrs., New York, 1965

11. G. M. C. Fisher and M. J. Leitman, "A Correspondence Principle for Free Vibrations of a Viscoelastic Solid," J. Appl. Mech., ASME Trans. Ser. E., 88:924-926 (Dec. 1966)

12. Lord Rayleigh, "Theory of Sound," 1 (Dover Publications, New York), 1945

13. T. K. Caughey and M. E. J. O'Kelley, "Classical Normal Modes in Damped Linear Dynamic Systems," J. Appl. Mech., Trans. ASME Ser. E, 87:583-588 (Sept. 1965)

14. T. K. Caughey, "Classical Normal Modes in Damped Linear Systems," J. Appl. Mech., Trans. ASME Ser. E, 82:269-271 (June 1960)

15. P. Hertelendy and W. Goldsmith, "Flexural Vibrations of an Elastic Plate with Two Symmetric Viscoelastic Coatings," J. Appl. Mech., ASME Trans. Ser. E, 87(1):187-194, Mar. 1967

16. M. A. Biot and F. V. Pohle, "Validity of Thin-Plate Theory in Dynamic Viscoelasticity," J. Am. Acoust. Soc., 36(6):1110-1117 (June 1964)

17. R. A. DiTaranto and W. Blasingame, "Composite Damping of Vibrating Sandwich Beams," Paper No. 67 - Vibr-6, Vibrations Conf., Boston, Mass., Mar. 29-31, 1967, American

18. R. A. DiTaranto and W. Blasingame, "Effect of End Constraints on the Damping of Laminated Beams," J. Am. Acoust. Soc., 39(2):405-407 (Feb. 1966)

19. J. E. Ruzicka et al., "Damping of Structural Composites with Viscoelastic Shear-Damping Mechanisms," NASA Contractor Rept., CR-742, Mar. 1967

20. I. W. Jones, V. L. Salerno, and A. Savacchio, "An Analytical and Experimental Evaluation of the Damping Capacity of Sandwich Beams with Viscoelastic Cores," Paper No. 66 - WA/UNT-3, Am. Soc. Mech. Engrs., New York, 1966

21. G. R. Cowper, "The Shear Coefficient in Timoshenko's Beam Theory," J. Appl. Mech., Paper No. 66-APM-C, Am. Soc. Mech. Engrs., New York, 1966, in press

DISCUSSION

Y. K. Liu (Univ. of Mich.): I am curious about the dynamic correspondence principle. Could you briefly summarize why it is valid?

Mr. Fitzgerald: The general correspondence principle is given by Biot. Essentially, it says that under certain conditions the viscoelastic response is either the Fourier transform or the Laplace transform of the response of an associated elastic problem. The time can be transformed out of the problem under certain conditions and, if that is true, then the stresses and displacements will be the same, both in the elastic and in the viscoelastic problem. In the case of harmonic motion the transform is trivial because it turns out it would just be necessary to substitute the complex modulus for the real modulus.

* * *

DAMPING OF MULTISPAN STRUCTURES BY MEANS OF VISCOELASTIC LINKS

David I. G. Jones
Air Force Materials Laboratory
Wright-Patterson Air Force Base, Ohio

In this paper, a normal mode analysis is presented for the response of a typical multispan skin stringer structure having viscoelastic links connecting points on the skin to points on beams joining the frames. It is shown that certain conditions arise for which no damping is introduced into the structure and others for which relatively high damping occurs. An example is given.

INTRODUCTION

Many structures that are subject to vibrational problems contain within them elements that are parallel or nearly so. Examples are: (a) Commercial aircraft fuselage, where the trim in the passenger area is essentially parallel to the outer skin and is separated from it by the frames, and (b) control surface and wing structures, where the upper and lower skins are separated by bulkheads. In such structures the vibrational characteristics of the parallel elements are often different and the proper use of viscoelastic links joining antinodal points of the parallel surfaces can lead to introduction of significant amounts of damping into the structure at the expense of very little added weight.

In this paper, a normal mode analysis is developed for the response of a typical multispan skin stringer structure having the frames joined across each bay by beams and with each beam joined to the skin by a viscoelastic link. This idealized representation of what might be done in a real structure is examined with reference to a specific example, and it is shown that a significant reduction of the response level can be achieved by proper choice of link and beam stiffness, provided that a natural frequency of a beam is not identical to (or close to) any natural frequency of the structure. In this case, it is shown that no damping can be achieved and that an optimum value of the link stiffness exists for which the response is a minimum.

NOMENCLATURE

- A See Eq. (17)
- A_n See Eq. (16)
- B See Eq. (18)
- D $Eh^3/12\,(1-\nu^2)$; flexural rigidity of skin
- E Young's modulus of skin material
- E_b Young's modulus of beam material
- f_m mth normal mode of beam
- F_j Force transmitted to skin by link at location (x_j, y_j)
- h Thickness of skin
- i $\sqrt{-1}$
- I_b Second moment of area of beam cross section
- j Number of spans of structure
- J Total number of spans
- k Stiffness of link
- ℓ Breadth of structure between frames
- L Length of each span between stringers

m Mode number for beam

n Mode number of structure

N Total number of modes in first band

$P(x,y)$ Amplitude of loading on skin

Q Amplification factor

S See Eq. (11)

t Time

$W_b(y)$ Amplitude of transverse displacement of beam

$W(x,y)$ Amplitude of transverse displacement of skin

x Station on skin parallel to frame

x_j Station of link in jth span

y Station on skin normal to frame

y_j Station of link in jth span

α_m See Eq. (5)

β_m See Eq. (6)

Γ Link stiffness parameter

δ Dirac delta function

η Loss factor of link

λ Ratio of beam fundamental frequency to structure fundamental frequency

μ_b Linear density of beam (mass per unit length)

ν Poisson's ratio of skin material

ξ $(\rho\omega^2 L^4/D)^{1/4}$ — frequency parameter

ξ_n $(\rho\omega_n^2 L^4/D)^{1/4}$

ξ_{bm} $(\mu_b \omega_{mb}^2 \ell^4/E_b I_b)^{1/4}$

ξ_b $(\mu_b \omega^2 \ell^4/E_b I_b)^{1/4}$

ρ Density of skin material

ϕ $\mu_b \ell/\rho \ell L$ — mass parameter

ϕ_n nth normal mode of undamped structure

χ See Eq. (19)

ω Circular frequency

ω_1 Fundamental frequency of structure

ω_{1b} Fundamental frequency of beam

ω_n nth natural frequency of undamped structure

∇^4 Biharmonic operator

ANALYSIS

Consider a multispan skin stringer structure of the type illustrated in Fig. 1. One of the simplest possible means of introducing viscoelastic link damping into the system is by joining the frames across the center of each panel by identical clamped-clamped beams. The centers of each beam are then joined to the skin by identical links as in Fig. 1.

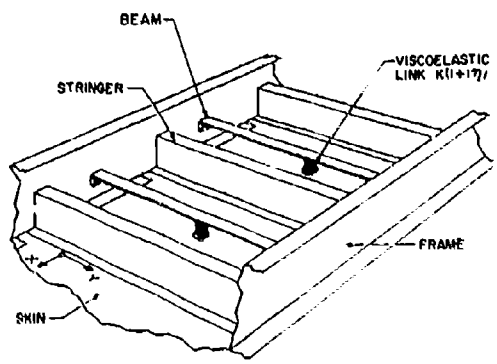

Fig. 1. Typical structure geometry

Equation of Motion of the Beam

Consider the jth beam, crossing the jth span of the structure. Let $W_b(y)\exp(i\omega t)$ be the transverse displacement of the beam. Let the link be at the point (x_j, y_j), and let $W(x,y)\exp(i\omega t)$ be the transverse displacement of the skin. Then the equation of motion of the beam is

$$E_b I_b (d^4 W_b/dy^4) - \mu_b \omega^2 W_b = -k(1+i\eta)(W_b - W)\,\delta(y_j - y) . \qquad (1)$$

We now expand the response of the beam as a series of beam normal modes $f_m(y/\ell)$, which satisfy the homogeneous equation:

$$\frac{d^4 f_m}{dy^4} - \frac{\xi_{bm}^4}{\ell^4} f_m = 0 \qquad (2)$$

where the ξ_{bm} are the eigenvalues of a clamped-clamped beam [1]. Putting Eq. (2) into Eq. (1), solving in the usual manner and neglecting all terms apart from the fundamental, we get

$$W_b = \frac{(k\ell^3/E_bI_b)(1+i\eta)\,\beta_1 W(x_j,y_j)\, f_1(y_j/\ell)}{\xi_{b_1}^4 - \xi_b^4 + (k\ell^3/E_bI_b)(1+i\eta)\,\alpha_1} \qquad (3)$$

where

$$\xi_{b_1}^4 = \mu_b\,\omega_{b_1}^2\,\ell^4/E_bI_b \qquad (4)$$

$$\alpha_m = f_m^2(y_j/\ell)\Big/\int_0^1 f_m^2(y/\ell)\,d(y/\ell) \qquad (5)$$

and

$$\beta_m = f_m(y_j/\ell)\Big/\int_0^1 f_m^2(y/\ell)\,d(y/\ell)\,. \qquad (6)$$

For the particular case of a clamped-clamped beam with $y_j/\ell = 0.5$, $f_1(1/2) = 1$,

$$\int_0^1 f_1^2(y/\ell)\,d(y/\ell) = 0.397$$

so that $\alpha_1 = \beta_1 = 2.519$ and $\xi_{b_1}^4 = 500$ [1]. The reason for retaining only the first term in the series for W_b is that we shall generally be confining attention to the case when the higher beam modes have frequencies well above those of primary interest with respect to the response of the main panel system. The higher order terms can always be retained if the need arises, but the term ξ_{bm}^4 in the denominator will insure their irrelevance to the present analysis.

Force Transmitted to Skin of Structure

The force F_j transmitted back to the skin at the point (x_j, y_j) by the link is

$$F_j = k(1+i\eta)\,[W(x_j,y_j) - W_b(x_j,y_j)]$$

$$= \frac{k(1+i\eta)(\xi_{b_1}^4 - \xi_b^4)\,W(x_j,y_j)}{\xi_{b_1}^4 - \xi_b^4 + (k\ell^3/E_bI_b)(1+i\eta)\,\alpha_1} \qquad (7)$$

after some simplification. It is convenient at this point to introduce some of the nondimensional parameters that govern the response of the total system. Let $\lambda = \omega_{1b}/\omega_1$ be the ratio of the beam fundamental frequency to the undamped structure fundamental frequency. Let $\phi = \mu b\ell/\rho L$ be the ratio of the mass of a beam to the mass of a panel. Let $\xi_1 = (\rho\omega_1^2L^4/D)^{1/4}$ be the first eigenvalue of the undamped skin stringer panel system and let $\Gamma = kL^3/\ell D$ be a measure of the ratio of the link stiffness to the structure stiffness. Then, after some rearrangement, F_j can be written

$$F_j = \frac{k(1+i\eta)[1-(\xi/\xi_1)^4/\lambda]\,W(x_j,y_j)}{1-(\xi/\xi_1)^4/\lambda^2 + (\alpha_1\Gamma/\phi\lambda^2\xi_1^3)(1+i\eta)}\,. \qquad (8)$$

A number of interesting facts may be noted directly from an examination of Eq. (8). F_j represents both the damping and stiffening effects of the link. It is seen that $F_j = 0$ whenever $\xi^4 - \xi^4/\lambda^2 = 0$. If, at the same time $\xi = \xi_n$, where n is the nth mode of the structure, we see that this implies $\omega_{1b} = \omega_n$, that is, the beam fundamental frequency is equal to the nth natural frequency of the structure. Whenever this is the case, the links have no effect whatsoever and no damping is introduced at all. Graphs of the amplification factor of the system against the parameter λ will therefore have singularities at these points. Equation (8) also shows that the maximum value of F_j is

$$(F_j)_{max} = \frac{-k(1+\eta^2)\,W(x_j,y_j)}{i\eta}\,. \qquad (9)$$

Equation of Motion of the Structure

The equation of motion of the structure with allowance made for the isolated loads F_j may be written

$$D\nabla^4 W - \mu\omega^2 W + S\sum_{j=1}^{J} W(x_j,y_j)\,\delta(x-x_j)\,\delta(y-y_j) = P(x,y) \qquad (10)$$

where

$$S = \frac{k(1+i\eta)[1-(\xi/\xi_1)^4/\lambda^2]}{1-(\xi/\xi_1)^4/\lambda^2 + (\alpha_1\Gamma/\phi\lambda^2\xi_1^4)(1+i\eta)}\,. \qquad (11)$$

An approximate solution to Eq. (10) has already been derived [2] for the case where the points (x_j, y_j) are located at the centers of the panels. This solution is

$$W = \sum_{n=1}^{N} \frac{(P_nL^4/D)\,\phi_n(x/L, y/\ell)}{\xi_n^4 - \xi^4 - SL^3A_n/\ell D} \qquad (12)$$

where ϕ_n is the nth mode of the undamped structure, ξ_n is the nth eigenvalue of the undamped structure, and

$$P_n = \frac{\int_0^J \int_0^1 P(x,y)\,\phi_n(x/L, y/\ell)\,d(x/L)\,d(y/\ell)}{\int_0^J \int_0^1 \phi_n^2(x/L, y/\ell)\,d(x/L)\,d(y/\ell)} \quad (13)$$

$$A_n = \frac{\sum_{j=1}^{J} \phi_n^2(x_j/L, y_j/\ell)}{\int_0^J \int_0^1 \phi_n^2(x/L, y/\ell)\,d(x/L)\,d(y/\ell)} \quad . \quad (14)$$

Finally,

$$\frac{DW}{L^4} = \sum_{n=1}^{N} \frac{P_n \phi_n(x/L, y/\ell)\,\exp(i\omega t)}{\xi_n^4 - \xi^4 + \dfrac{\Gamma A_n(1+i\eta)(\xi_1^4 - \xi^4/\lambda^2)}{\xi_1^4 - \xi^4/\lambda^2 + (\Gamma a_1/\phi\lambda^2)(1+i\eta)}} \quad (15)$$

$$\frac{DW}{L^4} = \sum_{n=1}^{N} \frac{P_n \phi_n(x/L, y/\ell)\,\exp(i\omega t)}{\xi_n^4 - \xi^4 + A_n(A + iB)} \quad (16)$$

where

$$\frac{A}{\Gamma} = \frac{\chi(\chi + 1 + \eta^2)}{(\chi+1)^2 + \eta^2} \quad (17)$$

$$\frac{B}{\eta\Gamma} = \frac{\chi^2}{(\chi+1)^2 + \eta^2} \quad (18)$$

and

$$\chi = \frac{\xi_1^4 - \xi^4/\lambda^2}{\Gamma a_1/\phi\lambda^2} \quad . \quad (19)$$

Typical graphs of A/Γ and $B/\Gamma\eta$ against χ are shown in Figs. 2 and 3. The solution of Eq. (16) is straightforward. For a given structure, with known modes, and for given excitation P, the P_n and the A_n are calculated. For each value of ξ^2, within the frequency range of interest, χ is calculated and A and B derived from Eqs. (17) and (18). The eigenvalues ξ_n of a typical skin stringer structure usually fall within an octave band of frequency or less. The fundamental mode ϕ_1, with frequency ω_1, is often known as the stringer torsion mode and forms the lower bound of the band. The number of modes N is usually equal to the number of spans J and the Jth mode, with frequency ω_J,

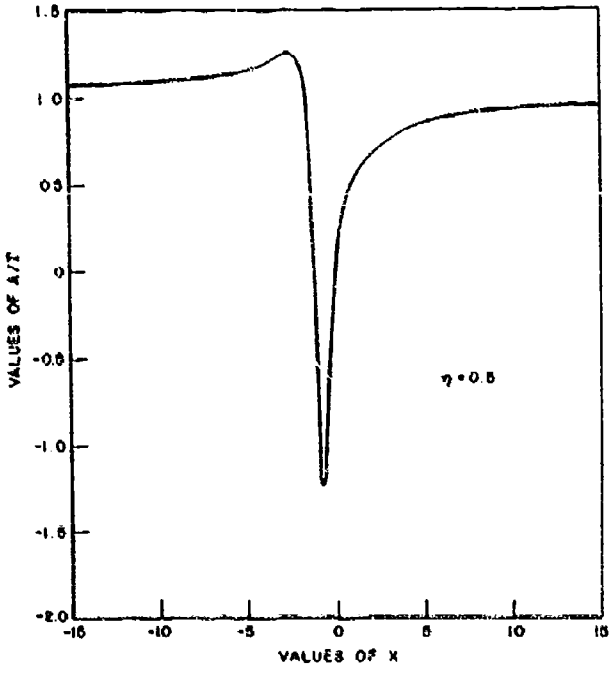

Fig. 2. Graph of A/Γ against χ

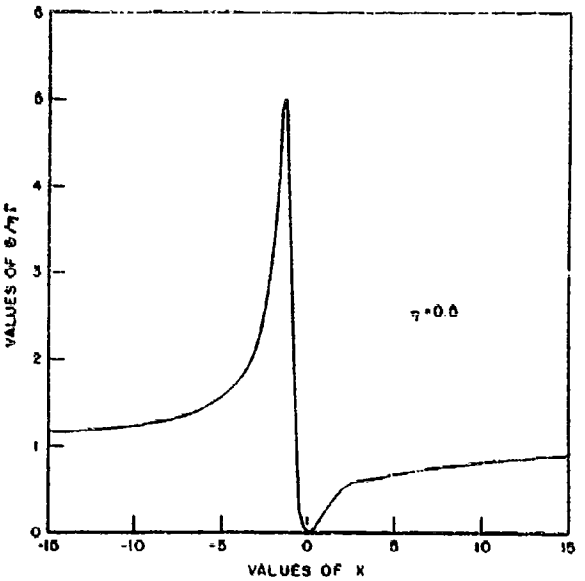

Fig. 3. Graph of $\Phi/\eta\Gamma$ against λ

forming the upper bound is often referred to as the stringer bending mode. The second modal frequency ω_{b2} of the beam must lie well above ω_J for the present analysis to be valid. Otherwise, terms involving ξ_{b2}^2, and so forth, must be added into Eq. (16). This is not difficult but makes the equation far more cumbersome. Therefore this particular matter will not be pursued further.

EXAMPLE

To demonstrate the damping that can be achieved by means of viscoelastic links in multispan structures, it is convenient to consider as simple a case as possible. It is particularly convenient to consider an example which has already been examined [2,3] from a somewhat different point of view. Consider a five-span supported structure in which the length, L, is not greater than $\ell/2$. Then the normal modes of a multisupported beam may be used to represent those of the structure with some accuracy [2]. Let the excitation be a uniform loading, P. Then $\xi_1^4 = \pi^4$, $\xi_3^4 = 187.4$, $\xi_5^4 = 428.6$, $a = 2.519$, $\phi_1 = 1$ at the center of the center span, $P_1/P = (4/\pi)(+0.255)$, $P_2/P = 0$, $P_3/P = (4/\pi)(-0.618)$, $P_4/P = 0$, $P_5/P = (4/\pi)(+1.647)$, $A_1 = 4.000$, $A_3 = 4.13$, $A_5 = 4.79$. We further let $\eta = 0.5$ and $\phi = 0.1$. Then the expression of Eq. (16) can be simplified to

$$\frac{\pi DW}{4PL^4} = \frac{0.255[(\pi^4 - \xi^4 + 4A) - 4iB]}{(\pi^4 - \xi^4 + 4A)^2 + 16B^2} - \frac{0.618[(187.4 - \xi^4 + 4.13A) - 4.13iB]}{(187.4 - \xi^4 + 4.13A)^2 + (4.13B)^2} + \frac{1.647[(428.6 - \xi^4 + 4.79A) - 4.79iB]}{(428.6 - \xi^4 + 4.79A)^2 + (4.79B)^2} \quad (20)$$

which may be evaluated numerically for given λ and Γ over a range of values of the frequency parameter ξ^2. Typical graphs of $\pi D|W|/4PL^4$ against ξ^2 are shown in Figs. 4 to 8.

It is seen from these figures that for each λ a definite value of Γ exists for which the output level is minimized. If we let Q_{min} be the minimum value of the peak amplification factor as Γ is varied, a very gross measure of the amount of damping introduced may be obtained by plotting $1/Q_{min}$ against λ as in Fig. 9. It is seen that high damping can be achieved if $\lambda > 6$ and that very little damping can be achieved for $\lambda < 2.1$ in this example. More generally, it would appear that the beam fundamental frequency must be greater than that of the stringer bending mode or less than that of the stringer torsion mode for significant amplitude reductions to be attainable.

CONCLUSIONS

Analysis has been developed for predicting the response of multispan structures with

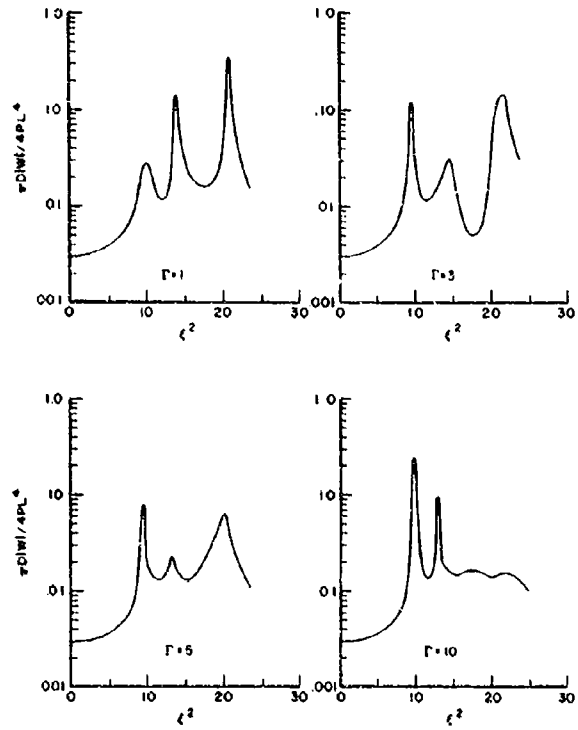

Fig. 4. Typical graphs of $\pi D|W|/4PL^4$ against ξ^2 for $\lambda = 0.8$

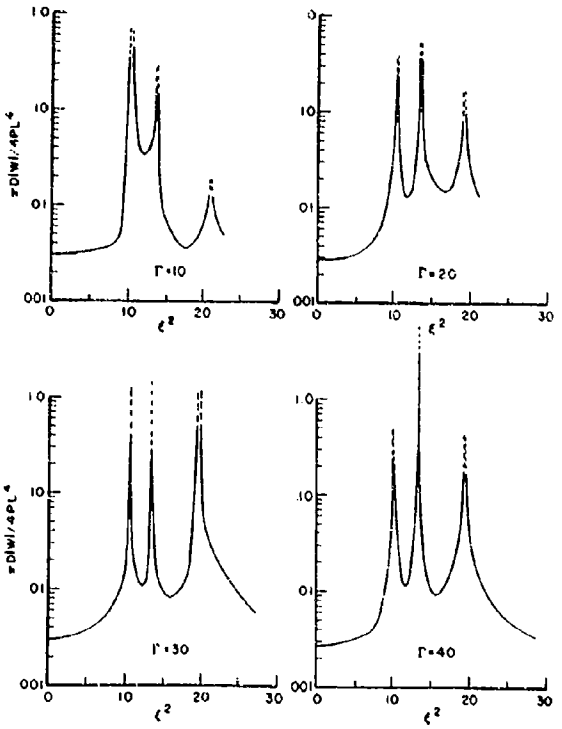

Fig. 5. Typical graphs of $\pi D|W|/4PL^4$ against ξ^2 for $\lambda = 1.2$

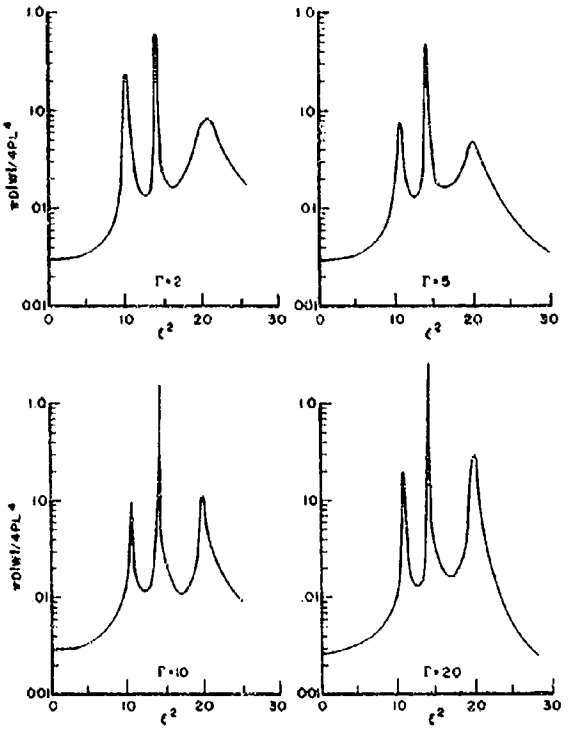

Fig. 6. Typical graphs of $\pi D|W|/4PL^4$ against ζ^2 for $\lambda = 1.7$

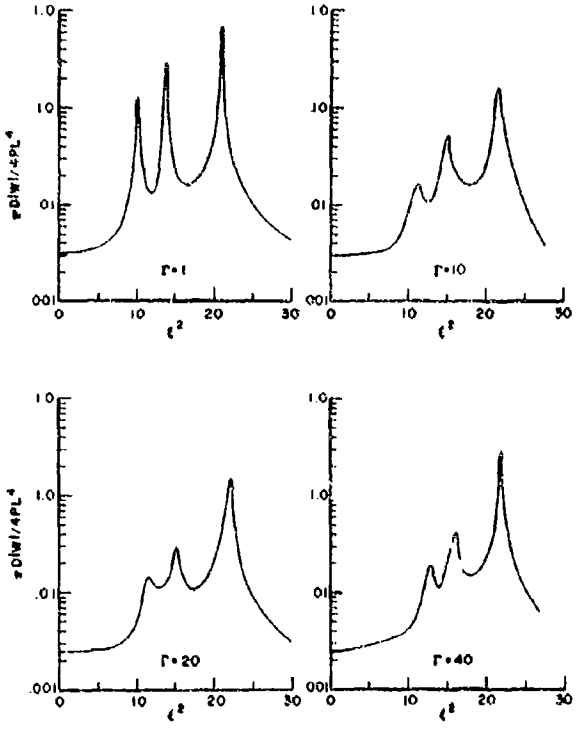

Fig. 7. Typical graphs of $\pi D|W|/4PL^4$ against ξ^2 for $\lambda = 3$

viscoelastic link damping to harmonic loading. It has been shown by means of an example that significant amounts of damping can be introduced into the structures by proper choice of link stiffness.

ACKNOWLEDGMENTS

Thanks are given to W. J. Trapp, Chief, Strength and Dynamics Branch, for his support; T. Raab for assistance with the computations; and Connie Gillmore for preparation of the manuscript. The work described in this paper was carried out under Project No. 7351, "Metallic Materials," Task No. 735106, "Behavior of Metals." This paper may be reproduced for purposes of the U.S. Government.

REFERENCES

1. R. E. D. Bishop and D. C. Johnson, The Mechanics of Vibration (Cambridge Univ. Press), 1960

2. D. I. G. Jones, "Effect of Isolated Tuned Dampers on Response of Multispan Structures," J. Aircraft, 4(4):343-346 (July-Aug. 1967)

3. D. I. G. Jones and G. H. Bruns, "Effect of Tuned Viscoelastic Dampers on Response of Multispan Structures," 36th Shock and Vibration Bull., Part 4, NRL, Washington, D.C., 49-64, 1967

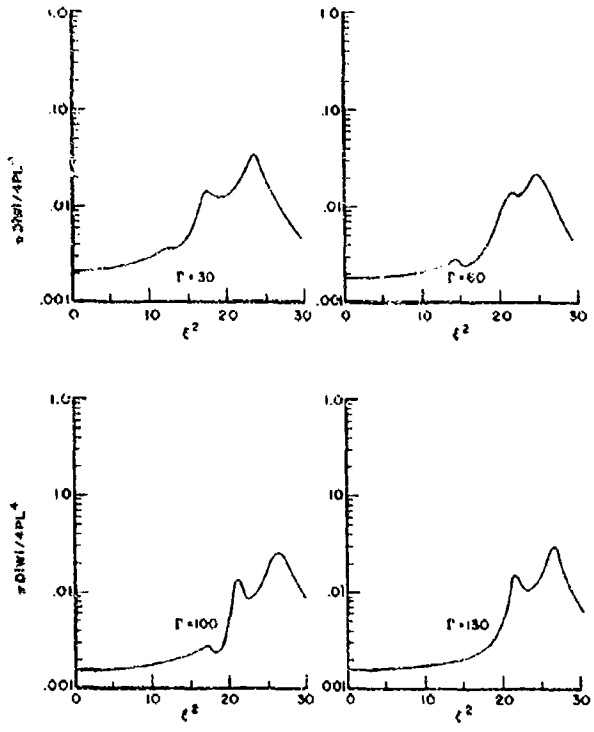

Fig. 8. Typical graphs of $\pi D|W|/4PL^4$ against ξ^2 for $\lambda = 6$

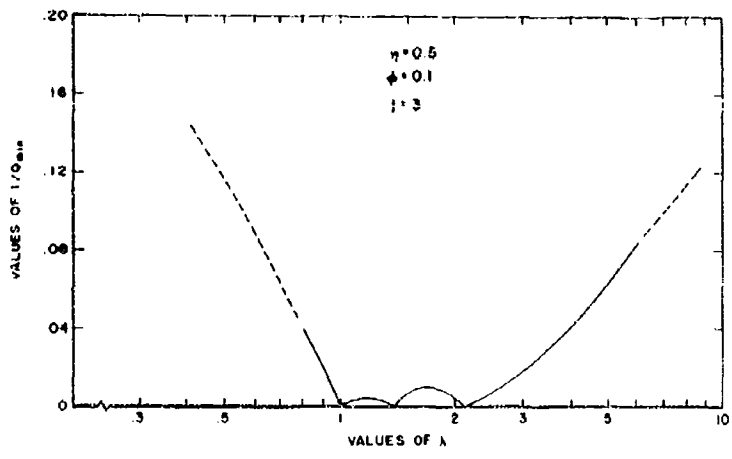

Fig. 9. Typical graph of $1/Q_{min}$ against λ

DISCUSSION

K. McConnell (Iowa State Univ.): It was not clear to me whether the modes were for the plate or for the beam.

Dr. Jones: The modes we assumed in this particular example were for the plate. We assumed an aspect ratio greater than two. I think quite a few previous investigations have shown that where the stringers are of very low stiffness in torsion, one can approximate the modes by this case. Of course this was purely an illustration and,for any particular problem, one must take the appropriate modes. It would be a good deal more than three modes.

Mr. McConnell: What modes did you assume for the beam then?

Dr. Jones: The standard ones that are available in Bishop and Johnson, for example. We assumed a clamped-clamped beam for which Bishop and Johnson have a whole catalog of mode shapes.

Mr. McConnell: Well, did you assume for the beam the first, second, third, fourth?

Dr. Jones: No, I forgot to make this point. In the analysis, we assumed that the second mode of the beam was irrelevant because the link was at the center in this particular example. One would have to consider it in a more general case. The third mode is approximately six times as high in frequency as the first. Therefore, in this particular problem it was outside the frequency range of interest. In general, of course, it has to be incorporated.

Mr. McConnell: So you used just the first mode.

Dr. Jones: In this particular examples, yes.

* * *

DAMPING MEASUREMENTS ON SOFT VISCOELASTIC MATERIALS USING A TUNED DAMPER TECHNIQUE

C. M. Cannon and A. D. Nashif
University of Dayton
Dayton, Ohio

and

D. I. G. Jones
Air Force Materials Laboratory
Wright-Patterson Air Force Base, Ohio

A variation of the classical resonance technique for measuring the damping properties of soft viscoelastic materials in tension-compression is described. It is shown that, from the measured amplification factor at resonance and the resonant frequency, the Young's modulus and loss factor of a material are easily derived. An error analysis was also performed to show the effects of measuring errors on the computed properties. This analysis shows that measuring errors in the amplification factor and resonant frequency do not have large effects on the computed properties. It is also shown that the error in the loss factor calculated from measured phase angles, owing to errors in phase measurement, becomes significant at and below the natural frequency of the system.

To demonstrate the effectiveness of this technique, a relatively stiff elastomer was selected so that reliable test results could be obtained by both this technique and the Brüel and Kjaer apparatus. Good agreement is demonstrated. It is concluded that the resonance technique is capable of measuring the damping properties of very soft viscoelastic materials (Young's modulus less than 1000 lb/in.^{2}) and is complementary to the Brüel and Kjaer technique (Young's modulus greater than 1000 lb/in.^{2}).

The effects of specimen geometry on the measured elastic modulus are also investigated and described.

INTRODUCTION

Many techniques have been used to determine the complex stiffness characteristics of viscoelastic materials. Each technique has its own particular advantages and disadvantages. For example, the well-known Brüel and Kjaer cantilever beam technique [1] can be used to measure accurately the complex Young's modulus of stiff viscoelastic materials only (usually $E \geq 10^3$ lb/in^2), resulting primarily from a serious effect of errors in measurement on the calculated results for soft materials. For stiff materials, the effect of these errors on the calculated results is small. The Fitzgerald technique is useful for low frequencies only. Several currently used techniques [2] depend on phase-angle measurements in a fixed-mass/viscoelastic-link system. These techniques suffer from the necessity of obtaining phase measurements of the required accuracy, which is generally difficult to achieve without sophisticated instrumentation. If, however, one is prepared to accept the slight inconvenience of making a variable-mass/viscoelastic-link system and repeating forced vibration tests for several masses so as to cover a wide range of resonant frequencies, the need for phase measurement is completely eliminated.

The present paper describes such a technique in which cylindrical specimens of a soft viscoelastic material are joined on one flat surface to a variable mass and on the other to a vibrating shaker table.

NOMENCLATURE

A	Amplification factor at resonance
b	Width of cantilever specimen in B & K technique
$d\eta$	Difference between measured and actual loss factor
$d\phi$	Difference between measured and actual phase angle
d	Diameter of cylindrical specimen
E	Real part of Young's modulus of viscoelastic material (lb/in.^{2})
f	Frequency (Hz)
h_{Al}	Thickness of aluminum beam in B & K technique (in.)
h_{BJ}	Thickness of one Paracril-BJ layer in B & K technique
L	Length of cantilever specimen in B & K technique
M	Tuning mass (slugs)
r	Radius of cylindrical specimen
S	Area of material cross section (in.^{2})
t	Time (sec)
X	Amplitude of shaker table displacement (in.)
$\ddot{X}$	Amplitude of shaker table acceleration (g's)
y	Response of mass M (in.)
$\ddot{Y}$	Amplitude of acceleration of mass M (g's)
ϵ_1	Strain in 1-direction
ϵ_2	Strain in 2-direction
ϵ_3	Strain in 3-direction
η	Loss factor of viscoelastic material
ν	Poisson's ratio
ξ	Frequency parameter
ρ_{Al}	Density of aluminum (slug/in.^{3})
ρ_{BJ}	Density of Paracril-BJ (slug/in.^{3})
σ_1	Normal stress in 1-direction
σ_2	Normal stress in 2-direction
σ_3	Normal stress in 3-direction
τ	Thickness of material (in.)
ϕ	Phase lag between response of mass M and shaker table (radians)
ω	Circular frequency (rad/sec)
ΔA	Fractional error in A
ΔE	Fractional error in E
$\Delta\eta$	Fractional error in η
$\Delta\phi$	Fractional error in ϕ
$\Delta\omega$	Fractional error in ω

ANALYSIS

Consider an idealized tuned damper as shown in Fig. 1. Let the net mass be M, the area of the material cross section S, the material thickness τ, and the complex Young's modulus $E(1+i\eta)$. Let the shaker table be excited harmonically with amplitude X and let the response of the mass M be $y = Y\exp(i\omega t)$. Then the equation of motion is

$$M\frac{d^2y}{dt^2} + \frac{ES}{\tau}(1+i\eta)(Y-X)\exp(i\omega t) = 0 \qquad (1)$$

or

$$\left[-M\omega^2 + \frac{ES}{\tau}(1+i\eta)\right]Y = \frac{ES}{\tau}(1+i\eta)X. \qquad (2)$$

Therefore

$$\frac{Y}{X} = \frac{\ddot{Y}}{\ddot{X}} = \frac{1+i\eta}{1+i\eta - M\tau\omega^2/ES} = \frac{1+i\eta}{1+i\eta-\xi^2} \qquad (3)$$

where

$$\xi^2 = \frac{M\tau\omega^2}{ES} \qquad (4)$$

and $\ddot{Y}$ and $\ddot{X}$ are the output and input accelerations, respectively, and can be measured by suitable accelerometers.

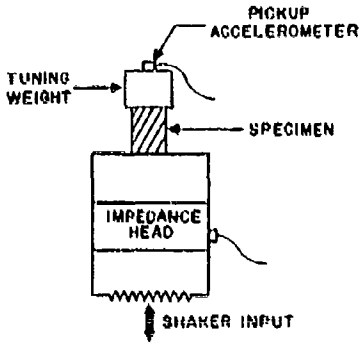

Fig. 1. Sketch of experimental setup

At resonance $\xi = 1$, provided that E and η are not strong functions of frequency, and the resonant amplification factor A becomes, from Eq. (3),

$$A = \left| \frac{1 + i\eta}{i\eta} \right|_2 = \sqrt{\frac{1 + \eta^2}{\eta}} .$$

Therefore

$$\eta = 1 \sqrt{A^2 - 1} . \tag{5}$$

The condition $\xi = 1$ for resonance gives, if ω is known,

$$E = M\pi\omega^2/S \tag{6}$$

so that both E and η are readily obtained from measured values of A and ω.

An alternative relationship between η and the lagging phase angle between the output Y and the input X may be derived from Eq. (3), namely

$$\frac{Y}{X} = \frac{(1 + \eta^2 - \xi^2) - i\eta\xi^2}{(1 - \xi^2)^2 + \eta^2} \tag{7}$$

so that

$$\tan \phi = \eta\xi^2/(1 + \eta^2 - \xi^2) . \tag{8}$$

Equation (8) gives a comparatively simple relationship between η and the phase angle ϕ. However, it will be noted that small errors in measuring ϕ will have serious effects on the calculated value of η whenever the frequency is well below resonance or at the natural frequency.

ERROR MAGNIFICATIONS

Whenever the characteristics of a material or system are not measured directly, but are calculated from other measurements, the question of the effect of errors in these measurements on the calculated characteristics must be considered. In this particular instance, one must consider the effect of errors in measuring the resonant frequency ω, the amplification factor A, and the phase angle ϕ. Each of these will now be considered in turn.

Error in ω

Let the measured resonant frequency $\omega(1 + \Delta\omega)$ where ω is the true resonant frequency and $\Delta\omega$ is the fractional error. Thus, from Eq. (6), if $\Delta\omega \ll 1$, the measured value E' of the Young's modulus is $E' = (M\pi\omega^2/S)(1 + 2\Delta\omega)$. Let $\Delta E = (E' - E)/E$ be the fractional error in E. Then

$$\Delta E/\Delta\omega = 2 \tag{9}$$

so that a certain fractional error in ω will give rise to twice that error in E.

Error in A

Let the measured amplification factor be $A(1 + \Delta A)$ where A is the true amplification factor and ΔA is the fractional error. Thus, from Eq. (5), the measured value η' of the loss factor is, if $\Delta A \ll 1$,

$$\eta' = \frac{1}{\sqrt{A^2(1 + 2\Delta A) - 1}}$$

$$\simeq \frac{1 + A^2\Delta A/(A^2 - 1)}{(A^2 - 1)^{1/2}} .$$

Let $\Delta\eta = (\eta' - \eta)/\eta$ be the fractional error in η. Then

$$\Delta\eta/\Delta A = A^2/(A^2 - 1) \tag{10}$$

$$= 1 + \eta^2 \tag{11}$$

by Eq. (5). The effects of errors are not magnified for small η.

Error in ϕ

The error in η owing to a measurement error in ϕ can be determined by taking the derivative of Eq. (8). Thus,

$$\sec^2\phi \, d\phi = \left[\frac{\xi^2(1+\eta^2-\xi^2) - 2\eta^2\xi^2}{(1+\eta^2-\xi^2)^2}\right] d\eta$$

or

$$\left\{1 + \frac{\eta^2\xi^4}{(1+\eta^2-\xi^2)^2}\right\} d\phi = \left\{\frac{\xi^2(1+\eta^2-\xi^2) - 2\eta^2\xi^2}{(1+\eta^2-\xi^2)^2}\right\} d\eta.$$

Therefore

$$\frac{d\eta}{d\phi} = + \frac{(1+\eta^2-\xi^2)^2 + \eta^2\xi^4}{\xi^2(1-\eta^2-\xi^2)} \qquad (12)$$

or

$$\left|\frac{d\eta}{d\phi}\right| = \left|\frac{(1+\eta^2-\xi^2)^2 + \eta^2\xi^4}{\xi^2(1-\eta^2-\xi^2)}\right|. \qquad (13)$$

Graphs of $|d\eta/d\phi|$ against ξ for various values of η are shown in Fig. 2. From these graphs it can be seen that, especially for higher loss factors, measuring errors in ϕ rapidly become serious at frequencies below resonance.

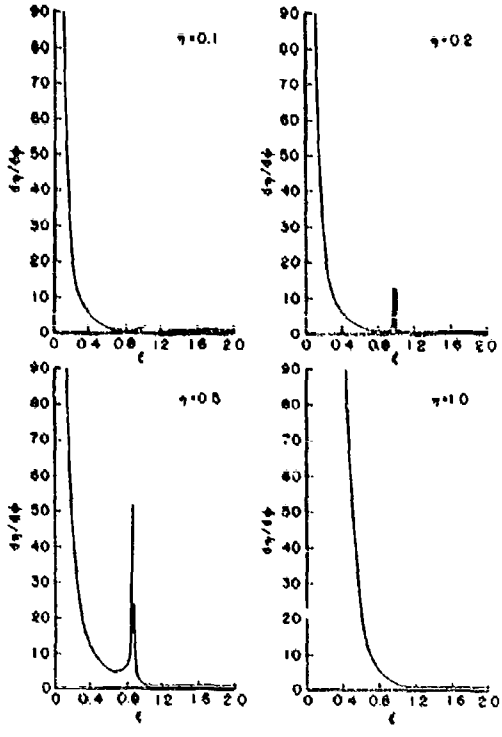

Fig. 2. Graphs of $|d\eta/d\phi|$ against frequency parameter, ξ

DAMPING MEASUREMENT PROCEDURE

If the mass M can be changed, the resonant frequency can also be changed and η and E calculated from measured value of A and ω, as functions of frequency.

A technique for determining E and η for soft viscoelastic materials is therefore possible, using cylindrical material specimens with adjustable masses attached at the free end and with the other end attached to a vibrating shaker table. The advantage of the technique is that no phase-angle measurements are involved at any time. Because accurate phase measurements can be made only with the most sophisticated electronic instrumentation, this potential source of difficulty is totally avoided. However, amplification factor and natural frequency measurements using accelerometers are relatively easy to make, although some difficulty may be encountered in determining A and ω when the loss factor η is large and resonant peaks are low and wide.

The experimental procedure involves (a) the preparation of a specimen with suitable mass M, thickness τ, and area S, (b) the measurement of the response amplitude $\hat{Y}$ as a function of frequency by means of an accelerometer, for given shaker table input $\hat{X}$, (c) the determination of the amplification factor A at the resonance frequency ω, and (d) the use of Eq. (5) and (6) to determine η and E, respectively. Tests are carried out over the entire temperature range of interest and the mass M and/or the dimensions of the specimen are then changed to get results at different frequencies. Finally, graphs of E and η against frequency are plotted for various temperatures.

EXPERIMENTAL DEMONSTRATION

Effects of Specimen Geometry on Calculated Modulus

During the preliminary experimental investigations, specimens were used with radius-to-height ratios of 0.125, 0.290, 0.325, 0.500, 0.780, 1.185, 1.975, and 2.425. Apart from the specimens with a radius-to-height ratio of less than 0.5 the calculated values of Young's modulus were higher than expected; that is, they were higher than those determined using the Brüel and Kjaer technique.

This phenomenon may be accounted for in terms of the state of stress in the specimen.

The analysis in this paper assumes a state of plane stress. This assumption is valid only for specimens whose heights are large compared to their radii. In this case, taking the longitudinal axis of the specimen as the 3-axis, it is easily shown [3] that $\sigma_3 = E\epsilon_3$, $\sigma_2 = 0$, and $\sigma_1 = 0$, where ϵ_3 is the strain in the longitudinal direction, and 1, 2, 3 are axes in a three-dimensional, orthogonal coordinate system. On the other hand, for specimens whose height-to-radius ratios are small, the assumption of a state of plane strain is more accurate. For this case, Poisson's ratio effects must be taken into account and it can be shown [4] that

$$\epsilon_3 = \frac{\sigma_3}{E}\left[\frac{(1-2\nu)(1+\nu)}{(1-\nu)}\right]$$

In this case as effective observed modulus E_{eff} can be defined as

$$E_{eff} = \frac{E(1-\nu)}{(1-2\nu)(1+\nu)}$$

so that $\epsilon_3 = \sigma_3/E_{eff}$.

In the case of plane stress, E_{eff} is the same as Young's modulus of the material whereas in the case of plane strain, E_{eff} is equivalent to the bulk modulus of the material.

The experimentally determined values of E, using the equations developed in this paper, are always equivalent to E_{eff}. The values of E_{eff} then lie somewhere between the true Young's modulus and the bulk modulus, as neither a state of plane stress nor of plane strain actually exists.

To determine a specimen size that will yield results that can be unambiguously interpreted in terms of either the Young's modulus or the bulk modulus, it was necessary to conduct preliminary experiments in which E_{eff} was determined for specimens of various radius-to-height ratios. Typical results for Paracril-BJ with 60 PHR SAF carbon are shown in Figs. 3 and 4. It is seen that for low radius-to-height ratios the values of E_{eff} tend to flatten indicating a range of values of the radius-to-height ratio over which E_{eff} is essentially equal to E.

Such tests must necessarily be conducted for each material to choose acceptable specimen sizes. In this case, the 1/2-in. diameter by 1/2-in. high specimen was chosen. The results obtained from this size specimen agreed quite well with those for the Brüel and Kjaer technique.

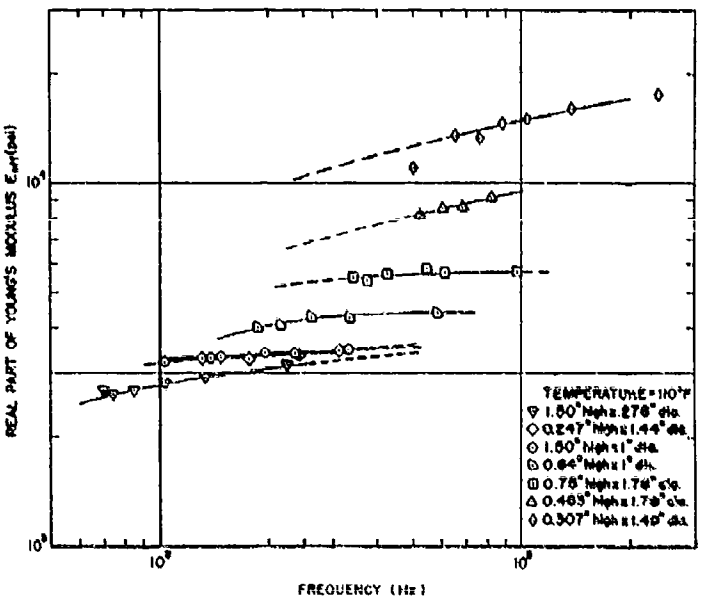

Fig. 3. Graph of experimentally measured values of effective Young's modulus against frequency

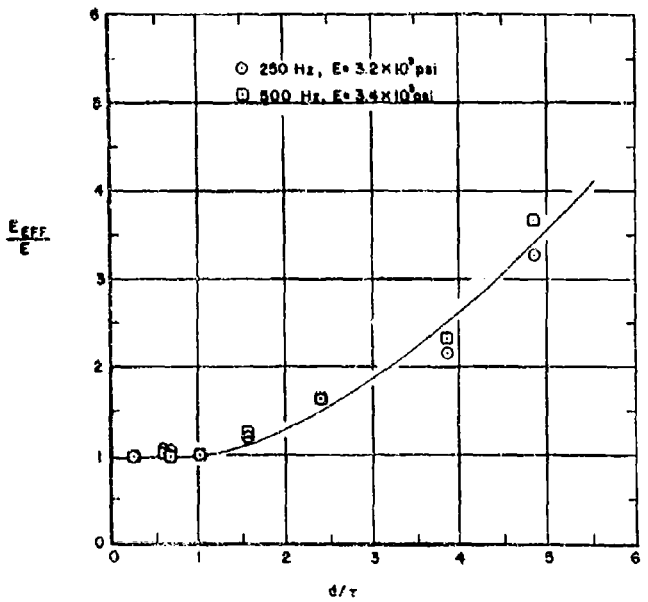

Fig. 4. Graph of ratio of effective Young's modulus to Young's modulus against diameter-to-height ratio of specimen

Effects of Temperature and Frequency

To verify the general accuracy and effectiveness of the tuned damper measurement technique, tests were carried out on simple cylindrical specimens of a particular elastomer (Paracril-BJ with 50 parts per hundred super abrasive carbon black) for which accurate measurements of E and η had already been made using a cantilever beam technique [1]. The specimen dimensions were a 0.5-in. diameter by a 0.5-in. depth. In accordance with elementary spring theory, one-third of the mass of the viscoelastic element was added to the nominal mass of the added weight and accelerometer to give the true mass M. Tests were carried out at various masses M, input accelerations $\ddot{X}$, and temperatures for the specimens and the results are given in Tables 1 and 2. For the given values of M, τ, and S, η and E were calculated from the measured values of A and ω. Both E and η were found, as seen in Table 3, to be independent of strain for low input accelerations. This is the linear region for the material, and measurements in this range only were used for comparison with the cantilever beam test results.

Graphs of E and η against frequency for various temperatures are shown in Figs. 5 through 8. Cross plots of E and η against temperature for a frequency of 500 Hz are shown in Fig. 9.

For the sake of comparison, data previously taken on aluminum beams, coated on both sides with equal thicknesses of the same elastomer as in Fig. 10, and excited as a cantilever beam in a complex modulus apparatus [1] are included. The results are given in Table 4. Measured values of E and η are plotted against frequency in Figs. 5 through 8.

CONCLUSIONS

An analysis has been developed to describe the dynamic response of a variable-mass/viscoelastic-link system in tension-compression. This analysis shows that the Young's modulus and loss factor of a viscoelastic material are easily determined from frequency and amplitude measurements at resonance. The analysis also showed that there is a simple relationship between the loss factor and phase lag between the input and output.

To determine the effects of amplitude, frequency, and phase measurement errors on the calculated properties, an error analysis was

TABLE 1
Experimental Values of Loss Factor and Young's Modulus for Paracril-BJ With 50 Parts SAF C for a 1/2-in. Diameter, 1/2-in. High Cylindrical Specimen Using the Tuned Damper Technique[a]

Temp °F	M (gm)	f (Hz)	Output (g)	A	η	E (psi)
50	63.5	400	2.4	2.4	0.460	6.00×10^3
	132.0	274	2.55	2.55	0.426	5.70×10^3
	268.5	185	2.70	2.70	0.400	5.25×10^3
110	63.5	310	5.0	5.0	0.204	3.50×10^3
	132.0	207	5.1	5.1	0.200	3.25×10^3
	268.5	133	4.9	4.9	0.207	2.70×10^3
132	63.5	286	5.7	5.7	0.178	2.98×10^3
	132.0	194	5.6	5.6	0.182	2.86×10^3
	268.5	125	5.1	5.1	0.200	2.70×10^3
161	63.5	274	5.95	5.95	0.171	2.74×10^3
	132.0	175	5.3	5.3	0.192	2.34×10^3
	268.5	116	5.1	5.1	0.200	2.08×10^3

[a]Input = 1 g.

TABLE 2
Experimental Values of Loss Factor and Young's Modulus for Paracril-BJ with 50 Parts SAF C for Three 1/2-in. Diameter, 1/2-in. High Cylindrical Specimens Joined in Parallel Using the Tuned Damper Technique[a]

Temp °F	M (gm)	f (Hz)	Output (g)	A	η	E (psi)
50	102.6	596	1.90	1.90	0.620	6.95×10^3
	244.7	363	2.20	2.20	0.510	6.20×10^3
	433.2	284	2.15	2.15	0.526	6.73×10^3
	711.2	216	2.18	2.18	0.516	6.32×10^3
110	102.6	409	4.42	4.42	0.232	3.28×10^3
	244.7	266	4.8	4.80	0.213	3.31×10^3
	433.2	197	4.8	4.80	0.213	3.24×10^3
	711.2	150	4.05	4.05	0.255	3.07×10^3
132	102.6	387	5.0	5.0	0.204	2.94×10^3
	244.7	238	4.30	4.3	0.240	2.68×10^3
	433.4	185	4.90	4.9	0.207	2.85×10^3
	711.2	137	4.10	4.10	0.251	2.57×10^3
161	102.6	363	5.25	5.25	0.194	2.59×10^3
	244.7	—	—	—	—	—
	433.4	171	5.0	5.0	0.204	2.45×10^3
	711.2	128	4.10	4.10	0.251	2.43×10^3

[a]Input = 1 g.

TABLE 3
Typical Variation of Experimentally Determined Values of Loss Factor and Young's Modulus With Input Acceleration for a 1/2-in. Diameter, 1/2-in. High Specimen of Paracril-BJ With 50 Parts SAF Carbon[a]

f (Hz)	Input (g)	Output (g)	A	η	E (psi)
210	0.5	2.6	5.20	0.196	3.33×10^3
207	1.0	5.1	5.10	0.200	3.25×10^3
202	2.0	8.95	4.97	0.230	3.10×10^3
188	5.0	21.7	4.34	0.237	2.67×10^3

[a] Temperature = 110°F, M = 132.0 gm.

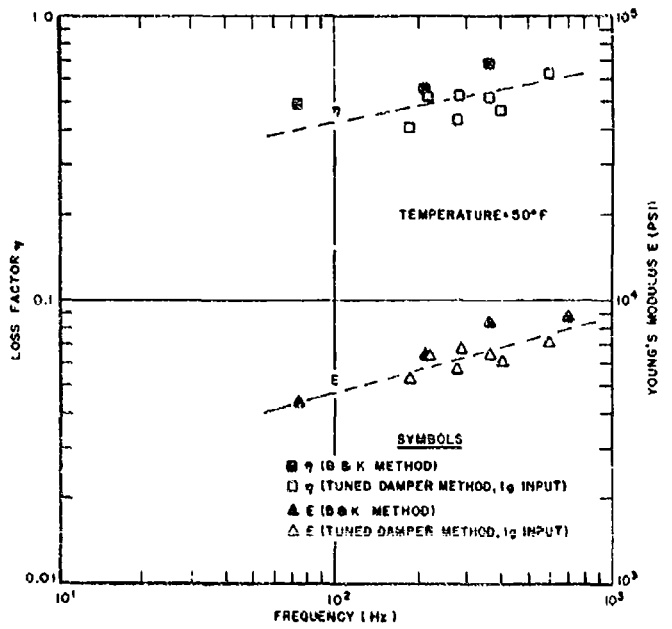

Fig. 5. Graph of experimentally measured values of loss factor and Young's modulus against frequency at 50°F

performed. This analysis showed that for a soft viscoelastic material with a small loss factor, the effect of small errors in measured frequency and amplitude are not serious.

The analysis showed that small errors in phase measurement can become quite serious at and below the resonant frequency of the system.

An investigation of the effects of specimen geometry on the measured Young's modulus was also conducted to determine a suitable specimen size. This investigation showed that for cylindrical specimens with a radius-to-height ratio of 0.5 or less, Poisson's ratio effects could be neglected. The investigation also indicated that Poisson's ratio may be 0.5 or very nearly 0.5 for the particular material used. For radius-to-height ratios of 0.5 or less, the measured properties were in good agreement with those obtained using the Brüel and Kjaer technique.

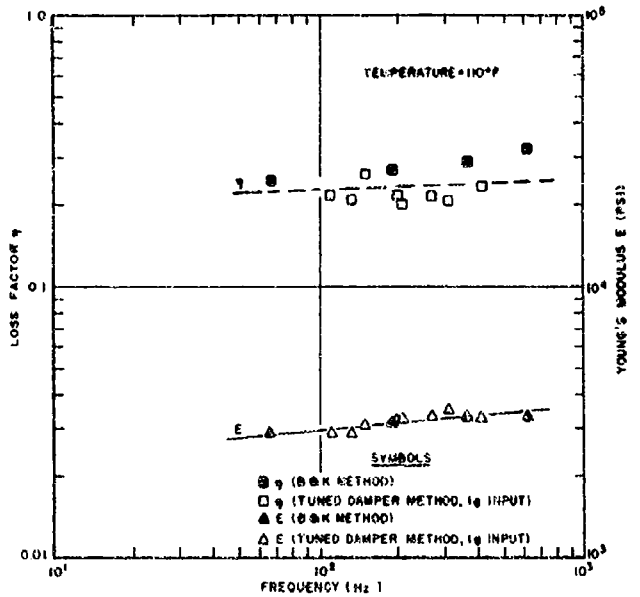

Fig. 6. Graph of experimentally measured values of loss factor and Young's modulus against frequency at 110°F

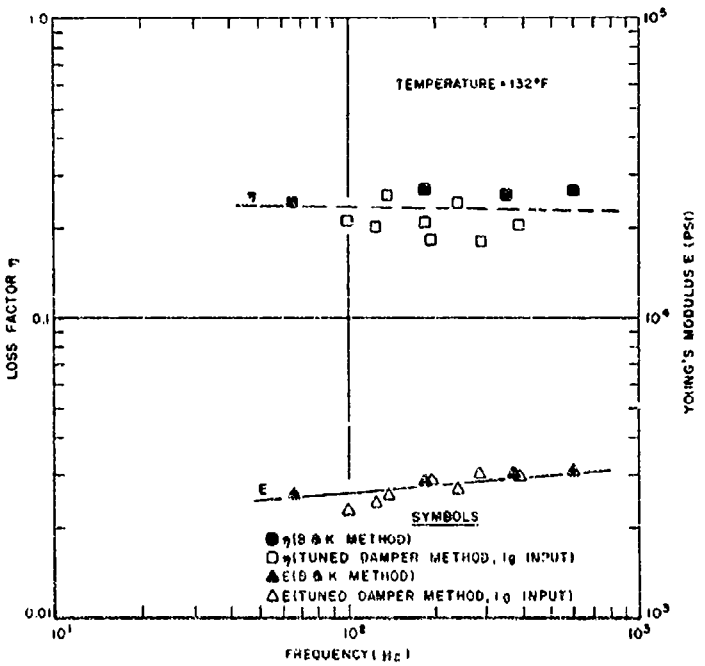

Fig. 7. Graph of experimentally measured values of loss factor and Young's modulus against frequency at 132°F

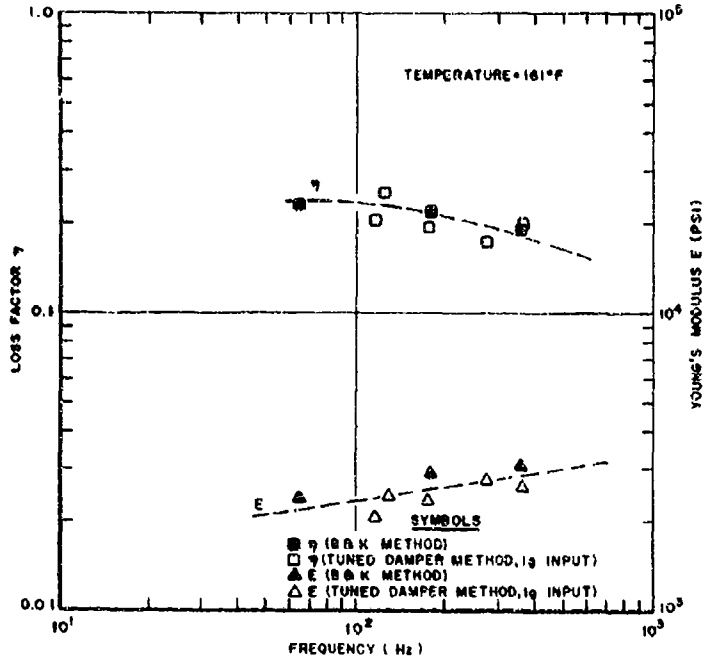

Fig. 8. Graph of experimentally measured values of loss factor and Young's modules against frequency at 161°F

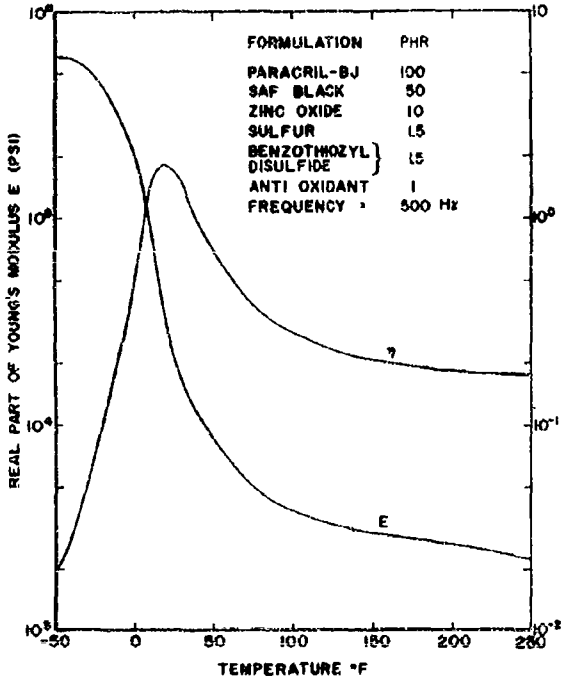

Fig. 9. Graph of experimentally measured values of loss factor and Young's modulus against temperature

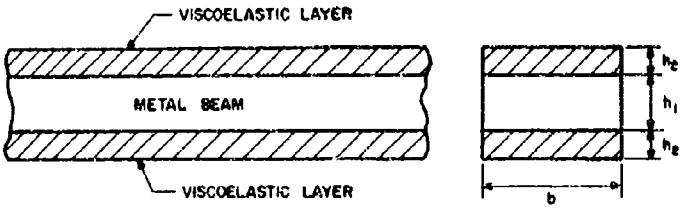

Fig. 10. Sketch of metal beam with viscoelastic layers

TABLE 4
Experimental Values of Loss Factor and Young's Modulus for Paracril-BJ With 50 Parts SAF C Using the Brüel and Kjaer Technique[a]

Temp (°F)	f (Hz)	η	E (psi)
50	72.9	0.397	5.42×10^3
	212.3	0.548	7.04×10^3
	426.3	0.887	8.21×10^3
110	67.2	0.245	2.84×10^3
	190.4	0.266	3.15×10^3
	374.5	0.286	3.28×10^3
	618.8	0.320	3.28×10^3
132	66.1	0.239	2.65×10^3
	186.5	0.265	2.83×10^3
	368.1	0.252	3.01×10^3
	609.4	0.266	3.07×10^3
160	64.6	0.229	2.42×10^3
	183.4	0.216	2.88×10^3
	361.9	0.189	3.05×10^3

[a] h_{BJ} = 0.0119 in., L = 7 in., ρ_{BJ} = 0.041 lb/in.^{3}, h_{Al} = 0.032 in., b = 0.45 in., and ρ_{Al} = 0.1 lb/in^3.

ACKNOWLEDGMENTS

The authors would like to thank W. J. Trapp, Chief of the Strength and Dynamics Branch, for his support of the Air Force Materials Laboratory damping research program of which this paper represents a part. The work reported in this paper was sponsored by the U.S. Air Force under Project No. 7351, "Metallic Materials," Task No. 735106, "Behavior of Metals," and Contract No. F33615-67C1187. Equipment used in this investigation was purchased by the Directors' Fund of the Air Force Materials Laboratory. The authors would also like to thank F. S. Owens for assistance with preparation of the elastomer specimens, Constance M. Gillmore for typing the manuscript, and T. Nicholas for many helpful discussions.

REFERENCES

1. A. D. Nashif, "New Method for Determining Damping Properties of Viscoelastic Materials," 36th Shock and Vibration Bull. 36, Part 4, pp. 4-7, NRL, Washington, D.C., Jan. 1967
2. G. W. Painter, "Dynamic Properties of BTR Elastomer," paper presented at SAE Natl. Aeron. Meeting, Los Angeles, Calif., 1958
3. F. B. Seely and J. O. Smith, Advanced Mechanics of Materials (John Wiley & Sons, Inc., New York), 1952, p. 65
4. J. C. Jaeger, Elasticity, Fracture and Flow (John Wiley and Sons, Inc., New York), 1956, pp. 57-59

DISCUSSION

D. S. Nokes (Tufts Univ.): Could you comment on how this technique would work for a material with very high loss factor? For a loss factor of the order of 1, can you still measure a resonant frequency?

Mr. Cannon: I think it would be rather difficult because the amplification factors might tend to be quite low. Once they got down to the order of say 1-1/2 or so, then the amplification factor could have quite a serious effect on the calculated results.

P. J. Conlisk (Monsanto): Would you care to comment on the softest material you have tested and what success you had? Have you measured any material with a modulus in the range of 100?

Mr. Cannon: I do not think we measured any material of around 100, but for moduli of around 500 or 600 psi the results have been quite good.

Mr. Conlisk: What were the loss factors of those?

Mr. Cannon: The loss factor for this material, a silicone rubber compound, was from about 0.1 to 0.3.

Mr. Conlisk: And you had very good results?

Mr. Cannon: Yes.

Dr. Jones (Air Force Mat. Lab.): I would like to add a comment. We have measured properties down to about 150 psi. Charles wouldn't have known about that because I did it.

K. McConnell (Iowa State Univ.): I was very interested in the penalty curves or error curves using the phase technique. I would like to suggest that you can considerably improve these by using a slightly different arrangement. Apply a sinusoidal force to the mass instead of to the base, and then at extremely high dissipation factors, you can also use the phase shift between the driving force and the response as an indication of resonance. I have used this technique in a highly damped fluid system and it is extremely precise. With the system you have, there is a 90-degree phase shift if you drive with a purely linear system. Because you are driving through the material you really do not know what the phase relationships are. This is why you have such high error penalties.

Mr. Cannon: We never tried the technique that you suggested. It might be good to look into, though.

Mr. Forkois (NRL): Have you concerned yourself at all with the thermodynamics of the material itself? In other words, you said you have a 150-degree F external temperature and, of course, the material itself may be 50 degrees higher. How long would it take for the material itself to deteriorate as the damping is increased?

Mr. Cannon: You mean just because of the heat dissipation within the material as it builds up the heat? During the testing I noticed that if the system is left at resonance for several minutes or so, there is very little difference either in frequency or in the loss factor.

Mr. Forkois: I once embedded thermocouples in a block of polyurethane and, over a period of time, there was quite a temperature rise in the material. I suspect that this can cause some error in determining the damping factor.

Mr. Cannon: Yes, it would, but, for materials that are in a range where the moduli and loss factors are fairly flat or in the rubbery region, the effect of even a 5- or 10-degree change within the material would not affect its properties very much. However, at the glass

transition temperature where there is a change of slope in the elastic curve and the loss factor curve is at its peak, then a several-degree change in temperature within the specimen would cause a serious effect, particularly if the material is quite temperature sensitive.

D. Kraft (Univ. of Dayton): In the paper that Mr. Newman and I presented this morning, we had a shear system which is not dissimilar to what Charles is talking about. We embedded thermocouples in our viscoelastic material which was 1 by 1 by 1/4 in. thick. We ran this at different levels of acceleration and monitored the temperature variations within the viscoelastic material. It might be of interest that this is somewhat a function of the magnitude of the acceleration. One can get outside the linear range and perhaps get into some difficulties, but in the area of very small accelerations, up to 3 or 4 g's, which is the region we monitored, and we had the system running 10, 15, 20 min, we would get variations of temperatures of maybe ±1-1/2 degrees. So it was relatively small and as mentioned, one would have to be in an extremely sensitive temperature region in terms of the real part of the modulus to affect the results significantly.

Mr. Brooks (NASA, Langley): There is certainly a great deal of effort in this area. Looking at materials that have very high loss factors, I wonder if anyone has given any consideration to just simply looking at the damping of critically damped systems when you approach very high values of damping. I remember a few years ago I was faced with this problem and I found that I could get a pretty good answer on the damping, or loss factor if you like, by simply integrating the decay curve for a critically damped system. This is a technique which some of you may find interesting when you have very high loss factors.

* * *

AIRCRAFT STRUCTURAL RESPONSE DUE TO GROUND IMPACT

Jack D. Weber
Conv. r Division of General Dynamics
San Diego, California

A method is developed for computing the dynamic response of a free-free elastic aircraft structure while impacting with the ground. This problem, which is complicated by nonlinear force characteristics and structural feedback, has been brought into the realm of practical solution by a unique transformation. The mathematical model consists of a lumped parameter system. The ground load is idealized by a series of nonlinear partially restoring springs. These springs represent the vertical crushing characteristics of the lower fuselage structure. The method of analysis employed computes the rigid body plus the transient elastic response of the structure. Basic kinetics are used to determine the rigid body response and load. The modal acceleration technique is used to compute the vibratory response of the structure. To facilitate a solution, the load-deflection characteristics of the lower fuselage structure are transformed into load-time curves. The load-time curves are generated as the solution progresses and thus represent the effect of structural feedback. The results of a sample problem are presented as time varying displacements, velocities, accelerations, and fuselage bending moments. A comparison is made between the loads and accelerations developed in a typical fuselage during a crash (fuselage contact) and those developed during a landing (two-wheel contact) under the same initial conditions. The results of fuselage model impact tests are presented, and a comparison is made with the theoretical decelerations and bending moments.

INTRODUCTION

Passenger safety and survivability are becoming ever more important with the advent of larger and larger aircraft. The maintaining of fuselage structural integrity during ground impact is the area under consideration in this paper. Primary consideration is given to a practical method of determining the loads developed in a fuselage during ground impact.

A number of controlled crash tests have been made with aircraft. With other participating organizations, the FAA conducted a full-scale dynamic crash test of a Lockheed Constellation Model 1649 aircraft [1]. Similar tests have been made on other aircraft. In all cases the fuselage broke at one or more places. Recently the FAA, in conjunction with Convair, performed crash tests on models of fuselages. These models were 4 ft in diameter and 30 ft long.

If one considers the loads developed in a fuselage as a design parameter, the possibility of a fuselage remaining intact during a limited crash can be significantly improved. The problem is twofold: First, the lower fuselage structure must be designed to absorb the energy attributed to the velocity of the aircraft normal to the ground. The energy attributed to the forward motion of the aircraft must be absorbed by ground friction. Second, the fuselage structure must have adequate strength to withstand the loading during ground impact. These two objectives can be improved by only a minor weight increase using new design considerations [2].

The objective in developing the present method of solution has been to arrive at a technique with enough flexibility so that it can be used readily and still produce results with reasonable engineering accuracy. The ability to handle not only the fundamental modes but higher frequencies was of prime consideration in the development of the present method of analysis. The test results presented in Ref. [1] show the importance of higher modes. The results of previous analytical work [3] and test results [1] have been helpful in deriving the present technique. Certain parameters such as longitudinal vibrations that were determined to have an insignificant effect [3] were not considered.

The determination of the response of an elastic aircraft structure during ground impact is complicated by the nature of the forcing functions. If the forces were predetermined functions

of time, the solution would be straightforward. Instead, they are functions of both displacement and permanent set.

BASIC EQUATIONS

The method of analysis employed computes the rigid body plus the transient elastic response of the structure. Basic kinetics are used to determine the rigid body response and load. The modal acceleration technique is used to compute the vibratory response of the structure; the mathematical model consists of a lumped parameter system; the ground load is idealized by a series of nonlinear partially restoring springs. These springs represent the vertical crushing characteristics of the lower fuselage structure. To facilitate a solution, the load-deflection characteristics of the lower fuselage structure are transformed into load-time curves. The load-time curves are generated as the solution progresses and thus represent the effect of structural feedback.

In deriving the basic equations, the following assumptions are made:

1. The crash is symmetric. That is, the airplane is allowed to pitch and translate vertically but cannot yaw, roll, or translate laterally. Longitudinal motion has been excluded from the present consideration.

2. The normal force applied to the fuselage while impacting with the ground is derived from a series of nonlinear partially restoring springs.

3. The beam flexural stiffness remains constant during the crash.

4. The lift on the wing is completely destroyed at impact.

5. The stiffness of the ground is relatively high in comparison to the lower fuselage structure; therefore, it can be neglected.

The basic equations or phases to the solution have been divided into three parts: force determination, rigid body equations, and elastic body equations.

The coordinates and sign convention used in deriving the equations of motion are given in Fig. 1, where

X_i = location of ith mass station,

Z_i = distance between ground and undeformed underside of fuselage at the ith mass station (a negative displacement indicates deformation of the lower fuselage structure),

$\dot{Z}_i$ = velocity of the ith mass station,

$\ddot{Z}_i$ = acceleration of the ith mass station, and

F_i = spring force on the ith mass station.

Force Determination

A typical force-deflection curve of a lower fuselage structure at a given mass station, i, is given in Fig. 2. By transforming this curve into one of force vs time, the response of the fuselage can be determined by a closed form solution. The transformation is accomplished by estimating the distance a station will travel

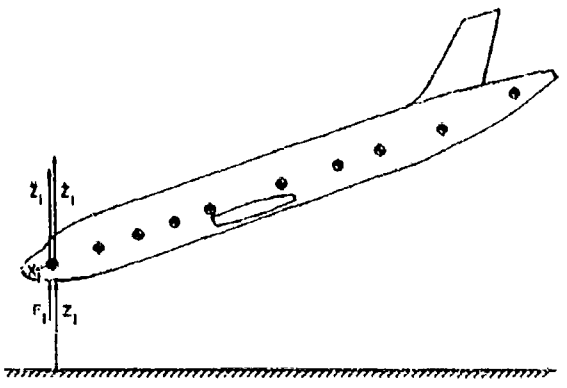

Fig. 1. Coordinates and sign convention

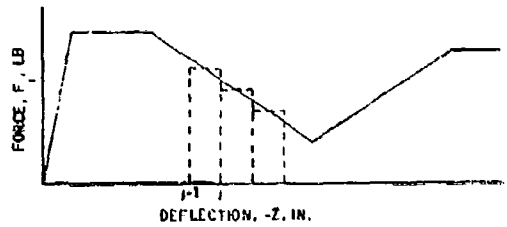

Fig. 2. Force-deflection characteristics of a lower fuselage structure

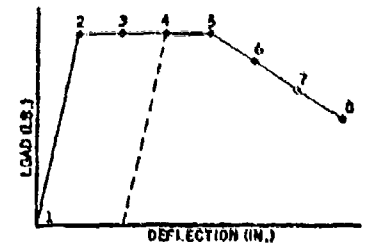

Fig. 3. Load-deflection curve with permanent set

in a given time increment, t_{j-1} to t_j. The estimated displacement is determined by Eq. (1), which is based on the value of displacement, $Z_{i_{j-1}}$; velocity, $\dot{Z}_{i_{j-1}}$; and acceleration, $\ddot{Z}_{i_{j-1}}$, at time, t_{j-1}.

$$Z_{i_j} = Z_{i_{j-1}} + \dot{Z}_{i_{j-1}}(t_j - t_{j-1}) + \frac{1}{2}\ddot{Z}_{i_{j-1}}(t_j - t_{j-1})^2. \tag{1}$$

From the force-deflection curve, values of force are determined for the displacement at time t_{j-1} and t_j. The constant force, F_i, acting on mass station i during a given time increment is taken as the average of the force at $Z_{i_{j-1}}$ (actual) and Z_{i_j} (estimated). The procedure is repeated for each mass station. These forces are then used to determine the response of the structure for the given time increment. Test cases show the estimated displacements to agree within four digits of accuracy with the subsequently computed actual displacements. Because of this accuracy the computed forces fall well within engineering accuracy. Thus this technique has proven to be very powerful with respect to both accuracy of solution and minimum computer time.

Permanent set can be represented by letting the load-deflection characteristics of the lower fuselage structure for each station be represented as a series of load-deflection coordinates. A straight line is assumed between each set of points. A separate curve is used for each station. Figure 3 illustrates a portion of a load-deflection curve with permanent set.

As a solution progresses, the curve can be modified to account for plastic deformation of the lower fuselage structure. The procedure is to progressively destroy the curve as deflection increases. For example, when the deflection is between points 3 and 4, the value of load at point 2 is set to zero; and then the deflection is between points 4 and 5, the load at point 3 is set to zero, and so forth. These values of load will remain at zero. Thus, when the deflection decreases, the value of applied load computed from these modified curves will also be zero.

A limited amount of elastic springback is represented by a modified curve. For example, if points 2 and 3 have been set to zero, the new elastic region of the structure is as shown with a dashed line in Fig. 3. By proper selection of the points not only can the load deflection curve be represented, but springback characteristics can be varied along the curve. Depending on the structure involved, a high elastic springback is possible in one region and a low value in another. The potential of this feature is dependent on the proper selection of the points to represent a load-deflection curve.

Rigid Body Equations

The following equations are used to describe rigid body motion of the aircraft center of gravity and the individual mass stations. The total normal force on the fuselage is

$$F = \sum_1^n F_i. \tag{2}$$

The total pitching torque about the aircraft center of gravity (cg) is

$$T = \sum_1^n F_i(X_i - X_{cg}). \tag{3}$$

Equating the applied forces to the inertia forces,

$$F = M\ddot{Z} - Mg \tag{4}$$

$$T = I\ddot{\alpha} \tag{5}$$

where

M = mass of aircraft,

I = pitching moment of inertia of aircraft,

g = acceleration attributed to gravity,

$\ddot{Z}$ = relative acceleration of aircraft center of gravity, and

$\ddot{\alpha}$ = aircraft pitching acceleration.

Combining Eqs. (4) and (5), the acceleration of the ith point is

$$\ddot{Z}_i = \frac{F}{M} + g + \frac{T\,(X_i - X_{cg})}{I}. \tag{6}$$

Assuming that the applied force and the resulting acceleration, $\ddot{Z}_{i_j}$, are constant for a given time increment, t_{j-1} to t_j, the velocity and displacement of the ith mass station at the end of the jth time increment is

$$\dot{Z}_{i_j} = \ddot{Z}_{i_j}(t_j - t_{j-1}) + \dot{Z}_{i_{j-1}} \tag{7}$$

$$Z_{i_j} = \dot{Z}_{i_{j-1}}(t_j - t_{j-1}) + \frac{1}{2}\,\ddot{Z}_{i_j}(t_j - t_{j-1})^2 + Z_{i_{j-1}}. \tag{8}$$

These equations then represent the rigid body motion of an aircraft during impact.

Flexible Body Equations

The elastic response of a complex multi-degree-of-freedom system is best determined by the use of generalized coordinates. The generalized coordinates or modes will be considered to be orthogonal; thus the total vibratory response is the superposition of the individual modes. In terms of generalized coordinates, the equation of motion for the kth mode is

$$M_{kk}\,\ddot{q}_k + M_{kk}\,\omega_k^2\,q_k = F_{q_k} \tag{9}$$

where

M_{kk} = generalized mass in the kth mode,

ω_k = frequency of kth mode, and

F_{q_k} = generalized force of kth mode.

The generalized mass for an orthogonal mode is

$$M_{kk} = \sum_{1}^{n} m_i\,\phi_{i_k}^2 \tag{10}$$

where

m_i = mass at the ith mass point, and

ϕ_{i_k} = modal displacement at the ith mass point in the kth mode.

The generalized force is also based on the applied force remaining constant during a given time increment. Thus the generalized force is represented as a step-curve. The generalized force for the kth mode during the jth time increment is

$$F_{q_{k_j}} = \sum_{1}^{n} F_{i_j}\,\phi_{i_k}. \tag{11}$$

The solution of the equation of motion for the kth mode in terms of generalized displacement, Q_{k_j}, velocity, $\dot{Q}_{k_j}$, and acceleration, $\ddot{Q}_{k_j}$, at the end of the jth time increment is

$$Q_{k_j} = \frac{F_{q_{k_j}}}{M_{kk}\,\omega_k^2} + \left(Q_{k_{j-1}} - \frac{F_{q_{k_j}}}{M_{kk}\,\omega_k^2}\right)\cos\omega_k(t_j - t_{j-1}) + \frac{\dot{Q}_{k_{j-1}}}{\omega_k}\sin\omega_k(t_j - t_{j-1}) \tag{12}$$

$$\dot{Q}_{k_j} = -\omega_k\left(Q_{k_{j-1}} - \frac{F_{q_{k_j}}}{M_{kk}\,\omega_k^2}\right)\sin\omega_k(t_j - t_{j-1}) + \dot{Q}_{k_{j-1}}\cos\omega_k(t_j - t_{j-1}) \tag{13}$$

$$\ddot{Q}_{k_j} = -\omega_k^2\left(Q_{k_{j-1}} - \frac{F_{q_{k_j}}}{M_{kk}\,\omega_k^2}\right)\cos\omega_k(t_j - t_{j-1}) - \omega_k\,\dot{Q}_{k_{j-1}}\sin\omega_k(t_j - t_{j-1}) \tag{14}$$

where $Q_{k_{j-1}}$ and $\dot{Q}_{k_{j-1}}$ are the generalized displacement and velocity at the beginning of the time increment. The solution is propagated by letting the final conditions of one increment become the initial conditions of the next. The effect of structural damping, G, has been added by multiplying Eqs. (12), (13), and (14) by

$$e^{-0.5\,G\omega_k(t_j - t_{j-1})}. \tag{15}$$

The total vibratory response of the ith mass point is obtained by transforming the above response factors from generalized to structural coordinates and summing the response of the individual modes. Thus the transient response at the end of the jth time increment is

$$Z_{i_j} = \sum_k^m Q_{k_j} \phi_{i_k} \tag{16}$$

$$\dot{Z}_{i_j} = \sum_k^m \dot{Q}_{k_j} \phi_{i_k} \tag{17}$$

$$\ddot{Z}_{i_j} = \sum_k^m \ddot{Q}_{k_j} \phi_{i_k} . \tag{18}$$

These equations represent the vibratory response of an aircraft during impact. The total response is the sum of the rigid body plus the transient response.

DIGITAL COMPUTER PROGRAM

A digital computer program has been developed based on the preceding equations. The program computes the dynamic response of a free-free elastic aircraft structure while impacting with the ground. The program computes as a function of time the displacement, velocity, and acceleration of each control station. Bending moments along the fuselage are also determined. These are compared with the maximum allowable bending moments. The normal computer output is in the form of both printed output and SC-4020 plots. A complete description of the program is given in Ref. [2]. The program has been written in Fortran IV and has been run on the IBM 7094/44, the IBM 360 model 65/40, and the CDC 6400

STUDY AND TEST RESULTS

To demonstrate the method developed in this paper, the results of two different problems are presented. The first is an analytical study using the physical characteristics of a medium-size, four-engine jet transport. The second is a comparison between analytical prediction and test results for a model fuselage.

Jet Transport Study

The fuselage of a jet transport was idealized as a beam with ten mass stations (Fig. 1). In the model the vertical flexural stiffness was considered to vary linearly between mass stations. Wing weight was included as part of the fuselage weight. The vertical crushing characteristics of the lower fuselage structure were represented as a nonlinear partially restoring spring at each of the forward nine mass stations. The free-free orthogonal vibration modes and frequencies for the idealized structure were computed from stiffness, mass, and geometric data.

The dynamic response of the jet transport impacting the ground was determined by the computer program and is in the form of printed output and SC-4020 plots. To illustrate the results, selected plots are presented in Fig. 4. The plots of displacement show progressive contact of the ground by the various stations. Contact is made at a displacement of zero. Negative displacements represent deformation of the lower fuselage structure. By comparing the displacements between stations, pitching of the fuselage can be observed. The plots of velocity also illustrate pitching of the fuselage. The plots of acceleration show the pronounced effect of the vibratory modes, especially higher frequencies. The plots of bending moment show that the higher frequency modes have a more pronounced effect at the ends of the beam and that the fundamental modes produce the primary response near the center of the beam. Actual test data [1] have also brought out the importance of multiple elastic modes. One of the features of the computer program that uses the method of this paper is its ability to handle six elastic modes at a minimum of computer time (1.5 min on the IBM 7094/44).

A parameter study was made for the jet transport impacting the ground. Angle of attack and contact velocity were varied. Results of these studies are presented in the form of fuselage vertical decelerations (Fig. 5) and bending moments (Fig. 6). Impact velocity has a pronounced effect on decelerations and bending moments. Angle of attack also increases the fuselage response. The increase attributed to angle of attack is the result of the application of load at the end of a beam and the relative stiff nose structure. Except for the wing fuselage intersection and the nose, the remainder of the lower fuselage structure of present jet transports possesses fairly good energy-absorbing characteristics. The maximum allowable fuselage bending moments are included in Fig. 6 to serve as a basis for evaluating the severity of the loads attributed to ground impact.

Figure 6 shows that it does not take much of an impact (zero degree and 10 ft/sec) before the maximum positive (compression in upper surface) allowable bending moment is exceeded. The reason for this is that aircraft fuselages are not designed for high positive bending moments. The typical crash situation is shown in Fig. 4(H) where the initial impact produces a large positive bending moment at 0.13 sec. A fuselage to be more survivable must be designed not only to withstand large negative bending

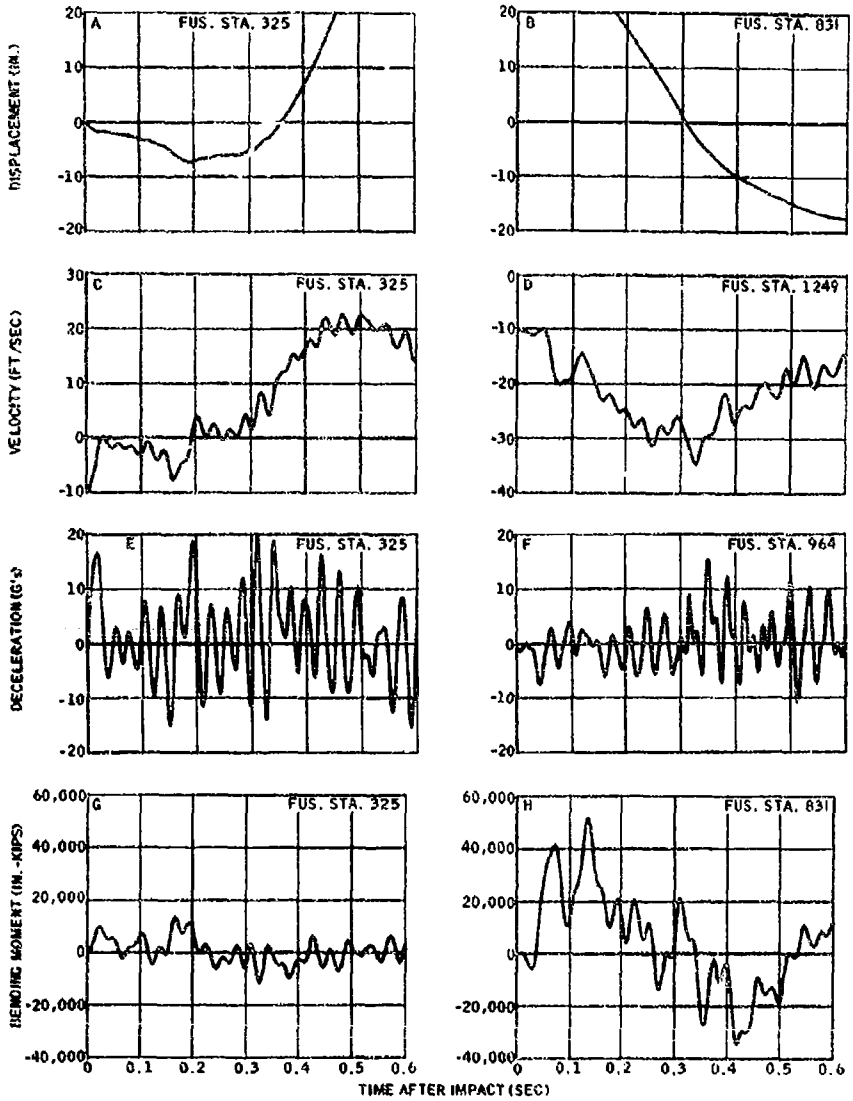

Fig. 4. Jet transport fuselage--5° impact angle, 10 ft/sec, normal velocity

moments, as they now are, but also to withstand high positive moments. In Ref. [2] the problem of maintaining the structural integrity of a fuselage during impact is discussed further. Also, methods are outlined to improve the energy-absorbing characteristics of a lower fuselage structure.

The results of a two-wheel symmetric landing analysis are also presented in Figs. 5 and 6 for a 10 ft/sec descent velocity. Landing produces much larger negative than positive bending moments. Comparison with the ground impact shows the landing condition to be less severe for both positive or negative bending moments. This is because of two factors: One, the landing gear is a better energy absorber than the lower fuselage structure; two, the distance from the airplane center of gravity to the applied load is less for a landing. Thus, the result shown by this comparative study is that ground contact is a more severe design condition than landing.

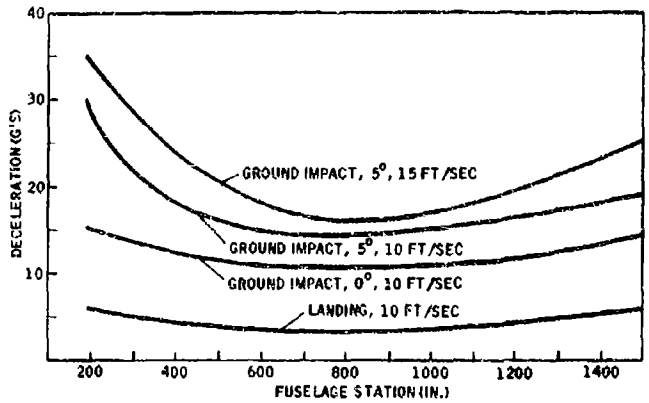

Fig. 5. Deceleration--jet transport fuselage, landing comparison

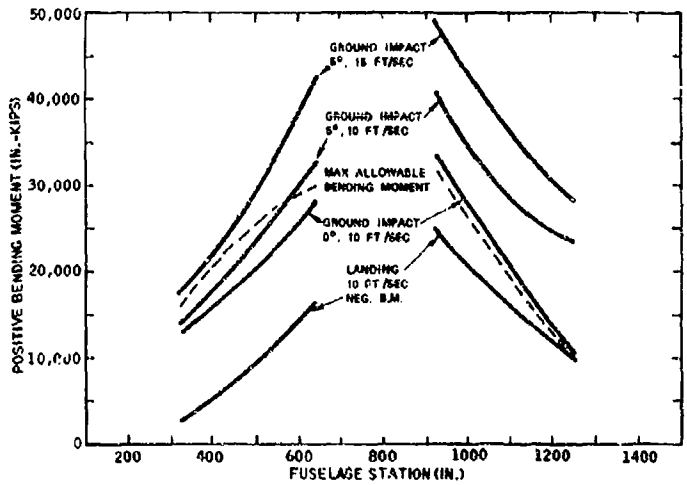

Fig. 6. Bending moments--jet transport fuselage, landing comparison

Fuselage Model Tests

Fuselage scale models 4 ft in diameter and 30 ft long have been built and used in crash tests. The objective has been to demonstrate the method presented in this paper. The improved crashworthy types of lower fuselage structure, as presented in Ref. [2], were also tested.

Two models, each with a different fuselage bending strength and lower fuselage structure, were shot off a catapult at 75 mph into a 6-degree hill. The impact area for the first test was relatively soft fill. A steel plate was laid down on the impact area for the second test and acceleration and strain gage measurements were recorded during impact. Test results for model 1 are presented in Figs. 7 (decelerations) and 8 (bending moments), and the results for model 2 are shown in Figs. 10 (decelerations) and 11 (bending moments). The fundamental vibratory bending mode along with the higher frequency modes are presented in the test data (Figs. 9 and 12).

Prior to testing, analytical predictions were made for each model. The models were idealized as 10 mass lumped parameter systems. Associated with each of the forward nine

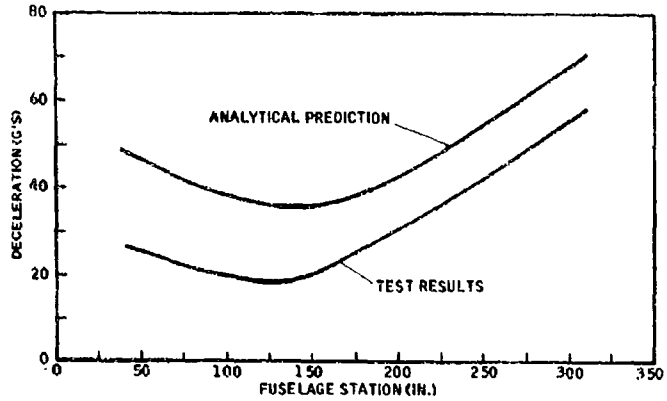

Fig. 7. Deceleration--fuselage model 1, impact on soft ground

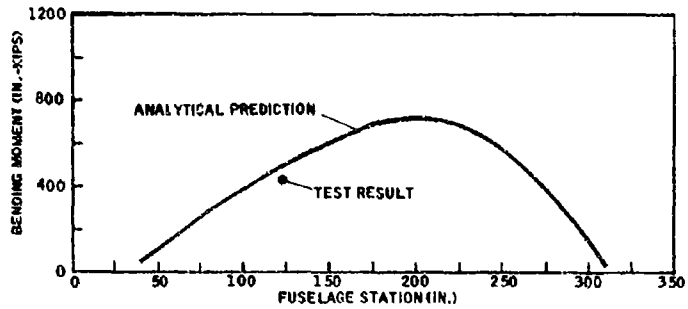

Fig. 8. Bending moment--fuselage model 1, impact on soft ground

stations was a nonlinear partially restoring spring. The first six free-free orthogonal vibration modes and frequencies were computed. The computer program was used to determine the dynamic response of the models under the test conditions.

The analytical results for model 1 are presented in Figs. 7, 8, and 9 with the test results. In the analysis the ground was assumed infinitely stiff, which accounts for the difference between the theoretical and predicted results. The greatest difference occurs in the accelerations (Fig. 7). This is primarily because of the high frequencies, which produce the high accelerations, being attenuated by the soft ground. The bending moments (Fig. 8) that are more closely related to fundamental mode (Fig. 9(C)) have better correlation. Figure 9 illustrates the correlation that exists on the basis of time for two select decelerations and a bending moment. In general the test results and analytical predictions have the same peaks and frequency content.

The analytical and test results for model 2 are presented in Figs. 10, 11, and 12. In the test of model 2 a steel plate (which approaches the assumption made in the analysis) was placed on the impact area. Figures 10 and 11 show good correlation between theory and test for both decelerations and bending moments. The response time variation is also good for model 2 (Fig. 12). Thus, the theory and method of this paper have been demonstrated to give reasonable correlation with test results.

CONCLUSIONS

A practical method has been developed that can be used to determine the dynamic response

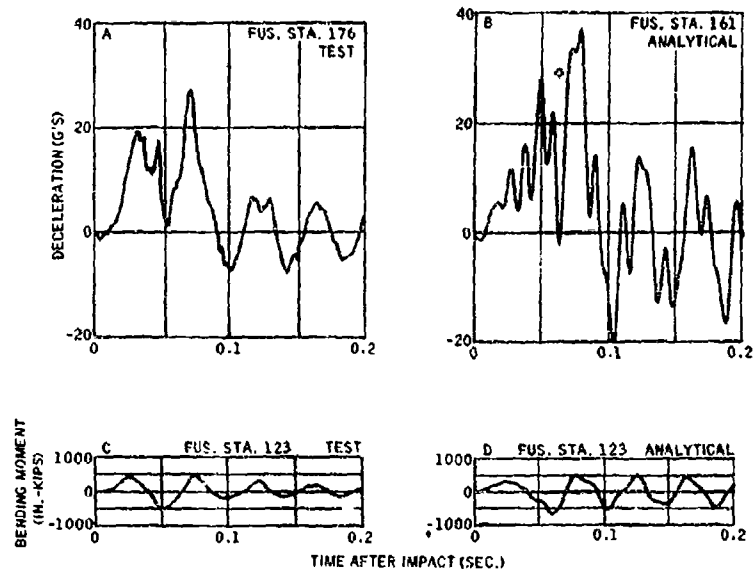

Fig. 9. Deceleration and bending moment--fuselage model 1

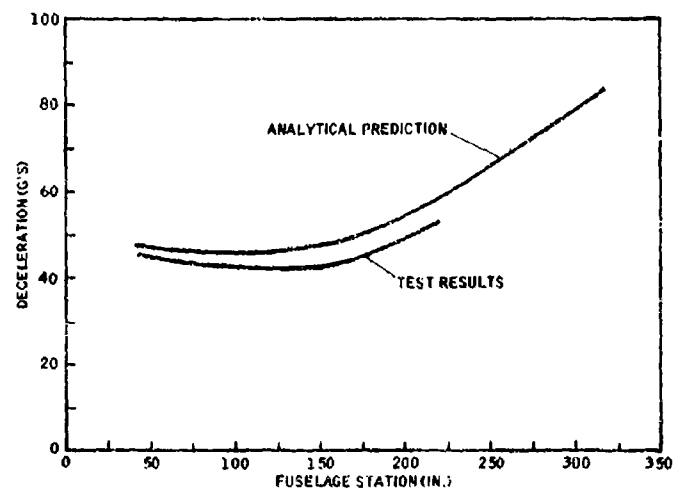

Fig. 10. Deceleration--fuselage model 2, impact on steel plate

of a free-free elastic aircraft structure while impacting the ground.

The fundamental and higher modes must be considered when determining crash loads and decelerations.

The upper fuselage compressive strength is the design condition when ground impact is considered.

The loads developed in a fuselage for the same initial condition are more severe for fuselage contact than for a two-wheel landing.

The method developed in this paper compares well with test results.

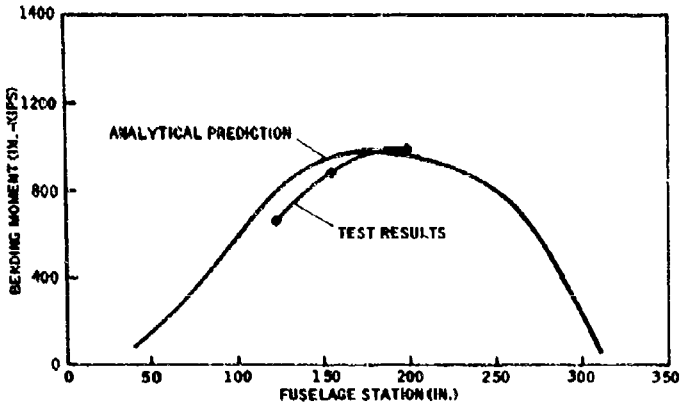

Fig. 11. Bending moment--fuselage model 2, impact on steel plate

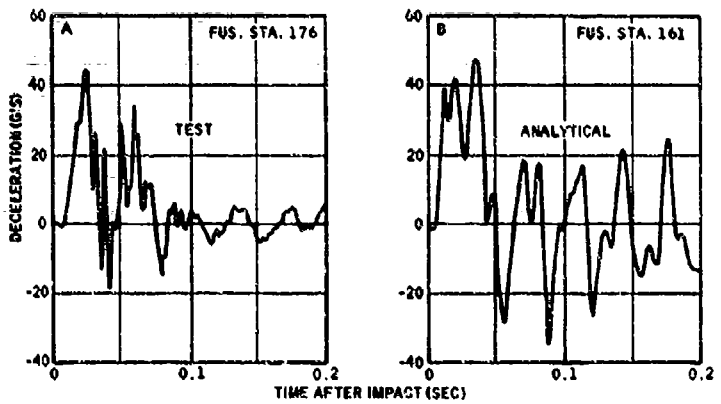

Fig. 12. Deceleration--fuselage model 2

REFERENCES

1. W. H. Reed et al., "Full Scale Dynamic Crash Test of a Lockheed Constallation Model 1649 Aircraft," Federal Aviation Agency, Tech. Rept. ADS-38, Washington, D.C., Oct. 1965

2. D. L. Greer, T. L. Held, and J. D. Weber, "Design Study and Model Structures Test Program to Improve Fuselage Crashworthiness," Federal Aviation Agency, Tech. Rept. DS-67-20, Oct. 1967

3. J. P. Bigham, Jr. and W. W. Bingham, "Theoretical Determination of Crash Loads for a Lockheed 1649 Aircraft in a Crash Test Program," Federal Aviation Agency, Tech. Rept. ADS-15, July 1964

* * *

EFFECT OF TEMPERATURE ON THE VISCOELASTIC HIGH POLYMER MATERIALS

John M. Ohno
The Aerospace Systems Division
The Bendix Corporation
Ann Arbor, Michigan

A chemorheological approach was introduced to interpret mechanical behaviors, such as creep, elastic recovery, retarded recovery, stress relaxation, permanent set, and stiffening. Five stages in three types of stress-strain diagrams were discussed. Temperature dependency of thermoplastic open- and closed-cell foam materials was tested at -50°F (45.5°C), room temperature, and at 160°F (71°C). In the case of silicone, the upper limit test temperature was raised to 300°F (149°C). The materials selected were polystyrene (rigid foam), polyvinylchloride (flexible closed cell), polyetherurethane (flexible open), polyethylene (flexible closed), and silicone (rubbery closed cell). The thermal effects on the stress-strain curve, change in hysteresis area, compression set, and retarded recovery were studied quantitatively. Mechanical and thermal (low temperature) stiffening phenomena were demonstrated clearly. Transmissibility of vibrational energy was also studied at various temperatures.

INTRODUCTION

Unlike most of the structural materials, the relationship between process parameters and properties of end products is not well known. The moduli of high polymers at room temperature depend on the type of filler materials, blowing agent, thermal treatment, and so forth. Temperature dependency of viscoelastic materials is significant because these foam materials are thermoplastic. Transition temperature varies depending on the molecular structure and, in some materials, two transition temperatures are observed: for example, dimethyl silicone which transforms from an amorphous state to crystalline at -70°F, then to a glassy state at approximately -190°F. Polyethylene foam is flexible at room temperature, but is glassy at subzero temperatures. The effective use of high polymers depends substantially on the user's modification. The modification for the particular application requires some background knowledge on materials and processes. Designers must be aware of these properties. Therefore, a study was made on the temperature dependency of high polymer foam materials such as polyurethane, polyethylane, polyvinylchloride, silicone, and polystyrene.

A chemorheological approach is introduced to interpret some differences between various groups.

CHEMORHEOLOGICAL APPROACH

Classification of the Group

Viscoelastic properties of high polymer materials are derived from the following five mechanisms: (a) stretching of primary and secondary bonds, (b) distortion of valence bond angles, (c) rotation of bond axes, (d) stress-activated jumping of molecular elements, and (e) entanglement and chain scission. The first two mechanisms represent elastic property observed in the case of rigid polymers or glassy states below the second-order transition temperature. The next two mechanisms, (c) and (d), represent nonlinear property which involves a relaxation or retardation; this relaxation is called chemical stress relaxation.

Molecular jumping or rotation against intermolecular forces requires a finite time and depends greatly on temperature. The secondary bonds between molecular chains, with the entropy effect, tend to force these chains into a random

contracted configuration. This molecular movement indicates a characteristic viscoelasticity. The last mechanism, (e), is related to permanent entanglement called "set" and degradation caused by chain scissions.

Thus, depending on the property, high polymers are divided into the following groups:

1. amorphous linear high polymers
2. cross-linked amorphous high polymers
3. crystalline high polymers
4. semicrystalline high polymers.

Amorphous Linear High Polymers

The viscoelastic property depends greatly on molecular rotations. An example is shown in Fig. 1(a). Deformation results from movements of segments of the long chain molecules. These movements, which consist of the chains coiling and uncoiling, require a finite time and are delayed by intermolecular and intrasegmental forces.

The flexibility of linear polymer molecules is largely because of the possibility of rotation around single bonds. There is no rotation around the double bond.

As the temperature is raised, the retarded elastic response is gradually dominated by flow. Conversely, if the temperature is lowered, the effect of flow disappears and the configurational elastic response is significantly retarded. The mechanical behavior, thus, depends on temperature.

Cross-Linked Amorphous High Polymers

Cross-linking has a significant effect on mechanical behavior, because a highly cross-linked polymer can not flow, even at elevated temperatures. Thus, a cross-linked polymer has simpler viscoelastic properties than a linear polymer. As the temperature is raised, the retardation in elastic response of a cross-linked polymer simply decreases without the appearance of flow (see Fig. 1(b)).

Crystalline High Polymers

This material has two transition temperatures; namely, glass transition temperature

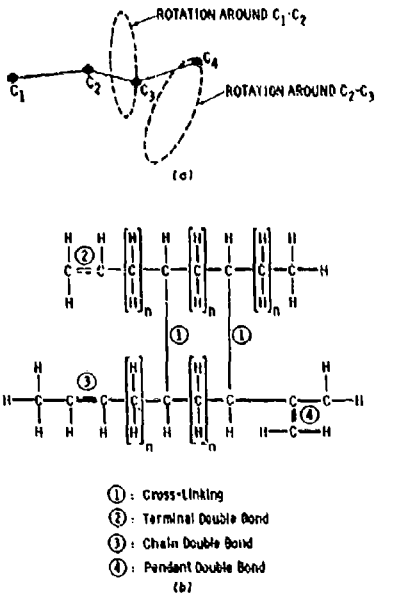

Fig. 1. (a) Molecular rotation around C-C single bonds, and (b) cross-linking and double bond in polyethylene (combination of amorphous and crystalline compounds)

(T_G) and crystalline transition temperature (T_C). Its modulus is the highest at temperatures below T_G. As temperature is raised, the modulus indicates a plateau which is called "rubbery plateau stage." At a certain temperature (T_C), the material transforms from a crystalline state to an amorphous state. As temperature is raised above T_C, flow will occur as a linear amorphous polymer. This is clearly illustrated in Fig. 2 (see Ref. [1]). The stress relaxation modulus Er (t sec) in Fig. 2 is defined as the stress per unit strain necessary to maintain the sample at constant extension for t seconds (such as 10 sec).

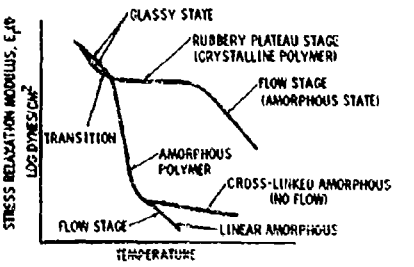

Fig. 2. Modulus-temperature curves

CHARACTERISTICS AND LIMITATIONS OF VARIOUS TYPES OF FOAMS

Silicone

The molecular linkage of silicone (Fig. 3) is relatively simple and, unlike hydrocarbon polymers, silicone has good heat resistance.

The organic groups, R, modify what otherwise would be a purely inorganic silicon oxide or silica glass and provide the desired degree of flexibility.

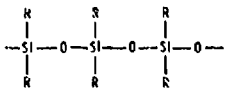

Fig. 3. Molecular structure of silicone

In practice, the R groups are almost always methyl groups (CH_3), but occasionally phenyl (C_6H_5) or ethyl (C_2H_5) groups.

Silicone is made by hydrolyzing pure dimethyl-dichlorosilane and extending the resulting linear polymers to very high molecular weight, so that the chains consist of thousands of dimethyl siloxane units (Fig. 4).

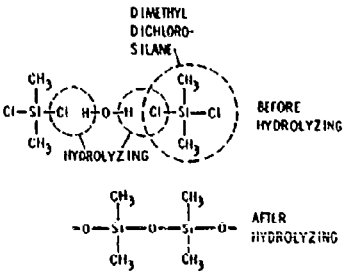

Fig. 4. Hydrolyzing process of dimethyl silicone

Major suppliers of silicone base materials in the United States are Dow Corning, General Electric, and Union Carbide. The so-called RTV silicone rubber, meaning room-temperature vulcanized silicone, requires only the addition of a catalyst for cure at room temperature.

The base compound comprises a reactive silicone prepolymer, a blowing agent, and fillers. The addition of an active catalyst to the system initiates two reactions: vulcanization, and evolution of hydrogen gas. The rate of hydrolyzing reaction must be carefully controlled to obtain consistent results. The addition of fumed silicas as a filler increases the strength of silicone rubber, but also decreases the shelf life of the base compound. Therefore, any modification with strongly acidic or basic materials must be carried out carefully. Table 1 shows an example of modification and the effect of modification on density and deflection [2].

A. V. Tobolsky [3] et al. studied the vulcanized silicone rubbers and emphasized the effect of a catalyst on SiO linkage. Tobolsky attributed the stress relaxation phenomena to an ionic interchange of SiO linkage catalyzed by some unknown reagent (Fig. 5). The chemical stress relaxation phenomena depend greatly on a reagent and temperature.

Polyurethane

The foam material is supplied in many grades which can be distinguished by their load-bearing properties, commonly referred to as "load deflection"; for example, load value at 25 percent, 50 percent, and at 75 percent deflections. ASTM D-1564-61T "Tentative Specifications and Methods of Test for Flexible Urethane Foam" was issued in 1958 (Table 2). However, an increasing variety of applications necessitated many additions to this specification.

The reaction and the final molecular structure of polyurethane are shown in Fig. 6.

There are many modifications depending on other ingredients. Table 3 shows the classification of Polyfoam which is a flexible, open-cell, polyether-based urethane foam material supplied by the General Tire and Rubber Co. Nominal 2 pcf foams have heat distortion temperatures in the range of 200 to 265°F.

Polyethylene

Polyethylene foam is made by mixing a foaming agent with a molten polymer under high pressure. The foaming agent expands under reduced atmospheric pressure and forms an individual cell. The basic molecular structure is $-CH_2-CH_2-CH_2-CH_2-$. However, the actual structure polymerized at a very high pressure is strongly branched. (See Fig. 1(b) for cross-linked and branched structure.) Polyethylenes are classified by density: (a) low density, (b) medium density, and (c) high density. Low density polyethylene foam is flexible and displays high impact strength, but is relatively low heat resistant. The maximum service temperature

TABLE 1
Effect of Blend Formula on Density and Deflection[a]

Blend Formula	Thickness (in.)	Compression Deflection ($lb/in.^2$)			Density (lb/ft^3)
		10%	25%	50%	
RTV-7	0.125	0.5	1.0	2.9	16.7
RTV-7 + RTV-11 (100 pts) (25 pts)	0.125	0.8	1.9	5.3	19.4
RTV-7 + RTV-60 (100 pts) (25 pts)	0.125	0.8	1.7	5.7	21.2
RTV-7 + RTV-90 (100 pts) (25 pts)	0.125	1.1	2.2	8.3	24.8

[a]See Ref. [2].

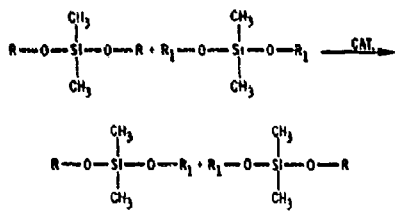

Fig. 5. Chemical stress relaxation by a catalyst

TABLE 2
Flexible Urethane Foam (ASTM D-1564)

	Foam Type	
	Polyether	Polyester
Density (lb/ft^3)	1.1 to 2.3	1.6 to 2.0
Tens st (psi)	9 to 22	25 to 33
Ult elong (%)	222 to 310	250 to 500
Tear st (lb/linear in.)	2 to 4	2.3 to 4.2
Compression deflection at (psi):		
25% comp	0.15 to 0.6	0.46 to 0.48
50%	0.2 to 0.7	0.56 to 0.80
75%	0.4 to 1.6	1.29 to 2.09
Compression set 158°F, method B, at:		
50% comp 22 hr	3 to 4	3.5 to 6.0
90% comp 22 hr	6 to 8	8 to 20

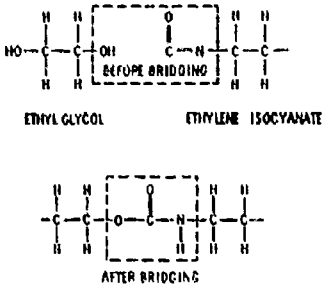

Fig. 6. Formation of polyurethane

recommended is only 175°F. It becomes stiffer at low temperatures and has a strong tendency to crystallize. However, because this foam is a thermoplastic material, it becomes increasingly flexible at higher temperatures. Although the foam has some thermal insulation property, it is not normally considered as a thermal insulator, but rather a shock and vibration isolator.

According to MIL-C-46842 (8 Nov. 1965), the low density polyethylene foam must satisfy the following properties: density, 1.0-2.6 lb/ft^3; compression strength, < 8 psi; compression set, <10 percent.

The cushioning ability of polyethylene at lower temperatures is much less than at room temperature because of the stiffening phenomena. Polyethylene is more heat-stable than polystyrene. The reaction products for polyethylene contain paraffins with up to 50 carbon atoms, and contain little monomer. Degradation starts at about 310°C.

Polyvinylchloride

Polyvinyl foams are available as either open- or closed-cell structures in both flexible and rigid foams. Flexible polyvinyl foams are very sensitive to temperature. Flexible foams can not be used continuously at temperatures over 150°F. Rigid foams, however, retain 80 percent of their mechanical properties at 200°F, and can withstand 300°F if the service is intermittent.

The molecular structure of polyvinyl chloride is a simple, head-to-tail linear high polymer (Fig. 7). Flexible PVC is a plasticized material that often contains, in addition to plasticizers, other ingredients such as stabilizers and pigments.

VS 400 CG-PVC is made by B. F. Goodrich under the trade name Koroseal Foam. This is the most flexible grade closed-cell foam material.

Polystyrene

Rigid thermoplastic polystyrene foams are available in densities ranging from about 1 pcf to over 20 pcf. Foams are made from the polystyrene beads by applying heat which causes the beads to expand, crushing them together in a closed container (or mold), and fusing them into a closed-cell material. The beads are expanded over 45 times their original volume. The disadvantages follow: (a) high compression set, (b) poor acoustical resistance, (c) creep, (d) poor heat resistance, and (e) nonuniformity. However, the thermal insulation properties are excellent, and their K-factor compares favorably with many other insulation materials.

Polystyrene is a thermoplastic material that is easily distorted by heat. One modification called polymethylstyrene has a relatively high heat distortion point (310°F).

Degradation of polystyrene is divided into three categories: (a) degradation in vacuum, (b) oxidative degradation, and (c) mechanical degradation.

Degradation in Vacuum — The weak points in the polymer chains are indicated by the arrows in Fig. 8. The reaction products for polystyrene consist mainly of monomer and dimer.

Oxidative Degradation — The mechanism can be assumed to be as follows:

Polystyrene + O_2
↓
Polystyrene hydroperoxide
↓
Chain scission.

Degradation of polystyrene was observed at 103°C. However, under ultraviolet radiation, the degradation was initiated even at 60°C (Fig. 9).

Mechanical Degradation — Bimolecular and monomolecular reactions are considered. The rate of degradation (Fig. 10) as a function of chain length was calculated by N. Sato et al. and H. Jellinek et al. The primary break of polystyrene is coupled with a migration of a labile hydrogen atom.

TABLE 3
Grades of Polyfoam

	P-7	P-10	P-12	P-17	P-22	P-25	P-55	P-65	P-137	P-200	P-220	P-230
Load deflection (based on 4 x 5 x 15 in.)												
At 25% deflection	8-11 lb	12-17 lb	16-21 lb	22-27 lb	28-33 lb	34-40 lb	53-63 lb[a]	40-48 lb	26-31 lb	15-20 lb	21-26 lb	27-32 lb
At 65% deflection	16 lb min	23 lb min	31 lb min	45 lb min	54 lb min	70 lb min	—	80 lb min	50 lb min	—	—	—
80% Compression set	—	—	—	15% max	15% max	15% max	15% max	15% max	15% max	—	15% max	15% max
50% Compression set	20% max	20% max	20% max	—	—	—	—	—	—	15% max	—	—
Dry heat resistance (max change in tensile strength)	±20%	±20%	±20%	±20%	±20%	±20%	±20%	±20%	±20%	±20%	±20%	±20%
Humidity resistance (percent change in load deflection after 5 hr at 250°F)	±10%	±10%	±10%	±10%	±10%	±10%	±10%	±10%	±10%	±10%	±10%	±10%
Tensile strength (psi) min	4.0	5.0	5.0	10.0	10.0	12.0	12.0	12.0	10.0	6.0	8.0	10.0
Tear strength (lb/in.) min	0.5	1.0	1.0	1.5	1.5	1.5	0.8	1.0	1.5	1.2	1.4	1.5
Elongation (%) min	175	175	175	180	150	150	100	120	175	150	150	150
Flex fatigue (max percent loss in ILD after 250 kc to 75% deflection)	—	—	—	30	30	30	30	30	30	20	20	20

[a] Load values are based on a 15 x 15 x 2 in. specimen.

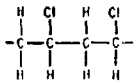

Fig. 7. Molecular structure of typical PVC

Fig. 8. Weak points in polystyrene polymer

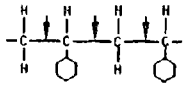

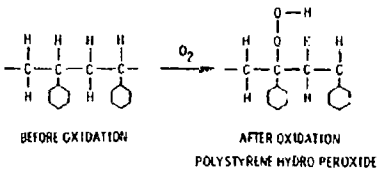

Fig. 9. Oxidative degradation

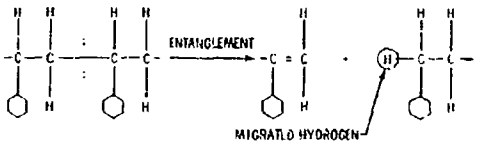

Fig. 10. Chemomechanical degradation

TEST SPECIMENS AND PROCEDURES

Selection of Foam Materials

Applications of foam materials (either shape, block, or pad) are grouped into four purposes: (a) isolation of shock and vibration, (b) thermal insulation, (c) electrical insulation, and (d) acoustical insulation. The selection of foam materials must be based on the particular application. Mechanical properties are a function of base plastic resin, the density, type of cells (open or closed), blowing agent, and cell size.

Table 4 lists the foam materials selected for this study, and Table 5 includes specimen sizes for the static test. Unfortunately, the manufacturers' specifications are not consistent. Table 6 lists the properties of RTV-7 silicone rubber foam manufactured by General Electric Co. In Table 4, selected grades of polyfoam supplied by the General Tire & Rubber Co. are shown.

Static Test Procedure

This static test is run to investigate the thermal effect on the stress-strain curve, change in hysteresis area, compression set, and retarded recovery.

A load was applied at a constant compression rate of 180 lb/min on 6- x 6-in. samples. A linear displacement variable transformer was used to observe the strain of each sample.

For comparison, a 50 percent deflection load, based on the stress-strain diagram, was determined for each sample. The plastic deformation was recorded twice: immediately after the removal of load, and after 4 hr.

TABLE 4
Foam Materials Selected for the Test

Types	Group	Cell	Trade Name and Grade
Polyether-Urethane	Flexible	Open cell	Polyfoam P-12, P-25, P-65 (General Tire & Rubber Co.)
Polyethylene	Flexible	Closed cell Expanded	Ethafoam 2 lb/ft^3 (Dow Chemical)
Polyvinyl Chloride	Flexible	Closed cell	Koroseal Foam VS400, 4 lb/ft^3 (B. F. Goodrich)
Polystyrene	Rigid	Closed cell Expanded	Falconfoam 1 lb/ft^3 (Falcon Manufacturing Co.)
Silicone	Rubbery	Closed Cellular	RTV-7 silicone 12.5 lb/ft^3 (General Electric)

TABLE 5
Foam Specimens (6 in. x 6 in. x thickness)

Sample No.	Type	Grade	Thickness (in.)
1	Silicone	RTV-7 (12.5 pcf)	0.55
2	Silicone	RTV-7 (12.5 pcf)	0.87
3	Silicone	RTV-7 (12.5 pcf)	1.05
4	PVC	Flexible PVC (4-5 pcf)	0.5
5	PVC	Flexible PVC (4-5 pcf)	1.03
6	PVC	Flexible PVC (4-5 pcf)	2.0
7	Polyether-Urethane	Flexible, open, P-12	0.5
8	Polyether-Urethane	Flexible, open, P-12	0.98
9	Polyether-Urethane	Flexible, open, P-12	2.0
10	Polyether-Urethane	Flexible, open, P-12	4.0
11	Polyether-Urethane	Flexible, open, P-12	6.0
12	Polyether-Urethane	Flexible, open, P-25	0.52
13	Polyether-Urethane	Flexible, open, P-25	1.0
14	Polyether-Urethane	Flexible, open, P-25	2.03
15	Polyether-Urethane	Flexible, open, P-25	4.0
16	Polyether-Urethane	Flexible, open, P-25	6.0
17	Polyether-Urethane	Flexible, open, P-65	0.5
18	Polyether-Urethane	Flexible, open, P-65	1.05
19	Polyether-Urethane	Flexible, open, P-65	2.03
20	Polyether-Urethane	Flexible, open, P-65	4.0
21	Polyether-Urethane	Flexible, open, P-65	6.0
22	Polystyrene	Rigid, closed, expanded, 1 pcf	0.52
23	Polystyrene	Rigid, closed, expanded, 1 pcf	1.0
24	Polystyrene	Rigid, closed, expanded, 1 pcf	1.98
25	Polyethylene	Flexible, closed, expanded, 2 pcf	0.5
26	Polyethylene	Flexible, closed, expanded, 2 pcf	1.0
27	Polyethylene	Flexible, closed, expanded, 2 pcf	1.97

TABLE 6
Specification of RTV-7 Silicone Rubber Foam[a]

Base Compound	
Viscosity, cps at 77°F	7000-9000
Color	Black
Specific gravity	1.11 ± 0.02
Shelf life	3 months
Cured TRV-7 (5 wt % Stannous Octoate) 50% relative humidity	
RTV tack free time	5 ± 2 min
Density, max	12.5 lb/ft^3
Tensile strength (0.08-in. thick, ASTM)	20 psi
Elong (ASTM)	70%
Compression set of post cured sample[b]	
50% compression for 22 hr at 212°F	5%

[a]See Ref. [2].
[b]Post curing: 1 hr at 212°F.

Selection of Test Temperature

The test temperature should stay within the limits of service temperature. Therefore, Table 7 is based on a state-of-the-art study of the heat-resistance capability of various foam materials.

Table 7 shows that PVC and polystyrene have poor capability. A range of -50°F to +160°F was selected for the study of foam specimens with the exception of silicone. Silicone, which has an excellent heat and low temperature capability, was tested at 300°F to -50°F.

EFFECT OF TEMPERATURE

Transition Temperature

The transition from an amorphous to a glassy state or from a crystalline to a glassy state takes place at a definite temperature (or within a certain temperature range). The midpoint transition temperature (T_m) is determined by taking a rms value between the glassy and the rubbery moduli. (See Table 8 and Refs. [1] and [4].)

T_G is often called the second-order transition temperature. Some materials (such as dimethyl silicone) have a so-called crystalline transition temperature (T_C) which is a transition temperature from an amorphous state to a crystalline state.

Dimethyl and Methyl-Phenyl Silicones

If one of the methyl groups (CH_3) is replaced by phenyl group (C_6H_5), a special low temperature silicone called methyl-phenyl silicone is obtained. Dimethyl silicone transforms from amorphous to crystalline at approximately -70°F, but methyl-phenyl silicone does not have such a transformation. Both types, however, transform to glassy state at approximately -190°F. The change in length vs temperature for these two silicones is illustrated in Fig. 11 (see Ref. [5]). Figures 12 (see Refs. [5] and [6]) and 13 (see Ref. [6]) are the results of tensile

TABLE 7
Approximate Service Temperature Limits (°F)

Polymer	Lower Limit (°F)	Upper Limit (°F)
Silicone { Dimethyl	-80	500
Silicone { Methyl-phenyl	-160	500
Polyurethane	-50	200 265
Polyethylene	-50	175
Phenolics	-32	250
PVC	20	150
Polystyrene	RT	170

TABLE 8
Glass Transition Temperature (T_G) and Midpoint Glass Transition Temperature (T_m) (°F)

Polymer	T_G	T_m
Polystyrene	100*	116* 92 to 105†
Polyvinylchloride (rigid)	74* 82†	90*
Polyurethane (ester base)	-35*	--
Polyethylene	--	-5 to 0*
Silicone	-123†	--

*See Ref. [4].
†See Ref. [1].

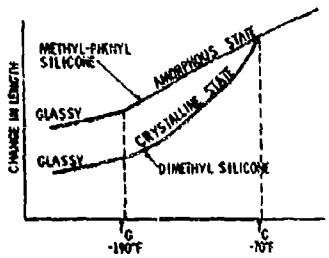

Fig. 11. Change in length vs temperature for two types of silicone

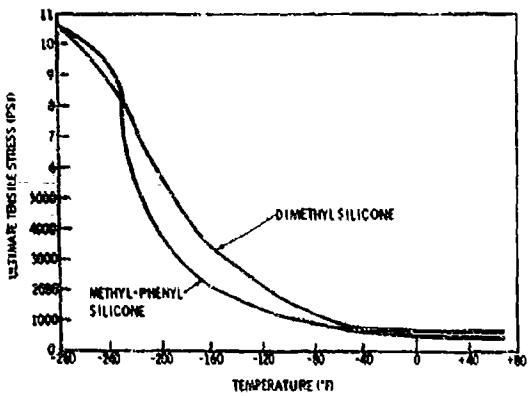

Fig. 12. Ultimate tensile stress vs temperature (RTV-silicone)

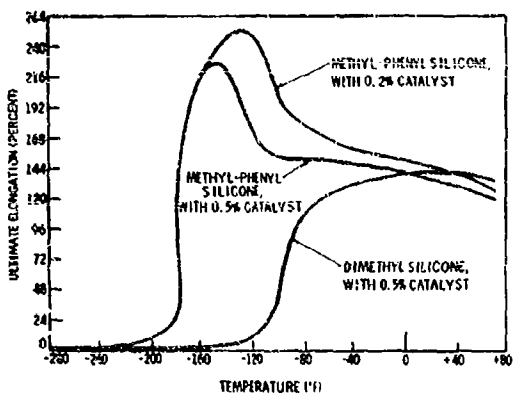

Fig. 13. Ultimate elongation vs temperature (RTV-silicone)

tests at various temperatures; Fig. 12 illustrates the difference in percent elongation.

CHANGES IN HYSTERESIS DIAGRAM

Classification

Flexible or rubbery foam materials, unlike metallic materials, indicate characteristic buckling and bottoming. Bottoming is defined as a drastic increase in stress with negligible increase in strain. Often called stiffening, bottoming must not be confused with low temperature stiffening. To distinguish these two phenomena, in this paper the former is called deformation stiffening, and the latter low temperature stiffening. The other feature noticed in the compressive stress-strain diagram is a buckling, which is an opposite phenomena. It is defined as a drastic change in height with negligible increase in stress. In other words, a typical stress-strain diagram of flexible foam materials is composed of five stages: buckling, transition, bottoming, stress relaxation, and recovery. Depending on grades or types of material and temperature, buckling, transition, and recovery vary significantly. Careful examination of the stress-strain curves and hysteresis diagrams revealed that there are actually three types: type 1 – flexible or rubbery type materials such as silicone foam, polyether-urethane foam, room temperature very soft PVC; type 2 (mixed type) – semiflexible and semiglassy materials such as polyethylene (Ethafoam); and type 3 – rigid type for glassy materials such as polystyrene foam and cold temperature PVC.

Silicone

Figure 14 illustrates the compressive stress-strain curves for dimethyl silicone foams. The five typical stages (buckling, transition, stiffening, rapid stress relaxation, and rapid recovery) are shown in both a room temperature test and a -50°F test. Low temperature stiffening was clearly observed at -50°F. This temperature is still above the glass transition temperature of dimethyl silicone. Therefore, a complete rapid recovery was observed even though the foam was stiffened considerably. When the test temperature approaches the glass transition temperature (approximately -190°F), the diagram indicates much greater hysteresis and a definite retardation in recovery because of significant low temperature stiffening. Figure 15 [6] shows an example of methyl-phenyl silicone (low temperature silicone) which was tested at -180°F by Robinson and Schreihans.

Polyether-Urethane

Figure 16 illustrates the stiffening effect of low temperature (-50°F) on polyfoam (P-12).

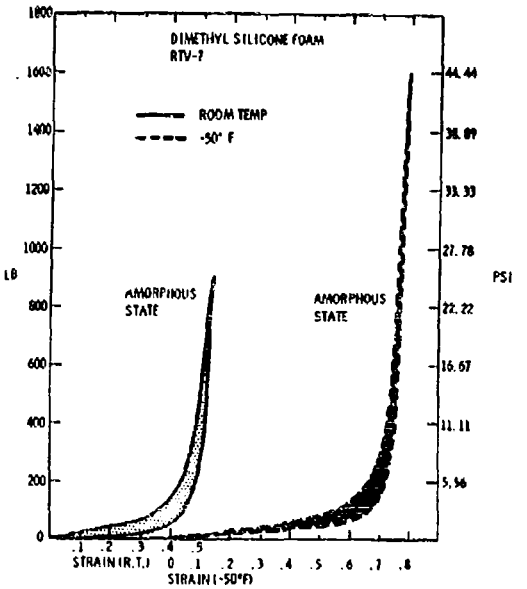

Fig. 14. Stress-vs-strain curve for dimethyl silicone at room temperature and -50°F

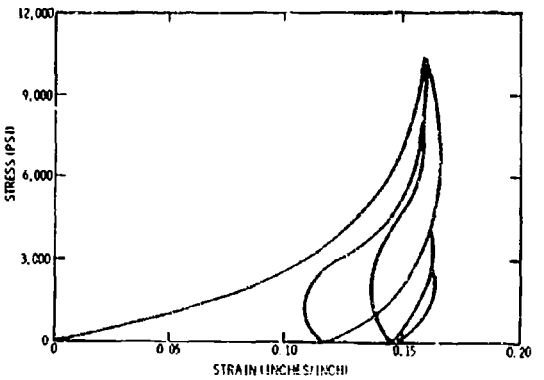

Fig. 15. Stress-vs-strain curve for methyl-phenol silicone at -180°F

The diagram is very similar to that of silicone, and is classified as type 1. The only difference is the fifth stage (recovery stage) in which a definite retardation in recovery was observed. About 90 percent of compression set is shown in Fig. 16. This deformation set recovers at room temperature and not at subzero temperatures. Reexaminations after 4 hr at room temperature indicate almost complete recovery. Based on this static test, the cushioning ability is inferior to that of silicone. Static conditions do not simulate actual dynamic conditions. However, this study could be used at least to predict qualitatively dynamic behaviors of this material at various temperatures.

PVC Foam

The hysteresis diagram of a very soft flexible PVC foam is similar to that of silicone. In other words, the stress-strain diagram is in the category of type 1. However, PVC foam is in glassy state at -50°F, and the curve is entirely different (Fig. 17). Elastic buckling was not observed in this case. Lower temperature

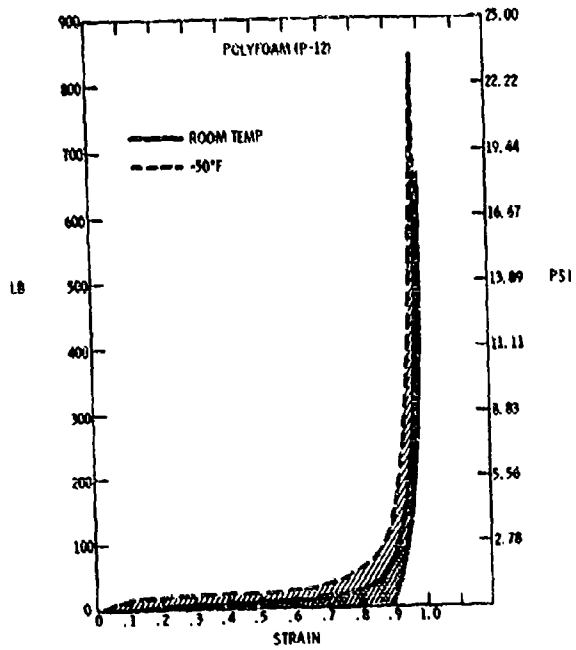

Fig. 16. Stress-vs-strain curve for polether-urethane at room temperature and -50°F

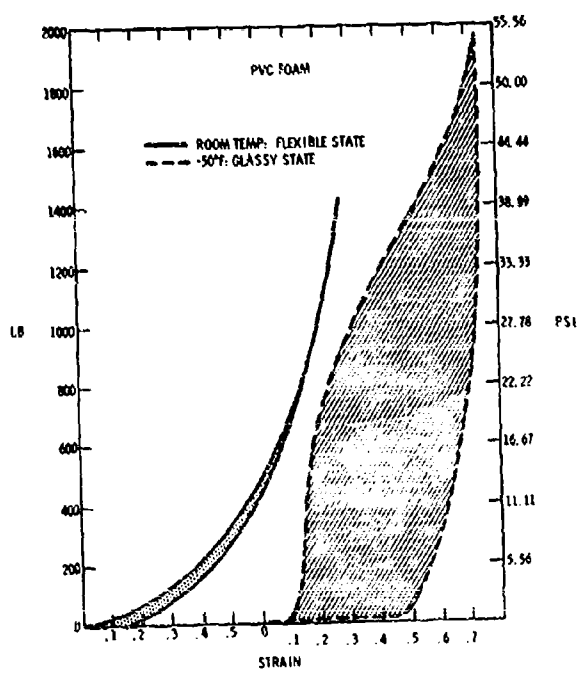

Fig. 17. Stress-vs-strain curve for PVC foam at room temperature and -50°F

stiffening retarded the recovery, and the larger hysteresis area was observed. The glassy state PVC and rigid-type polystyrene are therefore grouped in type 3. A great percentage of permanent set and a large hysteresis area are the major disadvantages of this type of foam. The application is therefore limited.

Polyethylene

The stress-strain curve of polyethylene is between the rubbery and glassy types, and can be classified as type 2. Careful examination of Fig. 18 revealed five stages: initial hardening, retarded buckling, strain hardening, rapid stress relaxation, and retarded recovery. The effect of low temperature stiffening is clearly shown in Fig. 18. Larger hysteresis areas were observed as temperature was lowered.

Effect of Cold Temperature on Hysteresis Diagram

Table 9 is a summary of hysteresis diagrams. As temperature is lowered, the stiffening of a material causes a gradual increase in the hysteresis area without changing the type. Upon further decrease in temperature, it will finally transform from type 1 to type 2, or type 2 to type 3, or from type 1 to type 3, directly.

Table 10 shows a quantitative study of hysteresis diagrams. Cold temperatures increase the hysteresis area without exception.

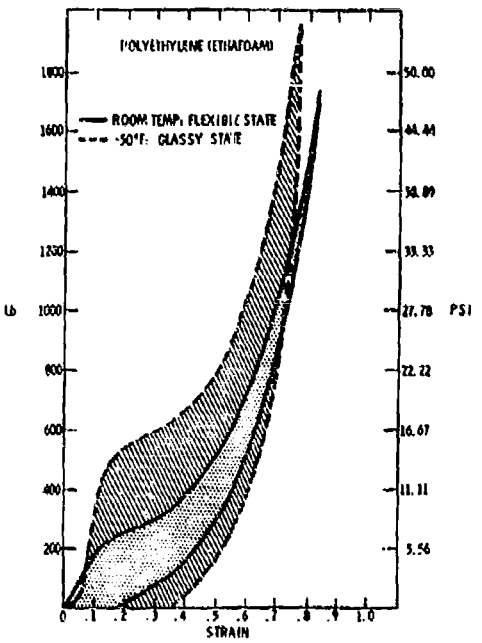

Fig. 18. Stress-vs-strain curve for polyethylene at room temperature and -50°F

RETARDED RECOVERY

Table 11 shows two compression sets and a 50-percent deflection load for each specimen. Falconfoam, because it is a rigid type, indicated the highest permanent compression set.

TABLE 9
Five Stages in Three Types of Stress-Strain Diagrams

Stage	Type 1 (Flexible, Rubbery Type)	Type 2 (Semi-Type)	Type 3 (Rigid Type)
1	Elastic buckling	Initial hardening	Initial hardening
2	Transition stage	Retarded buckling	Gradual yielding
3	Elastic bottoming	Strain hardening	Strain hardening
4	Rapid stress relaxation	Rapid stress relaxation	Rapid relaxation
5	a. Complete recovery b. Retarded complete recovery	a. Partial recovery b. Retarded recovery	Incomplete recovery
Example	Silicone Polyether Urethane (Polyfoam) Very soft PVC (room temp.)	Polyethylene	Polystyrene PVC (cold temp.)
Hysteresis Area	Smallest →	Medium →	Largest

TABLE 10
Effect of Cold Temperature on Hysteresis Diagrams

Specimen No.	Temp. (°F)	Area (lb-in.)		Hysteresis Area	Change in Hysteresis Area
		Loading	Unloading		
Silicone No. 1	Rm	0.127	0.067	0.060	
	-50	0.225	0.155	0.070	Increase
Silicone No. 2	Rm	0.165	0.060	0.095	
	-50	0.257	0.157	0.100	Increase
PVC No. 5 (Polyvinyl-chloride)	Rm	0.859	0.766	0.093	
	-50	1.852	0.298	1.554	Increase
	2nd Rm	1.005	0.715	0.290	
PVC No. 6	Rm	1.503	1.275	0.138	
	-50	3.014	0.824	2.190	Increase
Polyfoam No. 8 (Polyether)	Rm	0.079	[illegible]	0.054	
	-50	0.141	0.025	0.116	Increase
	2nd Rm	0.056	0.005	0.051	
Ethafoam No. 26 (Polyethylene)	Rm	1.162	[illegible]	0.302	
	-50	1.460	0.424	1.036	Increase
	2nd Rm	1.279	0.674	0.605	
Ethafoam No. 27	Rm	1.944	1.214	0.730	
	-50	2.490	0.980	1.510	Increase

TABLE 11
Room Temperature Compression Test of Foam Materials
(Pressure Rate, 180 lb/min)

Type	Sample No.	Thickness (in.)	Max Comp			Comp at 50%		Comp Set (%)	
			lb	psi	%	lb	psi	Immediate	After 4 hr
Silicone	1	0.55	675	19.0	73	120	3.3	0	0
	2	0.87	940	26.0	60	200	5.5	17	0
	3	1.05	1340	37.0	77	50	1.4	0	0
PVC	4	0.5	1350	37.5	86	300	8.4	0	0
	5	1.03	1450	40.0	85	325	9.0	12.6	6
	6	2.0	1125	31.0	80	500	14.0	6	2
Polyfoam P-12	7	0.5	275	8.0	98	5	0.14	84	2
	8	0.98	670	19.0	98	5	0.14	86	0
	9	2.0	340	9.5	91	5	0.14	75	0.5
	10	4.0	1000	28.0	98	5	0.14	0	0
	11	6.0	1350	37.5	97	5	0.14	0	0
Polyfoam P-25	12	0.52	365	10.0	98	20	0.56	48	2
	13	1.0	740	21.0	99	20	0.56	5	1
	14	2.03	595	16.5	91	20	0.56	75	0.5
	15	4.0	1300	36.0	95	30	0.84	0	0
	16	6.0	1500	41.5	96	30	0.84	0	0
Polyfoam P-65	17	0.5	395	11.0	99	30	0.84	0	4
	18	1.05	520	14.5	99	30	0.84	6	4
	19	2.03	475	13.0	94	30	0.84	10	1
	20	4.0	1300	36.0	94	40	1.1	8	0
	21	6.0	1600	44.5	95	40	1.1	8.4	0
Falconfoam	22	0.52	1700	47.0	70	900	25.0	50	32.7
	23	1.0	1850	51.0	85	900	25.0	50	50
	24	1.98	1740	48.0	86	770	21.0	84	79.5
	25	0.5	1600	44.5	82	550	15.0	16	0
	26	1.0	1740	48.0	83	530	15.0	15	5
	27	1.97	1600	44.5	74	620	17.0	15	3

Therefore, the subsequent tests of this material were abandoned. Other specimens indicated significant recoveries during 4 hr at room temperature.

Table 12 is a summary of cold tests at -50°F. Retarded recoveries are shown under the immediate compression set column. These are much greater than those at room temperature; silicone is the exception. The differences between two columns of compression sets represent recovered portions during 4 hr at room temperature. Silicone indicated a complete recovery even at -50°F.

EFFECT OF ELEVATED TEMPERATURE

Creep

Thermoplastic foam materials creep more at higher temperatures regardless of their type. Figure 19 [7] is an example. Compressive creep of the ethafoam at 73°F and 155°F is compared under varying stress conditions. A load of 1-psi static stress indicates negligible creep at room temperature, but the same load condition showed a significant creep at 155°F.

Recovery

The difference between room temperature recovery and elevated temperature recovery of rubbery foam such as silicone is negligible, because silicone is the most heat-resistant material (Table 13). Silicone also indicated negligible difference in recovery time at subzero temperatures (Table 12). Silicone always indicated a complete recovery immediately.

All other thermoplastic foams recover their original height much faster at elevated temperatures. The difference between room

TABLE 12
Cold Test at -50°F
(Pressure Rate, 180 lb/min)

Type	Sample No.	Thickness (in.)	Max Comp			Comp at 50%		Comp Set (%)	
			lb	psi	%	lb	psi	Immediate	After 4 hr at RT
Silicone	1	0.55	1600	44.5	84	60	1.7	0	0
	2	0.87	1600	44.5	83	60	1.7	0	0
	3	1.05	1650	44.5	67	100	2.8	0	0
PVC	4	0.5	2040	57.0	75	1500	42.0	34	12
	5	1.03	1960	54.0	70	1350	37.0	42	6.8
	6	2.0	1840	51.0	67	1150	32.0	32	2
Polyfoam P-12	7	0.52	820	23.0	85	15	4.2	68	7.7
	8	0.98	850	24.0	95	20	0.56	90	—
	9	2.0	1600	44.5	79	20	0.56	90	1
	10	4.01	1600	44.5	99	25	0.7	95	0
	11	6.05	1200	33.0	95	30	0.84	91	0
Polyfoam P-25	12	0.52	810	22.5	96	75	2.1	70	5.7
	13	1.0	1130	31.5	94	75	2.1	75	7
	14	2.03	1740	48.5	97	75	2.1	80	2.5
	15	3.99	1850	51.5	99	125	3.5	80	0
	16	5.95	2000	55.5	98	75	2.1	60	0
Polyfoam P-65	17	0.50	840	23.5	98	75	2.1	80	8
	18	1.05	840	23.5	90	75	2.1	80	5
	19	2.03	730	20.0	88	100	2.8	71	4.9
	20	3.99	1850	51.5	97	110	3.0	75	0
	21	5.96	2000	55.5	94	80	2.2	66	0
Falconfoam	22	—	—	—	—	—	—	—	—
	23	—	—	—	—	—	—	—	—
	24	—	—	—	—	—	—	—	—
Ethafoam	25	0.5	1950	54.0	82	800	22.0	37	2
	26	1.0	1970	55.0	76	800	22.0	34	5
	27	1.97	1970	55.0	72	850	24.0	30	5

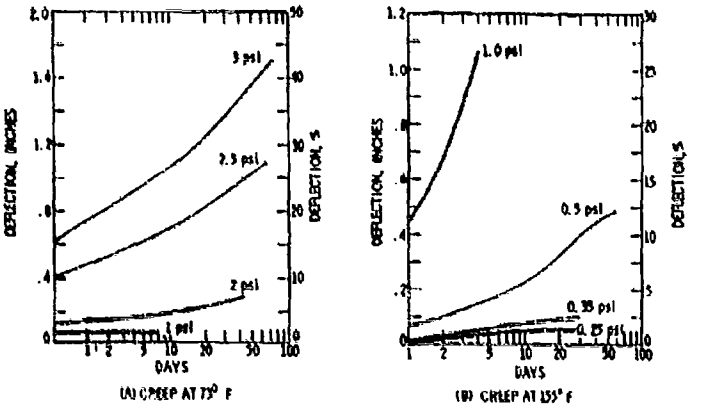

Fig. 19. Effect of temperature on compressive creep of 4- x 4- x 4-in. ethafoam

TABLE 13
Static Compression Tests at 300°F

Type	Sample	Thickness (in.)	Max Comp			Comp at 50%		Comp Set	
			lb	psi	%	lb	psi	Immediate	After 4-hr Recovery
Silicone	1	0.54	1630	45.5	95	65	1.8	—	0
Silicone	2	0.92	1800	50.0	97	80	2.2	0	0
Silicone	3	1.08	2000	55.5	95	30	0.84	0	0

temperature recovery and elevated temperature recovery of ethafoam from 50 percent compression is shown in Fig. 20 [7].

The room temperature recovery of falconfoam after hot tests at 160°F was extremely slow, and the next was ethafoam as shown in Table 14.

A comparison of 50 percent compression stress indicated softening tendency of materials at 160°F (Table 15).

VIBRATION STUDY

Effect of Temperature on Natural Frequency

The natural frequencies of component parts of the packaged item have been estimated by using the following formula:

$$f_n = \frac{2G}{\sqrt{H}}$$

where

f_n = natural frequency,

G = designated G factor, and

H = drop height (in.).

Figure 21 [7] gives the relationship between natural frequency and static stress for four thicknesses of ethafoam at -40°F, +73°F, and +165°F. The above formula is given only to provide a rough estimate. If the estimated f_n is close to the input frequencies, a vibration test must be performed to determine experimentally the resonant frequency and effects on the item.

Vibration Test Procedure

The vibration test was performed using the Ling 249 vibration exciter with the fixture mounted as shown in Fig. 22(a). A sample-mass-sample arrangement was placed in the fixture as shown in Fig. 22(b). The plate above the top sample merely held the latter in place and did not load the setup. Restraining leads of nylon cord were attached to the mass to

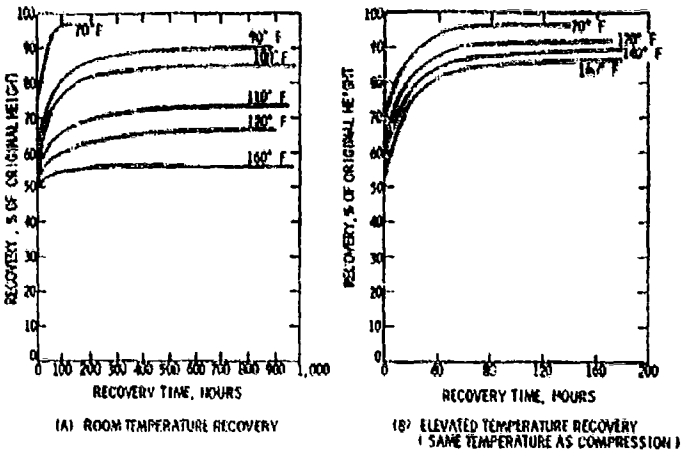

Fig. 20. Effect of temperature on recovery speed after 50 percent compression for 22 hr at various temperatures (ethafoam)

TABLE 14
Static Compression Tests at 160°F

Type	Sample No.	Thickness (in.)	Max Comp			Comp at 50%		Comp Set (%)	
			lb	psi	%	lb	psi	Immediate	After 4-hr Recovery
Silicone	1	0.54	1600	44.5	97	70	1.95	0	0
	2	0.92	1900	53.0	97	60	1.7	0	0
	3	1.08	2000	55.5	95	10	0.28	0	0
PVC	4	0.50	2000	55.5	94	280	7.9	10	6.0
	5	1.00	2250	62.5	93	300	8.4	10	7.0
	6	2.06	2450	68.0	92	300	8.4	10	5.8
Polyfoam P-12	7	0.54	600	16.8	99	5	0.14	10	0
	8	0.97	750	21.0	98	5	0.14	80	0
	9	2.00	920	26.0	99	5	0.14	70	0
	10	3.99	1050	29.0	98	5	0.14	80	0
	11	5.89	1340	38.0	98	5	0.14	80	0
Polyfoam P-25	12	0.51	615	17.0	99	30	0.84	0	0
	13	1.02	800	22.0	99	15	0.4	50	0
	14	2.05	1100	31.0	99	25	0.7	50	0
	15	3.94	1470	41.0	98	30	0.84	10	0
	16	5.98	1750	48.5	98	30	0.84	8	0
Polyfoam P-65	17	0.51	735	20.0	98	30	0.84	0	0
	18	1.01	1465	41.0	99	30	0.84	0	0
	19	2.01	1600	44.5	99	30	0.84	7	0
	20	3.98	1750	48.0	98	30	0.84	6	0
	21	5.95	2000	55.5	97	30	0.84	8	0
Falconfoam	22	0.52	2300	64.0	92	—	—	75	44
	23	1.03	2650	73.6	95	—	—	50	43
	24	2.01	2850	79.0	90	—	—	75	49
Ethafoam	25	0.52	2450	68.0	94	300	8.4	40	23
	26	1.03	2600	72.2	95	450	12.5	25	19
	27	2.05	2850	79.0	94	450	12.5	12	10

TABLE 16
Comparison of 50% Compression Stress

Type	Sample No.	RT		160°F	
		lb	psi	lb	psi
Silicone	1	120	3.3	70	1.95
	2	200	5.5	60	1.7
	3	50	1.4	10	0.28
PVC	4	300	8.4	280	7.9
	5	325	9.0	300	8.4
	6	500	14.0	300	8.4
Polyfoam P-12	7	5	0.14	5	0.14
	8	5	0.14	5	0.14
	9	5	0.14	5	0.14
	10	5	0.14	5	0.14
	11	5	0.14	5	0.14
Polyfoam P-26	12	20	0.56	30	0.84
	13	20	0.56	15	0.4
	14	20	0.56	25	0.7
	15	30	0.84	30	0.84
	16	30	0.84	30	0.84
Polyfoam P-60	17	30	0.84	30	0.84
	18	30	0.84	30	0.84
	19	30	0.84	30	0.84
	20	40	1.1	30	0.84
	21	40	1.1	30	0.84
Falconfoam	22	--	—	—	—
	23	900	25.0	—	—
	24	770	21.0	—	—
Ethafoam	25	560	15.0	300	8.4
	26	630	16.0	450	12.5
	27	620	17.0	450	12.5

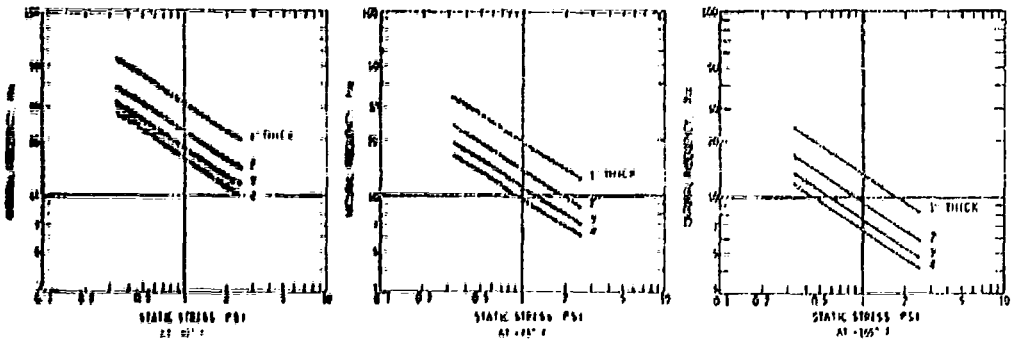

Fig. 21. Natural frequency vs static stress of ethafoam

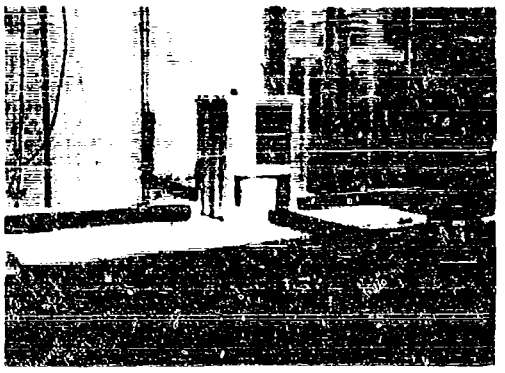

(a)

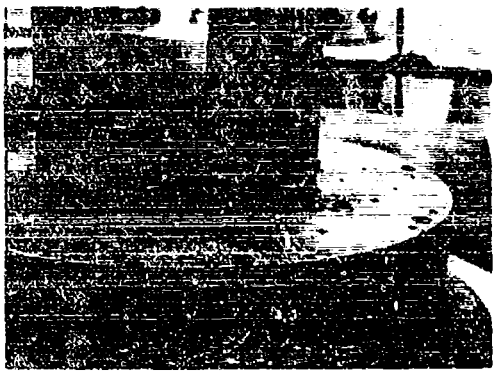

(b)

Fig. 22. Room temperature transmissibility study of foam specimens

prevent cross-axis movement during the vibration test.

An accelerometer was mounted on the fixture base to control the vibration input to the test item. The accelerometer was the detector for a constant velocity/acceleration servo system, its output being measured with a true rms voltmeter and recorded on an X-Y recorder. A response accelerometer was mounted in the central mass, and during the tests its output was compared with the input accelerometer and recorded on an X-Y recorder to obtain the required transmissibility data.

The sensitivity of each accelerometer system was checked prior to the test by subjecting the accelerometers to a sinusoidal vibration of 0.25-in. double amplitude at a frequency of 44 Hz to give an acceleration of 25 g peak. Vibration displacement was measured with an optical wedge, frequency was measured with an electronic counter, and the accelerometer system output was monitored with a true rms voltmeter.

A styrofoam enclosure-electric heater system was placed over the test setup for the elevated temperature tests. The temperature was held to within ± 3°F of the required level.

For subzero temperature tests, the enclosure was placed over the test setup, and liquid nitrogen was pumped into the system. The temperature was held to within ± 3°F of the required level.

The foam samples were stabilized at the specified temperature for a minimum of 2.5 to 3 hr before the test. The temperature was monitored by thermocouples located close to the samples being conditioned and at the test fixture.

TRANSMISSIBILITY

Room Temperature Test

The dynamic responses of foam samples are shown in Tables 16 and 17. Table 18 is a comparison of various materials at room temperature with a constant static stress of 0.22 psi. The excellent cushioning capability of silicone is also shown in Table 16. Samples No. 13 and 18 are used to compare the different grades of polyfoam. Samples 4, 5, and 6 show the effect of thickness in the case of very soft flexible PVC. Similarly, samples 26 and 27 demonstrate the effect of thickness in ethafoam.

Table 17 investigates the relationship between transmissibility and weight on foam samples that varied from 7.75 lb (0.22 psi) to 33 lb (0.92 psi). The natural frequency depends on both stiffness ($dF/d\delta$) and weight of a body (W).

$$f_n = 3.13 \sqrt{\frac{dF/d\delta}{W}} .$$

Therefore, transmissibility peak shifts depending on the ratio of stiffness and weight.

Effect of Temperature on Transmissibility

Table 18 is a summary of tests at -50°F, room temperature, and at +150°F. Under the specified dynamic input, the difference in transmissibility data was not significant.

TABLE 16
Vibration Study at Room Temperature
(Static Stress, 0.22 psi)

Sample No.	Foam Material	Dynamic Input (Hz)	Dynamic Input (g)	Peak (Hz)	G_o/G_i
3	Silicone, 1 in.	5 to 20 20 to 50 50 to 250	1.25 to 5 10 20	7	6.5 0.5 0.09
13	Polyfoam (P-25), 1 in.	5 to 20 20 to 50 50 to 250	1.25 to 5 10 20	10	28 0.3 0.1
18	Polyfoam (P-65), 1 in.	5 to 20 20 to 50 50 to 250	1.25 to 5 10 20	9	5 0.4 0.15
4	PVC, 0.5 in.	20 to 50 50 to 250	10 20	50	24 0.7
5	PVC, 1.0 in.	20 to 50 50 to 250	10 20	28	7 0.3
6	PVC, 2.0 in.	20 to 50 50 to 250	10 20	24	6.5 0.5
26	Ethafoam, 1 in.	20 to 50 50 to 250	10 20	35	16 1.5
27	Ethafoam, 2 in.	20 to 50 50 to 250	10 20	50	2.5 1.2

TABLE 17
Vibration Study at Room Temperature
(Static Stress, 0.22 to 0.92 psi)

Sample No.	Material	Mass (lb)	Static Stress (psi)	Dynamic Input (Hz)	Dynamic Input (g)	Peak (Hz)	G_o/G_i
13	Polyfoam P-25	7.75	0.22	5 to 20 20 to 50 50 to 250	1.25 to 5 10 20	10	28 0.3 0.1
		12.25	0.34	5 to 20 20 to 50 50 to 250	1.25 to 5 10 20	38	23 0.15
		17.25	0.48	5 to 20 20 to 50 50 to 250	1.25 to 5 5 10	10	8.4 3.0 0.15
		33	0.92	20 to 50 50 to 250	5 10	20	10 0.15
27	Ethafoam, 2 in.	7.75	0.22	20 to 50 50 to 250	10 20	50	2.5 1.2
		12.25	0.34	20 to 50 50 to 250	10 20	25	5.5 1.0
		17.25	0.48	20 to 50 50 to 250	5 10	20	12 0.5
		33	0.92	5 to 20 20 to 50 50 to 250	1.25 to 5 5 10	15	11 1.2 0.3

TABLE 18
Effect of Temperature on Transmissibility (0.22 psi)

Material	Temperature (°F)	Dynamic Input (Hz)	Dynamic Input (g)	Peak (Hz)	G_o/G_i
Silicone, 1 in.	-50	5 to 20	1.25 to 5	7	2.4
		20 to 50	10		1.0
	+160	5 to 20	1.25 to 5	10	2.4
		20 to 50	10		1.0
Polyfoam, 1 in. (P-12)	-50	20 to 50	10	—	2
		50 to 250	20	55	2.5
	+160	20 to 50	10	26	1.7
		50 to 250	20	—	0.3
PVC, 1 in.	-50	20 to 50	10	50	2.5
		50 to 250	20	—	1.0
	R.	20 to 50	10	28	7
		50 to 250	20	—	0.3
	+160	20 to 50	10	38	10
		50 to 250	20	—	0.6
PVC, 2 in.	-50	20 to 50	10	41	2.7
		50 to 250	20	—	0.8
	RT	20 to 50	10	24	6.5
		50 to 250	20	—	0.5
	160	20 to 50	10	25	13
		50 to 250	20	—	0.2
Ethafoam, 2 in.	-50	20 to 50	10	22	5
		50 to 250	20	—	0.06
	RT	20 to 50	10	5	2.5
		50 to 250	20	—	1.2
	160	20 to 50	10	25	12
		50 to 250	20		0.25

CONCLUSIONS

The modulus of high polymer materials is extremely sensitive to temperature variations. Therefore, a study was made of the temperature effect on the viscoelastic behavior of high polymer materials such as flexible open-cell polyether-urethane, flexible closed-cell polyethylene, very soft closed-cell polyvinylchloride, rigid polystyrene, and rubbery silicone foams.

The scope of the study included (a) chemorheological analysis, (b) three types of stress-strain curves, (c) quantitative analysis of hysteresis diagrams, (d) time dependent recovery, and (e) vibrational transmissibility.

The following conclusions were obtained:

1. Low temperature stiffening was observed in all materials.

2. Silicone indicates the best high temperature and subzero cushioning capability. Conversely, rigid polystyrene and flexible PVC have poor viscoelastic capability.

3. Based on stress-strain relationship at various temperatures, the materials were divided into three types.

4. Five stages of stress-strain relationship were clearly demonstrated for three types of high polymer materials.

5. The vibrational response of high polymer foam materials can be at least qualitatively predicted from the above static study, and by using the following formula:

$$f_n = 3.13 \sqrt{\frac{dP/dS}{W}} .$$

However, because of so many variables in practice, considerably more dynamic data are needed under various simulated conditions although such simulation is very time consuming.

ACKNOWLEDGMENTS

The author wishes to acknowledge the support of Mr. George A. Cantrick, President, G. A. Cantrick Co., Detroit, Mich., for making some of the foam specimens, and also wishes to acknowledge the valuable assistance of Mr. David Brown, Bendix Aerospace Systems Division Testing Engineer, in carrying out these tests.

REFERENCES

1. A. V. Tobolsky, Properties and Structure of Polymers (John Wiley & Sons, Inc., New York), 1960

2. "RTV-7 Silicone Rubber Foam," G.E., Silicone Products Dept., Supplementary Data, S-3C-2

3. A. V. Tobolsky, "Stress Relaxation Studies of the Viscoelastic Properties of Polymers," J. Appl. Phys., pp. 673-685 (July 1956)

4. J. D. Ferry, Viscoelastic Properties of Polymers (John Wiley & Sons, Inc.) New York), 1961

J. A. Thorn[illegible] Effect of Extreme Low Temperatures on Silicone Elastomeric Materials," Dow Corning Corp. Rept. No 172, 15 Oct. 1965

6. D. E. Robinson and F. A. Schreihans," RTV Silicones as Sealants and Adhesives for Cryogenic Applications," Eng. Dev. Lab. North Am. Aviation Inc., 28 Feb. 1964

7. "Packaging with Ethafoam," Dow Chemical Co., 1963

BIBLIOGRAPHY

Alfrey, T., Jr., Mechanical Behavior of High Polymers (Interscience Publishers, New York), 1948, pp. 93-94, p. 234

Becker, G. W. and H. J. Rademacher, "Mechanical Behavior of High Polymers under Deformations of Different Time Function, Type, and Magnitude," J. Polymer Sci., 58: 621-631 (1962)

Brenner, W., "Foam Plastics, Materials & Methods Manual" (127), June 1956

Carmichael, A. J. and H. W. Holdaway, "Phenomenological Elastomechanical Behavior of Rubbers," J. Appl. Phys., 32(2) (Feb. 1961)

Cooper, S. L. et al., "Properties of Linear Elastomeric Polyurethanes," AD 633.787, Princeton Univ., May 1966

Crede, C. E., Vibration and Shock Isolation (John Wiley & Sons, New York), 1951, p. 155

"Cushioning Materials Study Program," G.E., R58EML43

Eller, S. A., "Investigation of the Physical Properties of Resilient Polyurethane Foam Materials," Lab. Proj. 4981-23, New York Naval Shipyard, Materials Lab., 26 Jan. 1959

General Tire & Rubber Co., Chemical Plastics Div., Tech. Bull. - Polyfoam

Gigliotti, M. E., "Design Criteria for Plastic Package-Cushioning Materials," PLASTEC Rept. No. 4 AD273 400, Dec. 1961

Halpin, J. C., "Nonlinear Rubberlike Viscoelasticity: A Molecular Approach," AFML-TR-65-107, Oct. 1965

Jellinek, H., Degradation of Vinyl Polymers (Academic Press), 1955

Kolsky, H., "The Mechanical Testing of High Polymers," Progress in Non-Destructive Testing (Heywood & Co., London), 1959

Krakovar, S. M., "The Theory and Operation of a Dynamic Tester for Evaluating Package Cushioning Material," WADC TR56-342, May 1956

Krakovar, S.M. and A. Olevitch, "Investigation of Design Criteria for Cushioning Materials," WADC TR58-639, Mar. 1959

Kresser, T. O., Polyethylene (Reinhold Publishing Co., New York)

Lethersich, W., "The Rheological Properties of Dielectric Polymers," British J. Appl. Phys., pp. 294-301 (Nov. 1950)

McClintock, F. A. and A. S. Argon, Mechanical Behavior of Materials (Addison-Wesley Co., Reading, Mass.), 1966, pp. 215-262

"Military Standardization Handbook Package Cushioning Design," MIL-HDBK-304, 25 Nov. 1964

Osgood, C. C., Packaging with Foam, Machine Des[illegible] Per[illegible] Publishing Company. Cle[illegible]land, Ohio, 9 Nov. 1967, pp. 17[illegible]-181

Parfitt, G. G., "Damping in [illegible] High Polymers," 9th Intnat. Cong. Appl. Mech., Univ. Bruxelles, 5:360-369 (1957)

"Plastic Foams. Materials & Processes Manual" ([illegible]), May 1968

Rand, J. L. et al., "Dynamic Compression Testing of Shock Mitigating Materials," NOLTR 66-39, U.S. Nav. Ord. Lab., 9 Jan. 1966

Rempel, J. R., "Shock-Wave Attenuation in Elastic-Rigid Foams," RTD TDR-63-3056, Oct. 1963

Sullivan, M. B., "Modifications of Cellular RTV-Silicone Rubber," 8th Natl. Symp. Soc. Aerospace and Material Process Engrs., May 1965

"Tentative Specifications and Methods of Test for Flexible Urethane Foam," ASTM D1564-61T, 1958

Titus, J. B., "Effect of Low Temperature (0 to -65°F) on the Properties of Plastic," PLASTEC Rept., 30 July 1967

Tolley, W. B., "Low Temperature Properties of RMS-1[illegible]1172-1 Urethane Foam," Tucson [illegible] Lab. No. 4271.6/9, 24 Oct. 1969

[illegible]olley, W. B., "Low Te[illegible] Dynamic [illegible]rethane Fo[illegible] sh[illegible] Studies," Bull. 30, Shock & [illegible]ibration and Associated Environments, Part III, Feb. 1962

Treloar, L. R. G., The Physics of Rubber Elasticity (Clarendon Press), 1958

Zell, G., "Vibration Testing of Resilient Package Cushioning Materials," Picatinny Arsenal Tech. Rept. 3160, Aug. 1964

* * *

BROADBAND EXTENSIONAL DAMPING MATERIALS

Donald R. Blenner and Thomas J. Dudek
Lord Manufacturing Company
Erie, Pennsylvania

High polymer extensional damping materials, which have been especially formulated to possess very high internal damping properties over limited temperature and frequency intervals, have been used extensively as additive treatments to control resonant responses and to attenuate noise radiation and noise propagation in vibrating structures. This paper reports the properties of a new series of damping materials (Lord EXLD500), which effectively double the temperature range and increase the frequency range over which damping effectiveness (experimentally determined on coated beams) is maintained at a high level.

Criteria for comparing the effectiveness of damping materials are used to indicate the progress that has occurred in the development of various damping materials over the past 15 years. Because of the marked temperature dependence of the damping effectiveness of viscoelastic damping materials, one should always compare the relative merits of various damping treatments over a temperature range appropriate for the application under consideration. Data are presented to show that the temperature bandwidth of "effectiveness" for a damping material is usually more important than peak damping properties.

A comparison of composite loss factor data obtained on standardized steel test beams uniformly coated with 30 percent by weight of various extensional damping materials shows that the temperature range (temperature bandwidth) over which the composite loss factor (η_c) exceeds 0.1 (percent $c/c_o > 5$) has been limited to about 50°F. In the same test the new "broadband" materials have effective temperature bandwidths of 80°F. The increased temperature bandwidth of these materials, which has been obtained without decreasing the peak damping levels available, makes them practical damping treatments for many outdoor applications.

Predictions are made on temperature bandwidths and peak damping levels that can be expected as a result of future development work now underway on extensional damping treatments.

INTRODUCTION

To improve fatigue life problems and reduce acoustic noise transmission and reradiation, vibration damping materials have been used for many years to reduce resonant vibration amplitudes in metal structures. The internal damping inherent in viscoelastic damping materials is responsible for the dissipation of mechanical vibrational energy to heat.

Damping materials, which are applied to structures as coatings, are referred to as extensional damping material [1] and have been commercially available for over 15 years. These materials are particularly attractive because they can be used to add damping at optimum locations in a structure (that is, they are easily applied where they are needed) at a reasonable cost, and they can be formulated [2] to meet specified damping requirements over most temperature and frequency ranges (that is, various materials are readily available to match the specific requirements of almost any structural application). Additive damping treatments have been employed to reduce noise and resonant vibrations in aircraft and missiles, rapid transit, ships, refrigeration units, home appliances, automobiles, and machine enclosures.

The purpose of this paper is to describe the properties of a recently developed series of broad temperature range, broad frequency range extensional damping materials, and to compare the effectiveness of these materials with that of typical commercially available damping materials, taking into account the temperature and frequency dependence of the damping properties. The comparative study indicates the progress that has been made in the development of extensional damping materials over the last 15 years.

CRITERIA FOR EFFECTIVENESS COMPARISON OF DAMPING MATERIALS

The loss factor of a damped composite structure [1] is a measure of the amount of energy dissipated in it per vibration cycle and is probably the most useful criterion [3] for comparing the effectiveness of different damping treatments. Mead [3] has pointed out that other criteria, which include specific effects of the added mass and stiffness of the damping treatment, are important when the stiffness of the structure is significantly increased by the addition of the damping treatment. However, for practical additive weights of damping materials, the increase in stiffness of the system is usually quite small, that is, up to 40 percent added weight to steel and 70 percent to aluminum. Hence, a comparison of composite loss factors of metal bars uniformly coated with equal (small) weights of different extensional damping materials is sufficient to determine their relative merits for the suppression of structural response, that is, resonant vibration amplitudes (displacement, velocity and/or acceleration) and sound transmission and radiation.

In addition, loss factor comparisons (on an equal weight basis) should be made over a range of temperatures and frequencies, because in practical applications overall damping material effectiveness depends on the temperature and frequency ranges over which the loss factor remains above a minimum level (which varies with the application).

The practical problem, so far as the design engineer is concerned, is to select the minimum weight (and/or cost) of an additive damping treatment that will provide the required damping performance level over specified ranges of temperature and frequency. Unfortunately, this data is usually not made available in a form easily used by design engineers. Comparative data presented in this report will show that a detailed knowledge of the temperature and frequency dependence of the damping effectiveness (composite loss factor on equal weight basis) is essential to make a valid judgement on relative performance/cost effectiveness ratings for damping materials.

EXPERIMENTAL

Damping properties reported in this paper were determined over ranges of temperature and frequency using the B&K Model 3930 Complex Modulus Apparatus. A schematic diagram of this apparatus is shown in Fig. 1. More detailed descriptions of the instruments and experimental procedures used in the test method are available elsewhere [4]. Briefly, the method is similar to that developed by Oberst [ ] and uses a metal cantilever beam that is coated on one side with a layer of viscoelastic material as a test specimen. The test specimen is subjected to a harmonic force of fixed amplitude (generated by a magnetic force transducer) at its free end, and the frequency response of the bar is monitored by means of a second magnetic transducer. Composite loss factors are determined at the resonant frequencies of the test bars by measuring either the time rate of free decay of the resonant vibration or the half-power bandwidth of each resonant peak. The complex dynamic modulus of the viscoelastic coating material $[E^* = E'(1+i\eta)]$ can be computed using this experimental data, the geometry of the test bar, and properties of the uncoated bar [5].

The test bars used in this investigation were $0.25 \times 0.30 \times 0.032$-in. steel bars and/or $10\ 3/4 \times 0.30 \times 0.061$-in. steel bars that were coated with about a 30 percent added weight of damping material (to allow comparisons at equal weights of damping treatment). The damping materials were applied and bonded to the steel bar in accordance with the instructions of suppliers.

RESULTS

Composite Loss Factor Results

Typical Complex Modulus Apparatus test results are shown in Fig. 2 were the composite loss factors of a steel bar coated with a 30 percent added weight of EXLD500 damping material are plotted vs frequency at various temperatures. From Fig. 2 it is seen that at low temperatures the composite loss factor is low with a slight negative frequency dependence and that as temperature is increased, the composite loss factor increases to a peak value and then decreases while the frequency dependence of the composite loss factor changes from a negative to a positive slope.

This characteristic behavior of damping-material-coated test bars is shown more clearly in Fig. 3 where the composite loss factor data from Fig. 2 are plotted vs temperature for frequencies of 100 and 1000 Hz. Figure 3 shows that at 100 Hz, a steel bar treated with 30 percent added weight of EXLD500 has a peak loss factor of 0.23 (11.5 percent c/c_o) at 58°F and that the loss factor is 0.10 (5 percent c/c_o) or higher over the temperature range of 16-96°F (a temperature bandwidth of about 80°F). At

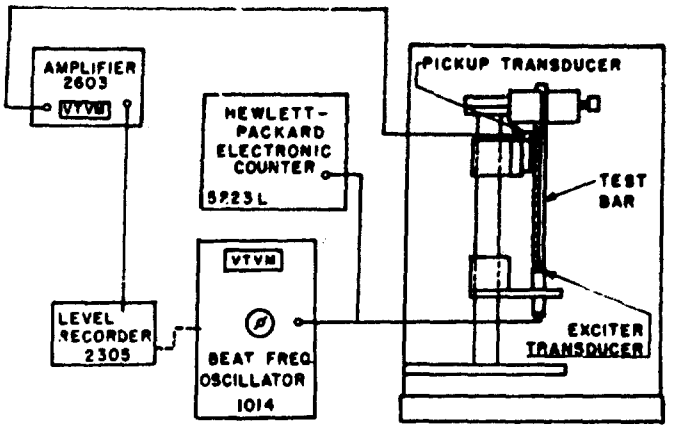

Fig. 1. Schematic of B&K Complex Modulus Apparatus, Model 3930

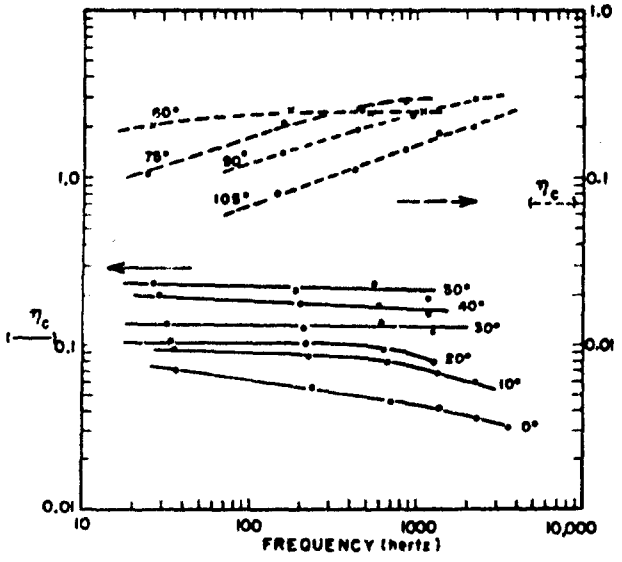

Fig. 2. Composite loss factor vs frequency at various temperatures (°F) for a steel bar uniformly coated with 30 percent added weight of EXLD500

1000 Hz, the η_c vs T damping curve is seen to shift in the direction of higher temperatures. However, it is important to note that the frequency change effects a change in shape of the damping curve, that is, not just a horizontal translation of the 100-Hz curve. This is mainly a result of the increased frequency dependence of the modulus of the damping material at the higher temperatures. At 1000 Hz, the peak damping temperature of the EXLD500 (30 percent added weight) coated steel bar occurs at 75°F, and the temperature range over which the composite loss factor exceeds 0.1 is 25 to 115°F or a temperature bandwidth of 90°F.

From Fig. 3 it is also seen that if a composite loss factor of 0.1 is required for a 100 to 1000-Hz frequency range, the effective temperature range for a 30 percent added weight treatment of EXLD500 would be 25 to 95°F (or a ΔT of 70°F). If effective damping performance is required over a broader frequency range, for example, 10^2 to 10^4 Hz, the effective temperature range of the damping treatment would be

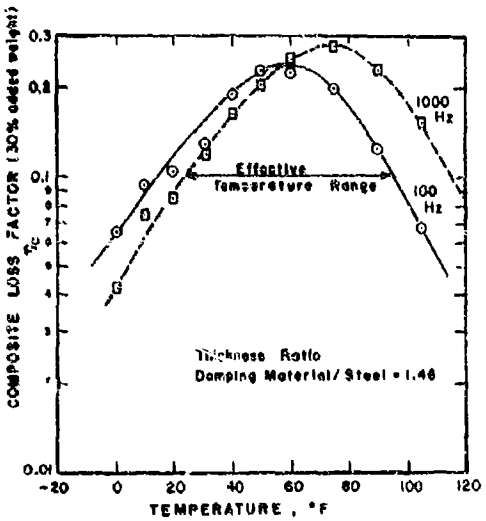

Fig. 3. Composite loss factor vs temperature at 100 and 1000 Hz for a steel bar uniformly coated with 30 percent added weight of EXLD500

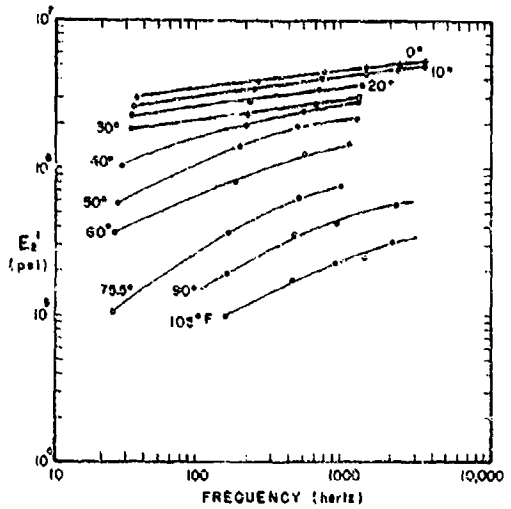

Fig. 4. Real part of the complex dynamic Young's modulus of EXLD500 as a function of frequency at various temperatures (°F)

decreased to about 60°F, that is, the effective temperature range would be about 35 to 95°F.

Although all damping material treatments generally show the same qualitative behavior as EXLD500 in Figs. 2 and 3, it will be shown that significant quantitative differences in temperature bandwidth and effective temperature range properties do exist among different materials; these differences can be traced back to important differences in the temperature and frequency dependence of the dynamic properties of the different materials.

Material Dynamic Properties – EXLD500

The theory developed by Oberst and Frankenfeld [5] was used to compute the dynamic mechanical properties of EXLD500 from the composite loss factor and resonant frequency data determined with the Complex Modulus Apparatus. In Fig. 4, the results obtained for the real part of the complex dynamic Young's modulus (E') of EXLD500 are plotted as a function of frequency at various temperatures and the material loss factor ($\eta_2 = E_2''/E_2'$) of EXLD500 is plotted as a function of the same parameters in Fig. 5. With the material properties of EXLD500 known

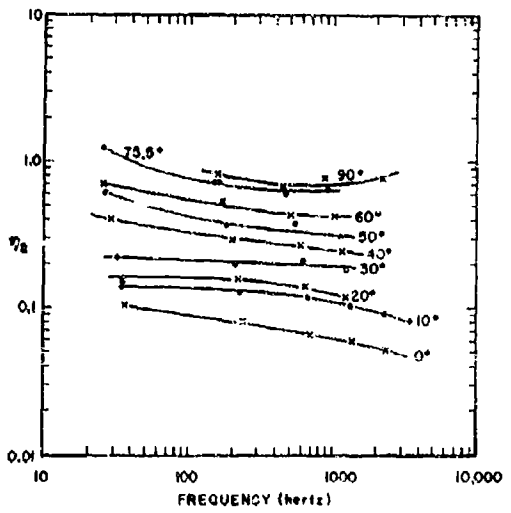

Fig. 5. Loss factor (E_2''/E_2') of EXLD500 as a function of frequency at various temperatures (°F)

over the range of temperatures and frequencies studied, that is, 0 to 105°F and 25 to 200 Hz, one can compute the composite loss factors of a bar coated with any thickness of EXLD500 over this same temperature/frequency range.

EFFECT OF EXLD500 TREATMENT WEIGHT ON COMPOSITE LOSS FACTOR VS TEMPERATURE

In Fig. 6, the composite loss factor vs temperature curves at 100 Hz, computed for steel bars coated with various added weights (5.1, 10, 20 and 30 percent) of EXLD500 damping material, are shown. As expected, the range of temperature (temperature bandwidth) over which the composite loss factor exceeds a specified value, for example, 0.10, is a function of the amount of damping material applied. It is also interesting that the temperature of peak damping is also a function of the amount of damping material added, for example, peak damping occurs at 40°F for a 5.1 percent EXLD500 treatment weight and at 58°F for a 30 percent treatment weight.

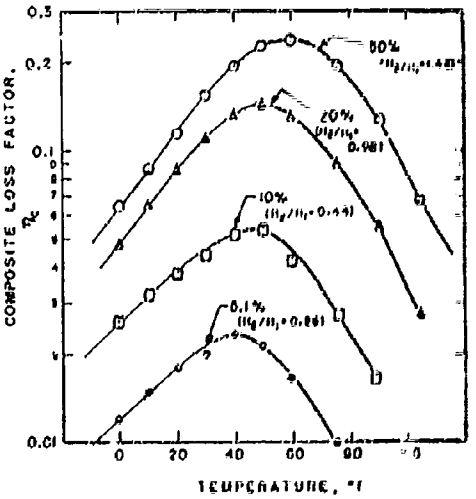

Fig. 6. Composite loss factor vs temperature at 100 Hz for a steel bar coated uniformly with various weights of EXLD500

In Fig. 6, data could have also been included at 1000 Hz at each added weight of damping material. This was not done because it would have made interpretation of the figure difficult because of overcrowding.

The level of damping and temperature and frequency range of interest is determined by the specific application for the damping material. The frequency and temperature range requirement for a damped structure determines the minimum amount of damping material that has to be applied to the structure. This minimum damping material weight requirement can be estimated without difficulty using curves like those in Fig. 6. It should be clear from what has already been said that the broader the effective temperature range of a material, the smaller the added weight required to encompass the temperature and frequency requirements.

It is possible to define the effective temperature range of a material for any required level of composite loss factor (damping) and added weight. Automotive "sound deadeners" are an example of damping materials that are tested [6] and compared at 5.1 percent added weight on steel and temperature bandwidths at a composite loss factor level of 0.005 (or less) are used as one measure of material effectiveness. Vibration damping materials for U.S. Navy ship applications are tested at about a 30 percent added weight on steel and the temperature range over which the composite loss factor exceeds 0.1 (5 percent c/c_c) is of interest.

ADJUSTABLE PEAK DAMPING TEMPERATURE

The EXLD500 broadband damping materials can be formulated to position the peak damping temperature at any temperature between -60 and 250°F. This is illustrated in Fig. 7 where the composite loss factor vs temperature curves at 100 Hz are plotted for steel bars coated (30 percent added weight) with three commercially available sprayable damping materials with peak damping temperatures located at 55°F (LD5500), 70°F (LD5501), and 120°F (LD5502).

The LD5500 type materials are further characterized by being resistant to water and oil absorption and are flame retardant.

COMPARISON OF EXLD500-TYPE DAMPING MATERIALS WITH OTHER MATERIALS

We have found that damping properties can be determined over a broader temperature range with test bars coated with close to 30 percent added weight of damping material. Also, we have found it convenient to define temperature bandwidth as the temperature range over which the composite loss factor of a coated (30 percent added weight) steel bar exceeds 0.1.

In Fig. 8, the damping effectiveness at 100 Hz of LD5501 is compared with that of a polyvinyl acetate (PVAc) water-based commercially available sprayable material. It is seen that the

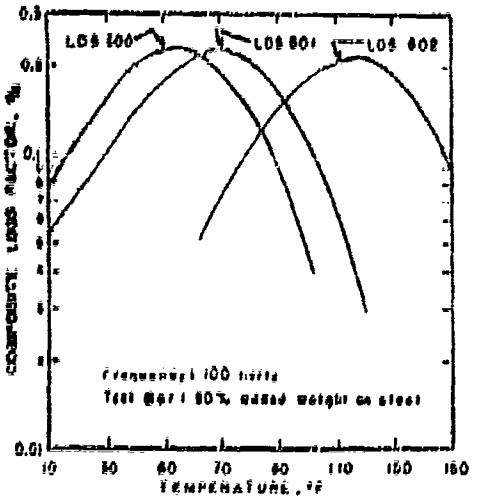

Fig. 7. Damping effectiveness of Lord Manufacturing Co.'s Sprayable Damping Materials, LDS500, LDS501, and LDS502

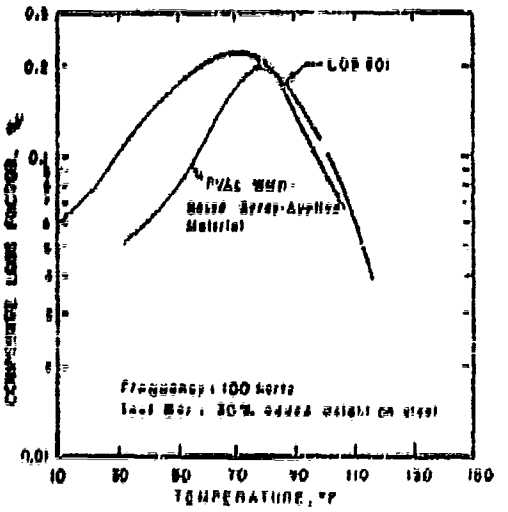

Fig. 8. Damping effectiveness of LDS501 compared with a PVAc water-based sprayable damping material

temperature bandwidth of LDS501 is about 72°F compared with 41°F for the PVAc-based material. The temperature bandwidth and peak damping results shown for the PVAc-based damping material are comparable to the results of Oberst and coworkers [2,7] for the most effective damping materials available to them in 1964. It is also interesting to point out that a 20 percent added coating weight of LDS501 would have a temperature bandwidth of more than 40°F, but with a peak damping level below that of the PVAc-based damping material.

In Fig. 9, the damping effectiveness of LDS500 is compared with LD403, a Lord Manufacturing Co. vibration damping material supplied in sheet and tile form. Again, the broader temperature bandwidth capability of the LDS500 is clearly evident. The LD403 material has damping properties comparable to the MRC-OG4 damping material developed by Ball and Salyer [8] for the U.S. Navy.

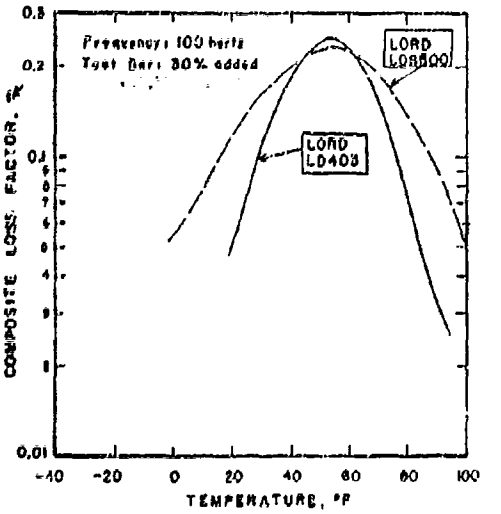

Fig. 9. Damping effectiveness of LDS500 compared with LD403 (Lord Manufacturing Co.)

The temperature bandwith of LD403 at 100 Hz is about 47°F. A comparison of damping effectiveness curves for LD403 and LDS500 in Fig. 9 shows that the improved temperature bandwidth properties of the 500 materials were obtained without a significant reduction in peak damping level.

Continued development work is in progress in our R&D laboratory to further improve the effectiveness (temperature and frequency bandwidths) of extensional damping materials so that present application requirements can be met at lower additive weights of damping material, and so that the use of extensional damping materials can be extended to more applications requiring

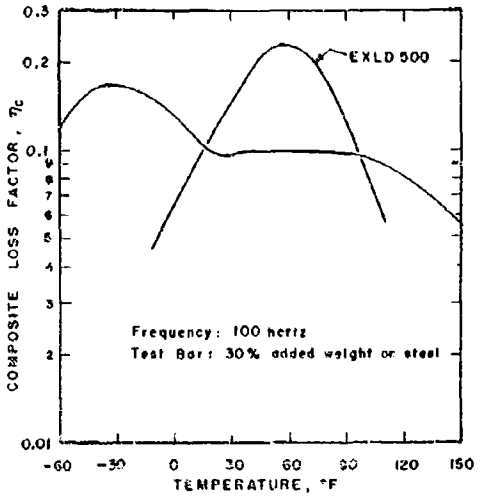

Fig. 10. Damping effectiveness of EXLD500 compared with a next-generation damping material now under laboratory development

very broad temperature bandwidths (for example, high performance aircraft applications). Figure 10 compares the damping properties of a broadband damping material, which is still in the laboratory phase of development, with those of EXLD500. It is seen that the next generation material produces a loss factor of 0.095 or higher over a temperature range of -65 to 95°F (a temperature bandwidth of 160°F) at a 30 percent added treatment weight on steel; however, to accomplish this, peak damping had to be sacrificed.

CONCLUSIONS

A new class of LD500 damping materials has been shown to have significantly broader temperature/frequency range capabilities when compared with present state-of-the-art materials.

Viscoelastic damping materials are used primarily because of their broadband frequency temperature damping capabilities. If these properties were not required in an application, a tuned damper would probably be more efficient. Temperature bandwidth data are required for the selection of minimum weight damping treatments that maintain a specified damping level (or higher) over the temperature and frequency ranges of interest. Hence, temperature bandwidths, defined in this report as the temperature range over which the composite loss factors of test bars coated with 30 percent added weights of various damping materials are equal to or greater than 0.1, are an important characteristic of damping materials (but often neglected on product data sheets).

A comparison of composite loss factor vs temperature curves determined at 100 Hz on standard test bars (30 percent added weight on steel) for several commercially available damping materials shows that materials, which were available on the market during the period 1955-1967, can be characterized by temperature bandwidths of 40 to 50°F and peak composite loss factors of 0.15 to 0.25. The new LD500 type materials are characterized (using the same test methods) by temperature bandwidths of 70 to 80°F and peak loss factors of 0.20 to 0.25. Extensional damping materials with temperature bandwidths of 150°F should be available in a few years.

If material effectiveness comparisons are made at different frequencies (for example, 100 Hz) or with a different standard test bar (for example, 5 percent or 20 percent weight of damping material), different temperature bandwidths would be obtained, but the relative ranking of the various materials would not be altered.

REFERENCES

1. J. E. Ruzicka, "Structural Damping," Am. Soc. Mech. Engrs., Section 3, New York (1959)
2. H. Oberst, L. Bohn, and F. Linhardt, Kunststoffe 51:1 (1961)
3. D. J. Mead, Noise Control 7:27 (1961)
4. Complex Modulus Apparatus Instruction Manual, B&K Instruments, Inc., Cleveland, Ohio
5. H. Oberst and K. Frankenfeld, Acustica 2:181 (1952)
6. "Society of Automotive Engineers Handbook," Spec. SAE-J671, 1964, p. 850
7. H. Oberst, G. W. Becker, and K. Frankenfeld, Acustica 4:433 (1954)
8. G. L. Ball and I. O. Salyer, J. Am. Acoust. Soc. 39:663 (1963)

DISCUSSION

D. Thrasher (B.F. Goodrich): If I recall Oberst's expression for extensional damping correctly, I do not see how it predicts a shift in the maximum damping with temperature. If I remember, the expression includes only thickness ratios and the moduli, and so forth of the material. None of these factors would account for shifting the peak damping with temperature as you increase the thickness.

Mr. Blenner: The values that we obtained were actually run through the Oberst equations and computed from one added weight. What really happens is that, at the lower added weight, the predominant characteristic is the stiffness of the viscoelastic material. As you increase the thickness of the damping material, the thickness effect of the treatment is beginning to dominate. Also, from the nature of viscoelastic materials, the material loss factor normally lags the composite loss factor. In other words, the material loss factor will normally occur at a higher temperature than the composite loss factor. So as you increase in thickness you begin to approach the material loss factor just as though there were no steel there. This normally occurs at a higher temperature.

Mr. Thrasher: You are saying this is due actually to the extensional stiffness factor?

Mr. Blenner: That is right.

Mr. Thrasher: Considering the relaxation mechanism in any polymer, to broaden the response like this you effectively are increasing the distribution of relaxation times. Yet, if you spread out the distribution function then the maximum loss factor should decrease. You show a very, very small loss, and I really do not understand this either.

Mr. Blenner: This is the secret of our material. We have overcome this particular effect which is characteristic of most damping material. On some of those slides you noticed that we did sacrifice any peak damping, except for the last material that we talked about. With all other compounds that we show, we maintain the peak or the maximum damping that could be attainable. This is probably unique to this particular class of materials because they depend on a completely different kind of mechanism. It actually broadens out the relaxation mechanism that you are talking about without sacrificing any of the peak damping attainable.

Mr. Thrasher: Then you do not have a standard copolymer material. You must have added something, otherwise you would be defying the laws of nature.

Mr. Blenner: That is right. The basis for this is really a new composition which, of course, is company confidential.

* * *

A SINUSOIDAL PULSE TECHNIQUE FOR ENVIRONMENTAL VIBRATION TESTING

James T. Howlett and Dennis J. Martin
NASA, Langley Research Center
Hampton, Virginia

Currently, many environmental tests are based on shock spectra and the test specifications frequently require a slowly swept sinusoidal input. For this type of test, the input amplitude required to produce a response equivalent to that resulting from a transient is highly dependent upon the damping of the system under test. The procedure that is usually followed is based on a single value of damping and results in a considerable overtest of low damped systems.

This paper proposes a test method that accounts for the variation of response with damping. The test input consists of a spaced sequence of sinusoidal pulses. The frequency, amplitude, and number of cycles of each pulse are selected to adequately meet specified shock spectra for various levels of damping. Application of the method to a realistic test specification indicates a significant improvement over slow-sweep procedures.

INTRODUCTION

Many current environmental vibration tests intended to simulate transients are based on shock spectra. The specifications frequently require a slowly swept sinusoidal input with the amplitude controlled to produce responses that meet a specified shock spectrum based on only one value of damping. One disadvantage of this type of test is that the input amplitude required to produce the desired response at a particular frequency is highly dependent upon the damping of the system under test. To avoid undertesting, the input amplitude is usually based on the highest value of damping present. As a result, systems with low values of damping are severely overtested.

This paper presents a test method that overcomes the above difficulty. The test method produces response levels that adequately meet specified shock spectra for various levels of damping.

SLOW-SWEEP TEST

Consider the system shown in Fig. 1. The equations of motion are

$$\ddot{x}_i + 2\lambda_i \omega_i(\dot{x}_i - \dot{x}_g) + \omega_i^2(x_i - x_B) = 0,$$

$$i = 1, \ldots, n \qquad (1)$$

where

$$\omega_i = \sqrt{\frac{k_i}{m_i}}$$

$$\lambda_i = \frac{c_i}{2\sqrt{k_i m_i}}.$$

It should be noted that the results of this paper are applicable only to systems of the form illustrated in Fig. 1. As shown in Ref. 1, the results should not be applied to other systems, such as more general multidegree-of-freedom systems.

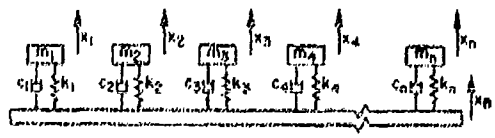

Fig. 1. Physical system

Let $y_i = x_i - x_B$. Then Eq. (1) becomes

$$\ddot{y}_i + 2\lambda_i\omega_i\dot{y}_i + \omega_i^2 y_i = -\ddot{x}_B . \qquad (2)$$

Damping is frequently specified in terms of Q, which is defined as $Q = 1/2\lambda$. In the shock spectrum method, the initial conditions for Eq. (2) are assumed to be

$$y_i(0) = \dot{y}_i(0) = 0 . \qquad (3)$$

The response shock spectrum for a particular motion input to a system is determined from the maximum response of a single-degree-of-freedom system having a given damping and frequency. The maximum response is found for several single-degree-of-freedom systems having the same damping but different frequencies. These maximum responses may then be plotted vs frequency to determine the shock spectrum. For environmental vibration test specifications the maximum absolute acceleration is the variable usually considered. The test specification is obtained by enveloping the shock spectra of all significant flight inputs.

The input that is used in the environmental vibration test is that required to produce responses equal to or greater than the desired response shock spectrum. In this paper, all inputs are acceleration time histories at the base of the system ($\ddot{x}_B$).

A slowly swept sinusoidal test input is frequently used to satisfy the above requirements. The amplitude is adjusted to satisfy the test specification. For this type of test, the input amplitude required to produce a desired response at a particular frequency is highly dependent upon the damping of the system at that frequency. Although the input amplitude of a slow-sweep test can be adequately specified for one particular value of damping, the input amplitude so selected is inadequate for any other value of damping. Some examples that illustrate this point are shown in Figs. 2 to 4. In Fig. 2, the solid lines indicate response levels to flight inputs for three different assumed values of Q. These response levels are similar to those obtained in deriving test specifications for Lunar Orbiter. Although the flight response levels for Q's of 10 and 30 are shown as a single curve, actually the levels for a Q of 30 are very slightly higher than those for a Q of 10.

The upper dashed line in Fig. 2 is the response level for a slow-sweep test input which is adjusted to produce conservative responses in systems having a Q = 30. If the systems being tested actually have a Q of 30, then this input test level produces response levels that are

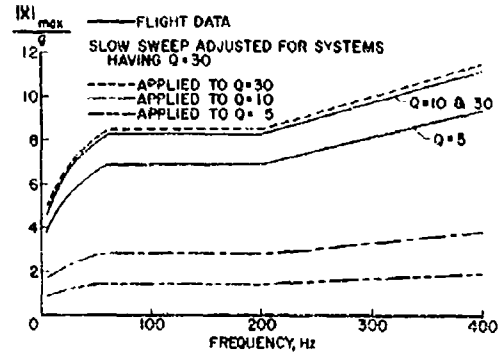

Fig. 2. Shock spectra of slow sweep adjusted for conservative response in systems having Q = 30

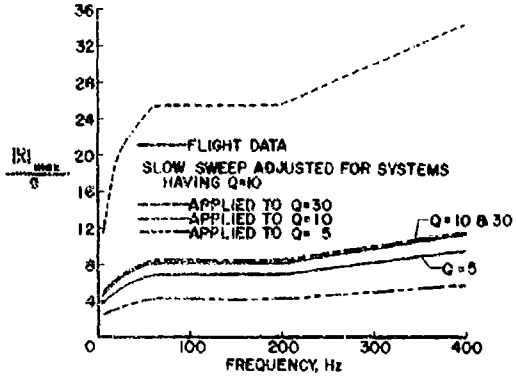

Fig. 3. Shock spectra of slow sweep adjusted for conservative response in systems having Q = 10

adequate. However, if the systems being tested have a Q of 5 or 10, then the response levels are seen to be too low. Hence, the test levels are too low.

Figure 3 shows the shock spectra for a test input adjusted to produce conservative responses in systems having a Q of 10. As Fig. 3 indicates, if the systems being tested actually have a Q of 10, then this test input produces adequate response levels. If the systems being tested have a Q of 30, the response levels are much higher than desired; if the systems being tested have a Q of 5, the response levels are too low.

To assure adequate response levels for all three values of Q, the amplitude of the slow-sweep test input must be based upon a Q of 5.

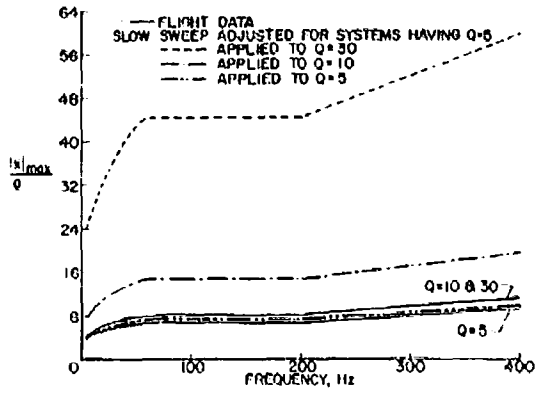

Fig. 4. Shock spectra of slow sweep adjusted for conservative response in systems having Q = 5

The response levels for this case are shown in Fig. 4. As the figure indicates, the response levels for systems with a Q of 10 are almost twice as high as the flight response levels for a Q of 10 and the response levels for systems with a Q of 30 are more than five times higher than the flight response levels for a Q of 30. Thus, systems with Q's of 10 and 30 are severely overtested.

For systems of the type shown in Fig. 1, several of the springs and masses may have the same natural frequency, but the values of damping may be different. Also, the damping of a particular system may not be accurately known. In these situations, it is highly desirable to have a test input that will produce adequate response levels for various values of damping without severely overtesting any system. As the above examples have shown, a slowly swept sinusoidal test input cannot accomplish this objective.

SINUSOIDAL PULSE TEST

The above overtesting can be overcome by testing at a sequence of discrete frequencies instead of using a continuous sweep. For a particular input frequency, the response of a system to a sinusoidal input is dependent upon the number of cycles of input. If the number of cycles of input is numerically equal to the Q of the system, then essentially steady state conditions are obtained. If the number of cycles of input is less than the Q of the system, then the variation of the response with damping will be shown to be less significant. A system with a natural frequency of 20 Hz was subjected to a varying number of cycles of sinusoidal input with a frequency of 20 Hz. Figure 5 shows the variation of the maximum response as a function of the number of cycles of sinusoidal input for four different values of Q. For one cycle of input, the maximum response of the system is practically the same for all values of Q shown. As the number of cycles of input is increased, the curves begin to disperse until the steady state values are reached. This phenomenon can be used to provide an environmental vibration test that accounts for the variation of response with damping.

As an example of the procedure, suppose that response shock spectra envelopes of flight data have been computed for Q's of 5, 10, and 50. Suppose, further, that the shock spectrum levels for a Q of 10 are 50 percent higher than the levels for a Q of 5 and the levels for a Q of 50 are twice as high as the levels for a Q of 5. An inspection of Fig. 5 indicates that for a system with a natural frequency of 20 Hz, 4 cycles of sinusoidal input will produce the desired variation with damping. The input amplitude is selected so that test levels are higher than specification levels for all three values of damping. Curves similar to those in Fig. 5 are easily obtained for other values of frequency and damping.

APPLICATION

The procedure has been applied to the test levels given earlier. Because, as shown by the flight data in Fig. 2, the required response

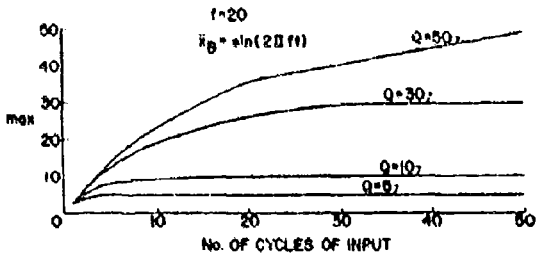

Fig. 5. Variation of maximum response with number of cycles of input for various values of Q

levels are very nearly the same for Q = 10 and Q = 30, and only 20 percent less for Q = 5, it is believed that this example is as difficult a case as would ordinarily be encountered.

As indicated by Fig. 5, the test input may consist of a single cycle at each of the necessary frequencies because the specification levels are practically equal for all three values of Q over the frequency range considered. The actual discrete frequencies used for the test input were selected as explained below. The only requirement is that the shock spectrum of the test input be at least as high as the specified levels for all three values of Q. The following procedure was used to determine the test input. An input frequency was selected and the shock spectra were computed for the three values of Q for a single cycle of input with 1 g amplitude. Based on this information, an input amplitude was selected that produced responses slightly higher than the required levels over a small frequency range. This process was continued until the entire frequency range had been covered. Note that the results are essentially a first try. No attempt was made to determine the optimum combination of test frequencies and amplitudes. The final test input is a series of 16 sinusoidal pulses, each pulse consisting of single cycle sine wave with a specified frequency and amplitude. The actual frequencies and amplitudes are shown in Table 1 along with the frequency range tested by each pulse.

To avoid superimposing the responses from consecutive pulses, the pulses must be spaced a short time apart. The space between consecutive pulses should be based on the highest value of Q. Preliminary studies indicate that between consecutive pulses the systems being tested should be allowed to undergo a number of cycles about equal to twice the highest value of Q. For example, in the present case, the time between pulses should be long enough to allow the systems being tested to undergo about 60 cycles of oscillation. With this spacing the total test required slightly less than 0.5 min, which is approximately one-third of the time required by a four oct/min sinusoidal sweep.

TABLE 1
Test Input

Input Frequency (Hz)	Input Amplitude (g)	Frequencies Tested (Hz)
5	1.90	5-7
8	1.98	8-10
14	2.33	13-18
20	2.36	20-24
26	2.48	26-30
32	2.63	32-38
40	2.80	40-48
50	2.93	50-62
64	3.05	64-86
88	3.05	88-120
122	3.05	122-166
168	3.05	168-210
230	3.30	212-260
280	3.58	262-296
325	3.90	298-374
400	4.20	376-400

The results are shown in Figs. 6 to 8. Note that for all three values of Q over the frequency range considered the shock spectra for the test input are slightly higher than the required levels. Comparison of these results with the slow sweep levels indicates a significant improvement. The sine pulse test produces response levels that are very nearly proportional to the levels received from flight inputs. All systems are conservatively tested, but no system is subjected to a drastic overtest.

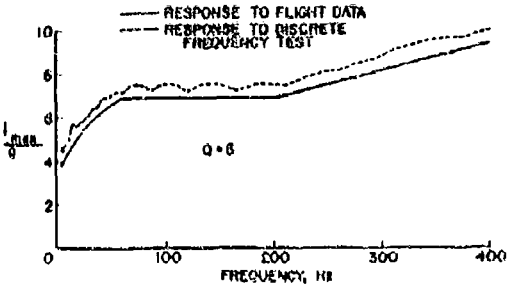

Fig. 6. Shock spectrum with Q = 5 for discrete frequency input

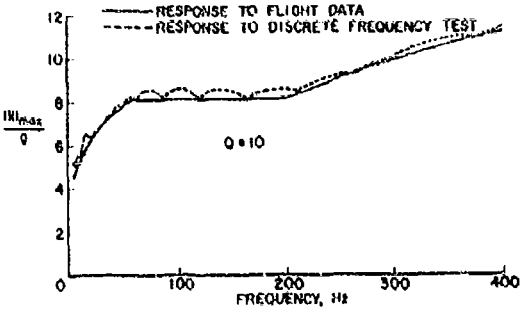

Fig. 7. Shock spectrum with Q = 10 for discrete frequency input

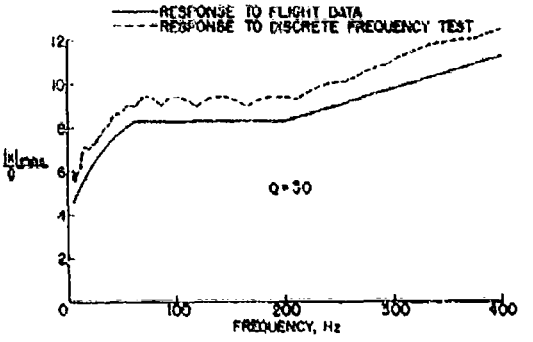

Fig. 8. Shock spectrum with Q = 30 for discrete frequency input

CONCLUSIONS

A test method that accounts for the variation of shock spectra with damping has been presented and applied to a realistic test specification. The test consists of a spaced sequence of sinusoidal pulses with the frequencies and amplitudes selected to meet specified shock spectra for different values of damping. The results indicate a significant improvement over slow sweep procedures.

REFERENCE

1. J. T. Howlett and J. P. Raney, "A New Approach for Evaluating Transient Loads for Environmental Testing of Spacecraft," 36th Shock and Vibration Bull., Part 2, Jan. 1967, pp. 97-105

DISCUSSION

Mr. K. W. Volkman (Lawrence Radiation Lab.): I am curious as to why you call that a shock spectrum. If I recall correctly, the maximum value of a shock spectrum is about 2 for an undamped system with a sawtooth pulse input. You are talking of values of 8 and 10, or 48. It just seems incompatible with the nature of what I know as a shock spectrum.

Mr. Howlett: Dr. Cronin, have you something to say on that?

Dr. D. L. Cronin (TRW Systems): Some people think in terms of simple shock when we say shock spectrum. I have been using the words response spectrum because, in your case, you are considering a collection of tests

which you consider as a single test. You are talking about enveloping the whole test and are getting something other than the classical or conventional shock spectrum. We can go up to a Q of 50; there is no limit.

Mr. Volkman: I think it is mislabeled then.

Dr. Cronin: Yes, I guess if we are going to speak of applications like these, we just have to stop calling them shock spectra.

Mr. Howlett: I should have said response spectra. These curves are envelope curves of flight data. Several different pulses were used and then the total was enveloped.

Dr. A. Curtis (Hughes Aircraft Co.): I found your technique very interesting. Could you envision the use of this technique to simulate a gun firing excitation on an aircraft?

Mr. Howlett: I cannot offhand see anything that would prevent its use in any situation for a transient input. You have to know the input motion to the base of the system and compute the shock spectrum for that input. Once you have this information, you could use this technique to determine proper test loads.

Dr. Curtis: Did I hear correctly that the results you showed on the slides were all computed values and were not values obtained in the laboratory?

Mr. Howlett: The flight data were obtained from actual vehicle flights. The curves were very similar to the curves used to obtain test specifications for Lunar Orbiter. The results for the test input were computed values, yes.

Dr. Curtis: Have you made any attempt to apply this technique in the laboratory? I can foresee at least a few difficulties.

Mr. Howlett: We have made a very preliminary attempt to indicate the feasibility of doing this. I talked to some of the men in the laboratory one day and, about two days later, they had a test on the head of a shaker which was reasonably like what I suggested. We made no attempt to control the frequencies or amplitudes of the pulses, but we did put in a spaced sequence of single pulses which were not exactly sine waves but were very similar to them. The equipment men tell me that the main problem in this area is getting a tape recording of the input. Once this is done, it is usually not difficult to apply it to a shaker head.

Dr. Curtis: I would like to suggest that they may be a little optimistic.

Mr. Howlett: Yes, I think you are probably right.

* * *

ISOLATION

A STUDY OF THE PERFORMANCE OF AN OPTIMUM SHOCK MOUNT

Kenneth T. Cornelius
Naval Ship Research and Development Center
Washington, D.C.

A mathematical model of a particular type of shock mount is presented and its response to several analytically specified foundation velocity input motions studied. The model was developed as a result of an earlier study of the response of linearly damped resilient mounts. This shock mount consists of a resilient element in parallel with a damper. The damping force produced by this damper is a linear function of velocity only at very low velocities. At higher velocities the damping force is limited to a constant value and is not sensitive to velocity at all. The damping force always acts to oppose the motion in the normal fashion. Because the damper performance is somewhat similar to that of certain types of automotive shock absorbers, the mount is termed double-acting. The performance of the mount is judged by comparison with those of the ideal shock mount and the linearly damped resilient mount. It is found that the double-acting mount efficiency approaches 100 percent in contrast to the linearly damped mount which seems inherently limited to a much lower efficiency. The mount is also capable of maintaining an equilibrium position, something the ideal mount cannot do. Although the performance of the mount is affected somewhat by the nature of the input motions, it is in all cases better than that of the other two types.

INTRODUCTION

The problem of protecting shipborne equipment from damage resulting from a nearby underwater explosion is well known. Attempts to solve it have usually taken the form of either designing the equipment to withstand the shock mounts, or a combination of both methods.

Because shock mounts do require that a certain relative motion be allowed, there are some things that obviously cannot be shock mounted. However, many items can be protected by using shock mounts.

This article was written to describe the operating characteristics and behavior of one promising shock mounting device and to compare it with both the ideal shock mount behavior and that of a linearly damped resilient mount.

BACKGROUND

The concept of an ideal shock mount has already been developed elsewhere [1,2]. Briefly, such a mount was one that produced a constant force to oppose any deflection, independent of the rate at which this occurred. This behavior resulted in the minimum possible deflection for any given transmitted force to the equipment for a particular input motion. The allowable magnitude of the transmitted force in a practical situation was determined by the shock resistance of the equipment to be protected. The mount deflections were then set by the input motion and mount efficiency. The shock resistance was expressed in terms of a quasi-static acceleration that could not be exceeded without damage, a fragility level, and was quantified with either the aid of experiment or specification. However, this was another

problem and will not be considered further here. For any given input motion, a curve showing the deflection requirements of an ideal mount over a range of transmitted accelerations was drawn. This was used as a standard with which to judge the performance of both proposed and existing shock mounts. The ideal shock mount concept was also useful in that it provided insight into what was required of a practical mount and whether it could be obtained. An ideal isolator would act the same as a dry-friction device whose static and dynamic friction coefficients were equal. It would do a good job of protecting against a single shock, but would never recover its equilibrium position. Repeated shocks would cause it to allow excessive deflections, and it would not function as a vibration mount at all. It was desirable to go on to develop an optimized shock isolator and the device under consideration here was felt to be a marked improvement.

Resilient elements, springs both damped and undamped were used extensively as shock mounts. A computer investigation was made of the manner in which linearly damped spring systems responded to typical shipboard shock motions (1). This study included undamped springs as a special case. Although the exact damping characteristics of many of the common commercial mounts were not known, it was likely that there, too, the damping force was a reasonably linear function of velocity so that the results of the study applied to them as well. It was found that the damped springs were able to handle particular motions fairly efficiently, but that in general they were not very good. Undamped springs were generally not very good.

STUDY OF THE OPTIMUM ISOLATOR

The manner in which the behavior of the damped systems varied with the character of the input motions suggested that improvement would result from using a different kind of damper, one largely insensitive to velocity. With this in mind, the characteristics shown in Fig. 1 were developed. The sole purpose of the resilient element was to provide an equilibrium position. At very low velocities the damping was linear, while at the higher velocities the damping force was limited. This was similar to the action of certain automotive shock absorbers. These absorbers were intended to insure passenger comfort and were not much more efficient than linear damped springs on shipboard. Because of the similarity, however, the optimum mount was named double-acting. The resilient, linear-damped mount was named simply damped.

A program was written for the small time-sharing computer available at the Naval Ship Research and Development Center (NSRDC) to study the response of the double-acting mount, as well as the ideal mount and the damped mount. This program used methods of numerical analysis and was checked against a different program (3) written for the large computer and based on the exact solution of the equations. The smaller computer was used for this study because of its fast reaction time. The program used was sufficiently versatile to include both ideal behavior and linear damping as special cases. It is available on request.

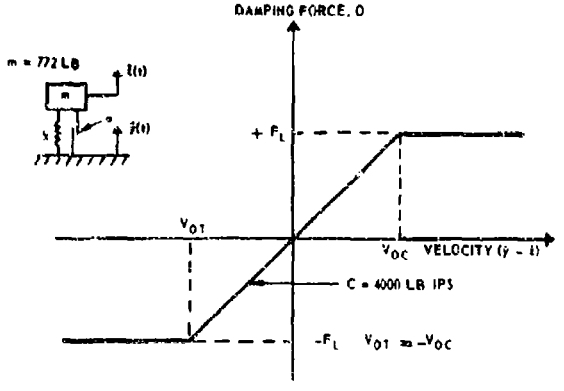

Fig. 1. Optimized shock isolation system (F_L is adjusted by varying V_{0C})

Foundation Input Velocities Used

Analytic representation of foundation velocity was used so that the effects of changing its shape would not be obscured by the irrelevant excursions normally found in experimental records. The response of the mounts could just as well have been calculated for any arbitrary input, however, had this been desired. The basic input velocity, Type I, is shown in Fig. 2. Here the velocity was represented by a versed-sine rise to 120 in./sec in 26 ms, followed by a deceleration of 4 g to rest. Three other foundation velocities, Types II, III, and IV, were obtained by decreasing the rise time to 0.5 ms and the deceleration to zero.

Mount Efficiency

The performance of various shock mounts was evaluated by comparing the deflections required to limit the mass accelerations with the same value. The mount requiring the smallest deflection, was, of course, the most efficient. The efficiency of a mount was quantified by comparing its deflection requirements with that of the ideal: *Efficiency = (ideal deflection/calculated deflection) × 100 percent.*

Mounts Investigated

The responses of three different types of mounts to each of the four input velocities were calculated. These were the ideal mount, the damped mount, and the double-acting mount. The damped mounts were specified in the usual way by fixed-base natural frequency and damping ratio. The double-acting mounts were specified by fixed-base natural frequency and the damping force limit, F_L, expressed as mass acceleration in g's. The mount configurations studied were tabulated in Table 1. Only one set of calculations was necessary to completely define the response of the ideal mount to each motion, so it was not tabulated.

TABLE 1
Mount Configurations Used[a]

Damped Mount	Double-Acting Mount
Damping Ratio	Damping Force Limit, g's
0	1
10	2
20	5
40	10
100	20

[a]Natural frequency: 5 and 10 Hz.

Presentation of Data

The behavior of each mount was described in terms of the maximum acceleration in g's transmitted to the mounted mass and the rattle-space, the sum of the positive and negative maximum excursions in inches of the mass from its equilibrium position.

RESULTS

The responses of the various mounts to each foundation velocity are shown in Figs. 3 through 6.

CONSIDERATIONS

Performance of the Damped Mounts

It can be clearly seen that as the damping ratio was increased from zero the transmitted

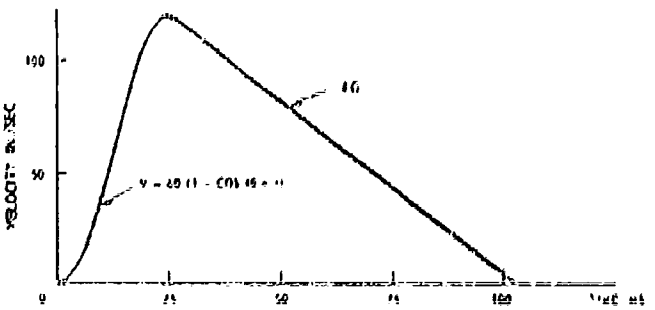

Fig. 2. Type I foundation velocity

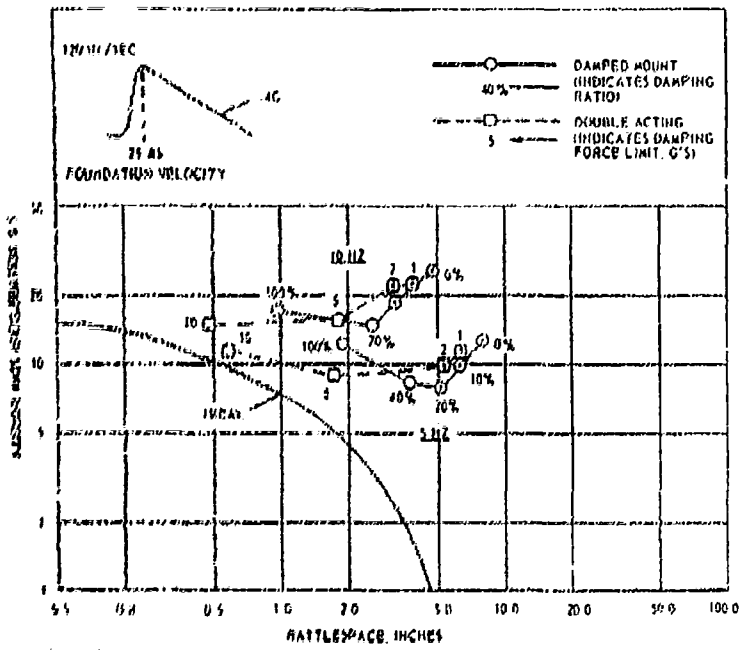

Fig. 3. Response of shock mounts to Type I foundation velocity (points with included dot indicate maximum acceleration observed in downward direction)

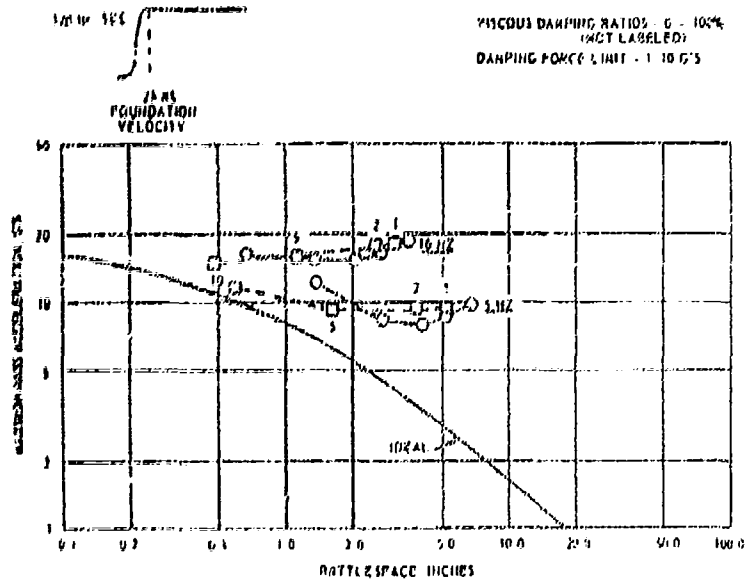

Fig. 4. Response of shock mounts to Type II foundation velocity

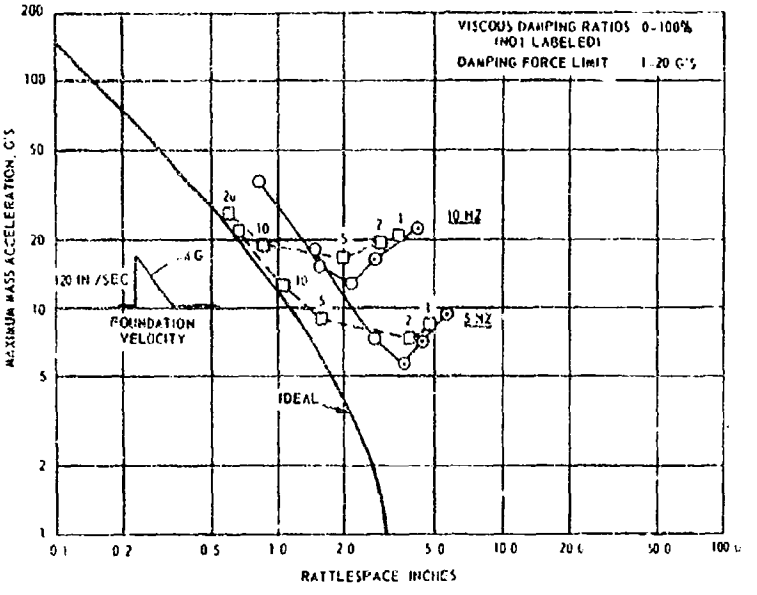

Fig. 5. Response of shock mounts to Type III foundation velocity

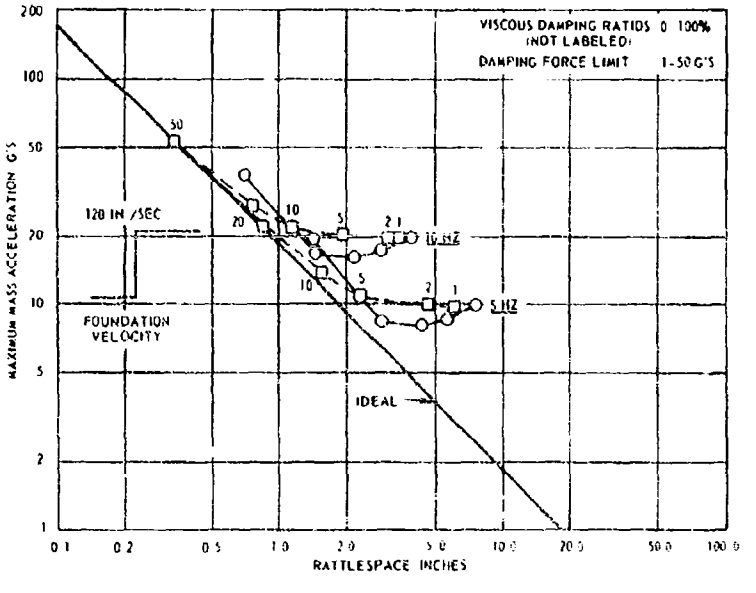

Fig. 6. Response of shock mounts to Type IV foundation velocity

acceleration typically first decreased and then increased while the rattlespace decreased continuously. The efficiency of the mount did not improve after the damping ratio was increased beyond a given value. This is apparent in all the figures, but is most obvious in Fig. 5. Here the efficiency of both the 5- and 10-Hz damped mounts reached a maximum of about 50 percent at a damping ratio of 40 percent and did not improve with a further increase in damping.

The efficiency of the damped mount was best where the foundation velocity increased abruptly (Figs. 5 and 8). Here the damper exerted its accelerating force on the mass from the very beginning. Where the velocity increased at a slower rate, the damper exerted less force initially and time was lost while the spring force built up. It was partly this effect which led to the idea of the double-acting mount.

Performance of the Double-Acting Mount

The efficiency of the double-acting mount was not limited in the same manner as that of the damped mount. In fact, as the damping force limit was increased, the efficiency invariably approached 100 percent. That it was not 100 percent efficient at the lower limits was a result of energy stored in the spring; an efficient mount does not store energy. As the damping force limit was increased, the spring energy becomes relatively less important. As would be expected, the behavior of the double-acting mount approached that of the undamped spring as the damping force limit was decreased. In this region the magnitude of the transmitted acceleration was determined roughly by the fixed-base natural frequency associated with the spring used. The efficiency of the mount, however, was determined by the damping force limit as this limit was increased. Because the mount was potentially extremely efficient, the deflection requirements were limited ultimately by the ideal.

One of the practical engineering problems involved in the design of damped mounts was that of obtaining enough damping force. Where large masses must be mounted, the forces required to yield significant benefits became very large. The requirements could have been lessened by lowering the mounting frequency, of course, but that method was limited. Thus, any way of decreasing the damping force requirements of a mount was desirable, even if it did not result in improving the efficiency of the mount.

The performance of the 10 Hz-, 40-percent damped system was identical to that of the 10-Hz, 5-g double-acting system (Fig. 3), so that these two configurations were used to compare damping force requirements. It was assumed that the weight supported by these mounts was 772 lb so that, by definition, the damping force exerted by the double-acting mount was 3960 lb. Inspection of the velocity-time history for the damped mount showed that the maximum damping force was 6032 lb, 52 percent greater, although the efficiencies were the same. This behavior was typical.

The linear damping coefficient of 4000 lb/in./sec used for the low velocity damping of the double-acting mount seemed to require that the deflected mount must take a very long time to recover its equilibrium position. However, for large deflections the spring force was sufficient to overpower the damper and return the mass most of the way to equilibrium rather rapidly. For example, the spring force was greater than the damping force limit for the 10-Hz, 5-g double-acting mount when the deflection was greater than about 1/2 in. The slow return, then, would start nearer than this point, rather than from some point further out. If a faster return were found to be necessary the low-velocity damping coefficient could be reduced with some slight cost to mount efficiency.

CONCLUSIONS

The double-acting shock mount was found to be capable of attaining very high efficiencies. Even at lower efficiencies it required less damping force than a linearly damped mount of comparable performance. In contrast to the ideal mount, it was capable of maintaining an equilibrium position. The double-acting mount appeared to combine the best features of the ideal and the linearly damped mounts with few of their disadvantages.

REFERENCES

1. K.T. Cornelius, "Rational Shock Mount Design, Investigation of the Efficiency of Damped, Resilient Mount," NSRDC Rept. 2383, July 1967
2. W.D. Pilkey, "Optimum Mechanical Design Synthesis," IIT Res. Inst. Rept. M 6069, June 1966

3. R.R. Lilliston, "A Computer Solution for the Response of a Simple Base-Excited Mechanical Oscillator with a Particular Type of Non-Linear Damping," NSRDC Rept. 2521, Nov. 1967

DISCUSSION

Mr. Sevin (IIT Research Inst.): I might make a comment that these ideal or optimum curves refer to a tradeoff between the constraint of rattlespace, in this instance, and the performance index of acceleration attenuation. They are functions of either the time details or the input in the deterministic case of this paper, or in the frequency distribution functions of Prof. Paul's paper. If you change the inputs, whatever the characterization might be, you change the nature of the optimum. There is evidence that suggests that these curves are relatively insensitive to reasonable variations in the input. That does not necessarily mean that an isolator designed to be optimized for a given input would itself have a small deviation from the optimum according to another input. The tradeoff curves themselves are reasonably insensitive.

* * *

AN INVESTIGATION OF THE PERFORMANCE OF GAS-BEARING MACHINERY SUBJECTED TO LOW-FREQUENCY VIBRATION AND SHOCK

Peter W. Curwen and Alan Frost
Mechanical Technology Incorporated
Lathan, New York

The use of gas or steam bearings in certain types of naval shipboard machinery offers several advantages. However, such machinery must operate in a dynamic environment. The question of bearing reliability and ruggedness under dynamic conditions thus arises. To gain initial insight into this question, a gas-bearing machine having a 61.5-lb shaft has been experimentally subjected to low-frequency nonimpulsive frame oscillations and also to frame impact. Maximum acceleration, measured at the upper journal bearing housing, was 4 g's during the oscillation tests and 38 g's during the shock tests. Capacitive displacement transducers, mounted within the bearings, were used to measure dynamic bearing responses throughout the tests.

Over 1000 shock cycles were imposed on each of two externally pressurized bearing systems and on one self-acting system. During each shock interval, a dozen or so momentary bearing contacts were observed. Nonetheless, all bearing parts were in excellent or good condition at the end of the tests.

Momentary bearing contacts were observed ov- at quite low shock levels. Compatibility, wear rate, and integrity of bearing materials th .s become the key factors in establishing gas-bearing reliability in a shock environmen: Additional data pertaining to these factors are badly needed.

An analytical procedure has been formulated for designing gas bearings that will be subjected to frame oscillations. Comparison of calculated and measured bearing displacements confirms that the design procedure is valid.

INTRODUCTION

Process-fluid lubrication of rotating machinery has made very significant advances within the last decade. By definition, a process-fluid-lubricated machine is one in which the working fluid flowing through the machine, or the environmental fluid surrounding the machine, is also utilized to lubricate the shaft bearings. The working or environmental fluid may be a liquid, vapor, or gas. In this paper only gas and steam-lubricated bearings are discussed.

Since 1958, the U.S. Atomic Energy Commission (AEC) has installed and operated a total of 17 gas-bearing machines in nuclear reactor experimental test loops. Very successful operation, totaling over 65,000 hours, has been accumulated with this machinery [1]. The U.S. National Aeronautics and Space Administration (NASA) is currently procuring and testing gas-lubricated turbomachinery for closed Brayton cycle auxiliary space-power systems [2].

Gas and steam-lubricated bearings are now being investigated for use in naval shipboard machinery. A study [3] performed in 1965 indicated that definite benefits would result for various types of naval machinery if process-fluid lubrication (specifically, steam or gas lubrication) of shaft bearings could be utilized. Improved reliability and maintainability, reduced size and noise, and elimination of auxiliary systems were some of the advantages identified.

In parallel with the above study, Contract Nonr-4358(00) was conducted to obtain a first assessment of the ability of gas-bearing

machinery to survive the shipboard vibration and shock environment. This is probably the most crucial question with respect to practicability of gas (or steam) bearings in naval applications. The aforementioned AEC machinery operates in static environments, while the NASA space-power machinery will be subjected to appreciable shock and vibration only during the relatively short launch period. Shipboard machinery, on the other hand, will experience an almost continuous spectrum of vibration and shock. Moderate seastates will produce low-frequency roll and pitch motions of the ship. Bow slap in heavy seas, firing of heavy guns, bomb or torpedo explosions will produce shock loads. Bow slap in particular, while not a necessarily severe shock condition, is nonetheless a potentially critical condition because hundreds of thousands of such impacts may be accumulated during a normal cruise.

As reported in Ref. [4], the initial assessment of gas-bearing performance under dynamic conditions was conducted with a 10,000 rpm gas-bearing machine having a 61.5-lb rotor. The machine was subjected to low-frequency non-impulsive frame oscillation and also to frame shock. Both self-acting and externally pressurized bearings were tested. The results of these initial tests, which are reviewed in the following sections of this paper, were sufficiently promising to warrant expansion of the shock test phase under Contract N000-14-66-C0282. At the same time, Contract Nonr-4966(00)M-2 was awarded for development of a 700-hp turbine-driven forced-draft blower using superheated turbine steam as the lubricant for externally pressurized journal and thrust bearings. This contract marks the first application of steam bearings to a major piece of shipboard equipment. A cross-section schematic of the blower is shown in Fig. 1.

The balance of this paper briefly documents the effects of low-frequency frame oscillation and frame shock on the performance of gas bearings. Although the investigation was limited to gas bearings, the dynamic responses of superheated steam bearings should be essentially the same. From a theoretical standpoint, superheated steam can be treated as a gas. However, if significantly different coating and/or structural materials are selected for either steam or gas-bearing parts (compared with those that have so far been tested), the consequencies of the dynamic bearing responses could be different. Because bearing contacts do occur under shock conditions, final proof of bearing reliability and ruggedness must come from shock tests on parts that have been fabricated with the same materials as proposed for the specific application.

TEST MACHINE

A schematic view of the gas-bearing test machine is shown in Fig. 2. Significant parameters of the shaft assembly are —

Weight	61.5 lb
Distance between journal centers	32 in.
Overall length	39.75 in.
Polar moment of inertia	0.55 in.-lb-sec^2
Transverse moment of inertia about c.g.	20.9 in.-lb-sec^2
Locations of c.g.	17.1 in. from thrust bearing

The shaft is driven by a four-pole, three-phase induction motor mounted between the journal bearings. A variable frequency generator set is used to control motor speed.

Two identical journal bearings and a double-acting thrust bearing are used to support the shaft. The journals are 2.375 in. in diameter and have a length-to-diameter ratio of 1.5. The thrust runner has an OD of 6.28 in.

Two easily interchangeable bearing systems were designed for the test machine. One system consists of externally pressurized (hydrostatic) bearings. The journal bearings are cylindrical sleeve bearings with two rows of 18 mil diameter orifices (eight orifices per row). The main thrust bearing is a 5-in. OD by 3.5-in. ID, single-row bearing with 36 orifices. The second bearing system consists of self-acting (hydrodynamic) bearings. The journal bearings are four-pad pivoted-pad bearings that operate at a preload ratio of 0.5 to 0.7. The main thrust bearing is a 6.28-in. OD by 2.75-in. ID spiral-grooved (Whipple plate) bearing of inwardly pumping configuration.

Figure 3 is a photograph of the shaft assembly and the parts for the self-acting bearing system. Figure 4 shows one of the externally pressurized journal bearing sleeves. Additional design and test data pertaining to the two gas-bearing systems are given in [4].

INSTRUMENTATION

To gain insight into the performance of gas bearings under condition of low-frequency frame

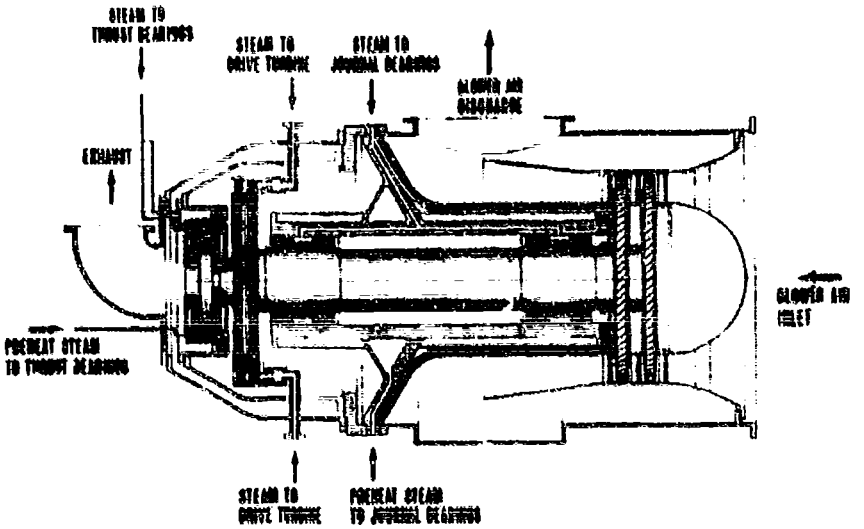

Fig. 1. Schematic cross section of steam-lubricated forced-draft blower

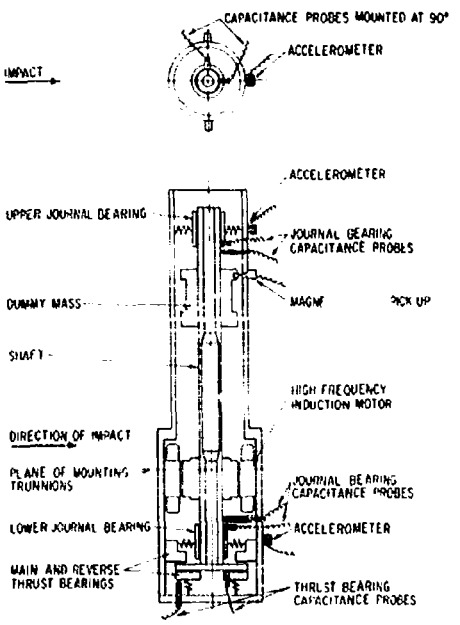

Fig. 2. Schematic of gas-bearing test machine showing location of instrumentation

oscillation and shock, the following experimental data were obtained via appropriate instrumentation:

(1) Normal bearing system performance under static conditions.

(2) Frame acceleration and/or displacement during oscillatory and impact excitation.

(3) Displacement response of the bearing system to the oscillatory and impact excitation.

Identical bearing system instrumentation was used for both the oscillation and shock tests. As might be expected, the shock condition imposed the most severe demands on instrumentation frequency response. In this respect, the instrumentation for measurement of impulsive displacements was less than optimum.

Bearing System Instrumentation

The most meaningful indications of bearing system dynamic performance are measurements of (a) position of the rotating journals within the bearing clearance, and (b) film thickness in the thrust bearing.

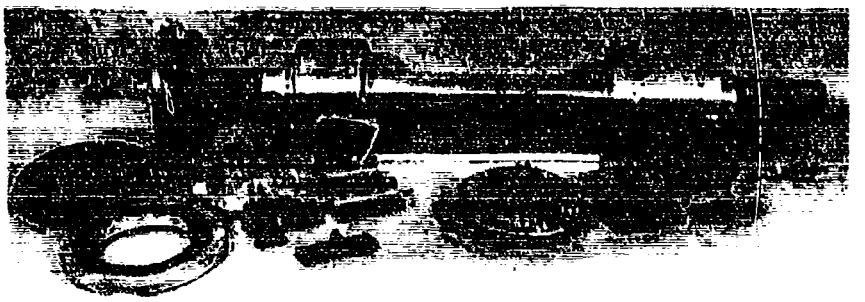

Fig. 3. Shaft assembly and self-acting bearing parts for the gas-bearing test machine

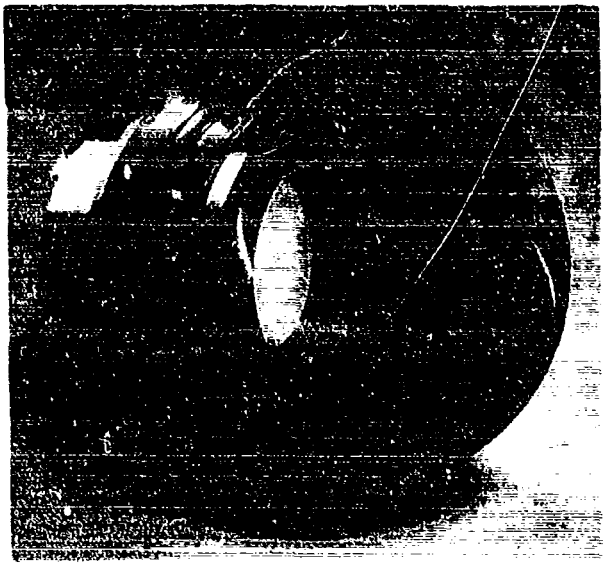

Fig. 4. Externally pressurized journal bearing for the gas-bearing test machine

These measurements were obtained by mounting capacitive displacement transducers within the bearings as shown in Fig. 2. Two probes were mounted in each journal bearing, circumferentially displaced 90 degrees from each other. Two probes were likewise mounted in the main thrust bearing, also circumferentially displaced 90 degrees.

Readout of the bearing probes was obtained from dual-beam oscilloscopes. With the signals from the 90-degree displaced journal bearing probes applied to the CRO X and Y deflection plates, orbital traces (or loci) of the journals within the clearance space could be obtained. By switching the CRO to common time base, X and Y components of bearing clearance could be displayed as a function of time. Common time-base readout of the two thrust bearing film thickness traces permitted some indication as to whether parallel alinement of the bearing surfaces was maintained under dynamic conditions. Theoretically, however, three film thickness readings are required to accurately define the relative positions of these surfaces.

Because both the journal and thrust bearings were "flexibly" mounted, additional capacitive displacement transducers were used to measure motion of the rotating journals and the thrust-bearing stator relative to the test machine casing.

The noncontacting capacitive displacement measuring system selected for these tests had the following characteristics:

(1) Excellent linearity over the complete range of possible bearing displacements.

(2) High output sensitivity (0.1 volt/mil).

(3) Stable output up to temperatures of 400° F (up to 1000° F with special lead wire).

(4) Excellent long-term stability.

(5) Flat frequency response from D-C to 1000 Hz.

Although duration of the shock pulses was expected to be 50 to 100 ms, it was recognized that frequency response of the capacitive transducer system left something to be desired. However, for the immediate purposes of the study, the 1000-Hz response was judged to be adequate. (It should be noted that flat frequency response of the capacitive system has recently been increased to 5000 Hz by use of an improved filter design.)

Additional Instrumentation

Shaft speed of the test machine was detected by means of a magnetic pickup. Digital display of speed was obtained from an electronic counter. No attempt was made to measure dynamic variations in speed.

During the shock tests, dynamic displacements of the shock table were measured with a linear-variable-differential transformer (LVDT). Dynamic accelerations were measured with crystal accelerometers mounted on the test machine casing in the planes of the two journal bearings. Readout of the LVDT and accelerometer signals was obtained via time-base CRO traces. The traces were triggered by the shock hammer just prior to hammer impact.

Frequency response to the LVDT was down 3 db at 100 Hz. Hence, accuracy of the shock table displacement amplitudes is in question. The main value of the LVDT was to obtain an approximate indication of pulse shape. Frequency response of the accelerometer system was flat from 20 to 10,000 Hz when displayed directly on the CRO. Peak acceleration values should thus be quite accurate.

All significant instrumentation signals were recorded on magnetic tape using FM electronics having a flat frequency response from 0 to 5000 Hz. Comparison of direct-display CRO signal traces and magnetic-tape playback traces indicated no degradation of signal waveform caused by the tape recorder.

BEARING PERFORMANCE DURING LOW-FREQUENCY VIBRATION

An Oscillation Test Stand was designed to subject the gas-bearing test machine to oscillatory (periodic) angular displacements about a fixed pivot axis. Figure 5 shows the test machine mounted on the oscillation stand. The stand had a continuously variable oscillation frequency of from 0 to 65 cpm. Oscillation amplitudes, measured from the vertical, could be set at ±11.5, ±23.5 or ±36.5 degrees.

The Oscillation Test Stand was not designed to simulate actual wave-induced shipboard motions. (Such motions would, in fact, be the result of simultaneous rotations and translations of the ship's hull and would not, in general, be truly periodic.) The primary function of the test stand was to provide a means whereby the validity of proposed gas-bearing design procedures for low-frequency vibration conditions could be experimentally determined. Exact simulation of shipboard motions was not felt to be necessary for this purpose. Because wave-induced motions have very low fundamental frequencies relative to the critical speeds of rotating machinery, it was hypothesized that the dynamic bearing reactions could be accurately calculated on the basis of a simply supported rigid shaft. The bearings could then be sized on the basis of static load capacity and eccentricity considerations. Validity of this design approach could be experimentally assessed using a simple test stand, provided accurate measurements of the frame and bearing displacements were obtained. Once the basic design hypothesis were verified, the analytical design procedures could readily be extended to the case of complex frame motions, and confidently applied to any specific situation without the necessity of additional experimental testing.

Figure 6 shows oscilloscope photographs of the upper journal-bearing loci obtained during testing of the externally pressurized gas-bearing system at supply pressures of 50 and 75 psig. (The photos are also typical of data

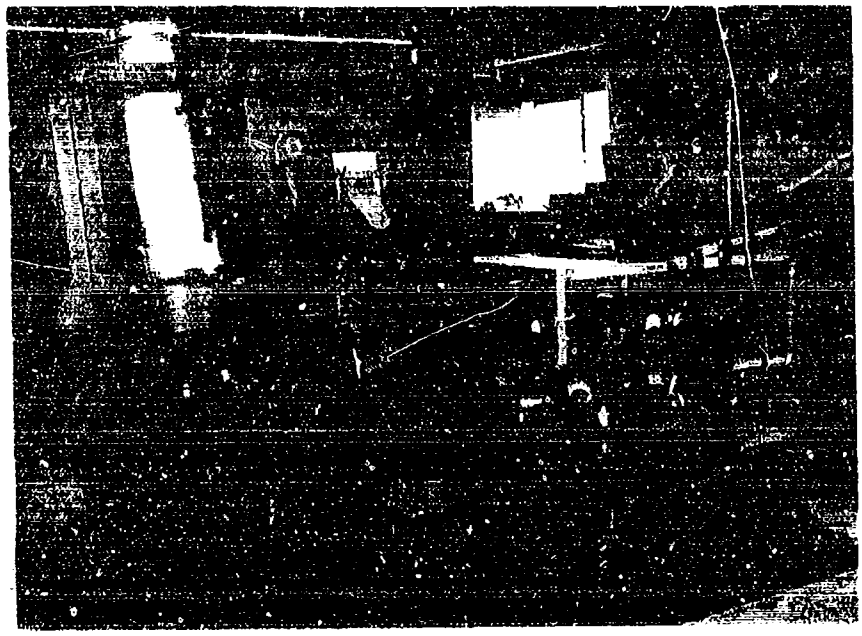

Fig. 5. Test machine mounted on oscillation test stand

obtained during testing of the self-acting bearing system.) The effects of frame oscillation, with and without shaft rotation, are clearly shown. It is seen from the lower photographs of Fig. 6 that the locus of the journal center is an ellipse under simultaneous conditions of 10,000-rpm shaft speed and 62-Hz oscillation frequency. This reflects the fact that the resultant bearing load consists of a gyroscopic component acting 90 degrees from the in-plane acceleration component.

Figure 7 shows a comparison of the measured and calculated response for the upper journal bearing during frame oscillation. This figure illustrates that the bearing forces, and resulting bearing eccentricities, can be calculated with sufficient accuracy for engineering design purposes. Details of the analysis procedure, as well as additional test and calculated data for both the externally pressurized and self-acting bearing systems, are given in Ref. [4].

In summary, a design procedure was experimentally validated whereby the load capacity of steam and gas-lubricated bearings could be investigated for any specified condition of low-frequency shipboard motion. In the process of verifying the design procedure, satisfactory operation of two practical gas-bearing systems was demonstrated at oscillation rates of up to 62 Hz and corresponding peak accelerations at the upper journal bearing of 4.05 g's. Both the self-acting and the externally pressurized bearing systems were able to carry the dynamic loads at safe film thicknesses (that is, without film rupture and rubbing contact).

BEARING PERFORMANCE DURING SHOCK

A Shock Test Stand was designed to subject the gas-bearing test machine to unidirectional impact loads. Figure 8 shows the test machine mounted on the shock stand. The Shock Test Stand is patterned after the Navy Hi-Shock Machine for Lightweight Equipment as defined in MIL-S-901B (Navy). The significant differences are that only the pivoted shock hammer has been provided (only horizontal impacts can be applied) and the hammer weight is 200, rather than 400 lb. It should be noted that the Shock Test Machine was not designed for the immediate objective of producing high-impact shock displacements as required by Navy qualification specifications (although this does remain an ultimate objective). It was designed primarily to produce shock pulses that would have shape

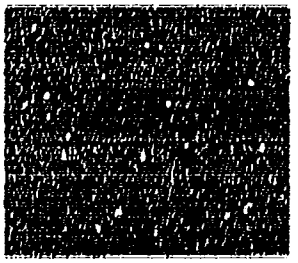

(a) Residual unbalance orbit at 10,000 rpm and 75 psig supply pressure (stationary frame)

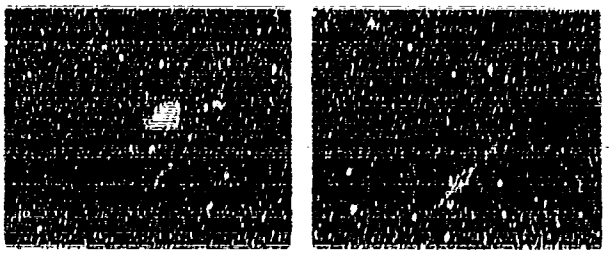

75 PSIG SUPPLY 50 PSIG SUPPLY

(b) Journal center loci at zero shaft rpm during 1 cycle of frame oscillation

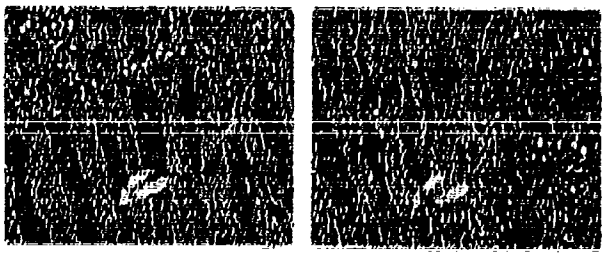

75 PSIG SUPPLY 50 PSIG SUPPLY

(c) Journal center loci at 10,000 rpm during 1 cycle of frame oscillation

Fig. 6. Loci of the externally pressurized upper journal bearing during frame oscillation; oscillation amplitude: ±11.5°; oscillation frequency: 62.7 hz. CRO calibration: 0.2 mils/major grid

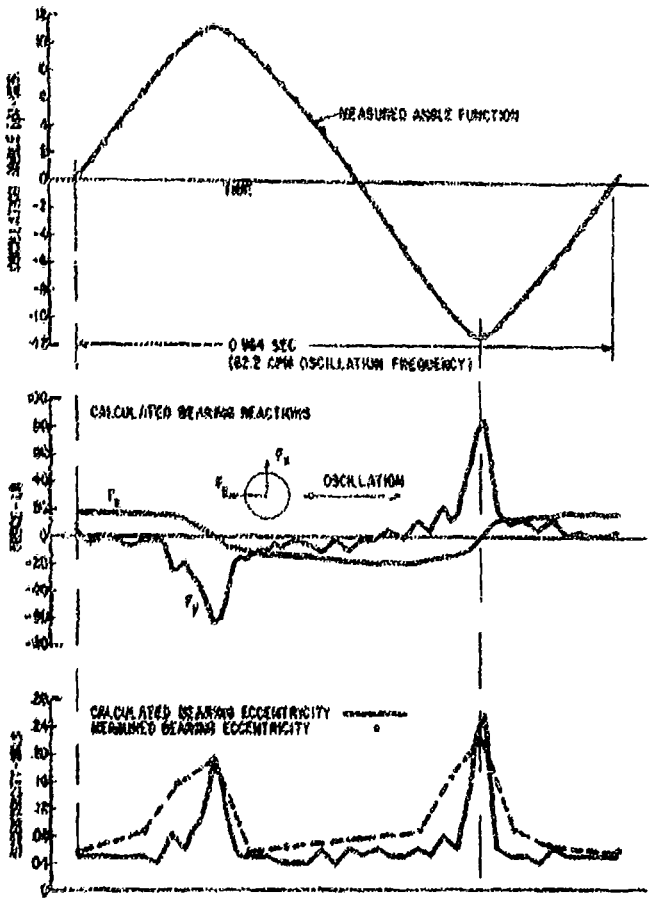

Fig. 7. Comparison of measured and calculated response of the externally pressurized upper journal bearing during frame oscillation; shaft speed: 10,000 rpm; bearing supply pressure: 75 psig

and duration characteristics similar to those produced by Navy hi-shock machines. A realistic basis would thus be provided for assessing gas-bearing performance and identifying any problem areas.

The first series of shock tests, with the test machine running at 10,000 rpm, consisted of a small number of impacts at increasing heights of hammer drop. It was noted that momentary rupture of the thrust-bearing film began at a drop height of 0.25 in. (that is, at very low impact levels). Momentary rupture of the journal bearing films began at a drop height of approximately 1.7 in. The film rupture characteristics were similar for both the externally pressurized and self-acting bearings; that is, onset of film rupture did not appear to be a function of bearing type.

Hammer drop height was gradually increased to 14.1 in., at which point performance of the test machine was noticeably impaired. The impaired performance was subsequently found to have resulted from permanent deformation (bending) of the shaft, not from bearing failure. In spite of the momentary contacts that had occurred during most of the shock intervals, there was no observable damage to the bearing parts. However, the extent of the shock series, in terms of number of impacts, was too

Fig. 8. Test machine mounted on shock test stand

limited to permit conclusions regarding bearing life under repeated shock conditions.

Several facts became clear from the first series of shock tests:

(1) Momentary bearing contacts should be anticipated in a gas-bearing system when the bearing housing is given an impulsive displacement of noticeable amplitude.

(2) Compatibility of bearing materials is of prime importance in any application where frame impact may occur. The bearing materials must be able to survive many momentary high-speed contacts without noticeable degradation of bearing performance.

(3) Structural design of the shaft and bearing system must be sufficient to assure that permanent deformation of the various parts cannot occur under the maximum possible impact condition.

(4) Performance of self-acting and externally pressurized bearings during impact is not significantly different.

To obtain an indication of bearing life capability under shock conditions, a second series of shock tests was undertaken. The test machine shaft assembly was first redesigned so that shaft bending would not be a problem. An extended series of impacts was then applied to each of three bearing systems (one self-acting system and two externally pressurized systems). The types of bearings and bearing materials used are listed in Table 1.

Figure 9 shows a typical CRO display of the various instrumentation signals during one impact interval. These data were obtained during the extended tests on the third (externally pressurized) bearing system. Shaft speed was 8,000 rpm, drop height was 9.6 in., and bearing supply pressure was 60 psig.

The upper left-hand photograph in Fig. 9 shows a journal bearing locus prior to impact. The locus is a small orbit owing to residual shaft unbalance.

The remaining five photographs in Fig. 9 show various responses during the shock interval. The shock table displacement pulse was approximately half-sine, with a peak indicated amplitude of 0.18 in. and a duration of 70 ms. Peak acceleration at the journal bearing housing was approximately 38 g's. This peak occurred within the first several milliseconds of the displacement pulse.

TABLE 1
Description of Bearing Systems Used for the Second Series of Shock Tests

	Bearing System Designation		
	First	Second	Third
Type of bearing system	Externally pressurized	Self-acting	Externally pressurized
Type of journal bearings	Carbon graphite sleeve with double orifice row	Chrome-oxide-coated pivoted-pad, 4 pads per bearing	Chrome-oxide-coated sleeve with double-orifice row
Coating on shaft journals	Chrome oxide (the same shaft journals were used throughout the shock tests)		
Type of main thrust bearing	Chrome-oxide-coated annular bearing with single-orifice row	Chrome-oxide-coated, spiral-grooved bearing (grooves on stator)	Same parts as used in first bearing system
Coating on thrust runner for main thrust bearing	Chrome oxide (the same thrust runner was used throughout the shock tests)		

The upper right hand photograph in Fig. 9 shows the journal orbit during the impact interval. It is seen that a dozen or so momentary bearing contacts occurred during the shock interval. Time-base traces of the journal motion and the thrust bearing film thickness are also shown below the journal locus trace. It is seen that one thrust bearing contact occurred during the first 90 ms of the shock response.

Figure 10 shows an oscillograph recording of several of the instrumentation signals for a period of approximately 0.5 sec. It is seen that the residual bearing responses persist for an appreciable period of time after the shock pulse. This reflects the generally low level of damping that exists in a gas-bearing system.

The total number of impacts to which the three bearing systems were subjected is given in Table 2, together with the associated values of hammer-drop height, casing acceleration, and test-stand displacement amplitude. (In addition to the data given in Table 2, recent testing with the third bearing system has been performed at drop heights of 17.2 in.)

The externally pressurized bearing systems survived the test series without any noticeable degradation of performance. However, at the conclusion of tests on the self-acting bearing system, readjustment of the journal bearing setup clearances was required. It was subsequently found that a slight flattening (deformation of the bearing pivots was responsible for the change in bearing clearance.

All of the bearing parts were carefully examined at the conclusion of the tests. The thrust bearing surfaces, and the externally pressurized journal bearing sleeves, were in excellent condition. Although evidence of the momentary rubs could be visually detected, measurements indicated actual wear in the bore of the journal sleeves to be of the order of only 25 μin.

Considerably more wear occurred on the shaft journals. Wear of the upper and lower journals was measured to be 150 and 350 μin., respectively. Most of this wear occurred during testing of the self-acting pivoted-pad journal bearings. Figure 11 shows the lower journal at the conclusion of tests on the self-acting bearing system. A total of 3061 shock cycles had been accumulated at this point. The shaft was reinstalled, without any touching-up of the journal surfaces, and an additional 1262 shock cycles accumulated during testing of the third bearing system. The journals were still smooth and in good operating condition after 4323 shock cycles.

The wear area on the self-acting journals pads is shown in Fig. 12. It is seen that wear occurred only in the central area of the pad (that is, under the pivot point). Because both the pads and the shaft journals were initially machined to a straightness tolerance of 50 μin.,

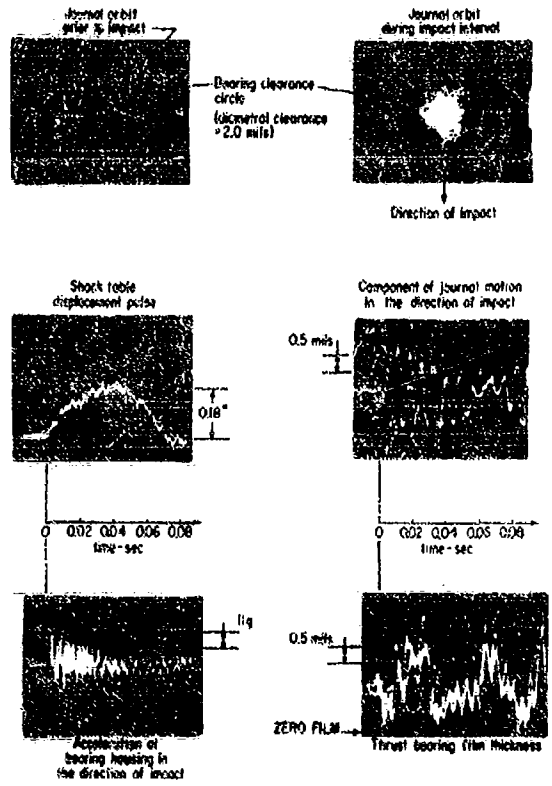

Fig. 9. Response of externally pressurized bearing system to a 9.6-in. hammer drop; shaft speed: 8,000 rpm; bearing supply pressure: 60 psig

it is concluded that the gas film, at the instant of contact, had sufficient stiffness to bend the ends of the pads away from the shaft. Aside from the previously mentioned flattening of the pivots, the self-acting pivoted-pad journal bearings were in good conditions for continued running.

CONCLUSIONS

Under conditions of low-frequency nonimpulsive shipboard vibration, gas (and steam) bearings should be designed so that fluid film lubrication is maintained at all times (that is, so that sliding contact does not occur). An analytical procedure for designing gas bearings to satisfy this criterion has been formulated and verified by test data. The procedure is described in Ref. [4].

Under conditions of frame impact as represented by the Navy high-shock qualification tests, momentary bearing contacts will occur in machinery containing gas- (or steam-) lubricated bearings. Additionally, it is clear that gas bearings can experience momentary contacts at relatively low-impact levels, such as may be produced by bow slap in heavy seas. Therefore, in addition to passing the high-shock qualification tests, reliability of gas bearings must also be demonstrated over hundreds of thousands of low-level impacts. The first step in this direction will be taken shortly. The third bearing system of Table 1 is to be subjected to 25,000 low-level impacts.

It has been clearly established that the reliability of gas bearings under shock conditions will be almost solely dependent upon the compatibility, the wear rates, and the long-term

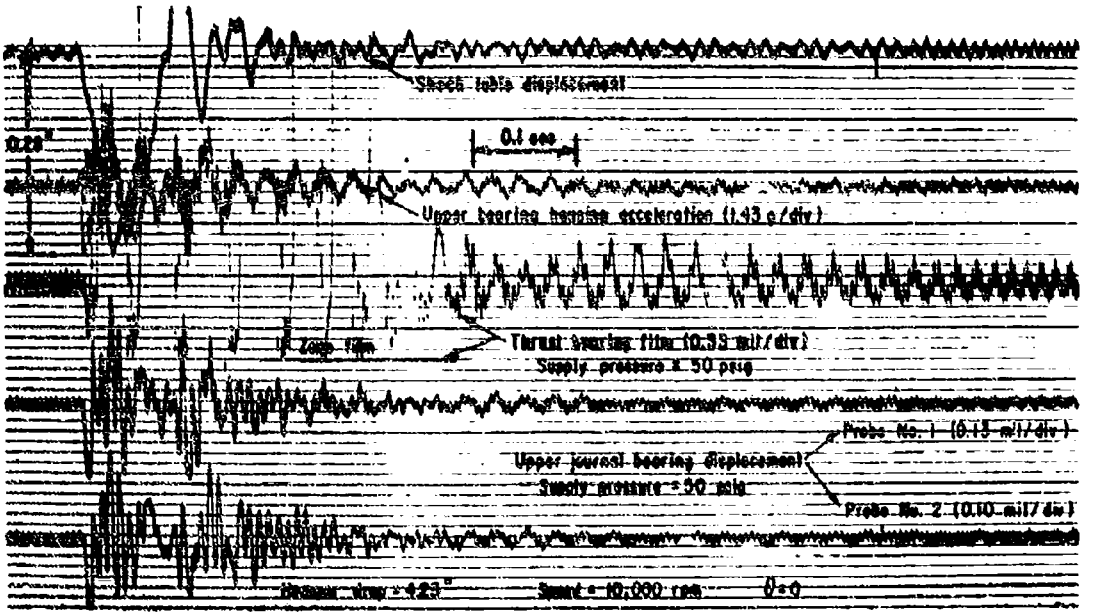

Fig. 10. Response of externally pressurized bearing system to a 4.3-in. hammer drop

TABLE 2
Data Acquired During Second Series of Shock Tests

Bearing System Designation	Height of Hammer Drop (in.)	Number of Impacts[a]	Rotor Speed (rpm)	Peak Acceleration Measured at Journal Bearing Housings (g)		Test Stand Displacement Amplitude (in.)	Shock Pulse Duration (ms)
				Lower Brg.	Upper Brg.		
First	2.61	200	0	13.8	21.3	0.222	60
	2.61	900	8000	13.0	19.3	0.210	72
	9.67	100	0	20.6	34.7	0.298	80
	9.67	500	8000	-	-	0.300	80
Second	2.89	510	8000	13.0	26.5	0.238	55
	9.67	851	8000	15.0	36.0	-	65
Third	9.67	1262	8000	21.8	38.5	0.238	75

[a]Total number of impacts on shaft journals and thrust runner = 4323.

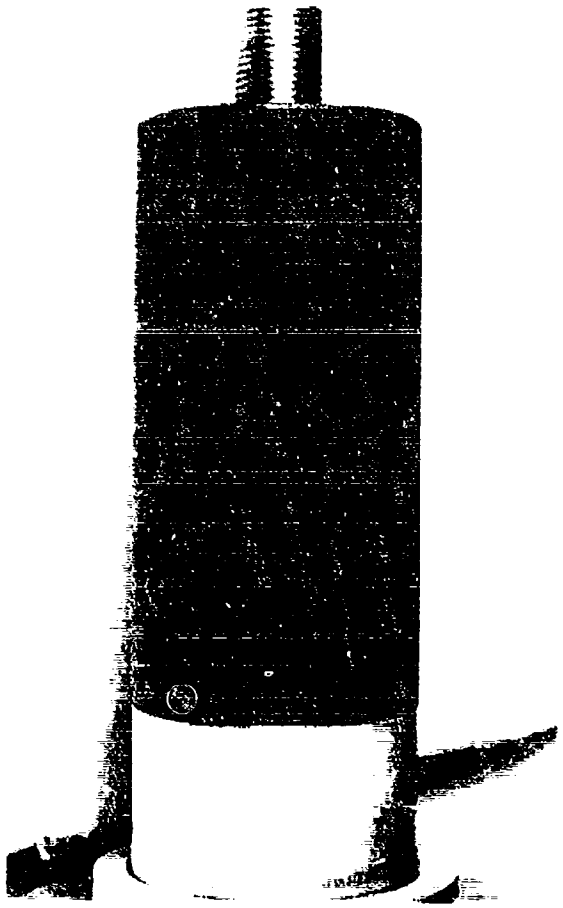

Fig. 11. Lower shaft journal after 3061 impacts at the conditions of Table 2

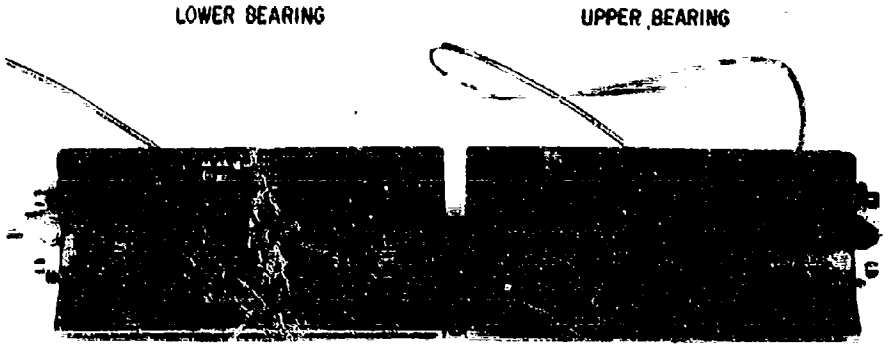

Fig. 12. Pads from self-acting journal bearings after 1361 impacts at the conditions of Table 2

integrity of the bearing materials. To permit quantitative prediction of bearing life and selection of optimum bearing materials, the above mentioned basic performance information must be obtained for various bearing materials as a function of —

(1) impact level

(2) bearing surface velocity

(3) bearing geometry

(4) bearing temperature

(5) bearing lubricant.

Extensive, carefully controlled testing under actual shock conditions appears, at present, to be the most meaningful way of obtaining these data.

Finally, it still remains to be determined whether gas- or steam-bearing machinery will ever be able to meet Navy high-shock specifications, with or without shock isolation. To this end, testing must continue to progress to increasing heights of hammer drop until the high-shock specification conditions are obtained and adequate bearing performance is demonstrated over the specified number of shock cycles.

REFERENCES

1. P. W. Curwen, "Operational Experience With Gas-Bearing Turbomachinery," paper presented (without publication) at a panel discussion on Gas Bearing Applications at the ASME 1966 Winter Annual Meeting, New York

2. "Space Power Systems Advanced Technology Conference," NASA Rept. SP-131, published by the Lewis Res. Ctr., Ohio, Aug. 23-24, 1966, pp. 100-126

3. J. W. Bjerklie, "Categorization of Shipboard Machinery for Applicability to Gas Bearings," MTI Rept. 65TR5-III, 1 Apr. 1965, prepared under Contract Nonr-4535(00)

4. P. W. Curwen, "Evaluation of Gas Bearings for Use in Naval Machinery Under Conditions of Frame Oscillation and Impact," MTI Rept. 65TR1, 12 Jan. 1965

DISCUSSION

Mr. Pakstys (General Dynamics/Electric Boat): Why did you build and use a special shock machine instead of using the regular Navy shock test machine?

Mr. Curwen: Mainly because this type of testing extends over a long period of time. Because of the amount of instrumentation that we had to carry around with us, it was much more economical to build that machine. It did not cost that much to build at our own facility so that we did not have to integrate with the rest of the Navy.

Mr. Brooks (NASA, Langley Res. Ctr.): What is the relative effect of density and pressure of the gas that is in the journal?

Mr. Curwen: With respect to the shock response, we tested both pressurized bearings and self-acting bearings, which run the gamut as far as pressure in the bearing goes. We saw no significant influence. The machine does not know what type of bearing is in there. The contacts occur just as readily in either type. We varied supply pressure up and down on the hydrostatic bearings and could detect no difference in the response.

* * *

AN EXPERIMENTAL INVESTIGATION OF AN ACTIVE VIBRATION ABSORBER*

T. D. Dunham
Southwest Research Institute
San Antonio, Texas

and

D. M. Egle
University of Oklahoma
Norman, Oklahoma

While the linear dynamic vibration absorber has seen application in practical vibration suppression, because it is effective in only a narrow band of frequencies near the tuned frequency, its usefulness is limited. A vibration absorber that changes its tuned frequency to match that of the exciting frequency would eliminate this fundamental difficulty and would be a more useful device. This paper reports on the conception, construction, and experimental investigation of just such a vibration absorber.

The active vibration absorber is an electromechanical device consisting of three main subsystems. The first is a spring-mass system of variable natural frequency. It consists of a mass with a threaded hole on a threaded cantilevered rod. The rod is attached to the main vibratory system by bearings and the mass is prevented from rotating so that if the rod rotates the mass will travel along the rod. The second subsystem is the power source, an electric motor that is capable of rotating the rod in either direction. The third part of the absorber is the control system which is an off-on device that activates the motor when the vibration amplitude of the main vibratory system reaches a predetermined level. Limit switches prevent the absorber mass from overtravel and reverse the travel direction. The control system deactivates when the vibration amplitude decreases below the chosen level.

To determine the effectiveness of the active vibration absorber, it was attached to a single-degree-of-freedom system subjected to a harmonic force. The response with the absorber operational was compared with the response with the absorber attached but not operating and with the response of the main system without the absorber. The response was evaluated in each case for constant excitation frequency of the original single-degree-of-freedom system. The response was also determined for several rates of increasing excitation frequency to verify the ability of the control system to track the applied frequency. In every case, the absorber was effective in eliminating the increase in amplitude caused by resonances. Additional experiments indicate that although it is possible to have instability in the control system, it may be eliminated by increasing the frequency bandwidth over which the absorber may be tuned.

INTRODUCTION

A vibration absorber may be defined as a device that, when attached to a vibrating system, reduces the vibration amplitude without dissipating energy. The device must be capable of producing a reaction force on the main system which counteracts the applied force causing the large amplitude vibration. The simplest example of such a device is the conventional linear dynamic vibration absorber, sometimes called the Frahm absorber, which generates the reaction force by resonating the absorber spring and mass. While the Frahm absorber has seen application in practical vibration suppression, its usefulness is limited because it is effective in only a narrow band of frequencies near the tuned frequency. Attempts to increase the effective

*This paper is based on a thesis submitted to the University of Oklahoma in partial fulfillment of the requirements for the degree of Master of Engineering (Mechanical), 1968.

bandwidth of the absorber may be divided into two classes: those using nonlinear, passive elements such as in Ref. [1] and [2], and those incorporating an external energy source or an active system as in Ref. [3] through [7]. Of special interest are Ref. [4] through [7], which are investigations of closed loop active systems.

This paper reports on experiments conducted with a closed loop active vibration absorber which is in part similar to the device described in Refs. [7] and [8]. It produces the reaction force by resonating a variable spring-mass system, the spring rate being varied by the control system so that the amplitude of the primary system remains below a preset level.

DESCRIPTION OF THE ACTIVE VIBRATION ABSORBER

The vibration absorber, shown in Fig. 1, consists of a threaded, cantilevered rod attached to the primary system with bearings so that the rod is free to rotate about its axis but is otherwise clamped. The absorber mass has a threaded hole and is placed on the rod and restrained from rotating. As the rod rotates, the mass will travel along the rod, thus changing the natural frequency of the absorber. The ac induction motor, coupled to the absorber rod with a small V-belt, is used to change the natural frequency of the absorber system. Also shown in Fig. 1 is the primary system which consists of a frame of mass, M_1, supported by four flat bars providing the restoring force, K_1. The primary system is excited by an electrodynamic vibrator coupled to M_1 by the relatively soft spring, K_0. The detailed properties of the absorber and the primary system are given in Ref. [9].

The control system, while appearing to be complex, is actually a very simple on-off device that activates the motor when the vibration amplitude of the main vibratory system reaches a predetermined level. Limit switches prevent the absorber mass from overtravel and also reverse the travel direction. The control system deactivates when the vibration amplitude decreases below the chosen level.

In Fig. 2, the control system is illustrated. The signal A_1, provided by a displacement transducer mounted on the primary mass, is amplified by a power amplifier and then rectified. The capacitor, in parallel with the coil resistance in the relay CR3, smooths the full rectified signal.

The amplifier has a gain control which is used to set the turn-on criteria for the relay CR3. When the amplitude X_1 reaches a predetermined level, relay CR3 is energized. Upon energization of CR3, contact CR3-1 closes; thus, relay CR1 is energized. Upon energization of CR1, contacts CR1-1 and CR1-2 close; thus, the one-fourth-hp electric motor starts. The direction of rotation of the electric motor depends upon whether relay CR2 is energized or not.

Relay CR2 is controlled by the Direction Control Circuit illustrated in Fig. 2(c). Switches SW-1 and SW-2 are activated by a control rod that trips the switches at the upper and lower limits of the absorber frequency band. Switch SW-1 is tripped at the upper absorber frequency limit. This occurs when the absorber mass is in the lowest position on the absorber rod. When switch SW-1 is tripped, relay CR4 is energized; thus, contacts CR4-1 and CR4-2 are closed. Contact CR4-2 makes relay CR4 a holding relay; thus, it will stay energized until the circuit is broken. The de-energization of relay CR4 is accomplished by the use of switch SW-2. As long as relay CR4 is energized, relay CR2 will remain energized; thus, contacts CR2-3 and CR2-4 will be closed, and contacts

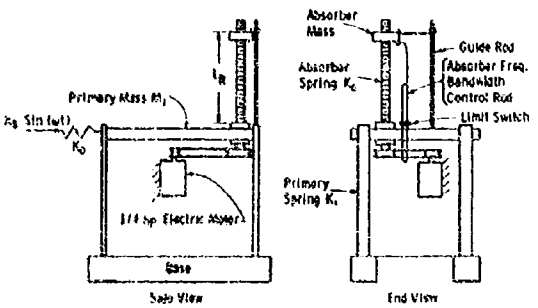

Fig. 1. Experimental apparatus

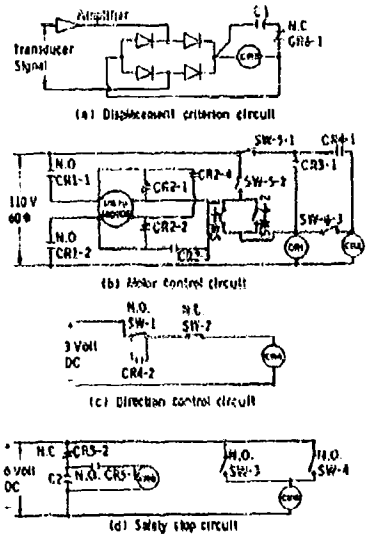

Fig. 2. Control system circuitry

CR2-1 and CR2-2 will be open. Therefore, the direction of rotation of the electric motor reverses when contacts CR2-3 and CR2-4 are open and CR2-1 and CR2-2 are closed.

The Direction Control Circuit will change the direction of rotation of the 1/4-hp electric motor at the upper and lower limits of the absorber frequency band and maintain that direction of rotation until the opposite limit is reached.

The Safety Stop Circuit illustrated in Fig. 2(d) is necessary to provide a momentary stoppage of the electric motor to permit reversing of the direction of rotation of the motor. Because of the time lag in the circuitry, the motor will only stop if instantaneous reversing does not take place. If the motor is stopped to reverse the direction of rotation, it is only stopped for an average of 1.9 sec.

A manual control of the operation of the electric motor is provided in the circuitry by switches SW-5 and SW-6. These two switches are both three-position switches. Switch SW-5 is a holding switch which is used to change from AUTOMATIC to MANUAL. When switch SW-5 is placed in either AUTOMATIC or MANUAL, it will remain in position until disengaged.

Switch SW-6 is a spring-return switch and will return to center position when it is released. It is used to manually control the electric motor in clockwise or counterclockwise rotation which in turn moves the absorber mass up or down. When contact SW5-1 is closed, the circuit is in AUTOMATIC mode of operation, and the manual up and down switch will not affect the operation. When contact SW5-2 is closed, the circuit is in MANUAL mode of operation, and the manual up and down will control the motor rotation.

EXPERIMENTAL INVESTIGATION

After constructing the experimental apparatus consisting of a 2-degree-of-freedom system and a control system, the experimental investigation was undertaken. This investigation was principally concerned with the response X_1 of the primary mass M_1 to a harmonic force (that is, $F_o \sin \omega t$) with a constant frequency ω and to a harmonic force with a slowly changing frequency. With the changing frequency, the acceleration $\omega^2 X_s$ (not F_o) was held constant. The response X_1 of the primary mass M_1, excited by a constant frequency harmonic force and with the control system of the absorber deactivated, was used to determine the absorber frequency bandwidth. The responses X_1 of the primary mass M_1 with and without the controlled frequency absorber system attached to the primary mass were used to determine the feasibility and effectiveness of the active vibration absorber.

The absorber frequency bandwidth is defined as the range of natural frequencies over which the absorber can be varied. This frequency bandwidth was determined by manually controlling the location of the absorber mass on the rod. Then, the frequency of the applied force f_s was varied until the primary mass displacement X_1 was at a minimum. At this point, the frequency was recorded as the absorber natural frequency f_2. The maximum and minimum absorber natural frequencies are the bounds for the absorber frequency bandwidth. The absorber natural frequency bandwidth is 12.33 to 26.30 Hz.

To illustrate the forced response of the primary spring-mass system, oscilloscope photographs in Figs. 3(b), 4(b), 5(b), and 6(b) were taken for different rates of change for the applied force frequency f_s. For the above photographs, the components of the absorber system that are normally attached to the primary mass during operation of the absorber and that have an effect on the natural frequency of the primary mass.

In Figs. 3, 4, 5, and 6 the acceleration of the shaker table was 0.5 g, and the ordinate represents displacement of the primary mass.

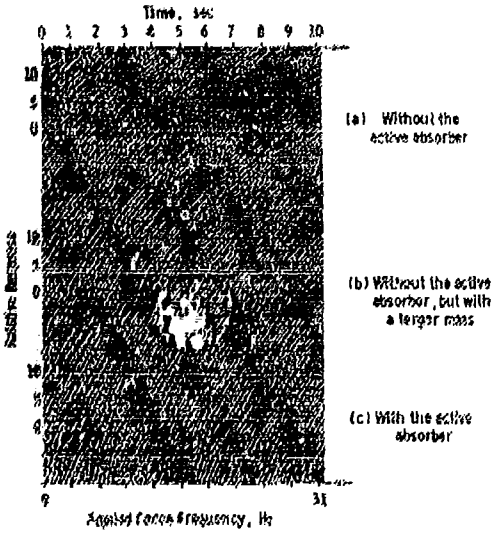

Fig. 3. Response of the primary mass to a harmonic force with increasing frequency $f_0 = 9$ Hz, $a = 0.124$ sec^{-1}

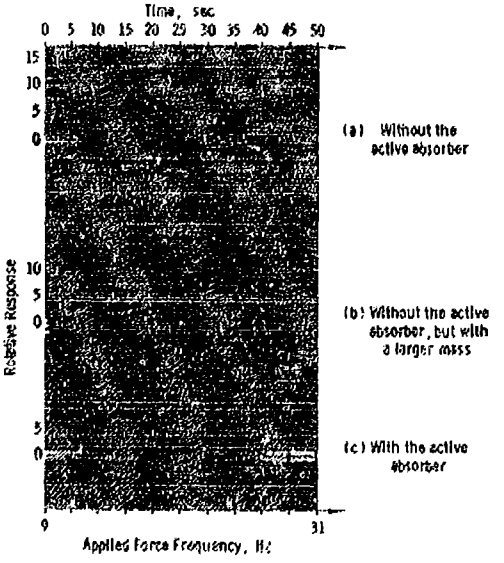

Fig. 5. Response of the primary mass to a harmonic force with increasing frequency $f_0 = 9$ Hz, $a = 0.0247$ sec^{-1}

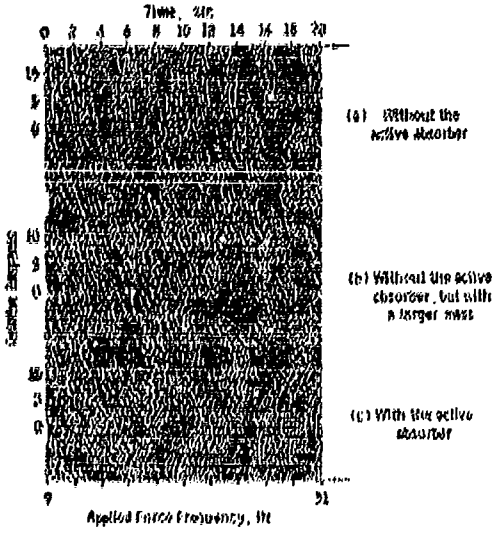

Fig. 4. Response of the primary mass to a harmonic force with increasing frequency $f_0 = 9$ Hz, $a = 0.0618$ sec^{-1}

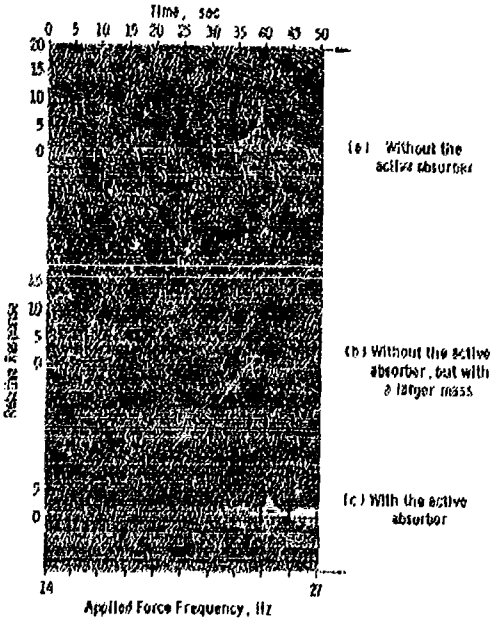

Fig. 6. Response of the primary mass to a harmonic force with increasing frequency $f_0 = 14$ Hz, $a = 0.0131$ sec^{-1}

The natural frequency of the primary system as described above is $f_1 = 23.30$ Hz.

The frequency of the applied force f_a plotted across the bottom of the aforementioned figures is in logarithmic scale because the frequency change from the vibrator is logarithmic. The frequency expressed as a function of time is $f_a = f_0 e^{at}$. The values of f_0 and a are given in each figure.

Figures 3(a), 4(a), 5(a), and 6(a) illustrate the need for a dynamic vibration absorber. As previously mentioned, the knowledge of how to design a vibration absorber to reduce the amplitude of vibration to a minimum has been developed and used for a number of years. However, the problem associated with the application of a dynamic vibration absorber is the commonly known problem of two resonant frequencies for the 2-degree-of-freedom system which is the primary system with the absorber system attached. After demonstrating with the responses shown in Figs. 3(a), 4(a), 5(a), and 6(a) that the primary and absorber systems are modeled by the experimental apparatus, the effectiveness of the active vibration absorber was investigated.

Previous work with an absorber constructed of a flat steel bar as the spring with a mass attached to the end had produced reductions in the primary mass displacement X_1 up as high as 98 percent. The flat bar system was clamped very rigidly to the primary mass. It was observed in using the rod system that the rigidity of attachment of the absorber system to the primary system has a significant effect on the percent of reduction which can be obtained.

With the absorber system constructed from the one-half-in. diameter threaded rod with the movable mass, the reduction in the primary mass displacement X_1 with the absorber operating close to the primary system resonant frequency was 0.09-0.005 = 0.085 in., or 100× 0.085/0.09 = 94.45 percent reduction.

To further illustrate the effectiveness of the active vibration absorber on this model system, photographs in Figs. 3(c), 4(c), 5(c), and 6(c) were taken of the forced response of the primary mass with the absorber operating. Photos with the absorber operating should be compared with those of the absorber not attached as shown in Table 1. The photographs listed under "absorber completely off" are the forced responses of the primary system without any of the absorber components attached.

TABLE 1

Absorber OFF		Absorber OPERATING
Completely	Partially	
3(a)	3(b)	3(c)
4(a)	4(b)	4(c)
5(a)	5(b)	5(c)
6(a)	6(b)	6(c)

Because the slowest rate of change of the frequency of the applied force results in the largest response at the resonant frequency of the primary system, a comparison of the maximum peak-to-peak (p-p) amplitudes in Figs. 6(b) and 6(c) illustrates the effectiveness of the active vibration absorber. In Fig. 6(b) the largest p-p amplitude occurs at t = 33.5 sec, and the p-p amplitude is 30 units. In Fig. 6(c) the p-p amplitude at 41.5 sec is 10 units. Therefore, the comparison of the amplitude yields a 67 percent reduction. Comparing the amplitudes at 41.5 sec in Figs. 6(a) and (c) results in a 74 percent reduction.

Two important considerations in evaluating the effectiveness of the active vibration absorber are —

(1) Will the control system lag the response so that excessive amplitude will develop?

(2) Will the absorber go unstable and be unable to find a tuned frequency?

For consideration of the first question, the responses for comparable conditions in Figs. 3 through 6 illustrate that the control circuitry response is certainly capable of maintaining control.

For consideration of the second question, there was a problem during the investigation with the absorber mass M_2 not stabilizing. This occurred when the absorber frequency bandwidth was 18 to 23 Hz, and the frequency of the applied force f_a was 15 Hz. It is hypothesized that in this narrow absorber frequency bandwidth there was no frequency at which the absorber would reduce the primary mass displacement X_1 below the cutoff criterion; therefore, the control system would continue to seek a frequency, and, consequently, the absorber mass did not stop but kept changing positions.

To provide another check on the effectiveness of the active vibration absorber, the

peak-to-peak displacement at various applied frequencies was taken for the following conditions:

(1) The primary system without any of the absorber components attached.

(2) The primary system with the absorber attached and operating.

For the collection of the above described data, the primary mass p-p displacement was determined from the displacement transducer in the control system. The frequency of the applied force was moved from one frequency to another by running the frequency sweep and then stopping at a given frequency and allowing the displacement to stabilize, or, in the case of the absorber operating, by allowing the displacements of both the absorber and the primary system to stabilize. It is observed in Fig. 7 that the attachment of the absorber components to the primary mass has the effect of lowering the natural frequency of the primary system. This, of course, is the result of increasing the primary system's effective mass while the effective spring constant remained constant.

The data with the absorber on (denoted by Δ) were taken with the applied frequency increasing from 8.5 Hz. The primary system response remained about the same with a slight downtrend until the applied frequency reached approximately f = 12.4 Hz. At that point, the absorber started providing a reduction in the response.

The slow increase in the displacement X_1 and then the sudden drop in displacement X_1 are the result of the amplitude reaching the turn-on criterion for the absorber and the absorber adjusting to a different tuned frequency. Therefore, the primary mass response X_1 with the absorber operating has a sawtooth appearance.

The analysis and investigation of the control circuit were not attempted in this work because of the nature and scope of the problem of nonlinear control elements.

CONCLUSIONS

The results of this study show that the active vibration absorber described above can be very effective in eliminating large displacements caused by resonances over a wide range of frequencies. The absorber was also shown to be effective in suppressing large amplitudes caused by a "harmonic" exciting force of changing frequency.

It is evident that this investigation has only scratched the surface of a most complex topic. The problem needs to be formulated and studied analytically to assess the effects of the design parameters on the operation of the absorber. The mechanical and electrical systems obviously need to be redesigned before this absorber could be given practical consideration. There is need for further experimental work to study not only the response of the primary mass to harmonic forces but also to transient, complex periodic and random excitation.

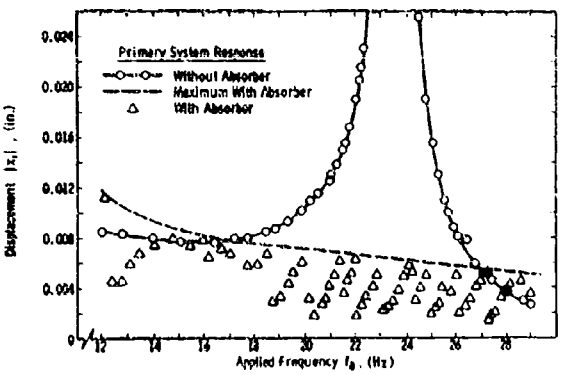

Fig. 7. Response of the primary mass to a steady harmonic force

REFERENCES

1. R. E. Roberson, "Synthesis of a Nonlinear Dynamic Vibration Absorber," J. Franklin Institute, 254:205-220 (Sept. 1952)

2. D. M. Egle, "An Investigation of an Impact Vibration Absorber," Trans. ASME, 89(4): 653-661, Ser. B (J. Engr. Indus.) (Nov. 1967)

3. R. Jones, "The Gyroscopic Vibration Absorber," Trans. ASME, 89(4):706-712, Ser. B (J. Engr. Indus.) (Nov. 1967)

4. T. H. Rockwell and J. M. Lawther, "Theoretical and Experimental Results on Active Vibration Dampers," J. Acoust. Soc. Amer., 36(8):1507-1515 (Aug. 1964)

5. T. H. Rockwell, "Investigation of Structure Borne Active Vibration Dampers," J. Acoust. Soc. Amer., 38(4):623-628 (Oct. 1965)

6. A. K. Abu-Akeel, "The Electrodynamic Vibration Absorber as an Active or Passive Device," Trans. ASME, 89(4):741-753, Ser. B (J. Engr. Indus.) (Nov. 1967)

7. J. A. Bonesho and J. G. Bollinger, "How to Design a Self-Optimizing Vibration Damper," Machine Design, 40(5):123-127 (29 Feb. 1968)

8. J. A. Bonesho and J. G. Bollinger, "Theory and Design of a Self-Optimizing Damper," Proc. 7th Internat. MTDR Conf., Birmingham, England, Sept. 1966, pp. 229-241

9. T. D. Dunham, "Experimental Investigation of an Active Vibration Absorber," Master's Thesis, Aerospace and Mech. Eng., Univ. Okla., 1968

DISCUSSION

Mr. Forkois (NRL): What happens if you put a shock input into this system?

Mr. Dunham: There was no shock testing actually performed with this system.

Mr. Sevin (IIT Research Institute): What happens if the threaded shaft is turning in the wrong direction?

Mr. Dunham: If the frequency is decreasing and the rod is turning in the wrong direction so that its mass is going wrong, it will go to the limit of the frequency, turn around and go back and search for a frequency which will give a primary displacement below the turn-on criterion.

* * *

INTEGRATED SHOCK AND ACOUSTIC MODULAR DESIGN CONCEPT FOR SUBMARINES

Michael Pakstys, Jr. and George A. Ziegra
Electric Boat Division of General Dynamics
Groton, Connecticut

This paper presents a new concept in submarine design, the Integrated Shock and Acoustic Modular (ISAM) concept, which demonstrates the possibilities of a greatly improved acoustic and shock resistant submarine. Past development of this concept at Electric Boat Division of General Dynamics is summarized. Problem areas in construction and maintenance and possible solutions are discussed. Development and construction of a scale model and proposed acoustic tests and underwater explosion shock tests on the model are presented.

INTRODUCTION

In recent years, extensive research has been carried out to produce quieter and more efficient submarines. Tentative radiated noise levels for future class submarines are considerably lower than those set for present submarines. It is probable that these goals cannot be achieved using present design methods. Therefore a new concept is proposed that represents a dramatic departure from current design philosophy and shows much promise for helping to bring about the step reduction in radiated noise which is sought for future submarines.

Also recognizing that, in present submarines, the internal equipment is substantially less resistant to underwater explosion shock than the hull, shock specifications for internal equipment and structures have been modified in recent years to require qualification shock testing, and improved analytical methods and inputs to obtain greater shock resistance. In addition, considering that the shock damage results from the motion of the hull, an attempt has been made in more recent designs to remove equipment from the hull structure to decks and bulkheads, to reduce or eliminate the effects of localized motions, and to attenuate inputs through structure.

These efforts have created greatly improved shock hardness in new submarines, but present designs for internal components still do not approach the shock resistance of the pressure hull. Hence, a logical conclusion might lead to a radical departure from present design philosophy.

The purpose of this paper is to present this new concept in submarine design, the Integrated Shock and Acoustic Modular (ISAM) concept, and to review the development of this concept at Electric Boat Division of General Dynamics.

ISAM CONCEPT

The basic concept is to provide, within a submarine, a shock-limited environment that existing equipment and personnel can tolerate, and that is designed so that equipment and personnel can withstand the same shock severity as the pressure hull.

To create such an environment, a number of modules (one per compartment) supporting the equipment and personnel within the pressure hull were conceived. These modules are envisioned as a system of beams and trusses. All internal equipment would be mounted to the modules. Elastomeric resilient mounts are envisioned to join the modules to the pressure hull in one of the following ways: (a) at bulkheads of the pressure hull, (b) at frames of the pressure hull, or (c) a combination of (a) and (b).

The mounts will act as two-way filters to dissipate the effects of the shock motion of the hull; in addition, sound transmission isolation provided by the elastomeric mounts would increase the ability of the submarine to remain undetected.

At this point, some of the advantages and the supporting reasons which demonstrate that the modular concept should be superior to present designs will be presented:

1. The average structural path length which structureborne noise must follow is increased. Thus, inherent and applied structural damping of the path will result in less noise for the longer transmission path.

2. Because the structureborne noise from all machines must reach the sea by traveling through the same foundation and bulkhead, path damping treatments may be economically concentrated to benefit all machinery noise.

3. Isolation mounting of each machine on rubber mounts in some cases may be abandoned in favor of a single set of isolation mounts located at the points where the foundation meets the hull or bulkhead.

4. For modular designs, the radiated and self-noise levels of the ship could be indirectly monitored on a continuous basis by a small number of permanently installed vibration pickups located at the junction points of the modules and the hull. Baseline measurements could be established for the various transducers, and then monitored to detect changes. It is possible that these transducers could be used to detect deterioration in plant performance and also for determining what operating conditions and ship's speed provide a minimum noise output. Thus, improved tactical performance of the submarine may be maintained.

5. Preliminary calculations show that the mounting system for a module supported only on frames can be designed to withstand and attenuate shock. The shock loading at a bulkhead is significantly less than that experienced at intermediate frame positions. However, additional supports at hull frames might be necessary to support the modules for shock loading caused by the large magnitude of the total module weight.

6. Bulkheads offer a readily accessible and extensive region in which to control structureborne noise. Because of their large area it should be possible to design very efficient damping systems integrally with them. They also offer an area that can be designed for very high impedance, considerably higher than that available at hull frames.

7. There are indications that structureborne energy reaching the bulkhead will not be easily radiated from the hull, because the bulkhead coupling to the hull appears to be poor by comparison with radiation from on-frame mounting positions.

8. The pressure hull will be clean because unsymmetric deep frames may be eliminated. This should increase structural efficiency of the hull, and enable greater use of automatic welding in fabrication of the hull.

9. Independent of acoustic and shock considerations, such a design should open a way to more efficient construction techniques. The modules with the equipment installed might be fabricated and assembled as a unit independent of the hull structure. The hull plating and frame sections could then be placed in the position around the module assembly at the final stages of construction with a consequent saving in time. Work scheduling would be simplified, because the order of assembly would not be as important as it is in the present procedure, which involves the installation of equipment into an almost completed hull.

RESPONSE TO UNDERWATER EXPLOSIONS

The stresses experienced by internal equipment and foundations caused by the underwater explosion shock result from the motion of the hull. This motion is, in general, quite complex, consisting of one or a combination of the following:

1. The overall body motion of the submarine cross section, including the rigid body motion and possible beam bending vibrations of the hull. The average lateral motion measured on submarine bulkheads consists principally of the body motion.

2. The local motion of the hull plating and the hull stiffeners including hull shell vibration. This motion is of relatively short duration and is most important for light equipment attached directly to the hull.

3. Local motion resulting from interaction of the hull and the responding equipment-foundation system. This feedback motion depends on the relative masses and frequencies involved. This effect modifies the motion of

the hull in the way of larger components, reducing the resultant relative motion between the component and the hull.

Two extreme types of shock response can be calculated analytically for broadside underwater attack: the rigid body velocity of the hull and the early portion of the local radial motion of the hull-stiffener velocity caused by the impingement of the steep front of the shock wave. These analytical methods advanced by Murray and Taylor, respectively, are reviewed in Ref. 1. The peak-stiffener velocity and its initial acceleration are always higher than the peak-body velocity and its initial acceleration.

The body velocity, especially for a nuclear charge, is considered to be the more significant indicator of damage for most of the submarine equipment, except for the equipment directly attached to the hull frames in line-of-sight between the center of the submarine and the charge. Therefore we will concentrate on the prediction of the body velocity. The peak-body velocity of the submarine for nuclear charges approaches the peak velocity of the water particles in the shock front as shown in Fig. 1. The peak-body velocity thus can be related by a constant, to the peak-shock pressure. To introduce some numbers, let us assume that a submarine will be subjected to a body velocity history shown in Fig. 2.

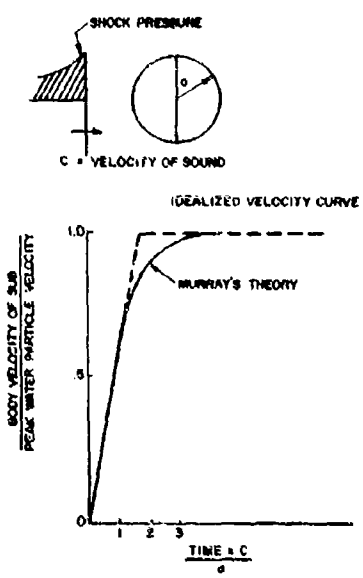

Fig. 1. Bodily velocity of submarine

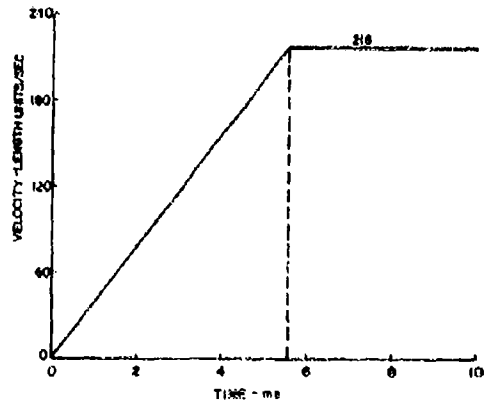

Fig. 2. Base-velocity input for example problem

The simplest rational treatment of shock response of equipment to a given shock motion of the hull utilizes a shock spectrum that gives the maximum absolute response of one-degree-of-freedom systems to input motion. For frequencies up to nearly the cutoff frequencies for the velocity history shown in Fig. 2, the input motion consists of a constant velocity region equal to the peak-input velocity, and a constant acceleration region equal to twice the input acceleration for frequencies somewhat above the cutoff frequency. The shock spectrum is plotted on quadralog paper in Fig. 3. It can easily be seen that for this sample problem much of the hardmounted shipboard equipment would be subjected to limiting acceleration. Resiliently mounted equipment, as can be seen in Fig. 3, would be subjected to considerably lower g-loading if the mounts were properly designed to attenuate the shock loading.

Recognizing that both acceleration loads and relative displacements of the modules are of prime concern, use of nonlinear hardening mounts is desirable. During normal operating conditions involving small displacements, these mounts respond as a linear system. Shock loading, however, distorts the mounts into the nonlinear range. Such behavior is exhibited by elastomer mounts.

To obtain some insight into the shock-isolation characteristics of modules mounted on elastomer mounts, let us examine the behavior of a one-degree-of-freedom system representing such a modular concept. Let us assume that the system will have a 6-Hz natural frequency in the small displacement range of the mount (desirable for sound isolation) and its

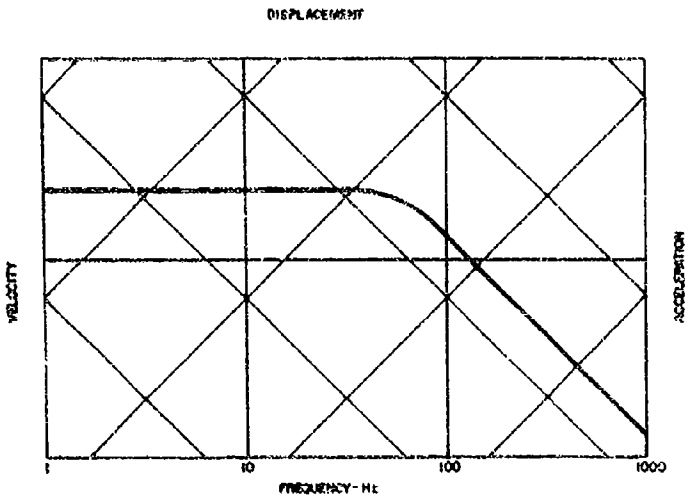

Fig. 3. Shock spectrum for example problem

stiffness increases to 7.5 times in the high displacement range (as shown in Fig. 4(a)). The shock input at the base of the system is as shown in Fig. 2, representing the body velocity of the hull.

For a nonlinear mount, the maximum relative deflection (Fig. 4(b)), was restricted to 3.5 length units in 22 ms. This is 60 percent of the excursion of the linear system. The maximum response acceleration of the bilinear mount shown in Fig. 4(c), exceeds that of the linear mount by 20 percent, but is still only 26 percent of the input acceleration.

Both acceleration and deflection of the nonlinear mount attain their maximum values very rapidly and diminish to a low level before the linear mount has reached its peak.

ISAM CONCEPT DEVELOPMENT AT ELECTRIC BOAT DIVISION

Company sponsored research [2] was initiated at Electric Boat Division in 1963 to study the feasibility of the Integrated Shock and Acoustic Modular concept. At that time, emphasis was placed on finding a mounting device that would support a module and equipment, and also exhibit desired vibrational and acoustical characteristics.

Prior to the evaluation of a system's response to environmental conditions, the environment as well as the limitations on the

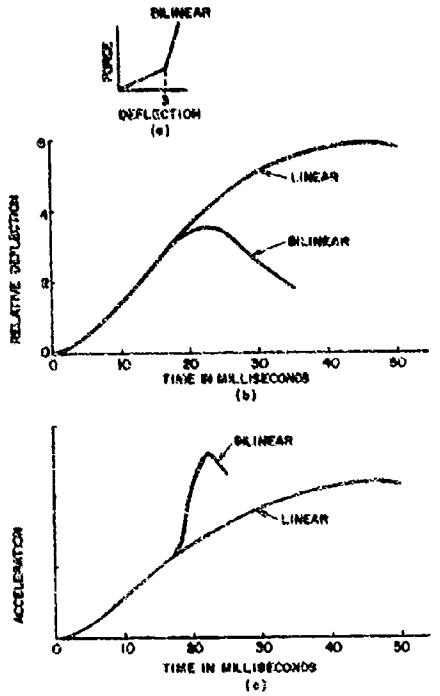

Fig. 4. Shock responses for example problem

response must be defined. This includes dynamic input and response, sound transmission characteristics, and sensitivity to environmental changes in temperature and fluid surrounding.

Additional criteria include reliability, weight, and cost to incorporate into present construction techniques. The following is a discussion of the criteria that are considered of primary pertinence to design.

Because of interconnecting piping, relative deflections between compartments and the hull must be limited. The limitation is a function of each intercompartmental piping system. Present piping schemes may not possess the flexibility to permit relative deflections large enough to make shock absorption effective. Although this problem is acknowledged, a detailed investigation of it is not a purpose of this study. A maximum limit of 3 in. in relative deflections has been chosen for this study which is believed to be reasonable if sufficient flexibility is built into each intercompartmental piping system.

Certain space limitations are imposed on the system; mainly that the module be large enough to accommodate existing inboard equipment and that the outer hull not be significantly larger than present hulls. These requirements thereby restrict the distance between the two structures. Two ft is considered a practical upper limit.

The total weight of the suspension system shall be small in comparison with the weight of module and enclosed equipment. Because the pressure hull is to remain essentially the same size, too much additional weight would result in a boat incapable of neutral or positive buoyancy. A realistic goal might be a system that weighs not more than 15 percent of the total weight.

Overall reliability of the system is another important consideration. Under all possible operating conditions, a low probability of failure for the system is required. Operating conditions include steady state vibrations, shock, and operational insensitivity to environmental variation in temperature, humidity, air, sea water, oil, and all fluids circulated intra- or intercompartmentally that might come in contact with the system.

Four systems have been proposed; namely, honeycomb material, pneumatic devices, helical springs, and elastomeric media. Each is evaluated from the very basic considerations contained in the design criteria.

Honeycomb Material

Honeycomb material has been proposed to absorb shock energy as it is crushed between the modular structure and the pressure hull. Although for one given shock this arrangement might be a feasible shock mitigator, theoretically the system must be able to contend with from one to a large number of shock waves. Once the honeycomb material has been crushed, it is no longer useful as an energy absorber or sound isolator. For this reason this material was deemed unacceptable and further investigation was abandoned.

Pneumatic Devices

Pneumatic devices, either alone or in combination with other springs, have been proposed to satisfy the design criteria. Envisioned is the module supported radially by a number of pistons in airtight cylinders.

The device must necessarily act in the plus X and minus X directions and therefore the seal must be airtight. If this were not true, essentially only one-half of the devices would absorb energy for radial shock and the resultant efficiency of the system as a whole would be low. Closer investigation demonstrated that spring constants for this device would be much too low even when many such devices are used in parallel. This would necessitate the use of auxiliary devices in parallel with the pneumatic devices.

From these very basic considerations, pneumatic devices of this kind do not appear to possess the dynamic characteristics necessary for effective shock attenuation. The feasibility and effectiveness of pneumatic devices are also impaired by the following characteristics: (a) limitations of the system in the longitudinal and rotational modes because of the one-dimensional characteristics of each device, (b) decreased reliability of the system compared with an elastomeric or helical spring arrangement because of the possibility of air leakage, (c) need of an auxiliary system to introduce damping, (d) temperature sensitivity of the system's dynamic properties, and (e) high cost because of strict tolerances and intricacy inherent to the system.

Helical Springs

A system is proposed whereby the module is connected to the outer hull by means of radial helical springs. Rings containing n number of springs would be equally spaced longitudinally at every frame (about 24 in.). Each spring is assumed to act in tension and compression with a spring constant of K lb/in.

Assume the pressure hull and modular structure rigid; only rigid body displacements will be considered. This system was considered unfeasible for the following three reasons:

1. For small displacements in the longitudinal and rotational directions, the spring constant is essentially zero. A helical spring has essentially one-dimensional load carrying qualities. For longitudinal displacements, Δ, the net resisting force, F_L, in the longitudinal direction is $F_L = 32\,k(\sin\theta)^2\,\Delta$ where k is the stiffness and θ is the angle.

For small θ, $\sin^2\theta$ is approximately equal to zero. To make clear the seriousness of this situation, theoretically (neglecting friction and direct shear resistance) a force of 200 lb, roughly the weight of one man, would cause a relative longitudinal deflection of 1 in.

2. Springs made of steel are susceptible to corrosion from salt water. Protective measures such as continual painting would be necessary to deter corrosion resulting from bilge water, and so forth.

3. Because structural damping in helical springs is only about 3 to 5 percent of critical, an additional mechanism must be incorporated into the design to increase damping to approximately 15 to 20 percent. Resulting will be an increase in weight which is already too high, and a decrease in the reliability of the system.

Elastomeric Foundation

Typical preliminary investigations were made on elastomer compounds. These studies indicated that a good approximation to satisfy design criteria could be obtained with 360-degree rubber rings, rectangular in cross section, and bonded to the pressure hull and modules. As a result of these preliminary studies, elastomer was deemed most feasible for the following reasons:

1. Elastomers have relatively high energy-absorption capability per unit weight which results in a lightweight design for the system.

2. Increasing modulus of elasticity with increasing compressive strain provide ideal properties for both sound and shock isolation; namely, a "soft" spring for small displacement, steady state behavior and a "hard" spring for large displacements resulting from shock.

3. Elastomers can be compounded to possess optimum damping characteristics which of course are then inherent to the material.

4. A bonded elastomeric system will provide three-dimensional shock and sound isolation.

5. Primarily because of the simplicity of a bonded design and the ability of elastomers to withstand strains on the order of from 200 percent to 300 percent, the reliability of elastomeric system is considered very high.

6. Although a cost analysis is not within the scope of this paper, it seems evident that the relative cost of an elastomeric system would be low.

Company sponsored research [3,4] was continued in 1964 with the emphasis on producing an elastomer compound that would have desired characteristics, and producing a design for a scale model to simulate the structural and vibrational characteristics of a compartment in a submarine.

First, an analytical study was conducted to formulate a design for a scale model. This led to the scale model of a submarine compartment as shown in Fig. 5. It should be noted that this module does not appear like the truss-like structures previously mentioned. Stiffened-end bulkheads were designed to have at least the stiffness of full-scale bulkheads. Free flooding truncated conical extensions that are attached to the ends of the model were designed to produce low-frequency beam responses similar to an actual submarine. The module itself was designed as an innerstiffened hull. Holes will be cut in this hull so that the remaining structure will resemble the previously mentioned trusses and still retain the desired structural and vibrational characteristics. Various equipment will be simulated within the module by vibrating machines mounted on simulated foundations during acoustic tests for simulation of internal machinery noise, and replaced by masses for subsequent underwater explosion shock tests. Not shown in the figure will be a sea-connected section of piping that will be attached to the module through several pressure-balanced, ball-type flexible pipe connectors.

The second study concerned the development of a suitable elastomeric compound. As a starting point in designing the elastomer rings

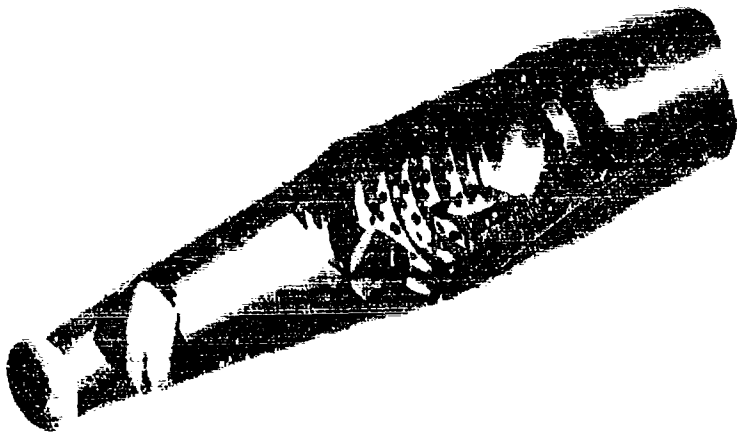

Fig. 5. Electric Boat Division ISAM model

for the model, the module-ring-hull system was idealized as a simple spring-mass system.

The mass represents the weight of the module and the simulated compartmental equipment, and the spring represents the elastomer ring. The assumption that the outer hull is rigid with respect to the inner system is supported by the fact that the weight of the outer hull plus the weight of the displaced water (the virtual mass) is approximately 10 times that of the module and equipment. Similarly, it was found that the radial stiffness of the hull stiffener was much greater than the stiffness of the elastomer ring. Within the limitations of these assumptions, then, the stiffness of the elastomer rings was calculated so that the frequency of the system would be 6 Hz (the desired value for acoustic considerations).

Elastomeric samples with desired properties were compounded, and were subjected to both static and dynamic tests. (See Appendix for a more detailed discussion.) Based on these test results, it was decided that, with further study, an elastomer with the necessary characteristics could be compounded.

Using the design that was produced in 1964, construction of the one-fifth scale model was initiated in 1965. All major components were fabricated at that time.

PROPOSED SHOCK AND ACOUSTIC TEST PROGRAM

To verify past and future analytical studies, both acoustic and shock tests have been proposed. Two series of each test will be made, one with the elastomer mounts functioning as proposed and one with steel blocks fastened between the hull and module to "short out" the elastomer mounts. This second series nearly simulates present designs; results from this series will be used as a basis for comparison.

During the acoustic tests, the model will be suspended with the longitudinal axis of the cylinder vertical at a depth of 40 ft. It will be excited at a single point by a shaker over a frequency range of 20 to 5K Hz. Radiated sound will be measured by three hydrophones located at depths of 30, 40, and 50 ft, and about 40 ft from the model. The above frequency range will be covered by using a sweeping oscillator and measuring the sound pressure levels for 22 1/2-degree increments of model rotation over half the model surface. Also, point mechanical impedance and several accelerations measurements on the inner and outer hull will be made. Damping for the two configurations will be determined by measuring the Q at the major resonances.

The effect of mechanical shock on internal components in the ISAM model will be studied by subjecting the model to two series of underwater explosions, each series consisting of five explosions of increasing severity as shown in Fig. 6. For each shot, strains, accelerations, velocities, displacements, and free-field shock pressures will be recorded. Comparison of shock inputs will be made on the same basis as for the acoustic tests.

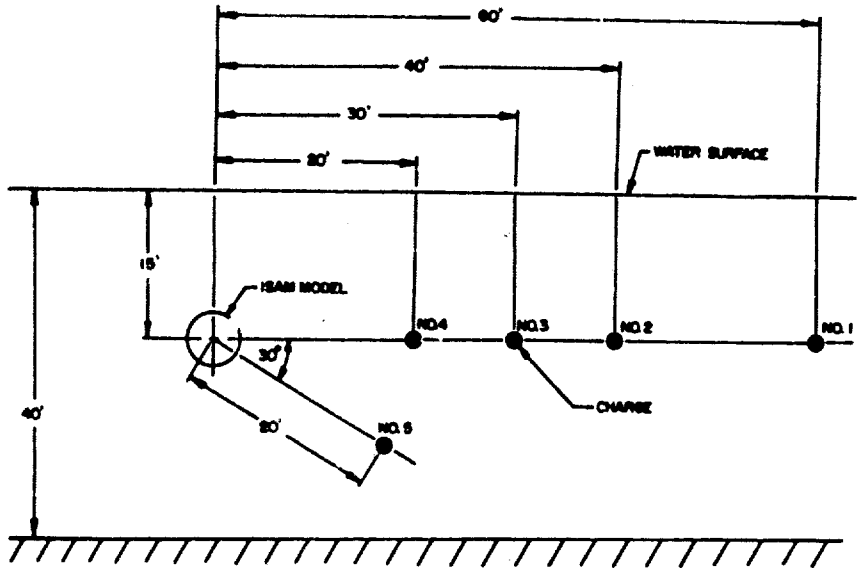

Fig. 6. Proposed ISAM shock test geometries

EFFECTS ON SUBMARINE DESIGN AND CONSTRUCTION

Recognizing that the basic concept is a significant departure from conventional design, and that it is in the development stage, one must expect that many changes might be required to conventional design and construction techniques to convert the concept into hardware.

The mobility of the resiliently mounted modules with respect to the hull requires that special consideration be given to mounting complete systems on a single module, and providing flexible connectors in systems that are supported on a number of modules or that connect with the hull. Relative displacements of several inches are anticipated. Although many systems already employ flexible connectors, the magnitude of motion accommodated is considerably less than that which would be required in the modular design concept.

Piping systems, particularly sea-connected piping systems [5], main propulsion shafting, and periscopes, have been cited as examples where changes would have to be made to conventional designs.

Considering sea-connected piping, pressure-balanced, ball-type flexible connectors are presently being used in systems that sustain high internal pressure and support nearly unresisted relative motions. With some development they should be quite suitable for adapting to nearly all piping needs. Novel submerged propulsion systems that do not require mechanical coupling may be proposed as possible design alternatives to the main shaft problem. As for certain hull-connected equipment, such as periscopes, they may be shock hardened and remain mounted on the hull.

The weight of a truss-like module that would support the weight of the engine room components was calculated to be approximately 5 percent of the weight of the components themselves for an acceleration of 15 g. This weight will increase with increasing g-levels.

There are many problems inherent in the elastomeric system which have yet to be investigated. These include creep, strain rate, mechanical and chemical properties over long periods of time, bonding material properties, and bonding and installation techniques. Construction techniques will have to be conceived to allow efficient installation and maintainability of the modules.

CONCLUSIONS

This paper has presented the ISAM concept of submarine design, the development of the concept at Electric Boat Division of General Dynamics, and the proposed tests on a scale model of an elastomerically mounted compartment. An insight into problem areas was also discussed.

The following conclusions are considered to be the principal reasons for continuation of the development of the ISAM concept.

Feasibility studies during the past 5 years have demonstrated that, by mounting submarine compartments on elastomeric mounts, the attenuation of underwater explosion shock and reduction of machinery noise radiated from a submarine is greatly enhanced.

Because this concept is a radical departure from present design philosophy, numerous problems will be created, especially with intercompartmental and compartment-to-hull connections. However, continuation of present development in this area should eliminate most of these problems.

Both the size and weight of an ISAM submarine will be increased, but proper design of the module will limit this increase to a reasonable level.

Construction of an ISAM submarine should reduce the scheduling and construction time because the modules and hull could be fabricated independently.

ACKNOWLEDGMENTS

This work is a summary of company-sponsored research. The authors wish to acknowledge the outstanding work performed in the project by Mr. V. D. Godino and Mr. J. C. Flynn and other Electric Boat Division engineers.

REFERENCES

1. M. Pakstys, "Analytical Methods for Prediction of Mechanical Shock Environment for Shipboard Equipment of Submarines to Underwater Explosions," 34th Shock and Vibration Bull., Part 1, Feb. 1965
2. V. D. Godino, "A Comparative Investigation of Integrated Shock and Acoustic Modular Foundation Systems for Submarine Machinery and Equipment," Electric Boat Div. Rept. No. U411-63-053, Dec. 1963
3. V. D. Godino and J. C. Flynn, "Integrated Shock and Acoustic Hull Study," Electric Boat Div. Rept. No. P411-64-048, Dec. 1964
4. V. D. Godino, "A Method to Predict the Shock Response of Simple Systems Supported on Elastomeric Mounts," Electric Boat Div. Rept. No. U411-64-049, Dec. 1964
5. E. Beauchamp-Nobbs and Y. Wang, "Development of Rational Design Criteria for Submarine Sea Water Systems," J. Nav. Engrs., Dec. 1966

BIBLIOGRAPHY

Cole, R. H., Underwater Explosions (Princeton Univ. Press), 1948

Keil, A. H., "Introduction to Underwater Explosion Research," UERD Rept. 19-56, Dec. 1956 (Confidential)

Keil, A. H., "The Response of Ships to Underwater Explosions," DTMB Rept. 1576, Nov. 1961

"The Floating Shock Platform for Shock Testing Equipment up to 30,000 Pounds," UERD Rept. 7-61, May 1961

Appendix

Samples of the elastomeric compound subjected to three different curing times (20, 30, and 40 min) were bonded to test fixtures, and tested in tension and compression on the Tinius Olsen testing machine. Two more samples were compounded using the curing time found to yield the best results, one for shear investigations on the Tinius Olsen testing machine, and one for dynamic investigations. The samples were a scale representation of a 28-in. strip of an actual ring. The shape factor was 0.37.

Compression tests were conducted on samples subjected to three different curing durations. Each sample was cycled three times

under a maximum compression of ~40 percent (0.35 in.). A comparison of the load-deflection curves indicates that the 30-min curing time produced the best compromise for our purposes. The specimen had an initial static-spring constant of 2800 lb/in. The static damping was computed by evaluating the change in area in the load and unload cure. Damping = $\Delta A/A$ = 26 percent (static).

Tensile tests were also conducted on the samples of all three curing durations. Each sample was subjected to a 50 percent elongation and cycled three times as in the compression tests. Again the 30-min curing time appeared to be the best for our purposes. The initial spring constant calculated from the experiment curve was found to be 1900 lb/in.

In addition to cycling each specimen from 0- to 50-percent elongation, each specimen was loaded to failure. The 40-min cure specimen appeared to have an imperfection in the bond and failed first as a separation of the rubber from the metal on the top front edge as shown below.

Even with this imperfection, failure (but not complete failure) did not occur until the load reached 800 lb and the elongation was ~140 percent.

The 20-min cure specimen failed as a bond failure at 1100 lb. The recording equipment was not working and therefore no record of elongation was obtained.

The 30-min cure specimen was the best test of the three because the bond held throughout the test. The failure in this case was a tearing of the rubber that appeared to start to initiate as a stress raiser around an imperfection on one of the free ends of the sample. The failure load and elongation were 1340-lb and 247-percent elongation, respectively.

Shear tests were conducted on specimens, all of which were cured for a 30-min duration. The specimens were first subjected to a longitudinal load resulting in approximately 80 percent deflection and cycled three times at these conditions. There appeared to be a considerable amount of slippage in the test fixture so that the force-displacement charts recorded during the test are difficult to evaluate. It was necessary to load the specimen and then unload to the point where a decrease in load did not affect the deflection, then reload to obtain a meaningful record.

The shear specimens were also cycled twice to approximately 80 percent deflection in the horizontal direction and then loaded to failure. The ultimate load was 3600 lb and the deflection was approximately 350 percent. The failure was mainly a tearing failure similar to the tensile failure; however, the bond did fail in a few isolated areas prior to reaching the ultimate load. The recording mechanism reached its limit of travel at approximately 1.8 in. of deflection; however, the failure load was recorded and the load-deflection curve was extrapolated to the failure load. The failure load was 3900 lb with an extrapolated deflection of ~2.1 in.

The dynamic characteristic of the compounds was investigated by determination of the mechanical impedance of the system shown in Fig. A-1.

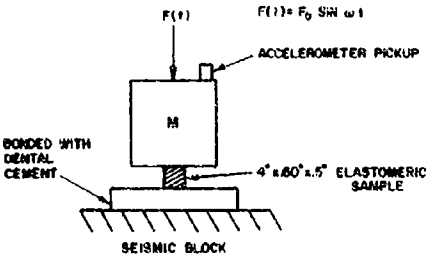

Fig. A-1. Dynamic elastomer test setup

The system has essentially one degree of freedom in the vertical direction. The mass, m, was calculated to produce the actual static psi loading on the rubber for a scale model. For a 360-degree elastomeric ring, m is approximately 10 lb. The sinusoidal driving force, F(t), was produced by means of a 10-lb electrodynamic shaker and was measured with a Endevco (force gage). Slight coupling with a rocking mode about the long axis of the rubber sample was evidenced by resonant frequencies of 106 and 129 Hz (Fig. A-2). Because the sound requirements dictate a resonant frequency of approximately 50 Hz, the mount was redesigned considering only one-fourth of an entire elastomeric ring which in effect increases the mass from 10 to 40 lb. The impedance test was repeated for this design revision.

The resonant frequency (Fig. A-2) of this system was found to be 49 Hz, and therefore 7 Hz for the full-scale ring. The 10-lb model

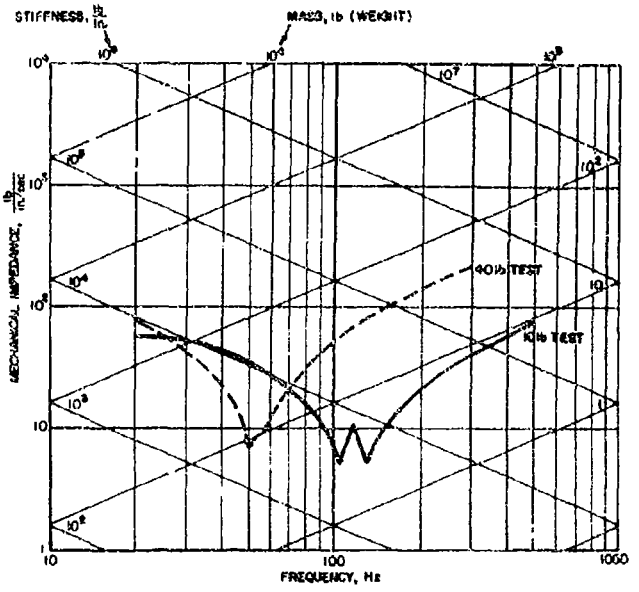

Fig. A-2. Impedance curves for elastomeric samples

showed a stiffness of 11,000 lb/in. and 16 percent of critical damping; the 40-lb model showed a stiffness of 10,000 lb/in. and 11-1/2 percent of critical damping.

These tests indicated that the strain rate in the 50-100 cycle range will not have an appreciable effect on the stiffness; however, further tests would have to be conducted to determine this effect below and above this range. The results also indicate that to obtain the desired dynamic natural frequency of the system, the rings should be designed for a stress of 40/2 = 20 psi. It should be noted here that stress is assumed to be unaffected by the scaling factor. This assumption amounts to neglecting the effects of gravity which will be small with respect to the magnitude of shock forces.

* * *

CYCLIC DEFORMATION CREW ATTENUATOR STRUTS FOR THE APOLLO COMMAND MODULE

David L. Platus
Mechanics Research, Inc
El Segundo, California

An advanced crew attenuator strut is described that was developed by Mechanics Research, Inc., under subcontract from the North American Rockwell Corp., for use in the Apollo Command Module to fulfill a requirement for improved land impact capability. The new attenuators absorb energy through cyclic plastic deformation of a ductile metal, by rolling a series of ring elements supported on toroidal retainers and compressed between two concentric tubes. These units offer performance advantages over the previously developed crushable aluminum honeycomb struts, the major advantages being tension-compression capability at a prescribed load level, tight load tolerances, capability for acceptance testing prior to use, and lighter weight.

A series of static and dynamic tests was conducted on a prototype, using drop test facilities and special hydraulic test fixtures, with stroking velocities up to 52 ft/sec. The force-time behavior displays a characteristic short duration overshoot followed by a steady dynamic value. The peak value of the overshoot is dependent on loading rate. The unit demonstrated an average dynamic force variation within ±6 percent over a total cumulative stroke of 112 in.

INTRODUCTION

The crew attenuator struts support the crew couch within the Command Module, as shown in Fig. 1, and serve to limit deceleration loads on the crew during landing impact.

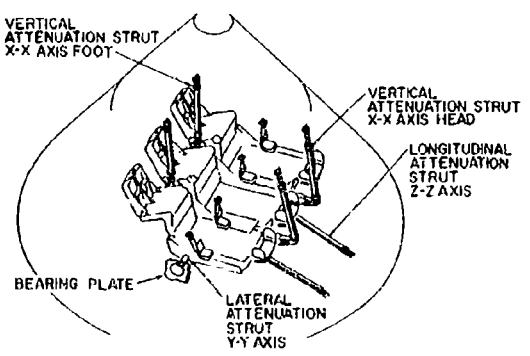

Fig. 1. Apollo crew couch-support structure

A sketch of the cyclic deformation strut is shown in Fig. 2. The unit consists of a pair of concentric tubes that are held together by a cluster of compressed ductile metal ring elements supported on toroidal retainers. The rings are compressed into the plastic range through an interference fit. Stroking of the device in tension or compression causes the elements to roll in their compressed state and absorb energy by cyclic plastic deformation, thereby producing a constant resisting force. The Apollo crew attenuators utilize type 6Al-4V titanium alloy tubes and Maraging steel ring elements supported on aluminum retainers.

THEORY OF CYCLIC DEFORMATION ENERGY ABSORBING DEVICES

The attractive features of a cyclic deformation energy-absorbing device result from some well-known properties of ductile metals under cyclic plastic straining:

1. Cyclic plastic straining of a ductile metal at a fixed strain range produces a hysteresis

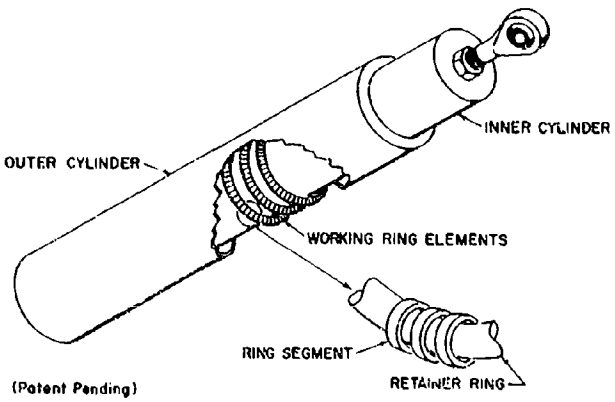

Fig. 2. Cyclic deformation crew attenuator strut

loop that stabilizes during the first few cycles. Repeated cycling results in almost constant energy absorption per cycle until eventual fatigue failure.

2. Plastic strain or low-cycle fatigue behavior for most ductile metals follows a simple power law relating plastic strain range (width of hysteresis loop) and fatigue life.

3. The narrower the hysteresis loop, the greater the cycles to failure, and the greater the total energy absorption at failure.

4. Cyclic plastic straining to failure results in considerably greater energy absorption than unidirectional straining to failure. Specific energy absorption (SEA) for N cycles to failure is approximately N times SEA for unidirectional straining to failure.

Plastic strain fatigue behavior of ductile metals is described, for example, in Ref. [1] to [5], and a general discussion of cyclic deformation energy-absorbing devices is presented in Ref. [6]. Some of the properties are illustrated in Figs. 3 to 5. Figure 3 shows fatigue data for several metals [1]. Figure 4 shows, schematically, the relation between size of hysteresis loop, cycles to failure, and specific energy absorption, and compares cyclic straining with unidirectional straining. For purposes of illustration the stress in Fig. 4 is shown as constant. In general, ductile metals under cyclic plastic straining will exhibit some strain hardening, which results in higher stresses for greater plastic strain range. Figure 5 shows approximate specific energy-absorption capacities for several metals as a function of cycles to failure [6]. At 1000 cycles to failure, for example, specific energy absorption is approximately 700,000 to 800,000 ft-lb/lb.

In the rolling ring configuration of Fig. 1, the rings are compressed slightly out-of-round into the plastic range. Stroking of the device causes the rings to roll and produce cyclic plastic bending deformation as the points of maximum strain are translated around a ring. Referring to Fig. 6, the material is cycled through a complete hysteresis loop when point A moves to B then to A'.

To insure that the rings roll rather than slide, the ratio of squeeze force to roll force is selected so that the sliding friction force is always greater than the roll force; that is (coefficient of friction) × (squeeze force) > roll force. However, it is desirable to maintain the squeeze force only as high as necessary to minimize tube wall thickness and strut weight.

APOLLO CREW ATTENUATOR STRUT DESIGN

Three attenuator struts, identified in Fig. 1 as the XX-Head, the XX-Foot, and the ZZ, were designed as summarized in Table 1. A design objective on load tolerance was ±5 percent at stroking velocities from quasi-static to 52 ft/sec, over a total cumulative stroke of 112 in. Additional design requirements included compressivie stroking of the units in their fully extended condition under the lateral G-loads indicated in Table 1, and certain tightness requirements under a prescribed loading history simulating reentry conditions. For example, permenent deformation of the prototype ZZ strut could not exceed 0.090 in. after loading at less

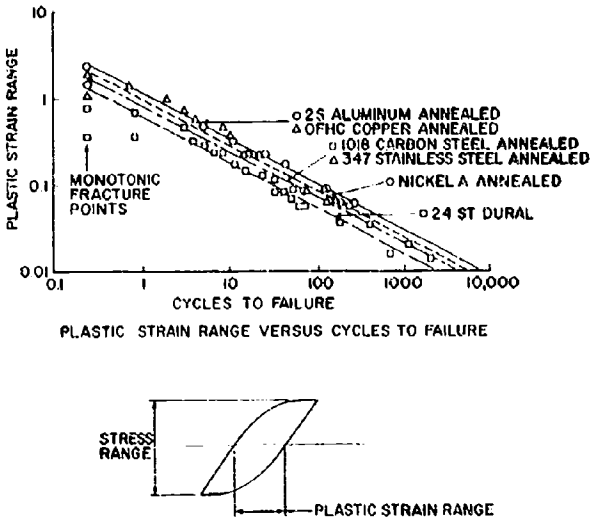

Fig. 3. Low-cyclic fatigue data (see Ref. [1])

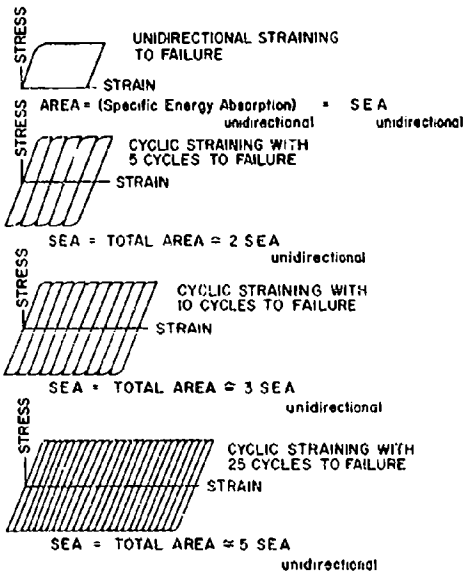

Fig. 4. Relation between hysteresis loop and specific energy absorption

than 110 lb/sec to 8528 lb, holding at this load for 1 sec, then reducing the load to 100 lb.

Ring element design data were generated for various materials using specially designed test fixtures. Maraging steel was selected for the rings because of its combined high strength and superior low-cycle fatigue behavior. Type 6A1-4V titanium alloy was used for the tubes because of its high strength-to-weight ratio and other desirable features.

The ZZ strut presented the most difficult design problem because of its higher stroke requirements in relation to strut size and load level. A sketch of this strut is shown in Fig. 7 and a photograph of the disassembled prototype is shown in Fig. 8.

PROTOTYPE ZZ STRUT TEST SUMMARY

A test program was conducted for design verification of a prototype ZZ strut. Static and quasi-static tests were performed on a Tinius-Olsen tensile tester. Dynamic tests were performed using drop-test facilities and special strut testing facilities.

Final design verification tests of the prototype strut under dynamic conditions were performed on two special strut-testing facilities at the North American Rockwell Corp. The Low-Velocity facility at the Hydraulic Laboratory was used for stroking velocities up to 10 to 15 ft/sec, and the High-Velocity facility at the Structures Laboratory was used for velocities up to 52 ft/sec. Stroking force was obtained from strain-gaged load links. Strut position in the Low-Velocity facility was obtained by a rotary

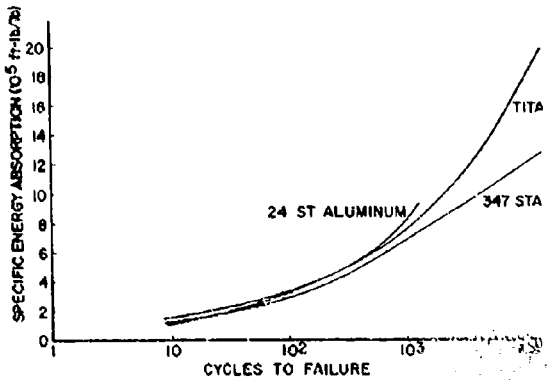

Fig. 5. Approximate specific energy absorption vs cycles to failure for several metals (See Ref. [4])

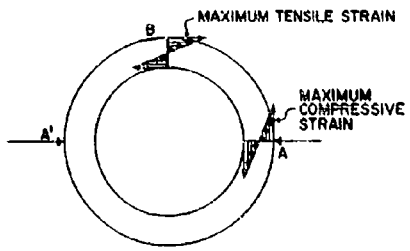

Fig. 6. Strain distributions in compressed ring

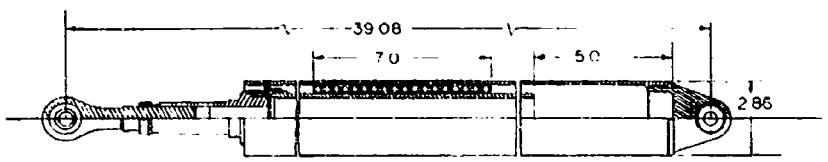

Fig. 7. Sketch of ZZ strut

TABLE 1
Design Summary

Strut	Initial Length[a] (in.)	Maximum Diameter (in.)	Force Level (lb)	Tension Stroke (in.)	Compression Stroke (in.)	Lateral G Factor	Strut Weight (lb)
XX-Head	36.68	2.80	5580	16.50	1.00	33.5	9.80
XX-Foot	31.70	2.80	9300	16.00	1.00	32.4	13.57
ZZ	39.08	2.86	9300	18.50	5.00	32.4	13.60

[a]Distance between spherical bearing centerline.

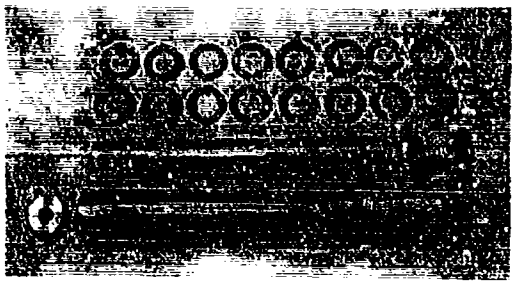

Fig. 8. Photograph of disassembled prototype ZZ strut

potentiometer connected to a pulley, and an inductance transducer was used in the High-Velocity facility. A backup system of break wires was also used for position/time measureurements in the High-Velocity facility. Associated instrumentation permitted readout of stroking force and stroke position on a conventional direct writing oscillograph. Estimated system frequency response was in excess of 200 Hz.

The force-time behavior shows a characteristic short-duration overshoot, followed by a fairly steady force level, as illustrated in Fig. 9. Typical results for one set of ring elements are presented in Tables 2 and 3 which summarize data for the low-velocity and high-velocity tests. Both peak and average force values are given in Tables 2 and 3, as well as the loading rate, which appears to affect the overshoot. Figures 10 to 12 show typical force and acceleration histories reproduced from the oscillograph records, and velocity histories determined from the position transducer data. The effect of loading rate on overshoot is shown in Fig. 13, where overshoot is defined as the difference between peak and average forces, divided by the average force.

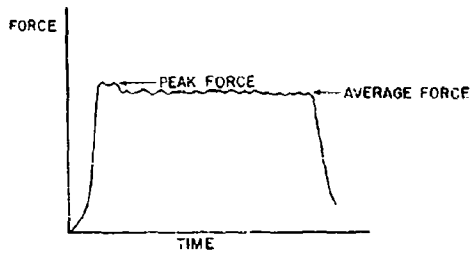

Fig. 9. Characteristic force-time behavior

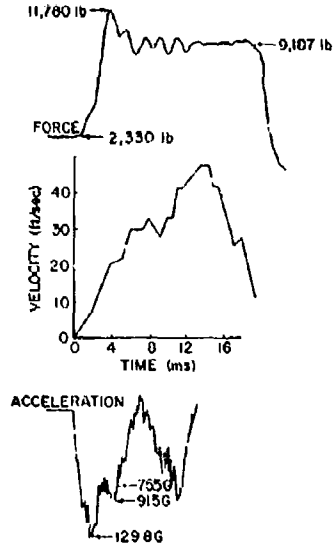

Fig. 10. Typical high-velocity data -- run no. 1

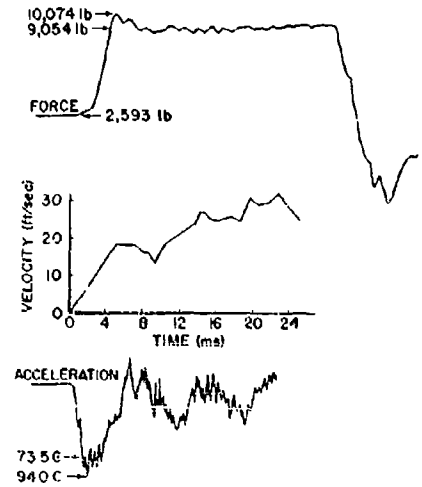

Fig. 11. Typical high-velocity data -- run no. 3

A summary of the average dynamic force behavior in terms of cumulative stroke is shown in Fig. 14, based on the results of Tables 2 and 3. The data points in Fig. 14 are identified in terms of maximum stroke velocity and onset rate.

A pronounced effect of loading rate on overshoot is indicated in Fig. 13. It is believed that this effect is a result of the inertia of the

TABLE 2
Prototype ZZ Strut Low-Velocity Test Summary

Run	Direction	Velocity (ft/sec)	Stroke (in.)	Peak Force (lb)	Average Force (lb)	Loading Rate (10^6 lb/sec)
1	Tens.	7.9	5.38	10,800	9,570	1.76
2	Comp.	–	3.5	–	–	–
3	Tens.	–	3.5	–	–	–
4	Comp.	8.95	5.38	9,560	9,200	1.62
5	Tens.	0.02	5.30	10,300	10,220	–
6	Comp.	0.02	5.10	10,000	9,920	–
7	Tens.	7.50	5.38	10,800	9,750	1.74
8	Comp.	8.25	5.38	9,550	9,300	1.63
9	Tens.	8.45	5.38	10,250	9,750	1.25
10	Comp.	0.02	5.38	10,300	10,250	–

TABLE 3
Prototype ZZ Strut High-Velocity Test Summary

Run	Direction	Maximum Velocity (ft/sec)	Stroke (in.)	Peak Force (lb)	Average Force (lb)	Loading Rate (10^6 lb/sec)
1	Tens.	46.0	6.25	11,780	9,187	5.6
2	Tens.	46.8	6.06	12,010	9,091	6.7
3	Comp.	32.7	6.19	10,070	9,054	3.3
4	Comp.	29.7	6.13	10,610	9,245	4.5
5	Tens.	46.8	6.94	10,800	9,127	3.9
6	Tens.	32.7	6.44	12,070	9,399	6.4
7	Comp.	27.3	5.16	11,170	9,116	7.5
8	Comp.	18.2	5.91	10,770	9,458	4.4
9	Tens.	40.9	7.84	10,350	9,076	4.0
10	Tens.	30.7	5.20	11,540	9,129	5.8

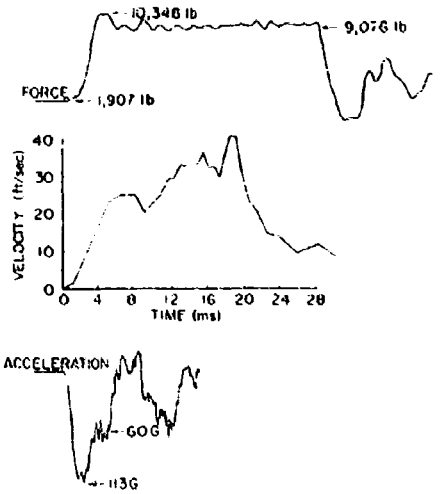

Fig. 12. Typical high-velocity data -- run no. 9

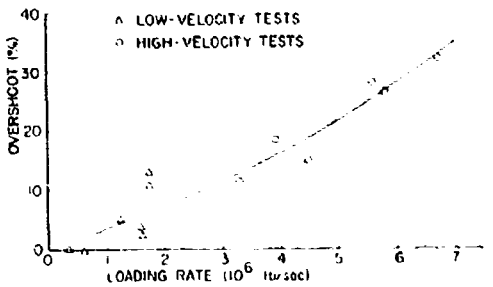

Fig. 13. Effect of loading rate on overshoot

ring and retainer elements and friction between the moving parts, and is not inherent in the cyclic deformation behavior of the working metal. The loading rates experienced in these tests are considerably greater than those anticipated during landing impact of the Apollo Command Module.

The relation between average dynamic force and cumulative stroke of Fig. 14 shows a rather steady force behavior with increasing stroke, for the total stroke range indicated. The data also indicate a slight negative rate sensitivity at the very low levels of stroking velocity. This may be a result of internal friction between the moving parts, which decreases as the coefficient of friction decreases with increased velocity.

CONCLUSIONS

An advanced crew attenuator strut for the Apollo Command Module has been described. The new attenuators absorb energy by cyclic deformation of a ductile metal and offer significant advantages over the previously developed crushable aluminum honeycomb struts.

The theory of cyclic deformation energy-absorbing devices has been discussed. It has been shown that cyclic plastic straining to failure of a ductile results in considerably greater energy absorption than unidirectional straining to failure. The formation of a stabilized hysteresis loop under cyclic straining of a ductile metal enables these devices to provide an almost constant resisting force during repeated operation in tension and compression.

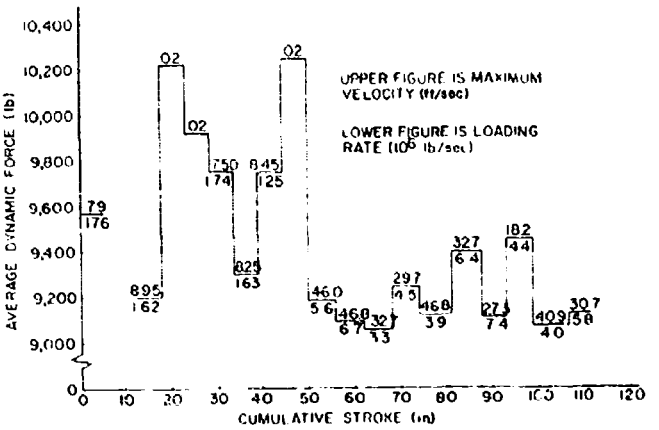

Fig. 14. Average dynamic force vs cumulative stroke

Tests on a prototype Apollo crew attenuator strut at stroking velocities up to 52 ft/sec indicated force-deformation behavior in tension and compression approaching that of an ideal energy absorber. The average dynamic force variation was within ±6 percent over a total cumulative stroke of 112 in. with very low-rate sensitivity.

It is expected that these devices will find wide application where high weight and volume efficiency, repeated operation in tension and compression, and precise force levels are required. They are ideally suited to structural overload applications because negligible deformation occurs until the design load is reached. The units can be designed for a wide range of load and stroke capability and require little or no maintenance.

REFERENCES

1. J. F. Tavernelli and L. F. Coffin, Jr., A Compilation and Interpretation of Cyclic Strain Fatigue Tests on Metals," Trans. Am. Soc. Metals, 51:438-453, 1959

2. S. I. Liu et al., "Low Cycle Fatigue of the Aluminum Alloy 24ST in Direct Stress," Trans., AIME, 175:469, 1948

3. L. F. Coffin, Jr. and J. F. Tavernelli, "The Cyclic Straining and Fatigue of Metals," Trans. Met. Soc. AIME, 215:794-806, Oct. 1959

4. R. W. Smith et al., "Fatigue Behavior of Materials Under Strain Cycling in Low and Intermediate Life Range," NASA TN D-1574, Apr. 1963

5. S. S. Manson, "Behavior of Materials Under Conditions of Thermal Stress," NACA Rept. 1170, 1954

6. D. L. Platus et al., "Concepts of Multiple-Impact Study of Energy Absorption," NASA-CR-273, Aug. 1965

DISCUSSION

Mr. Davis (Fairchild Hiller): I have noticed some designs in the literature that include rubber, and yours has the steel inserts. I am interested in automotive applications. What range or performance would you get under environments such as temperature or humidity? Can we get reasonably predictable properties over extreme temperature ranges?

Mr. Platus: I am glad you asked that question. We are interested in automotive applications also. Because of the mechanism employed here, namely the deformation of the ductile metal, I think we can expect good performance over extreme environments. We are dealing with essentially plastic flow of metals and the variation in force behavior will pretty much follow that for straining of ductile metals. Of course, there are high temperature alloys which will perform over quite a wide temperature range. So I think we can expect to get pretty good behavior over a wide range of environmental extremes.

* * *

DEVELOPMENT OF THE KINEMATIC FOCAL ISOLATION SYSTEM FOR HELICOPTER ROTORS

Rodney W. Balke
Bell Helicopter Company
Fort Worth, Texas

Because of out-of-balance forces and the asymmetric airflow over the rotor disk of a helicopter, the vehicle is subjected to considerable low-frequency excitation. To enhance crew and passenger comfort and improve component reliability, some form of isolation system is generally desirable. Conventional methods of isolation are compromised by the requirement that the large steady forces and moments and the long-duration transients resulting from maneuvers not cause excessive pylon deflection. A simple, highly effective isolation system, based on a new concept, has been developed for this environment. This concept utilizes linkages for properly placing the elastic axis to achieve zero-angular response at the desired frequency produced by a balance of inertial, spring, and exciting forces. The optimum focal regions for the isolation of rotor inplane forces at discrete harmonics and subharmonics, defined in terms of focal distance and spring rate, are shown by analysis. Branches of the optimum loci are shown to exist for some configurations above and below but not at the pylon-fuselage interface or mounting plane. Design criteria are developed and discussed for each of the two branches.

The development of an isolation system that achieves greater focal distances than the focal elastomeric mounting, while providing a high degree of restraint to rotor thrust and torque, is followed from initial concept through analysis, fractional and full-scale model tests, and ground-vibration and flight tests. The resulting kinematic focal isolation system, weighing less than 1 percent of design gross weight, provides theoretical isolation of 78 percent in pitch and 92 percent in roll. Ground- and flight-test data show that the theoretical values are approached. Field experience with this isolation system--which is used in the Model 206A, TH-57A, and OH-58A helicopters--has proved the components to be rugged and the system to be reliable.

INTRODUCTION

Current trends in mission and design objectives are toward higher speeds and better performance. Coupled with these objectives are requirements for low frontal area, lighter, more powerful turbine engines, and more efficient structure and dynamic components. With the increase in airspeed and power, there is an attendant increase in rotor-generated oscillatory loading and vibration.

Four considerations are involved in minimizing fuselage vibrations and improving component reliability: (a) minimization of oscillatory airloads, (b) optimization of rotor dynamics, (c) optimization of fuselage dynamics, and (d) attenuation of the excitation forces through isolation.

Efforts to reduce the oscillatory forces have been of limited success. Tailoring the rotor and/or fuselage to avoid resonance is usually attempted but is not by itself adequate to insure low vibration. Therefore, to enhance crew and passenger comfort and improve component reliability, some form of isolation system is generally desirable. This is particularly true for a two-bladed teetering rotor, because of the frequency and magnitude of the rotor hub forces produced. For rotors with three or more blades, isolation is not always mandatory but is often desirable to reduce sensitivity to out-of-balance and out-of-track forces and high frequencies. For rotors with articulated blades, mechanical stability considerations either preclude the use of isolaters or otherwise limit the control of vibrations.

The number of isolation techniques have been proposed [1-6] that include passive, servo-null, fully active, and hybrid systems. In practice, only a few systems meet the necessary design criteria and are efficient, light weight, and rugged.

CONVENTIONAL ISOLATION SYSTEMS

Conventional methods for isolating black boxes such as electronic packages – using elastomeric springs or metal springs and friction dampers – represent one of the best known fields of vibration isolation. These methods, however, can not be applied directly to helicopter rotor isolation. In the helicopter, two free bodies – pylon and fuselage – are suspended to the g-field by the rotor's thrust, while for most configurations, rotor counter-torque, engine torque, and steady rotor inplane forces act across the isolating system.

Conventional isolation requires that the natural frequency of the system be below the frequency to be isolated. For common rotor-generated frequencies, this requirement makes it necessary to use a relatively soft system. The large steady forces and moments and the long-duration transients would result in large static and transient deflections across the pylon-fuselage interface – deflections that could not be accommodated by the control system and other functional components. The small motions allowable for steady and transient loading make it necessary to provide a high degree of vertical restraint. A conventional system, combining a vertical restraint with mounts having high horizontal spring rates (Fig. 1), can be used to isolate the fuselage from inplane rotor excitations which tend to produce pitch and roll. Typical plots of angular pylon response a_p and angular fuselage response a_f are shown in the figure, along with the rigid-body response a_{rb}. The first peak is a pendular mode resulting from the assumption that the thrust force is vertical and invariant. This assumption is not valid for extremely low frequencies. In this mode, the rotor thrust and the g-field act as restoring forces. The second or pylon mode, which involves deflection about the elastic axis, is usually located below normal rotor operating speed.

With this system, the best isolation is achieved with the softest springs or elastomeric mounts that other considerations will permit. Two of these considerations are: (a) the requirement to minimize torsional deflections which cause input-shaft misalinements if the engine is not rigidly attached to the pylon, and (b) the requirement to minimize pylon response to pilot control inputs and subharmonic oscillations produced by gusts. These considerations set a lower limit, which is higher than desired for isolation, on the spring rates.

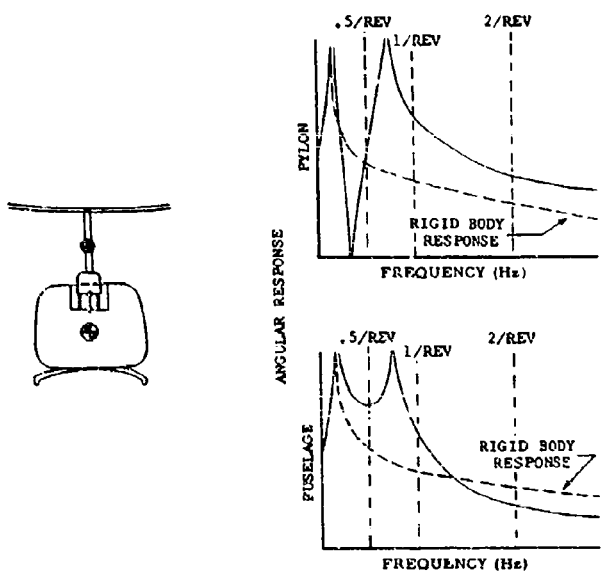

Fig. 1. Conventional helicopter isolation system with vertical restraint

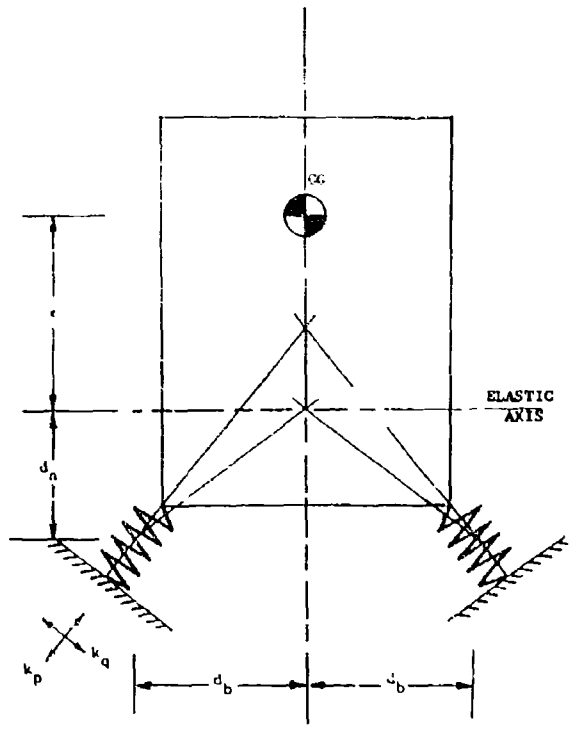

Fig. 2. Focal elastomeric isolation system

FOCAL ISOLATION SYSTEMS

Focal elastomeric mounts [7] are often used to decouple the translational and rotational modes in the mounting of black boxes. This system (Fig. 2) is limited in focal depth d_a unless large mounting breadths $2d_b$ and an extremely high ratio of the spring rates K_p to K_q along the two principal elastic axes are used. If utilized for rotor isolation where there are large cg offsets, the large mounting breadths would increase fuselage frontal area, which would also increase drag. Decoupling is usually achieved only in a single plane, and there is limited restraint to rotor thrust and torque.

A better method for achieving large focal distances is the use of a pair of kinematic linkages (Figs. 3(a) and 3(b) attached by pinned joints across the pylon-fuselage interface and directed toward the desired focal axis. A metal or elastomeric mount provides the necessary restoring spring. For the undamped case that is shown, both the pylon and the fuselage exhibit optimum (theoretically zero) response points. The upper focal arrangement is relatively stiff, and the pylon mode may occur at frequencies above normal rotor speed. These arrangements permit the thrust of the rotor to be rigidly restrained and provide pitch and roll (angular) isolation to inplane shear forces. The available focal depth, which is independent of the mounting breadth, is virtually unlimited.

ANALYSIS AND RESPONSE CHARACTERISTICS

A simplified analysis [8] has been used to study the behavior of the helicopter in flight. The equations for the angular pylon response α_p and the angular fuselage response α_f to rotor hub forces and moments were derived. Only the shear force excitation case is considered in the isolation of the Bell semirigid rotor system. The rigid-body response α_{rb} is found by considering the two bodies, pylon and fuselage, locked together ($1/K_t = 0$).

An idealized response plot and the related mode shapes are shown in Fig. 4. With the proper combination of system parameters, focal depth, and spring rate, it is possible to minimize the pylon's response to rotor

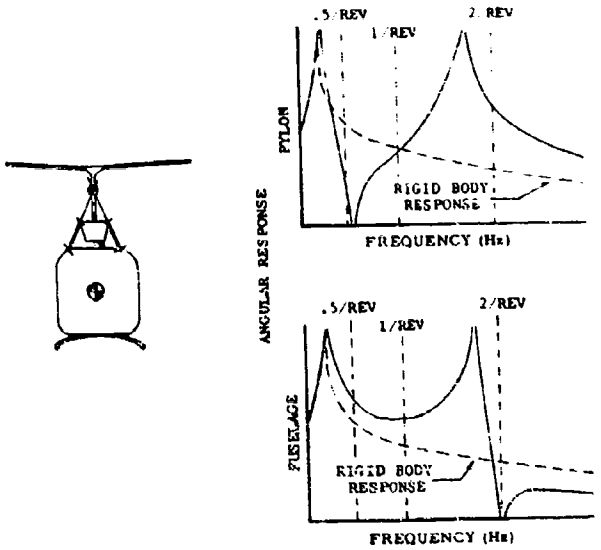

(a) Focal point above mounting plane

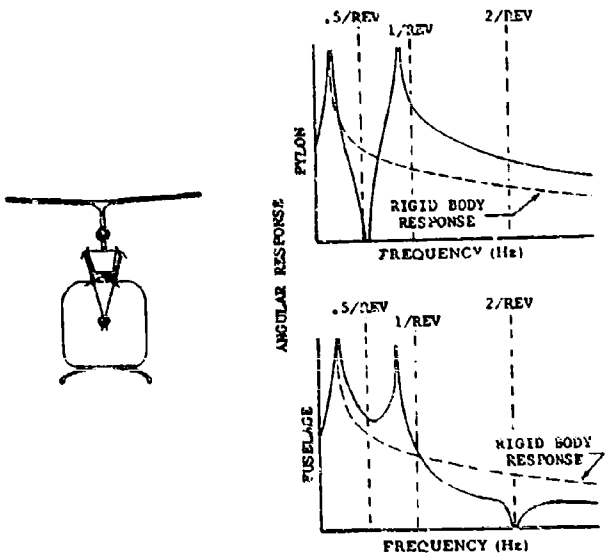

(b) Focal point below mounting plane

Fig. 3. Kinematic focal isolation system

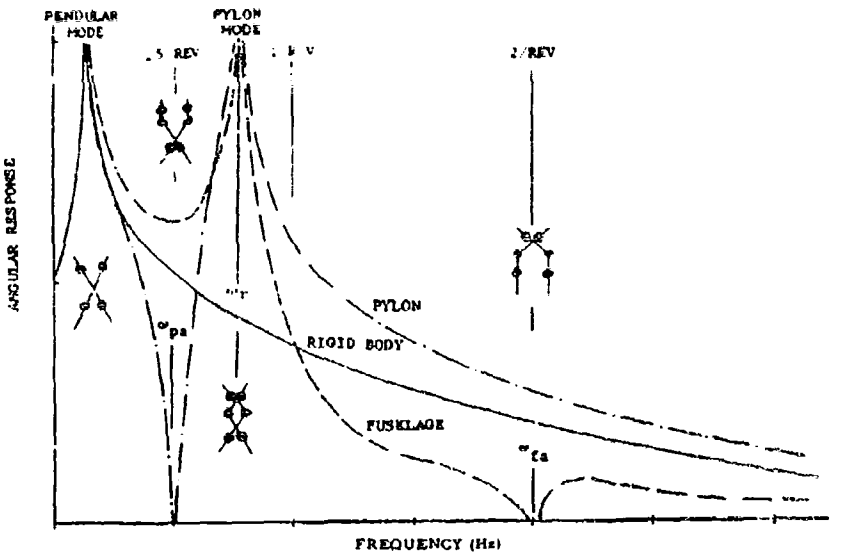

Fig. 4. Idealized frequency-response plot and related mode shapes

subharmonics and simultaneously to minimize fuselage response to higher integral multiples (n/rev) of the rotor speed without amplification at the fundamental rotor frequency ($n = 1$). The angular transmissibility is defined as

$$T = \frac{\alpha_f}{\alpha_{rb}}$$

A three-dimensional plot of fuselage-roll angular transmissibility at 2/rev as a function of spring rate and focal distance is shown in Fig. 5. The peaks and valleys of Fig. 5 correspond to maximum and minimum fuselage response loci, respectively.

Equations for minimum pylon response α_{pa} loci and minimum fuselage response α_{fa} loci are derived in the Appendix. These equations and the equation for maximum response are written in the form $Q_2c^2 + Q_1c^1 + Q_0K_tc^0 = 0$, which is the equation for a K_t parabola [9].

The coefficients Q_2, Q_1, and Q_0 are quadratics in ω^2. Therefore, the characteristics of the conics defining the loci of maximum and minimum response vary with ω as shown in Fig. 6. Figure 6(a) shows the locus of minimum pylon response at low frequency; Fig. 6(b) shows the loci of maximum pylon and fuselage response; and Fig. 6(c) shows the loci of minimum fuselage response. For configurations that place the pylon's center-of-gravity above that of the fuselage and that use a focal point below the rotor hub, the conics open upward. The optimum response characteristics to each pitch and roll excitation can thus be defined for any helicopter configuration.

DEVELOPMENT

Design Configuration

The Bell Model 206, a 2900-lb-gross-weight helicopter, has a silhouette that is conventional for single-lifting-rotor helicopters. The pylon, which consists of the main transmission, rotor shaft, and rotor, is entirely above the fuselage structure. The engine is mounted on top of the fuselage and is connected to the main transmission through a floating shaft with spherical-tooth-gear couplings. The pylon is essentially symmetrical, is light weight (a pylon-to-fuselage ratio of 0.173), and has low inertia (a pylon-to-fuselage ratio of 0.011 in pitch and 0.030 in roll). The Model 206 uses the Bell semirigid two-bladed rotor, which transmits oscillatory forces, but no significant vibratory moments, into the rotor shaft. The predominant excitation frequencies are 1/rev (6.57 Hz) as a result of out-of-track and out-of-balance and 2/rev (13.14 Hz) as a result of aerodynamic loading and dynamic blade response.

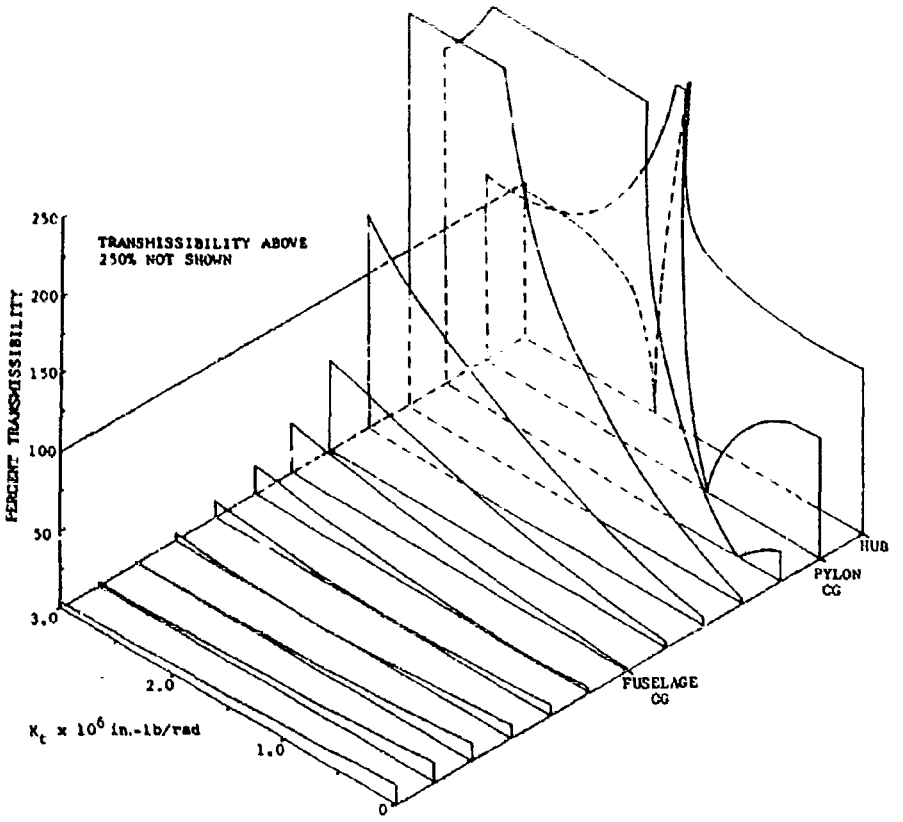

Fig. 5. Fuselage roll angular transmissibility at 2/rev

Design Criteria and Torque Restraint Requirements

Although focal-point choices were theoretically unlimited and the use of kinematic focal linkages overcame the difficulty of obtaining large focal distances, there remained a number of practical considerations. Extensive efforts were made to establish definitive criteria for static, dynamic, and transient deflections to insure the compatibility of the pylon-isolation system and the structural and functional components of the vehicle. The static criteria which were chosen to prevent excessive input-coupling misalinement and to insure clearance between the rotor and the fuselage, are shown in Table 1, along with dynamic criteria for isolation and oscillatory deflections.

The steady-state torque vectors that act upon the pylon (main rotor countertorque, engine-input torque, and lateral hub shear to balance tail-rotor thrust) are shown in Fig. 7. The resultant torque vector is aft, at an angle θ of 10 degrees from the vertical. Each of these torque vectors is interrelated and for most flight conditions varies in the same proportion, thus minimizing the variations in the angle θ.

Fractional-Scale Model Tests

Fractional-scale models were used in the development of the Model 206 focal isolation system. The first was an unsophisticated, unidirectional plywood model with rigid-body pylon and fuselage; it was the first attempt to use linkages to achieve focal distances. Positive and negative focal regions, as well as a parallelogram arrangement, were investigated. In addition, the effect of engine-to-transmission coupling friction was evaluated.

The second, smaller model was bidirectional providing isolation in both pitch and roll. It permitted the evaluation of a flexible fuselage.

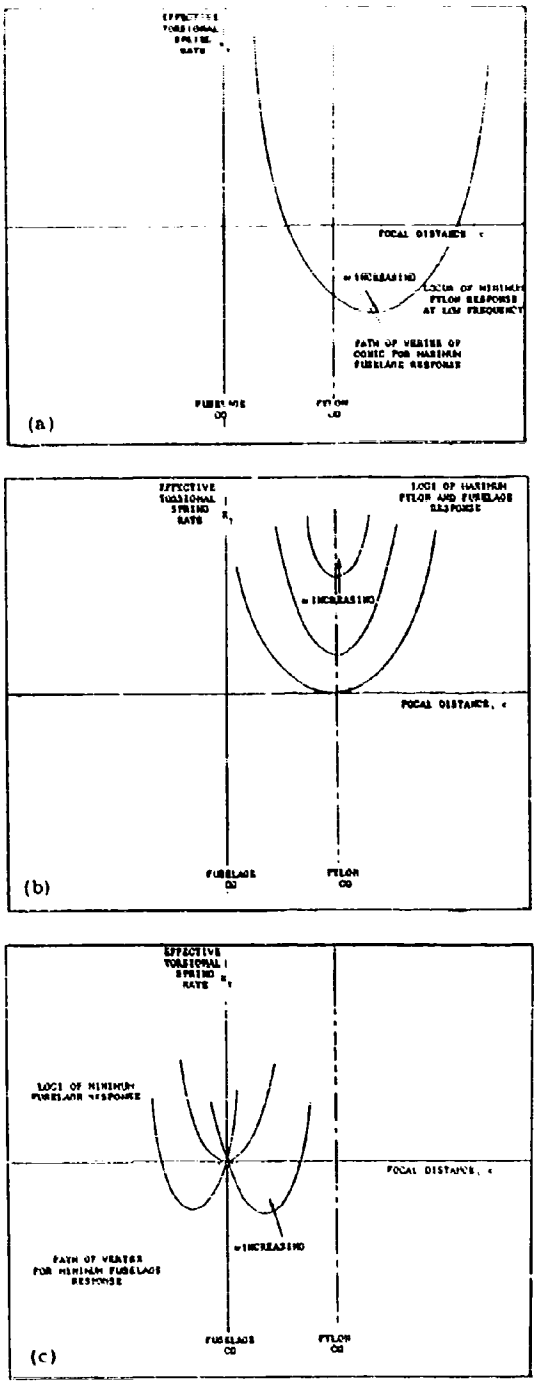

Fig. 6. Variation with excitation frequency of conics defining the loci of minimum and maximum response; (a) Minimum pylon response, (b) Maximum pylon and fuselage response, and (c) Minimum fuselage response

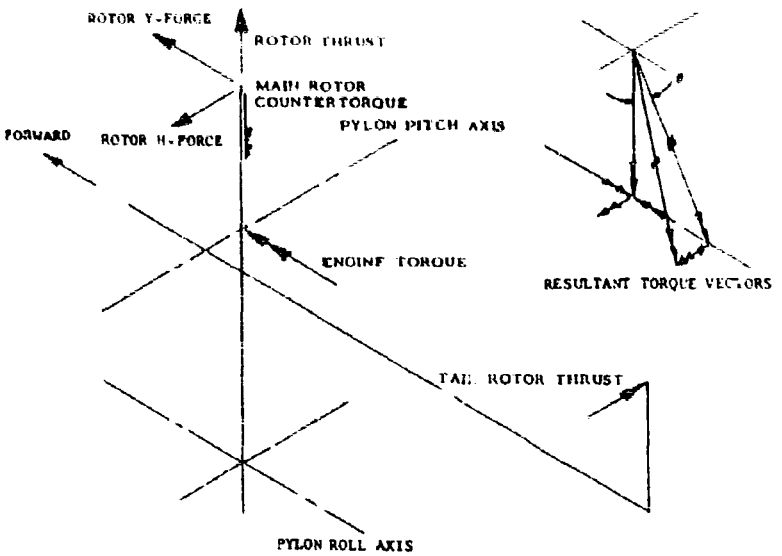

Fig. 7. Torque restraint requirements

TABLE 1
Design Criteria

Static Criteria		
Plane	**Steady Force (lb)**	**Rotation (degrees)**
Pitch	200	1.00
Roll	200	1.25
Dynamic Criteria		
Plane	**Oscillatory Force**	**Isolation (% transmissibility)**
Pitch	0.04 × gross weight	20
Roll	0.10 × gross weight	20
Vertical	0.10 × gross weight	100 or less (No amplification)
Transmission Input Shaft Motions		
Direction	**Shaft Misalinement (degrees)**	**Relative Oscillatory Motion (in.)**
Vertical	±0.5	±0.13
Lateral	±0.75	±0.13
Axial	—	±0.10
Component Life: 1200 hr		

Qualitative and some rough quantitative data were obtained from these models. The significant results of the preliminary tests were as follows:

1. Good isolation was achieved for focal regions both above and below the mounting plane.

2. Large relative motions occurred at focal points near the pylon center of gravity.

3. Input shaft friction was found to be quite detrimental to pitch isolation when using low or negative focal points.

These results were sufficiently promising to warrant more detailed study.

Investigations of the rotor shaft bending mode, which if improperly located could significantly alter the isolation of the focal system, were later made, both analytically and on the third fractional-scale model shown in Fig. 8. Typical response curves are shown in Fig. 9. The rotor shaft bending mode was calculated as a function of focal depth and the calculated data were compared with measured data (Fig. 10). These results show that there is no problem with regard to the Model 206, because the low 1/rev and 2/rev transmissibility is preserved, but results do indicate the capability of the focal system to vary the rotor shaft bending frequency, particularly when the system is focused near the pylon center of gravity. Although the presence of the rotor shaft bending mode can modify the response characteristics, the general trends defined by the rigid-body analysis still hold. The qualitative model 1/rev and 2/rev response data, shown in Figs. 11(a) and 11(b), respectively, demonstrate this.

Full-Scale Model

Construction of a full-scale, bidirectional model (Fig. 12), with mass and stiffness values approximating the Model 206, permitted the investigation of isolation in both pitch and roll. Seats were installed so that personnel could sit in the model and directly evaluate the effect on vibration of several parameters. These parameters included a wide range of positive and negative focal distances and variations in pylon spring rates.

Initial tests of this model resulted in a poor ride because of the friction in the spherical bearings in the linkages connecting the pylon and fuselage. Replacing the metal-to-metal bearings with self-lubricating Teflon fabric-lined bearings provided good isolation. The tests showed a rotor shaft bending mode near 20 Hz which is high enough to have little effect on low-frequency isolation.

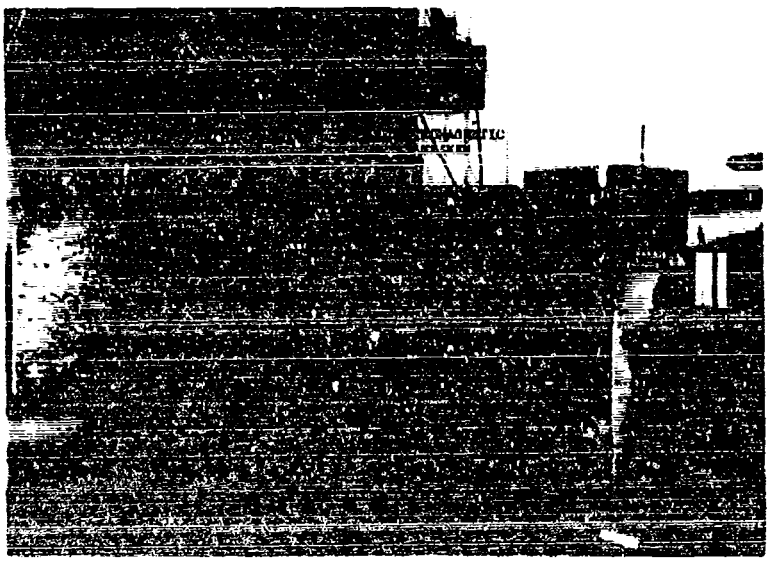

Fig. 8. Fractional scale model used to investigate rotor shaft flexibility

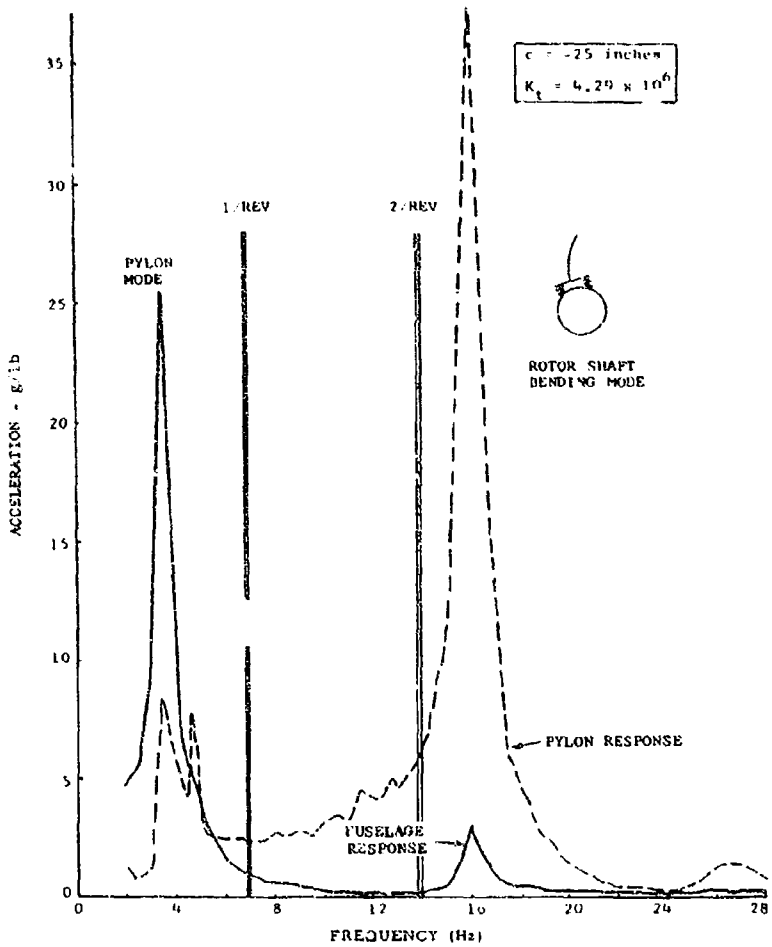

Fig. 9. Typical data plot from fractional scale model

APPLICATION

Conics for Design Configuration

The equations shown in the Appendix were used to calculate the maximum and minimum response loci in pitch and roll as shown in Figs. 13 and 14, respectively. Loci for 0.5/rev, 1/rev, and 2/rev pylon response are shown in Figs. 13(a), 13(b), and 13(c), respectively. Figures 14(a), 14(b), and 14(c) are similar plots for roll response. The static limit in pitch of 1.0-degree rotation for 200-lb hub shear force is shown in Fig. 13. The corresponding limit in roll of 1.25 degrees rotation for 200-lb hub shear is shown in Fig. 14. Three-dimensional contours, as shown in Fig. 15, were constructed and found to be quite useful in the study.

Design Selection

Careful review of the analytical and quantitative model data and consideration of the design criteria showed that optimum 2/rev roll isolation could be achieved when $c = -18$ in. and the spring rate is 1.0×10^5 in.-lb/rad and at the same time meet the static criteria. This system would have a pylon or natural frequency ω_r of 3.0 Hz. The optimum isolation could also be obtained with $c = +39$ in., a spring rate of 0.3×10^6 lb/rad and a pylon frequency 8.3 Hz.

Similarly, the optimum pitch isolation could be obtained at $c = -21$ in., $K_t = 1.3 \times 10^6$ in.-lb/rad, and $\omega_r = 3.0$ Hz, or at $c = +38.5$ in., $K_t = 0.35 \times 10^6$ in.-lb/rad and $\omega_r = 5.0$ Hz. In either case, optimum isolation could be obtained with

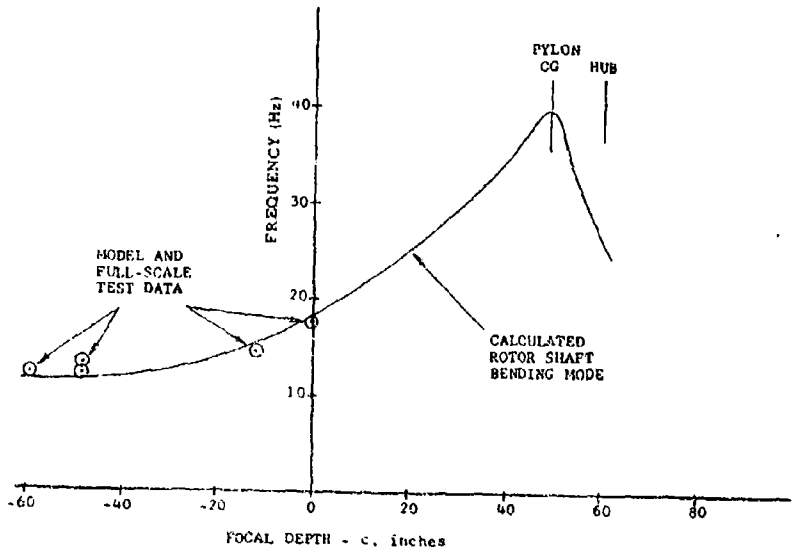

Fig. 10. Correlation of measured and calculated rotor shaft bending frequencies as a function of focal depth

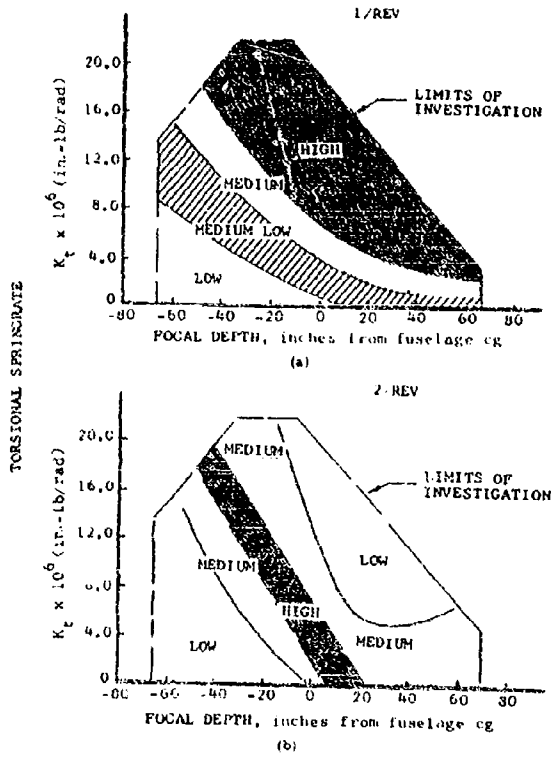

Fig. 11. Qualitative model data showing response characteristics with flexible rotor shaft

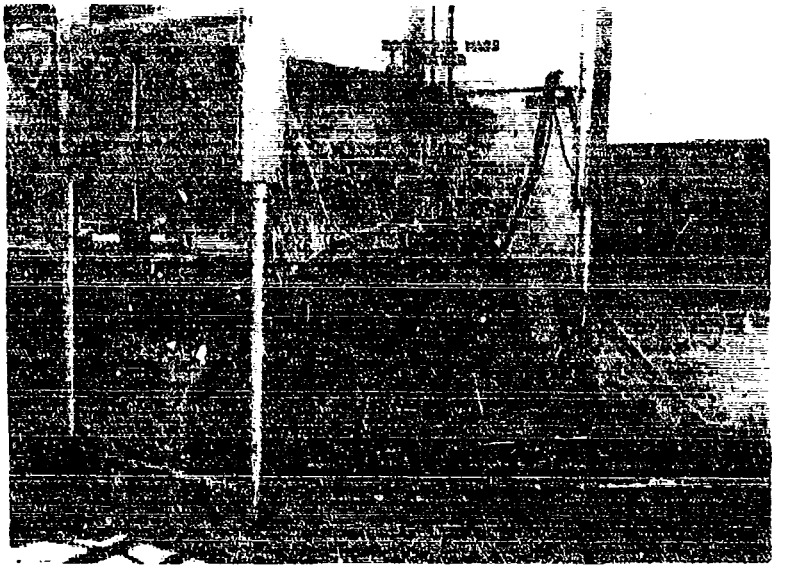

Fig. 12. Full-scale model

higher values of K_t by choosing the proper focal depth along the curve of the loci of zero response; however, for increasingly stiffer springs structural deflections become more and more significant.

Because the oscillatory hub forces in the lateral direction are higher than those in the fore-and-aft direction, and the fuselage roll inertia is lower than the pitch inertia, primary emphasis was placed on roll isolation. However, the consideration of rotor shaft flexibility led to the selection of a higher focal point than that indicated by the rigid body analysis. The lateral focal point was chosen at $c = 0$, defined by point P in Fig. 14. Roll response takes advantage of inertial amplification to provide good isolation and to minimize transient response to rotor-force variations.

The strong influence of input-shaft friction on pitch response for low and negative values of c led to the selection of a high focal point at the input-shaft axis, defined by point P in Fig. 13. This choice also precluded the very high relative motions across the pylon-fuselage interface associated with focal points slightly farther from zero. Tests of the full-scale model incorporating the final design geometry including the flexible rotor shaft of the Model 206 showed good 2/rev isolation.

The two kinematic links used on the full-scale model to obtain the desired pitch and roll elastic axes were canted to form a plane of intersection perpendicular to the resultant torque vector. This arrangement minimizes steady state pylon deflections resulting to torque. A single elastomeric mount is used to provide restraint in pitch and roll. The final design configuration is shown in Fig. 16.

Isolation System Weight

The isolation system used in the Model 206 weighed 23.2 lb or less than 1.0 percent of design gross weight. The weights of its components are shown in Table 2. If no isolation system were employed, some of this weight would be required to secure the gearbox to the fuselage.

Ground Vibration Tests

Ground vibration tests were made by suspending the helicopter by its rotor hub with a shock cord to put the rigid body vertical frequency below 1 Hz. A mechanical oscillator attached to the rotor hub produced lateral excitations. The oscillator and ballast were used to simulate the weight of the blades. A roll-response

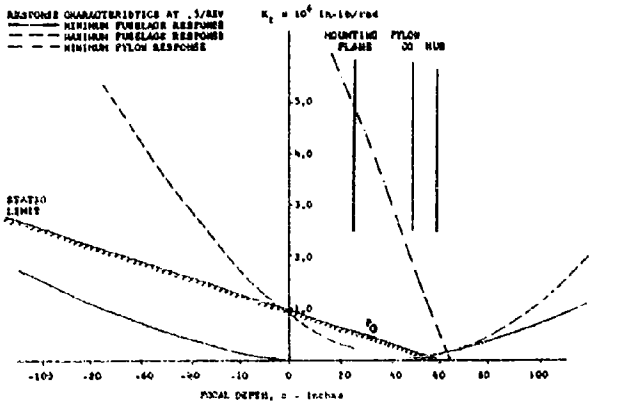

(a) At 0.5/rev

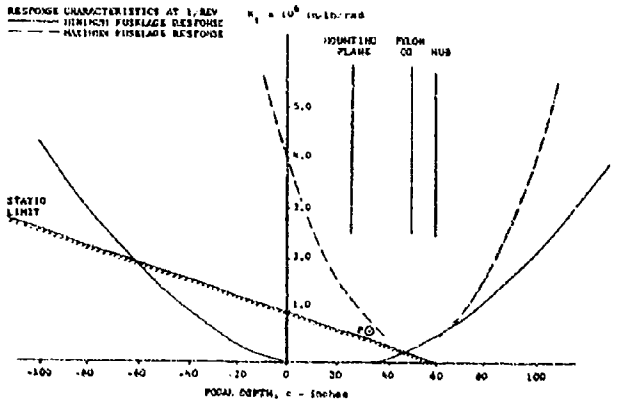

(b) At 1/rev

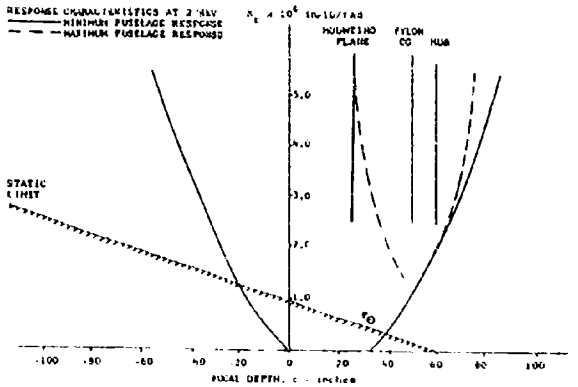

(c) At 2/rev

Fig. 13. Maximum and minimum pitch-response loci for Model 206 helicopter

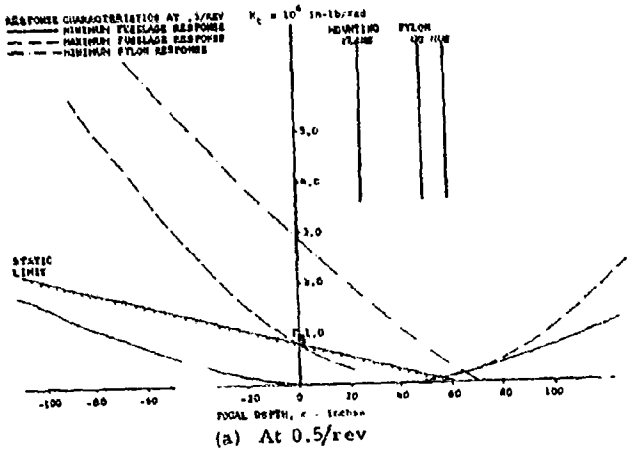

(a) At 0.5/rev

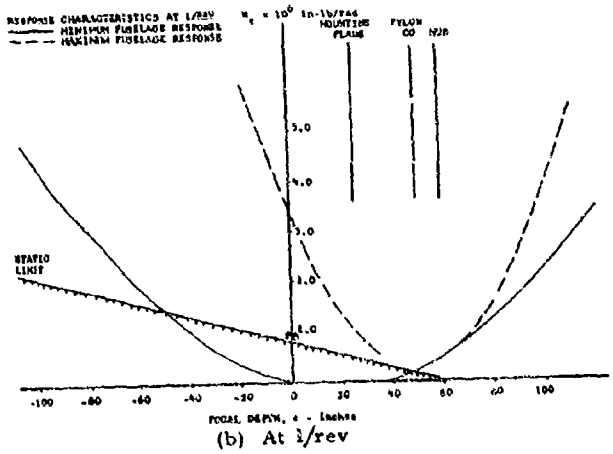

(b) At 1/rev

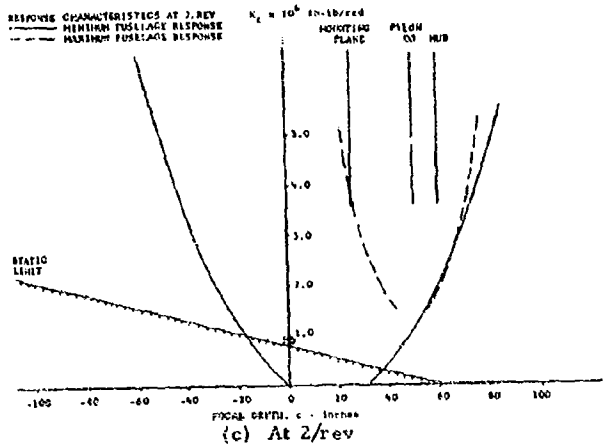

(c) At 2/rev

Fig. 14. Maximum and minimum roll-response loci for Model 206 helicopter

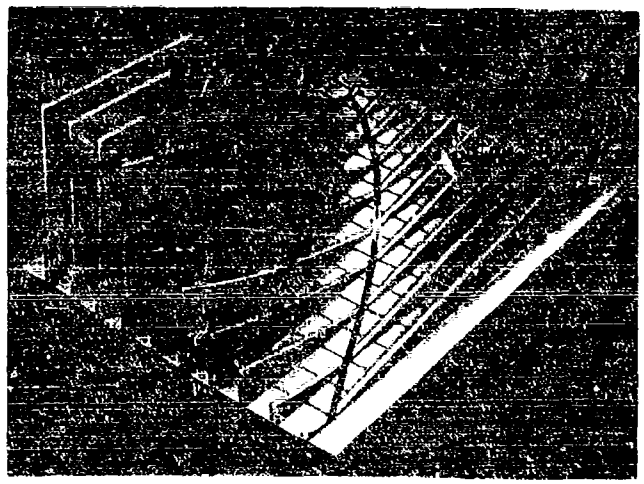

Fig. 15. Typical three-dimensional contour; transmissibility as a function of focal distance and effective torsional spring rate

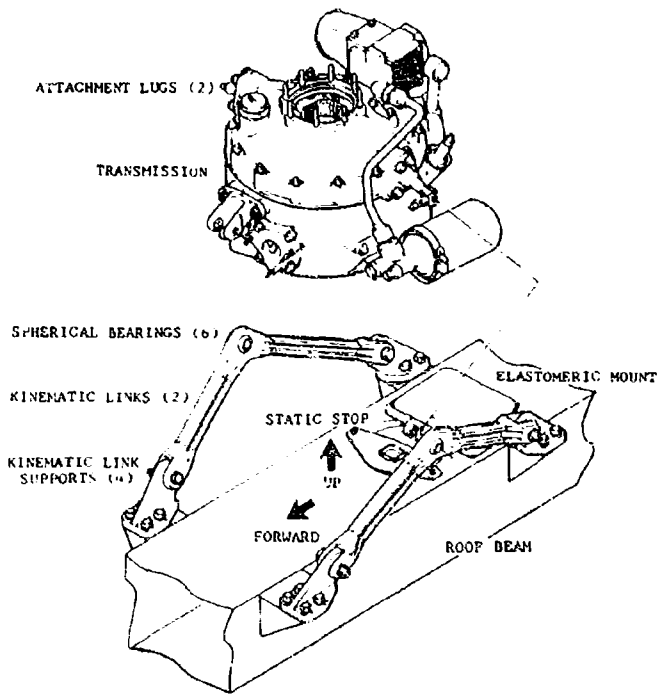

Fig. 16. Final design configuration of Model 206 kinematic focal isolation system

TABLE 2
Weight of Model 206 Kinematic Focal Isolation System

Component	Quantity	Weight
Upper link attachments	2	2.20
Kinematic links	2	4.00
Lower link attachments	4	3.09
Elastomeric mount	1	4.10
Mount attachment to gear box	1	1.10
Static stop	1	0.65
Fuselage roof beam fittings	6	4.85
Washers, shims, bolts, nuts	–	3.19
Total weight		23.18
Percent of design gross weight		0.799

plot of vertical acceleration of the pilot's seat per pound of lateral hub force is compared in Fig. 17 with the calculated data. Good pitch isolation, similar to that shown in roll, was also obtained.

Flight Tests

Flight-test evaluation by the U.S. Army of the OH-4A helicopter, the military version of the Bell Model 206 [10], found that "Qualitatively, the over-all vibration characteristics of the OH-4A were exceptionally good." Quantitative 1/rev and 2/rev data presented in Ref. [10] are shown in Fig. 18. These data are well within the specified limits of MIL-H 8501-A. The commerical Model 206A (Fig. 19), which uses the same kinematic focal isolation system, exhibits similar low vibration characteristics (Fig. 20).

Service Experience and Future Applications

Experience with the OH-4A and the Model 206A to date has proven this system to be rugged and reliable. Helicopters with more than 1000-hr flight time are still using the initial elastomeric mounts and spherical bearings. The isolation system is also used on other Bell models including the TH-57A, Model 206A-1, and OH-58A. Additional variations of this concept are under study.

CONCLUSIONS

The significant conclusions derived in the development of the subject rotor-pylon isolation system follow:

1. The kinematic focal isolation system functions to isolate rotor inplane forces efficiently in the helicopter environment. The system is both light weight and rugged.

2. The kinematic focal isolation system may be used to achieve focal depths far in excess of focal elastomeric mountings. At the same time the large deflections resulting from steady state and transient forces associated with conventional and focal elastomeric mounting are minimized.

3. The kinematic focal isolation system is adaptable to variations in gross weight, pylon-fuselage mass and inertia ratios, configuration geometry, type of excitation, and frequency of excitation.

Additionally, the conclusions regarding the analytical and functional aspects are:

4. The theoretical loci of optimum isolation, determined by the rigid-body analysis, are realized at low frequencies for systems having high rigidity and relatively low damping.

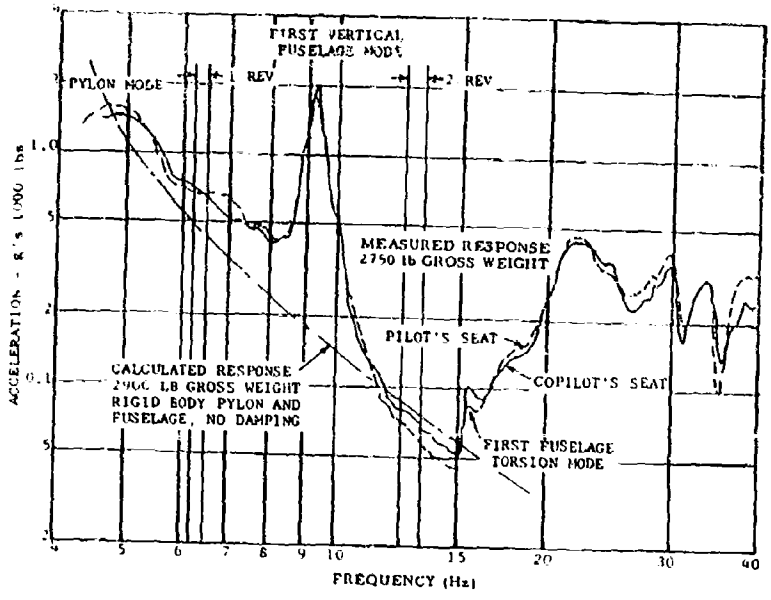

Fig. 17. Results of ground vibration test in roll response and correlation with calculated data

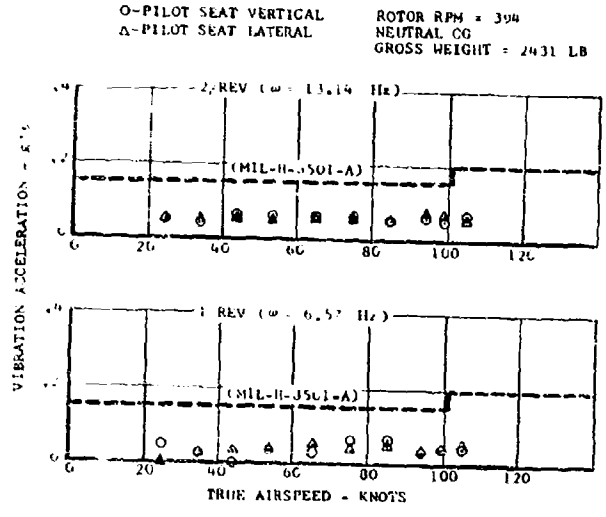

Fig. 18. Vibration-response data for OH-4A helicopter (Ref. [10])

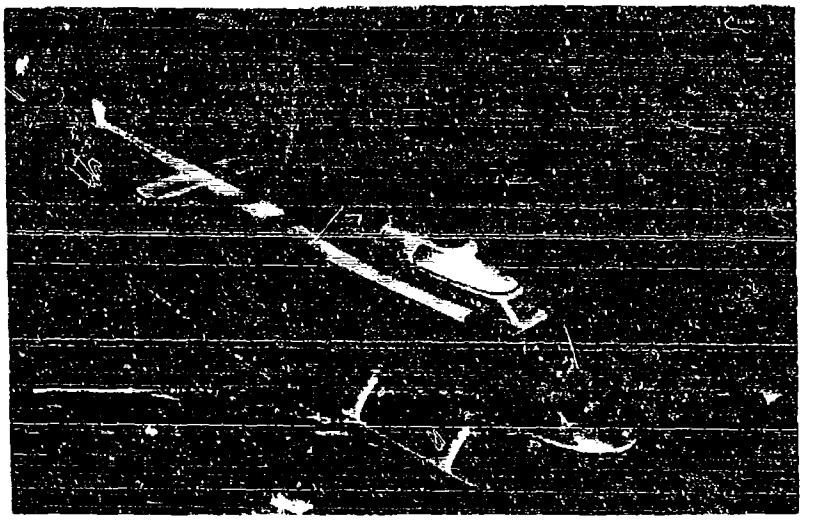

Fig. 19. Model 206A helicopter

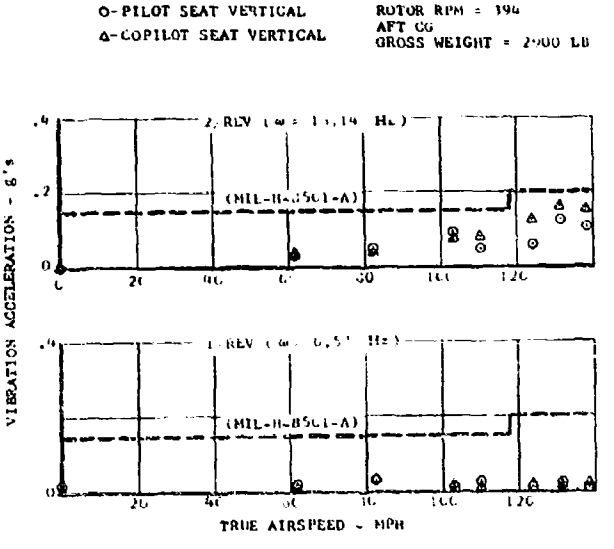

Fig. 20. Vibration-response data for Model 206A helicopter

5. The predicted loci of optimum isolation are shifted in the presence of rotor shaft flexibility, particularly for positive focal distances.

6. Variations in the focal depth of the kinematic focal isolation system can be used to shift the rotor shaft bending frequency.

7. The rigid-body analysis is useful for approximating the regions of low response, however, more extensive analyses are necessary to determine the effect of pylon and fuselage flexibilities.

8. Fractional- and full-scale models are useful in optimizing the isolation system design and are particularly valuable in evaluating the effect of friction on the vibration response characteristics.

ACKNOWLEDGMENTS

The author wishes to acknowledge the work of D. L. Kidd who instigated the use of linkages for pylon mounting; of J. M. Drees who conducted the initial analyses of the free-body system; of D. C. Faecke who programed the analysis; and of D. R. Neumeyer for his help in preparing the figures.

Also the continued guidance and interest of D. L. Kidd and J. M. Drees during this program are gratefully acknowledged.

REFERENCES

1. C. E. Theobald, Jr. and R. Jones, "Isolation of Helicopter Rotor Vibratory Forces From the Fuselage," WADC Tech. Rept. 57-404, Sept. 1957

2. C. E. Crede, R. D. Cavanaugh, and H. N. Abramson, "Feasibility Study of an Active Vibration Isolator for a Helicopter Rotor," WADC Tech. Rept. 56-163, Oct. 1956

3. "Technical Proposal for an Analytical Study of Helicopter Rotor-Pylon Isolation Systems," Bell Helicopter Co. Rept. 299-099-291, 30 Sept. 1965

4. P. C. Calcaterra and D. W. Schubert, "Isolation of Helicopter Rotor-Induced Vibrations Using Active Elements," 37th Shock and Vibration Bull., Part 6, Jan. 1968

5. D. A. Bies and T. M. Yang, "Hybrid Vibration-Isolation System for Helicopters," 37th Shock and Vibration Bull., Part 6, Jan. 1968

6. R. Jones and W. G. Flannelly, "Application of the Dynamic Antiresonant Vibration Isolator to Helicopter Vibration Control," 37th Shock and Vibration Bull., Part 6, Jan. 1968

7. C. E. Crede, Vibration and Shock Isolation (John Wiley & Sons, Inc., New York), 1951, pp 73-82

8. R. W. Dalke and D. C. Faecke, "Analysis of the Rigid-Body Pitch and Roll Modes of the Helicopter in Flight," Bell Helicopter Co. Rept. 599-114-901, Fort Worth, Tex., Apr. 1968

9. R. S. Underwood and F. W. Sparks, Analytic Geometry (Houghton Mifflin Co., Boston, Mass.), 1948

10. J. R. Melton and J. C. Watts, "Report of the Engineering Flight Test Performance Phase of the OH-4A Helicopter, Unarmed (Clean) and Armed with the XM-7 or SM-8 Weapon Subsystem," USATECOM Project No. 4-3-0250-11/12/13, U.S. Army Aviation Test Activity, Edwards AFB, Calif., Aug. 1964

Appendix

CONICS FOR MINIMUM AND MAXIMUM RESPONSE

NOMENCLATURE

a Distance from fuselage cg to common cg (positive when pylon cg is above the fuselage cg); in.

b Distance from pylon cg to common cg (positive when pylon cg is above the fuselage cg); in.

c Distance from fuselage cg to hinge (positive when hinge is above the fuselage cg); in.

d Distance from pylon cg to hinge (positive when hinge is below the pylon cg); in.

F Hub shear force; lb

g Acceleration of gravity; in./sec^2

I_p Inertia of the pylon about the pylon cg; in.-lb-sec^2

I_f Inertia of the fuselage about the fuselage cg; in.-lb-sec^2

K_t Effective torsional spring rate about hinge; in.-lb/rad

h	Distance from hinge to hub (positive when hinge is below hub); in.
T	Rotor thrust; lb
M	Hub moment; in.-lb
M_p	Mass of pylon; lb-sec^2/in.
M_f	Mass of fuselage; lb-sec^2/in.
d	Distance from pylon cg to hub; in.
t	Time; sec
α_p	Angular deflection of the pylon; rad
α_f	Angular deflection of the fuselage; rad
α_{rb}	Rigid body angular deflection; rad
ω	Excitation frequency; rad/sec

ANALYSIS

The general behavior of the helicopter in flight is shown by the use of a grossly simplified analytical model (Fig. A-1) in which both the pylon and the fuselage are considered to be rigid bodies. The rotor is treated as a mass acting at the top of the rotor shaft. An elastic axis between the two bodies is assumed to be at any arbitrary location along a line through the rotor-shaft axis, either on or off the pylon or fuselage. A restoring spring acts about the elastic axis. The rotor's thrust is considered to be vertical, invariant, and equal to the gross weight. An inplane oscillatory force or moment of variable frequency acts at the rotor hub. The equations of motion are derived by considering the forces on the free body of each the pylon and the fuselage. Additional assumptions are zero damping, small angle displacements, and sinusoidal motion. The resulting equations are —

$$\begin{vmatrix} A_{11} & A_{12} \\ A_{21} & A_{22} \end{vmatrix} \begin{Bmatrix} \alpha_p \\ \alpha_f \end{Bmatrix} = \begin{Bmatrix} E_1 \\ E_2 \end{Bmatrix} \qquad \text{(A-1)}$$

where

$$A_{11} = -I_p\omega^2 - \beta d^2\omega^2 - M_p gd + K_t + hT .$$

$$A_{12} = A_{21} = -\beta dc\omega^2 - K_t .$$

$$A_{22} = -I_f\omega^2 - \beta c^2\omega^2 + M_f gc + K_t .$$

$$E_1 = F_o h + M_o - \beta dF_o .$$

$$E_2 = \xi cF_o .$$

and

$$\beta = \frac{M_p M_f}{M_p + M_f} ,$$

$$\xi = \frac{M_p}{M_p + M_f} ,$$

$$\zeta = \frac{M_f}{M_p + M_f} ,$$

and

$$T = (M_p + M_f)g$$

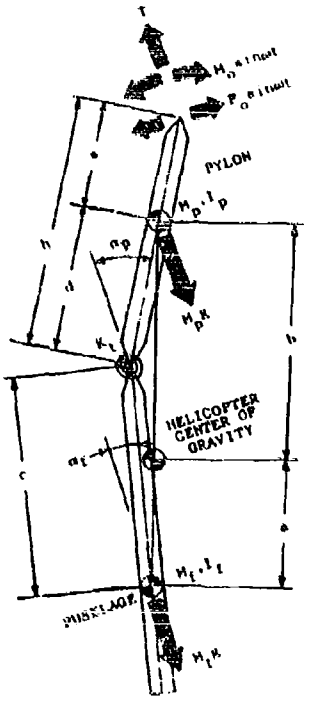

Fig. A-1. Analytical model

The equations for minimum fuselage response ($\alpha_{fs} = 0$), minimum pylon response ($\alpha_{ps} = 0$), and natural frequencies, that is, the maximum response, are, respectively

$$A_{11}E_2 - A_{21}E_1 = 0 . \qquad \text{(A-2)}$$

$$-A_{12}E_2 + A_{22}E_1 = 0 . \qquad \text{(A-3)}$$

and

$$+A_{11}A_{22} - A_{12}A_{21} = 0 \qquad \text{(A-4)}$$

Expanding these equations and making the substitutions

$$d = a + b - c ,$$

$$h = a + b + s - c$$

and observing that equivalent values for ξ and λ may be written

$$\xi = \frac{b}{a + b} ,$$

$$\lambda = \frac{a}{a + b} ,$$

the resulting equations are of the following form:

$$Q_2 c^2 + Q_1 c^1 + Q_0 K_t c^0 = 0 . \qquad \text{(A-5)}$$

This is the equation for a K_t parabola. The coefficients Q_2, Q_1, and Q_0 are quadratics in ω^2, that is,

$$Q_n = Q_{n4}\omega^4 + Q_{n2}\omega^2 + Q_{n0}\omega^0 . \qquad \text{(A-6)}$$

The resulting equations for shear excitation ($M_0 = 0$) follow.

Minimum Fuselage Response

The equation for minimum fuselage response is

$$B_2 c^2 + B_1 c^1 + B_0 K_t c^0 = 0 , \qquad \text{(A-7)}$$

where

$$B_{24} = B_{14} = B_{04} = 0 ,$$

$$B_{22} = -s\beta ,$$

$$B_{20} = (g - M_f)\beta ,$$

$$B_{12} = \beta s(a + b) - I_p\beta ,$$

$$B_{10} = M_f g(a + b + s) - g\beta(a + b) ,$$

$$B_{02} = 0 ,$$

and

$$B_{00} = b + s .$$

Minimum Pylon Response

The equation for minimum pylon response is

$$C_2 c^2 + C_1 c^1 + C_0 K_t c^0 = 0 . \qquad \text{(A-8)}$$

where

$$C_{24} = C_{14} = C_{04} = 0 ,$$

$$C_{22} = (a + b)(\xi - \lambda)\beta - (a + b + s)\beta ,$$

$$C_{20} = -M_f g + g\beta ,$$

$$C_{12} = I_f(1 + \delta) ,$$

$$C_{10} = M_f g c(a + b + s) - g\beta(a + b) ,$$

$$C_{11} = -I_f(a + b + s) - \delta(a + b) ,$$

and

$$C_{00} = (a + b + s) - \delta(a + b)$$

Maximum Pylon and Fuselage Response

The equation for maximum response is

$$D_2 c^2 + D_1 c^1 + D_0 K_t c^0 = 0 . \qquad \text{(A-9)}$$

where

$$D_{24} = (I_p - I_f)\beta ,$$

$$D_{22} = M_f\beta g(a + b) - \beta g s(M_f + M_p) ,$$

$$D_{20} = -(M_f g)^2 ,$$

$$D_{14} = -2\beta I_f(a + b) ,$$

$$D_{12} = M_f g(I_f - I_p) - \beta g(a + b)^2 ,$$

$$D_{10} = M_f^2 g^2 (a + b + s) - M_f M_p g^2 s ,$$

$$D_{04} = I_p I_f - I_f(a + b)$$

$$D_{02} = -K_t(I_p - I_f) - \beta g(a + b)^2$$

$$- M_f g(a + b + s) - I_f M_p g s ,$$

and

$$D_{00} = M_f g(a + b + s) + M_p g s$$

* * *

A TOOL FOR PARAMETRIC ANALYSIS OF COMPLEX ISOLATION SYSTEMS

Paul J. Jones and Frank A. Smith
Martin Marietta Corporation
Denver Division
Denver, Colorado

This paper presents the general methodology and a unique computer program for analysis of complex equipment suspension systems subjected to sinusoidal or random excitation. As an example, the analytical results of an isolated gyro system are presented showing the utility of the Fortran IV computer program. The method defines as variables the following parameters: (a) suspension system spring rates, (b) suspension system damping values, (c) center-of-gravity location, (d) isolated mass inertial properties, and (e) electromechanical transfer functions, for example, gyro voltage response characteristics.

The responses of the isolated unit are plotted as a part of the computer program. These graphs show the gyro response in voltage spectral densities as well as response acceleration spectral densities.

The matrix equations of motion for the system are written with the capability of excitation through any combination of up to 10 support points.

The final equations for the system transfer functions are developed in discrete coordinates with the free stiffness and damping matrices providing the exciting force. A discussion of the extension of this analysis to complex structures (that is, equipment trusses and payload trusses) excited by random vibration is included.

INTRODUCTION

The design of a complex vibration isolation system requires the evaluation of many dynamic parameters to insure compatibility between the evolved design and its intended application. Considerations must include the isolators design tolerances of stiffness and damping properties as well as tolerances on mass properties and center-of-gravity location. Many of these complex applications relate to guidance systems where it is necessary to evaluate both translational and rotational responses to estimate vibration-induced guidance errors. The evaluation of the response parameters can be a very time consuming task, especially for these complex systems with many isolators. Usually, tradeoff studies are performed to determine allowable tolerances for various segments of the isolator system. Because of the number of computations required to determine the response characteristics, many complex isolation system response parameters are "approximated"; the design is built and tested to evaluate its acceptability. In most cases, cost penalties are paid on these complex designs as a result of limitations placed on manufacturing tolerances or very selective matching of isolators. This cost penalty might have been averted with a parametric analysis, had an analytical tool been available. This paper presents an analytical design tool in the form of a computer program which permits the analyst to readily evaluate complex isolation systems. As an example, a rate gyro system is hypothesized and analyzed using the computer program to illustrate its utility.

TECHNICAL DISCUSSION

The vibration isolation program (VIP) was written in standard Fortran IV language for the purpose of analyzing complex systems employing up to 10 isolators. This program is presently adapted for the CDC 6400 computer. The isolated unit is considered rigid in the frequency range of isolator resonance. The geometry and

center of gravity of the rigid unit are completely general and can be specified as desired. The utility of the computer program can best be indicated by listing some of its features:

1. Up to 10 individual isolators may be used. For each isolator up to 3 translational degrees of freedom can be defined, that is, the user may use 0, 1, 2, or 3 different spring rates for the 3 orthogonal axes.

2. The isolator stiffness and damping values may be uniquely defined. No two isolators need have the same spring rates or damping values.

3. The stiffness matrix is computed and unstable systems can immediately be eliminated. The stability of the proposed configuration is readily determined by evaluation of the inverted stiffness matrix.

4. Product of inertia terms may be included in the mass matrix.

5. The forced phase relation between any degrees of freedom at isolator bases can be either in phase or out of phase. Also, any isolator base degree of freedom can be stationary, that is, no forcing function need be applied.

6. Rigid body mode shapes and associated undamped frequencies are determined for 6 rigid body degrees of freedom. The modes are described for the center of gravity of the rigid body.

7. The transfer functions for the rigid body center of gravity for up to 6 degrees of freedom are presented graphically. These plots provide visual information on damped translation frequencies, damped angular frequencies, amplification factors, and degree of coupled modal response. The transfer functions are continuous over the designated frequency interval.

8. The applied forcing function may be either sinusoidal or random. A limitation exists that all applied forces must be equal at the designated points of application. In the case of random excitation the spectral density need not be constant but must be a combination of straight lines when plotted on log-log paper.

9. The dynamic response may be either sinusoidal or random, commensurate with the prescribed forcing function. In the case of random excitation, response spectral densities in terms of displacement, velocity, and acceleration are plotted (if all are desired). Additionally, a transfer function describing the response characteristics for any electromechanical device relating to linear or angular acceleration can be supplied, and its response will be determined and plotted. An example of this application could be a rate gyro and the vibration-induced noise could be computed in terms of voltage spectral density.

10. The response calculations can start at any frequency, stop at any frequency, and perform the calculations at any delta frequency desired up to a total of 1000 delta frequency intervals.

11. The root-mean-square of all computed random responses is tabulated and printed by the computer.

12. The relative root-mean-square displacement across the isolator for each degree of freedom is determined and printed by the computer for random forcing functions. This information permits the evaluation of isolator compatibility under the prescribed dynamic loading.

13. Up to 6 degrees-of-freedom responses can be determined for up to 11 locations, one of the 11 being the center of gravity response. For example, if six isolators were used, the responses at four additional positions plus the center of gravity could be determined.

The methodology used in establishing the VIP analytical tool is discussed in the following section.

ANALYTICAL METHODOLOGY

To illustrate the methodology for determining the response of an isolation system to a vibrational input, consider the general system shown in Fig. 1.

The free stiffness matrix for the system may be obtained from the potential energy expression

$$2PE = \begin{Bmatrix} \vdots \\ X_i - X_{i_b} \\ Y_i - Y_{i_b} \\ Z_i - Z_{i_b} \\ \vdots \end{Bmatrix}' \begin{bmatrix} \begin{bmatrix} k_x & & \\ & k_y & \\ & & k_z \end{bmatrix}_i \end{bmatrix} \begin{Bmatrix} \vdots \\ X_i - X_{i_b} \\ Y_i - Y_{i_b} \\ Z_i - Z_{i_b} \\ \vdots \end{Bmatrix}$$

or simply

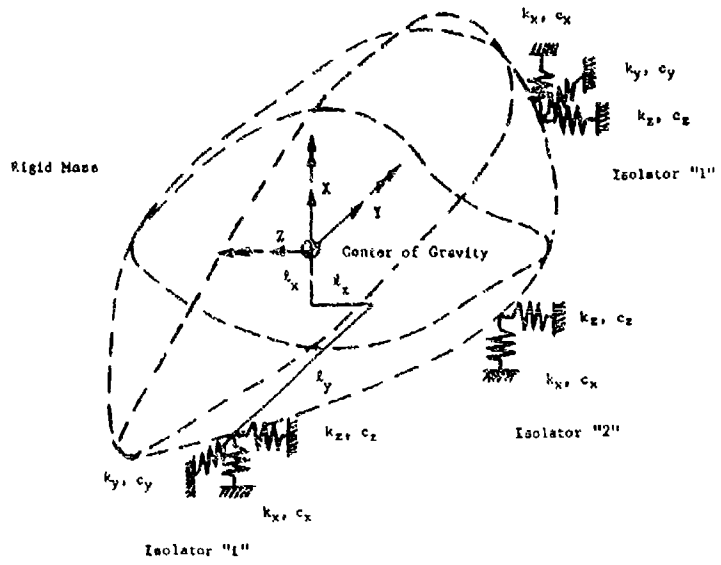

Fig. 1. General isolation system for any number (n) of isolators; number of isolators: n; center of gravity motion: X_{cg}, Y_{cg}, Z_{cg}, θ_x, θ_y, θ_z; motion of isolator "i" on isolated mass: X_i, Y_i, Z_i; motion of isolator "i" base: X_{ib}, Y_{ib}, Z_{ib}

$$2PE = \{\delta_R\}'[k]\{\delta_R\} \qquad (1)$$

where $\{\delta_R\}$ represents the relative motion across the isolators and $[k]$ is the uncoupled (diagonal) stiffness matrix for the isolators.

A transformation may be formed that relates the isolator attach-point motion to center-of-gravity motion. For the relative motion used in the potential energy expression, this transformation is

$$\begin{Bmatrix} \vdots \\ X_i - X_{i_b} \\ Y_i - Y_{i_b} \\ Z_i - Z_{i_b} \\ \vdots \end{Bmatrix} = \begin{bmatrix} 1 & & & -\ell_z & \ell_y & & -1 & & \\ & 1 & \ell_z & & -\ell_x & \cdots & & -1 & \cdots \\ & & 1 & -\ell_y & \ell_x & & & & -1 \\ & & & & & i & & & \end{bmatrix} \begin{Bmatrix} X_{cg} \\ Y_{cg} \\ Z_{cg} \\ x \\ y \\ z \\ \vdots \\ X_{i_b} \\ Y_{i_b} \\ Z_{i_b} \\ \vdots \end{Bmatrix}$$

or

$$\{\delta_R\} = [T]\{\delta\} \qquad (2)$$

where $[T]$ is the transformation matrix, and $\{\delta\}$ is the motion of the center of gravity and the isolator bases. The size of the transformation matrix is $3n \times 3n + 6$ with 3 degrees of freedom (DOF) for each isolator and 6 degrees of freedom for the center of gravity.

Substitution of the transformation matrix into the potential energy expression yields the free coupled stiffness matrix $[K]$ as follows:

$$2PE = \{\delta\}'[T]'[k][T]\{\delta\}$$

or

$$2PE = \{\delta\}'[K]\{\delta\}. \qquad (3)$$

The damping matrix $[C]$ can be formed in a similar manner by considering energy dissipation. The same transformation can again be used and the resulting matrix is similar to the coupled stiffness matrix with damping coefficients c replacing isolator spring constants k. The restrained matrices are $[\bar{K}]$ and $[\bar{C}]$.

The forced equations of motion are determined by manipulations of the coupled stiffness

and damping matrices. The degrees of freedom associated with the matrices, as explained previously, are displacement and rotation of the center of gravity (6 DOF) and displacement of the isolator bases (3n DOF). The isolator base(s) degree(s) of freedom are either restrained or forced in the restrained system. Consider the forced equations of motion:

$$[M]\{\ddot{\delta}_{cg}\} + [\bar{C}]\{\dot{\delta}_{cg}\} + [\bar{K}]\{\delta_{cg}\} = \{F\} \qquad (4)$$

where $[M]$ is the center-of-gravity mass matrix containing, on the diagonal, system mass and inertia (products of inertia, if applicable, are off-diagonal terms). The matrix $\{\delta_{cg}\}$ is a 6×1 representing the cg motion only. The forcing matrix $\{F\}$ is formed by the columns of the free damping and stiffness matrices corresponding to forced isolator DOF's times the known isolator base motion δ_o:

$$\overset{(6\times 1)}{\begin{Bmatrix} \vdots \\ F_j \\ \vdots \end{Bmatrix}} = \begin{Bmatrix} \vdots \\ -\sum_{i=1}^{m} K_{ji}\delta_o - \sum_{i=1}^{m} C_{ji}\dot{\delta}_o \\ \vdots \end{Bmatrix} \qquad (5)$$

where m is the total number of forced isolator base DOF's with a maximum value of $3n$.

If the base motion is sinusoidal the following substitutions can be made:

$$\delta_o = \bar{\delta}_o e^{i\omega t} \qquad (6)$$

and

$$\dot{\delta}_o = i\omega\bar{\delta}_o e^{i\omega t} \qquad (7)$$

where ω is the forcing frequency.

The resulting force matrix becomes

$$\begin{Bmatrix} \vdots \\ F_j \\ \vdots \end{Bmatrix} = \begin{Bmatrix} \vdots \\ -\sum_{i=1}^{m} K_{ji}\bar{\delta}_o e^{i\omega t} - \sum_{i=1}^{m} iC_{ji}\omega\bar{\delta}_o e^{i\omega t} \\ \vdots \end{Bmatrix} \qquad (8)$$

or factoring the $\bar{\delta}_o$ terms yields

$$\{F\} = \{F'\}\,\bar{\delta}_o e^{i\omega t}. \qquad (9)$$

The equations of motion can now be written as follows:

$$[M]\{\ddot{\delta}_{cg}\} + [\bar{C}]\{\dot{\delta}_{cg}\} + [\bar{K}]\{\delta_{cg}\} = \{F'\}\,\bar{\delta}_o e^{i\omega t}. \qquad (10)$$

If the steady state response is desired the following equations are available:

$$\{\delta_{cg}\} = \{\bar{\delta}\}\,e^{i\omega t} \qquad (11)$$

and

$$\{\dot{\delta}_{cg}\} = i\omega\{\bar{\delta}\}\,e^{i\omega t} \qquad (12)$$

and

$$\{\ddot{\delta}_{cg}\} = -\omega^2\{\bar{\delta}\}\,e^{i\omega t}. \qquad (13)$$

Substitution into the equations of motion yields

$$-\omega^2[M]\{\bar{\delta}\}e^{i\omega t} + [\bar{C}]\{\bar{\delta}\}e^{i\omega t} + [\bar{K}]\{\bar{\delta}\}e^{i\omega t} = \{F'\}\delta_o e^{i\omega t}. \qquad (14)$$

Solving for the center-of-gravity motion results in

$$\{\delta_{cg}\} = \left[-\omega^2[M] + i\omega[\bar{C}] + [\bar{K}]\right]^{-1}\{F'\}\,\delta_o. \qquad (15)$$

The ratio of output motion to input motion is

$$\frac{\{\delta_{cg}\}}{\delta_o} = \left[-\omega^2[M] + i\omega[\bar{C}] + [\bar{K}]\right]^{-1}\{F'\}. \qquad (16)$$

The system transfer function can be obtained by taking the absolute value of the above equation

$$\{|H(\omega)|\} = \left|\left[-\omega^2[M] + i\omega[\bar{C}] + [\bar{K}]\right]^{-1}\{F'\}\right|. \qquad (17)$$

If the input is known in the form of a power spectral density, the response spectral densities of the center of gravity may be obtained:

$$S_j(\omega) = |H(\omega)|_j^2\, S_{input(\omega)} \qquad (18)$$

where $S_{input(\omega)}$ represents the input spectral density at frequency ω and $S_j(\omega)$ represents the output spectral density at degree-of-freedom j.

This development is representative of the methodology for determining the response of an isolation system to a random excitation. The methodology can be used for any number of isolators, any location of equipment center of gravity, and excitation through any combination of isolators. For any system the amount of computations involved necessitates the use of a digital computer. A listing of the Fortran IV computer program based on the previously developed methodology is presented in Appendix A. To verify the program and the methodology, a check case was taken from pp. 3 through 29 of Ref. [1]. This provided a check on the computation of the stiffness and damping matrices, of modal properties, and of the transfer functions.

The results of the check case are presented in Appendix B. The computed values agreed exactly with the check case values from the reference. The verification of the program allowed its use in a parametric analysis of a gyro system.

EXAMPLE OF HYPOTHESIZED GYRO SYSTEM

Consider an isolation system as shown in Fig. 1 for a three-axis rate sensor employing rotational rate integrating gyros. It is desired to isolate the rate gyro package from a random vibration environment by four resilient mounts. Unless this system is a true center-of-gravity mount, the isolated package motion will be a combination of translation and rotation when subjected to a single-axis random input. This coupled motion, particularly rotational, experienced by the gyros has a deleterious effect on the guidance system accuracy by increasing the total integrated rate errors. As stated previously, to eliminate the coupled motion would require a true center-of-gravity isolation system which, owing to inherent manufacturing tolerances, is never achieved. In addition, it is desirable to specify the maximum permissible manufacturing tolerances to maintain minimum cost and schedule impacts. An analysis for this system was conducted to determine the coupled response and the vibration-induced noise response from the gyros. The gyro noise response was computed in terms of voltage spectral density.

Consider the location system depicted in Fig. 2 forced at the base in one axis by broadband random acceleration as defined by Fig. 3. The elastic centers of the four isolators are assumed to lie within a common plane. The gyro response function relating gyro voltage response to angular acceleration is shown in Fig. 4.

The parameters affecting the rotational response of this isolation system excited by random excitation in a single axis are:

1. Mismatch of suspension system spring rates.

2. Mismatch of suspension system damping values.

3. Center-of-gravity location.

4. Inertial properties of isolated unit.

Assume the following tolerances for the system of Fig. 2:

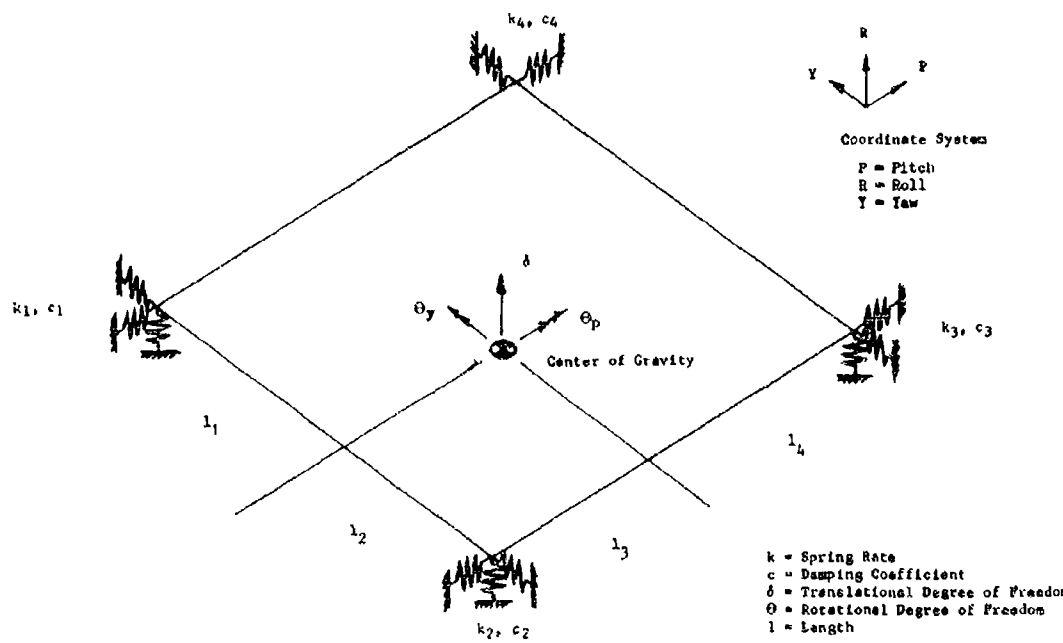

Fig. 2. Typical isolation system

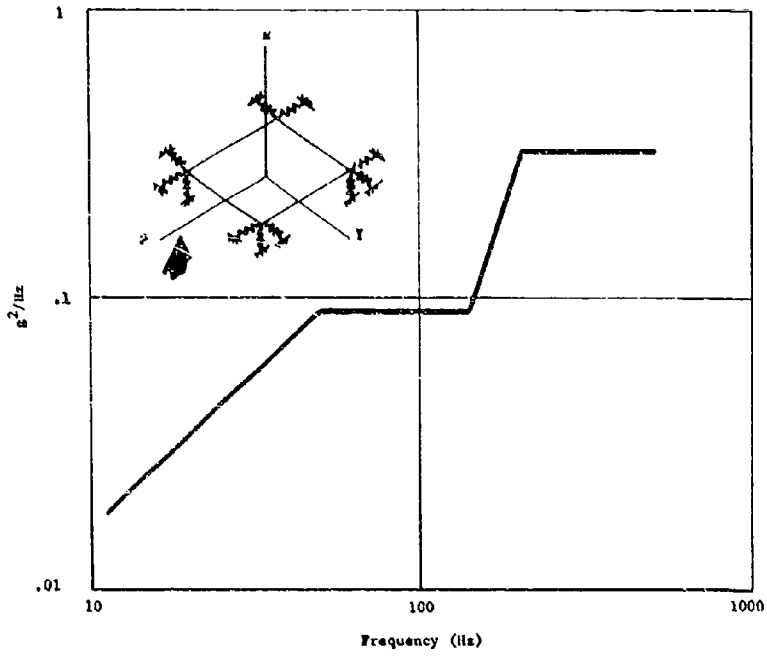

Fig. 3. Input acceleration spectral density

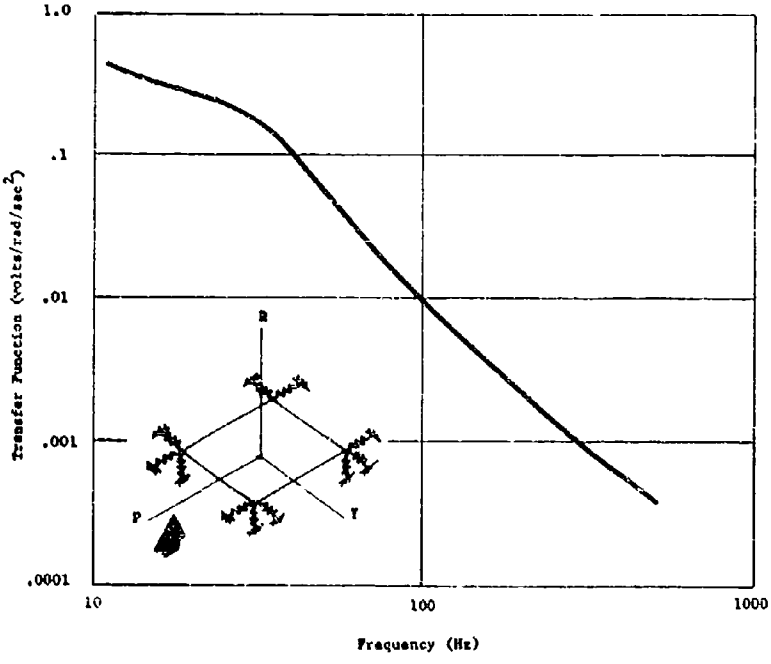

Fig. 4. Electromechanical transfer function

1. Individual isolator natural frequency of 80 Hz ± 10 Hz when loaded.

2. Maximum individual frequency difference in a set of four matched isolators of 5 Hz. The frequency of an individual isolator of a matched set could be between 70 and 90 Hz, but the frequencies of all isolators of a set must be within 5 Hz of each other.

3. Maximum individual isolator transmissibility (Q) of 3.7 at resonance.

4. Maximum individual isolator transmissibility difference for a set of four matched isolators of 0.5. The transmissibility of an individual isolator must not be greater than 3.7, but the transmissibilities of all isolators of a set must be within 0.5 of each other.

5. The center of gravity must be within a circle having a radius of 0.17 in. and lying in the plane of the isolators' elastic centers.

Based on these design tolerances, input acceleration values, and gyro response characteristics, a parametric analysis was performed to determine the gyro rotational response. The numerous cases analyzed are presented in Table 1.

For this gyro configuration, the total computer running time for each case was 100 sec. Consequently, a sufficient quantity of runs to determine the effects of each parameter was made at very little cost. Further, all data were plotted by the computer permitting rapid evaluation of each case analyzed.

The resulting root-mean-square (rms) values for the various cases are presented in Table 2. An example of the computer plotted translational transfer function for case 01 of Table 1 is shown in Fig. 5. The rotational transfer function is shown in Fig. 6. The gyro voltage response spectral densities for the two axes of rotation are shown in Figs. 7 and 8.

CONCLUSIONS

1. An analytical tool has been developed to rapidly determine the response characteristics of complex isolation systems subjected to sinusoidal or random excitation. A listing of the computer program (VIP) is included in Appendix A for ready use.

2. The computer program (VIP) is written in standard Fortran IV language and readily adaptable for most any computer. The program

TABLE 1
Gyro System Parametric Study[a]

Case No.[b]	Isolator Spring Rates (lb/in.)				Isolator Transmissibility (in./in.)				Center-of-Gravity Location			
	k_1	k_2	k_3	k_4	Q_1	Q_2	Q_3	Q_4	ℓ_1	ℓ_2	ℓ_3	ℓ_4
01	1905	1620	1905	1620	3.2	3.7	3.2	3.7	3.475	3.225	3.225	3.275
02	1905	1620	1905	1620	3.7	3.2	3.7	3.2	3.475	3.225	3.225	3.475
03	1397	1154	1397	1154	3.2	3.7	3.2	3.7	3.475	3.225	3.225	3.475
04	1397	1154	1397	1154	3.7	3.2	3.7	3.2	3.475	3.225	3.225	3.475
05	1154	1154	1397	1397	3.2	3.2	3.7	3.7	3.35	3.35	3.18	3.52
06	1154	1154	1397	1397	3.2	3.2	3.7	3.7	3.35	3.35	3.52	3.18
07	1154	1154	1397	1397	3.7	3.7	3.2	3.2	3.35	3.35	3.18	3.52
08	1620	1620	1905	1905	3.2	3.2	3.7	3.7	3.35	3.35	3.18	3.52
09	1154	1154	1154	1620	3.2	3.2	3.2	3.7	3.475	3.225	3.225	3.475
10	1397	1154	1154	1397	3.7	3.2	3.2	3.7	3.52	3.18	3.35	3.35
11	1397	1154	1154	1397	3.7	3.2	3.2	3.7	3.52	3.18	3.35	3.35

[a]See Fig. 2.
[b]Case 01 through 10 were analyzed with random excitation at all four isolators, simultaneously, representing a shake table input. Case 11 was run with excitation at isolators 1 and 2 only.

TABLE 2
RMS Values of Rate Gyro Response Spectral Densities

Case No.	Center-of-Gravity Acceleration	Rotational Rate (Pitch)	Rotational Rate (Yaw)	Output Voltage (Pitch)	Output Voltage (Yaw)
	GRMS	RMS Rad/Sec	RMS Rad/Sec	RMS Volts	RMS Volts
01	6.507	0.098	0.090	0.688	0.643
02	6.518	0.094	0.086	0.676	0.631
03	5.934	0.107	0.098	1.018	0.945
04	5.952	0.102	0.093	0.998	0.924
05	5.809	0	0.307	0	3.058
06	5.936	0	0.112	0	1.037
07	5.911	0	0.334	0	3.260
08	6.393	0	0.261	0	1.933
09	5.677	0.269	0.242	2.602	2.391
10	5.787	0.333	0	3.299	0
11	2.893	0.166	0.749	1.650	16.549

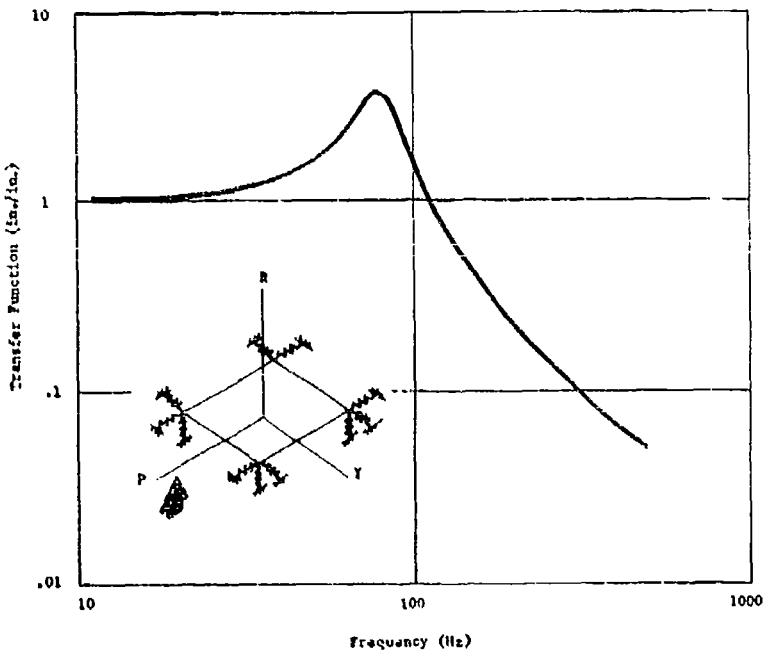

Fig. 5. Translational transfer function

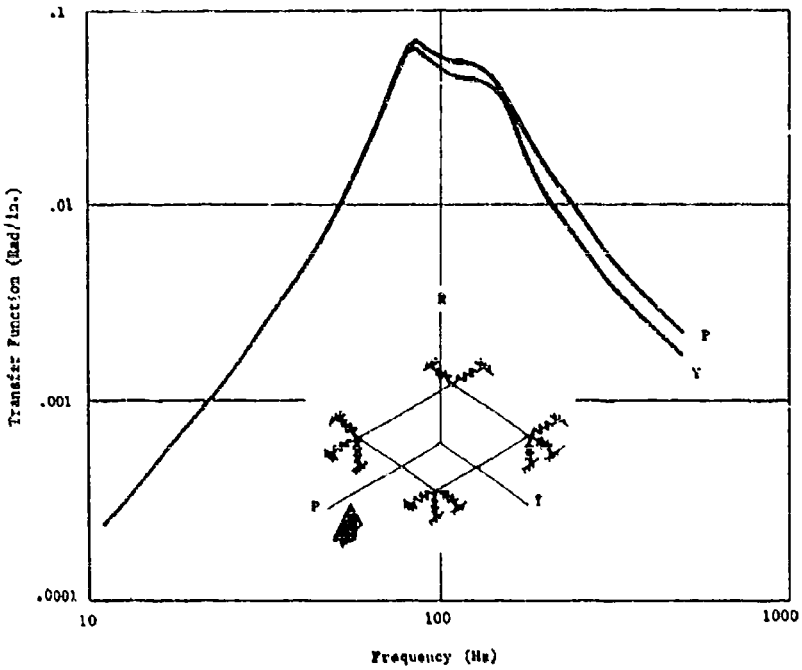

Fig. 6. Rotational transfer function

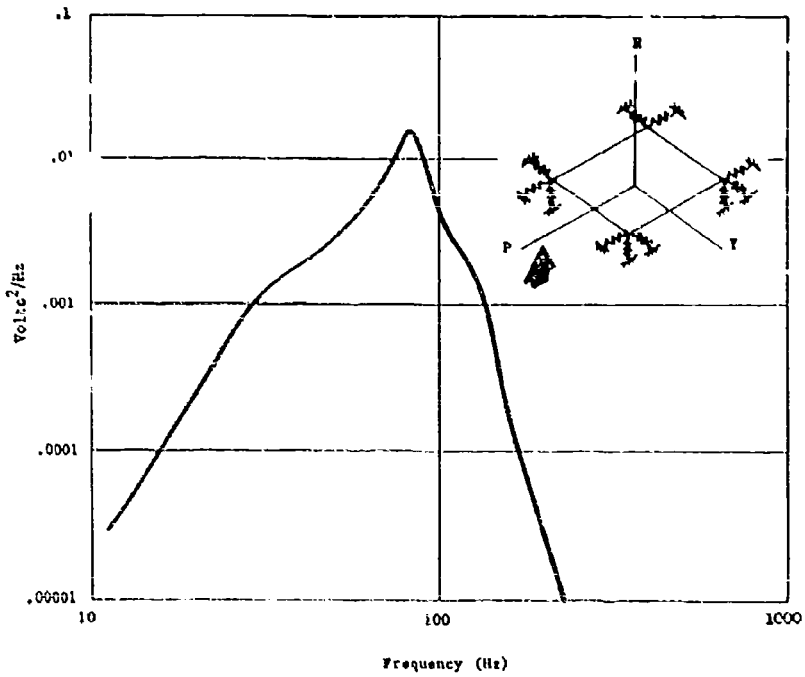

Fig. 7. Rate gyro-voltage spectral density (pitch axis)

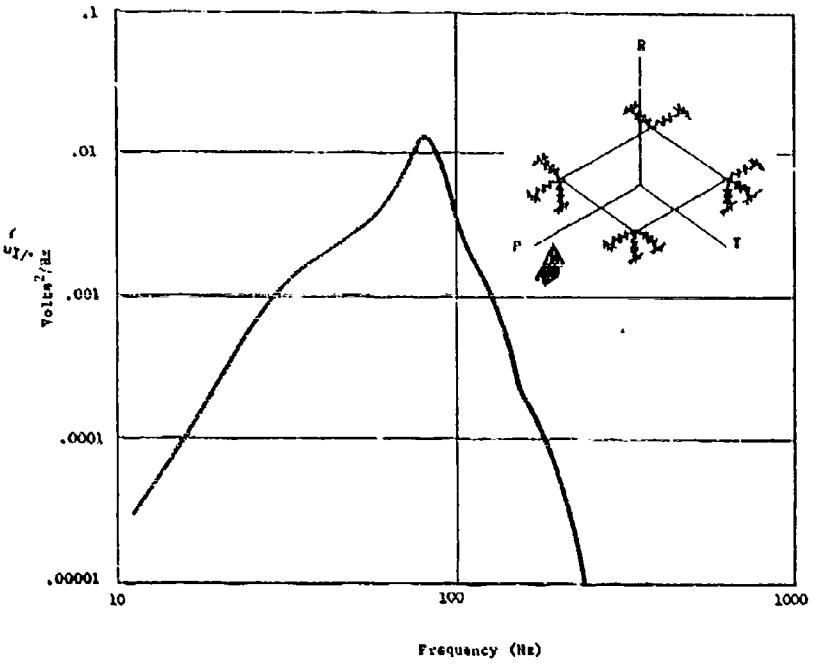

Fig. 8. Rate gyro-voltage spectral density (yaw axis)

as listed in the Appendix is currently being used on the CDC 6400 computer.

3. For any single computer run, the isolation system response at 11 discrete positions may be determined for up to 6 degrees of freedom at any location.

4. The system transfer functions, eigenvalue and eigenvector solutions and responses are tabulated and plotted automatically. No subsequent hand plotting is required.

5. All significant response characteristics are presented in a visual manner to permit rapid data evaluation. This assumes the computer facility has plotting capability.

RECOMMENDATIONS

The present method of analysis requires a rigid representation of the isolated unit. For most systems, this representation is valid in the frequency range desired for isolator resonance. However, for response calculations in the higher frequency range, the flexibility of the isolated unit may be important. The methodology used in the analysis is general and can be applied to flexible systems mounted on resilient isolators. For example, if the flexible system's mass matrix and free stiffness matrix can be determined, the equations of motion as developed previously can be modified to include the flexible system. However, a problem exists in the formation of a discrete damping matrix for the flexible system. There are various methods of forming damping matrices in discrete coordinates, but none that are straightforward and without problems. One possible way of circumventing this problem is the use of modal coordinates. With modal coordinates, modal damping can be used and also the inversion of the complex matrix is simplified because of the diagonal matrices resulting from modal coordinates. However, a technique must be developed for forming the discrete forcing function. It may be possible to form the forcing function by using a combination of modal and discrete coordinates, that is, modal damping for the flexible system and discrete damping for the isolators. In any event, additional work needs to be performed to incorporate the flexibility of the isolated unit in the computer program. With the inclusion of the flexible parameters, the methodology would then be applicable to any complex system and not limited to isolator applications. Possible applications would be

response analyses of complex equipment trusses installed in structural shells or any complex subsystem. The inclusion of flexible characteristics would further enhance the usefulness of the computer tool.

REFERENCE

1. C. M. Harris and C. E. Crede, Shock and Vibration Handbook (McGraw-Hill, New York), 1961, pp. 3-19–3-33

Appendix A

COMPUTER PROGRAM

A listing of the response computer program for the CDC 6400 computer and the DD 280 plotter is provided on the following pages. Comment cards are provided throughout the program for clarity.

The program uses the following matrix manipulation subroutines which are not provided in the listing but are generally available at companies with computer facilities: BTABA – B matrix transposed times A matrix times B matrix, result stored in A; INTAPE, LTAPE, PAGEHD, READ, RTAPE, START, WRITE, WTAPE – subroutines associated with tape operations, writing, and reading matrices; INV1, INVJ – matrix inversion; JACOBI, MODE 1 – subroutines for determining modal properties; MULTA – A matrix times B matrix, result stored in A; MULTB – A matrix times B matrix, result stored in B; and PLOT2, PLOT3 plotting subroutines.

The input and input formats for the program are provided in Table A-1. For further definition of the input and examples, refer to the program listing.

TABLE A-1
Program Input

Item	Format
Run No.	A6
Title 1 (title card)	12A6
Title 2 (title card)	12A6
Mass matrix (6 × 6) including products of inertia, if applicable (units: mass (lb-sec^2/in.), inertia (in.-lb-sec^2)).	*
Center-of-gravity location X, Y, Z from some 0, 0, 0, origin in a right-hand coordinate system (inches).	10X, 3E17.8
Total number of isolators including dummy points where output transfer functions are desired – maximum of 10 isolators.	I5
Isolator parameters	
Attach point location (elastic center of isolator) in right-hand coordinate system (inches). Principal axes of isolator are parallel to coordinate axes.	10X, 3E17.8

TABLE A-1 (Cont'd.)

Item	Format
Isolator parameters (Cont'd.)	
Spring rates (X, Y, Z) (lb/in.).	10X, 3E17.8
Damping coefficients (C) (lb-sec/in.).	10X, 3E17.8
Forced isolator code (X, Y, Z) for all isolators: 1 = forced, 0 = not forced. Output transfer function for isolator (or dummy point) relative if forced and absolute if not forced.	3I5
Input power spectral density frequencies and corresponding PSD valves (linear interpolation on log-log plots used between points supplied) (g^2/Hz).	*
Code for additional system transfer functions (X, Y, Z, theta X, theta Y, theta Z): 1 = transfer function supplied, 0 = transfer function not supplied. Transfer function supplied must relate to acceleration of system's center of gravity.	I6
Systems transfer functions if above code(s) = 1; (see explanation of input PSD) (example of units: volts/g or volts/rad/sec^2).	*
Title for plot of spectral density of systems response.	4A10
Name for Y-axis of plot.	A6
Starting frequency, delta frequency, end frequency for all computations.	10X, 3E17.8
Output code for displacement spectral densities, velocity spectral densities, acceleration spectral densities: 1 = computed, 0 = not computed.	3I5
Stop card (or next run number if applicable).	A6
*Matrix supplied as follows:	
Matrix name, number of rows, number of columns.	A6, I4, I5
Data Cards: row/column location of first element, elements.	2I5, 4E17.8
Zero card: 10 zeros.	

```
      PROGRAM VIP (INPUT,OUTPUT,TAPE5=INPUT,TAPE6=OUTPUT,FILMPL,
     *        TAPE1,TAPE2,TAPE3,TAPE4)
C
C ISOLATION SYSTEM RESPONSE TO RANDOM EXCITATION
C
C CODED BY PAUL JONES  MAY  1967
C
C VARIABLE PARAMETERS
C     SPRING RATES OF ISOLATORS
C     DAMPING OF ISOLATORS
C     EQUIPMENT INERTIAL PROPERTIES AND CG LOCATION-ISOLATED MASS RIGID
C     INPUT POWER SPECTRAL DENSITY
C     NUMBER OF ISOLATOR EXCITED
C     PLANE OF EXCITATION
C
C PROGRAM OUTPUT
C     TRANSFER FUNCTIONS FOR DISPLACEMENT AND ROTATION
C     RESPONSE POWER SPECTRAL DENSITIES
C     SYSTEM MODAL PROPERTIES-FREQUENCIES AND MODE SHAPES
C     RMS DISPLACEMENT ACROSS ISOLATORS
C     PLOTS OF TRANSFER FUNCTIONS AND OUTPUT PSDS
C
C DIMENSION SIZES
      DIMENSION EMASS(6,6),SX(10),SY(10),SZ(10),CX(10),CY(10),CZ(10),
     *          X(10),Y(10),Z(10),PSD(10,2),JX(10),JY(10),JZ(10),
     *          CMATP(36,36),SMATP(36,36),SMAT(3,3),CMAT(3,3),
     *          TRAN(3,36),W(6),SMATR(6,6),EMATR(6,6),W2(6),
     *          FREQ(6),DBP(10),ALP(10),DBPAL(10),SM(6),CM(6),
     *          ZR(6,6),WK1(6,6),Z1(6,6),WK2(6,6),TR(1000,6),
     *          PSDO(1000,6),FN(1000),SFN(1000),TRANP(3,6),
     *          DTITL1(4),VTITL1(4),ATITL1(4),TTITL1(4),
     *          STITLE(4),CR2(1000),PTITLE(4,10),TRFN(50,2,6),
     *          NR1(6),NC1(6),SLOPE(50),RNAME(6),IFTR(6),RTITLE(4,6),
     *          DTITL2(4),VTITL2(4),ATITL2(4),TTITL2(4),ON(1000),RMS(6)
C
C
C*********************************************************************
C************************  FORMAT STATEMENTS  ************************
C*********************************************************************
C
C
 9999 CALL START
C
C FORMAT STATEMENTS
 1001 FORMAT (10X,4E17.8)
 1002 FORMAT (6I5)
 1003 FORMAT (4A10)
 1004 FORMAT (A6)
C
 2001 FORMAT (///,5X,29HRMS X DISPLACEMENT AT CG (IN),5X,1F15.8)
 2002 FORMAT (///,5X,29HRMS Y DISPLACEMENT AT CG (IN),5X,1F15.8)
 2003 FORMAT (///,5X,29HRMS Z DISPLACEMENT AT CG (IN),5X,1F15.8)
 2004 FORMAT (///,5X,36HRMS THETA X DISPLACEMENT AT CG (RAD),5X,1F15.8)
 2005 FORMAT (///,5X,36HRMS THETA Y DISPLACEMENT AT CG (RAD),5X,1F15.8)
 2006 FORMAT (///,5X,36HRMS THETA Z DISPLACEMENT AT CG (RAD),5X,1F15.8)
C
 3001 FORMAT (///,5X,29HRMS X VELOCITY AT CG (IN/SEC),5X,1F15.8)
```

```
3002 FORMAT (///,5X,29HRMS Y VELOCITY AT CG (IN/SEC),5X,1F15.8)
3003 FORMAT (///,5X,29HRMS Z VELOCITY AT CG (IN/SEC),5X,1F15.8)
3004 FORMAT (///,5X,52HRMS ROTATIONAL VELOCITY AT CG ABOUT X AXIS (RAD/
    *SEC),5X,1F15.8)
3005 FORMAT (///,5X,52HRMS ROTATIONAL VELOCITY AT CG ABOUT Y AXIS (RAD/
    *SEC),5X,1F15.8)
3006 FORMAT (///,5X,52HRMS ROTATIONAL VELOCITY AT CG ABOUT Z AXIS (RAD/
    *SEC),5X,1F15.8)
C
4001 FORMAT (///,5X,22HGRMS X DIRECTION AT CG,5X,1F15.8)
4002 FORMAT (///,5X,22HGRMS Y DIRECTION AT CG,5X,1F15.8)
4003 FORMAT (///,5X,22HGRMS Z DIRECTION AT CG,5X,1F15.8)
4004 FORMAT (///,5X,59HRMS ROTATIONAL ACCELERATION AT CG ABOUT X AXIS (
    *RAD/SEC**2),5X,1F15.8)
4005 FORMAT (///,5X,59HRMS ROTATIONAL ACCELERATION AT CG ABOUT Y AXIS (
    *RAD/SEC**2),5X,1F15.8)
4006 FORMAT (///,5X,59HRMS ROTATIONAL ACCELERATION AT CG ABOUT Z AXIS (
    *RAD/SEC**2),5X,1F15.8)
C
5001 FORMAT (///,5X,27HRMS X DISPLACEMENT,ISOLATOR,2X,I2,2X,1F15.8)
5002 FORMAT (///,5X,27HRMS Y DISPLACEMENT,ISOLATOR,2X,I2,2X,1F15.8)
5003 FORMAT (///,5X,27HRMS Z DISPLACEMENT,ISOLATOR,2X,I2,2X,1F15.8)
C
      XNAME=6HFN(HZ)
      DNAME=5HD2/HZ
      VNAME=5HV2/HZ
      ANAME=5HA2/HZ
      TNAME=4HTRFC
      SNAME=5HG2/HZ
C
      DATA DTITL1/10HLINEAR DIS,10HPLACEMENT ,10HSPECTRAL D,
     *            10HENSITY CG /
      DATA DTITL2/10HROTARY DIS,10HPLACEMENT ,10HSPECTRAL D,
     *            10HENSITY CG /
      DATA VTITL1/10HLINEAR VEL,10HOCITY SPEC,10HTRAL DENSI,
     *            10HTY CG     /
      DATA VTITL2/10HROTARY VEL,10HOCITY SPEC,10HTRAL DENSI,
     *            10HTY CG     /
      DATA ATITL1/10HLINEAR ACC,10HELERATION ,10HSPECTRAL D,
     *            10HENSITY CG /
      DATA ATITL2/10HROTARY ACC,10HELERATION ,10HSPECTRAL D,
     *            10HENSITY CG /
      DATA TTITL1/10HDISPLACEME,10HNT TRANSFE,10HR FUNCTION,
     *            10H CG  IN/IN/
      DATA TTITL2/10HROTATIONAL,10H TRANSFER ,10HFUNCTION C,
     *            10HG  RAD/IN /
      DATA STITLE/10HINPUT POWE,10HR SPECTRAL,10H DENSITY (,
     *            10HCOMPUTED) /
      DATA PTITLE/10HTRANSFER F,10HUNCTION FO,10HR ISOLATOR,
     *            10H 1  X,Y,Z ,
     *            10HTRANSFER F,10HUNCTION FO,10HR ISOLATOR,
     *            10H 2  X,Y,Z ,
     *            10HTRANSFER F,10HUNCTION FO,10HR ISOLATOR,
     *            10H 3  X,Y,Z ,
     *            10HTRANSFER F,10HUNCTION FO,10HR ISOLATOR,
     *            10H 4  X,Y,Z ,
     *            10HTRANSFER F,10HUNCTION FO,10HR ISOLATOR,
     *            10H 5  X,Y,Z ,
     *            10HTRANSFER F,10HUNCTION FO,10HR ISOLATOR,
     *            10H 6  X,Y,Z ,
```

```
     *            10HTRANSFER F,10HUNCTION FO,10HR ISOLATOR,
     *            10H 7  X,Y,Z ,
     *            10HTRANSFER F,10HUNCTION FO,10HR ISOLATOR,
     *            10H 8  X,Y,Z ,
     *            10HTRANSFER F,10HUNCTION FO,10HR ISOLATOR,
     *            10H 9  X,Y,Z ,
     *            10HTRANSFER F,10HUNCTION FO,10HR ISOLATOR,
     *            10H 10  X,Y,Z/
C
      KA=16
      KB=2
      KC=6
      KD=56
      KE=3
      KF=1000
      NRK=3
      KG=50
C
      CALL IN(1,80
C
C DISC UNITS
      NWT=2
      MWT=3
      LWT=4
C
      REWIND NWT
      REWIND MWT
      REWIND LWT
C
C*****************************************************************
C*************************  INPUT DATA  ****************************
C*****************************************************************
C
C     SYSTEM MASS MATRIX 6X6  X,Y,Z,THETA X,THETA Y,THETA Z
      CALL REAL (EMASS,NRM,NCM,KC,KC)
C
C     CENTER OF GRAVITY LOCATION
      READ (5,1001) XCG,YCG,ZCG
C
C     NUMBER OF ISOLATORS
      READ (5,1002) NISOL
C
C     ISOLATOR PROPERTIES  LOCATION,SPRING RATES,AND DAMPING
C     0 VALUES OF SX,SY,SZ AND CX,CY,CZ PERMISSIBLE
C     FORCING POINTS CORRESPONDING TO INPUT FOR SPRING RATES
C     1=FORCING FUNCTION APPLIED,0=FORCING FUNCTION NOT APPLIED
C     -1=FORCING FUNCTION APPLIED IN NEGATIVE DIRECTION
C     ALL POINTS WITH FORCING FUNCTION ASSUMED TO BE CORRELATED
      DO 10 I=1,NISOL
      READ (5,1001) X(I),Y(I),Z(I)
      READ (5,1001) SX(I),SY(I),SZ(I)
      READ (5,1001) CX(I),CY(I),CZ(I)
      READ (5,1002) JX(I),JY(I),JZ(I)
   10 CONTINUE
C
C
C     INPUT POWER SPECTRAL DENSITY  FREQUENCY AND G**2/CPS VALUES
C     LINEAR INTERPOLATION ON LOG-LOG PLOTS USED BETWEEN SUPPLIED
C     VALUES
      CALL REAL (PSD,NRP,NCP,KA,KB)
```

```
C
C     CODE FOR INPUT OF ADDITIONAL TRANSFER FUNCTIONS RELATING
C     SYSTEM RESPONSE TO CG ACCELERATION   GS FOR DISPLACEMENT
C     AND RAD/SEC**2 FOR ROTATION  TRANSFER FUNCTIONS
C     0 TRANSFER FUNCTION NOT SUPPLIED
C     1 TRANSFER FUNCTION SUPPLIED
      READ (5,1002) IFTR(1),IFTR(2),IFTR(3),IFTR(4),IFTR(5),IFTR(6)
C     CORRESPONDING TO CG DOF  X,Y,Z,THETAX,THETAY,THETAZ
C
C
C     READ TRANSFER FUNCTIONS  FREQUENCY AND CORRESPONDING TRANSFER
C     FUNCTION VALUE 50 POINTS MAXIMUM  LINEAR ITERPOLATION USED
C     BETWEEN POINTS  VALUES MUST ENCOMPASS START FREQUENCY AND
C     END FREQUENCY
C     READ PLOT TITLE FOR OUTPUT PSD PLOT
C     READ NAME FOR Y AXIS OF PLOT
C
      DO 15 I=1,6
      IF (IFTR(I).EQ.0) GO TO 15
      CALL READ (TREN(1,1,I),NRT(I),NCT(I),KG,KB)
      READ (5,1005) (RTITLE(N,I),N=1,4)
      READ (5,1004) RNAME(I)
   15 CONTINUE
C
C     STARTING FREQUENCY,END FREQUENCY,DELTA FREQUENCY
C     FREQUENCY RANGE MUST BE COVERED BY INPUT PSD
C     START FREQUENCY MUST BE WITHIN FIRST PSD INTERVAL
      READ (5,1001) FSTA,DELT,FEND
C
C
C
C     CODE FOR OUTPUT PLOTS AND RMS VALUES CALCULATED (CG MOTION)
C     0=NOT CALCULATED 1=CALCULATED
      READ (5,1002) IDISP,IVEL,IACC
C
C
C
C
C*****************************************************************
C***************  COUPLED STIFFNESS AND DAMPING MATRICES  ************
C*****************************************************************
C
C
C FORM UNCOUPLED STIFFNESS AND DAMPING MATRICES,TRANSFORMATION
C MATRICES RELATING ISOLATOR ATTACH POINT MOTION TO CG MOTION,
C FORM COUPLED STIFFNESS AND DAMPING MATRICES.
C
      NDOF=6+3*NISOL
      KDOF=6
C     NUMBER OF DEGREES OF FREEDOM
C     CG KDOF + 6,3 KDOF FOR EACH ISOLATOR
C
C
      DO 40 I=1,NDOF
      DO 40 J=1,NDOF
      CMATP(I,J)=0.0
   40 SMATP(I,J)=0.0
C     SMATP FREE STIFFNESS MATRIX
C     CMATP FREE DAMPING MATRIX
C
```

```
C
      DO 50 KK=1,NISOL
C
      DO 55 I=1,3
      DO 55 J=1,3
      SMAT(I,J)=0.0
   55 CMAT(I,J)=0.0
C     SMAT 3X3 STIFFNESS MATRIX FOR ONE ISOLATOR (DIAGONAL)
C     CMAT 3X3 DAMPING MATRIX FOR ONE ISOLATOR (DIAGONAL)
C
      SMAT(1,1)=SX(KK)
      SMAT(2,2)=SY(KK)
      SMAT(3,3)=SZ(KK)
C
      CMAT(1,1)=CX(KK)
      CMAT(2,2)=CY(KK)
      CMAT(3,3)=CZ(KK)
C
      DO 70 I=1,3
      DO 70 J=1,NDOF
   70 TRAN(I,J)=0.0
C     TRAN TRANSFORMATION RELATING ISOLATOR ATTACH
C     POINT MOTION TO CG MOTION
C
      XL=XCG-X(KK)
      YL=YCG-Y(KK)
      ZL=ZCG-Z(KK)
C     XL,YL,ZL DISTANCE FROM CG TO ATTACH POINT OF ISOLATOR
C
      TRAN(1,1)=1.0
      TRAN(2,2)=1.0
      TRAN(3,3)=1.0
      TRAN(1,5)=-ZL
      TRAN(1,6)=YL
      TRAN(2,4)=ZL
      TRAN(2,6)=-XL
      TRAN(3,4)=-YL
      TRAN(3,5)=XL
      DO 75 I=1,3
      KDOF=KDOF+1
   75 TRAN(I,KDOF)=-1.0
      CALL WRITE (TRAN,NRK,NDOF,4HTRAN,KE)
C
C     WRITE DISC UNIT (MWT)
      WRITE (MWT) TRAN
C
C
      DO 90 J=1,NDOF
      DO 80 I=1,3
      W(I)=0.0
      DO 80 K=1,3
   80 W(I)=W(I)+SMAT(I,K)*TRAN(K,J)
      DO 90 L=1,NDOF
      DO 90 M=1,3
   90 SMATP(L,J)=SMATP(L,J)+TRAN(M,L)*W(M)
      CALL WRITE (SMATP,NDOF,NDOF,5HSMATP,KE)
C
      DO 120 J=1,NDOF
      DO 110 I=1,3
      W(I)=0.0
```

```
      DO 110 K=1,6
  110 W(I)=W(I)+CMAT(I,K)*TRAN(K,J)
      DO 120 L=1,NDOF
      DO 120 M=1,6
  120 CMATP(L,J)=CMATP(L,J)+TRAN(M,L)*W(M)
      CALL WRITE (CMATP,NDOF,NDOF,5HCMATP,KC)
   50 CONTINUE
C
C
C
C*****************************************************************
C*******************  MODAL PROPERTIES  ***************************
C*****************************************************************
C
C DETERMINE MODAL PROPERTIES  MODE SHAPES AND FREQUENCIES FOR
C ISOLATED SYSTEM USING 6X6 MASS MATRIX AND 6X6 RESTRAINED
C STIFFNESS MATRIX
C
      DO 130 I=1,6
      DO 130 J=1,6
  130 SMATR(I,J)=SMATP(I,J)
C
C     INVERT STIFFNESS MATRIX  POOR INVERSION CHECK INDICATES AN
C     UNSTABLE SYSTEM
      CALL INV1 (SMATR,EMATR,NRM,KC)
      CALL WRITE (EMATR,NRM,NRM,5HEMATR,KC)
C
      WRITE (NWT) EMASS
      CALL MODE1 (EMASS,SMATR,W2,W,FREQ,NRM,1.E-15,1.E-15,KC,1)
      CALL WRITE (FREQ,NRM,1,4HFREQ,KC)
      CALL WRITE (EMASS,NRM,NRM,5HMODES,KC)
      REWIND NWT
      READ (NWT) EMASS
C
C
C*****************************************************************
C*******************  INPUT PSD SLOPES  ***************************
C*****************************************************************
C
C DETERMINE SLOPES OF PSD CURVES FOR INTERPOLATION
C
      NN=NRF-1
      DO 140 I=1,NN
      DBP(I)=10.*ALOG(PSD(I+1,2)/PSD(I,2))
      ALP(I)=ALOG(PSD(I+1,1)/PSD(I,1))/.301
  140 DOPAL(I)=DBP(I)/ALP(I)
C
C
C
C*****************************************************************
C*******************  DISCRETE FORCING FUNCTION  ******************
C*****************************************************************
C
C FORM DISCRETE FORCING FUNCTION
C
      DO 165 J=1,NRM
      SM(J)=0.0
      CM(J)=0.0
      L=6
      DO 165 I=1,NISCL
```

```
      L=L+1
      IF (GX(I)) 141,155,156
  141 SM(J)=SM(J)+SMATP(J,L)
      CM(J)=CM(J)+CMATP(J,L)
      GO TO 155
  156 SM(J)=SM(J)-SMATP(J,L)
      CM(J)=CM(J)-CMATP(J,L)
  155 L=L+1
      IF (GY(I)) 142,160,161
  142 SM(J)=SM(J)+SMATP(J,L)
      CM(J)=CM(J)+CMATP(J,L)
      GO TO 160
  161 SM(J)=SM(J)-SMATP(J,L)
      CM(J)=CM(J)-CMATP(J,L)
  160 L=L+1
      IF (GZ(I)) 143,165,166
  143 SM(J)=SM(J)+SMATP(J,L)
      CM(J)=CM(J)+CMATP(J,L)
      GO TO 165
  166 SM(J)=SM(J)-SMATP(J,L)
      CM(J)=CM(J)-CMATP(J,L)
  165 CONTINUE
      CALL WRITE (SM,NRM,1,2HSM,KC)
      CALL WRITE (CM,NRM,1,2HCM,KC)
C
C
C*********************************************************************
C*********************  TRANSFER FUNCTION  ***************************
C*********************************************************************
C
C FORMATION OF TRANSFER FUNCTION
C
      NTIME=(FEND-FSTA)/DELT
      K=1
      REWIND NWT
      FRB=FSTA-DELT/2.
C
C
      DO 200 II=1,NTIME
C
      FRB=FRB+DELT
      OMB=6.2831853072*FRB
      OMB2=OMB*OMB
      ON(II)=OMB
      ON2(II)=OMB2
      FN(II)=FRB
C
      DO 171 I=1,NRM
      DO 171 J=1,NRM
      ZR(I,J)=SMATP(I,J)-OMB2*EMASS(I,J)
  171 ZI(I,J)=OMB*CMATP(I,J)
C
C     INVERT COMPLEX MATRIX BY PARTS ZR REAL ZI IMAGINARY
      CALL INVJ(ZR,WK1,NRM,KC)
      CALL MULTB(ZI,WK1,NRM,NRM,NRM,KC,KC)
      CALL MULTA(WK1,ZI,NRM,NRM,NRM,KC,KC)
      DO 172 I=1,NRM
      DO 172 J=1,NRM
  172 WK1(I,J)=ZR(I,J)+WK1(I,J)
      CALL INVJ (WK1,WK2,NRM,KC)
```

```
C     WK2 IS NOW REAL PORTION OF INVERSION
C
C
C     WRITE DISC UNIT (LWT)
      WRITE (LWT) WK2
      CALL INVC (ZI,WK1,NRM,KC)
C
      CALL MULTC (ZR,WK1,NRM,NRM,NRM,KC,KC)
      CALL MULTA (WK1,ZR,NRM,NRM,NRM,KC,KC)
      DO 173 I=1,NRM
      DO 173 J=1,NRM
  173 WK1(I,J)=-ZI(I,J)-WK1(I,J)
      CALL INVC (WK1,ZI,NRM,KC)
C ZI IS NOW THE IMAGINARY PORTION OF THE INVERSION
C
C
C     WRITE DISC UNIT (LWT)
      WRITE (LWT) ZI
C
      DO 180 I=1,NRM
      ZR1=0.0
      ZR2=0.0
      ZI1=0.0
      ZI2=0.0
      DO 185 J=1,NRM
      ZR1=ZR1+WK2(I,J)*SM(J)
      ZI1=ZI1-ZI(I,J)*OMB*CM(J)
      ZR2=ZR2+ZI(I,J)*SM(J)
  185 ZI2=ZI2+WK2(I,J)*OMB*CM(J)
  180 TR(II,I)=((ABS(ZR1+ZI1))**2.+(ABS(ZR2+ZI2))**2.)**.5
C TR IS NOW THE TRANSFER FUNCTION AT CG
C
C CALCULATION OF INPUT PSD VALUES AT FREQUENCIES
C
      ALPHA=(ALOG(FRB/PSD(K,1)))/.301
      DB=.4343*ALPHA*DBPAL(K)
      SF=PSD(K,2)*(10.**(DB/10.))
      SFN(II)=SF
C
      IF (FRB-PSD(K+1,1)+DELT/2.) 200,210,210
  210 K=K+1
  200 CONTINUE
      CALL WRITE (TR,NTIME,NRM,2HTR,KF)
      CALL WRITE (SFN,NTIME,1,3HSFN,KF)
      CALL WRITE (FN,NTIME,1,2HFN,KF)
C     WRITE DISC UNIT (LWT)
      WRITE (LWT) TR
      CALL PLOT3 (FN,TR,NTIME,NRK,XNAME,TNAME,TTITL1,3,KF,4)
      CALL PLOT3 (FN,TR(1,4),NTIME,NRK,XNAME,TNAME,TTITL2,3,KF,4)
      REWIND LWT
      READ (LWT) TR
      CALL PLOT2 (FN,SFN,NTIME,1,XNAME,SNAME,STITLE,3,KF)
C
C
      DO 201 J=1,NTIME
      DO 201 I=1,NRM
  201 TR(J,I)=TR(J,I)**2
C TR IS TRANSFER FUNCTION SQUARED
C
```

```
C*****************************************************************
C***************  RESPONSE PSD CENTER OF GRAVITY  ******************
C*****************************************************************
C
      IF(IDISP) 191,193,191
  191 DO 202 I=1,NRM
  202 RMS(I)=0.0
C
      DO 192 I=1,NRM
      DO 192 J=1,NTIME
      PSDO(J,I)=(1./ON2(J)**2)*TR(J,I)*SFN(J)*148996.
  192 RMS(I)=RMS(I)+PSDO(J,I)*DELT
C
      DO 203 I=1,NRM
  203 RMS(I)=RMS(I)**.5
C
      CALL WRITE (PSDO,NTIME,NRM,6HPSDDIS,KF)
      CALL PLOT3 (FN,PSDO,NTIME,NRK,XNAME,DNAME,DTITL1,3,KF,4)
      CALL PLOT3 (FN,PSDO(1,4),NTIME,NRK,XNAME,DNAME,DTITL2,3,KF,4)
C
      WRITE (6,2001) RMS(1)
      WRITE (6,2002) RMS(2)
      WRITE (6,2003) RMS(3)
      WRITE (6,2004) RMS(4)
      WRITE (6,2005) RMS(5)
      WRITE (6,2006) RMS(6)
C
C
  193 IF (IVEL) 194,196,194
  194 DO 204 I=1,NRM
  204 RMS(I)=0.0
C
      DO 195 I=1,NRM
      DO 195 J=1,NTIME
      PSDO(J,I)=(1./ON2(J))*TR(J,I)*SFN(J)*148996.
  195 RMS(I)=RMS(I)+PSDO(J,I)*DELT
C
      DO 206 I=1,NRM
  206 RMS(I)=RMS(I)**.5
C
      CALL WRITE (PSDO,NTIME,NRM,6HPSDVEL,KF)
      CALL PLOT3 (FN,PSDO,NTIME,NRK,XNAME,VNAME,VTITL1,3,KF,4)
      CALL PLOT3 (FN,PSDO(1,4),NTIME,NRK,XNAME,VNAME,VTITL2,3,KF,4)
C
      WRITE (6,3001) RMS(1)
      WRITE (6,3002) RMS(2)
      WRITE (6,3003) RMS(3)
      WRITE (6,3004) RMS(4)
      WRITE (6,3005) RMS(5)
      WRITE (6,3006) RMS(6)
C
  196 IF (IACC) 197,199,197
  197 DO 207 I=1,NRM
  207 RMS(I)=0.0
C
      DO 198 I=1,NRK
      L=I+3
      DO 198 J=1,NTIME
      PSDO(J,I)=TR(J,I)*SFN(J)
      PSDO(J,L)=TR(J,L)*SFN(J)*148996.
```

```
      RMS(I)=RMS(I)+PSDO(J,I)*DELT
  198 RMS(L)=RMS(L)+PSDO(J,L)*DELT
C
      DO 205 I=1,NRM
  205 RMS(I)=RMS(I)**.5
C
      CALL WRITE (PSDO,NTIME,NRM,OHPSDACC,KF)
C     WRITE DISC UNIT (LWT)
      REWIND LWT
      WRITE (LWT) PSDO
      CALL PLOT3 (FN,PSDO,NTIME,NRK,XNAME,ANAME,ATITL1,3,KF,4)
      CALL PLOT3 (FN,PSDO(1,4),NTIME,NRK,XNAME,ANAME,ATITL2,3,KF,4)
      REWIND LWT
      READ (LWT) PSDO
C
      WRITE (6,4001) RMS(1)
      WRITE (6,4002) RMS(2)
      WRITE (6,4003) RMS(3)
      WRITE (6,4004) RMS(4)
      WRITE (6,4005) RMS(5)
      WRITE (6,4006) RMS(6)
C
C
C*********************************************************************
C*************************  SYSTEM PSD  ******************************
C*********************************************************************
C
      DO 220 I=1,6
      IF (IFTR(I).EQ.0) GO TO 220
      K=1
      LENR(I)=1
      DO 221 J=1,L
  221 SLOPE(J)=(TRFN(J+1,2,I)-TRFN(J,2,I))/(TRFN(J+1,1,I)-TRFN(J,1,I))
      DO 224 M=1,NTIME
  223 IF (FN(M).GE.TRFN(K+1,1,I).AND.FN(M).LE.TRFN(K+1,1,I)) GO TO 222
      K=K+1
      GO TO 223
  222 TRF=SLOPE(K)*(FN(M)-TRFN(K,1,I))+TRFN(K,2,I)
  224 PSDO(M,I)=(TRF**2)*PSDO(M,I)
      CALL PLOT3 (FN,PSDO(1,I),NTIME,1,XNAME,RNAME(I),RTITLE(1,I),3,KF,
     *            4)
  220 CONTINUE
  199 CONTINUE
C
C*********************************************************************
C*******************  RMS ISOLATOR DISPLACEMENT  *********************
C*********************************************************************
C
C
      REWIND RWT
      DO 255 K=1,NISOL
      READ (RWT) TRAN
C
      DO 260 I=1,3
      DO 260 J=1,6
  260 TRANP(I,J)=TRAN(I,J)
      CALL WRITE (TRANP,NRK,6,5HTRANP,KE)
C
      REWIND RWT
      XDRMS=0.0
```

```
      YDRMS=0.0
      ZDRMS=0.0
C
      DO 250 II=1,NTIME
      READ (NRT) WK2
      READ (NRT) Z1
C
C
      CALL MULTB (1,WANP,WK2,NRK,NRM,NRM,KE,KC)
      CALL MULTB (1,WANP,Z1,NRK,NRM,NRM,KE,KC)
C
C
      DO 309 I=1,3
      ZR1=0.0
      ZR2=0.0
      ZI1=0.0
      ZI2=0.0
      DO 305 J=1,NRM
      ZR1=ZR1+WK2(I,J)*SN(J)
      ZI1=ZI1+Z1(I,J)*CN(J)
      ZR2=ZR2+Z1(I,J)*SN(J)
  305 ZI2=ZI2+WK2(I,J)*CN(J)
C
      IF (I.EQ.1.AND.DX(K).EQ.0) GO TO 308
      IF (I.EQ.2.AND.DY(K).EQ.0) GO TO 308
      IF (I.EQ.3.AND.DZ(K).EQ.0) GO TO 308
C
  307 TR(II,I)=((ABS(ZR1+ZI1-1.))**2.+(ABS(ZR2+ZI2))**2.)**.5
      GO TO 309
  308 TR(II,I)=((ABS(ZR1+ZI1))**2.+(ABS(ZR2+ZI2))**2.)**.5
  309 CONTINUE
C
      XDRMS=XDRMS+(1./GK2(II)**2)*(TR(II,1)**2)*SFN(II)*148996.
      YDRMS=YDRMS+(1./GK2(II)**2)*(TR(II,2)**2)*SFN(II)*148996.
  250 ZDRMS=ZDRMS+(1./GK2(II)**2)*(TR(II,3)**2)*SFN(II)*148996.
C
      XDRMS=XDRMS**.5
      YDRMS=YDRMS**.5
      ZDRMS=ZDRMS**.5
C
      CALL WRITE (IR,NTIME,NRK,3HTRI,KF)
      CALL PLOTJ (IR,TR,NTIME,NRK,XNAME,TNAME,PTITLE(1,K),3,KF,4)
C
      WRITE(6,5001) K,XDRMS
      WRITE(6,5002) K,YDRMS
  255 WRITE(6,5003) K,ZDRMS
C
      GO TO 9999
      END
$
DTABA
INTAPL
INVI
INVJ
JACOBI
LTAPE
MODEI
MULTA
MULTB
PAGEHD
```

```
PLOT2
PLOT3
READ
RTAPE
START
WRITE
WTAPE
R
CHECK
CHECK CASE
REF. SHOCK AND VIBR. HANDBOOK (PG 3-31)
EMASS     6     6
    1     1     .1166
    2     2     .1166
    3     3     .1166
    4     4    2.2570
    5     5    3.0322
    6     6    2.4668
0000000000
              5.25                  3.5              6.5
    7
              0.                    0.               0.
            525.                  525.            1050.
              0.3905                0.3905           0.5522
    1     0     0
              0.                    7.               0.
            525.                  525.            1050.
              0.3905                0.3905           0.5522
    1     0     0
              10.5                  7.               0.
            525.                  525.            1050.
              0.3905                0.3905           0.5522
    1     0     0
              10.5                  0.               0.
            525.                  525.            1050.
              0.3905                0.3905           0.5522
    1     0     0
              10.25              -0.90              12.00
               0.                0.               0.
               0.                0.               0.
    0     0     0
               2.25               5.80              10.50
               0.                0.               0.
               0.                0.               0.
    0     0     0
               0.75               5.00               4.00
               0.                0.               0.
               0.                0.               0.
    0     0     0
PSD       6     2
    1     1        1.                .016
    2     1       50.               .09
    3     1      140.               .09
    4     1      200.               .32
    5     1      700.               .32
    6     1     2000.               .015
0000000000
    0     0     0     0     0     0
              1.                    0.5             500.
    1     1     1
```

```
CASE01
RATE GYRO
RESPONSE TO RANDOM EXCITATION
EMASS     6     6
    1     1      .0275
    2     2      .0275
    3     3      .0275
    4     4      .05000
    5     5      .1080
    6     6      .0861
0000000000
                 0.0                 3.225                -3.475
    4
                0.0                 0.0                 0.0
                 1905.               0.0                0.0
                 1.05               0.0                 0.0
    1     0     0
                0.0                 0.0                -6.7
                1620.                0.0                1620.
                 .84                 0.0                 .84
    1     0     0
                0.0                 6.7                -6.7
                1905.               1905.                1905.
               1.05                 1.05                1.05
    1     0     0
               0.0                 6.7                  0.0
                1620.                1620.                0.0
                .84                 .84                 0.0
    1     0     0
PSD       6     2
    1     1       10.                 .016
    2     1       50.                .09
    3     1      140.                .09
    4     1      200.                .32
    5     1      700.                .32
    6     1     2000.                .015
0000000000
    0     0     0     0     1     1
VTSEC2   32     2
    1     1      11.                .197
    2     1      13.                .151
    3     1      15.                .122
    4     1      17.                .102
    5     1      19.                .0870
    6     1      21.                .0760
    7     1      23.                .0650
    8     1      25.                .0571
    9     1      27.                .0475
   10     1      29.                .0384
   11     1      31.                .0313
   12     1      33.                .0253
   13     1      35.                .0196
   14     1      37.                .0151
   15     1      39.                .0119
   16     1      41.                .0090
   17     1      43.                .0071
   18     1      45.                .0056
   19     1      47.                .0045
   20     1      49.                .0036
   21     1      51.                .0029
```

```
   22    1     54.          .0463
   23    1     60.          .0350
   24    1     65.          .0284
   25    1     70.          .0227
   26    1     75.          .0189
   27    1     80.          .0161
   28    1     85.          .0138
   29    1     90.          .0118
   30    1     99.          .0095
   31    1     150.         .0033
   32    1     200.         .0020
   33    1     250.         .0013
   34    1     300.         .00095
   35    1     350.         .00074
   36    1     400.         .00057
   37    1     450.         .00046
   38    1     500.         .00038
0000000000
VOLTS**2 PER HZ VS FREQ THETAY
VTSEC2
VTSEC2  38    2
    1    1     11.          .444
    2    1     13.          .389
    3    1     15.          .349
    4    1     17.          .319
    5    1     19.          .295
    6    1     21.          .275
    7    1     23.          .255
    8    1     25.          .239
    9    1     27.          .218
   10    1     29.          .196
   11    1     31.          .177
   12    1     33.          .159
   13    1     35.          .140
   14    1     37.          .123
   15    1     39.          .109
   16    1     41.          .0951
   17    1     43.          .0844
   18    1     45.          .0750
   19    1     47.          .0670
   20    1     49.          .0598
   21    1     51.          .0540
   22    1     54.          .0463
   23    1     60.          .0350
   24    1     65.          .0284
   25    1     70.          .0227
   26    1     75.          .0189
   27    1     80.          .0161
   28    1     85.          .0138
   29    1     90.          .0118
   30    1     99.          .0095
   31    1     150.         .0033
   32    1     200.         .0020
   33    1     250.         .0013
   34    1     300.         .00095
   35    1     350.         .00074
   36    1     400.         .00057
   37    1     450.         .00046
   38    1     500.         .00038
0000000000
VOLTS**2 PER HZ VS FREQ THETAZ
VTSEC2
                11.          0.5          500.
    1    1    1
STOP
>
```

Appendix B

CHECK CASE FOR COMPUTER PROGRAM

To verify the methodology and associated computer program, an isolation system check case was taken from Ref. [1]. This isolation system, shown in Fig. B-1, has a rigid body weight of 45 lb and is supported by four resilient supports with a stiffness k_z of 1050 lb/in. for each isolator. The stiffness ratios for the other directions are $k_x/k_z = k_y/k_z = 1/2$. The critical damping ratio (C/C_c) used in the check case was 0.05. The corresponding damping coefficients were calculated using critical damping coefficients of

$$C_{cx} = 2\sqrt{k_x M/4}\,, \qquad C_{cy} = 2\sqrt{k_y M/4}\,,$$

$$C_{cz} = 2\sqrt{k_z M/4}\,.$$

with the expressions for the critical damping coefficients being developed from single-degree-of-freedom considerations with $M/4$ representing one-fourth of the rigid mass. The base motion was sinusoidal in the X direction so that the modal frequencies of importance were associated with coupled X and θ_y motion (15.1 and 44.0 Hz).

For the above parameters the translational transfer function for the center of gravity is shown in Fig. B-2 and the rotational transfer function is shown in Fig. B-3. The transfer functions for points 1, 2, and 3 of Fig. B-1 are shown in Figs. B-4, B-5, and B-6, respectively. Figure B-7 shows the transfer function for one of the isolators. The modal frequencies and transfer functions for points 1, 2, and 3 are in agreement with Ref. [1]. It should be noted that all transfer functions shown are for absolute motion except the X transfer function for the isolator, which is for relative motion between isolator attach point and the forced base. To check the random excitation portion of the computer program, an input power spectral density was assumed as shown in Fig. B-8. The corresponding response spectral densities for the center of gravity are shown in Figs. B-9 and B-10. The root-mean-square response displacement values for the four isolators and for points 1, 2, and 3 are presented in Table B-1.

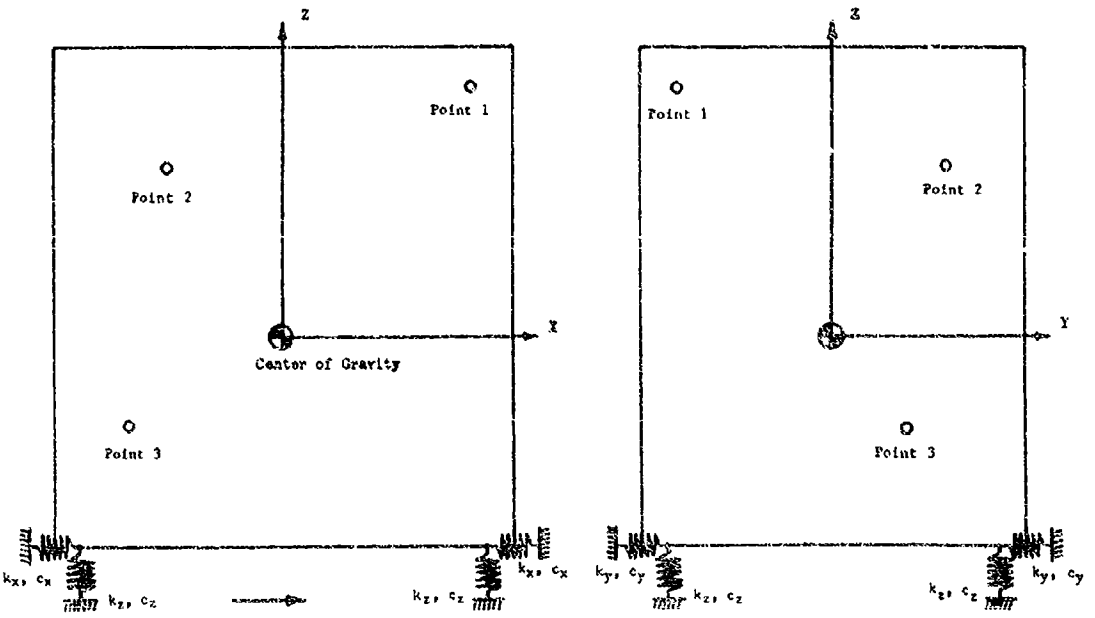

Fig. B-1. Four isolator check case (see Ref. [1])

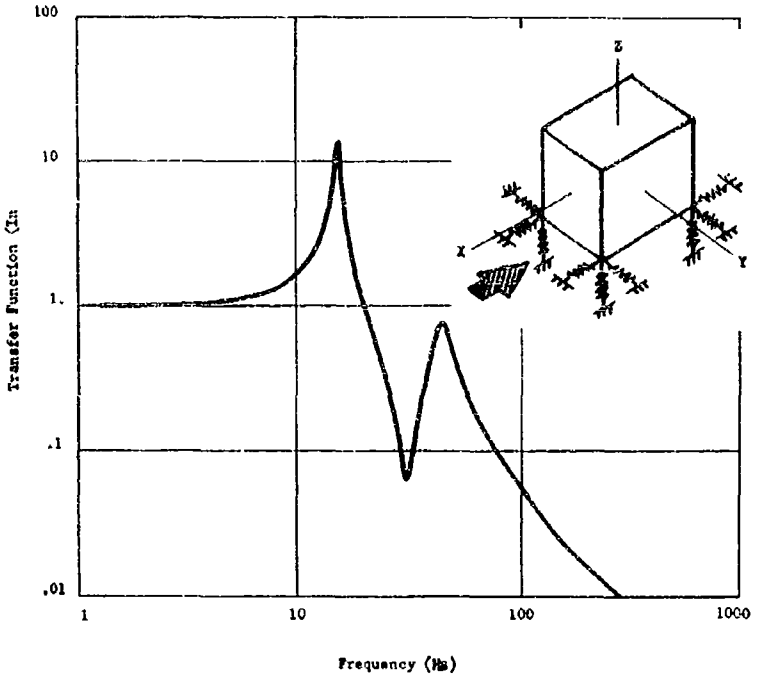

Fig. B-2. Translational transfer function (check case)

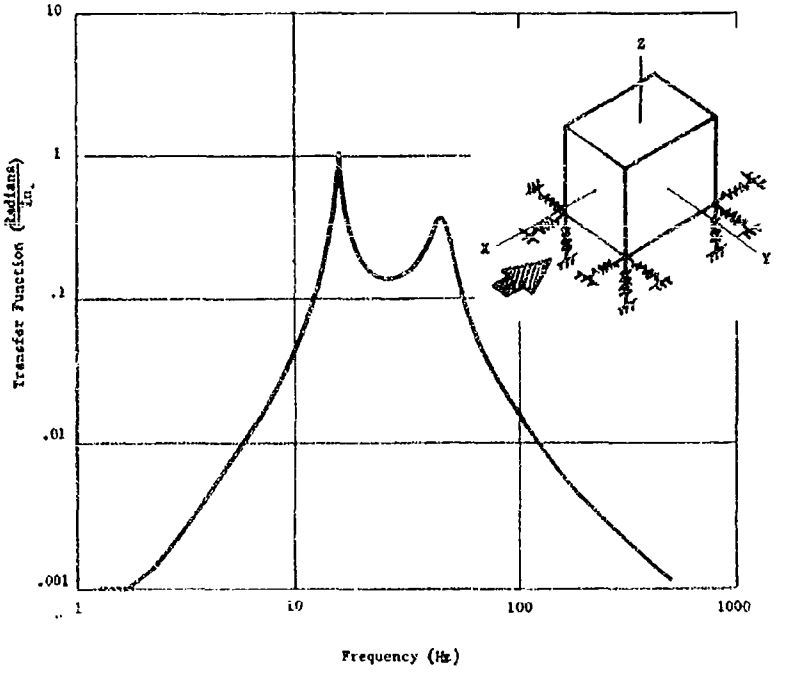

Fig. B-3. Rotational transfer function (check case)

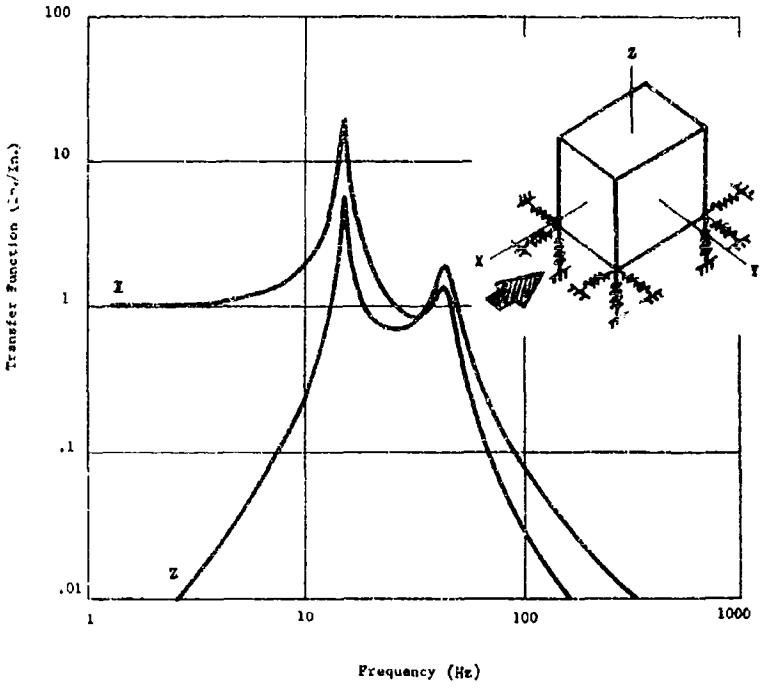

Fig. B-4. Transfer function for point 1 (check case) absolute motion

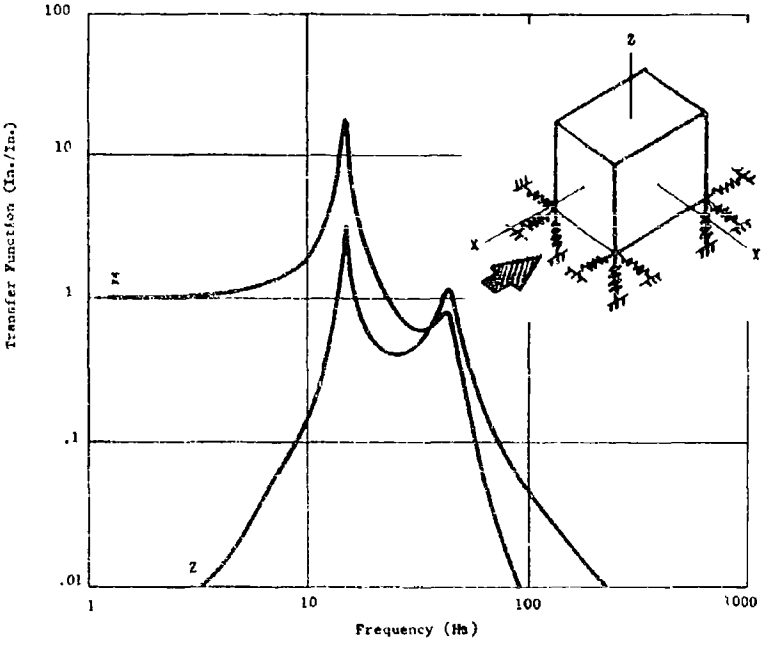

Fig. B-5. Transfer function for point 2 (check case) absolute motion

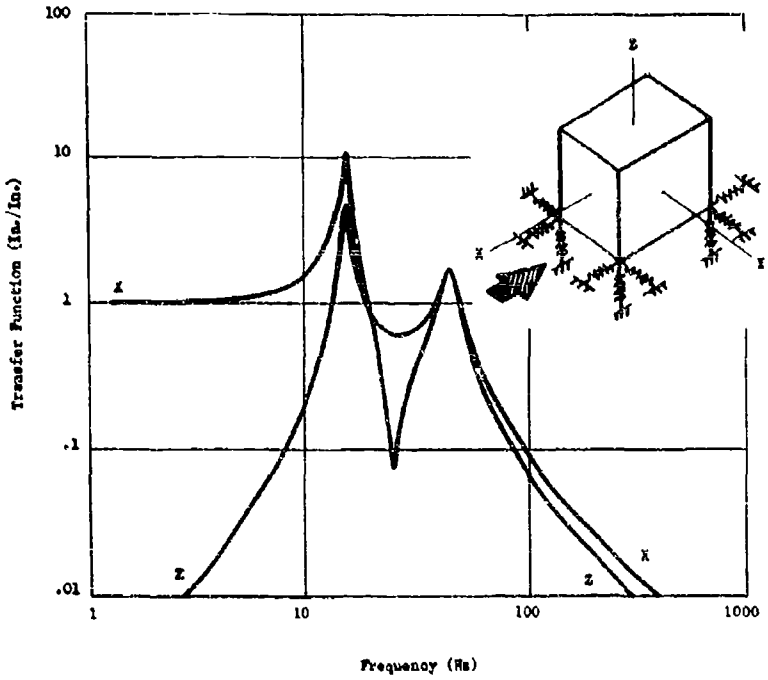

Fig. B-6. Transfer function for point 3 (check case) absolute motion

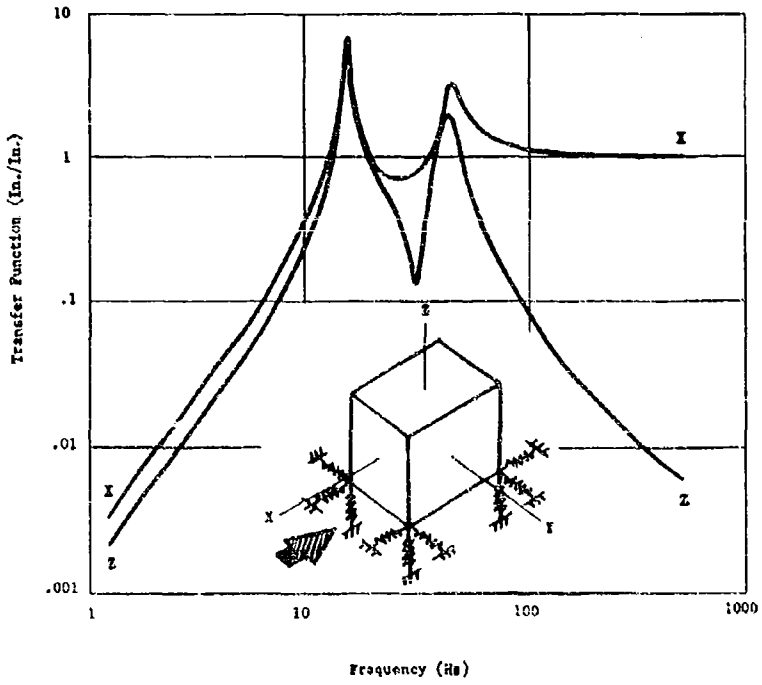

Fig. B-7. Transfer function for isolator (check case); X-axis, relative transfer function; Z-axis, absolute transfer function

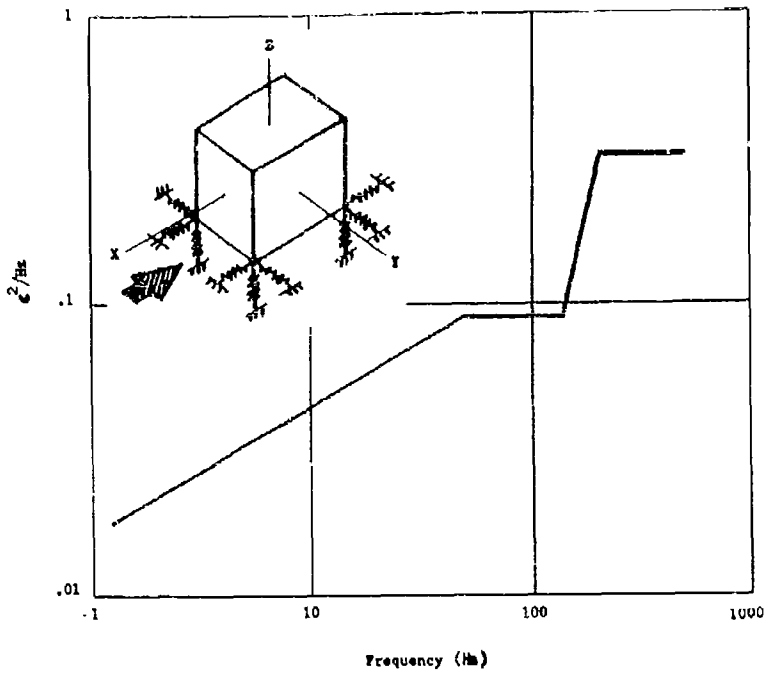

Fig. B-8. Input acceleration spectral density

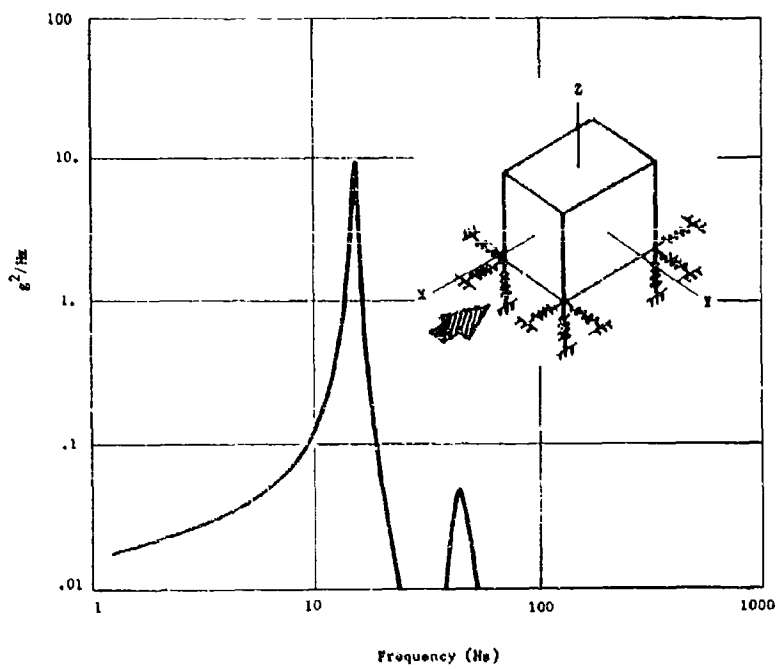

Fig. B-9. Translational acceleration spectral density (shock case)

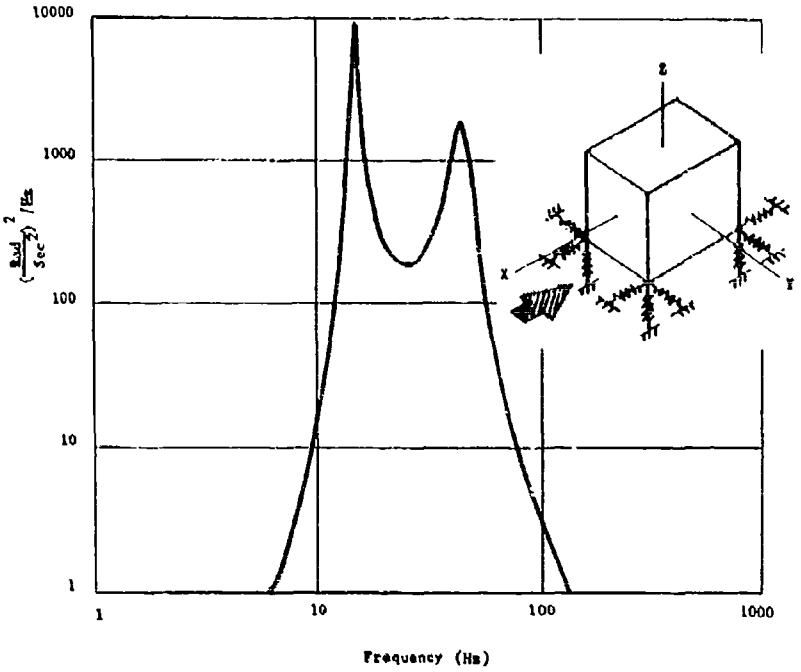

Fig. B-10. Rotational acceleration spectral density (check case)

TABLE B-1
Root-Mean-Squared Displacement (Check Case)

Isolator or Point	DRMS (inches)		
	X	Y	Z
Isolator 1	0.1220[a]	0	0.0987
Isolator 2	0.1220[a]	0	0.0987
Isolator 3	0.1220[a]	0	0.0987
Isolator 4	0.1220	0	0.0987
Point 1	1.1242	0	0.0940
Point 2	1.1145	0	0.0564
Point 3	1.0796	0	0.0846
Center of gravity	0.7718	0	0

[a] Relative displacement because X is the forced direction; all other displacements are absolute.

* * *

AN ACTIVE STABLIZATION SYSTEM FOR VEHICLES AND OTHER MASSIVE BODIES

T. H. Putman
Westinghouse Research Laboratories
Pittsburgh, Pennsylvania

The following paper describes an active inertia-controlled stabilization system developed for vehicles. Through active control the body mass is made to behave as if it were many times that of the actual mass. This results in reduction of the body resonant frequency and permits much greater damping of the body resonant mode than is possible for conventional suspensions. Because of the artificial character of the body-mass increase, the roll characteristics of the vehicle are not impaired. In fact, in the automotive installations the system was made responsive to lateral accelerations to provide banking while rounding curves. The paper gives a simple analytic treatment of the system to provide a basic understanding of its operation and discusses the actual hardware and system performance.

INTRODUCTION

The idea of using controlled force and velocity sources to modify the dynamic characteristics of a system is not new. Indeed, Westinghouse has maintained an interest in and actively worked from time to time on such systems for nearly 40 years. Within the past few years, a number of papers have been published in the area; many, of a theoretical nature, have explored the potential benefits obtainable from such systems.

There is a considerable gulf between theory and practice that must be bridged to make active systems a practical reality. The following paper describes an active inertia-controlled stabilization system that has been developed by Westinghouse and applied to automotive vehicles as well as a military gun carrier.

Isolation of an automobile or other vehicle body from the disturbances resulting from road undulations is conventionally achieved by a spring damper suspension. Two indices of performance of such a suspension system are the body resonant frequency on its springs and the body damping. It is usually desirable to reduce the body resonant frequency as much as possible, and this is conventionally done by using soft springs. However, there is a limit to how soft springs can be made because springs that are too soft result in poor roll characteristics when rounding curves and excessive changes in body level and attitude with load variations. A larger body mass also reduces the body resonant frequency, this accounts for the improved ride characteristics of some of the heavier automobiles.

Body damping is provided by shock absorbers which also provide damping of the wheel mass (the unsprung mass) on the tire stiffness. At the body resonant frequency body amplitude is limited only by the shock absorbers, and for this reason heavy damping is desirable. On the other hand, if the body is too heavily damped, excessive high frequency disturbances are transmitted to the body, causing a harsh ride. For conventional automobile suspensions, 15 to 20 percent critical damping is considered a reasonable compromise, and a resonant frequency of about 1 Hz is not unusual.

Increasing the mass of a vehicle body has the advantage not only of reducing the body resonance frequency but also of permitting higher body damping without any deterioration of the high frequency performance. Thus it appears that any means to increase the body mass is in the best interest of improving the ride. On the other hand, an actual increase in body mass has

the disadvantage of causing excessive roll and is impractical.

This paper describes a vehicle stabilization system that produces an artificial body mass increase and all the advantages attendant to increased mass without having an adverse effect on the roll characteristics. The system can in fact, cause the vehicle to stay level or even to roll in when rounding a curve.

The system has been applied to two automobiles and a military gun carrier (M-56) and has been shown to behave according to theory. Building reliable hardware with the required dynamic performance is, of course, a major undertaking and has been successfully completed.

Stabilization of massive bodies other than automobiles is simply an application of the concepts described herein.

DESIGN CONSIDERATIONS

The following points were taken into account in developing the system:

1. Failure of the system must not disable the vehicle.

2. The vehicle sensitivity to static loading changes must not be altered (no softening of springs).

3. Vehicle wheels must be adequately damped.

4. A fast roll response is required.

5. The body resonant frequency is to be reduced by a factor of 2 or more.

6. The system should involve only minor modifications of a conventional passive system.

OVERALL CHARACTERISTICS OF THE SYSTEM

In the automotive applications, the system takes the form of an inertial sensing element located at each corner of the vehicle; this controls the force of a hydraulic actuator which directly replaces the shock absorber located at the same corner. No change in the springs is necessary for this application. Figure 1 shows the general layout of sensing elements and actuators.

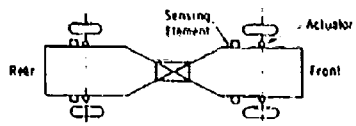

Fig. 1. Location of sensing elements and actuators for automobile stabilizer

The sensing elements are integral units that do all the required information processing hydraulically and supply the necessary hydraulic pressures to the actuators. The sensing elements basically respond to body accelerations although in the design of the damping requirements, one must take account of the body and the wheels. By appropriate design of the inertial weight and physical orientation of the sensing element itself, the element is made to respond to vertical and lateral accelerations of the body. The lateral acceleration response permits bank control so that the vehicle rolls in, rather than out, when rounding a curb.

A complete analysis of the system for the vertical, pitch, and roll modes requires an elaborate analog computer simulation. In the theoretical discussion which follows we shall concern ourselves with a simplified mechanical system that represents one corner of the vehicle for vertical motion only. Figure 2 shows such a system.

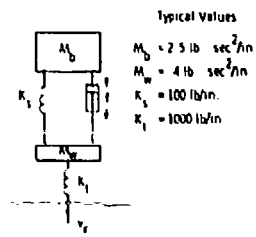

Fig. 2. Mechanical system for one corner of vehicle, vertical motion

Let M_b = lb×sec²/in., mass of body

M_w = lb×sec²/in., mass of wheel

K_s = lb/in., stiffness of springs

K_t = lb/in., tire stiffness

V_r = in./sec, velocity of road disturbance

f = lb, actuator force

s = sec^{-1}, complex frequency.

For purposes of analysis the mechanical system of Fig. 2 is represented by its electrical analog where voltage is analogous to velocity. Figure 3 shows the analog circuit.

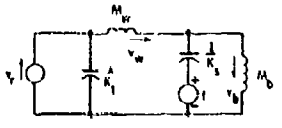

Fig. 3. Electric analog circuit of vehicle suspension

In the analog circuit the inductances shown are in henries and have numerical values equal to the actual mass to which they are analogous, while the capacitors are measured in farads and have numerical values equal to the reciprocal stiffness. Of course currents are measured in amperes and numerically equal the actual velocity (in./sec), and voltages are measured in volts and numerically equal the actual force (lb).

LOW FREQUENCY ANALYSIS

It is convenient to look first at the system behavior at low frequencies to determine the basic control law for the force source f. For frequencies well below the wheel-hop frequency ($\sqrt{K_t/M_w}$), the circuit of Fig. 3 reduces to that shown in Fig. 4.

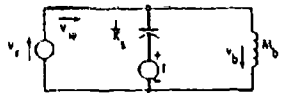

Fig. 4. Circuit representing low-frequency behavior of the suspension

The body experiences the force from the springs (K_s) and that caused by the actuator f. Now we must control the actuator force f so that two objectives are satisfied. First a force must be applied to the body to oppose its acceleration, and second, a damping force must be developed. If f is related to the body and wheel velocity, according to the relationship

$$f = -k_m M_b s V_b + (1 + k_d) R(V_w - V_b) , \qquad (1)$$

these objectives are satisfied.

A circuit that represents the suspension with the stabilizer is shown in Fig. 5. One can easily verify this by showing that the equilibrium equations for Fig. 4 reduce to those of Fig. 5 when the force source is related to the velocities as given by Eq. (1).

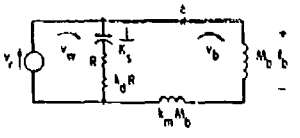

Fig. 5. Low-frequency representation of stabilized suspension

From Fig. 5 it is evident that the body mass M_b is augmented by the synthetic mass $k_m M_b$, and that the passive damping is $R(1 + k_d)$. The factor k_m is known as the mass multiplication factor. The hardware is built so that if the inertial weight is blocked the system will have a passive damping R. This damping is augmented by an amount $k_d R$ by means of a feedback force acting on the weight. Hence k_d is the passive damping multiplier. This particular aspect of the system will be discussed in relation to the actual hardware.

IMPEDANCE SEEN AT THE BODY

Let us now inquire as to the impedance one would observe by pushing on the body. An applied force would be resisted by the inertia reaction of the body plus the spring force plus the actuator force. Referring to Fig. 5 this would be the impedance seen at a pliers entry* into the network at point a or

*The descriptive term "pliers entry" is sometimes used because one would cut the wire at a, creating a pair of terminals between which we determine the impedance.

$$Z_s = M_b s + k_m M_b s + (k_d + 1)R + \frac{K_s}{s} . \qquad (2)$$

From Eq. (2) we see that by pushing on the body mass, an observer would not be able to discover that the body mass had not actually been increased.

IMPEDANCE SEEN BY THE ROAD

The road impedance is the impedance that we would see if we pushed on the wheel. The force would be the force on the body mass or f_b in Fig. 5, while the velocity would be V_r. Therefore one would observe the impedance f_b/V_r which, using the circuit diagram, is easily shown to be

$$Z_r = \frac{1}{\dfrac{1}{M_b s} + \dfrac{(1 + k_m)}{R(1 + k_d) + \dfrac{K_s}{s}}} . \qquad (3)$$

This expression is recognized as the impedance of two parallel elements: the body mass $M_b s$ and the series element composed of the springs and the damper whose impedance is reduced by the factor 1 plus the mass multiplier. Thus from the road one sees an impedance represented by the circuit of Fig. 6.

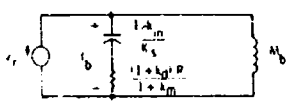

Fig. 6. Circuit representing impedance seen by the road

From this figure we discover that an observer pushing on the wheel would think the vehicle had the spring stiffness reduced by $(1 + k_m)$. Also he would see a similarly reduced damper

A physical explanation of the [illegible] mathematical result is as follows. First [illegible] are talking about low frequencies for which one can neglect the unsprung mass and tire stiffness. If a force is applied to the wheel [illegible] say 1 lb in the upward direction [illegible] will be transmitted to the [illegible] up the spring and actuator. Therefore the 1 lb force will be applied to the body mass causing a steady-state upward acceleration equal to $1/M_b$. The acceleration of the body will cause the actuator to apply a force in a direction to contract the spring equal to $k_m M_b$ for a 1-lb applied force. In the steady state the force applied to the spring is $1 + k_m$, and so the spring will contract an amount $(1 + k_m)/K_s$ under the action of a 1-lb force. Therefore the apparent spring stiffness is

$$\text{force displacement} = \frac{1}{\left(\dfrac{1 + k_m}{K_s}\right)} = \frac{K_s}{1 + k_m} .$$

To see how the damping is reduced we consider the situation that obtains at the first instant after the 1-lb force is applied; at this time the body velocity is zero and the displacement of the spring is zero. Because the spring displacement is zero, it has no force. Consequently, the 1-lb force is applied directly to the actuator. By Eq. (1), the actuator force is $f = -k_m M_b s V_b + (1 + k_d) R(V_w - V_b)$. We have $M_b s V_b = 1$, $V_b = 0$, and $f = 1$. Therefore

$$1 = -k_m + (1 + k_d) R V_w .$$

or

$$V_w = \frac{1 + k_m}{(1 + k_d)R} .$$

Because this is the velocity resulting from a 1-lb force, the effective damping must be $1/V_w$, or

$$\frac{(1 + k_d)R}{(1 + k_m)}$$

which confirms our previous result

HIGH FREQUENCY ANALYSIS

At high frequencies that is, frequencies equal to or greater than the wheel-hop frequency $\sqrt{K_t/M_w}$, the suspension springs have little influence on the motion. Therefore the circuit of Fig. 3 may be simplified as shown in Fig. 7

Fig. 7. High-frequency equivalent circuit

The actuator force is now applied essentially to the body mass M_b so that its velocity is

$$V_b = f\,(M_b s)$$

Elimination of V_b from the control law given by Eq. (1) yields the result

$$\frac{f}{V_w} = \frac{1}{\dfrac{1 + k_m}{(1 + k_d)R} + \dfrac{1}{M_b s}} \qquad (4)$$

which we immediately recognize as the parallel combination of the body mass and the damping resistance one observes at the wheels, and so Fig. 7 can be replaced by the circuit of Fig. 8 at high frequencies.

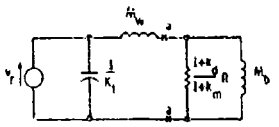

Fig. 8. Simplified high-frequency equivalent circuit

For an unstabilized vehicle, if R is the compromise damping that gives adequate body damping and acceptable high frequency transmission, then we will have the same high frequency transmission if we make k_d equal to k_m. The damping of the body mode is approximately

$$\zeta_b = \frac{(1 + k_d)R}{2\sqrt{K(1 + k_m)M}}$$

which becomes

$$\zeta_b = \frac{\sqrt{1 + k_m}\,R}{2\sqrt{KM}}.$$

Consequently, not only can we reduce the body resonance frequency, we can also increase the damping without causing harshness in the ride.

One can use the circuit of Fig. 8 to discover a very interesting property of vehicle ride stabilizers. By the use of Thermin's theorem one may replace everything to the left of points a-a' by an equivalent voltage source and a series impedance. The voltage source is simply the open-circuit voltage of E_t, $V_r(K_t/s)$, and the impedance is

$$Z_t = M_w s + \frac{K_t}{s}.$$

For the wheel-hop frequency

$$s = j\sqrt{K_t/M_w} = j\omega_w,$$

we have Z_t equal to zero and E_t equal to

$$V_r\frac{K_t}{j\omega_w} = -V_r\, j\omega_w M_w.$$

Because the impedance Z_t is zero, the voltage E_t appears at the terminals a-a' which is the voltage across M_b. Stated in mechanical terms, at the wheel-hop frequency the force on the body is $V_r(-j\omega M_w)$ regardless of what mechanical coupling exists between the body and wheels. The body velocity will be

$$V_r(-j\omega M_w)/j\omega M_b) = -V_r\frac{M_w}{M_b}.$$

Thus the road velocity V_r is attenuated by the ratio of the unsprung to the sprung mass. This points up the desirability of having the unsprung mass as low as possible because there is absolutely no possibility of improving the isolation at the wheel-hop frequency by active or passive means.

HARDWARE

Figure 9 shows a schematic diagram of the complete stabilization system. The heart of the system is the sensing element, which is a single unit containing the inertia weight, the pilot circuit, and the power valves.

The moment acting on the inertia weight resulting from vertical and lateral acceleration of the body, as well as the force from the feedback piston, is balanced by the pilot pressure. The pilot pressure acts on the power valves which regulate the actuator upper cylinder pressure essentially independently of actuator velocity.

The lower cylinder of the actuator is connected to the supply accumulator through the damper valves. The pressure drop across these valves is proportional to the actuator velocity and acts on the inertia member via the feedback piston. This is the means by which the body damping is increased.

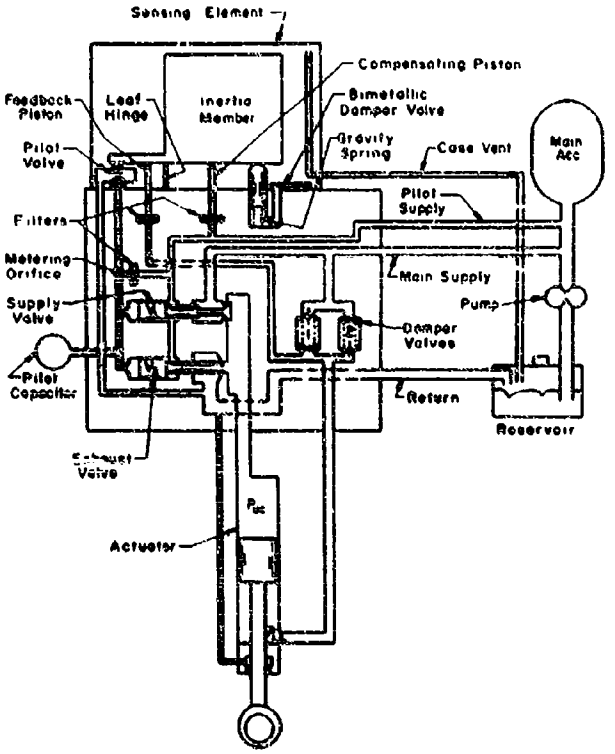

Fig. 9. Vehicle-stabilizer hydraulic circuit- nonleveling, Mod. 2

The inertia member is restrained by the pilot valve which mechanically is characterized as a stiffness, and the combination (inertia mass plus pilot-valve stiffness) forms a resonant system which must be damped. This is accomplished by the temperature-compensated damper valve which acts on the inertia member.

Figures 10 (a) and 10 (b) show the sensing element as it is physically realized.

PERFORMANCE OF COMPLETE SYSTEM

Figure 11 shows computer results of pitch characteristics for the M-56 military gun carrier; we see that the pitch resonant frequency for the unstabilized vehicle is about 1 Hz whereas with stabilization it is reduced to about 0.4 Hz. The reduction of resonant frequency comes about from an artificial increase in the pitch moment of inertia equal to $(1/0.4)^2$ = 6.3 times the normal moment of inertia. An even greater increase for the vertical mode was obtained. Also evident is the vast improvement in body damping that was obtained. Figure 12 shows the response of the actual vehicle when the pitch mode was excited by driving it across a ramp about 6 in. high and 20 feet long. The top trace in each view was made by a lamp attached to the muzzle of the gun; the middle trace by a lamp located near the center of gravity; and the bottom trace by a lamp on the front wheel hub.

HARDWARE LIMITATION

The question arises, is there any limit to the number of times by which the body mass can be multiplied up? Looking at our simplified analysis, one would be inclined to think not. However, when all factors are taken into account, as in actual hardware or on a computer simulation, there definitely is a point beyond which one can not go because of parasitic oscillations and system instabilities. Complete

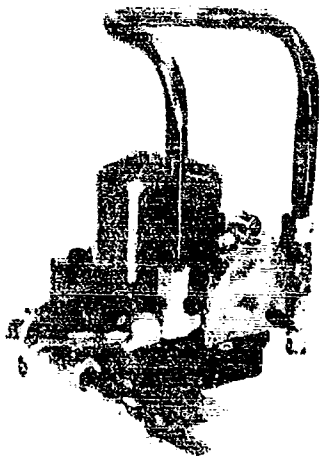

(a)

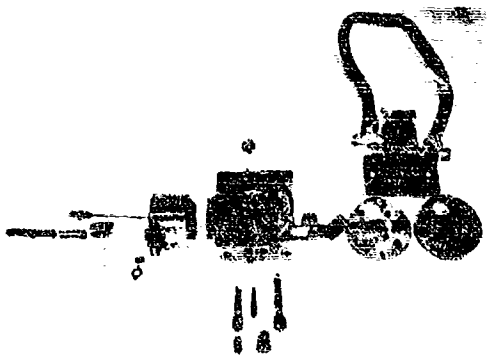

(b)

Fig. 10(a). Complete sensing element; (b) parts of sensing element: left-damper valve; feedback, pilot, and compensating piston; inertia weight; power valves (lower center); damper valves, pilot capacitor (right)

analog computer simulations are a great help in studying instabilities and devising appropriate

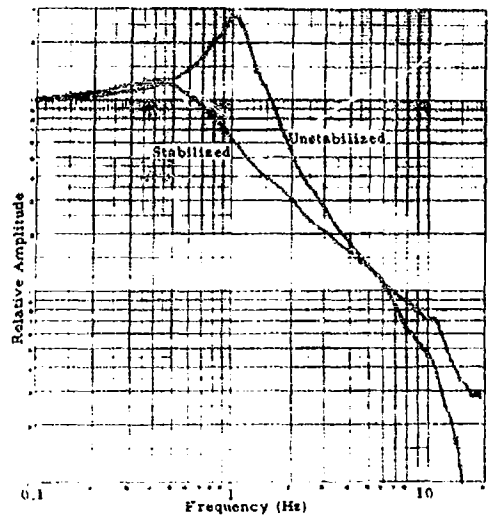

Fig. 11. Computer results, body motions for pitching mode

compensation. Unfortunately, simulations are no better than the equations that it solves. As a result, when one gets down to the point of actual hardware on a vehicle, unsuspected hydrodynamic effects and local structural resonances can cause the most carefully designed system to buzz. This problem is handled most effectively by empirical means.

CONCLUSIONS

Practical active ride stabilizers have been built and demonstrated for automotive vehicles. Such stabilizers can augment the body mass by from four to six times and provide 40 to 60 percent critical damping at the body resonance without causing harshness. Active systems need not be limited to ride stabilizers. They may be used to shock isolate any massive body such as a missile. Similar concepts can be applied to ships and submarines to reduce hull vibrations caused by propeller thrust pulsations.

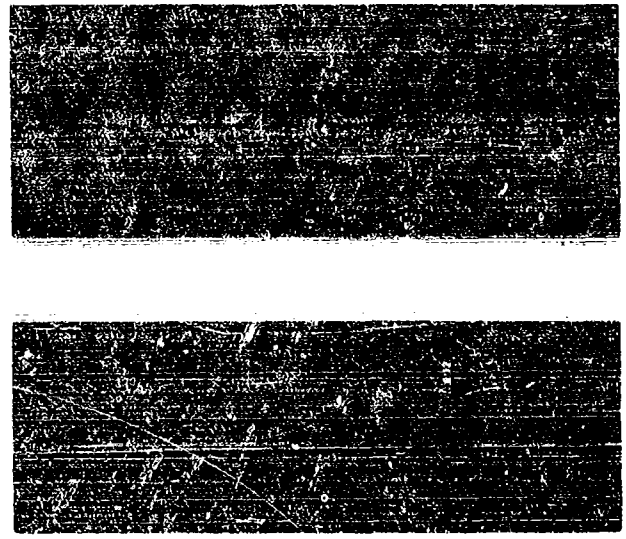

Fig. 12. Comparison of pitch performance of unstabilized (upper) and stabilized M-56 vehicles; top trace in each view is made by a light on the gun muzzle

DISCUSSION

Mr. Baruch (Kollsman Instrument Corp.): You used the active system in the automobile which you showed?

Mr. Putman: Yes, that is an active stabilizer.

Mr. Baruch: What kind of increase in performance did you notice? Was it substantial or did it become like a floating ride? I noticed that the car you put it in was not very heavy, and you were trying to get the added mass effect of a heavier car, such as a Cadillac. Was there a substantial difference?

Mr. Putman. There certainly was a great improvement in the ride characteristics. This actual job was completed for the Ford Motor Co. about 10 years ago. At that time they said it was a great improvement, but that we were 20 to 30 years ahead of our time. It has been a little discouraging, as far as acceptance of this sort of equipment is concerned. There is definitely a great improvement in performance of these vehicles.

Mr. Sevin (IIT Research Inst.): To what extent do the design details of your active system depend upon preknowledge or description of the environment of the roadways or the ground profile? Is that actually utilized in the design?

Mr. Putman: The technique which we used in design is basically a frequency response. Our guide rules were basically to reduce the resonant frequency and increase the damping without significantly hindering the high frequency ride. We did not use any spectrum of the road or anything like that. I noticed in Dr. Paul's paper, that he worries about the clearance that is available. We have not found this to be a particular problem in our case.

* * *

CRASH CONSIDERATIONS IN THE DESIGN OF THE NEW YORK STATE SAFETY SEDAN*

Sol Davis and Neil B. Nissel
Fairchild Hiller
Republic Aviation Division
Farmingdale, Long Island, N. Y.

This paper presents those aspects of vehicle design that are pertinent to the reduc- of crash injury to vehicle occupants when an accident occurs. Specifically, the considerations that defined the design configuration of the New York State Safety Sedan are reported.

System factors have been studied in an attempt to clearly define the critical criteria and design requirements, and to determine the subsystems that best satisfy the criteria and fulfill all the requirements. Thus, the roles of the driver, the environment, and the vehicle have been examined, and the relationship that each has to the overall problem of occupant crash safety has been established.

Three interrelated areas of engineering interest contribute significantly to the protection of occupants of a crashing car. First, the passenger compartment must retain a sufficient degree of structural integrity so that it will not deform to such an extent that the occupant is crushed, impaled, or otherwise injured by the deforming structure. Second, a passenger restraint system must be coupled to the seat and structural systems of the car in such manner that the accelerations of, and restraint forces on, the occupant remain within acceptable biological limits. Furthermore, maximum use must be made of the clearance distance between the occupant and the interior of the vehicle. Third, the vehicle interior must be designed to reduce the potential injury when the restrained or unrestrained occupant impacts the compartment interior, that is, to minimize the effect of the "second collision." All this has been accomplished without serious compromise on the ease and safety of vehicle operation under normal conditions.

INTRODUCTION

The New York State Safety Car Program grew out of problems encountered by the New York State Legislature in attempting to formulate laws that would bring about rapid improvement in automotive safety. The program was initiated in 1965 with the Phase I Feasibility Study [1] which provided the details of a general plan to accomplish the program objectives. These objectives included the design development, fabrication, testing, and evaluation of a prototype passenger vehicle embodying all feasible safety devices and features practical for limited mass production. The program was continued with the Phase II Engineering Design and Development [2] which created the Safety Sedan (Fig. 1), a practical, lifesaving vehicle that would reduce accidents and injuries and could be mass produced for public use.

SYSTEMS APPROACH TO AUTOMOTIVE SAFETY

The critical elements of automotive safety were examined and evaluated as a total system

*This paper reports on the crash injury aspects of the Design-Development Phase II of the New York State Safety Program, Contract No. C-0967, issued by the State of New York, Department of Motor Vehicles. This program was conducted under the cooperative direction of George Hildebrand, Program Manager, Republic Aviation Division, Fairchild Hiller, and John O. Moore, Director of Research Department of Motor Vehicles, State of New York. The authors were responsible for the structural mechanics aspects of the Safety Sedan described in this paper.

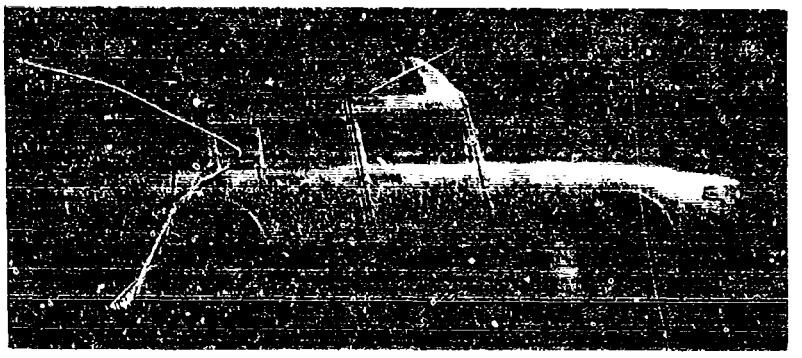

Fig. 1. The New York State Safety Sedan

within the matrix of the following five major safety categories:

1. Accident Avoidance — those aspects of safety associated with operation of the vehicle to prevent collisions with other vehicles, pedestrians, or fixed obstacles.

2. Crash Injury Reduction — those aspects of safety that reduce injury to the vehicle occupants when a crash occurs, including the effects of impact with the vehicle interior during the "second collision."

3. Pedestrian Injury Reduction — those aspects of vehicular design that tend to reduce injury to a pedestrian struck by the vehicle.

4. Post Crash Protection — those aspects of safety that apply after the accident, including rescue and the avoidance of further hazard at the accident site.

5. Nonoperating Safety — those aspects of safety that apply when the vehicle is not in traffic, including maintenance and repair, entry and egress, and the other hazards presented by a stationary vehicle.

Within these five safety categories, the basic safety criteria for passenger car performance, design, and construction can be realistically defined only as part of an overall systems concept for safe human transportation. This systems concept must recognize the contributing roles of the driver, the environment, and the vehicle in any accident situation. Each of these factors can help prevent accidents; and when an accident can no longer be avoided, each of these factors can help reduce the severity of the accident, particularly with regard to fatalities of the vehicle's occupants.

The subject of this paper emphasizes the second safety category of Crash Injury Reduction, which assumes that accident avoidance subsystems can not completely eliminate all accidents over the near term. It is noteworthy in this respect, that alcohol, with its adverse effect on the driver's decision-making process, has been established as a major cause of more than 50 percent of fatality-producing accidents [3].

SYSTEM FACTORS IN CRASH INJURY REDUCTION

The role of the driver in reducing the severity of the accident hinges on his ability and willingness to use the safety features that have been incorporated into his vehicle and his environment. The incorporation of an integrated seat and occupant restraint system that requires the occupant to fasten a seatbelt and harness is of little use unless the occupant consciously closes the loop in the safety design chain. Statistics collected in Wisconsin, the first state to make seatbelt installation mandatory, indicated that only 52 percent of all front occupants used seatbelts that were available [4]. The maximum protection of such safety devices as seatbelts depends not only on the occupant's cooperation but also on his understanding of the proper use of the devices. The occupant who tightens his seatbelt to a snug fit will start decelerating sooner and is likely to be less severely injured than the occupant who carelessly leaves 2 in. of space between himself and the belt.

The role of the environment in reducing the severity of accidents is clearly seen in terms of the potential hazards that exist in present road systems. The possibility of severe head-on

collisions of two vehicles traveling in opposite directions is being gradually reduced by the erection of effective crash barriers between opposing lanes of traffic on many of our heavily traveled, high-speed roadways. These crash barriers can prevent head-on collisions and can be designed to help the vehicle return to the normal direction of traffic [5]. The incidence of vehicle impact with trees and telephone poles, which usually results in penetration of the passenger compartment, will be significantly reduced as these objects are moved further away from the edges of the road [6].

The role of the vehicle in minimizing human crash injury depends on the structural interior and exterior design and the special safety features that may be included. The performance, design, and test criteria for the Safety Sedan focused on this area of the overall systems problem within the framework of current driver-environment boundary conditions.

CRASH THREATS

Crash threat situations that were considered in establishing the performance criteria of the New York State Safety Sedan included—

1. Frontal impact
2. Side impact
3. Rear impact
4. Rollover

These classifications are reasonable simplifications for typical crash situations; but vehicle impact point and object may significantly affect the safety performance. In side impact, for example, an impacting car that hits the passenger compartment area may cause severe compartment penetration. The same impacting car hitting the left rear side of the vehicle is generally a less severe impact situation. In frontal impact, a 30-mph crash into the rear of a stationary vehicle of similar design is much less severe than a 30-mph crash into a rigid barrier of the Society of Automotive Engineers type [7]. However, studies of real and potential crash threats for passenger vehicles have shown that certain problems of incompatibility exist that will require changes in the road environment or other types of vehicles. It would be impractical to design an improved passenger safety car to eliminate all hazards during the near term, as illustrated by the following examples:

1. Most objects passing above the hood through the windshield can not be guarded against effectively. These include pipes and lumber carried on a truck ahead, and falling rock or heavy missiles dropped from overpasses.

2. A passenger car occupant can not be fully guarded against compartment penetration caused by the car's running under the high floor or side of a truck.

3. Roadside barriers and guardrails are highly variable, and no single vehicle design can be optimum for the many different types of crash threats.

The crash design goals for the New York State Safety Sedan were established as (a) forward impact — 50-mph head-on impact into a rigid barrier; (b) side impact — 40-mph impact by a similar vehicle; (c) rear impact — 50-mph impact by a similar vehicle; and (d) rollover — 70-mph without collision. These goals were established by feasibility studies and knowledge that these criteria would cover more than 75 percent of accidents in urban-rural driving.

SAFETY GOALS

The areas of safety improvement for occupant crash injury reduction can be stated in terms of the following general goals:

1. Prevention of ejection through doors, windshield, or windows.

2. Reduction of occupant restraint forces.

3. Reduction of interior impact injury.

4. Maintenance of passenger compartment integrity.

These goals formed the basis for the crash safety performance criteria of the New York State Safety Sedan.

Ejection of the occupant from the vehicle was a high-priority area for safety improvement several years ago [8]. Studies based on numerous accidents and preplanned collision tests show that car doors spring open as a result of distortion of the vehicle body and/or actuation of the unlatching mechanism. The distortion of the automobile body may be caused by bending of the body outward in side impact, by torsional strain in corner collision, or by

column buckling in rollover. These factors involve the complete vehicle as a whole and generally involve large inertial force loadings with the door being literally torn away from its position without unlatching. The actuation of the door mechanism can be caused by inertial forces developed within the door lock system during crash conditions, by bending of the latch remote rod, by contact of the outside door handle with ground or object, or by inadvertent actuation by a vehicle occupant. Improvement of door lock designs [9], the use of seat belts, and the redesign of door handles to prevent accidental opening have reduced the present priority of this important goal.

Reduction of occupant restraint forces is concerned with the proper design of an integrated seat and occupant restraint subsystem. The optimum restraint system requires a tradeoff between the forces that the occupant will experience as a result of the restraint configuration and the greater forces that he will generally experience from abrupt impact with the vehicle interior. An unrestrained occupant experiences minimal restraint forces at the expense of serious injury from high decelerations during interior impact. Further tradeoffs are required for comfort, accessibility of controls, ease of entrance and egress, and to maintain the proper eye level of the driver for maximum visibility.

The proper choice of restraint system characteristics to minimize occupant injury is greatly influenced by the "tuning" relationship between the integrated seat and occupant restraint system, the dynamic characteristics of the vehicle structure, and the values of the crash safety performance requirements. The restraint system characteristics are also dictated by the maximum allowable displacement of the occupant within the confines of the vehicle interior. Thus, the optimum restraint system for a compact car may well be different from that for a full-size sedan.

In addition to optimizing the performance of a restraint system by proper design, the psychological acceptance of voluntary devices is a significant area of safety improvement. As indicated previously, statistics collected in Wisconsin indicated that only 52 percent of all front occupants used seat belts that were available. Women occupants used seat belts only 44 percent of the time and this sex disparity in restraint use may be greater for shoulder harnesses because of obvious differences in chest anatomy.

The conventional seat structure offers fairly good protection for downward or rearward accelerations (except for the head and neck). Statistics collected during the New York State Program indicated that, even though 44 percent of the accidents are rear-end collisions, only 7 percent of the fatalities occur in this mode. On the other hand, the same data indicated that noncollision (single-car involvement) includes only 12% of all accidents but 69 percent of the fatalities. Thus, the addition of adequate head and neck support to minimize the common whiplash injury, may be sufficient to reduce the priority of safety improvements for frequently occurring rear-end impacts. The greatest emphasis must be placed on reducing the fatalities resulting from single-car impact.

Some side-impact protection is afforded by bucket-type seats, and additional side protection can be incorporated either in the seat itself or in the adjoining door panel. In head-on collisions with other vehicles or roadside objects, however, the seat itself offers little protection for the unrestrained occupant who is frequently accelerated in an arc forward and upward leading with the head. An auxiliary method of restraint is required to control the deceleration rate of the occupant in frontal (±60 degree) collisions. This restraint system performance must consider the structural deformation characteristics of the forward vehicle structure itself. Considerable improvement in occupant loading is theoretically possible for a properly restrained occupant by optimizing the crush or deformation characteristics of the front end for forward impact.

Reduction of interior impact injury requires a tradeoff with occupant restraint system forces. A restraint system designed to avoid occupant interior impact will probably result in high occupant restraint forces. Proper consideration of a deliberately padded dash panel or collapsible steering wheel assembly must be included in the overall system design and analysis of an optimum restraint configuration for the range of occupants that represent the human population. Appropriate consideration in vehicle interior design must also be given to the many vehicle occupants who ignore the restraint systems provided for their protection.

After the occupant has been adequately restrained so that he does not suffer serious injury from contacting the vehicle interior or from the restraint system itself, the passenger compartment must be designed so that the interior does not move inward to impact the occupant. This area of safety improvement is generally called passenger compartment integrity. Problem areas have included the inward motion

of doors during side impact, the rearward movement of the steering column in forward impact, and roof collapse during rollover.

PRIORITIES FOR SAFETY IMPROVEMENT

Priorities for structural crashworthiness and the proper "packaging" of occupants to minimize crash injury were somewhat easier to establish than those for accident avoidance because of the existence of a substantial background of accident reports and analyses and documented crash-test programs. However, the variability and imprecision of most accident reports and the general difficulty experienced when the necessary variables are not specifically recorded hamper the analysis of accident data to determine the important factors. For example, recent data [10] that can be used to establish the statistical distributions of vehicle occupants are based on a small sampling and, therefore, may change as more data are included. However, these accident experience data, together with documented crash-test programs [11] and analyses [12], do provide guidelines for the identification of injury producing structure, components, and interior elements of vehicles.

Crash injury data [13,14] that list groups of injury-producing vehicle interiors are available. These injury levels produced by interiors are heavily dependent on the directional crash situations described earlier. Severe injury from impact with the windshield may occur in frontal collision but is unlikely in rear collision.

The available data can be misleading in two respects. First, for example, the steering wheel has been listed as a most frequent cause of injury, yet the absence of the steering wheel in the right front passenger seat in the same head-on crash situation can produce greater severity of injury by permitting head impact with the windshield at fatal velocities. Second, the data generally available are for unrestrained occupants: the interior areas of concern for the lap belted or lap-shoulder belted occupants are different and depend on the trajectories of the occupants under the restraint configuration.

FRONT IMPACT SUBSYSTEM

The New York State Safety Sedan has a bumper positioned at the extreme front of the vehicle and located at a standard height above the roadway (Fig. 2). The bumper is connected to a pair of parallel hydraulic energy-absorbing cylinders. The outer chambers of the shock absorbers also function as main structural members of the front structural system of the vehicle. Impact forces applied to the front end of the safety car, at bumper-level, are reacted by the bumper, and the energy generated by the forces of impact is partially absorbed by the displacement of internal fluid passing through a variable area orifice as the length of the cylinder is reduced or compressed in length.

The bumper is automatically extendable an additional 12 in. forward of the normal front boundary of the vehicle. As presently conceived, the bumper would be extended ahead of the safety car at speeds above 37 mph in highway traffic. At 37 mph, a circuit is energized to activate a linear actuator located between the midpoint of the bumper and the front crossover beam of the front structural system of the car. The extension of the actuator drives the bumper forward. The twin hydraulic energy-absorbing cylinders stabilize and guide the forward movement of the bumper into its final forward position. The circuit is deactivated after 12 in. of extension, and the bumper system is locked in position.

The bumper has the capability to pivot about the forward end of one of the hydraulic energy-absorbing cylinders and simultaneously compress the other energy-absorbing cylinder during an unsymmetrical impact at the front end of the vehicle. This is called the "swinging gate" feature and tends to deflect impacting objects and pedestrians to the side and away from the safety car. Bumper extension and retraction are fully automatic for normal over-the-road operation. A manual override is provided to avoid cycling the system when the car is operated in a dense traffic environment where the preset actuating speed is constantly being crossed.

The hydraulic shock-absorbing bumper is designed to apply the maximum forces of retardation as early as possible. The forces are applied early, in time to absorb the maximum energy at the highest velocities and permit the occupant's restraint system to start the deceleration process sooner than in conventional systems.

The hydraulic absorption of energy is the most efficient method known in terms of displacement and force. The absorbed energy is represented by the area under the force-stroke curve. Because the hydraulic peak force can be obtained very quickly compared with the straight line rise for typical elastic materials, the energy absorbed by the bumper system can be

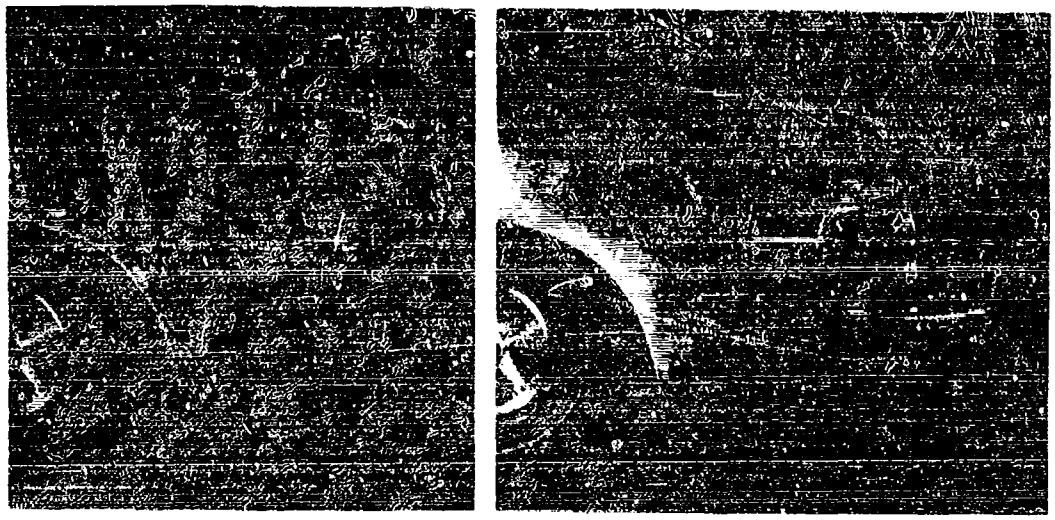

Fig. 2. Extendable hydraulic front bumper

greater for a given deflection and particularly for short strokes. For low-speed impacts, the deceleration forces are lower because they depend on the relative velocity of travel of the two ends of the bumper system.

For the design concept of the New York State Safety Sedan, a design goal of a 50 mph impact head-on into a rigid barrier appeared reasonable. The feasibility of a high force hydraulic bumper system required investigations into the dynamic characteristics of a bumper attached to a typical safety car.

The car was assumed to have a maximum loaded weight of 5300 lb. At an impact speed of 50 mph (880 in./sec), the hydraulic system acting alone must absorb 5.3165×10^6 in.-lb of kinetic energy. A maximum hydraulic stroke of 30 in. was considered feasible with 12 in. of stroke associated with an extension of the bumper beyond the normal front boundary of the car at higher speeds. The average force required from the hydraulic system was obtained on the assumption of a rigid car as

$$\text{Force} = \frac{\text{kinetic energy}}{\text{stroke}} = \frac{5.3165 \times 10^6 \text{ in.-lb}}{30 \text{ in.}}$$

$$= 1.7722 \times 10^5 \text{ lb.}$$

The average deceleration level that a rigid car (and rigid occupant) would experience is obtained as

$$\text{Deceleration (g's)} = \frac{\text{force}}{\text{weight}} = \frac{1.7722 \times 10^5 \text{ lb}}{5300 \text{ lb}}$$

$$= 33.44 \text{ g's.}$$

This deceleration level is within the known tolerable level for a properly restrained occupant.

SIDE IMPACT SUBSYSTEM

In contrast with frontal collision where the occupant has a certain amount of forward kinetic energy that must be dissipated by deceleration, the occupant during the side impact is accelerated from rest to some final velocity during the impact period. The vehicular protection against side impact must minimize the peak acceleration of the restrained occupant, prevent injury on vehicle interior impact, and maintain passenger compartment integrity. Occupant impact with the vehicle interior must be cushioned by appropriate design.

It is evident that the standard form of occupant restraint, that is, a lap belt and shoulder harness, can not provide adequate restraint during a side impact. Although the hip area is restrained by the belt, the occupant is free to rotate sideways about the hip and collide with the vehicle wall or window. The addition of a shoulder harness does not help much, because such harnesses allow considerable side sway. Therefore, an additional side restraint is required.

The New York State Safety Sedan provides the additional side restraint by the use of energy-absorbing material built into wings on the sides of the seats. The inboard wings are part of the seat while the outboard wings are built into the door (Fig. 3). This feature permits easy entrance and egress for the driver and passengers. The degree of protection afforded the occupant depends on the energy-absorbing characteristics and volume of material used. It is important to note here that only the plastic deformation of a structure can be considered to absorb and dissipate energy; elastic deformation absorbs energy from a system but then promptly returns an equal amount of energy back to the system.

The structural protection against passenger compartment penetration is provided in the New York State Safety Sedan by means of a thick door nested into the side sill of the platform which is a large longitudinal thin-wall beam at bumper height. Both of these structural elements are capable of undergoing moderate deformation without significant compartment intrusion. In the deformation process, they absorb a large amount of energy.

The problem of estimating the plastic deformation of the longitudinal beams, door posts, and doors of the struck car is one of predicting the following:

1. The percent of the kinetic energy of the striking car that remains as kinetic energy of rigid body motion immediately after impact.

2. The percent of energy loss as a result of friction during the impact.

3. The percent of the kinetic energy of the striking car A which is converted to plastic or permanent deformation.

4. The percent of the energy-causing plastic deformation in the striking car A and in the struck car B.

5. The percent of the energy absorbed in the struck car B by the longitudinal beams, door posts, doors, and the percent absorbed by other local structure.

The procedure is illustrated in Fig. 4 for center-side impact.

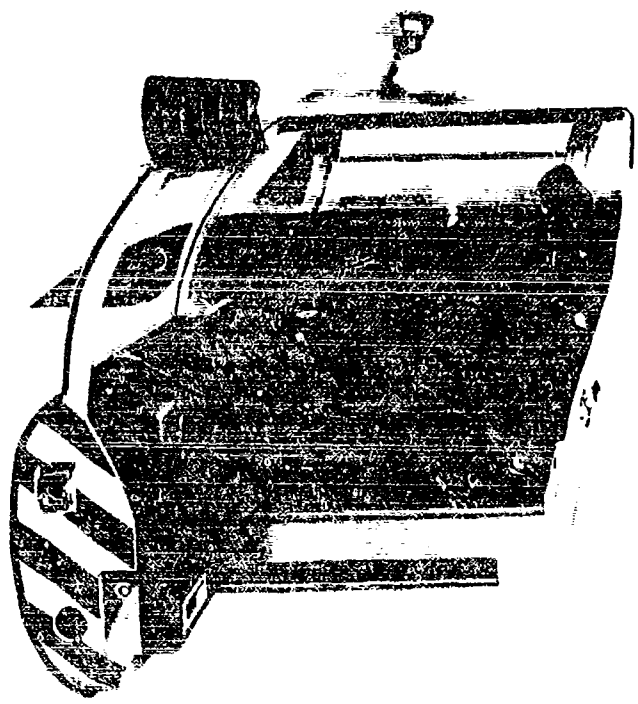

Fig. 3 Side impact passenger compartment protection

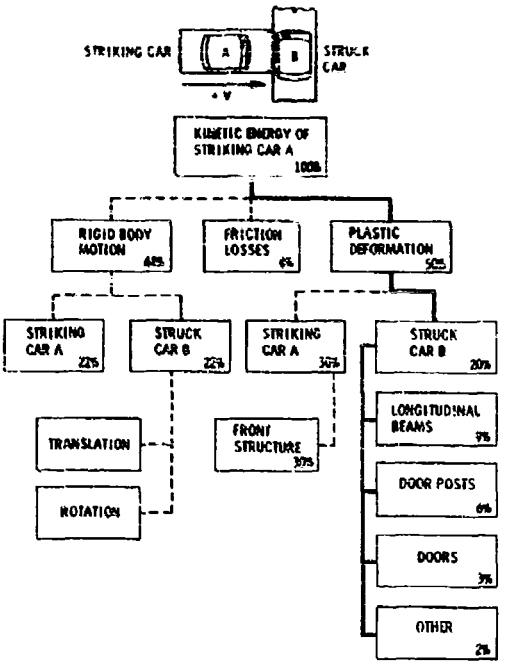

Fig. 4. Conversion of initial kinetic energy during side impact

Analysis of test results for typical vehicle crashes in the literature [11,15] indicates that up to 57 percent of the initial energy of the impacting vehicle can be lost during the collision. Classical impact theory suggests that even in perfectly plastic impact no more than 50 percent of the initial kinetic energy can be converted into permanent plastic deformation. The discrepancy of 7 percent can be attributed to friction losses in the tires and in internal vibration damping. The plastic deformation energy loss occurs in the crushing of the front end of the striking car A and in the crushing of the side of the struck car B. This energy loss is not equally distributed between the two cars, but depends on the relative stiffness of the crushing parts. For the Safety Sedan, a distribution ratio of 2/3 is reasonable with the smaller value for the side of the struck car B which will deform much less than the front of the striking car A. Thus only about 20 percent of the initial kinetic energy must be absorbed by the side structure of the impacted car. Estimates of the energy-absorption breakdown for major side structure components are indicated in Fig. 4. These estimates are helpful in preliminary design, but detailed dynamic nonlinear analysis [16-18] supported by actual test data is clearly needed to obtain better predictions of critical loads and energy absorbed for final design verification.

REAR IMPACT SUBSYSTEM

The Safety Sedan has the capability of preventing serious injury to the occupant when it is struck from behind by a vehicle of similar weight at a speed of 50 mph. In rear impact, as in side impact, the occupant in the struck vehicle is accelerated from an initial velocity associated with his vehicle's speed to an increased velocity caused by impact. The velocity increment is the significant parameter so that the potential severity of a 60-mph car hitting the rear of a 30-mph vehicle is the same as for a 30-mph car hitting a stationary car, because the relative velocity would be the same. In rear impact, the large impact area of the seat back, when coupled with adequate head restraint to prevent whiplash, minimizes the occupant injury potential for this crash situation. However, the energy-absorbing rear structure must not result in penetration of the passenger compartment.

The rear bumper of the Safety Sedan wraps around the car from wheel opening to wheel opening. It is backed up by a perimeter frame structure over its entire length. The bumper's principal attachment points are to the rear longerons and the base of the wheel arch.

The rear section connects to the passenger compartment "strong box" in such a way as to absorb major forces of impact, and a transverse bulkhead resists deformation and penetration by typical objects from the trunk or outside the vehicle. This bulkhead also acts as a rear firewall in case of fire caused by fuel spillage.

ROLLOVER SUBSYSTEM

An occupant of the Safety Sedan is protected in case of rollover by a stiff integrated system of pillars, rollbars, roofrails, and heavy-gage roof skin. The purpose of this structurally stiff system is to resist the severe roof loading without collapsing and crushing the occupant.

As the car may be skidding forward and sideways while in the inverted position, three types of loads on the roof have been considered. First and foremost is the vertical load resulting from the downward inertia force of the car. Second is the shear force in the fore-aft direction caused by friction while the car is sliding

forward on its roof. This introduces a transverse shear load. The third type of load is also caused by friction, this time as a result of the car sliding sideways, and this introduces a lateral shear load on the structure. Only a very stiff structure could avoid collapse under these combined conditions.

The roof structure of the Safety Sedan incorporates four transverse rollbars. The A, B, C and D pillars (Fig. 5) continue over the top to form rollbars. The A pillar is designed of high-strength steel to minimize cross-sectional area to afford optimum driver vision. It is then reinforced to act as the forward rollbar. The B pillar is integrated to the center transverse bulkhead and is of box section to form the rollbar structure over the top. The C and D pillars are interconnected, that is, they are spanned by a continuous reinforced box structure and thus become the primary rollover protection element.

The four rollbars are joined together and stiffened by the roof rails and the heavy-gage roof skin. The side-post structure has a high degree of "tumblehome" or curvature away from the vertical. Therefore, the semicircular cross section of the Safety Sedan above the belt line will give the vehicle improved safety performance in a rollover type accident by —

1. Avoiding high stress concentration at the square corner juncture between the roof and sides typical of vehicles.

2. Avoiding sudden high rotational or transverse acceleration on the passengers caused by square corner impacts with ground.

3. Avoiding elastic and plastic deflections during roll which can cause the doors to fly open or jam shut.

The interior surfaces of all roof structural members have no exposed edges and are padded for additional occupant protection. The periscope housing will collapse against the roof under moderate loads.

The Safety Sedan will withstand the loads associated with a 70-mph uncomplicated rollover without permitting significant deformation or penetration of the body structure.

OCCUPANT INTERIOR PROTECTION SUBSYSTEM

The Safety Sedan interior is designed to protect all occupants by means of an integrated seat and restraint subsystem, force distributing surfaces, and delethelized hardware installations (Fig. 3). Special consideration was required for the driver's position to maintain the proper eye level for optimum vision capability, and to assure accessibility to the controls.

The driver's seat in the Safety Sedan is an individual seat with a tubular peripheral frame, zig-zag springs and foam upholstery cushioning. The seat is attached on its vertical adjustment tracks to a transverse bulkhead at the B pillar (see Fig. 5). This vertical mounting provides greater resistance to failure of the seat during collision because the impact forces of the collision are primarily in the horizontal direction; with horizontal mountings, a large bending stress may develop, particularly when the shoulder harness loads are reacted by the upper seat back structure. Furthermore, with the seat mounted in the former manner, vertical adjustability is incorporated into the seat without reducing the strength of the anchorage.

The driver's head support, which has two inertia reels and the X type shoulder harnesses stored within it, is also rigidly attached to the bulkhead. Adjustability is not provided in the head support because the seat is vertically adjustable for a standard eye position. The head support affords protection against whiplash injuries in the event of a rear-end collision. It is padded to provide injury protection in all directions. This includes the possibility of unrestrained rear seat occupants striking the front seat head support during a frontal impact.

The most significant factors in occupant safety are that the occupant remain restrained in his seat and that the seat remain a controlled part of the vehicle during the entire crash period. Nonuse of a seat belt has been clearly established as a prime cause of serious injury or death in cases of accident. A loose or overly flexible lap belt can endanger the user by permitting impact with the vehicle's interior elements, by unnecessary amplification of crash loads, or by allowing ejection from the vehicle. To function properly, the restraint system used must be compatible with vehicle characteristics and with the human factors involved. Forward impact imposes the greatest forces on the vehicle occupant (50 percent of all injury- and fatality-producing accidents are frontal). The Safety Sedan has a system of restraints that arrest the occupant's forward motion with a minimum of injury and, at the same time, is compatible with his need for freedom and comfort during the time of normal or accident-free travel. Rearward impact presents a lesser problem because the occupant's back and head are impacted against the large, cushioned area of the seat and head support.

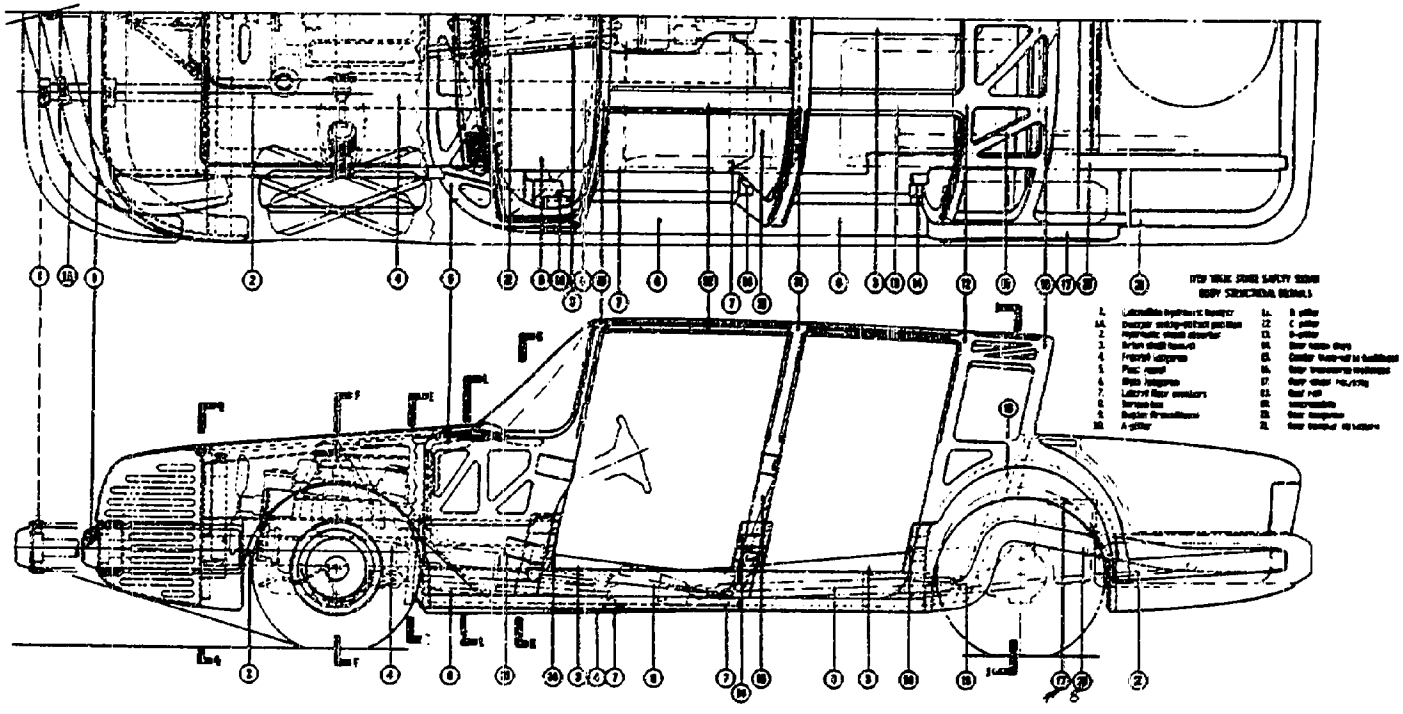

Fig. 5. Safety Sedan body structural details

In the selection process of an integrated restraint system for the Safety Sedan, a wide variety of restraints against forward impact were examined. The restraint system selected contains webbing that is integrally mounted on the seat structure; this minimizes the possibility of belts tearing loose and avoids the clutter and hazards of mountings that are on the floor or roof. Throughout the range of adjustment, the webbing has only a short distance to span between mountings and the occupant's torso. This means that the occupant can be snugly restrained, and the possibility of excessive g amplification is reduced. The lap belts are push-button recoil-mounted at an angle of 50 degrees with the seat cushion plane. The shoulder straps of X type are mounted integrally within the head support and are on rate-sensitive inertia reels.

Inertia reels are spring-loaded take-up spools on which harness belts are mounted. On impact, or any deceleration equivalent to more than 2 g's, the device will lock the belt automatically and restrain the occupant from being thrown forward; yet normal movements will not activate the locking mechanisms, so that the occupant has relative freedom of movement. The Safety Sedan uses a multiaxial rate-sensitive reel that has the advantage of allowing the occupant to check its working order by a quick yank on the harness. The headrest-mounted reels avoid the severe spinal compression inherent in floor or other low-level shoulder strap mountings.

The occupant restraint system crash loads are transmitted to the bulkhead so that the seat can be lightweight in comparison with normal safety seat construction; any significant occupant loadings beyond those of normal highway effects will be taken by the bulkhead. The bulkhead structure is designed to yield at 30 g's so that it will yield sufficiently during severe collisions to keep the occupant loading within tolerable physiological limits.

The harness-seatbelt assembly is usually thought to restrain a passenger precisely in the seat. This is not true because some stretch will occur; furthermore, the occupant-restraint system must be considered as a dynamic system. Tests of vehicle collisions [15] with conventional seatbelts show that an accelerometer on the passenger's hip indicates higher peak decelerations than one mounted on the chassis. The dynamic response of the seat and restraint system may magnify the chassis deceleration levels and cause seatbelt loads that exceed present belt load capability at the higher impact speeds. The shoulder straps must allow the occupant's shoulders to pitch forward at least until his weight is taken up by the lap belt to reduce the likelihood of submarining under the lap belt. This will distribute the high stresses on the anatomy, thereby avoiding excessive g's on the more vulnerable upper torso and directing higher decelerations to the pelvic area which can tolerate the higher loadings.

The allowable stretch of the belts, however, must limit the velocity of contact with the padded cowl, steering wheel, roof, or the rear of the front seat to velocities within the deformation design level of the area contacted.

Present safety belts will elongate during impact from 16 to 40 percent before failure. (Society of Automotive Engineers specifications limit elongation of a shoulder harness to 40 percent.) Owing to the particular characteristics of webbing currently in use, most of the elongation will be elastic and, therefore, there will be a return reaction. With large shoulder harness elongation and a high enough g load, it is possible to create whiplash, when the occupant rebounds into the seat back after a front-end impact.

A plastic or yielding belt is specified in the Safety Sedan to minimize rebound. The yield properties of the restraint are consistent with known human tolerance level. Loadings in excess of human capability will cause the transverse bulkhead to yield to keep the impact forces within human tolerance levels, that is, 30 to 40 g's.

The other seats in the sedan will be of the same type and basic structure; they will only lack the versatility of adjustment that the driver's seat needs for proper vision and reach to controls which is not considered as important a factor for the passenger. The passenger seats will still possess adjustability for comfort and accommodation.

The Safety Sedan interior is primarily designed to reduce occupant injuries in all types of collision when the specified restraints are in use; yet it is recognized that some occupants will neglect to use them. Therefore, every effort is made to also protect unrestrained passengers from injury. Occupants who neglect to use the restraint system will be significantly safer than in cars of conventional construction under similar conditions. Specific interior injury impact areas have been modified for increased safety.

The most severe damage is often produced by impacting into rigid, small-area surfaces

which concentrate impact pressures. Examples include knobs, hard metal edges, gearshift levers, rearview mirrors, and steering wheel hubs. Rigid flat areas do not penetrate the body, but they can generate very rapid deceleration and often cause limb or rib fractures as well as internal damage resulting from a relative internal displacement of organs such as the brain, heart, and viscera. Any reasonably sharp structure will lacerate with even moderate impact force. Very sharp structures such as open glove compartment doors, broken glass, or rearview mirrors will lacerate severely with very mild impact pressures. Based on accident studies, the instrument panel and associated knobs and controls inflict the greatest number of injuries. In the Safety Sedan, the primary display instruments are located along the cowl at the windshield and are flush with the cowl on crushable mountings. All controls are flush mounted on crushable structure and are configured to prevent injury. The controls are located on a small console to the left of the steering column, thus making contact with them by passengers and driver unlikely because of the shielding afforded by the steering wheel.

The "floor-mounted" gearshift lever is countersunk in the transmission hump. Interior lights are placed flush with the surface of interior cushioning and are covered with flexible plastic. Impact injury-producing structures have been removed from the sphere of contact with head, shoulders, and chest of the restrained occupant wherever possible. Where this is not possible, surfaces and structures are designed to minimize injury potential by limiting rigidity to avoid excessive unit pressures on the body.

The steering wheel accounts for a large percentage of driver injuries. It can be dangerous for both the lap-belted as well as the unbelted vehicle occupant. In forward collisions, the steering column may be displaced rearward into the compartment or the passenger may be projected forward against the wheel. For this reason, the Safety Sedan incorporates an energy-absorbing, collapsible steering column. The steering wheel hub is level with the rim to provide a broader area for torso contact. The wheel rim will deform under impact to match the angle of the upper torso. The center hub is 10 in. in diameter and padded to reduce chest injuries. The traditional glove compartment is eliminated, and maps, gloves, and other personal paraphernalia are carried in center compartments placed between both the front and rear seats. The traditional dashboard is replaced by a controlled-energy-absorbing cowl placed 40 in. forward of the eye point, at the base of the windshield. It consists of a yielding backup structure covered by foamed padding.

The front seats form a padded barrier in front of the rear passengers that will not break away under the crash loading by the front passengers, nor under impact loading by the rear passengers. The doors provide the outboard lateral support and cushioning from the shoulder down to the pelvis. They are contoured to provide arm-rest space, and the arm-rest is itself the door-operating handle.

The windshield, as a transparent part of the "strongbox" concept of automobile safety design, is a compromise of conflicting requirements. The Safety Sedan windshield consists of simple curved surfaces (to eliminate visual distortion) well removed from the seated front occupant position. It is made of laminated glass especially formulated to reduce head impact injury for the unrestrained occupant. This laminate consists of thin plies of annealed outer glass and a chemically toughened inner glass with a 0.030-in. thick controlled adhesion polyvinyl-butyral interlayer. According to tests, this glass has less weight and less stiffness — and takes up to three times greater head velocity to fracture — than the recently introduced improved laminated windshield glass used in 1967 vehicles. Other tests indicate that flying glass created by severe impact of this material is of such size and shape as to cause minimal laceration.

The side window area is extensive and requires the use of the best glass characteristics available to minimize ejection of the unrestrained occupant and impact injury from the glass itself. Automobile side impact tests show that, when side windows shatter, some parts of the passenger may be forced outside the car and injured. Use of a proper laminated glass will help prevent such ejection. In the Safety Sedan, the side glass is similar to the windshield, except that thinner plies are used for greater resiliency in occupant impact.

The side windows are flush with the padded interior door frame to reduce the likelihood of occupant-injurious contact with frames and door posts. The interior roof or ceiling area provides added head protection with a uniform 3-in. thickness of energy-absorbent padding under the finished headlining material.

CONCLUSIONS

The Engineering Design and Development phase of the New York State Safety Car Program has, through a systematized study, created an optimized configuration for a safety sedan which

is capable of greatly reducing the severity of injury that an occupant will experience in a collision. The dynamic response of the vehicle structure together with the responses of the integrated seat and restraint systems have been studied and designed to minimize intrusion, control the magnitude and distribution of the loads transmitted to the occupants, and minimize occupant injury caused by vehicle interior impact. The occupant who neglects to use the available restraint system is also protected to a greater extent than in current practice.

New York State has no immediate plans for continuing with the next phase, that of building and testing prototype safety sedans. However, they have presented the designs to the Federal Government for possible development of such a car as part of the nationwide emphasis on traffic safety. The Safety Sedan is an important step forward on the road to greater automotive safety; for whether or not the Safety Sedan is built in its present form, the odds are that its ideas and concepts will effect your car of the future.

REFERENCES

1. "Feasibility Study – New York State Safety Car Program," FHR 3040-3, Fairchild Hiller Republic Aviation Div., 31 Aug. 1966

2. "Phase II Final Report – New York State Safety Car Program," I, FHR 3520-1, Fairchild Hiller Republic Aviation Div., 27 Nov. 1967

3. D. Gardner, "New York's Safety Car," in Health News, New York State Dept. of Health, July 1967

4. "A Study of Seat Belts in Wisconsin Automobile Accidents," CAL Rept. VJ-1823-R3, Cornell Aeron. Lab., Buffalo, N. Y., 9 Sept. 1963. Tables 4 and 7

5. R. R. McHenry, "Research for Better Barriers," Research Trends, Cornell Aeron. Lab., X(3), 1962

6. K. A. Stonex and P. C. Skeels, "Development of Crash Research Techniques at the General Motors Proving Ground," Highway Research Record (4), Highway Research Board, Washington, D. C., 1963

7. "Barrier Collision Tests, "Society of Automotive Engineers' Standard No. J850, 1967

8. B. Tourin, "Ejection and Automobile Fatalities," Public Health Reports, 73(5):381-391, May 1958

9. J. W. Garrett, "The Safety Performance of 1962-63 Door Latches and Comparison with Earlier Latch Designs," Cornell Aeron. Lab. Rept. No. VJ-1823-R7, 1964

10. "Occupant Injury Tabulations," Cornell Aeron. Lab. Rept. No. VJ-1823-R27, Sept. 1967 (advance copy)

11. D. M. Severy et al., "Auto Crash Studies," Univ. of Calif. Rept. No. 59-10, Jan. 1959

12. R. R. McHenry, "Analysis of the Dynamics of Automobile Passenger-Restraint System," 7th Stapp Car Crash Conference Proc., 1965

13. J. K. Kihlberg, "Driver and His Right Front Passenger in Automobile Accidents," Cornell Aeron. Lab. Rept. No. VJ-1823-R16, Nov. 1965

14. B. J. Campbell and T. Hopens, "Automobile Glazing as an Injury Factor in Accidents," Cornell Aeron. Lab. Rept. No. VJ-1625-R-1, Dec. 1964

15. D. M. Severy et al., "Automobile Side-Impact Collisions, Series II," SAE Rept. SP-232, Mar. 1962

16. W. Flügge, Handbook of Engineering Mechanics (McGraw-Hill, New York), 1962, Ch. 49

17. J. A. Seiler and P. S. Symonds, "Plastic Deformation in Beams under Distributed Dynamic Loads," J. Appl. Phys., 25, 556-563 (1954)

18. J. A. Seiler, B. A. Cotter, and P. S. Symonds, "Impulsive Loading of Elastic-plastic Beams," J. Appl. Mech. 23, 515-521 (1956)

DISCUSSION

Mr. Paul (MIT): You put down all these criteria such as 50 mph frontal impact and 40 mph side impact. What degree of damage to the occupant is permitted? Is this keeping him alive, maiming him, or what?

Mr. Davis: The degree of injury is called minor injury. There is absolutely no danger of death. The detailed medical definition of minor injury may be listed in the paper. I do not recall at the moment.

Mr. Meyo (McDonnell Douglas Corp): Do you consider a human response? When you talk about human injury are you considering dynamic models of the head, the neck, and so on? If you do, what kind of springs and damping are postulated and where did you get them?

Mr. Davis: Frankly, the state-of-the-art, particularly in such directions as side impact, does not have such models as you refer to. The basic criterion that we have used to estimate the degree of injury is the allowable g level that human occupant can tolerate. We probably have used very simple dynamic models of the occupants to estimate what the dynamic response of the occupants will be.

Mr. Meyo: Are you saying that you really have a set of in-motion or in-car descriptions of the environment and you sort of let it go at that?

Mr. Davis: No. Some groups, such as Cornell Aeronautical Laboratory, for example, have an 11-degree-of-freedom model of a human in a forward crash impact. The details of the model have taken 3 years to validate finally. I think the basic approach we took was to look at approximately what the deceleration level of a semirigid occupant would be.

Mr. Bynum (Rocketdyne): I think you left out the most important thing. What does this thing cost compared to say the latest model Chevrolet or Ford? How much more would a production version of this car cost?

Mr. Davis: This can can be mass-produced at a cost in the range of the low-priced three. However, I would like to point out that this car is airconditioned. If you are going to compare it with a current car it should, of course, have the same features.

* * *

U.S. GOVERNMENT PRINTING OFFICE 1965 O—838-016